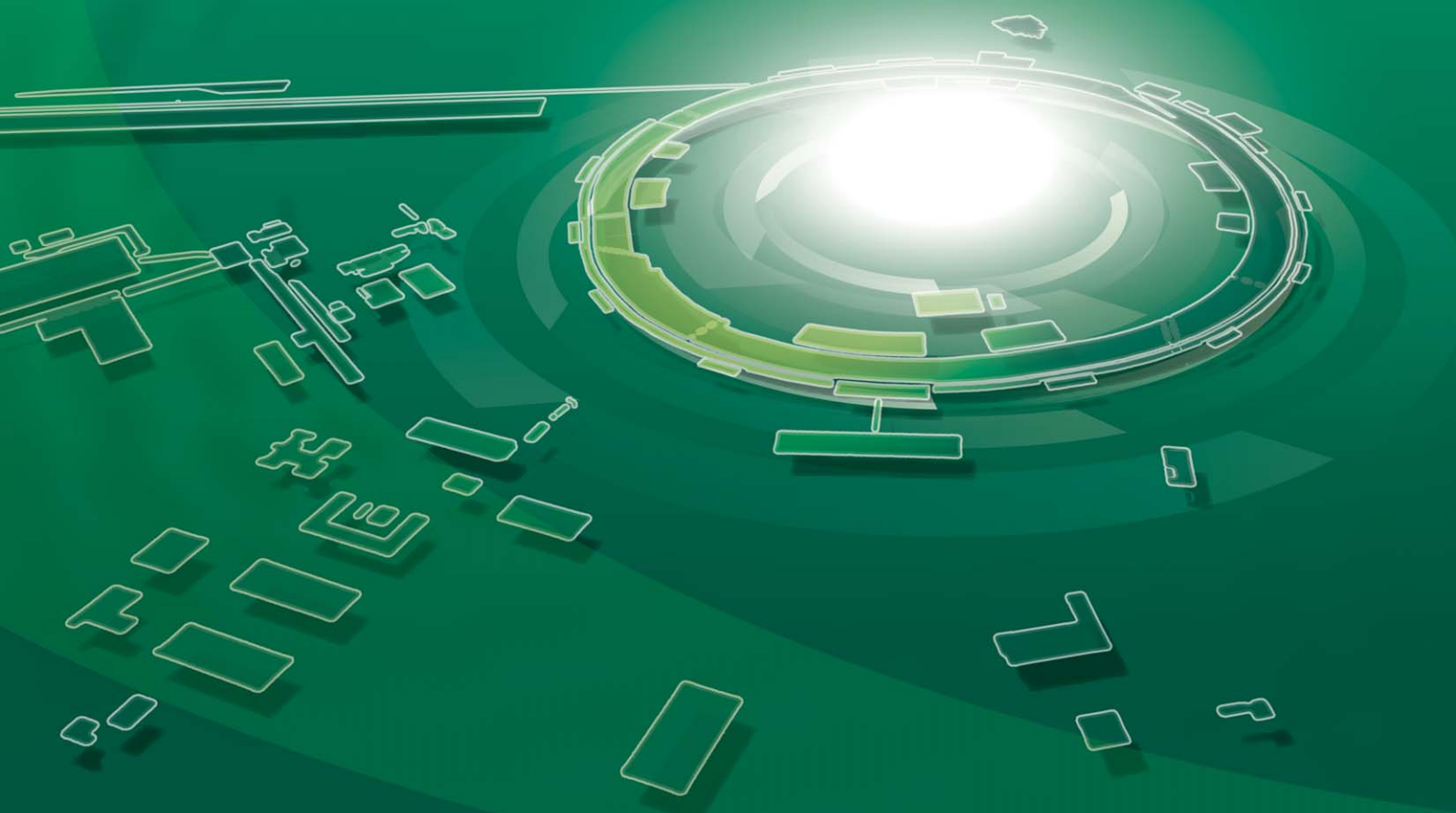
ISSN 1349-0087
SPring-8 Document D2009-005

SPring-8 Research Frontiers



2008

SPring-8
Research Frontiers
2008



CONTENTS
2008

Preface 9

Scientific Frontiers 10

A PLACE IN THE "X-RAY" SUN – Endeavors at Frontiers of Research 11
M. Takata

LIFE SCIENCE: STRUCTURAL BIOLOGY 16

The Structural Basis for an Essential Subunit Interaction in Influenza Virus RNA Polymerase 18
E. Obayashi, H. Yoshida and S.-Y. Park

Crystal Structure of an Active Form of BACE1, an Enzyme Responsible for Amyloid β Protein Production 20
H. Shimizu and N. Nukina

Protein Biotinylation Visualized Using a Complex Structure of Biotin Protein Ligase with a Substrate 22
N. Kunishima and B. Bagautdinov

Crystal Structure of the Oxidative-Stress Sensor SoxR Bound to DNA 24
S. Watanabe and K. Miki

Hypervalent Intermediate in the Oxidation of Archaeal Peroxiredoxin 26
T. Nakamura and T. Inoue

Structural Basis for the Exclusive Specificity of Slac2-a/Melanophilin for the Rab27 GTPases 28
M. Kukimoto-Niino, M. Shirouzu and S. Yokoyama

Structure of Squid Rhodopsin 30
M. Murakami and T. Kouyama

Crystal Structures of LOV1 Domains in *Arabidopsis* Phototropin 1 and 2 32
M. Nakasako and S. Tokutomi

Structural Versatility of a Bacterial Aconitase as Revealed by Small-Angle X-Ray Scattering Analysis 34
D. Tsuchiya

Structure and Function of Stationary Phase-Dependent Regulatory Protein from *Thermus thermophilus* HB8 36
Y. Agari and A. Shinkai

Conformational Changes upon Activation of a Replication Initiator Protein, RepE 38
A. Nakamura and K. Miki

Combined Study of Crystallography and NMR Reveals Structural Basis for a Reversible Switchable Fluorescent Protein 40
A. Kikuchi

LIFE SCIENCE: MEDICAL BIOLOGY 42

Structural Model Construction of the Photointermediate of Photoactive Yellow Protein by High-Angle X-Ray Scattering 44
H. Kamikubo and M. Kataoka

Structural Changes in the Muscle Thin Filament during Contraction Caused by Single and Double Electrical Pulses 46
T. Matsuo and N. Yagi

The Use of Microbeam X-Ray Diffraction for the Characterization of Crystal Structure of Rice Starch 48
A. Kubo, Y. Yuguchi and S. Kitamura

High-Resolution 4D *In Vivo*-CT for Visualization of Cardiovascular and Respiratory Motion of Small Animals 50
T. Sera

Assessment of the Pulmonary Circulation in Health and Disease Using Synchrotron Radiation Microangiography 52
D. O. Schwenke, K. Umetani and M. Shirai

Atherosclerotic Plaque Imaging Using Phase-Contrast X-Ray Computed Tomography 54
M. Shinohara, K. Hirata and A. Momose

MATERIALS SCIENCE: STRUCTURE 56

Time-Resolved Investigation of Nanosecond Crystal Growth in Rapid-Phase-Change Materials for Rewritable Digital Versatile Disc 58
S. Kimura, Y. Tanaka and M. Takata

Towards *In Situ* X-Ray Diffraction Imaging at the Nanometer Scale: Early Detection of Nanoparticle Growth in Light Metal Alloys 60
N. A. Zatsepin, A. Y. Nikulin, R. A. Dilanian and O. Sakata

In Situ X-Ray Diffraction Measurement of Hydrogenation and Dehydrogenation of Aluminum at High Pressure and Temperature 62
H. Saitoh and K. Aoki

Direct Observation of Motion in an Atom Cage 64
S. Tsutsui, H. Kobayashi and A. Q. R. Baron

Giant Negative Thermal Expansion in Magnetic Nanocrystals 66
X. G. Zheng

Recent Findings on Metal Nanoparticles as New-Type Hydrogen-Storage Materials 68
H. Kobayashi, M. Yamauchi, H. Kitagawa and M. Takata

Rational Design of Iron Oxides with Square Planar Coordination 70
H. Kageyama

Helical X-Rays Probe Crystal Chirality 72
Y. Tanaka, A. Chainani and S. Shin

MATERIALS SCIENCE: ELECTRONIC & MAGNETIC PROPERTIES 74

Resolving Subsurface Magnetism at Atomic Scale by "Diffraction Spectroscopy" 76
F. Matsui, T. Matsushita and H. Daimon

Magnetic Ordering and Fluctuation in One-dimensional Fe Nanowires 78
S. Shiraki

Nature of Magnetic Coupling between Mn Ions in As-Grown $Ga_{1-x}Mn_xAs$ – Systematic Temperature and Magnetic Field Dependent XMCD – 80
Y. Takeda

SR-PES and STM Observation of Metastable Chemisorption State of Oxygen on Si(110)-16×2 Surface 82
M. Suemitsu

Recoil Effect of Photoelectron in the Fermi-Edge of Simple Metals 84
Y. Takata and Y. Kayanuma

Detection of the Valence Band in Buried Co_2MnSi-MgO Tunnel Junctions by Means of Hard X-Ray Photoemission Spectroscopy 86
G. H. Fecher, C. Felser and K. Kobayashi

Experimental Magnetic Form Factors in $Co_3V_2O_8$: A Combined Study of *Ab Initio* Calculations, Polarized Neutron Diffraction and Magnetic Compton Scattering 88
N. Qureshi, M. Zbiri and Y. Sakurai

Phonons in the New Iron-Based High-Temperature Superconductors 90
T. Fukuda and A. Q. R. Baron

Pressure-Induced Valence Anomaly in TmTe Probed by Resonant X-Ray Emission Spectroscopy 92
I. Jarrige, J. P. Rueff and Y. Q. Cai

Infrared Magneto-Optical Imaging on Phase Separation of Solids 94
S. Kimura

Infrared Optical Probe of Carrier Doping by X-Ray Irradiation in Organic Dimer Mott Insulator κ-$(BEDT\text{-}TTF)_2Cu[N(CN)_2]Cl$ 96
T. Sasaki

CHEMICAL SCIENCE 98

Liquid Structure of Water: Observation of Two Structural Motifs 100
T. Tokushima, Y. Harada and S. Shin

Orientational Correlations in High-Pressure Fluid Oxygen and Nitrogen 102
L. Temleitner, L. Pusztai, Y. Akahama and S. Kohara

Crystal Structures of the Odd and Even Electron One-Dimensional Metal-Metal Bonded Chain Compounds 104
M. Mitsumi, Y. Ozawa and K. Toriumi

Structural Collapse of Fluorohydrogenate Anions in Molten $Cs(FH)_{2.3}F$ Detected by High-Energy X-Ray and Neutron Diffraction Studies Combined with RMC Calculation 106
R. Hagiwara, K. Matsumoto and S. Kohara

NifB-co, a Key FeMo-co Precursor, is a Fe_6S_9 Core with an Interstitial Light Atom 108
Y. Guo, S. J. George, L. M. Rubio and S. P. Cramer

Grasping Carbon — Bonding Nature of Penta- and Hexacoordinated Carbon by Experimental Electron Density Distribution Analysis 110
D. Hashizume

Selective Chemical Bond Breaking Induced by Resonant Inner-Shell Excitation of Acetone Molecule on the Ar Clusters 112
Y. Tamenori

A Molecular Knife – Control of Chemical Reactions Using Core Ionization – 114
S. Nagaoka, G. Prümper and K. Ueda

Ab Initio Structure Determination of Medium-Sized Pharmaceuticals 116
E. Nishibori, S. Aoyagi and M. Sakata

EARTH & PLANETARY SCIENCE 118

Chondrules in the Short-Period Comet 81P/Wild 2 120
T. Nakamura and A. Tsuchiyama

Composition of the Mantle Transition Region Constrained by Sound Velocity Measurements at High Pressure and Temperature 122
T. Irifune and Y. Higo

The Electrical Conductivity of Post-Perovskite in Earth's D" Layer 124
K. Hirose, K. Ohta and K. Shimizu

Melting Experiments on Fe_3C and FeH_x under High Pressures 126
Y. Nakajima, K. Sakamaki and E Takahashi

Oxygen *K*-edge X-Ray Raman Scattering Study of $MgSiO_3$ Glass at High Pressure 128
S. K. Lee

ENVIRONMENTAL SCIENCE 130

Micro-X-Ray Fluorescence Imaging and Micro-X-Ray Absorption Spectroscopy of Cadmium Hyperaccumulating Plant, *Arabidopsis halleri* ssp. *gemmifera*, Using High-Energy Synchrotron Radiation 132
A. Hokura, N. Kitajima, Y. Terada and I. Nakai

Origin of Difference in Solubility between Tellurium and Selenium into Water at Earth's Surface 134
Y. Takahashi

Snapshots of Metal Nanoparticles Generated on TiO_2 Photocatalyst: *In situ* Time-Resolved Energy-Dispersive X-Ray Absorption Fine Structure Analysis 136
K. Teramura and T. Tanaka

XAFS Study of Tungsten L_1-, L_3-Edges: Structural Analysis of Loaded Tungsten Oxide Species 138
S. Yamazoe, T. Shishido and T. Tanaka

Industrial Applications 140

Energy Band Bending Profile of Ultra-Shallow Junction in Silicon Studied by Hard X-Ray Photoelectron Spectroscopy 142
M. Yoshiki

Chemical Analyses of Heavily Doped Boron in Silicon-Based Shallow Junctions by Soft X-Ray Photoelectron Spectroscopy 144
K. Tsutsui, H. Iwai and T. Hattori

Excellent Crystallinity of Truly Bulk Ammonothermal GaN 146
R. Dwiliński, M. Zając and Y. Kanbara

Analysis of Electronic and Crystal Structures of Graphene Multi-layers by Hard X-Ray Photoelectron Spectroscopy and Grazing Incidence X-Ray Diffraction 148
D. Kondo, S. Sato, M. Nihei and Y. Awano

Effects of Ion Implantation in Fabrication of Bit Patterned Media by Micro-XMCD Measurement 150
Y. Kondo, J. Ariake and M. Suzuki

X-Ray Nanospectroscopic Characterization of Single Molecular Ferromagnetic $Ti_{1-x}Co_xO_2$ Nanosheet 152
K. Ono

Development of Hydrogen Storage Materials by Crystal Structure Analysis of Light Element Hydrides 154
T. Noritake, S. Towata and S. Orimo

Imaging of Damaged and Undamaged Hairs Using X-Ray Microtomography 156
K. Takehara, T. Inoue and K. Uesugi

X-Ray Diffraction Analysis of Intercellular Lipid Structure in Human Stratum Corneum Collected by Less Invasive Method 158
N. Kunizawa and I. Hatta

Instrumentation & Methodology 160

Precise Determination of Elastic Constants by Inelastic X-Ray Scattering 162
H. Fukui and A. Q.R. Baron

Construction and Development of Time-Resolved XMCD-PEEM System using Femtosecond Laser Pulse at BL25SU 164
K. Fukumoto

Is Lifetime-Broadening Free X-Ray Absorption Spectroscopy Really Feasible? 166
Y. Hikosaka and E. Shigemasa

NUCLEAR PHYSICS 168

First Production of the Σ^* Nucleon Resonance using the LEPS Spectrometer 170
K. Hicks

Photoproduction of $\Lambda(1405)$ and $\Sigma^0(1385)$ on the Proton at $E_\gamma = 1.5$–2.4 GeV 172
M. Niiyama

Accelerators & Beamlines Frontiers 174

Beam Performance 175
Developments and Upgrades of Storage Ring 175
Developments and Upgrades of Linac 185

Controls & Computing 188
Development of Flexible and Logic-Reconfigurable VME Boards 188

New Apparatus & Upgrades 190
Upgrade at Hyogo Prefectural Beamline BL24XU 190
Upgrade of the SAXS Apparatus at BL40B2 191
Stabilization of Double-Crystal Monochromator at BL41XU 192
Upgrade of Engineering Science Research III, BL46XU 194

Facility Status 196

Introduction 197
Machine Operation 198
Beamlines 199
User Program and Statistics 203
Budget and Personnel 207
Research Complex 208
Users Societies, Conferences and Other Activities 210

Project XFEL 212

Progress of the XFEL Project 213

NewSUBARU 220

Construction of a High-Resolution Beamline BL-5 for Soft X-Ray Spectroscopic Analysis on Industrial Materials 221

Note: The principal publication(s) concerning each article is indicated with all author's names in italics in the list of references.

Editor's Note

SPring-8 Research Frontiers 2008 covers advances achieved during two consecutive research periods, the second half of 2007 and the first half of 2008. SPring-8 Research Frontiers describes the remarkable scientific achievements obtained at the SPring-8 in various fields of basic and applied science including industrial applications, as well as the development of accelerators, beamlines and experimental apparatus and the present status of the SPring-8 facility. The progress of the XFEL project at SPring-8 toward completion in FY 2010 is also reported. In addition, activities using the NewSUBARU, which forms an integral part of the research complex at the SPring-8 campus, are introduced.

Five new beamlines are currently in operation or under construction, two of which use long straight sections. We are expecting that many excellent results will be produced owing to the characteristics of these beamlines.

This is the eleventh issue of SPring-8 Research Frontiers. Since we make it a practice to change the cover design every five years, the cover design has been changed for this issue. The coming five years will mark a mature phase in the development of the SPring-8.

Copies of SPring-8 Research Frontiers will be sent on request. Its full text is also available on the SPring-8 website (http://www.spring8.or.jp/). For the list of publications produced by the SPring-8 users and staff, please visit the publications database at https://user.spring8.or.jp/en/pubsch.

We extend our appreciation to the many specialists who have recommended excellent research results suitable for publication in SPring-8 Research Frontiers. We would also like to express our sincere gratitude to the users and staff of the SPring-8 for contributing their reports to this issue.

Editorial Board

Seishi KIKUTA (Editor in Chief)	SPring-8 / JASRI
Katsutoshi AOKI	SPring-8 / JAEA
Shunji GOTO	SPring-8 / JASRI
Tetsuya ISHIKAWA	SPring-8 / RIKEN·JASRI
Toyohiko KINOSHITA	SPring-8 / JASRI
Takashi KUMASAKA	SPring-8 / JASRI
Yasuo OHISHI	SPring-8 / JASRI
Haruo OHKUMA	SPring-8 / JASRI
Yoshitsugu SHIRO	SPring-8 / RIKEN
Masayo SUZUKI	SPring-8 / JASRI
Masaki TAKATA	SPring-8 / RIKEN·JASRI
Tomoya URUGA	SPring-8 / JASRI
Yoshio WATANABE	SPring-8 / JASRI
Naoto YAGI	SPring-8 / JASRI
Marcia M.OBUTI-DATÉ (Secretariat)	SPring-8 / JASRI

Preface

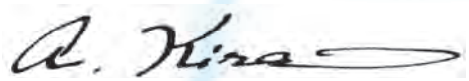


SPring-8 held an international peer review meeting called SPARC (SPring-8 Academic Research Council) in November 2008. This was the first peer review of the achievement of SPring-8: in the past reviews, the achievements were reviewed as one of the materials for the reviewing administration and operation. The report of SPARC is open on a SPring-8 web site.

I asked SPARC to select the best ten results in 10 years since inauguration and also to give us suggestions how to explain them to the public. Nowadays, the accountability to the public is as important as the reputation among scientists. We have published the SPring-8 Research Frontiers, which demonstrates the growth of the achievement in both quantity and quality. I believe that the Research Frontiers is appreciated by the science community but I am afraid that its contents are still too difficult for the public to understand.

The industrial utilization of SPring-8 has recently established good reputation in the public. The booklet which very compactly introduces the successful applications is favorably accepted by the public society including the Government and industries. We are now planning publication of an academic version for the public on the basis of the SPARC's selection.

Plans of construction of the X-ray free electron laser and relevant innovation of the present storage ring are being provided for a coming decade. I am sure that SPring-8 has enough potential to materialize these plans. But we should be keenly aware that the plans would gain the financial support if the present results as well as the future plans of utilization can convince not only the academia but also the public.



Akira Kira
Director General
SPring-8/JASRI



Scientific Frontiers



1. Watching DVDs in Real Time

Digital versatile discs (DVDs) are one of the most convenient ways of storing large amounts of information. However, despite two decades of development since the discovery of the materials on which they are based, details of how they work remain unclear. Researchers from RIKEN SPring-8 Center, JASRI, CREST and Matsushita Electric Industrial are filling the gaps in our understanding of these materials, using state-of-the-art time-resolved X-ray diffraction analysis to observe the change in the atomic level structure of these materials.

This is a report on the first successful outcome of time-resolved pump and probe X-ray diffraction in SPring-8 by the pilot project "*X-ray pinpoint structural measurement*" organized by Japan Science and Technology Agency (JST) as the Core Research for Evolutional Science and Technology (CREST) started since 2004 and to be completed by 2009. The *X-ray pinpoint structural measurement* system is developed at the BL40XU high flux beamline (Fig. 1). The aim of the project is to achieve a picosecond time-resolved X-ray diffraction experiment using a submicron-scale beam. This is why the project is called "pinpoint." The aimed specifications of the X-ray pinpoint structural measurement are ~100 nm spatial resolution and ~40 ps time resolution. Specialists in the field of accelerator science, laser physics, X-ray optics, diffraction physics, crystallography and chemistry are part of this project (Fig. 2).

The research group has combined high-speed X-ray diffraction with *in situ* time-resolved laser reflectometry to simultaneously probe the structural and optical properties of two different DVD materials, $Ge_2Sb_2Te_5$ (GST) and $Ag_{3.5}In_{3.8}Sb_{75.0}Te_{17.7}$ (AIST). This has enabled them to track microscopic processes that occur in these materials, in real-time, as they change from an amorphous state to a crystalline state. They found a gradual increase in both the reflectivity and emergence of diffraction peaks corresponding to the crystalline phase, proving the close relationship between the optical properties and structures of the materials. The differences in the widths of the diffraction peaks between the two materials and their evolution over time led the researchers to propose two subtly different models of the mechanisms taking place in each. In GST, they suggested that large crystal grains form over the entire volume of the material when the moment the process starts; however, in AIST, the process begins with the formation of small crystallites in different parts of the material, which gradually grow and merge to form

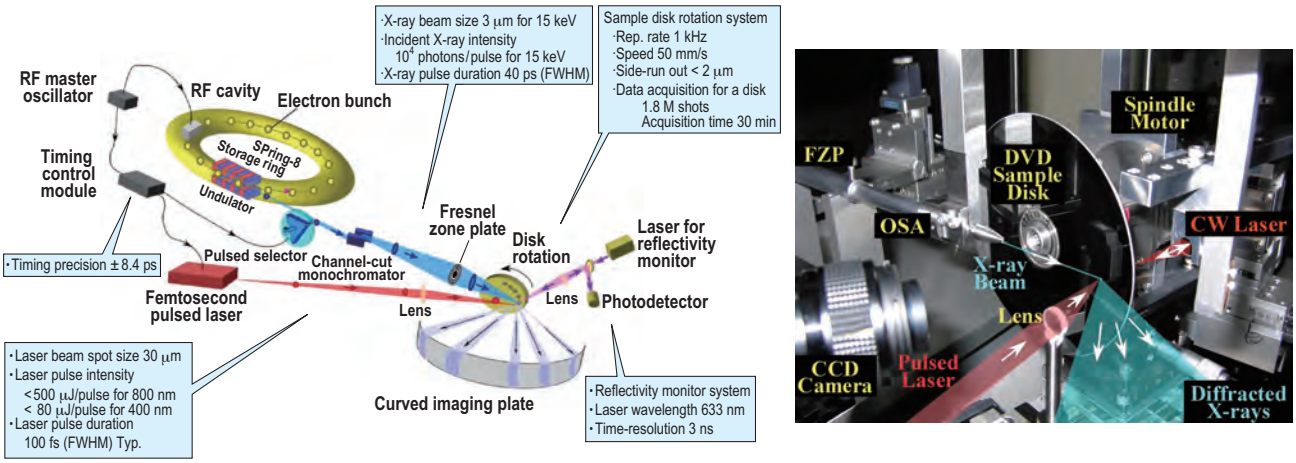


Fig. 1. Schematic representation and photograph of *X-ray pinpoint structural measurement system.*

larger grains. The level of detail enabled by this and future studies is likely to make a valuable contribution to the development of better and faster DVD materials.

The X-ray pinpoint structural measurement system is now close to completion in SPring-8. The system, which is an integration of a time-resolved experiment and a sub-micron beam technique, will be applied after its completion to the study of various phenomena such as photo-induced phenomena, and structural changes under applied AC electric field.

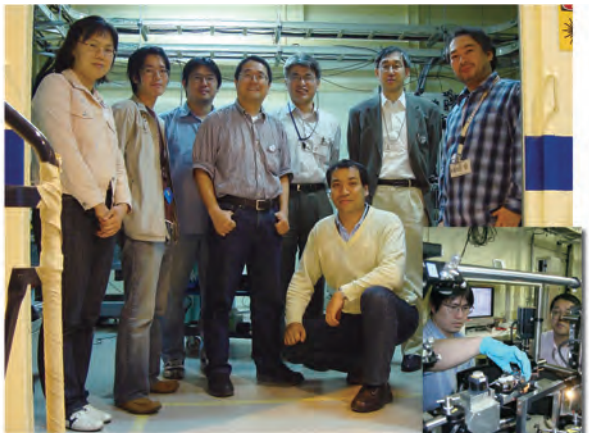


Fig. 2. Members of *X-ray pinpoint structural measurement project.*

2. Capturing a Heartbeat Motion

Internal motions such as heartbeat, and the pulsation of blood vessels, are inherent in all living creatures. In a hospital, we are told to hold our breath when chest X-ray or CT images are taken to avoid motion blur. However, it is impossible to control heartbeat. A research team composed of researchers from RIKEN, Kawasaki University of Medical Welfare and JASRI has designed and constructed a high-resolution, computed tomography (CT) system that can sharply visualize the motion and deformation of the heart, coronary arteries and small airways of live mice and rats, which are most often used as animal models of human diseases.

Mice and rats have heart and respiration rates higher than 300 and 100 per minute, respectively, making internal motions very fast. Since these animals are smaller than humans, the required spatial resolution is higher, making motion blur a more serious problem.

The RIKEN team solved this problem by controlling respiration with a ventilator and monitoring heartbeat using an electrocardiogram. Using a fast X-ray shutter, images were recorded only when the respiration and heartbeat were in their certain prescribed phases. By rotating the animal in the X-ray beam and collecting images, the team was able to accumulate data for the 3D reconstruction of the chest. For more details on this topic, see page 50 of this issue.

Figure 3 shows a comparison of the reconstructed cross sections of a mouse chest. The resolution is 12 μm per pixel. The left image (A) is without synchronization, showing severe blurring. The center image (B) is with only respiration synchronization, showing blurring of the heart. The right image (C) is with respiratory and cardiac

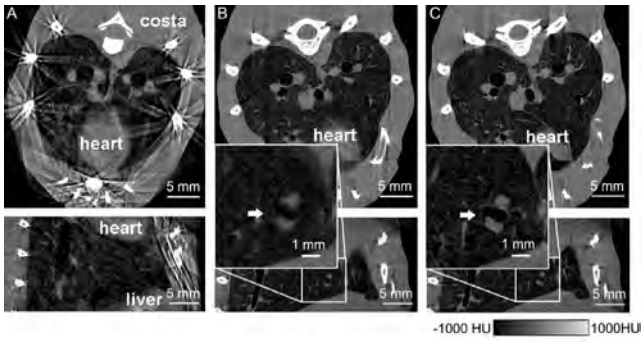


Fig. 3. Reconstructed cross-sections of mouse chest by high-resolution computed tomography (CT).

synchronizations. The blurring is much reduced and the bronchi and the heart are clearly visualized. Using this technique, they constructed sharp images of the lung after inspiration and expiration, and also those of the heart in systole and diastole.

This technique opens a way to high resolution imaging studies of live animals. The high-resolution dynamic structures of the lung and heart will help in our understanding of the function of these vital organs, especially by providing an experimental basis for the simulation of gas exchange in small airways and of shear stress in blood vessels using a supercomputer.

3. Coming Powerful Light

SPring-8 will soon start building a new beamline for inelastic X-ray scattering, i.e., the Quantum Nano Dynamics Beamline BL43LXU, which has been funded by MEXT through RIKEN. The new beamline will provide unprecedented flux using a short-period, small-gap undulator installed in one of SPring-8's 30-m straight sections. By operating in the fundamental to maximize the ratio of flux to power load, such a flux will be the world's most brilliant X-ray source in the 15 to 25 keV energy range, and provide the highest flux, as shown in Fig. 4.

Associate chief scientist Alfred Baron has been considering this project for more than 4 years and has a numerous discussions with scientists about the scientific goals for such a beamline - the members of the workshop in 2008 are shown (Fig. 5). The beamline's scientific target, i.e., inelastic X-ray scattering with energy resolutions from <1 to >40 meV covers some of the most challenging experimental regimes today: the high-resolution (1 to 3 meV) setup is aimed primarily at atomic dynamics in crystals and disordered materials, and the “medium-resolution” (6 to 40 meV) setup at nonresonant measurements of charge dynamics. This

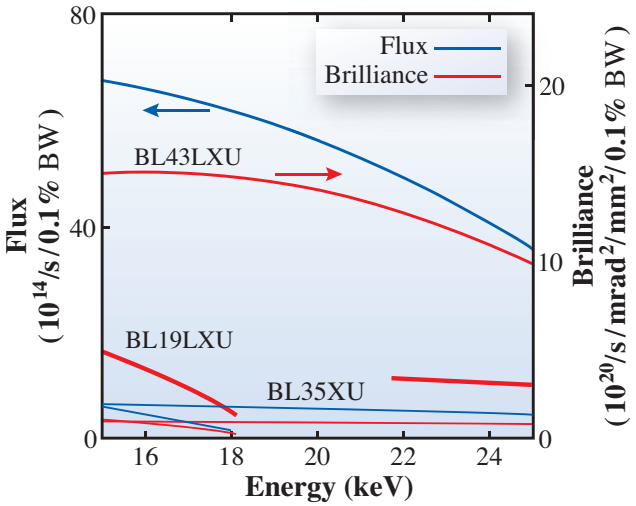


Fig. 4. Comparison of the flux and brilliance available from a standard insertion device (32 mm period by 4.5 m long) at BL35XU and the one planned for BL43LXU (19.4 mm period, 17.6 m). The brilliance of BL19LXU (32 mm period, 25 m) is included for reference.

is expected to provide a unique window on processes in many different types of material, and in different potentially extreme conditions. One area of application, for example, will be in the new iron-arsenic superconductors discovered by Hosono's group. With superconducting transition temperatures that are only exceeded by those of some copper oxides, this new class of high-temperature superconductors shows a complex electronic structure, magnetic order, and an extremely strong magneto-elastic coupling. The twin windows of meV resolution for investigating atomic dynamics and of ~40 meV resolution for investigating electronic dynamics are expected to lead to new results - in addition to the investigation of magneto-elastic interaction, for example, direct investigation of superconducting gap may be possible.



Fig. 5. Workshop for new beamline “Quantum Nano Dynamics Beamline.”

4. Heading to Next Goal: Sunbeam Consortium

In the last decade, the Sunbeam Consortium (Industrial Consortium for Beamline Construction and Applications) has contributed to new technology developments as the front runner in industrial utilization with the Industrial Consortium Beamline (BL16XU/B2). The Sunbeam Consortium is a private organization consisting of 13 companies (12 companies and 1 electric group): Kawasaki Heavy Industries, Ltd., Kobe Steel, Ltd., Sumitomo Electric Industries, Ltd., Sony Corp., Electric power group (Kansai Electric Power Co., Inc., Central Research Institute of Electric Power Industry), Toshiba Corp., Toyota Central R&D Labs., Inc., Nichia Corp., NEC Corp., Hitachi, Ltd., Fujitsu Laboratories Ltd., Panasonic Corp. and Mitsubishi Electric Corp.

The SPring-8 research of the Sunbeam Consortium has successfully been applied to the development and improvement of manufacturing processes for various types of product such as advanced semiconductor devices, high-density magnetic disks, laser diodes, optical fibers, high-corrosion-resistance steel, automotive catalysts and fuel batteries.

On the basis of the activities over the past 10 years and the next-term research plans, the Sunbeam Consortium renewed their contract with JASRI, who is in charge of SPring-8 operation, for the continuous installation and operation of the Industrial Consortium Beamline for the next 10 years starting from August 27th, 2008.

For the next term, a large-scale capital investment of approximately 320 million yen was made to renew the experimental equipment (Fig. 6). The main upgrades achieved are as follows:

(i) *X-ray diffractometer and scattering measurement system*

The system increased the number of movable axes of the sample stage from 4 to 8. This improvement can provide high measurement flexibility and reduce measurement time to half. The new large sample stage allows the mounting of a large wafer up to 300 mm diameter and the measurement of the entire product, instead of a test piece or a cut-out sample.

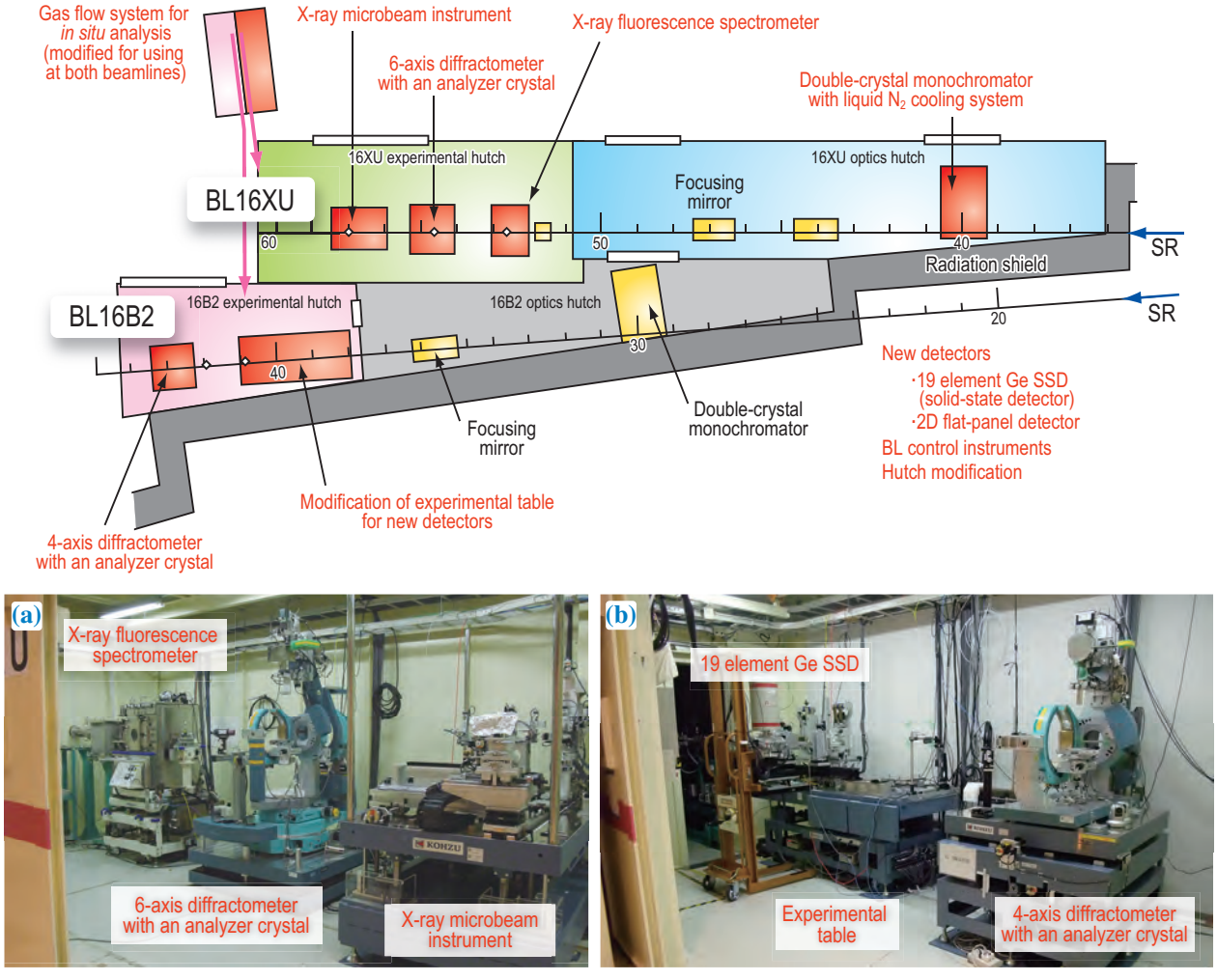


Fig. 6. Beamline diagram and photograph of the Industrial Consortium Beamline **(a)** BL16XU and **(b)** BL16B2. Upgraded parts of experimental equipment are indicated in red.

Consequently, the structure and interface structural analysis of a 1-nm silicon oxide layer on a 300-mm-diameter wafer used in the production line has been accomplished; it is the world's highest precision measurement. This achievement is also made possible by significant progress in the dynamic range of measureable data up to 12 orders of X-ray intensity magnitude from 10 orders of magnitude for the X-ray reflectivity measurement.

(ii) *X-ray fluorescence measurement system*

The element analysis is available even for ultra-dilute samples. The element mapping area also increased to be applicable to 200-mm-diameter wafers with 10 μm resolution. Chemical state analysis is also available as well as composition analysis with XAFS measurement. High-performance equipment will provide a solution to the various types of problem concerning devices, and contribute to the development of novel sustainable materials and commercial products such as hexavalent-chromium-free plating.

(iii) *Microbeam technique*

The function of X-ray diffraction analysis is related to the focused beam whose diameter is less than 300 nm. X-ray intensity increases over one order of magnitude at the sample position. This technique enables microstructure analysis, such as designing a micro-magnetic head for high capacity, analyzing head materials, and improving the fabrication process.

Full operation was restarted from the second half of the fiscal year 2008. The utilization of the new facilities and equipment will allow previously unattainable level of analyses and observations, such as ultrathin-film and sub-micrometer analysis, real-time observation and direct observation of commercial products.

6. Finding a Way to Overcome Diseases

From the beginning of modern drug discovery, any new drug is the result of complex efforts includes many steps such as assays, clinical trials and among others. Even today, drug development takes years, and the costs for screening and safety testing are very high and rising. Discovering drugs targeting infectious diseases has the added complication that a single mutation of the target virus or microbes may render the drug ineffective. Therefore, rapid drug discovery is even more important in this case; moreover, such drugs should target some essential biological process to limit survival of the pathogen.

Structure determination of drug-target proteins has long been recognized to assist drug discovery, because knowledge of the protein structure helps build drugs which fit into it and bind tightly. Recent developments in structural biology, including the improvement of synchrotron beamlines, have greatly accelerated the pace of protein structure determination, and enabled structural genomics groups to solve drug-target proteins very rapidly. Although the number of the results are not so much more but several important drugs has been developed.

For example, the influenza drugs zanamivir (Relenza) or oseltamivir (Tamiflu) target the viral neuraminidase, which is an essential protein for release of the virus from host cells. Unfortunately, influenza can develop resistance to these drugs, and new ones are urgently required to treat such resistant strains.

In 2008, Prof. Park and his group from Yokohama City University have determined the structure of a piece of the influenza RNA polymerase. This family of enzymes is essential to all biological species, being required to utilize genetic information stored in DNA. However, the influenza enzyme is assembled from three polypeptide chains unique to the virus, and disruption of its assembly blocks replication of the virus inside host cells. Two subunits, called PA and PB1, bind together through part of their structure to form a complex, which is necessary for the RNA polymerase to function. The structure of this complex revealed the interaction between subunits, and this structure is being used to guide new drug development (Fig. 7). Detail in this topic can be found in Park *et al.*'s report in this issue on page 18.

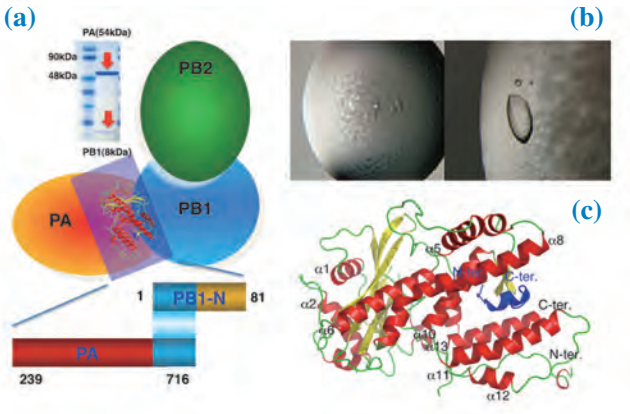


Fig. 7. Influenza RNA polymerase complex. **(a)** Schematic diagram of PA, PB1 and PB2 subunits of the influenza RNA polymerase. **(b)** Crystals of the complex. **(c)** An overall ribbon diagram showing the fold of PA, with helices in red, strands in yellow and coil in green. Helices are numbered from the N terminus. PB1 residues are in dark blue.

Masaki Takata

Life Science:



The finest X-ray beam produced from a synchrotron source is a powerful tool for protein crystallography, which reveals profound knowledge and details of structure-function relationship for extensive biological macromolecules. For adaptation to various experimental needs and requests, SPring-8 structural biology beamlines are continuously developed. Here, we present some selected reports from many fruitful results obtained this year.

One of the major expected contributions of structural analyses is the investigation of the mechanisms of diseases and biological responses to pathogeny or stress leading to the development of cure and prevention for health benefits. The structure of influenza RNA polymerase revealed the relationship between its assembly and function. Increasing dementia caused by Alzheimer's disease is a difficult problem not only for patients and caregivers but also for societies in aging populations. One of its major pathogenesis is the accumulation of an insoluble degraded protein produced by β-secretase and BACE1. The crystal structures of active and inactive forms of BACE1 reveal conformational changes during its catalytic reaction. As another marked health problem, metabolic syndrome associate with lifestyle-related diseases increases the risk for diabetes, thus its therapy is expected. Excessive nutrients are converted and stored as fatty acids. Biotin protein ligase is a key component in fatty acid synthesis and its structure reveals the activation mechanism of the synthetic pathway. These structures might be used for novel drug design.

Structural Biology

Stress is quite common and a serious problem for living organisms. Excessive oxidation and UV radiation cause severe damage to proteins and nucleotides by chemical reaction. SoxR is a transcription factor sensing oxidative stress by its own iron-sulfur cluster. Its structure reveals that the oxidative state of the metal cluster causes structural changes to adopt DNA binding and the promotion of transcription of antioxidant enzymes. An antioxidant enzyme, peroxiredoxin, showed the novel structure of its hypervalent sulfur compound in multiple oxidation states. Such structural and functional analyses of the ancestral protein from an archaeal bacterium might reveal biological evolution in stress resistance. Melanosome is a melanin vesicle, and its maturation and storage are essential for photoprotection. The X-ray analysis of Rab27-Slac2 responsible for melanosome transport reveals the structural basis of the specific interaction between them, and might be used for drug development for Griscelli syndrome caused by transport failure.

On the other hand, structural analysis of macromolecules is also opening the profound secret of life. One key mechanism of life is signal transduction, which is essential for survival because living things must respond to environmental signal or stimulus. The signal transduction pathway starts with sensors and the signal reaches regulators via messengers. Many of the sensors located in the cell membrane receive extracellular signals and transmit the signal to intracellular messenger. G-protein coupled receptors (GPCRs) are the largest family of such proteins, and thus, are considered as the most important drug targets. Rhodopsin is the largest subgroup of GPCR receiving light photons at the retina covering the back wall of the eye. The detailed analysis of squid rhodopsin elucidates its photoactivation mechanism. Plants have no eyes but sense light for controlling development such as flowering and the growth of shoot and root. Phototropin contains a chromophore, flavin, sensing blue light and induces structural changes leading to the transmission of the signal to downstream messengers. Its structure provides clues to the signaling mechanism.

To transfer the sensed signal to messengers and regulators correctly, the molecular interaction between the components is quite essential. The analysis of the interaction by crystallography is limited because of its weak, instant and dynamic features. Small-angle X-ray scattering is an effective tool to investigate such a weak protein-protein interaction and used to reveal structural variety and flexibility in a couple of molecules, aconitase and isocitrate dehydrogenase, in a carbon metabolic pathway.

The signal that reachs transcription factors affects the expression of gene information stored in DNA. Gene expression is mediated by the activation of transcription factors and their interaction with DNA. The structural analysis of SdrP showed its similarity with a well-known transcription factor, CRP, but also the novel features of the protein. In the mechanism of DNA replication, the structure of a key protein RepE working as both a repressor and a replication initiator is determined. Observed structural changes clarify its functions and further analysis might reveal the structural relationship with signaling from DnaK system.

As a scientific topic this year, Prof. Shimomura was awarded the Nobel Prize in Chemistry for the discovery of green fluorescent protein (GFP). This is widely used as a reporter of expression and there are many variants developed. One of the variants, Dronpa, was analyzed in terms of its structure and mechanism of photochromism. This might accelerate further developments of the reporter gene.

Yoshitsugu Shiro and Takashi Kumasaka

The Structural Basis for an Essential Subunit Interaction in Influenza Virus RNA Polymerase

Influenza kills more than 250,000 people worldwide every year on average, and estimates of the death toll in the 1918 pandemic range up to 50 million people worldwide [1]. Recent outbreaks of highly pathogenic avian influenza in Asia have rapidly spread across continents, and present vaccines and medication seem unlikely to alleviate greatly any epidemic or pandemic should these viral strains adapt to human hosts [2]. To prepare for such predictable next pandemic produced by mutated highly pathogenic virus like avian one, billions of dollars worth of oseltamivir, which is influenza neuraminidase (NA) inhibitor, were stockpiled, but resistant influenza is already emerging. Another useful anti-influenza drug amantadine targets the M2 protein, however a single residue change is sufficient to confer resistance, which has accordingly risen sufficiently to render the drug useless against many strains. There is therefore ample scope to develop new lead molecules disrupting other processes in the viral life cycle.

The viral RNA-polymerase is not yet a target of any approved pharmaceutical, but has recently become a focus for the development of new anti-influenza drugs since it is highly conserved in strains of avian and human influenza [3]. It carries out a number of essential processes in the viral life cycle, but many of these and their regulation remain poorly understood [4]. The three subunits, PB1, PB2 and PA play different roles within the polymerase, and are all essential for viral replication, but despite considerable functional analysis relatively little is known about their structure (Fig. 1). Here, we have solved the crystal structure of a complex formed by N-terminal fragments of PB1 and C-terminal domain of PA at 2.3 Å using **BL41XU** beamline [5].

PA C-terminal domain consists of 13 α helices and 9 β strands and three α helices, α10, α11 and α13, are positioned like the jaws of a clamp, grasping the N terminus of PB1 with the support of a β-hairpin loop made by β8 and β9 (Fig. 2(a)). The interaction region at PB1 lays from 1 to 15 which are visible in the electron density map, whether the rest of peptide of PB1 (16-81) is disordered. PB1 interacts with PA through an array of hydrogen bonds and hydrophobic contacts. Most inter-subunit hydrogen bonds form through main chain atoms of PB1. Residues *Asp 2* to *Asn 4* form anti-parallel β-sheet like interactions with Ile 621 to Glu 623 of PA (Fig. 2(b)). Hydrophobic interactions appear to contribute substantially to the binding energy. *Pro 5* packs between Ile 621 and Trp 706, and *Leu 8* makes contact with the side chains of Met 595, Trp 619, Val 636 and Leu 640 (Fig. 2(c)). Using this model, we designed deletions and point mutations in the C-terminal domain of PA which greatly weaken or abolish PB1 binding, and similarly reduce viral RNA synthesis in human cells (Fig. 3(a) and 3(b)). The levels of vRNA, cRNA, and viral mRNA synthesis were markedly lowered for all the mutants [5]. Further, influenza RNA polymerase shows a high level of sequence conservation across strains, since

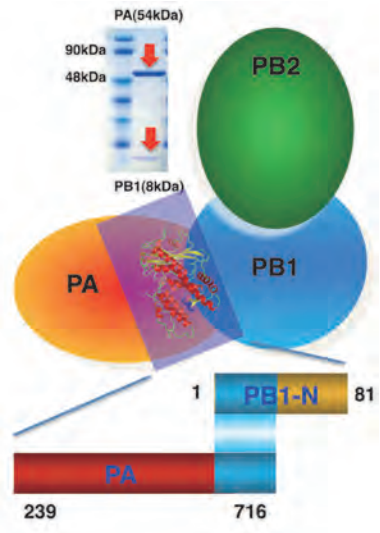


Fig. 1. Schematic diagram of PA, PB1 and PB2 subunits of the influenza RNA polymerase. PB1 binds to C-terminal domain of PA at N-terminus and to N-terminal of PB2 at C-terminus. Purified PA-PB1 complex in this study is analyzed by SDS-PAGE.

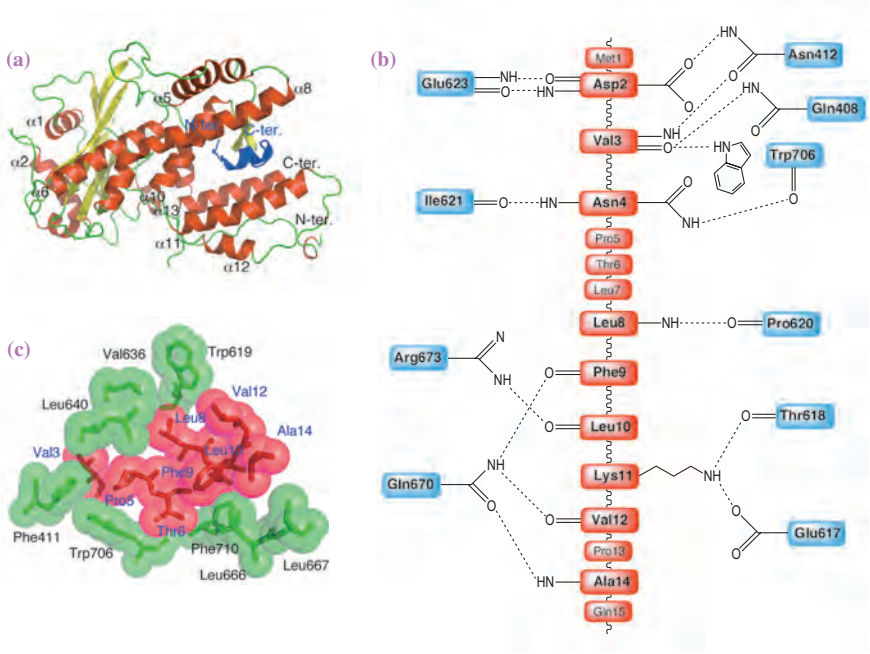


Fig. 2. Crystal structure of the C terminal domain of PA bound to the N terminal peptide of PB1. **(a)** An overall ribbon diagram showing the fold of PA, with helices colored red, strands yellow and coil green. Helices are numbered from the N terminus. PB1 residues are colored dark blue. **(b)** Schematic diagram showing the hydrogen bonds between PA (blue boxes) and PB1 (orange boxes). Black dashed lines indicate hydrogen bonds between 2.4 Å - 3.4 Å in length. **(c)** Space-filling representation, with PA residues show in green and PB1 residues red. Although the interface is largely tightly packed, unfilled space is found adjacent to *Pro 5*, *Thr 6* and *Phe 9* of PB1.

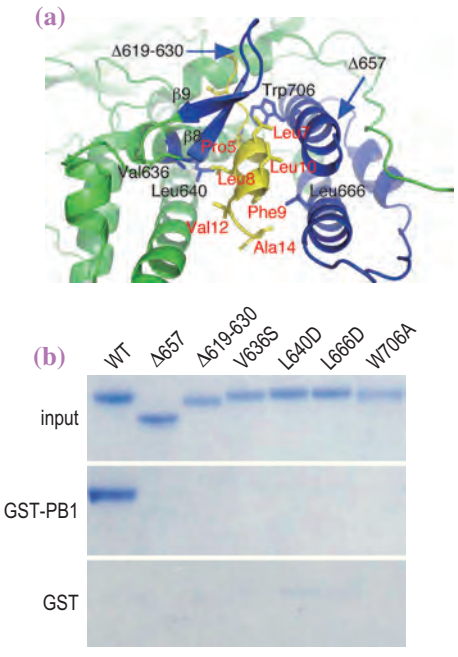


Fig. 3. PB1 binding to PA mutants. **(a)** Cartoon showing the Cα trace of PA in green, with residues selected for mutagenesis or deletion shown in blue. PB1 is shown in yellow (residues labelled in red). Val 636 touches *Leu 8*, Leu 640 lies close to *Leu 8* and *Pro 5*, Leu 666 packs against the side-chain of *Phe 9*, and Trp 706 interacts with *Asn 4*, *Pro 5* and *Thr 6*. **(b)** GST-pull-down assay. Wild-type PA and various mutants were tested for binding to GST-fused to the N-terminal 14 residues of PB1 (middle) or by GST alone as a negative control (bottom).

this PA-PB1 interaction manner is critical for viral replication for all types of influenza A virus, residues involving in the interaction between PA and PB1 are all conserved between those in human (H1N1) for this study and those in highly pathogenic avian (H5N1). From these results, it is concluded that the structure of the highly conserved PB1 binding site on PA presented here provides information to developed into new treatments effective against all types of influenza A virus, including avian strains.

Eiji Obayashi, Hisashi Yoshida and Sam-Yong Park*

Protein Design Laboratory, Yokohama City University

*E-mail: park@tsurumi.yokohama-cu.ac.jp

References

[1] World Health Organization. (2003) <http://www.who.int/mediacentre/factsheets/2003/fs211/en/>.
[2] J.S. Peiris *et al.*: Clin. Microbiol. Rev. **20** (2007) 243.
[3] J.K. Taubenberger *et al.*: Nature **437** (2005) 889.
[4] D. Elton *et al.*: Current Topics in Influenza Virology (Horizon Scientific Press, Norfolk, 2005).
[5] *E. Obayashi, H. Yoshida, F. Kawai, N. Shibayama, A. Kawaguchi, K. Nagata, J.R. Tame and S.-Y. Park: Nature **454** (2008) 1127.*

Crystal Structure of an Active Form of BACE1, an Enzyme Responsible for Amyloid β Protein Production

Alzheimer's disease (AD) is the most common neurodegenerative disorder and characterized by the extracellular deposition of insoluble amyloid plaques. The major component of amyloid plaques is the amyloid β-peptide (Aβ), which is derived from the amyloid precursor protein (APP) by sequential cleavage at the N-termini and C-termini of the Aβ domain by BACE1 and γ-secretase (Fig. 1(a)). Therefore, BACE1 is considered to be critical in the pathogenesis of Alzheimer's disease and one of the most promising pharmaceutical targets for treating AD.

During cellular trafficking, BACE1 is reinternalized from the cell surface to early endosomes and can recycle back to the cell surface via the trans-Golgi network (Fig. 1(b)). At the plasma membrane, both BACE1 and APP are located in lipid rafts on the cell surface where, at neutral pH (~pH 7), BACE1 is expected to show poor activity. BACE1 and APP follow similar trafficking routes and meet within endosomes, where BACE1 is activated due to an acidic pH environment (pH 4.5-6). When BACE1 is recycled to the cell surface, it becomes inactive again. Considering the long half-life of BACE1 and the recycling rate, BACE1 moves between the cell surface and the endosomal system many times throughout the course of its lifespan, showing an activation/inactivation transition during cellular trafficking [1]. The conformational transition of active and inactive states in BACE1 is interconvertible under physiological conditions and plays an important role in the localization-dependent activity of BACE1. However, never before has a structural view of active BACE1 been available. Here, we show the crystal structures of the catalytically active and inactive forms of BACE1 using beamlines **BL26B1**, **BL26B2** and **BL44B2** [2].

The active BACE1 has novel structural features involving the conformation of a flexible antiparallel β-hairpin, called a flap, and subsites that promote APP binding. The flap, which is believed to control substrate access to the active site and set the substrate into the correct geometry for the catalytic process, has adopted a more open conformation (Fig. 2(a)). In addition, the subsites show a new conformation, resulting in the formation of new spaces for APP binding (Fig. 2(b)). Inhibitor binding experiment suggests that these conformational

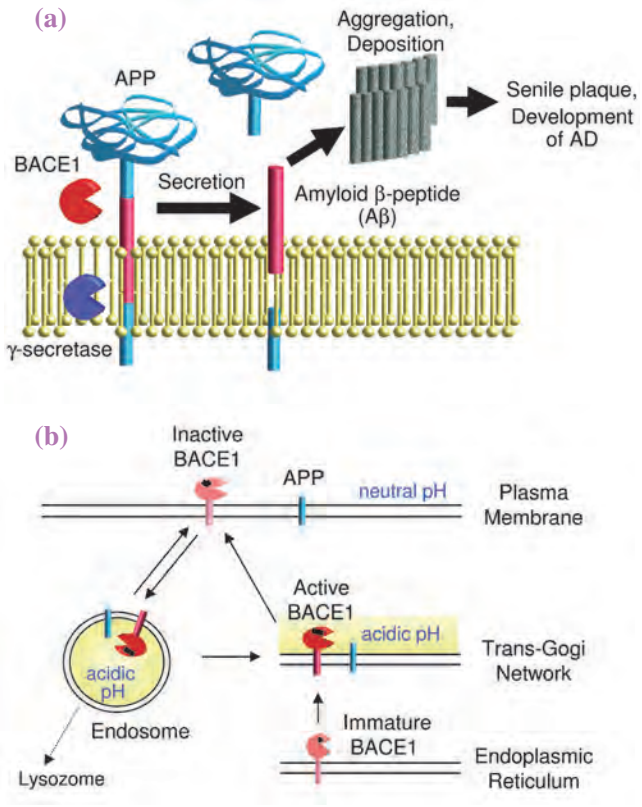


Fig. 1. **(a)** Schematic depicting generation of Aβ from APP. γ-secretase is another enzyme involved in the process. **(b)** Subcellular trafficking of BACE1.

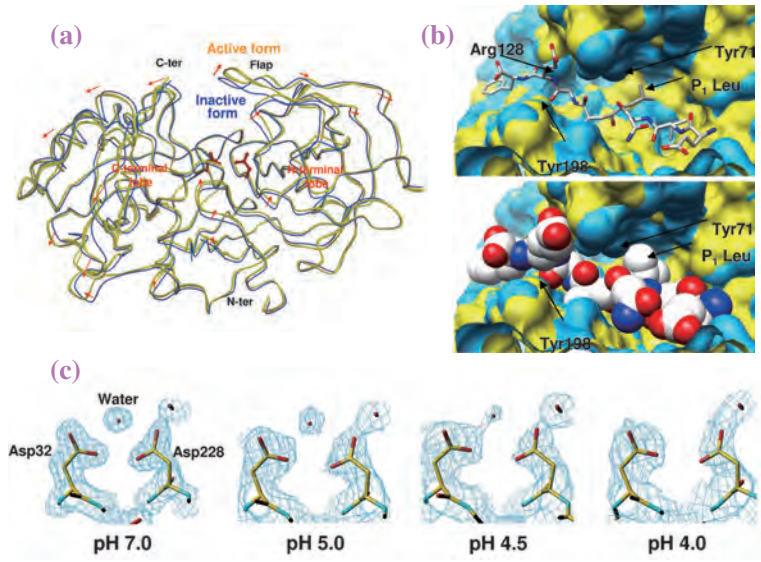


Fig. 2. Shape changes associated with activation of BACE1. **(a)** Overall structure of inactive BACE1 (dark blue) and active BACE1 (yellow). The displacement from inactive to active BACE1 is indicated by red arrows. **(b)** Composite surface representation in the APP binding site cleft with superimposed inhibitor OM99-2. Active BACE1 (yellow), inactive BACE1 (blue) and bound OM99-2 (white). **(c)** Electron densities of water molecule in the vicinity of Asp32 and Asp228.

changes are important in allowing the APP to bind. Thus, the active BACE1 could accommodate the substrate, leading to activation, whereas inactive BACE1 has a self-inhibition mode accounting for less APP binding and the loss of enzymatic activity.

Furthermore, we found that the active site water molecule –considered to be important in the chemical reaction through which BACE1 cleaves APP– became weaker as the pH was lowered, leading to the lack of activity at pH less than 4.0 (Fig. 2(c)). On the basis of these results, we propose that BACE1 has a dual regulatory mechanism of enzymatic activity at different pH values (Fig. 3).

As a template for novel inhibitor designs, the most suitable structure of BACE1 should be selected depending on the condition of the cellular compartment where the inhibitor reaches and binds to BACE1 [3]. Accordingly, information on the structure of active BACE1 would be of value in designing further selective drugs.

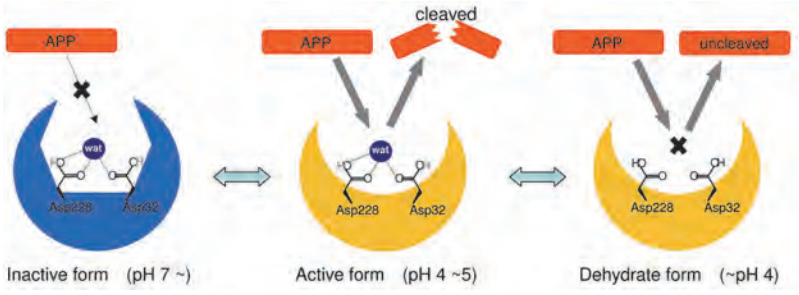


Fig. 3. Schematic representation of the regulatory mechanism of enzymatic activity in BACE1.

Hideaki Shimizu[a,b,*] and Nobuyuki Nukina[a]

[a] Laboratory of Structural Neuropathology, RIKEN Brain Science Institute
[b] Systems and Structural Biology Center, RIKEN Yokohama Institute

*E-mail: hshimizu@gsc.riken.jp

References

[1] *T. Sakurai, K. Kaneko, M. Okuno , K. Wada, T. Kashiyama, H. Shimizu, T. Akagi, T. Hashikawa and N. Nukina: J. Cell Biol.* ***183*** *(2008) 339.*
[2] *H. Shimizu, A. Tosaki, K. Kaneko, T. Hisano, T. Sakurai and N. Nukina: Mol. Cell Biol.* ***28*** *(2008) 3663.*
[3] L. Rajendran *et al.*: Science **320** (2008) 520.

Protein Biotinylation Visualized using a Complex Structure of Biotin Protein Ligase with a Substrate

We have determined the three-dimensional (3D) structure of a protein complex related to the metabolic syndrome. Organisms have an energy storage system in which excess calories are converted into adipose (fatty acid) for emergency. However, in human beings, this system could be the main reason for metabolic syndrome disorder including cardiac disorder and cerebral stroke. These diet-induced diseases and obesity can be overcome by regulating the activity of acetyl-CoA carboxylase (ACC), which is a key enzyme in fatty acid biosynthesis. It is reported that ACC-deficient mutant mice have a normal life span, a high fatty acid oxidation rate, and low amounts of fat [1]. In the living cell, ACC works only after the covalent attachment of biotin to its special lysine residue located at the biotin carboxyl carrier protein (BCCP) region. This biotinylation of BCCP is catalyzed by biotin protein ligase (BPL) in all organisms (Fig. 1). Therefore, one of the methods for

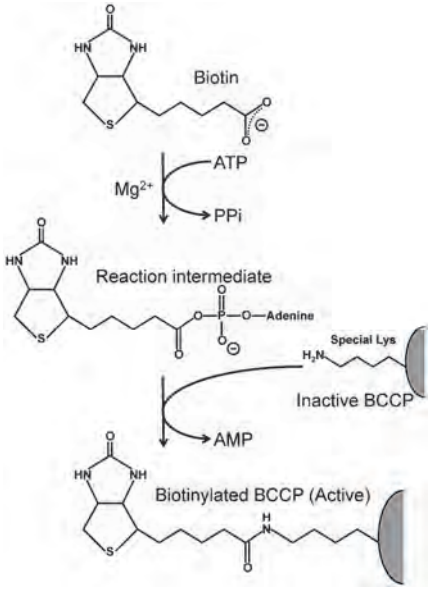


Fig. 1. Biotinylation of BCCP by BPL.

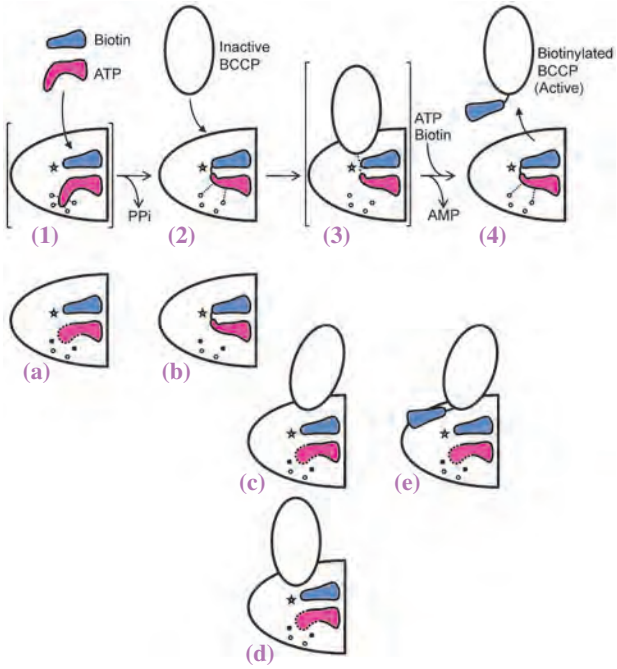


Fig. 2. Stabilization of reaction intermediates using BPL mutants. Objects (1)-(4) schematically denote the wild-type reaction procedure in which unstable states that cannot be observed by usual methods are indicated by parentheses. BPL is depicted as a half ellipsoid in which the amino acid residues to be mutated and the active site are indicated as circles and an asterisk, respectively. Covalent bonds, transition-state interactions and noncovalent interactions are indicated as thick solid lines, thick dotted lines and thin dotted lines, respectively. As derivatives from the substrates (ATP and biotin), the states (2) and (4) bind the reaction intermediate biotinyl-5'-AMP, and the state (3) binds the transition-state intermediate. Objects **(a)**-**(e)** schematically denote all the forms that were observed in the crystals of this work. The mutated residues of BPL are indicated by filled circles. The fuzzy boundary of the ATP molecule indicates a mutation-induced partial disorder due to the decrease in the number of noncovalent interactions. Presumably, in the crystals of mutant proteins, the substrate itself acted as an inactive intermediate analogue, thereby allowing the stabilization of BPL-BCCP complexes. The crystal forms **(a)** and **(b)** may correspond to the wild-type's states (1) and (2), respectively. Similarly, the forms **(c)** and **(d)** may correspond to intermediate states between (2) and (3), and the form **(e)** to a state between (3) and (4). The observation of forms **(b)** and **(e)** indicates that the mutants used retain essentially the same enzymatic function as that of the wild-type BPL.

the effective control of ACC in the human body would be the pharmaceutical inhibition of BCCP biotinylation. For the development of such medicine, scientists have to determine the 3D structure of BPL complexed with BCCP, which requires the preparation of BPL:BCCP complex crystals.

The crystallization of BPL:BCCP complexes is difficult because the complexes are inherently unstable as they are essentially intermediates (Fig. 2). Previously, we determined the crystal structure of archaeal BPL [2]. On the basis of the 3D structural information of BPL, eight mutants were designed to stabilize the intermediate complexes. By using these BPL mutants, the crystallization screening of BPL:BCCP complexes was performed and was successful for two mutants that could potentially form complexes but would only react slowly with BCCP. We have determined the crystal structures of BPL:BCCP complexes for the first time in the world using the synchrotron radiation at beamline **BL26B1** (Fig. 3). In this work, a huge number of combinations of mutants, ligands and crystallization conditions were carried out, and about 30 relevant crystal structures were determined to elucidate the BCCP biotinylation reaction. In one of the crystal forms, surprisingly, two different states of biotinylation were observed in a single crystal: one of the complexes was in the unbiotinylated state before the reaction and the other complex showed the biotinylated state after the reaction. On the basis of these various crystal structures, we could successfully discuss the activation mechanism of ACC [3].

The 3D structural information presented here will be useful for the development of drugs for metabolic syndrome. For instance, large structural changes were observed at the C-terminal domain during the reaction (Fig. 3). Therefore, a certain ligand to arrest the structural change in the C-terminal domain can be used to control the BCCP biotinylation effectively. As another perspective from this work, our approach using mutant proteins may be applied to the structural determination of other recalcitrant but important target proteins that are difficult to crystallize owing to their poor crystallizability or inherent instability.

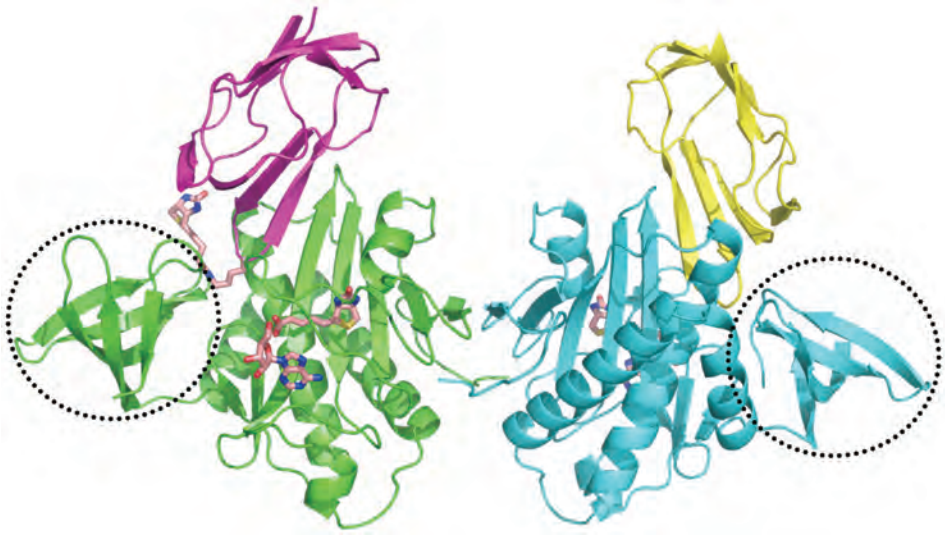


Fig. 3. Crystal structure of BPL:BCCP complex. BPL is a dimeric protein whose subunits are depicted as green and blue ribbon models. In the present crystal form of the BPL:BCCP complex, each BPL subunit binds a BCCP molecule (magenta or yellow model) to form a 2:2 complex. Two different states of the BCCP biotinylation reaction are observed in the same crystal: the right-side complex (blue and yellow models) and the left-side complex (green and magenta models) correspond to the states before and after the biotinylation, respectively. Dotted circles indicate the BPL's C-terminal domains that show large structural changes during the reaction, thereby suggesting a potential drug design target.

Naoki Kunishima* and Bagautdin Bagautdinov

SPring-8/RIKEN

*E-mail: kunisima@spring8.or.jp

References

[1] L. Abu-Elheiga *et al.*: Science **291** (2001) 2613.
[2] B. Bagautdinov *et al.*: J. Mol. Biol. **353** (2005) 322.
[3] *B. Bagautdinov, Y. Matsuura, S. Bagautdinova and N. Kunishima: J. Biol. Chem.* ***283*** *(2008) 14739.*

Crystal Structure of the Oxidative-Stress Sensor SoxR Bound to DNA

Reactive oxygen species (ROS) provide cellular and genetic damages to aerobic organisms, and cells have thus evolved defense systems against oxidative stress. In *Escherichia coli*, the *soxRS* regulon functions in the protection of cells against oxidative stress [1]. The *soxRS* regulon is induced in two steps: first, SoxR activates transcription of another transcription factor, SoxS in response to oxidative stress such as superoxide, nitric oxide; and then the increased level of the SoxS protein enhances the production of various antioxidant proteins and repair proteins. SoxR forms a homodimer in solution, with each 17-kDa subunit containing a [2Fe-2S] cluster. The [2Fe-2S] cluster is essential for activity of SoxR. In the absence of oxidative stress, the [2Fe-2S] cluster is maintained in reduced states and SoxR is inactive for transcription. Upon oxidative stress, the metal center is oxidized and SoxR is converted to the active form to enhance transcription of the *soxS* gene up to 100-fold. Apo-SoxR and reduced SoxR can bind to DNA with an affinity similar to that of oxidized SoxR, but only oxidized SoxR is able to activate transcription of the *soxS* gene. Therefore, it is suggested that structural changes between the oxidized and reduced forms of SoxR regulate the activity of SoxR.

SoxR belongs to the MerR family of transcriptional activators, which responds to various environmental stresses [2]. MerR family proteins have a homologous N-terminal DNA binding domain and a less conserved C-terminal sensor domain. The target promoter sequences of MerR family proteins have an unusual 19 or 20 bp spacer between the -35 and -10 elements, in contrast to the optimal 17 bp spacer. Hence, the MerR family is assumed to possess a common DNA distortion mechanism for transcriptional activation. To provide deep insights into the transcriptional activation mechanism by the redox regulation of SoxR, we have determined the crystal structures of SoxR from *E. coli* and its complex with the promoter DNA in the oxidized state at 3.2 Å and 2.8 Å resolution, respectively, using beamlines **BL41XU** and **BL44B2** [3].

The overall structure of SoxR consists of a DNA-binding domain, a dimerization helix (α5) and an Fe-S cluster-binding domain (Fig. 1(a)). The dimerization α5 helix forms an antiparallel coiled coil stabilizing the SoxR dimer. The overall architecture of the SoxR-DNA complex is similar to those of other MerR family proteins such as BmrR and MtaN [4,5]. Upon binding to DNA, the DNA binding domain undergoes an outward rotation of approximate 9° and the Fe-S cluster-binding domain receives an outward rotation of about 6°, resulting in a widening of the distance between the α2 and α2' helices from 29.3 to 31.5 Å (Fig. 1(b)). The dimerization helix connecting both domains shows an inner helical twist, which leads to a change in the relative positions of the dimerization helices. These conformational changes of SoxR are different from those observed in MtaN [5]. However, the observed movement of MtaN may result from the missing of a sensor domain of MtaN, which probably interacts with the DNA binding domain of the other subunit. Therefore, conformational changes similar to those observed in SoxR are expected to occur in other MerR family proteins during binding to their target promoters.

The [2Fe-2S] cluster of SoxR is coordinated by conserved four cysteine residues (Fig. 2(a)). The Fe-S cluster-binding domain is further stabilized by interactions with the conserved residues of the DNA binding domain from the other subunit (Fig. 2(b)). The remarkable feature of the [2Fe-2S] cluster of SoxR is its asymmetric environment (Fig. 2(a)). The lower

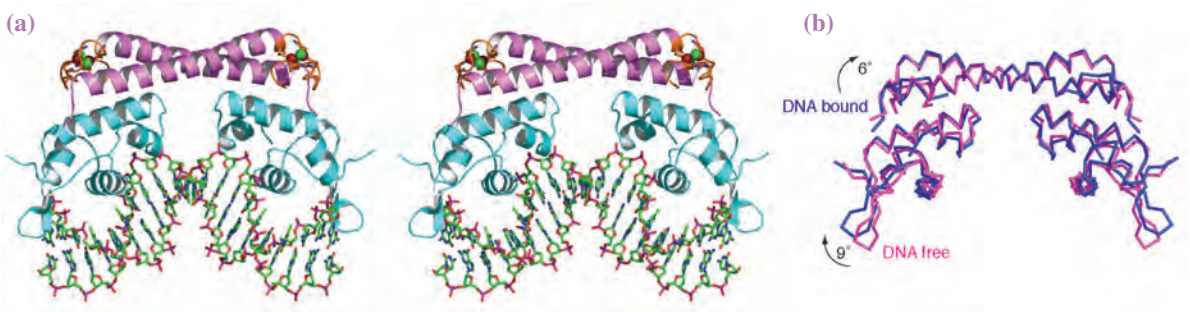


Fig. 1. Overall structure of the SoxR-DNA complex. **(a)** Stereo view of the overall structure of the SoxR-DNA complex. The SoxR dimer is shown in a ribbon representation and the DNA fragment appears in a stick model. The DNA binding domain, dimerization helix and Fe-S cluster binding domain are shown in light-blue, pink and orange, respectively. The two iron and two sulfur atoms of the [2Fe-2S] cluster are represented with brown and green spheres, respectively. **(b)** The Cα backbone of the DNA-bound (blue) and DNA-free (magenta) forms of SoxR. The two structures are superimposed based on the dimerization helices.

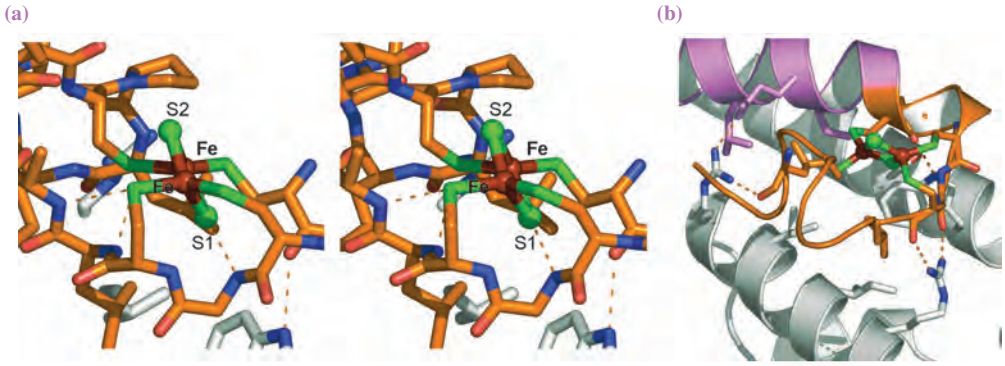


Fig. 2. Asymmetric environment of the [2Fe-2S] cluster of SoxR. **(a)** Stereo view of the [2Fe-2S] cluster environment in stick representation. Iron and sulfur atoms are indicated by brown and green spheres, respectively. NH-S hydrogen bonds are represented in orange broken lines. **(b)** Interactions between the Fe-S cluster-binding domain and the DNA-binding domain of the other subunit. The other subunit is shown in white.

sulfur atom (S1) of the cluster is surrounded by three positively charged amide groups of the main chain, while the upper sulfur atom (S2) is not able to interact with any amide groups but with the negatively charged carbonyl oxygen atom. These results suggest that asymmetric charge distribution of the [2Fe-2S] cluster environment causes redox dependent conformational changes of SoxR. Upon reduction, an additional negative charge on the sulfur atoms will attract the amide groups of the main chain and increase the charge repulsion with the oxygen atom, possibly resulting in large conformational changes of SoxR.

The promoter DNA in the SoxR-DNA complex is sharply bent at the middle (Figs. 1(a) and 3(a)). Although the half-site of the structure of the SoxR-DNA complex is similar to those of BmrR and MtaN, the DNA in the SoxR-DNA complex is further bent approximately 65° at the middle away from the protein, compare to 47~50° in BmrR and MtaN (Fig. 3(b)). Consequently, the overall end-to-end length of the 20-bp DNA fragment is further shortened by about 3.4 Å, which corresponds to the length of 1-bp, compared to those of the activated *bmr* and *mta* promoters. Therefore the DNA structure of SoxR is distorted and unwound by about 3-bp, compared to a B-form DNA. Comparison of the target promoter sequences of the MerR family indicates that the present DNA structure represents an activated conformation of the target promoter with a 20-bp spacer in the MerR family. In the target promoters with a 20-bp spacer, the DNA distortion observed in the SoxR-DNA complex unwinds the promoter by 3 bp and aligns the -35 and -10 elements for productive interactions with RNA polymerase.

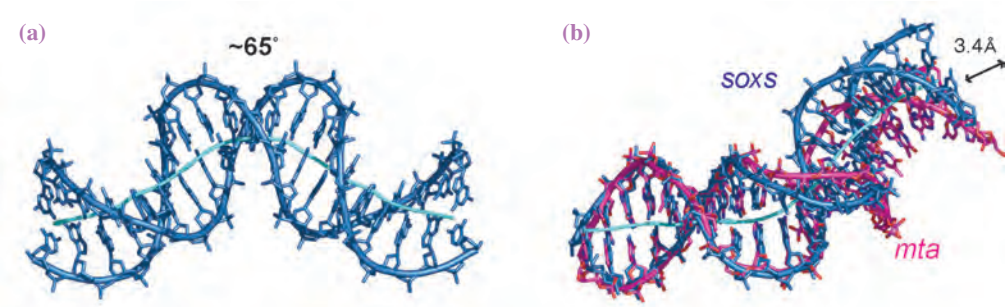


Fig. 3. Activated conformation of target promoter of SoxR. **(a)** The overall structure of the *soxS* promoter with the global DNA helical axis. **(b)** Comparison of the 20-bp promoter structures of SoxR (blue) and MtaN (magenta). Two promoter structures are superimposed on each half-site of DNA.

Satoshi Watanabe[a] and Kunio Miki[a,b,*]

[a] Dept. of Chemistry, Graduate School of Science, Kyoto University
[b] SPring-8/RIKEN

*E-mail: miki@kuchem.kyoto-u.ac.jp

References

[1] P.J. Pomposiello and B. Demple: Trends Biotechnol. **19** (2001) 109.
[2] N.L. Brown et al.: FEMS Microbiol. Rev. **27** (2003) 145.
[3] *S. Watanabe, A. Kita, K. Kobayashi and K. Miki: Proc. Natl. Acad. Sci. USA **105** (2008) 4121.*
[4] E.E. Heldwein and R.G. Brennan: Nature **409** (2001) 378.
[5] K.J. Newberry and R.G. Brennan: J. Biol. Chem. **279** (2004) 20356.

Hypervalent Intermediate in the Oxidation of Archaeal Peroxiredoxin

Increased levels of reactive oxygen species, such as hydrogen peroxide and alkyl peroxides, cause damage to biological macromolecules in aerobic cells, including lipids, proteins, and nucleic acids. Therefore, aerobic organisms have evolved mechanisms that protect them from oxidative damage. As a result, most cells have developed antioxidation proteins such as superoxide dismutase, catalase, thioredoxin, and peroxidase.

Peroxiredoxins (Prxs) are thiol-dependent peroxidases that reduce hydrogen peroxide and alkyl peroxides to water and the corresponding alcohols, respectively [1]. In addition to antioxidant functions, Prxs maintain the intracellular level of hydrogen peroxide that affects signal mediators such as protein tyrosine phosphatase and the lipid phosphatase PTEN through its self-inactivation mechanism [2]. These two distinct functions make Prx a switching molecule that regulates the cellular H_2O_2 level. In general, the oxidation of a cysteine side chain of protein is initiated by the formation of cysteine sulfenic acid (Cys-SOH) (Fig. 1). The same oxidation mechanism has been reported also for the oxidation process of Prx proteins. Prx contains a redox active peroxidatic cysteine (C_p) residue in its N-terminal region. It has been reported that the first step of the reaction of Prx is the formation of the single oxidation intermediate, cysteine sulfenic acid (C_p-SOH). Cysteine sulfenic acid is prone to further oxidation in aqueous solution, leading to a self-inactivation process by overoxidation to form cysteine sulfinic acid (C_p-SO_2H) and cysteine sulfonic acid (C_p-SO_3H). In the peroxidase process of Prx, the single oxidation intermediate is followed by disulfide linkage formation or reaction with a cellular reductant.

To gain insight into the oxidation mechanism of the archaeal Prx, we determined crystal structures of ApTPx in multiple oxidation states [3], using beamline **BL41XU**, and compared them with the reduced form [4] (Fig. 2). In the reduced state, the C_p side chain interacts with Arg126, which is invariant in all known Prxs. With the addition of hydrogen peroxide, the conformation around the C_p changes so that Arg126 swings away and His42 moves near to C_p50, while the side chain of C_p50 is still reduced. Oxidation of C_p50 results in the single oxidation form, in which an extra oxygen atom bonds covalently to the S^{γ} atom. In addition, the S^{γ} atom is situated near $N^{\delta 1}$ of His42. The distance between these atoms is so close (2.2 Å) that they are considered to form a covalent bond rather than a hydrogen bond. The bond angle formed around the S^{γ} atom shows a characteristic feature where the $N^{\delta 1}$, S^{γ}, and O^{δ} atoms are aligned linearly and the C^{β} atom of C_p50 bonds to the S^{γ} from the perpendicular direction (Fig. 3(a)). Simulation with quantum chemical calculations revealed that the single oxidation form represents a sulfurane derivative, which is a hypervalent sulfur compound (Fig. 3(b)). The crystal structure is considered to represent a mixture of the sulfurane derivatives with either a neutral or protonated imidazole moiety.

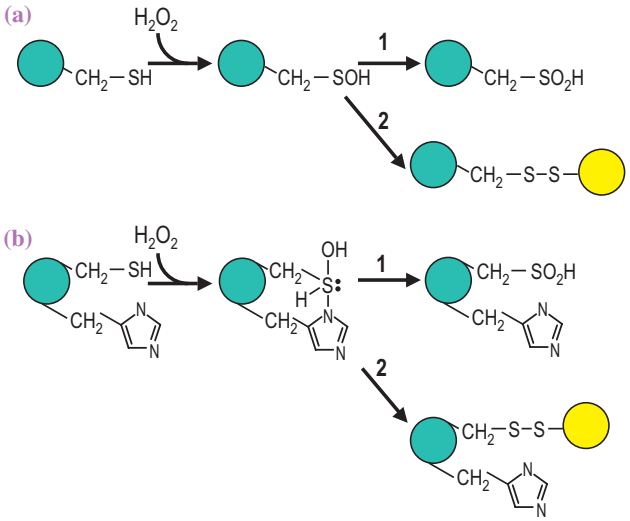


Fig. 1. Mechanism of thiol oxidation in proteins. Panel **(a)** represents the conventional mechanism of thiol oxidation involving cysteine sulfenic acid and panel **(b)** the novel mechanism involving hypervalent sulfur intermediate. Arrows 1 and 2 indicate further oxidation and disulfide bond forming pathways, respectively.

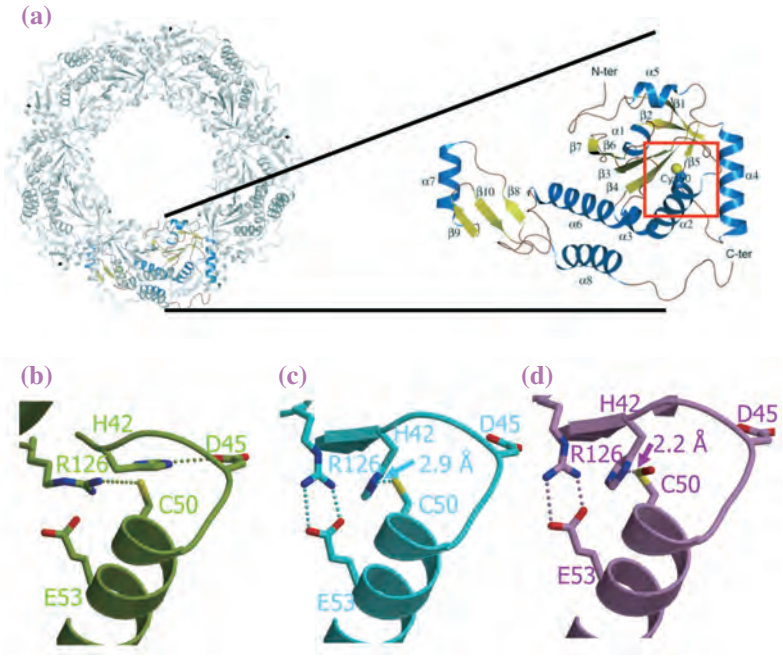
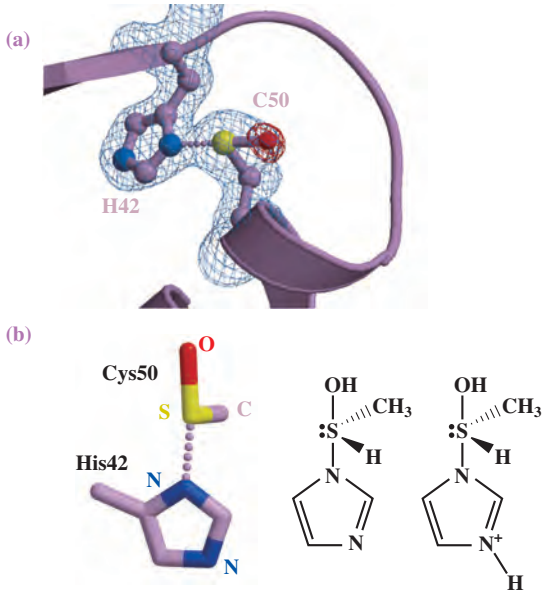


Fig. 2. Crystal structure of ApTPx in multiple oxidation forms. **(a)** shows decamer and monomer structures of ApTPx. **(b)**, **(c)** and **(d)** show the structure around the C_p residue (red box in a) in the reduced, preoxidation, and single-oxidation forms, respectively.



Angle (O-S-C) (˚)	**81.3 ± 2.8**	91.5	93.7
Angle (O-S-N) (˚)	**170.2 ± 4.5**	170.3	172.4
Angle (N-S-C) (˚)	**91.0 ± 3.7**	88.2	89.0
Distance (O-S) (Å)	**1.72 ± 0.01**	1.80	1.68
Distance (S-N) (Å)	**2.21 ± 0.13**	1.97	2.39

Fig. 3. Structure of the hypervalent sulfur intermediate. **(a)** Crystal structure around C_p50 and His42 of ApTPx in the single-oxidation form. **(b)** List of bond angles and lengths. Values for the crystal structure (shown on the left) are the average ± SD of the 10 subunits. The right columns show the calculated values of the neutral and protonated sulfurane models.

This study shows for the first time that sulfurane is involved in a biochemical reaction. Hypervalent compounds have been studied in the field of organic synthetic chemistry for about 50 years. Nowadays, hypervalent compounds are known as active reagents such as the Wittig reagent, a hypervalent phosphorus compound. This study expands the importance of hypervalent compounds with respect to the field of biochemistry by demonstrating that a sulfurane derivative occupies a crucial position in biochemical processes. The architecture of hypervalent sulfur in proteins will provide useful guidelines for methodological studies towards the synthesis of novel hypervalent compounds.

Tsutomu Nakamura[a,*] and Tsuyoshi Inoue[b]

[a] National Institute of Advanced Industrial Science and Technology
[b] Graduate School of Engineering, Osaka University

*E-mail: nakamura-t@aist.go.jp

References

[1] Z.A. Wood *et al.*: Trends Biochem. Sci. **28** (2003) 32.
[2] S.G. Rhee *et al.*: Curr. Opin. Cell Biol. **17** (2005) 183.
[3] *T. Nakamura, T. Yamamoto, M. Abe, H. Matsumura, Y. Hagihara, T. Goto, T. Yamaguchi and T. Inoue: Proc. Natl. Acad. Sci. USA **105** (2008) 6238.*
[4] T. Nakamura *et al.*: Proteins **62** (2006) 822.

Structural Basis for the Exclusive Specificity of Slac2-a/Melanophilin for the Rab27 GTPases

Melanin, a pigment found in hair and skin, plays important roles in protecting the human body against radiation damage, but leaves unfavorable dark pigments in the skin. Melanin is made by skin color cells known as melanocytes and is stored in intercellular vesicles called melanosomes. Melanosomes mature near the nucleus, transfer along microtubules and actin filaments to the cellular membranes, distribute to skin cells called keratinocytes, and then pigment skin and hair.

Rab27A, a member of the monomeric Ras-like GTPase superfamily, is a key player in melanosome transport in skin melanocytes, through interactions with two specific effector molecules, Slac2-a/melanophilin and Slp2-a/Exophilin4. In melanocytes, Rab27A forms a transport complex with Slac2-a and myosin Va (an actin-based motor). The resulting tripartite protein complex regulates melanosome transfer from microtubules to actin filaments as well as subsequent actin-based melanosome transport. After actin-based melanosome transport, Rab27A interacts with Slp2-a, another Rab27-specific effector, and promotes the anchoring of melanosomes to the plasma membrane. The former interaction seems to be more crucial for melanosome transport, because mutations of Rab27A or Slac2-a cause human Griscelli syndrome, which is characterized by pigment dilution in hair (i.e., defect in melanosome transport in melanocytes) as well as immunodeficiency.

More than 60 Rab isoforms have been reported in humans, and they appear to be present on distinct organelle membranes, where they regulate certain types (or distinct steps) of membrane trafficking. Rab27B, a closely related isoform of Rab27A (72% sequence identity), also binds all of the known effectors of Rab27A including Slac2-a and Slp2-a. Thus far, nothing is known about the structural basis of the Rab27•Slac2-a interaction, although this information is critical for the molecular diagnosis of human Griscelli syndrome as well as for understanding the mechanism by which Slac2-a specifically recognizes Rab27A/B, but not the other Rab proteins.

Rab, like other G proteins, functions as a molecular switch by cycling between two nucleotide-bound states, a GDP-bound inactive state and a GTP-bound active state. The GTP-bound active form of Rab27A interacts with its specific effector molecules, such as Slac2-a and Slp2-a, and the resultant Rab27A•Slac2-a and Rab27A•Slp2-a complexes promote melanosome transport. Because active Rab27 proteins are notoriously difficult to crystallize, we generated a GTPase-deficient mutant of Rab27B, and succeeded in crystallizing the active Rab27B complexed with the effector domain of Slac2-a and solved its crystal structure [1]. The structure analysis was carried out using beamline **BL41XU**.

The structure of the Slac2-a effector domain, in complex with Rab27B, comprises a coiled-coil and a zinc-binding subdomain (Fig. 1). The main interface of Slac2-a with Rab27B is formed by the coiled-coil. In the Rab27B side, the switch, interswitch and Rab complementarity-determining regions (RabCDR) are involved in the interaction. In the Rab27B•Slac2-a interface, we found many hydrophobic interactions and several electrostatic interactions. Most of the Slac2-a-interacting residues of Rab27B are conserved in Rab27A. These include the Rab27A residue Trp73, whose mutation to Gly is found in type 2 Griscelli syndrome patients (Fig. 2). The Slac2-a residue Arg35, whose mutation to Trp is found in type 3 Griscelli syndrome patients, is also involved in the Rab27B

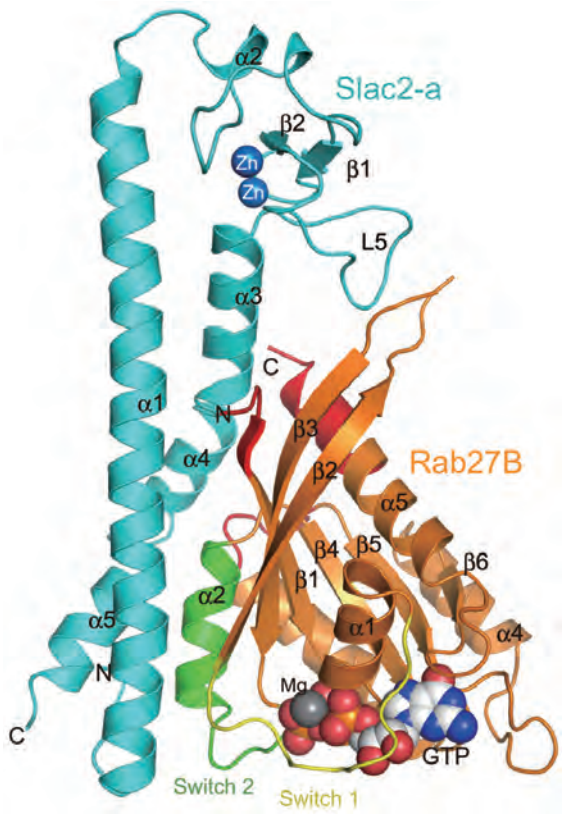


Fig. 1. Crystal structure of the Rab27B•Slac2-a complex.

interaction. Therefore, we suggest that Griscelli syndrome would be caused by the disruption of the complex formation between Rab27A and Slac2-a.

Rabphilin, a Rab effector, binds several subfamilies, including Rab3 and Rab27, while Slac2-a exclusively binds the Rab27 subfamily (Rab27A and Rab27B). Precise comparison of the Rab27B•Slac2-a complex with the previously reported Rab3A•rabphilin complex [2] revealed several intermolecular hydrogen bonds that are specific between Rab27B and Slac2-a. Rab27A mutations that disrupt any of these specific hydrogen bonds with Slac2-a resulted in the dramatic reduction of Slac2-a binding activity (Fig. 3(a)). Furthermore, we found that transplantation of only four Rab27-specific residues into Rab3A was sufficient to make the Rab3A mutant associate with Slac2-a (Fig. 3(b)).

The present Rab27B•Slac2-a complex structure may be used as a basis for the development of drugs for the treatment of rare, lethal Griscelli syndrome for which there is no effective treatment. It is also hoped that the regulation of melanosome transport in skin melanocytes will enable the development of cosmetics that are effective against skin pigmentation.

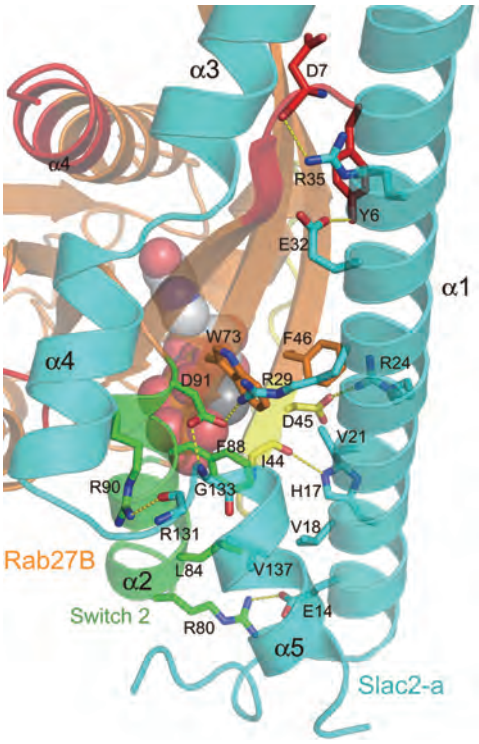


Fig. 2. Rab27B•Slac2-a interfaces, which can explain the structural basis of the human diseases caused by mutations in Rab27A and Slac2-a.

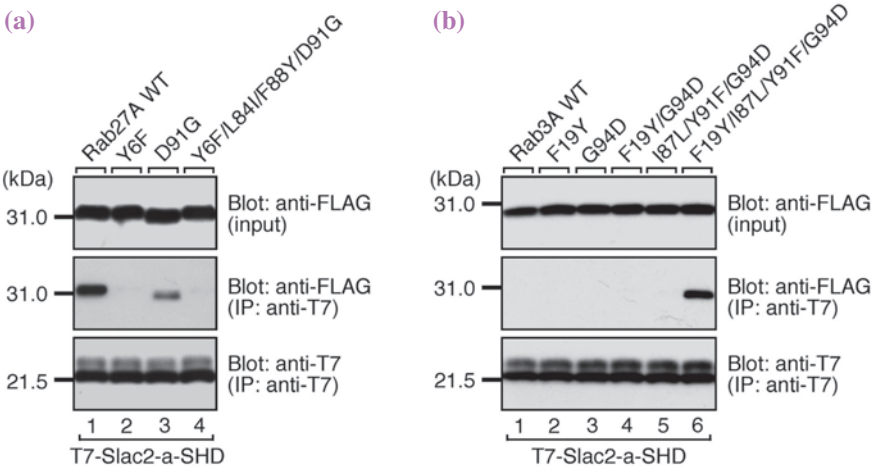


Fig. 3. Mutational analyses of Rab27A **(a)** and Rab3A **(b)** showing the requirement of specific hydrogen bonds for the Rab27A•Slac2-a interaction.

Mutsuko Kukimoto-Niino[a], Mikako Shirouzu[a] and Shigeyuki Yokoyama[a,b,*]

[a] Systems and Structural Biology Center, RIKEN Yokohama Institute
[b] Department of Biophysics and Biochemistry, The University of Tokyo

*E-mail: yokoyama@biochem.s.u-tokyo.ac.jp

References

[1] *M. Kukimoto-Niino, A. Sakamoto, E. Kanno, K. Hanawa-Suetsugu, T. Terada, M. Shirouzu, M. Fukuda and S. Yokoyama: Structure* ***16*** *(2008) 1478.*
[2] C. Östermeier and A.T. Brunger: Cell **96** (1999) 363.

Structure of Squid Rhodopsin

Rhodopsin is the primary molecule in the visual signaling cascade in vertebrate and invertebrate photoreceptor cells. Upon light absorption, the retinal chromophore in rhodopsin undergoes isomerization from the 11-*cis* to the all-*trans* configuration, which initiates the photoactivation process. In vertebrate retinas, the final photoproduct, meta-rhodopsin, activates a subtype of heterotrimeric G-protein, transducin (Gt), which in turn activates phosphodiesterase, an enzyme that degrades the second messenger, cGMP. In the retinas of many invertebrates such as insects and cephalopods, on the other hand, photoactivated acid meta-rhodopsin stimulates a Gq-type G-protein, and then the G-protein activates phospholipase C, an enzyme that hydrolyzes phosphatidyl inositol into the second messengers inositol trisphosphate and diacyl glycerol [1]. The same cascade is used by many G-protein-coupled hormone/neurotransmitter receptors such as serotonin and acetylcholine receptors, indicating that invertebrate rhodopsin is a prototypical member of the G-protein-coupled receptor (GPCR) family. The structural information of invertebrate rhodopsin would be useful to elucidate a common mechanism of Gq-type G-protein activation by GPCR.

We performed X-ray crystallographic analysis of invertebrate squid (*Todarodes pacificus*) rhodopsin. Squid rhodopsin contains 448 amino acids, i.e., 100 residues longer than those of vertebrate counterparts, mainly due to the unique C-terminal extension with repeated proline-rich sequences. After enzymatic deletion of the extended C-terminus, squid rhodopsin was extracted selectively from microvillar membrane with octylglucoside in the presence of zinc ion, and crystallized into the hexagonal *P62* crystal. We collected diffraction data from a frozen crystal of squid rhodopsin at beamline **BL38B1** and determined its crystal structure at 2.5 Å resolution [2].

The polypeptide of C-terminally truncated squid rhodopsin, which was traced from Glu 9 to Glu 358, is composed of seven transmembrane helices (from I to VII) and two cytoplasmic helices (VIII and IX) (Fig. 1). The overall structure revealed new features of Gq-coupled receptors. Helices V and VI extend into the cytoplasmic medium and, together with a hydrophilic helix IX, they form a highly organized structure of about 25 Å length from the membrane surface. The calculated map of electrostatic potential on the protein

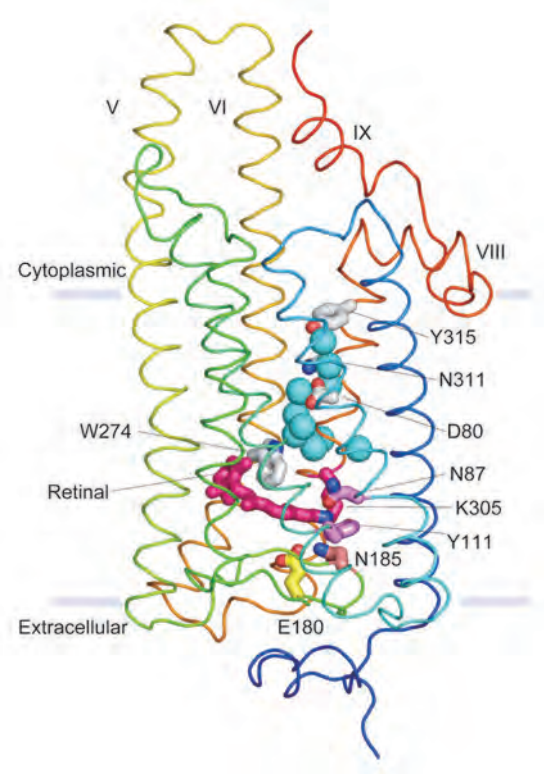


Fig. 1. Crystal structure of C-terminally truncated squid rhodopsin. Helices are color-coded from blue (helix I) to red (helix IX). Retinal-Lys305 chain (pink), water molecules in an interhelical cavity (cyan), and several key residues (yellow, orange, magenta, and white) are depicted.

surface shows that positively charged residues are crowded into the N-terminal end of helix IV and the second cytoplasmic (C2) loop, whereas negatively charged residues are clustered along helix IX. This structural motif and charge distribution in the cytoplasmic side seem to explain the selective interaction of squid rhodopsin with Gq-type G-protein.

Invertebrate rhodopsin is known to exhibit a bistable property; that is, its acid-meta state is thermally stable and reverts to the dark state upon absorption of a second photon, whereas vertebrate rhodopsin undergoes an irreversible photobleaching reaction. Reflecting this difference, squid rhodopsin has a unique feature in the retinal binding pocket, which is quite different from that of bovine rhodopsin [3]. The sole anionic residue Glu 180 in the retinal binding region is too far from the Schiff base to have a direct interaction; in fact, the side chain of Asn 185 is located between them. In the dark-state structure, the protonated Schiff base is stabilized by hydrogen bonds with either the side-chains of Asn 87 or Tyr 111. Because the OH group of Tyr 111 is kept neutral in both the dark state and the acid metarhodopsin state [4], it is suggested that in the acid-meta state, Asn 185 mediates an indirect interaction between Glu 180 and the protonated Schiff base. Thus, our structure provides a reasonable explanation for a bistable property of squid rhodopsin, in which the retinal chromophore is not released from its binding pocket after the photoactivation.

Squid rhodopsin possesses a large interhelical cavity that is filled by nine water molecules. Together with polar residues, these water molecules form a long hydrogen-bonding network, which extends from the retinal-binding pocket to the cytoplasmic surface. A recent FTIR study has shown that more than eight water molecules change their vibration frequencies upon formation of bathorhodopsin [5]. It is thus suggested that a light-induced conformational change propagates along the water cluster towards the cytoplasmic side during the photoactivation process. As the amino acid residues around the water cluster are highly conserved in GPCRs, the rearrangement of the water molecules in the interhelical region seems to play an important role in the activation process of G proteins.

In the $P6_2$ crystal, intramembrane dimerization is observed around a crystallographic twofold axis (Fig. 2). In this dimeric association, the protein-protein interactions are reinforced by phospholipids located at the intradimer interface. The crystal structure shows another type of protein-protein interaction that leads to intermembrane dimerization; i.e., the N-terminal polypeptides of neighboring monomers are tightly associated via salt bridges. It should be noted

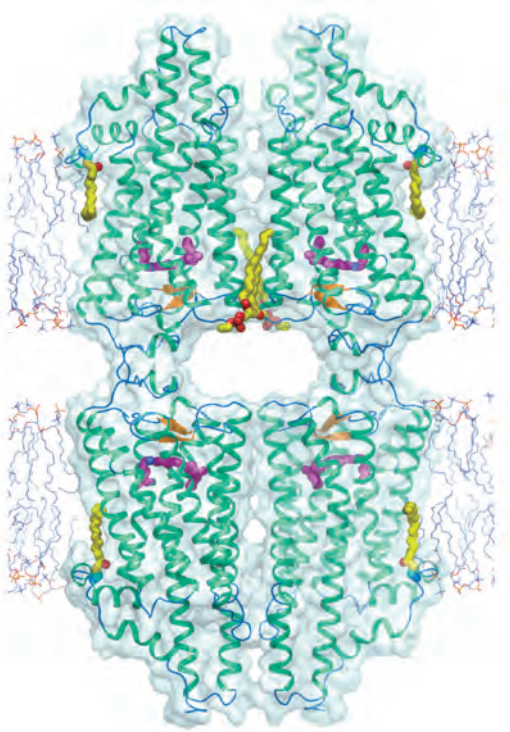


Fig. 2. A tetrameric structural model of squid rhodopsin incorporated into the lipid bilayer.

that two adjacent intramembrane dimers form a tetrameric structure around a noncrystallographic twofold axis. In this tetramer, four retinylidene chromophores are orientated nearly parallel with one another. It is possible that such tetramers are arranged in the apposed microvillar membranes so that the absorption dipole moments of all the retinal chromophores are aligned in parallel with the microvillar axis. As all the microvillar membranes in each photoreceptor cell are arranged in a particular direction, our crystal data provide a structural basis for the detection of polarized light by invertebrate eyes.

Midori Murakami and Tsutomu Kouyama*

Department of Physics, Nagoya University

*E-mail: kouyama@bio.phys.nagoya-u.ac.jp

References

[1] A. Terakita *et al.*: FEBS Lett. **439** (1998) 110.
[2] *M. Murakami and T. Kouyama: Nature **453** (2008) 363.*
[3] T. Okada *et al.*: J. Mol. Biol. **342** (2004) 571.
[4] M. Nakagawa *et al.*: Proc. Natl. Acad. Sci. USA **96** (1999) 6189.
[5] T. Ota *et al.*: Biochemistry **45** (2006) 2845.

Crystal Structures of LOV1 Domains in *Arabidopsis* Phototropin 1 and 2

In 1882, Charles Darwin wrote that blue light was effective for inducing the tropic response of plants in his famous book "The Power of Movement in Plants." Since then, many researchers reported the blue-light-regulated movements of plants, such as whole body, stem, leaf, cell, or micro-organ. In the last decade, molecular biological studies revealed that all these blue light responses are mediated by a single species of blue-light receptor named phototropin (phot) [1]. phot was first found as a receptor for phototropic responses and has since been revealed to regulate a variety of physiological activities for maximizing the efficiency of photosynthesis, such as chloroplast relocation, stomata opening, and leaf expansion. Most higher plants have two isoforms named phototropin1 (phot1) and phototropin2 (phot2). phot1 senses blue light in a wide range of light intensity, whereas phot2 acts as a light sensor under high irradiance. For instance, in *Arabidopsis*, phot1 and phot2 share phototropism and photoaccumulation responses (migration to appropriate light condition) of chloroplasts depending on the blue light intensity, while photoavoidance response (escape from intense light) of chloroplast is mediated solely by phot2. In contrast, stomata opening is mediated redundantly by both.

phot molecules comprise about 900 - 1000 amino acid residues and have two photoreceptive domains called LOV (light, oxygen and voltage-sensing) 1 and 2 in their N-terminal halves that bind flavin mononucleotide (FMN) noncovalently as a chromophore (Fig. 1). LOV is a subfamily of the PAS (PER-ARNT-SIM) superfamily involved in protein-protein interactions in cellular signaling. The C-terminal half forms a serine/threonine kinase domain (Fig. 1) inducing blue-light-activated autophosphorylation, which is considered to be the primary step in the light-signal transduction by phot. Thus, phot is thought to be a light-regulated protein kinase, in which LOV2 acts as a major molecular switch [2]. LOV1 is thought to regulate the sensitivity to blue light [2] and to work as a dimerization site [3].

In the present study, we determined the crystal structures of LOV1 domains of *Arabidopsis* phot1 (P1L1: Gly180-Lys329, Fig. 1) and phot2 (P2L1: Phe117-Lys265) in the dark at resolutions of 2.1 and 2.0 Å, respectively [4]. The P1L1 crystals appeared as bundles of thin needles. The X-ray diffraction data of P1L1 was collected from a crystal carefully broken off from a bundle at beamline **BL44B2** [5]. P2L1 crystal appeared as considerably stacked thin plates. The diffraction data was collected at beamline **BL41XU** by irradiating X-ray microbeam to a small volume likely composed of a few plates in a polycrystal [5]. The crystal structure of either LOV1 appears as a dimer in a face-to-face association mode of their β-scaffolds, which is composed of three antiparallel β-strands (Fig. 2). Three types of

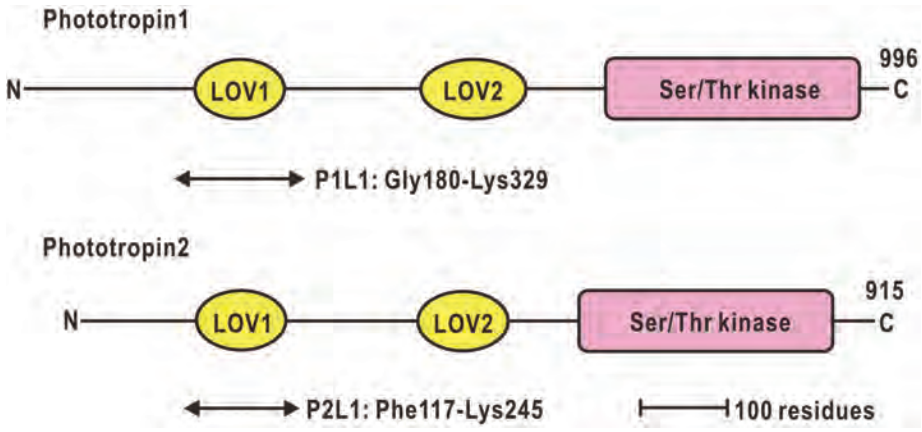


Fig. 1. Schematic of domain organization in *Arabidopsis* phot1 and phot2. P1L1 and P2L1 are the LOV1 domains targeted in this study and are indicated by solid lines.

interaction indispensable for stabilizing the dimer structures are contacts of side chains in the β-scaffolds, hydrophobic interactions induced by a short helix in the N-terminus of a subunit, and hydrogen bonds mediated by hydration water molecules confined in the dimer interface. In P1L1, the critical residue for dimerization is Cys261 that forms a disulfide bridge between subunits, and in P2L1, those are Thr217 and Met232 that may be involved in the difference in light sensitivity between phot1 and phot2. Putative models for the tertiary structures of full-length phot1 and phot2 based on the dimeric structures of their LOV1 domains are speculated (Fig. 3). In addition, the topologies in the homodimeric associations of the LOV1 domains also provide clues to understand the structural basis of the dimeric interactions of Per-ARNT-Sim protein modules in cellular signaling.

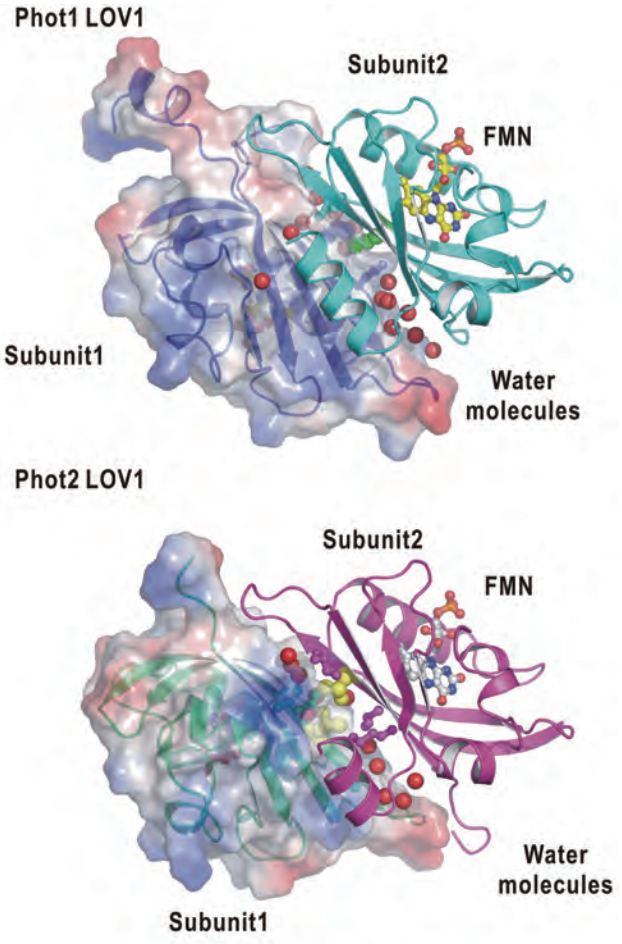


Fig. 2. Schematics of the crystal structures of P1L1 and P2L1 dimers. The structures of subunits are shown as ribbon models with cofactor FMN molecules shown as ball-and-stick models. The molecular surface of one of the subunits is also shown. Side chains of residues and hydration water molecules indispensable for the dimer association are shown in the space-filling models.

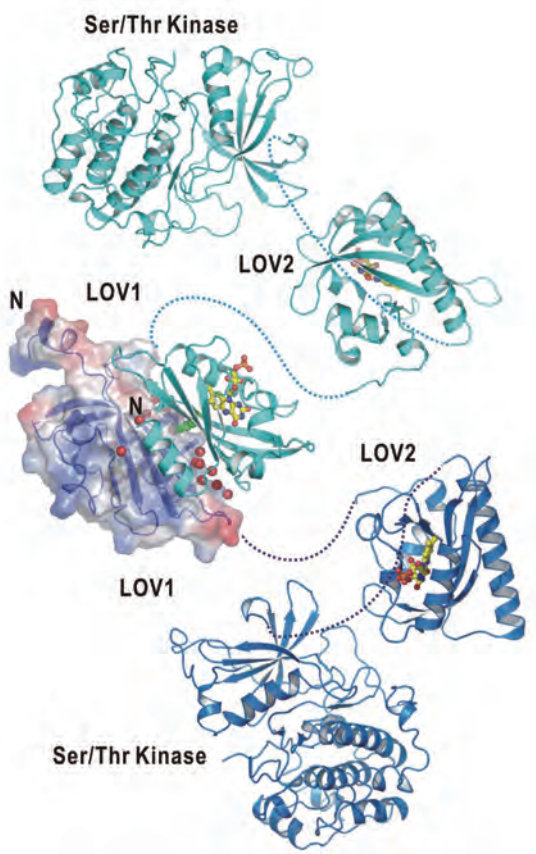


Fig. 3. A putative model for the quaternary structures of full-length phot1. The structures of LOV2 and the kinase domains are illustrated using the crystal structures of oat phot1 LOV2 (PDB accession code: 2V0U) and protein kinase A (1ATP), respectively. Protein kinase A has an amino acid sequence homologous to that of the phot serine/threonine kinase domain. The dashed lines are the linkers of the functional domains.

Masayoshi Nakasako[a,b,*] and Satoru Tokutomi[c]

[a] Department of Physics, Keio University
[b] SPring-8/RIKEN
[c] Graduate School of Science, Osaka Prefecture University

*E-mail: nakasako@phys.keio.ac.jp.

References

[1] J.M. Christie: Annu. Rev. Plant. Biol. **58** (2007) 21.
[2] D. Matsuoka and S. Tokutomi: Proc. Natl. Acad. Sci. USA **102** (2005) 13337.
[3] M. Nakasako *et al.*: Biochemistry **43** (2004) 14881.
[4] *M. Nakasako, K. Zikihara, D. Matsuoka, H. Katsura and S. Tokutomi: J. Mol. Biol.* ***381*** *(2008) 718.*
[5] M. Nakasako *et al.*: Acta Crystallogr. Sect. F **64** (2008) 617.

Structural Versatility of a Bacterial Aconitase as Revealed by Small-Angle X-Ray Scattering Analysis

Nowadays, to catalogue comprehensive three-dimensional folding patterns of proteins has an air of authenticity. On the other hand, the structural information of macromolecular complexes is still limited. Their structural analysis is an important task in modern structural biology, because many biological functions the require formation of complexes. In particular, macromolecular complexes maintained by weak protein-protein interactions are of considerable interest, because their versatile nature plays a vital role in dynamic biological processes. For instance, a multienzyme complex could exhibit an allosteric effect among the active sites. Temporal assembly of these enzymes yields a timely metabolic regulation, responding to different conditions. Although conventional biochemical studies focused on the catalytic properties of purified enzymes under diluted conditions, little is known about their proprieties under physiological conditions, where macromolecules are densely crowded. The intracellular environment could promote macromolecular association by weak interactions. Recent proteomic analyses results revealed several supramacromolecular complexes *in vivo*. However, their structural analyses are generally difficult, owing to their low stability *in vitro*.

Aconitase B (AcnB) from *Escherichia coli* is an iron-sulfur protein, catalyzing a reversible isomerization of citrate into isocitrate (Fig. 1). A previous study indicated that the protein could assume not only a monomer but also a homodimer in the cell [1]. The catalytic property apparently varied, depending on the oligomerization state. Consideration of the potential consequence tempted us to explore a linkage with a metabolon, that is, a multienzyme cluster catalyzing the consecutive reactions in the Krebs cycle [2]. The pairwise interactions between the component enzymes were too weak to detect *in vitro*. However, experimental data *in vivo* implied a possibility of a direct interaction between AcnB and isocitrate dehydrogenase (ICDH). ICDH catalyzes the next reaction of AcnB in the Krebs cycle (Fig. 1). Thus, the hypothetical interaction could affect the consecutive reactions.

We investigated the versatile architecture of AcnB and the interference in the reaction with ICDH [3]. Small-angle X-ray scattering (SAXS) is advantageous for analyzing protein structures with fragile interactions. The experimental data provide structural information of macromolecules in solution without any specific modifications. Although the data are of limited resolution, they could be interpreted using known atomic structures of the component proteins. Because direct binding of AcnB to ICDH was undetectable *in vitro*, a fusion protein of the two proteins was analyzed. The linker with 27 amino acid residues (about 80 Å), introduced by a genetic manipulation, connected the N-terminus of AcnB to the C-terminus of ICDH. The increased local concentration for each protein region promotes the weak intermolecular interaction. The SAXS data of *E. coli* AcnB, ICDH, and the fusion protein (AcnB-ICDH) were obtained with the synchrotron radiation at beamline **BL40B2**.

The conventional SAXS analysis indicated that all the three proteins formed homodimers in solution. These observations were consistent with the results of the chemical crosslinking [3]. The structural state of each protein was estimated, using the experimental SAXS data and the known three-dimensional structure (Fig. 2). The crystal structure of homodimeric ICDH reasonably explained the corresponding scattering profile. In contrast, only the monomeric structure was known for AcnB (PDB 1L5J). To account for the experimental SAXS data of AcnB, a three-dimensional model of the homodimeric AcnB was constructed by rigid-body modeling, using the atomic coordinates of the AcnB monomer. No structural state of the homodimeric AcnB-ICDH could be explained using

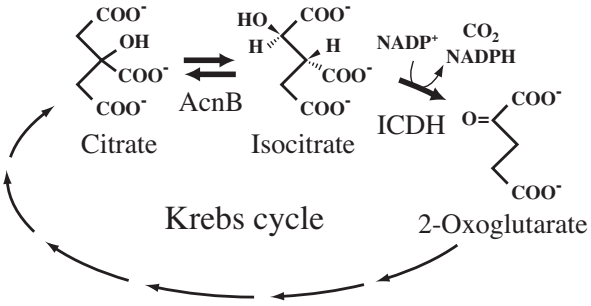


Fig. 1. Catalytic reactions of AcnB and ICDH.

any combination of the AcnB and ICDH homodimers, even though the linker was sufficiently long to form a hypothetical "heterodimer-of-homodimers." Instead, a rigid-body modeling with the SAXS data indicated that the fusion protein maintained only the homodimeric architecture of ICDH but not that of AcnB. Only one of the two monomeric AcnB regions associated with the homodimeric ICDH region.

The enzymatic assay revealed the variable catalytic property of AcnB, depending on the oligomerization state [3]. To perform the consecutive reaction from citrate to 2-oxoglutarate, AcnB-ICDH exhibited a slower catalysis than that observed in the mixture of the AcnB and ICDH proteins in an equimolar ratio. Considering the catalysis of each enzyme, monomerization of AcnB would attenuate the overall performance of the consecutive reaction, either by the decelerated hydration of the intermediate product in AcnB, or by the partial inhibition of ICDH activity. In addition, we observed that homodimerization of AcnB generated a substrate-dependent negative cooperativity between the two active sites [4]. This allosteric effect selectively promoted the isomerization from isocitrate, but not from citrate, at the intracellular substrate concentration. The dissociable homodimerization of AcnB, together with ICDH, may be involved in the complex control of the Krebs cycle.

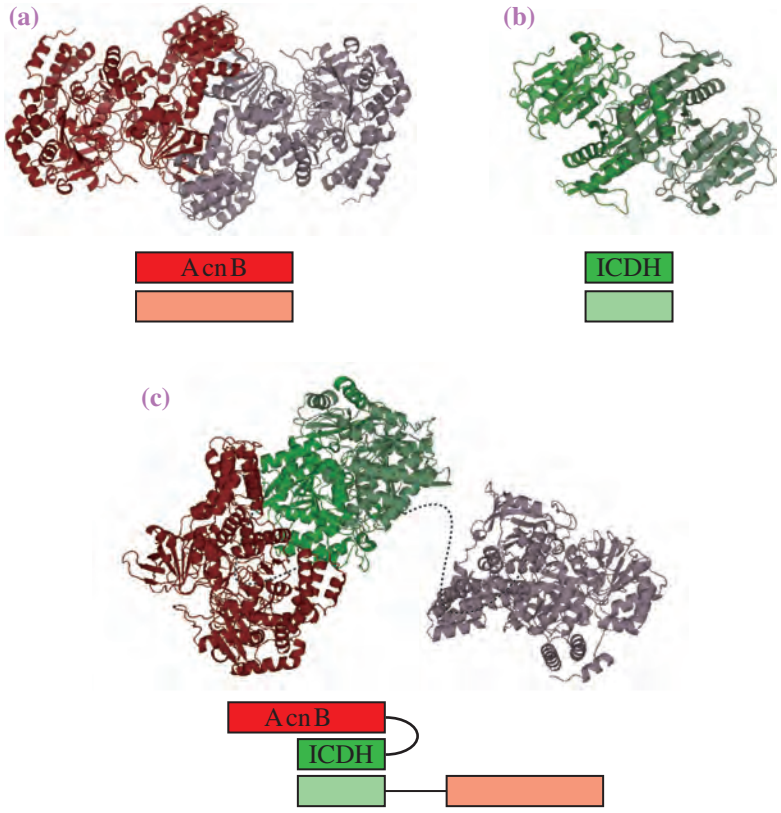


Fig. 2. Structural models of **(a)** AcnB, **(b)** ICDH, and **(c)** AcnB-ICDH in solution, which could account for the experimental SAXS profiles. The structure in **(b)** is the same as that observed in the crystal (PDB 3ICD). The models in **(a)** and **(c)** were constructed by a rigid-body modeling method [3], using the experimental SAXS profiles and atomic coordinates of PDB 1L5J (AcnB) and 3ICD (ICDH).

Daisuke Tsuchiya

Institute for Advanced Biosciences, Keio University

E-mail: dsktcy@ybb.ne.jp

References

[1] Y. Tang *et al.*: Mol. Microbiol. **56** (2005) 1149.
[2] P.A. Srere: Trends Biochem. Sci. **25** (2000) 150.
[3] *D. Tsuchiya, N. Shimizu and M. Tomita: Biochim. Biophys. Acta* ***1784*** *(2008) 1847.*
[4] *D. Tsuchiya, N. Shimizu, M. Tomita: Biochem. Biophys. Res. Commun.* ***379*** *(2009) 485.*

Structure and Function of Stationary-Phase-Dependent Regulatory Protein from *Thermus thermophilus* HB8

In order to survive, organisms have to respond to changes in environmental conditions. These switches are mediated by alternative σ factors of RNA polymerase or transcription factors, which regulate the transcription of genes to respond to changes. Bacterial cells enter the stationary phase upon nutrient depletion. During the stationary phase, the gene expression pattern changes globally, and genes that are required for adaptation and survival, including those involved in nutrient scavenging, DNA repair, protein turnover, and protection from oxidative damage, are expressed. We performed structural and functional analyses of the transcriptional regulator SdrP (stationary-phase-dependent regulatory protein) from an extremely thermophilic bacterium *Thermus thermophilus* HB8, the mRNA expression of which increases in the stationary phase [1] (Fig. 1). Using an *sdrP*-deficient strain, we found that the strain showed growth defects, particularly when grown in a synthetic medium, and increased sensitivity to disulfide stresses although the gene was nonessential. The expression of several genes was altered in the *sdrP* disruptant. Among them, we found eight SdrP-dependent promoters using *in vitro* transcription assays. The transcription activation *in vitro* was independent of any added effector molecule. On the basis of amino acid sequences and three-dimensional structures of the protein products of the genes regulated by these promoters, we speculate that they are involved in activities such as securing nutrient and energy supply, and protecting against oxidative damage to DNA [1] (Fig. 1).

The *T. thermophilus* SdrP belongs to cyclic AMP (cAMP) receptor protein (CRP), also referred to as catabolite activator protein, CAP/fumarate and nitrate reduction regulator (FNR) superfamily proteins, which are global transcriptional regulators widely distributed in bacteria and predominantly function as activators. In many cases, CRP/FNR regulators respond to a wide range of endogenous and exogenous signals such as cAMP, anoxia, redox state, oxidative and nitrosative stress, nitric oxide, carbon monoxide, 2-oxoglutarate, and temperature [2]. The cAMP-dependent regulatory mechanism of CRP has been extensively studied for *E. coli* CRP, a prototype of this family of proteins, in which two cAMP binding sites are present in each monomer [2,3]. *E. coli* CRP is a homodimer that contains a helix-turn-helix DNA-binding motif in its C-terminal domain. CRP undergoes conformational change upon cAMP binding

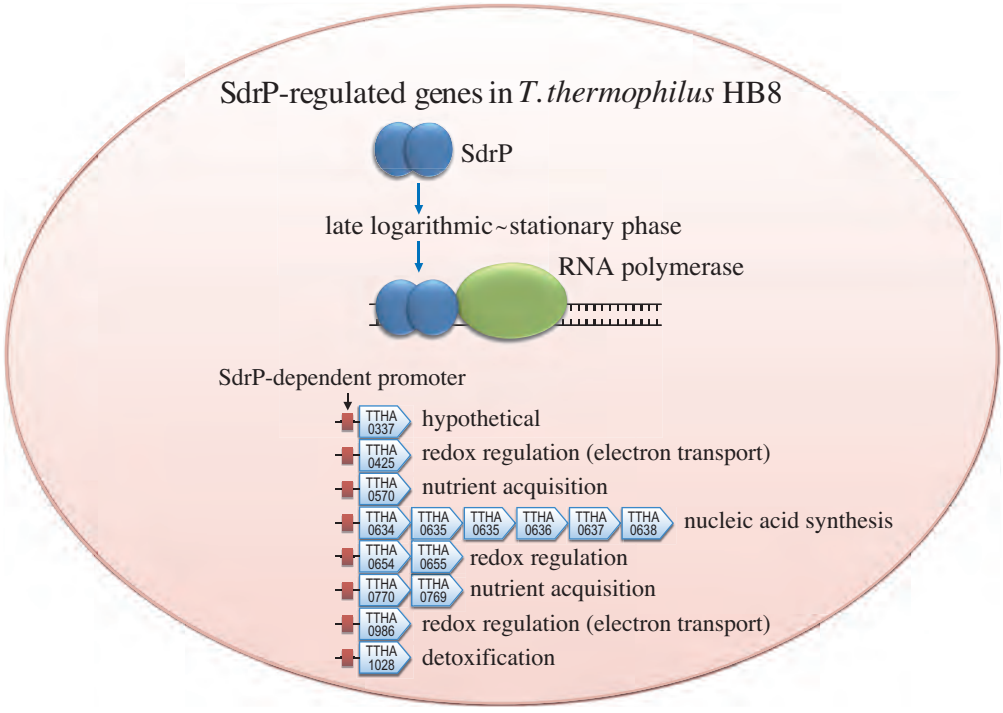


Fig. 1. Schematic representation of the activity of the *T. thermophilus* SdrP. The SdrP-regulated genes and their functions are indicated.

to the primary binding site in its N-terminal domain, and the CRP-cAMP complex interacts with a 22-bp DNA site exhibiting twofold symmetry that has the consensus sequence 5'-AAATGTGATCTAGATCACATTT-3' [4]. The N-terminal domain of *T. thermophilus* SdrP consists of one α-helix and eight β-strands that adopt a double-stranded β-helix fold with a jelly roll topology (Fig. 2(a)). The C-terminal domain of *T. thermophilus* SdrP consists of four α-helices and four β-strands that adopt a winged helix-turn-helix fold (Fig. 2(a)). These two domains are connected by a large α-helix as the linker. The three-dimensional structure of *T. thermophilus* SdrP is similar to that of the DNA-binding form of *E. coli* CRP [3]—the form complexed with cAMP and DNA—and has an r.m.s.d. of 2.3 Å (Fig. 2(b)). Superpositioning of the structure of SdrP with that of *E. coli* CRP revealed that residues G72, E73, L74, R83, S84, T128, and S129 of *E. coli* CRP, which are primary cAMP-binding sites, correspond to G59, E60, E61, R68, Y70, A106, and Y107 in SdrP (Fig. 2(c,d)). It should be noted that the side chains of E60, E61, Y70, and Y107 of SdrP penetrate into a space corresponding to the cAMP-binding pocket of *E. coli* CRP (Fig. 2(c)). The structure of SdrP suggests that cAMP cannot enter the site corresponding to the primary cAMP-binding site of *E. coli* CRP owing to steric hindrance by bulky residues. These structural properties of SdrP imply that this protein does not require an effector molecule to bind DNA, which is supported by the observation that this protein can positively regulate transcription independent of any effector molecule *in vitro*. Y70 of SdrP, which probably causes steric hindrance in cAMP binding, corresponds to S84 of *E. coli* CRP and possibly S86 of *T. thermophilus* CRP. At this position, a small residue might be necessary for a CRP family protein to act as a cAMP-dependent transcriptional regulator.

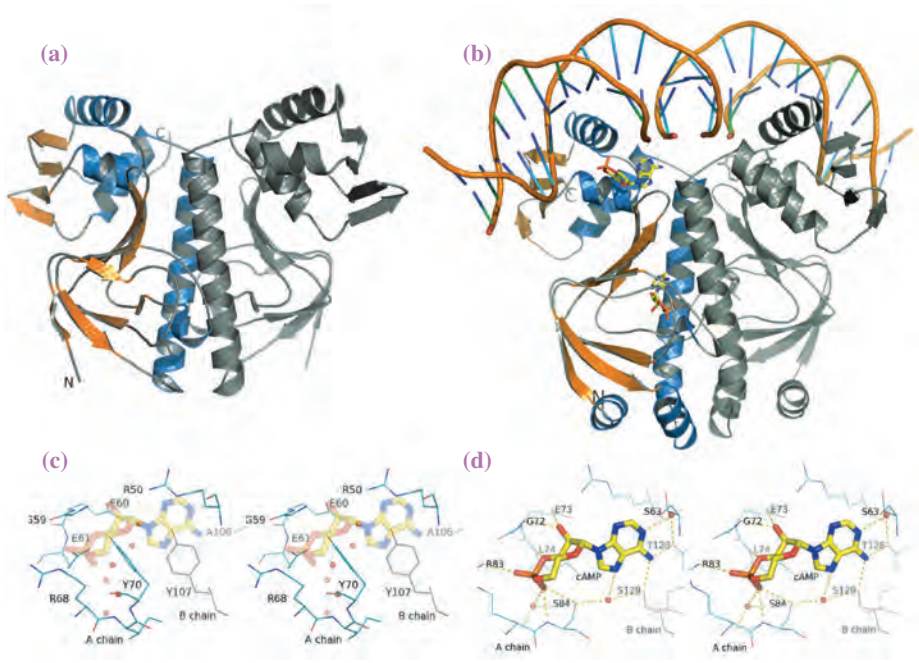


Fig. 2. **(a)** Ribbon diagram of the *T. thermophilus* SdrP dimer. The α-helices and β-strands in one chain are colored blue and orange, respectively, and the other chain is colored dark gray. **(b)** Ribbon diagram of the *E. coli* CRP-cAMP-DNA complex [3]. The color scheme is the same as in **(a)**. cAMP molecules are shown as stick models. **(c)** Stereoview of the site in *T. thermophilus* SdrP corresponding to the primary cAMP-binding site of *E. coli* CRP shown in **(d)**. A cAMP molecule of the *E. coli* CRP-cAMP-DNA complex is superimposed on SdrP as a transparent stick model. **(d)** Stereoview of the primary cAMP-binding site in the N-terminal domain of *E. coli* CRP. Residues involved in cAMP binding are labeled. A cAMP molecule is shown as a stick model.

Yoshihiro Agari and Akeo Shinkai*

SPring-8/RIKEN

*E-mail: ashinkai@spring8.or.jp

References

[1] *Y. Agari, A. Kashihara, S. Yokoyama, S. Kuramitsu and A. Shinkai: Mol. Microbiol. **70** (2008) 60.*
[2] H. Körner *et al.*: FEMS Microbiol. Rev. **27** (2003) 559.
[3] J.M. Passner and T.A. Steitz: Proc. Natl. Acad. Sci. USA **94** (1997) 2843.
[4] R.H. Ebright *et al.*: Nucleic Acids Res. **17** (1989) 10295.

Conformational Changes upon Activation of a Replication Initiator Protein, RepE

DNA replication is a fundamental and essential process for lives and is stringently regulated at the stage of its initiation. In a eukaryotic cell, genomic DNA is licensed to ensure its one-time replication during one cell-cycle by several protein complexes which are activated by other cell-cycle dependent proteins, such as CDK (cyclin-dependent kinase) [1]. The DNA replication of F plasmid in a prokaryote, *Escherichia coli*, is also controlled, which maintains the copy number of F plasmid against the host chromosome at 1 or 2. An F-plasmid encoded protein, called RepE, plays a crucial role for this regulatory mechanism. RepE has two molecular association states, that is, dimeric and monomeric states, and only the monomer can work as a replication initiator. However, RepE is usually found as an inert dimeric form in the *E. coli* cell, which functions as an autogenous transcriptional repressor [2] (Fig. 1). Both the dimer and monomer are able to bind DNA at the discrete regions, that is, the *repE* operator and iteron of the origin, respectively, in which an 8-bp DNA sequence is common. One of the other interesting points of this replication control is that the DnaK molecular chaperone system of *E. coli* is required for conversion from the RepE dimer to monomers in order to activate RepE as a replication initiator.

The crystal structure of RepE54, a monomeric RepE mutant, whose initiator activity is much higher than the wild-type protein, in complex with DNA was solved in 1999 [3] as the first crystal structure of a prokaryotic replication initiator protein (Fig. 2(a)). On the basis of this structure, it is found that RepE can be

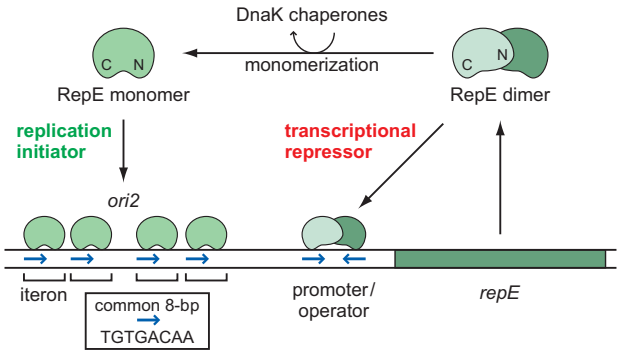


Fig. 1. Schematic draw of functions of the F-plasmid replication initiator protein, RepE. The predominant RepE dimer functions as an autogenous transcriptional repressor. RepE monomerization is mediated by the DnaK molecular chaperone system of *E. coli*. The dissociated monomer works as a replication initiator. Blue arrows indicate positions and directions of the common 8-bp DNA located in both the origin (*ori2*) and the operator region of the *repE* gene.

divided into N- and C-terminal domains related by a non-crystallographic 2-fold symmetry. The C-terminal domain interacts with the common 8-bp region, indicating that this domain is responsible for sequence-specific DNA-binding of RepE. The N-terminal domain also interacts sequence-nonspecifically with DNA, and this domain has been expected to be a scaffold of the dimeric structure. In addition, in case of dimer-to-monomer conversion, a large conformational change in the N-terminal domain has also been predicted. To elucidate structural details of this conformational change, we have determined the crystal structure of the dimeric RepE in complex with DNA using beamlines **BL41XU, BL26B1**, and **BL44B2** [4].

The crystal structure of the RepE dimer bound to the *repE* operator DNA (Fig. 2(b)) indicates structural difference as well as structural similarity between the two molecular association states of RepE. The C-terminal domain of the dimer also interacts with the common 8-bp as observed in the RepE monomer structure, while the N-terminal domain of the dimer does not contact with DNA but certainly plays a significant role for dimerization as expected. The discrete superimposition of the domain structures shows that each domain of RepE does not undergo a significant structural change during the dimer-to-monomer conversion. On the contrary, characteristic structural differences between the two molecular association states are found in a linker region tethering the two domains and in relative domain orientation. The dimer has a long α-helical structure as the domain-linker, whereas a shorter α-helix, an unstructured region and a β-strand construct the domain-linker of the monomer. This domain-linker consists of several hydrophobic residues, which should make a strong hydrophobic interaction with a hydrophobic core of the N-terminal domain. However, the domain-linker of the monomer protrudes outward from the core of the N-terminal domain, suggesting a weak interaction with the core. We think the domain-linker of the monomer can play a hinge role for alteration of the relative domain orientation compared to that in the dimeric structure.

The two crystal structures of RepE solved over the past decade in both molecular association states clearly demonstrated a conformational switch, in particular the domain-based structural transition, undertaken during the dimer-to-monomer conversion. We could also suggest a mechanism of the DnaK molecular chaperone system in dimer dissociation

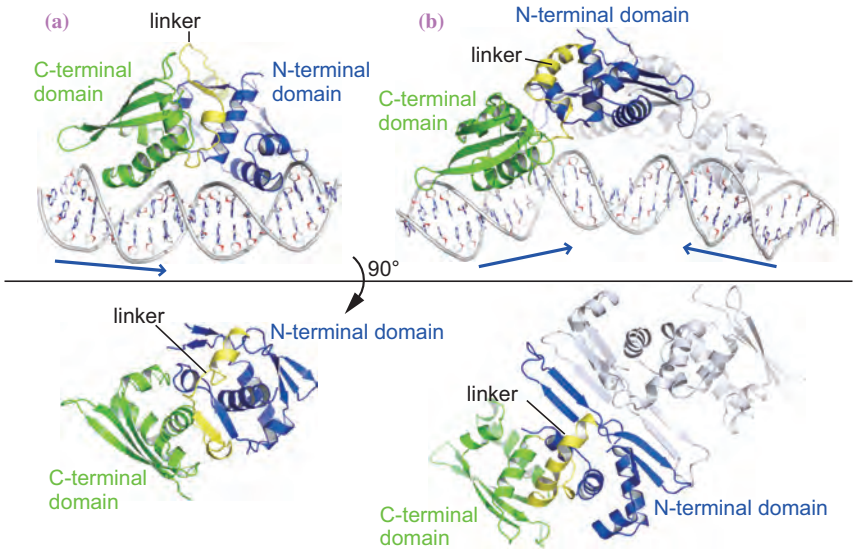


Fig. 2. Crystal structures of the RepE-DNA complexes. **(a)** Crystal structure of a monomeric RepE mutant (RepE54) in complex with the iteron DNA. **(b)** Crystal structure of the RepE dimer bound to the *repE* operator DNA. Side (upper panel) and top (lower panel) views of RepE-DNA complexes are displayed. The N-terminal domain, domain-linker, and C-terminal domain are shown in blue, yellow, and green, respectively. Blue arrows indicate the common 8-bp DNAs.

of RepE (Fig. 3). The DnaK and DnaJ proteins belonging to the DnaK system would interact with the hydrophobic region of the domain-linker and N-terminal domain of RepE, which has been indirectly indicated by sequence-dependent binding of chaperones and interaction of a homologous protein with DnaJ. The action of the DnaK chaperones may afford a structural alteration in the domain-linker of RepE, and thus variations of relative domain orientation and dissociation of the RepE dimer must be induced. With the aid of DnaK, the RepE monomer could adopt a form appropriate for origin-binding.

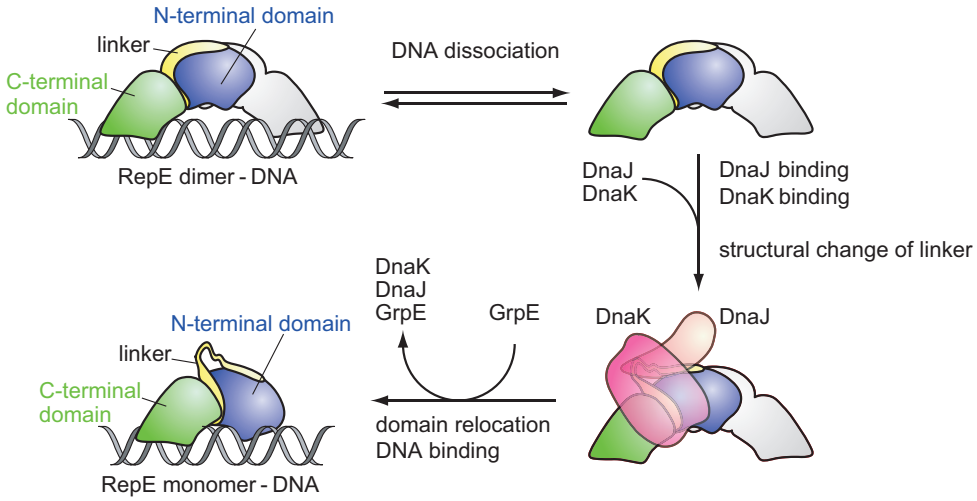


Fig. 3. Suggested activation mechanism of RepE. DnaK/DnaJ chaperone proteins would interact with the domain-linker region of RepE (upper right). Intermolecular hydrophobic interactions induce the conformational changes of the domain-linker (lower right). Structurally flexible hinge may allow domain relocation, followed by monomerization and activation of RepE.

Akira Nakamura[a] and Kunio Miki[a,b,*]

[a] Dept. of Chemistry, Graduate School of Science, Kyoto University
[b] RIKEN SPring-8 Center at Harima Institute

*E-mail: miki@kuchem.kyoto-u.ac.jp

References

[1] J.J. Blow and A. Dutta: Nature Rev. Mol. Cell Biol. **6** (2005) 476.
[2] M. Ishiai *et al.*: Proc. Natl. Acad. Sci. USA **91** (1994) 3839.
[3] H. Komori *et al.*: EMBO J. **18** (1999) 4597.
[4] *A. Nakamura, C. Wada and K. Miki: Proc. Natl. Acad. Sci. USA **104** (2007) 18484.*

Combined Study by Crystallography and NMR Reveals Structural Basis for a Reversible Switchable Fluorescent Protein

As affirmed by the 2008 Nobel Prize in Chemistry recognizing the initial discovery of green fluorescent protein (GFP) and a series of influential developments related to its biological applications, GFP and GFP-like proteins are now ubiquitous tools. The proteins enable us to visualize interesting, but otherwise invisible, phenomena such as gene expression, subcellular localization of protein, and protein-protein/DNA interaction in living cells. In recent years, interest has grown in the development of reversible switchable fluorescent proteins (RSFPs) that can be selectively and reversibly switched between a fluorescent (bright) state and nonfluorescent (dark) state by irradiation with light of appropriate wavelengths. Such ability promises more localized and/or precise studies of rapid protein movements within living cells. A successful example of RSFP includes Dronpa from the coral *Pectiniidae* [1]. Whereas Dronpa emits green fluorescence, strong irradiation at 488 nm can convert the protein into a dark state ($Dronpa^{D}$). The protein can be switched back to the original bright state ($Dronpa^{B}$) from the $Dronpa^{D}$ by brief and minimal irradiation at 403 nm. Despite the exquisiteness of the protein for not only biological application but also realization of a nondestructive read-out system, the structural basis for the reversible switching in Dronpa is still poorly understood.

To unravel the mechanisms, we determined the crystal structures of $Dronpa^{B}$ using beamlines **BL26B1**, **BL44B2** and **BL45XU** PX-station as well as 22 G, the obligate tetrameric precursor protein of Dronpa. The overall structures of both proteins were nearly identical to other GFP structures, namely, an 11-stranded β-barrel with a coaxial central α-helix holding a chromophore (so-called "β-barrel fold") (Fig. 1(b)). The chromophore formed spontaneously from the internal tripeptide Cys62-Tyr63-Gly64. The resulting 4-(*p*-hydroxybenzylidene)-5-imidazolinone moiety is typical for green-emitting GFP-like proteins. The chromophore adopted *cis* and coplanar conformation and the phenolate moiety hydrogen-bonded to Ser142. The imidazole ring of His193 was parallel to the phenolate ring of the chromophore, which is representative of a π-π stacking interaction. The structural comparison between $Dronpa^{B}$ and 22 G indicated little difference in the chromophore environment between the two proteins (Figs. 1(c) and 1(d)). This is in line with the fact that Dronpa acquired the reversible switchable ability during a mutagenesis study aimed at the monomerization of 22 G, and thus, the substituted six residues do not make direct contacts with the chromophore. Therefore, it was hypothesized that the monomeric property is essential for engineering RSFPs.

Next, we determined the crystal structure of $Dronpa^{D}$. Although the crystal of $Dronpa^{B}$ can be converted to $Dronpa^{D}$ by irradiation with a 514.5 nm argon laser at ambient temperature and turned back to the $Dronpa^{B}$ by irradiation with violet light, the electron density corresponding to the chromophore and the vicinity such as His193 in the $Dronpa^{D}$

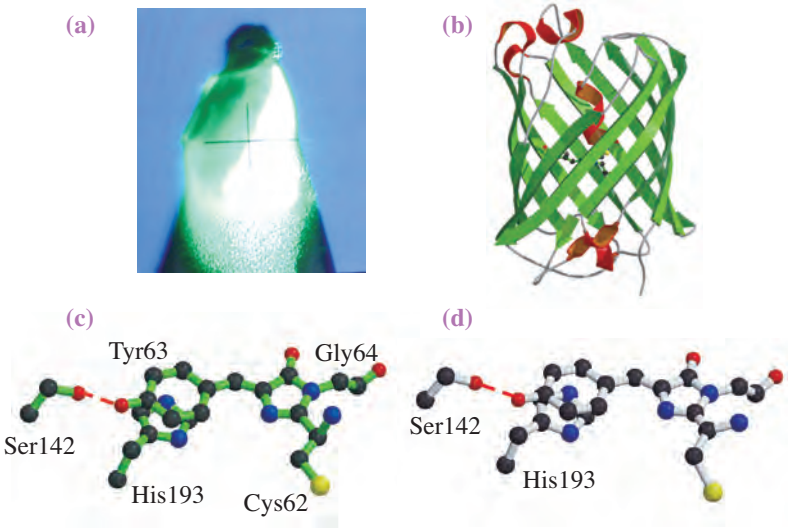


Fig. 1. **(a)** Crystal of $Dronpa^{B}$ on beamline BL44B2. **(b)** Overall structure of $Dronpa^{B}$. The chromophore is represented as a ball-and-stick model. The chromophore environments of $Dronpa^{B}$ **(c)** and 22G **(d)**. 22G is the precursor protein of Dronpa.

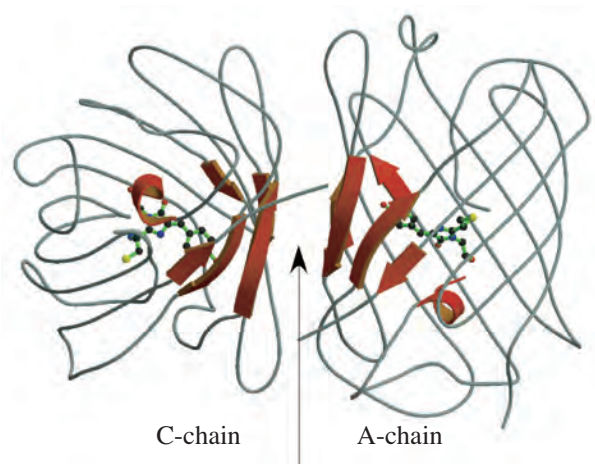


Fig. 2. Mapping of dimer interface, in which the residues in red were not sssigned to any peaks in NMR spectra of Dronpa^{D}, on the Dronpa^{B} crystal structure. The chromophores are represented as a ball-and-stick model.

structure was not well resolved, suggesting a disorder, i.e., the chromophore and surroundings may adopt various conformations in Dronpa^{D}.

Although the monomeric state of Dronpa was confirmed in solution, the crystal structure of Dronpa^{B} revealed that the crystallization of Dronpa enforced a dimer-of-dimer formation on the protein. The tetramer formation in the crystal was considered to be inappropriate for further investigation. Thus, we performed NMR analysis of Dronpa in solution at ambient temperature in combination with the crystallographic study. The NMR data conclusively demonstrated the structural flexibility around the dimer interface, where the peaks for Dronpa^{D} could not be assignable (Fig. 2). The ^{1}H-^{15}N heteronuclear sequential quantum correlation (HSQC) spectra also indicated the flexibility of a β-strand containing His193 that participated in the dimer interface. In addition, a peak for the proton assigned to the Ser142 hydroxyl group at 14.0 ppm was present in the ^{1}H NMR spectrum for Dronpa^{B} but not for Dronpa^{D}, indicating the loss of the hydrogen bond between Ser142 and the chromophore of Dronpa^{D}. Altogether, we proposed a structural basis for the reversible photoswitching in Dronpa as shown in Fig. 3; the deprotonated chromophore (phenolate form) tightly adopted the *cis*/coplanar conformation mainly because of non-covalent interactions from Ser142 and His193 in Dronpa^{B}. Upon irradiation, the chromophore is protonated (phenol form) and becomes free from the β-barrel in Dronpa^{D}. As a result, the chromophore and part of the β-barrel become flexible. The proposed mechanism focusing on the flexibility of the protein is perfectly consistent with the initial hypothesis, in which the monomeric property is essential for engineering RSFPs.

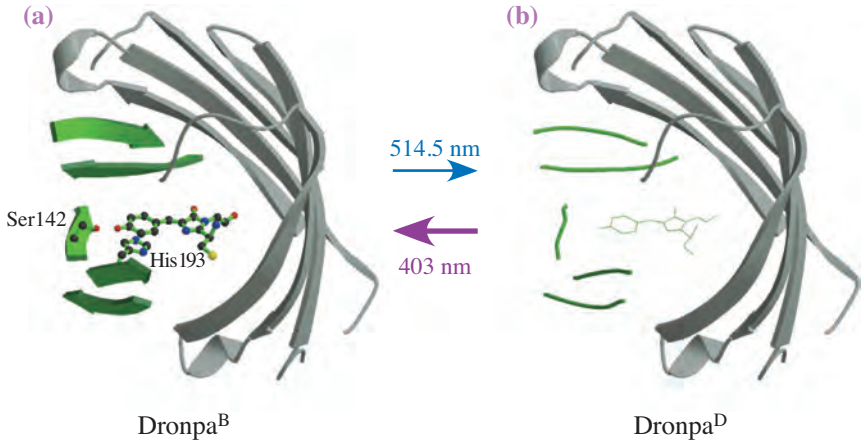


Fig. 3. Proposed mechanism for the reversible switching in Dronpa. The key to the reversible switching is a light-dependent regulation of the structural flexibility of the chromophore and part of the β-barrel in the protein. In Dronpa^{D}, strands highlighted with lime green and the chromophore are flexible **(b)**, while they have a rigid structure that is characteristic of GFP proteins in the Dronpa^{B} **(a)**, probably due to noncovalent interactions between the chromophore and surroundings such as Ser142 and His193.

Akihiro Kikuchi

SPring-8/RIKEN

E-mail: kikuchi@spring8.or.jp

References

[1] R. Ando *et al.*: Science **306** (2004) 1370.
[2] *H. Mizuno, T. K. Mal, M. Mächli, A. Kikuchi, T. Fukano, R. Ando, J. Jeyakanthan, J. Taka, Y. Shiro, M. Ikura and A. Miyawaki: Proc. Natl. Acad. Sci. USA* ***105*** *(2008) 9227.*

Life Science:



Medical Biology

The articles in this 2008 volume demonstrate the diversity of biological studies at SPring-8. Three diffraction studies in reciprocal space and three imaging studies in real space are reported.

Protein solution X-ray scattering is becoming a common tool in structural biology. Since this technique usually uses scattering data in a small-angle region, its spatial resolution is inherently low. However, Kamikubo and Kataoka proposed a method of analyzing wide-angle scattering data to obtain more detailed structure of a protein. They used photoactive yellow protein as a model. Its wide-angle scattering data contains information on secondary-structure packing and tertiary folds. By comparing scattering data from proteins with different chain lengths, they interpreted the wide-angle data and further demonstrated a change in the packing of secondary structures in the transient states of photoreception.

Matsuo and Yagi used X-ray fiber diffraction to study the regulation of contraction in frog skeletal muscles. Although the control of contraction by Ca in skeletal muscle is established, it has not been correlated in detail with the molecular changes associated with contraction. X-ray diffraction can give clues to both the binding of Ca to the regulatory protein troponin and the interaction of myosin heads with actin. The difference in the responses of these events to an electrical stimulus explains the phenomenon of summation in skeletal muscle contraction.

Kubo and her colleagues used microbeam X-ray diffraction for the structural analysis of starches in rice, the most important agricultural product in Japan. By scanning kernels of mutant rice with a 5 μm microbeam, they studied starch localization and the crystalline structure of starch. The results showed that the branch chain length of polyglucans is crucial in determining the starch crystalline structure.

There are three articles on imaging experiments. Sera overcame technical difficulties to record computed tomography (CT) images of a live mouse at different stages of cardiac and respiratory cycles. Since it is necessary to work on live animals in physiological studies, this "4D" tomography is essential for applying CT to important medical problems.

Schwenke and his colleagues used microangiography to study pulmonary arterial hypertension. They were able to visualize blood vessels down to 80 μm in diameter. The important finding is that there are few small vessels in this diseased state. This must be the causal factor for the increase in pulmonary arterial pressure.

Shinohara and his colleagues used phase-contrast tomography to examine a coronary atherosclerotic plaque. Owing to the high contrast resolution of this technique, collagen-rich and lipid-rich regions, which are important in differentiating stable and unstable plaques, were clearly visualized.

Both diffraction and imaging techniques are quite effective in studying biological structures in their native state. These articles show that SPring-8 is utilized by researchers from diverse fields of biology and medicine.

Naoto Yagi

Structural Model Construction of the Photointermediate of Photoactive Yellow Protein by High-Angle X-Ray Scattering

Solution X-ray scattering is an effective technique used for characterizing biomolecular structures and their changes in solution. The so-called *ab initio* shape prediction analysis enables us to construct a molecular envelope of a protein from an X-ray scattering profile without any assumptions. Scattering profiles of only up to $Q = 0.3$ Å^{-1}, which corresponds to a resolution of ~20 Å, are usually used in this analysis. High-angle profiles theoretically contain structural information at a high resolution, such as secondary structure packing and tertiary folds. Although the availability of third-generation synchrotron radiation sources with a two-dimensional detector has improved the quality of profiles even in the high-angle region by up to 6 Å^{-1}, high-angle scattering has not yet been applied systematically to derive solution structures. Here, we demonstrate the use of a promising method for analyzing structural changes in a protein by high-angle scattering combined with fluctuation analysis [1].

In this study, a light sensor protein, photoactive yellow protein (PYP), was used as a model protein [2]. PYP is a putative photoreceptor of a negative phototaxis in a purple phototropic bacterium, *Halorhodospira halophila*, which is composed of an N-terminal region and a chromophore-binding domain (see Fig. 1). The isomerization of the chromophore in the chromophore-binding domain upon light absorption triggers the subsequent thermal reaction. The blue-shifted intermediate PYP_M formed during the reaction is assumed to be an active state; therefore, it is essential to analyze the structural changes during PYP_M formation for the understanding of the molecular mechanism of photosignal transduction. The results of our previous studies on small-angle X-ray scattering and CD have revealed that the N-terminal region of PYP_M exhibits a deformation of its tertiary and secondary structures [3]. However, the essence of the structural changes in the chromophore-binding domain has not been clarified.

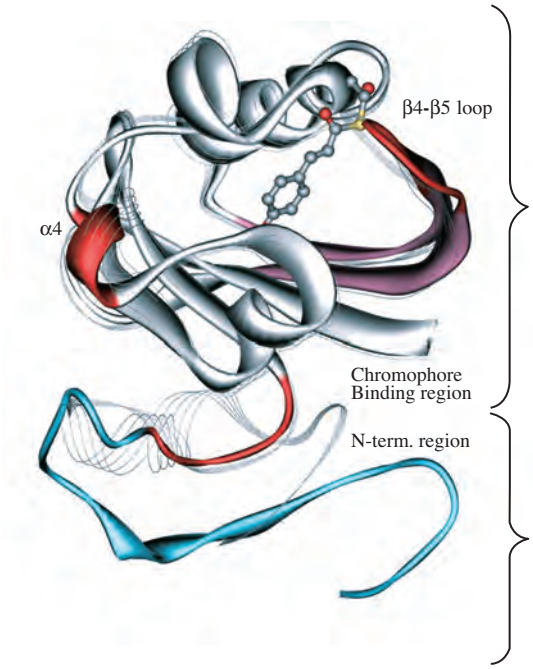


Fig. 1. Schematic model of PYP_M of the intact PYP (solid ribbon model). The crystal structure of the dark state of the intact PYP (line ribbon model) is superimposed on the model. Regions largely deviating from the dark state structure are shown in red color.

We have proposed an analytical method of high-angle scattering to characterize the tertiary structural change of PYP under illumination. In order to achieve the above-mentioned objective, we prepared several N-terminal truncated PYPs, in which the N-terminal 6 and 23 residues were cleaved by chymotrypsin treatment; these N-terminal truncated PYPs are referred to as T6 and T23, respectively. Scattering profiles of the intact PYP and the two truncated variants (T6 and T23) were observed at beamline **BL40B2** (Fig. 2(a)) [1]. The profile of the intact PYP shows two broad peaks at $Q = 0.35$ and 0.55 Å^{-1}, with a valley at around $Q = 0.41$ Å^{-1}. The peak position shifts toward a higher Q value, and concomitantly, the intensity of the peak at a high Q value decreases with an increase in the degree of N-terminal truncation. T23, which is completely devoid of the N-terminal region, exhibits a scattering profile with a single maximum around at $Q = 0.39$ Å^{-1}. These characteristic profiles indicate that the scattering profile observed in the Q region reflects the intramolecular interference. The theoretical profiles of the intact PYP, T6, and T23 well explained their respective observed profiles (Fig. 2(b)), indicating that the structures of T6 and T23 as well as that of the intact PYP can be explained by removing the corresponding residues from the crystal structure.

X-ray scattering profiles of T6 and T23 were measured under continuous illumination. Figure 3 shows the intensity profiles of the PYP_M of the truncated PYP variants compared with those obtained for their dark states. Significant differences between the two states were observed for each truncated PYP. Characteristic profile changes in T23 indicate rearrangements of the secondary structure packing in the chromophore-binding region during the formation of PYP_M. From the obtained profile, we attempted to

generate the plausible conformations of PYP_M from a variety of structures derived from the crystal structure of PYP, using the high-angle X-ray scattering profile as a boundary condition. A structural ensemble comprising 500 structures was constructed by fluctuation analysis. The high-angle scattering profile of each generated structure was calculated. While the profiles of most of the structures were similar to that of the dark state of T23 (a single broad peak at Q = 0.39 $Å^{-1}$), the profiles of some structures exhibited a bimodal shape, which was the same as that observed for the PYP_M of T23. From the structural pool, we selected structures whose scattering profiles were in good agreement with the characteristic features of the PYP_M of T23. Consequently, 51 structures from the 500 structures were selected and averaged to build a structural model of the chromophore-binding domain of PYP_M. According to this model, the loop between β4 and β5 and the α4 helix move away from each other to open the chromophore-binding pocket (Fig. 1). These structural changes agree well with the model predicted by a previous MD simulation study [4]. The schematic structural model for wild-type PYP_M can be obtained by combining the structural model of the chromophore-binding region of the PYP_M intermediate of T23 with the structural fluctuation of the N-terminal region predicted by a previous SAXS study (Fig. 1).

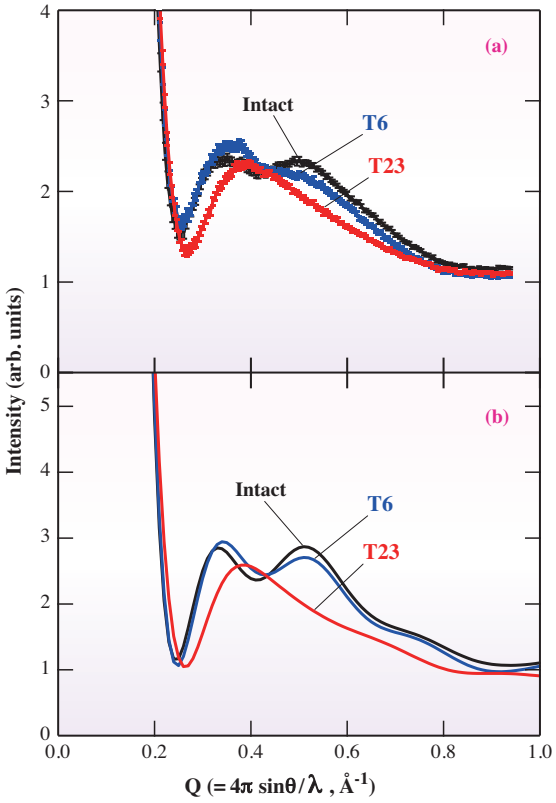


Fig. 2. High-angle X-ray scattering profiles of wild-type PYP, T6, and T23 measured in solution **(a)** and calculated from their respective atomic structural models **(b)**.

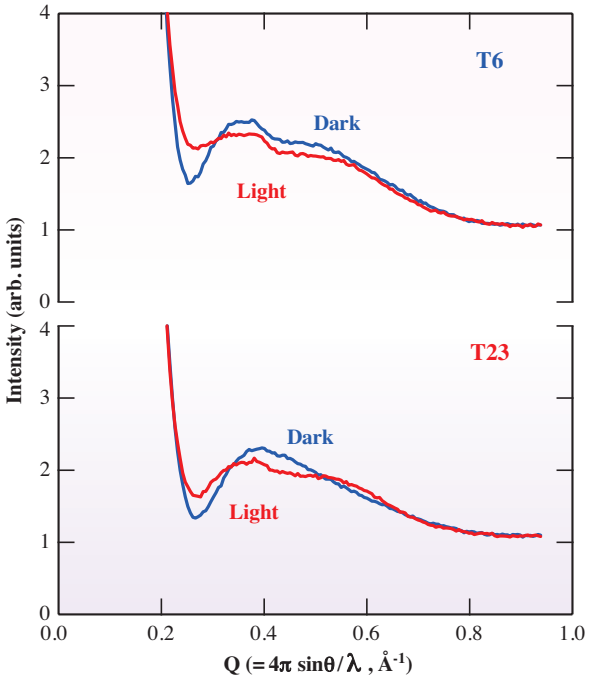


Fig. 3. High-angle X-ray scattering profiles of T6 and T23 under illumination (red). The profiles of the dark states are shown (blue) as reference.

This study confirms that high-angle X-ray scattering is quite effective and useful for determining structural properties under various solution conditions. In addition, it allows us to analyze structural changes in the transient states of proteins as well as their resting structures in solution. Fluctuation analysis combined with high-angle X-ray scattering is a promising technique for the solution structural studies of proteins.

Hironari Kamikubo* and Mikio Kataoka

Graduate School of Materials Science, Nara Institute of Science and Technology

*E-mail: kamikubo@ms.naist.jp

References

[1] *H. Kamikubo, N. Shimizu, M. Harigai, Y. Yamazaki, Y. Imamoto and M. Kataoka: Biophys. J.* ***92*** *(2007) 3633.*
[2] Y. Imamoto and M. Kataoka: Photochem. Photobiol. **83** (2007) 40.
[3] Y. Imamoto *et al.*: Biochemistry **41** (2002) 13595.
[4] M. Shiozawa *et al.*: J. Am. Chem. Soc. **123** (2001) 7445.

Structural Changes in the Muscle Thin Filament during Contraction Caused by Single and Double Electrical Pulses

Skeletal muscle undergoes a transient contraction (twitch) when stimulated by a single electrical pulse. In frog muscle, the duration of the twitch is about 100 msec at 16 °C. Skeletal muscle produces more tension when stimulated with a second pulse while the tension is high. This is called the "summation" of tension. Although this phenomenon has been known for many years [1], its molecular mechanism has not been understood clearly.

Skeletal muscle has a hierarchical structure (Fig. 1). The minimal contractile unit is called the sarcomere that consists of two kinds of filament, namely, the thin and thick filaments. The thin filament consists mainly of three proteins, namely, actin, troponin and tropomyosin. Actin is a globular protein that forms a filament to make the helical backbone of the thin filament. Tropomyosin is a rod-shaped protein that winds around the actin filament, and troponin binds to tropomyosin. The thick filament mainly consists of myosin molecules. Myosin has two globular domains (called myosin heads) and each head can bind to actin (crossbridge formation) and produce force utilizing the energy of ATP hydrolysis.

Contraction is regulated by Ca^{2+}, which is stored in an organelle called the sarcoplasmic reticulum in a muscle cell. After a stimulus, Ca^{2+} is released into the sarcomere. Troponin and tropomyoin regulate the binding of myosin to actin depending on the intracellular Ca^{2+} concentration: they inhibit the actin-myosin interaction in the absence of Ca^{2+}, but the inhibition is removed when Ca^{2+} binds to troponin. Summation may be due to an increase in Ca^{2+} concentration by repeated stimulation. However, studies with calcium-sensitive dyes showed that the intracellular Ca^{2+} concentration is not increased by repeated stimulation [2]. To verify the relation between Ca^{2+} concentration and tension, we performed a time-resolved X-ray fiber diffraction experiment that can provide information on the behavior of muscle proteins during summation [3].

The experiment was carried out at beamline **BL40XU**. The X-ray energy was 10.5 keV. The X-ray detector used was an X-ray image intensifier (V5445P, Hamamatsu Photonics) with a high-speed CCD camera (C7770, Hamamatsu Photonics). The specimen was a sartorius muscle of bullfrog. X-ray diffraction patterns were recorded at a time resolution of 1 msec during contractions caused by either single (SP) or double (DP) electrical pulses at 16 °C. In the case of DP experiments, the interval of the pulses was set at 15 msec.

The X-ray diffraction patterns from skeletal

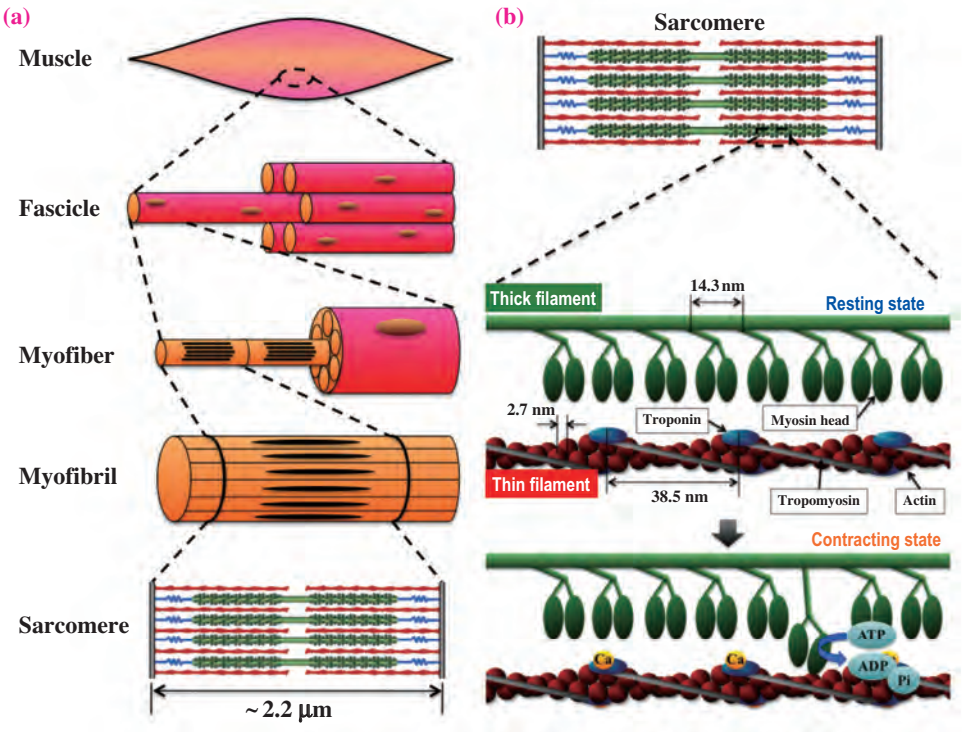


Fig. 1. **(a)** Hierarchical structure of skeletal muscle. **(b)** Schematic drawing of proteins within a sarcomere.

muscle consist of several diffraction peaks derived from the ordered array of muscle proteins in the sarcomere (Fig. 2). Figure 3 shows the time courses of the intensities of the (1,0) equatorial reflection ($I_{(1,0)}$) and the 38.5 nm meridional reflection ($I_{38.5}$). The (1,0) reflection arises from the hexagonal arrangement of the filaments and is related to the number of crossbridges. The 38.5 nm reflection arises from the regular axial arrangement of troponin molecules. In SP, $I_{(1,0)}$ decreased by 20% after the stimulus. In DP, it further decreased by 10% after the second stimulus, indicating that more crossbridges are formed, and $I_{38.5}$ increased by about 30% and then decreased as the tension developed. The initial intensity increase is considered to be due to the Ca^{2+}-induced structural change of troponin and the subsequent decrease due to crossbridge formation. In DP, $I_{38.5}$ decreased slowly after the second stimulus and dropped to about the same level as that observed in SP. This indicates that troponin molecules already undergo a maximal structural change in SP (twitch) and DP only prolongs it.

These results show that the conformational change in troponin is not enhanced by DP. Thus, the summation is not due to the increased Ca binding but due to the increased crossbridge formation. In SP, crossbridge formation takes longer than the dissociation of Ca^{2+} from troponin. Thus, only a small number of crossbridges are formed in SP. In DP, the second stimulus causes the release of Ca^{2+}, which prevents the dissociation of Ca^{2+} from troponin. Thus, more crossbridges are formed and tension looks summed. DP increases tension by maintaining troponin in the conformation that permits the actin-myosin interaction.

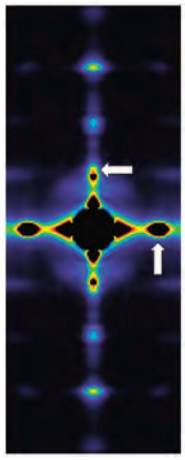


Fig. 2. X-ray diffraction pattern from frog skeletal muscle in a resting state. Muscle fibers are vertical. The horizontal arrow points the 38.5 nm meridional reflection and the vertical arrow the (1,0) equatorial reflection.

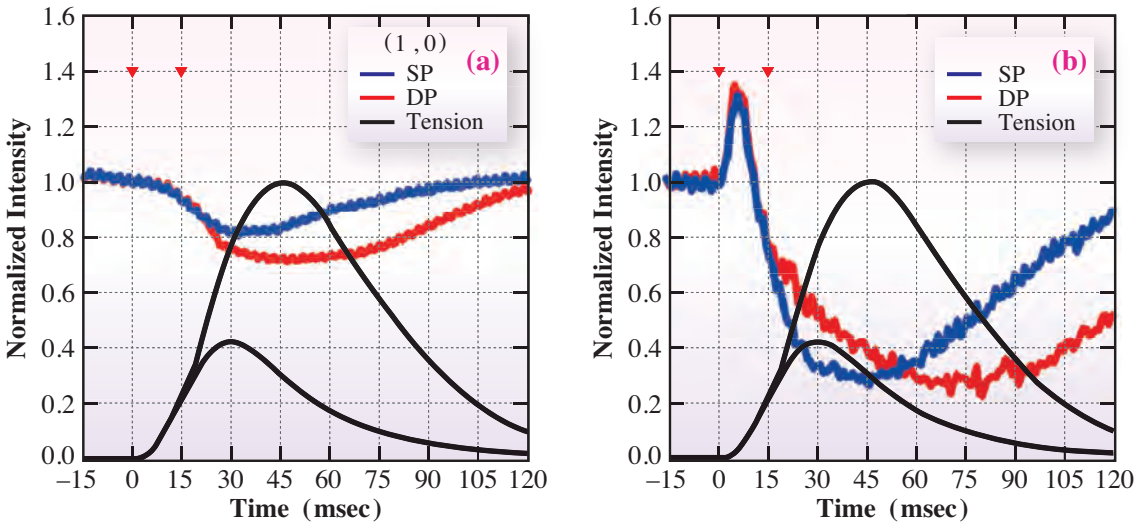


Fig. 3. Time courses of intensity changes of two diffraction peaks. The ordinate is the integrated intensity and the abscissa is time. The blue line denotes data obtained from SP experiments and the red line data obtained from DP experiments, and the black line shows tension. Red triangles indicate the onset time of the stimulus. **(a)** (1,0) reflection. **(b)** 38.5 nm reflection.

Tatsuhito Matsuo[a,b,*] and Naoto Yagi[b]

[a] Div. of Biophysical Engineering, Osaka University
[b] SPring-8/JASRI

*E-mail: tatsu@spring8.or.jp

References

[1] A.V. Hill: Proc. Royal Society of London B **138** (1951) 349.
[2] S.M. Baylor and S. Hollingworth: J. General Physiology **112** (1998) 297.
[3] *T. Matsuo and N. Yagi: J. Mol. Biol.* ***383*** *(2008) 1019.*

The Use of Microbeam X-Ray Diffraction for the Characterization of Crystal Structure of Rice Starch

Starch consists mainly of amylose and amylopectin. It occurs as water insoluble particles in the form of "starch granules" in plant tissue, and is generally classified into three types (A, B, and C) according to the wide-angle X-ray diffraction (WAXD) pattern given by their amylopectin crystalline structures. Cereal starch, including rice starch, had an A-type WAXD pattern, tuber starch a B-type, and bean and root starch a C-type (a mixture of A- and B-types) [1].

A genetic analysis using amylopectin mutants showed that a specific gene was important in determining the amylopectin structure and crystal pattern. The *amylose-extender* (*ae*) mutant, with a defect in the starch branching enzyme IIb function, accumulated starch which had a reduced ability to gelatinize due to a change in the fine structure of amylopectin with enriched long chains. The powder WAXD analysis of purified *ae* starch showed a B-type diffraction pattern, whereas wild-type rice starch showed an A-type. The *sugary1* mutant, with reduced isoamylase 1 activity, accumulated water-soluble polyglucans named as phytoglycogen. The phytoglycogen contained more short-glucan chains than wild type amylopectin, in contrast to the enriched longer glucan chains in *ae* amylopectin. In some *sugary1* lines, endosperm cells were clearly separated into a starch region and a phytoglycogen region as evidenced by iodine staining [2].

The localization of starch granules in the kernel is important, because it influences the gelatinization properties of rice. Powder WAXD analysis, which was typically used to characterize the crystalline structure of starch, tells us nothing about localization because the starch for this analysis is generally extracted and purified from tissue, destroying localization information and possibly damaging the starch granules. The aim of this study was to visualize starch localization and the starch crystalline structure by microbeam WAXD analysis.

We used mutant lines generated by treating of fertilized egg cells of japonica rice cv Kinmaze (wild type) with *N*-methyl-*N*-nitrosourea [3]. The use of double mutants that include a *waxy* (*wx*) defective gene ensures that the starch consists of essentially amylopectin, which makes up most of its crystal structure. The mature kernels from *ae*, *wx* double mutant (*wx/ae*) and *sugary1*, *wx* double mutant (*wx/sugary1*) were used as materials. The experiments were performed at beamline **BL40XU** with a high-flux beam ($\lambda = 0.083$ nm) of 5 μm in diameter. WAXD patterns were recorded using an image intensifier coupled to a cooled CCD camera [4]. 0.2 mm and 0.02 mm thick slices were cut from rice kernels using a cryostat, and the crystalline structure was scanned sequentially in constant intervals as shown by the arrows in Fig. 1.

Microbeam WAXD analysis visualized the starch localization and crystalline structure (Fig. 2). Amylose-free starches in the native rice kernels of the *wx* and *wx/ae* mutants showed A- and B-type WAXD patterns, respectively, with no difference between the outer and inner regions of the patterns. In contrast, the *wx/sugary1* mutant kernel showed an A-type diffraction pattern in the outer region and amorphous in the inner region. The higher intensity at small angles in the outer regions of *wx/sugary1* (scanning positions near 0 and near 1600) is likely due to scattering derived from density fluctuations in *sugary* amylopectin clusters. A chain-length distribution analysis of polyglucans in wild type and mutant kernels showed that *ae* amylopectin had more long chains and fewer short chains than the wild type and *waxy* amylopectin. In the *wx/sugary1* kernel, the phytoglycogen in the inner region had many more short chains than the amylopectin in the outer region had. These results indicate that the branch chain length in polyglucans is crucial in determining the starch crystalline structure [5].

Several lines of *ae* mutants with mutations at same locus but with varying phenotypes have been isolated previously. The starch from *ae* mutant line EM16 was a typical B-type detected by powder WAXD but that from EM129 was C-type. When microbeam WAXD analysis was applied to the EM129 kernel,

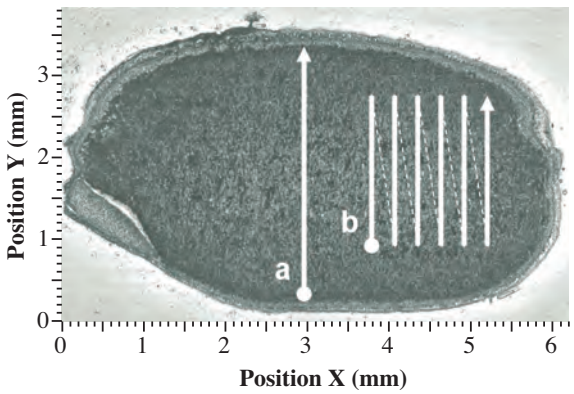


Fig. 1. A rice kernel slice of wild type under the microscope. WAXD profiles were scanned linearly **(a)** or two-dimensionally **(b)**.

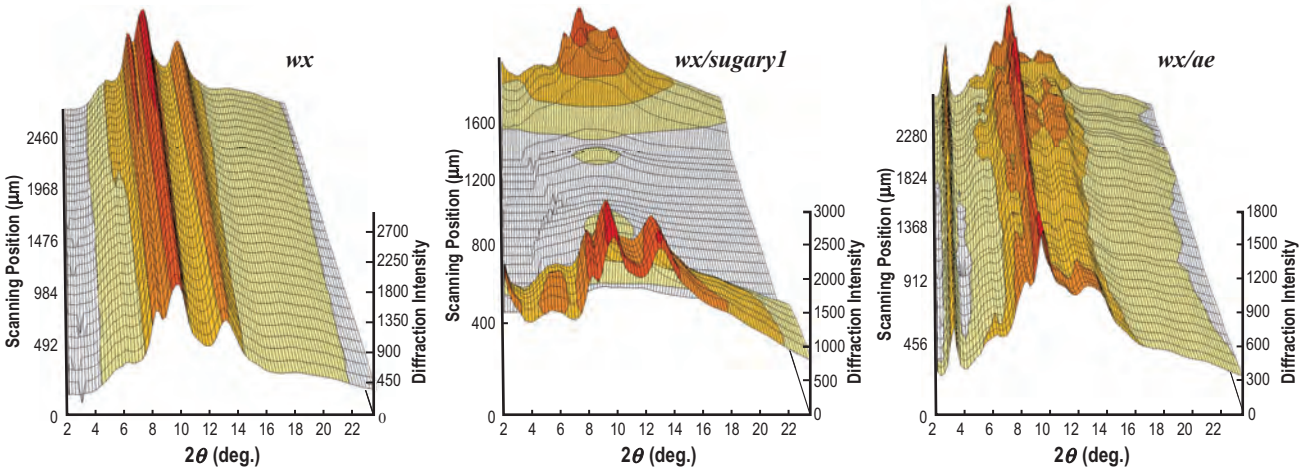


Fig. 2. Microbeam WAXD profiles of rice kernel starch granules. Diffraction patterns were recorded sequentially at intervals of 25 μm along the arrow **(a)** in Fig. 1.

C-type diffraction patterns scanned at different positions were classified to Ca- and Cb-type (Fig. 3). This result agreed with the idea that the C-type is the mixture of A- and B-type crystalline structures [1]. We did not observe any pattern in the regional distribution of Ca- and Cb-type starch. In conclusion, microbeam WAXD is a useful method to map the distribution of starch crystalline structures in the rice kernel.

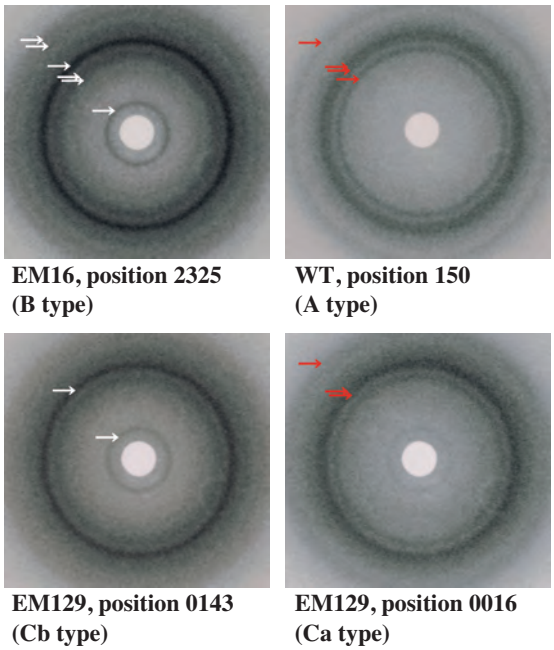


Fig. 3. Microbeam WAXD patterns detected using thin slices (20 μm). Diffraction patterns were recorded as shown in **(b)** of Fig. 1. White and red arrows show B- and A-type specific signals, respectively. C-type patterns from an *ae* kernel of EM129 were classified as Ca- and Cb-type.

Akiko Kubo[a], Yoshiaki Yuguchi[b] and Shinichi Kitamura[a,*]

[a] Graduate School of Life and Environmental Sciences, Osaka Prefecture University
[b] Faculty of Engineering, Osaka Electro-Communication University

*E-mail: skita@bioinfo.osakafu-u.ac.jp

References

[1] Hizukuri *et al.*: Nature **192** (1961) 239.
[2] Kubo *et al.*: Plant Physiol. **121** (1999) 399.
[3] Satoh *et al.*: J. Fac. Agr. Kyushu Univ. **24** (1979)165.
[4] Ohta *et al.*: J. Appl. Cryst. **38** (2005) 274.
[5] *A. Kubo, Y. Yuguchi, M. Takemasa, S. Suzuki, H. Satoh, S. Kitamura: J. Cereal Sci. **48** (2008) 92.*

High-Resolution 4D *In Vivo*-CT for Visualization of Cardiovascular and Respiratory Motion of Small Animals

We have constructed a high-resolution, computed tomography (CT) system that can visualize the motion and deformation of the heart, coronary arteries and small airways of live small animals (rat and mouse), which are most often used as models for human diseases [1].

In the past five years, several systems based on micro-CT have been proposed and developed for imaging the heart and lungs of live small animals, but none had enough resolution to detect the motion of coronary arteries and small airways. To obtain high-resolution CT images, the animal needs to be as still as possible. In the visualization of a live animal, breathing and cardiac motion cause serious motion artifacts in the reconstructed images, including blurring of the lung and heart. When imaging the heart, the movement of the lung needs to be minimized, and vice versa. Thus, the images need to be collected under a certain well-controlled condition.

The *in vivo*-CT system was constructed in the medical imaging beamline **BL20B2**. This system consists of a precision rotation stage, a high-resolution image detector (1 pixel = 12 μm), an X-ray shutter, a mechanical ventilator, an electrocardiogram (ECG) recorder, and PCs. To avoid the artifacts caused by breathing and heartbeats, the projection images were acquired prospectively in synchrony with respiratory and cardiac gatings. The sample rodent was anaesthetized, put onto a ventilator, and connected to the ECG recorder. To visualize the lung, we acquired data at controlled iso-airway pressures between heartbeats. To visualize the heart and arteries, a contrast agent was injected into the tail vein, and image acquisition was timed at the end of breath expiration. In both imaging procedures, the total scan time was approximately 10 min.

We are the first to visualize the deformation of the coronary arteries, aortic valves (Fig. 1), and small airways down to 125 μm in diameter (Fig. 2) of a live

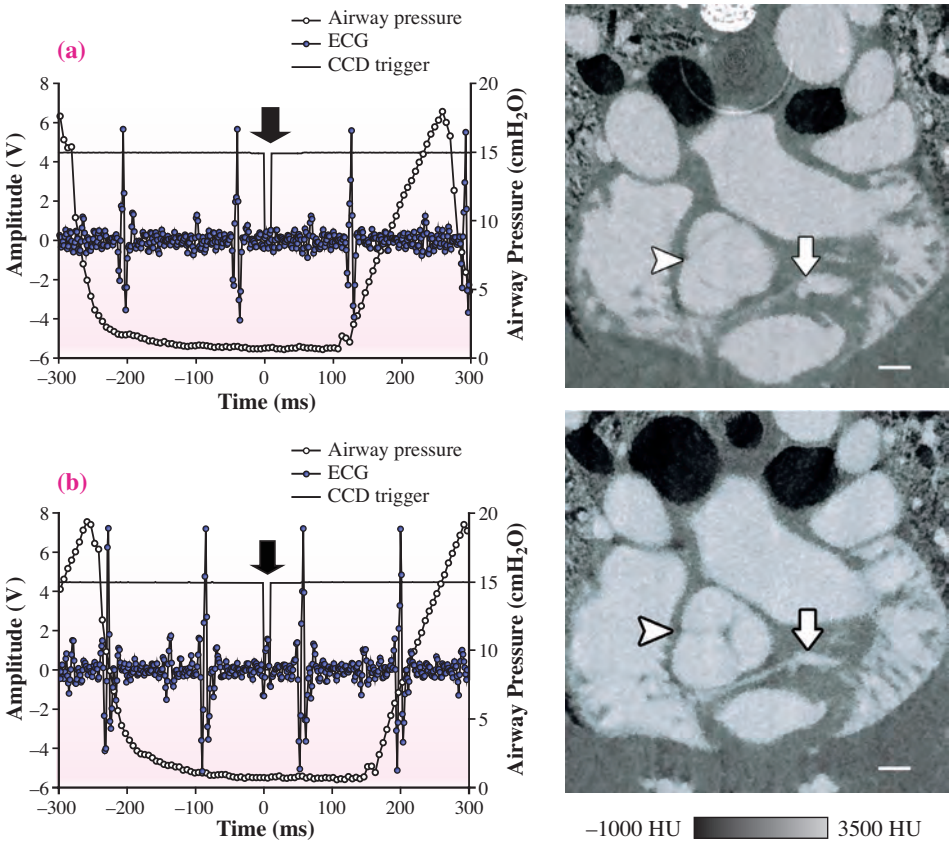


Fig. 1. Left: Timing charts of the time-resolved CT imaging. The airway pressure was controlled using a ventilator and repeated every 560 ms. The heart was beating spontaneously and the ECG was monitored. The X-ray exposure was made at a selected time (indicated by the black arrows) in the respiratory and cardiac cycles, which was at 45 ms **(a)** or 95 ms **(b)** after the R peak in the ECG. The exposure time was 10 ms. Right: axial images of the coronary arteries (arrows) and aorta valves (arrow heads) of a mouse recorded at the time shown in the timing diagrams. The diameters of the coronary arteries are 444 μm in **(a)** and 288 μm in **(b)**. Bar: 500 μm.

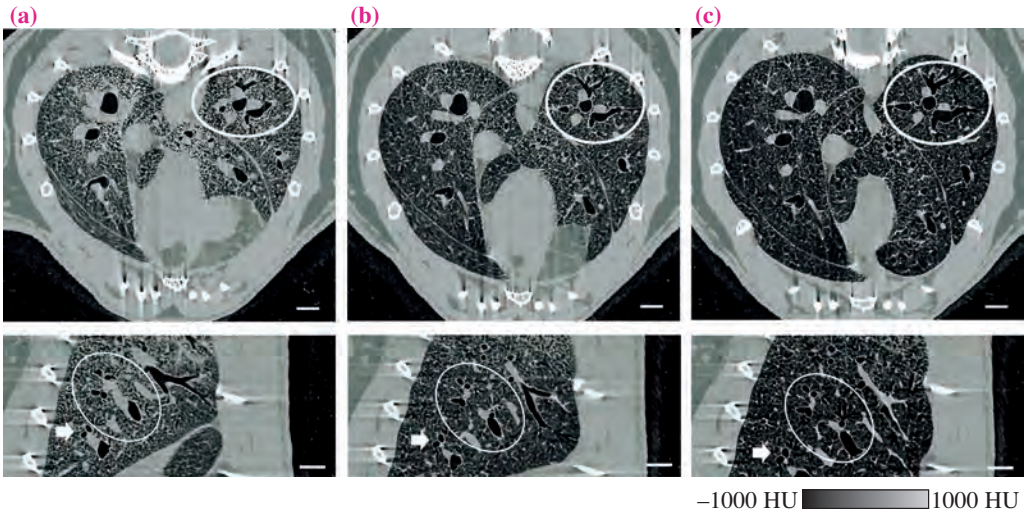


Fig. 2. Representative axial (top) and sagittal (bottom) images of a mouse chest recorded at different airway pressures: 0 cmH_2O (minimum pressure, **a**), 5 cmH_2O (during inspiration, **b**), 15 cmH_2O (maximum pressure, **c**). The circles and arrows show the deformation of the same airways. Bar: 1 mm.

mouse with acceptable radiation risk. To test the applicability of this 4D *in vivo*-CT system, we measured the airway diameters at different pressures. The results (Fig. 3) show that the change in diameter is large for small airways, and indicate that airways do not behave homogeneously *in vivo*. These high-resolution images taken at different phases of dramatic motions will allow the calculation of gas exchange in small airways, and of shear stress in blood vessels.

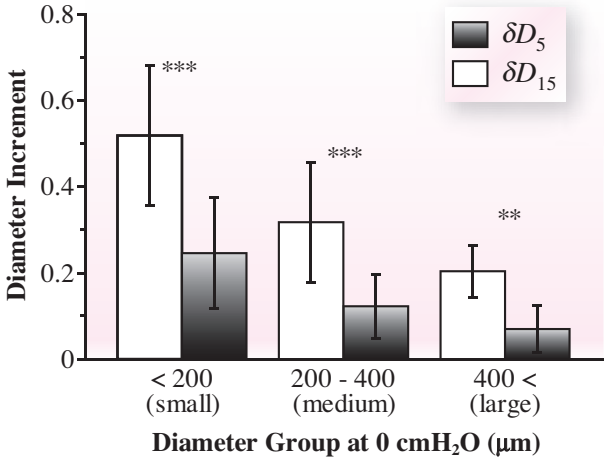


Fig. 3. Changes in the airway diameters of a mouse lung during inspiration. The airways were classified into three groups according to their diameters at an airway pressure of 0 cmH_2O: small (smaller than 200 μm), medium (between 200 and 400 μm), and large (larger than 400 μm). Relative increases in the diameter of each airway were measured at 5 cmH_2O (dark bars) and 15 cmH_2O (white bars). The airways with small diameters expand more than those with large diameters.

Toshihiro Sera

Computational Biomechanics Unit, RIKEN (Wako)

E-mail: sera@riken.jp

References

[1] *T. Sera, H. Yokota, K. Fujisaki, H. Tachibana, K. Uesugi, N. Yagi, R. Himeno: Physics in Medicine and Biology* ***53*** *(2008) 4285.*

Assessment of the Pulmonary Circulation in Health and Disease using Synchrotron Radiation Microangiography

Pulmonary arterial hypertension (PAH) is characterized by the irreversible remodeling and medial thickening of small peripheral pulmonary arteries (<500 μm), causing a reduction in vessel internal diameter (ID) and, consequently, an increase in pulmonary vascular resistance. The subsequent increase in the workload of the heart enhances the risk of heart failure and is, therefore, closely associated with an increased mortality.

Despite decades of research, the structural and functional changes of the pulmonary vasculature during the pathogenesis of pulmonary arterial hypertension (PAH) still remain to be fully elucidated. One of the limitations in understanding the pathology of the lung has been the inability to clearly visualize blood flow within the pulmonary vascular bed. Conventional angiography systems, which have previously been used for visualizing pulmonary vessels, have considerable resolution limitations so that protocols are limited to i) open-chest models that expose the lung, and ii) images of vessels no smaller than 200 μm.

In the last decade, technological advances in microangiography have utilized monochromatic synchrotron radiation (SR) as a powerful X-ray source, providing the ability to study microvessels of various organs in unprecedented detail. In contrast to conventional systems, SR is characterized by high brilliance and extreme collimation, allowing enhanced sensitivity to contrast material and superior image quality. Therefore, we have utilized the high definition X-ray source of SR at **BL28B2** beamline to visualize the pulmonary microvessels within an intact-chest rat model - a technique not previously possible with conventional X-ray systems.

Rats were anesthetized and surgically prepared as previously described [2]. Rats were positioned in front of the beam pathway, so that the synchrotron beam passed, from anterior to posterior, through the rat thorax and ultimately to a biomedical imaging SATICON X-ray camera (Fig. 1). An iodinated contrast agent (Iomeron 350) was injected at high-speed (0.4 ml @ 0.4 ml/s) into the right ventricle so as to provide a concentrated dose of agent within the pulmonary vasculature to ensure optimal contrast of microvessels.

Using SR, we could clearly visualize pulmonary vessels, ranging from the main axial artery (~1200 μm) to the 4th generation of branching (~100-200 μm), in the left lung of an intact-chest rat (Fig. 2(a)). The smallest vessels that could be clearly measured were ~80 μm. This resolution is suitable for the purpose of the present study because the majority of vessels responsible for an increase in vascular resistance in pathological conditions generally have an ID between 50 μm and 300 μm [2-4].

Subsequently, we imaged the pulmonary vasculature of rats with PAH. PAH was induced by exposing rats to chronic hypoxia (10% O_2) for 4 weeks [1]. Compared to the normal lung, we observed significant structural and functional differences in the hypertensive lung. Importantly, PAH-rats had significantly fewer perfused 3rd and 4th generation vessels (9 and 16 vessels, respectively) compared to normal-rats (14 and 30 vessels, respectively) (Fig. 2(a) *vs.* 2(b)). This reduction in parallel blood flow in the hypertensive lung is the leading causal factor for the increase in pulmonary vascular resistance and, consequently, pulmonary arterial pressure.

The pulmonary vascular reversibly constricts in response to acute hypoxia. Therefore, we were able to assess functional dynamic changes in pulmonary reactivity. We observed that acute exposure to hypoxia (8% O_2 for 4 min) caused a significant decrease in the ID of all vessels less than 500 μm,

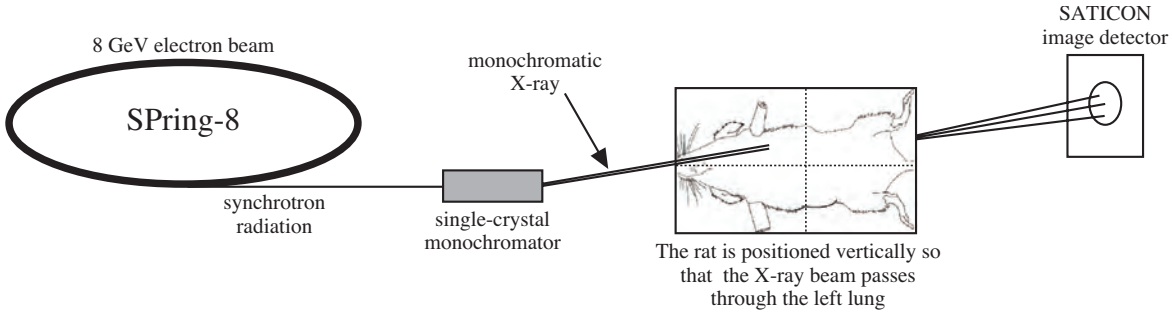


Fig. 1. A simplified schematic diagram showing the experimental set-up for pulmonary microangiography in a closed-chest rat model using SR.

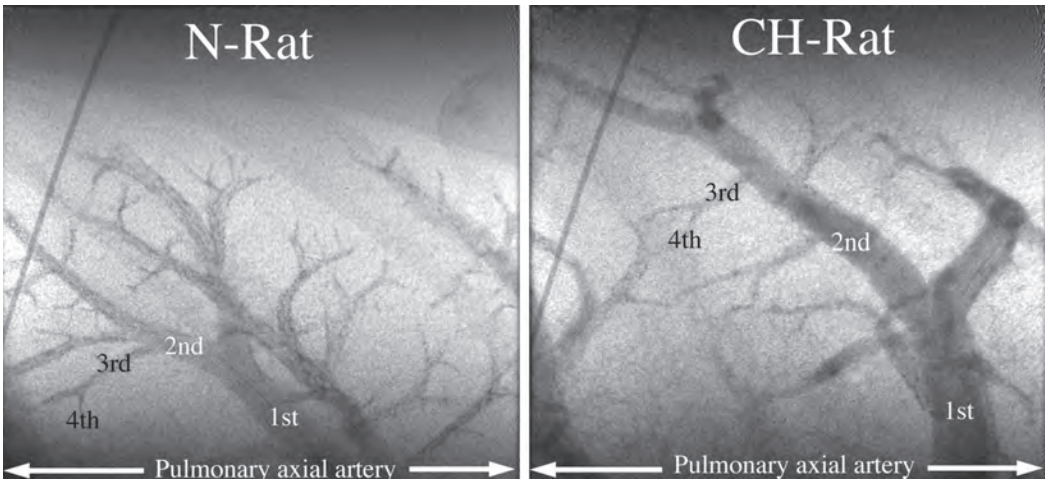


Fig. 2. Typical microangiogram images showing the branching pattern of small pulmonary arteries in **(a)** normal rats (N-Rat) and **(b)** hypertensive rats (CH-Rat). Pulmonary branches to the 4th generation from the left main axial artery (not in the image) were visible. The tungsten wire in the top left corner of each image is a reference of 100 μm diameter.

most noticeably in the 200-300 μm vessels (Fig. 3) - similar for both normal and PAH rats.

In summary, the use of SR provides a powerful tool for visualizing the pulmonary circulation in a closed-chest rat model. Furthermore, the high definition of SR permits detailed evaluation of the dynamic changes associated with acute pulmonary vasoconstriction and, more importantly, the gross structural changes in pulmonary vessel density of the hypertensive lung. Of particular importance, future use of SR will provide an effective method for assessing potential therapeutic treatments for PAH.

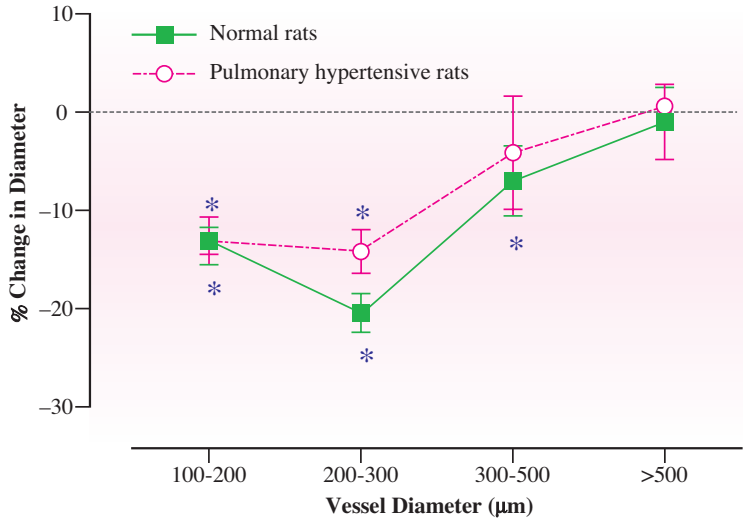


Fig. 3. The relationship between vessel size and the magnitude of pulmonary vasoconstriction (% decrease in vessel diameter) in response to acute hypoxia (8% O_2 for 4 min) in normal rats (n = 5) and pulmonary hypertensive rats (n = 5). * Significant vasoconstriction response to acute hypoxia ($P<0.05$).

Daryl O. Schwenke[a,*], Keiji Umetani[b] and Mikiyasu Shirai[c]

[a] Dept. of Physiology, University of Otago, New Zealand
[b] SPring-8/JASRI
[c] Faculty of Health Sciences, Hiroshima International University

*E-mail: daryl.schwenke@stonebow.otago.ac.nz

References

[1] *D.O. Schwenke, J.T. Pearson, K. Kangawa, K. Umetani and M. Shirai: J. Appl. Physiol.* ***104*** *(2008) 88.*
[2] D.O. Schwenke *et al.*: J. Appl. Physiol. **102** (2007) 787.
[3] R. Tokiya *et al.*: Acad. Radiol. **11** (2004) 1039.
[4] T. Yamashita *et al.*: Circ. J. **66** (2002) 1057.

Atherosclerotic Plaque Imaging using Phase-Contrast X-Ray Computed Tomography

Cardiovascular diseases are main life-threatening diseases in advanced countries. In particular, acute myocardial infarction often leads to sudden cardiac death. Prediction and prevention of this disease are strongly required in cardiovascular fields.

Recent studies revealed that there are mainly two different kinds of coronary atherosclerotic plaque: stable and unstable plaques. Stable plaque (Fig. 1(a)) consists of mainly collagen and smooth muscle cells. On the other hand, unstable plaque (Fig. 1(b)) consists of large lipid deposition, many infiltrating macrophages, and a thin collagen and smooth muscle cell layer (fibrous cap) that covers the lipid pool core. Unstable plaque often induces inflammatory changes near thin fibrous cap, and activated proteases weaken the fibrous cap and induce sudden rupture of unstable plaque. The lipid core contains many thrombogenic factors; therefore, the rupture of unstable plaque subsequently obstructs coronary blood flow, resulting in acute myocardial infarction. Clinical evidence suggests that plaque components rather than the severity of luminal stenosis are important predictors of plaque stability and clinical events.

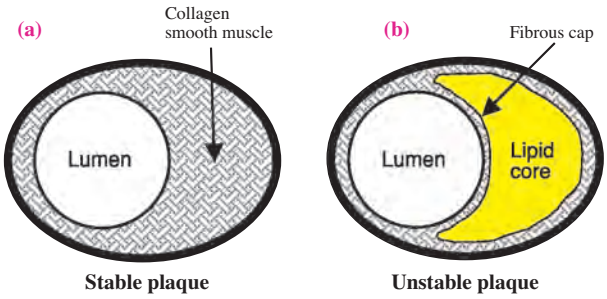


Fig. 1. Schematic diagram showing comparison of the characteristics of "stable" **(a)** and "unstable" **(b)** plaques.

Invasive investigations using a catheter technique can reveal the plaque volume and components. However, reliable noninvasive imaging modalities for the characterization of plaque components are clinically desirable. Currently, two emerging and promising techniques, namely, computed tomography (CT) and magnetic resonance imaging (MRI), are widely used by the medical community because they are noninvasive and have the potential to evaluate luminal stenosis and characterize plaque components. Technical developments over the past several years, especially the introduction of multislice CT scanners, have made coronary CT angiography quite reliable. However, the discrimination of noncalcified plaque components remains difficult. Noncalcified atherosclerotic plaques mainly consist of deposited lipids, inflammatory cells, smooth muscle cells, and collagen. The present clinical X-ray CT is based on absorption-contrast X-ray imaging, in which images are generated by the differences in X-ray absorption as determined by the linear attenuation coefficient. The differences in the X-ray absorption by biological soft tissues are very small, and therefore, the present X-ray CT is not highly sensitive in differentiating plaque components.

X-rays have the nature of waves, and the shift of the wave when it passes through an object is called the X-ray phase shift. Phase-contrast X-ray imaging has great potential to reveal the structures inside soft tissues because the sensitivity of this method to light elements is almost 1000 times greater than that of the absorption-contrast X-ray method. The purposes of this study were to image atherosclerotic lesions by phase-contrast X-ray CT [1] and to investigate whether this method could identify differences in plaque components that would lead to the detection of unstable atherosclerotic plaques.

The interferometric phase-contrast X-ray imaging experiments were performed at beamline **BL20XU** [2]. A sample cell filled with water was inserted into the beam path. Interference patterns were detected using a charge-coupled device (CCD) detector with a 10-μm luminescent screen and lens coupling. The CCD chip

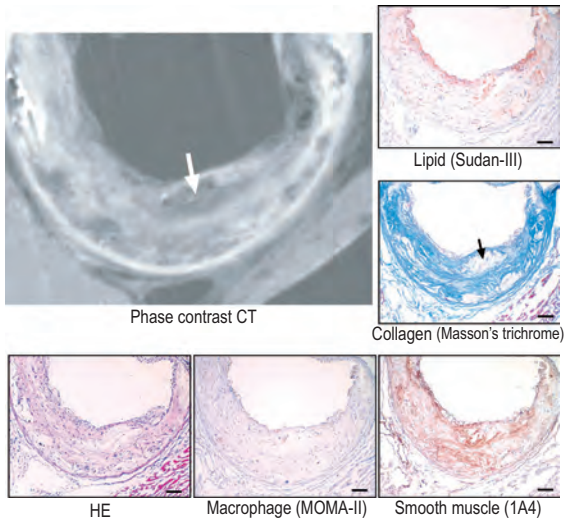


Fig. 2. Representative atherosclerotic lesion in the aortic sinus of the ApoE-KO mouse fed a normal diet. This lesion was investigated using phase-contrast CT; HE, Sudan-III, and collagen (Masson's trichrome) staining; and anti-macrophage (MOMA-II) and anti-smooth muscle (1A4) immunohistochemistry. Scale bars indicate 100 μm.

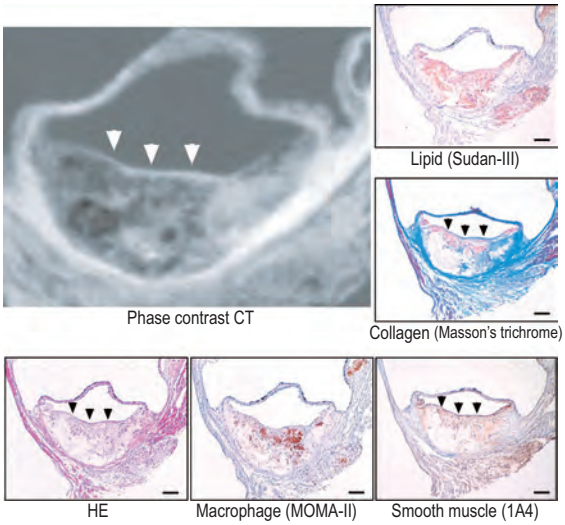


Fig. 3. Representative atherosclerotic lesion in the aortic sinus of the ApoE-KO mouse fed a high cholesterol diet for eight weeks. This lesion was investigated using phase contrast CT; HE, Sudan-III, and collagen (Masson's trichrome) staining; and anti-macrophage (MOMA-II) and anti-smooth muscle (1A4) immunohistochemistry. Scale bars indicate 100 μm.

had 3.14 μm × 3.14 μm pixels. The X-ray energy was set at 12.4 keV.

Atherosclerotic model mice, apolipoprotein E-deficient mice (ApoE-KO mice), were fed a normal diet or a high cholesterol diet. A high cholesterol diet was used to induce unstable like atherosclerotic lesions in mice.

Atherosclerotic lesions were fixed, and *ex vivo* investigations were performed by phase-contrast X-ray CT and histological analysis. Figure 2 shows a representative atherosclerotic plaque in a normal diet-fed ApoE-KO mouse and Fig. 3 that in a high cholesterol diet-fed ApoE-KO mouse. In the normal diet-fed ApoE-KO mouse (Fig. 2), the lipid plaque component was small and limited to its luminal surface. Almost the entire plaque area was positively stained by Masson's trichrome, showing that collagen is the main component of this plaque. Immunohistochemical analysis using 1A4 demonstrated the infiltration of smooth muscle cells into the plaque. Phase-contrast CT images as well as histological analyses enable the characterization of plaque components. The low refractive index (dδ) area in one of the CT images (arrow) corresponded to the area of low collagen content, as revealed by Masson's trichrome staining.

On the other hand, in the high cholesterol diet-fed ApoE-KO mouse (Fig. 3), Sudan-III staining showed that atherosclerotic plaque formed a large lipid pool. A strong invasion of many macrophages was indicated by MOMA-II immunohistochemistry. The low-dδ area in the CT image also corresponded to the less or no collagen-containing area, and it was filled with a large amount of lipid. Phase-contrast CT imaging can reveal the differences in atherosclerotic plaque components, particularly the lipid component.

For the quantitative analysis of the mass density of plaque components, the refractive indices dδ of these three components were measured. The measured dδ values and their association with mass densities are shown in Fig. 4. Phase-contrast X-ray CT can directly estimate tissue-mass density and reveal very small differences in mass density among the atherosclerotic plaque components.

The phase-contrast X-ray CT technique can achieve a higher sensitivity than absorption-contrast X-ray CT imaging for the evaluation of biological soft tissues and provide a new quantitative parameter - the "tissue-mass density."

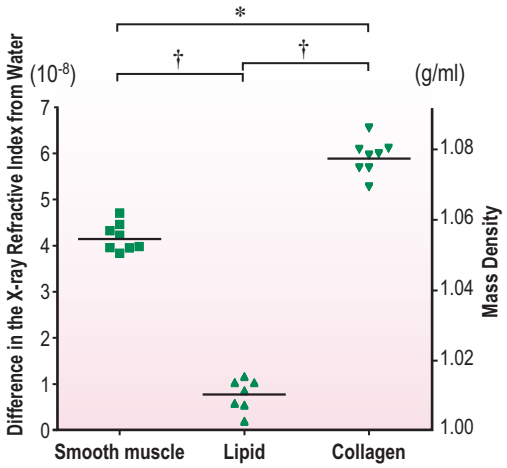


Fig. 4. The mean dδ values and specific mass densities of the various components of atherosclerotic plaques. *, P<.05; †, P<.01.

Masakazu Shinohara[a,*], Ken-ichi Hirata[a] and Atsushi Momose[b]

[a] Dept. of Internal Medicine, Kobe University Graduate School of Medicine
[b] Department of Advanced Materials Science, The University of Tokyo

*E-mail: shinodoc@med.kobe-u.ac.jp

References

[1] A. Momose *et al.*: Nat. Med. **2** (1996) 473.
[2] *M. Shinohara, T. Yamashita, H. Tawa, M. Takeda, N. Sasaki, T. Takaya, R. Toh, A. Takeuchi, T. Ohigashi, K. Shinohara, S. Kawashima, M. Yokoyama, K. Hirata and A. Momose: Am. J. Physiol. Heart Circ. Physiol.* ***294*** *(2008) H1094.*

Materials Science:

In situ structural investigation is one of the most attractive research areas in materials science, in which synchrotron radiation science can make significant contributions with highly specific light source characteristics. The first experiment regarding a nanosecond-scale time-resolved pump and probe X-ray diffraction in SPring-8 has been conducted for the phase change phenomena of digital versatile disc-random access memory (DVD-RAM) materials, as reported by Kimura *et al*. This experiment was carried out using the "X-ray pinpoint structural measurement" system developed at the BL40XU high-flux beamline. The system enable a picosecond time-resolved X-ray diffraction experiment using submicron scale beams and may expand of outcomes for the investigation of pinpointed information on chemical reactions. Nikulin *et al*. reported "Towards *in situ* X-ray diffraction imaging at the nanometer scale: Early detection of nanoparticle growth in light metal alloys," which is a nano-application of the 2D reciprocal space map (RSM) method developed by O. Sakata at BL13XU. Saitoh *et al*. performed an elaborated experiment, "*In situ* X-ray diffraction measurement of hydrogenation and dehydrogenation of Al at high pressure and temperature," at BL14B1. Tsutsui *et al.* explored the potential of "skutterudite" to become a novel thermoelectric material by high-resolution inelastic X-ray scattering (IXS) at BL35XU and reported "Direct observation of motion in atom cage."

In addition, the number of structural research studies on novel-functional nanosized materials has been increasing continuously. Zheng *et al*. reported their work, "Giant negative thermal expansion in magnetic nanocrystals," which is another structural research on nanomaterials conducted to create novel thermoelectric materials. Very recently, Kitagawa *et al*. successfully created a unique nanoparticle structure, that is, Pd(core)/Pt(shell), as a new type of hydrogen storage material and carried out *in situ* characterization at BL02B2 through hydrogen absorption/desorption. From the viewpoint of uniqueness, the results obtained in the study entitled "Rational design of iron oxides with square planar coordination" by Kageyama *et al*. is significant, indicating that the potentials of novel iron-oxide-related materials should be explored.

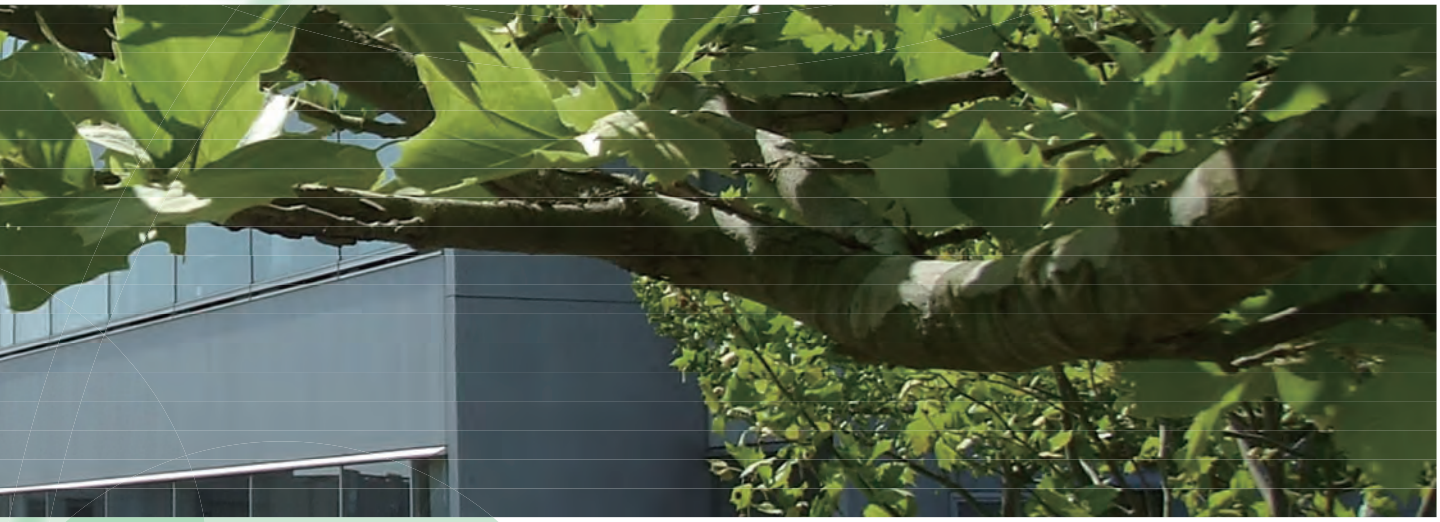


STRUCTURE



Finally, the work conducted by Tanaka *et al*. on "Helical X-ray probe crystal chirality," is the first successful attempt at investigating the crystal chirality of the quartz by a resonant X-ray diffraction experiment using polarized X-ray beams with the newly developed soft X-ray diffractometer at RIKEN beamline BL17XU. This new diffractometer is quite promising and widely applicable to research on liquid crystals, amino acids, and multiferroic materials as well as magnetic chirality. The newly developed instruments shall reinforce the new measurement technique critical for the emerging materials science.

Masaki Takata



Time-Resolved Investigation of Nanosecond Crystal Growth in Rapid-Phase-Change Materials for Rewritable Digital Versatile Disc

The rapid phase-change mechanism in DVD-RAM (digital versatile disc-random access memory) materials has been investigated using the "X-ray pinpoint structural measurement" system developed at the high flux beamline **BL40XU**. The measurement system has been constructed with support of the Core Research for Evolutional Science and Technology (CREST) project, organized by the Japan Science and Technology Agency (JST). The aim of the project is to accomplish picosecond time-resolved X-ray diffraction experiment using a submicrometer-scale beam. This is why the project is termed "pinpoint." Specialists in accelerator science, laser physics, X-ray optics, diffraction physics, crystallography, and chemistry have joined this project from several institutes, i.e., JASRI/SPring-8, RIKEN SPring-8 Center, Panasonic Corporation, Tsukuba University and University of Hyogo. The target specifications of the X-ray pinpoint structural measurement are ~100 nm spatial resolution and ~40 ps time resolution [1]. To ensure the precision of the time resolution, we devised a new precise timing control system, which allows us to keep the timing accuracy within 5 picosecond in any case [2].

In rewritable DVDs, such as DVD-RAM and DVD-RW, information is written to the phase-change materials composed of the alloys of Ge, Sb and Te, or those of Ag, In, Sb and Te, by changing their phase between amorphous and crystalline states using submicrometer-sized laser irradiation. Although recently developed DVD materials can complete their phase change with 20 ns of laser irradiation, the real-time *in situ* observation of the crystal growth process in the nanosecond time scale has never been reported. We therefore conducted a time-resolved X-ray diffraction experiment coupled with *in situ* photoreflectivity measurement using the X-ray pinpoint structural measurement system to study the crystallization processes of $Ge_2Sb_2Te_5$ and $Ag_{3.5}In_{3.8}Sb_{75.0}Te_{17.7}$ [3], which are thought to exhibit different crystallization behavior. To reveal the crystallization process of the amorphous phase in these rapid phase-change materials, it is necessary to know (i) the time constants of both crystallization and optical reflectivity changes, and (ii) the crystallization behavior. Thus, we employed avalanche photodiode (APD)/multi-channel scaling (MCS) measurement with

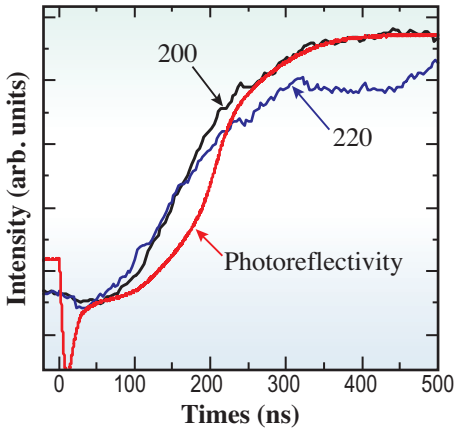


Fig. 2. Time evolution of photoreflectivity and X-ray diffraction intensity.

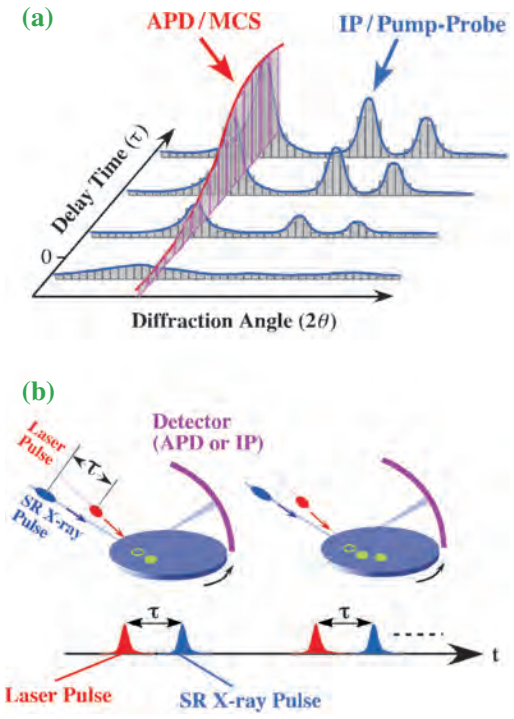


Fig. 1. **(a)** Schematic diagram of APD/MCS and IP/pump-probe measurement and **(b)** scheme of DVD rotating system and the time chart of pump-probe measurement.

a time resolution of 3.2 ns coupled with photoreflectivity measurement for (i) and imaging plate (IP)/pump-probe measurement of a time resolution of 40 ps for (ii), as schematically shown in Fig. 1(a). Figure 1(b) shows the experimental method and the time chart for pump-probe measurement using 40 ps X-ray pulses and synchronous femtosecond laser pulses. The DVD samples were prepared by depositing $Ge_2Sb_2Te_5$ and $Ag_{3.5}In_{3.8}Sb_{75.0}Te_{17.7}$ on a SiO_2 glass substrate (12 cm diameter and 0.6 mm thick) with a 2-nm-thick 80 mol% ZnS-20 mol% SiO_2 cap layer. The thickness of the sample was 300 nm, which gave sufficient X-ray diffraction intensities for structure characterization and sufficient stability of the amorphous phase to avoid spontaneous crystallization.

Figure 2 shows time dependence of the X-ray diffraction intensity of Bragg peaks (black and blue lines) together with the photoreflectivity profiles (red lines), measured by APD/MCS measurement. These show good agreement, which proves the close relationship between X-ray diffraction intensity and the photoreflectivity of the phase-change materials, i.e., between the structure and the electronic properties.

From the intensity profile measured by the APD/MCS method, the delay times, τ, were determined for the IP/pump-probe method. Figure 3(a) shows the diffraction patterns obtained by the IP/pump-probe method for a 40 ps snapshot. Since the intensity of each diffraction peak has a uniform time-dependent increase, there is no crystal-crystal phase transition in $Ge_2Sb_2Te_5$ or $Ag_{3.5}In_{3.8}Sb_{75.0}Te_{17.7}$ during the crystal growth. We estimated the grain sizes from the peak width of Bragg reflection, as shown in Fig. 3(b). In $Ge_2Sb_2Te_5$, the grain size is nearly constant (=70 nm), while the grain size significantly increases up to 1 μs in $Ag_{3.5}In_{3.8}Sb_{75.0}Te_{17.7}$. It is noteworthy that the volume fraction of the crystal phase is almost saturated at 300 ns (see Fig. 2). Thus these observations suggest the coalescence of the crystal domains after 300 ns.

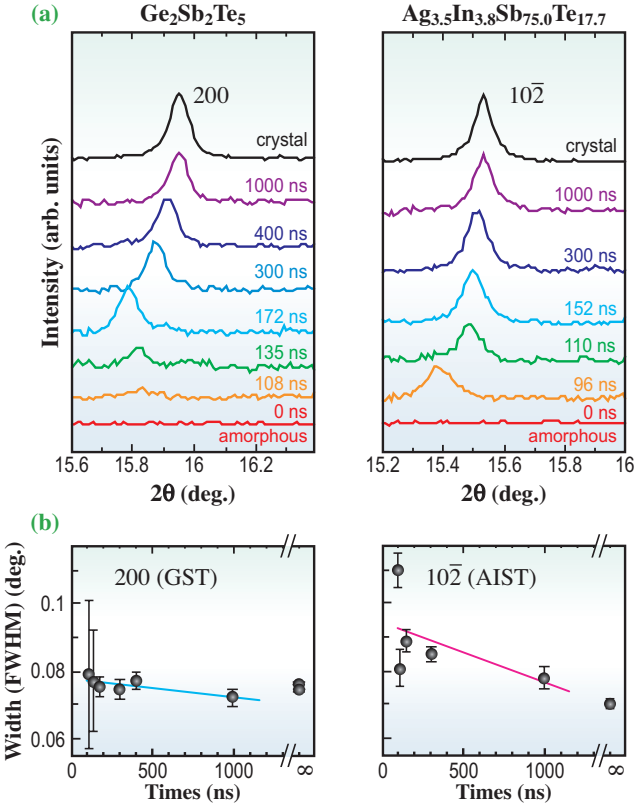


Fig. 3. **(a)** Snapshots of X-ray diffraction patterns and **(b)** changes in peak width.

On the basis of the above experimental findings, we propose schematic models for the crystallization processes of $Ge_2Sb_2Te_5$ and $Ag_{3.5}In_{3.8}Sb_{75.0}Te_{17.7}$. In $Ge_2Sb_2Te_5$, large crystal grains form over the entire volume of the material from the moment the process starts, while in $Ag_{3.5}In_{3.8}Sb_{75.0}Te_{17.7}$, the process begins with the formation of small crystallites in different parts of the material, which gradually grow and merge to form larger grains.

The X-ray pinpoint structural measurement system is now close to completion. The system, which is an integration of the time-resolved experiment and microbeam technique [4], will be applied to investigate, for example, photo-induced phase transition, and structural change under applied AC electric field, as well as the phase change of DVD materials.

Shigeru Kimura[a,*], Yoshihito Tanaka[b] and Masaki Takata[a,b]

[a] SPring-8/JASRI
[b] SPring-8/RIKEN

*E-mail: kimuras@spring8.or.jp

References

[1] S. Kimura *et al.*: AIP Conf. Proc. **879** (2007) 1238.
[2] Y. Fukuyama *et al.*: Rev. Sci. Instrum. **79** (2008) 045107.
[3] *Y. Fukuyama, N. Yasuda, J. Kim, H. Murayama, Y. Tanaka, S. Kimura, K. Kato, S. Kohara, Y. Moritomo, T. Matsunaga, R. Kojima, N. Yamada, H. Tanaka, T. Ohshima and M. Takata: Appl. Phys. Express* ***1*** *(2008) 045001.*
[4] Y. Tanaka *et al.*: Jpn. J. Appl. Phys. **48** (2009) 03A001.

Towards *In Situ* X-Ray Diffraction Imaging at the Nanometer Scale: Early Detection of Nanoparticle Growth in Light Metal Alloys

X-ray diffractive imaging is widely used for nondestructive, high-resolution bulk-material characterization. Coherent X-ray imaging, though very powerful, has stringent requirements on the spatial isolation of a small sample, optics stability and X-ray coherence, while suffering from limitations in detector pixel resolution and insufficient dynamical range. Transmission electron microscopy offers very high resolution, but sample preparation is destructive and multiple scattering limits the technique to surface studies or very thin samples (<0.5 μm).

Novel materials with properties governed by the dispersion of nanoparticles embedded *within* a continuous bulk matrix (such as technologically important light metal alloys) thus require a complementary technique that can offer nondestructive 3D characterization of the nanoparticle form and dimensions by averaging over a substantial volume of nanoprecipitates, rather than a single isolated particle. We have developed an innovative X-ray diffraction technique aimed specifically at characterizing such materials at the nanometer scale. Established on various embedded nanoparticles [1], we are extending the technique to potential real time *in situ* investigations. Due to the complexity of nucleation and growth kinetics of the nanoprecipitates, it is crucial for such *in situ* studies to be sensitive to the early stages of precipitate formation.

Principal experiments were performed on the high-resolution multi-axis diffractometer at beamline **BL13XU**. The nondispersive triple axis setup is shown in Fig. 1. The arrangement consisted of a double-reflection, channel-cut Si(400) monochromator (axis 1), used to select 10.9 keV X-rays, with slits limiting the beam size to 0.25 mm vertically and 1.00 mm horizontally. The sample was placed downstream of the monochromator, resulting in a modulated wave incident on the single-reflection Si(400) analyzer crystal (mounted on the goniometer stage, axis 2). A scintillation counter was mounted on the 2θ-arm (axis 3). The sample was 0.6-mm-thick single-crystal Al-2.0%wt Cu, polished and chemically etched with $[100]_{Al}$ normal to the surface. Solutionizing (530 °C for 1 h), water quenching, and ageing at 150 °C for 172 h resulted in randomly distributed, weakly diffracting, Al_2Cu nanoprecipitates, crystallographically oriented along the $<100>_{Al}$ planes (Fig. 2).

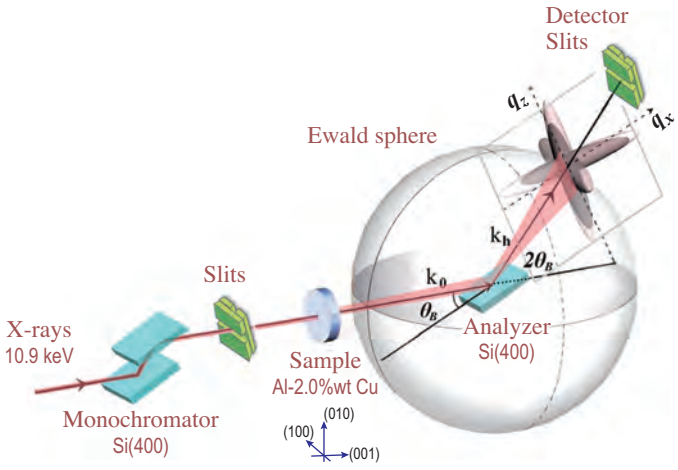


Fig. 1. Schematic of triple axis diffractometry setup.

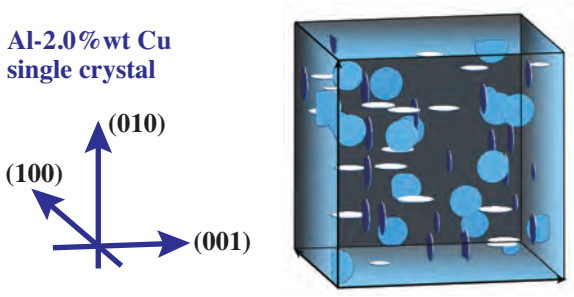


Fig. 2. Simulated volume of embedded nanoparticles, representative of the size spread of Al_2Cu nanoprecipitates in artificially aged Al-2.0%wt Cu.

We collected a 2D reciprocal space map (RSM) around the Si(400) Bragg reflection of the analyzer by performing α/2θ scans (along q_z in Fig. 1), with shifts of the analyzer, α, in between. Results from two sample orientations are shown in Figs. 3(c) and 3(d), and are compared with those of a plane wave incident on the analyzer (no sample) in Fig. 3(e). The results shown span an angular range of α = ±0.795°, and Δ2θ = ±1.590°, with nominal step sizes of 0.01° and 0.02°, respectively. Here, α and Δ2θ are deviations of the analyzer and detector-slit arrangement from their ideal Bragg configurations.

On a background of widespread diffuse scattering, there are dynamical and kinematical diffraction streaks. Along q_z is the crystal truncation rod, resulting from the abrupt change in electron density at the surface of the analyzer. The angular allowance of the detector slits (0.25 mm vertically and 5.0 mm horizontally) caused the thin, single-pixel,

detector streak at an angle of θ_B counterclockwise from the q_z axis, i.e., tangential to the Ewald sphere.

The diffracted wavefront emerging from the sample imitated the effect of mosaicity in the analyzer crystal, as evident in the horizontal streaks of Figs. 3(c) and 3(d), and simulated in 3(a). The shortened horizontal streak with more prominent asymmetry in Fig. 3(d) is due to a different projection (onto the Ewald sphere) of the 3D diffracted intensity of the sample, resulting from azimuthal sample rotation [1,4]. The simulated RSMs were calculated using Takagi equations [2] (Figs. 3(a) and 3(b)), assuming a weakly diffracting object, where the nanoprecipitates were approximated as flat cylinders with a Gaussian distribution of diameters (Fig. 1) [4].

By deconvolving the instrumental effects and applying a modified Fienup Gerchberg Saxton error-reduction algorithm [1,3,4], we reconstructed a pseudo-3D image using *a priori* knowledge about the symmetry of the nanoprecipitates. The reconstruction of a single Al_2Cu nanoprecipitate, in Figs. 3(g) and 3(h), is representative of the modal (most commonly occurring) nanoprecipitate size. A transmission electron micrograph of two randomly chosen nanoprecipitates is shown in Fig. 3(f).

In the present work, the sensitivity of the technique to the presence and crystallographic orientation of sparse, weakly diffracting embedded nanoprecipitates, was established. Not only is this a fundamental step in the characterization of static intermetallic nanostructures in bulk alloys, but it warrants the extension of the technique to real time *in situ* investigations. The first successful *in situ* experiments, in which the nucleation, clustering and very early stages of nanoprecipitate growth were examined have already been conducted at BL13XU [5]. The continuation of this work is now in progress.

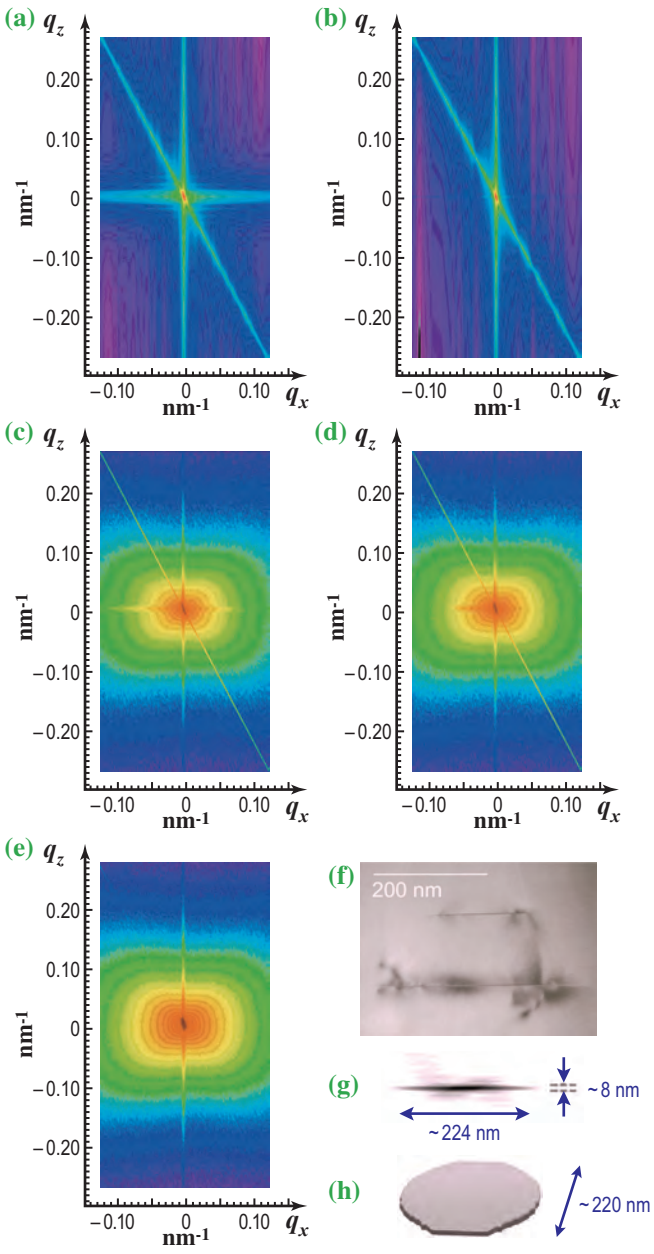


Fig. 3. Reciprocal space maps around the Si(400) analyzer reflection. Simulations: **(a)** Al-2.0%wt Cu single crystal, showing prominent horizontal streak; **(b)** no sample; Experimental results: **(c)** Al-2.0%wt Cu single crystal with nanoprecipitates parallel and perpendicular to diffracting plane; **(d)** nanoprecipitates at ±45° to diffracting plane; (e) no sample; **(f)** $<100>_a$ zone axis TEM micrograph showing 2 typical nanoprecipitates; Reconstructions: **(g)** 2D projected thickness of the modal nanoparticle (one variant shown); **(h)** pseudo-3D rendering of nanoparticle based on **(g)**.

N. A. Zatsepin[a], A. Y. Nikulin[a,*], R. A. Dilanian[a] and O. Sakata[b]

[a] School of Physics, Monash University, Australia
[b] SPring-8/JASRI

*E-mail: andrei.nikulin@sci.monash.edu.au

References

[1] A. Y. Nikulin *et al.*: Nano Letters **7** (2007) 1246.
[2] S. Takagi: Acta Cryst. **15** (1962) 1311.
[3] J.R. Fienup: Appl. Opt. **21** (1982) 2758.
[4] *N.A. Zatsepin, R.A. Dilanian, A.Y. Nikulin, B.M. Gable, B.C. Muddle and O. Sakata: Appl. Phys. Lett.* ***92*** *(2008) 134101.*
[5] N.A. Zatsepin *et al.*: submitted.

In Situ X-Ray Diffraction Measurement of Hydrogenation and Dehydrogenation of Aluminum at High Pressure and Temperature

Hydrogen is the ideal energy carrier since it can avert adverse effects on the environment and reduce dependence on imported oil for countries without natural resources. The safe and efficient storage of hydrogen is widely considered as one of the key technological challenges to realizing a hydrogen-based energy economy. Hydrogen can be store as pressurized gas, cryogenic liquid, and solid fuel in chemical or physical combinations with other materials; hydrogen forms metal hydrides with some metals and alloys leading to solid-state storage that provides the important advantage of safety over the gas and liquid storage methods.

AlH_3 is a metal hydride with the highest hydrogen content (10.1 mass%) and therefore is a promising candidate for hydrogen storage material. AlH_3 has been synthesized only by a desolvation reaction after the chemical reaction between $LiAlH_4$ and $AlCl_3$ in ether [1,2] and was shown to crystallize in seven polymorphs. In order to utilize AlH_3 as a practical energy source, it is necessary to develop a more efficient synthesis route. The hydrogenation of aluminum metal is the simplest method of synthesizing AlH_3. Thermodynamic studies show an equilibrium H_2 pressure of around 1 GPa at room temperature for the α phase, the most stable phase under ambient conditions. It is hence ruled out to synthesize AlH_3 from aluminum metal by the conventional hydrogenation technique using hydrogen gas pressurized up to 10 MPa, which is much lower than the estimated equilibrium pressure of 1 GPa. Understanding the simple hydrogenation reaction is indispensable to developing other synthetic methods for AlH_3. Herein, we attempted to hydrogenate pristine aluminum at high temperature and high pressure to clarify the hydrogenation mechanism of aluminum. The hydrogenation and decomposition processes were observed by *in situ* X-ray diffraction measurement [3].

High-pressure and high-temperature environments were generated with a cubic-type multi-anvil apparatus installed at beamline **BL14B1**. A schematic of the *in situ* X-ray diffraction measurement system and high-pressure cell is shown in Fig. 1. Highly pure aluminum (Nilaco Corporation, Japan, purity 6N) disks punched from 50-μm-thick foil were stacked to fill a pyrolytic boron nitride capsule 0.8 mm in diameter and 0.4 mm in length, and then placed in a hydrogen sealing capsule along with an internal hydrogen source. The aluminum foil was used as received. A photoelectron spectroscopy measurement indicated that the oxide layer was 35 Å thick. Incident X-rays were collimated to 50 μm × 300 μm square on the sample and diffracted X-rays were measured with a germanium solid-state detector mounted on a goniometer.

The sample was compressed to 10.0 GPa and then heated from room temperature to 600 °C at a rate of 10 °C/min. The hydrogen source decomposed at around 300 °C to supply free hydrogen, which condensed into hydrogen fluid and immersed the metal sample to be hydrogenated. The Bragg peak, which was assigned to the 012 reflection of α-AlH_3, appeared at 600 °C. The hydrogenation of pristine aluminum began at the pressure-temperature conditions. The pristine passivated aluminum foil was not hydrogenated at pressures below 7.5 GPa under pressure and temperature conditions at which α-AlH_3 is thermodynamically stable.

Figure 2 shows the temperature variation of X-ray diffraction profiles of the hydrogenated aluminum

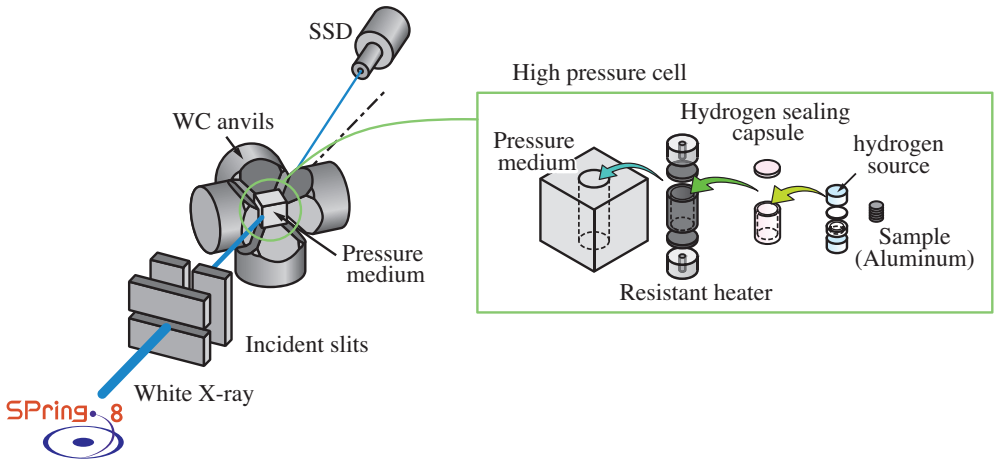


Fig. 1. Schematic of *in situ* X-ray diffraction measurement system and high-pressure cell.

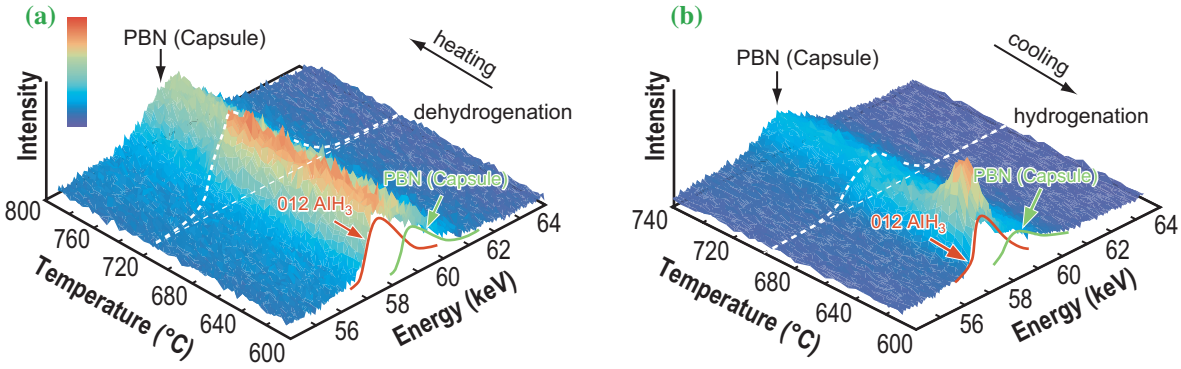


Fig. 2. Temperature variation of X-ray diffraction profiles taken at 10.0 GPa during **(a)** heating and **(b)** cooling.

taken at 10.0 GPa. When the sample was heated to 720 °C, 012 reflection of α-AlH_3 and other Bragg peaks from α-AlH_3 (these are not shown in Fig. 2) vanished; α-AlH_3 was dehydrogenated. These peaks reappeared upon successive cooling; aluminum was hydrogenated again to form α-AlH_3 .

After aluminum was hydrogenated at 10 GPa and the dehydrogenation-hydrogenation reaction was repeated, cyclic dehydrogenation and hydrogenation processes were observed at pressures lower than 7.5 GPa. The pressure-temperature diagram of the hydrogen-aluminum system was determined (Fig. 3). In the present study, all the hydrogenated aluminum has the α-AlH_3 structure, confirming that α-AlH_3 is the most stable phase. This activation effect for hydrogenation suggests the possibility of synthesizing AlH_3 under more moderate conditions, even below 4 GPa.

The hydride crystals thus prepared at high pressure and temperature were recovered under ambient conditions. They were colorless and transparent (Fig. 3 inset), and the grain size ranged roughly from a few to 50 mm. These grains were expected to be single crystals on the basis of polarized micrograph observation. The powder X-ray diffraction pattern of the recovered AlH_3 was measured. All the Bragg peaks can be indexed with the unit cell of α-AlH_3. Traces of other AlH_3 polymorphs were not found. The single phase of α-AlH_3 was obtained. EDS analysis did not detect impurities.

We succeeded in the hydrogenation of pristine aluminum with hydrogen fluid at high temperature and high pressure, and the recovery of AlH_3 crystals under ambient conditions. This synthesis method allows the preparation of a large amount of single crystals of AlH_3. The obtained single crystals will be useful for characterizing the thermodynamic and kinetic properties of AlH_3 as well as for studying the bonding nature. *In situ* X-ray diffraction measurement will be further applicable to a study of the dynamics of the hydrogenation and dehydrogenation cycles, which will lead to the improvement of the high-pressure synthesis method. The synthesis of aluminum-rich metal hydrides is being carried out at SPring-8.

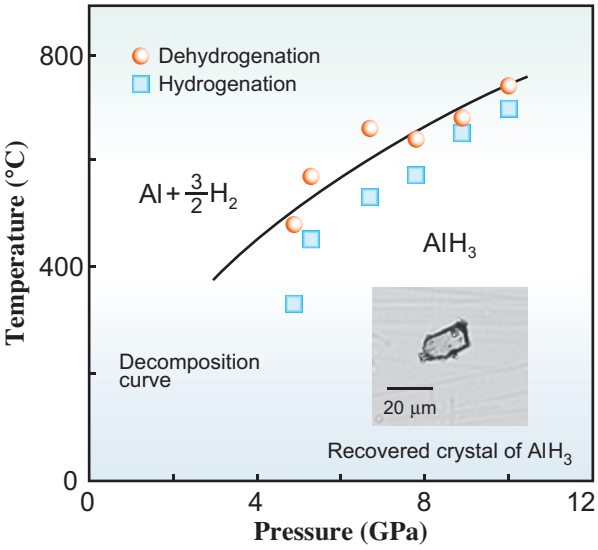


Fig. 3. Hydrogenation and dehydrogenation pressure-temperature conditions determined by *in situ* X-ray diffraction measurements. Inset shows a micrograph of a recovered AlH_3 crystal.

Hiroyuki Saitoh* and Katsutoshi Aoki

SPring-8/JAEA

*E-mail: cyto@spring8.or.jp

References

[1] F.M. Brower *et al.*: J. Am. Chem. Soc. **98** (1976) 2450.
[2] S. Orimo *et al.*: Appl. Phys. A **83** (2006) 5.
[3] *H. Saitoh, A. Machida, Y. Katayama and K. Aoki: Appl. Phys. Lett.* ***93*** *(2008) 151918.*

Direct Observation of Motion in Atom Cage

Thermoelectricity requires materials that are electrically conducting but thermally insulating. While important technologically, such materials are difficult to realize because electrons usually act as both electronic and thermal conductors. One option for their realization is a material which has low lattice conductivity, whereby the lattice contribution to thermal transport is removed. Since the proposal of the phonon-glass-electron-crystal (PGEC) model [1], cage compounds, such as filled skutterudites (see Fig. 1) and clathrates have been considered potential thermoelectric materials because of their low thermal conductivity. The central idea is that localized vibrational modes of the atoms inserted into the cages reduces thermal conductivity.

We employ a combination of two synchrotron techniques to investigate precisely the motions of atoms in cages of filled skutterudites. These materials, having the formula RT_4X_{12} (R: rare earth or actinide, T: transition metal, X: pnictogen), have a cage about atom "R" (see Fig. 1), which may lead to localized motion and reduce thermal conductivity. Using meV-resolved inelastic X-ray scattering (IXS), we show that nearly dispersionless modes exist, and using atom-specific nuclear resonant inelastic scattering (NRIS), we show that these modes are precisely those of the guest atom in the cage [2], as discussed below.

The left and middle panels of Fig. 2 show the phonon dispersion relations in $SmRu_4P_{12}$ obtained by IXS at beamline **BL35XU**. We found dispersionless modes in both longitudinal and transverse modes along the (1 0 0) and (1 1 0) directions. The obtained dispersion relations also show that the dispersionless modes hybridize with the heat-carrying acoustic modes. Meanwhile, the right panel of Fig. 2 shows the Sm PDOS in $SmRu_4P_{12}$ obtained by ^{149}Sm NRIS at beamline **BL09XU**. A strong single peak in the Sm

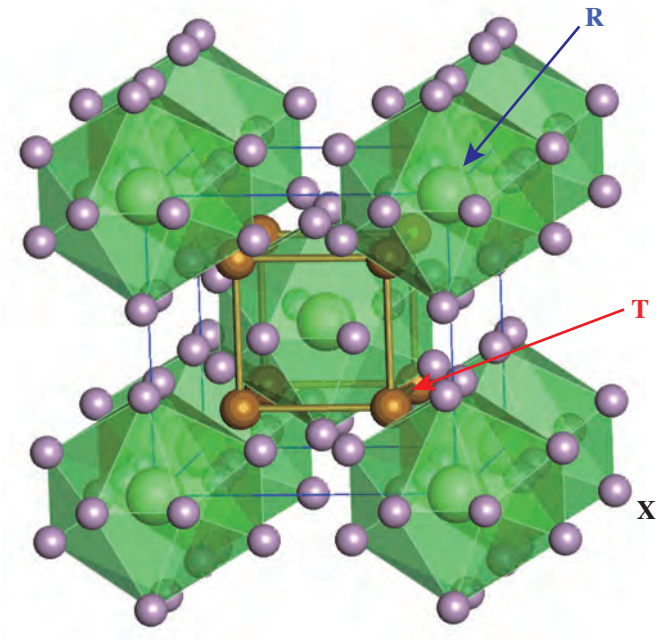


Fig. 1. Crystal structure of filled skutterudites. A rare earth atom (R), a Sm atom in the present case, is surrounded by 12 pnictogen atoms (X), P atoms in the present case, forming an icosahedral cage. A transition metal atom (T), Ru in the present case, is located between the icosahedral cages.

PDOS, suggesting the presence of a dispersionless mode, and its energy, 9 meV, agrees with that of the modes observed by IXS. This indicates that the dispersionless modes at 9 meV correspond to Sm atomic motion. The sharp PDOS also means that the contribution of Sm motion to the acoustic modes is small, similar to the localized mode.

To understand the thermoelectricity in filled skutterudites, the relation between the dispersionless mode and the heat-carrying acoustic modes is important. Investigating the precise atomic motion makes it possible to clarify the contribution of the phonon to the reduction of the thermal conductivity. In particular, the hybridization of the dispersionless mode with the acoustic mode, as we observe here, is not expected from the PGEC model, which is one of the candidate theories for explaining the reduction of thermal conductivity [1]. Our recent work suggested that such hybridization is the common property in the series of filled skutterudites [3-6], as did subsequent neutron scattering work [7,8]. Since the temperature dependence of the NRIS spectra indicates that the Sm modes in $SmRu_4P_{12}$ are anharmonic [6], the present work hints that the hybridization of the anharmonic dispersionless modes owing to the inserted atoms with acoustic modes might reduce the thermal conductivity due to phonons in cage-structured compounds.

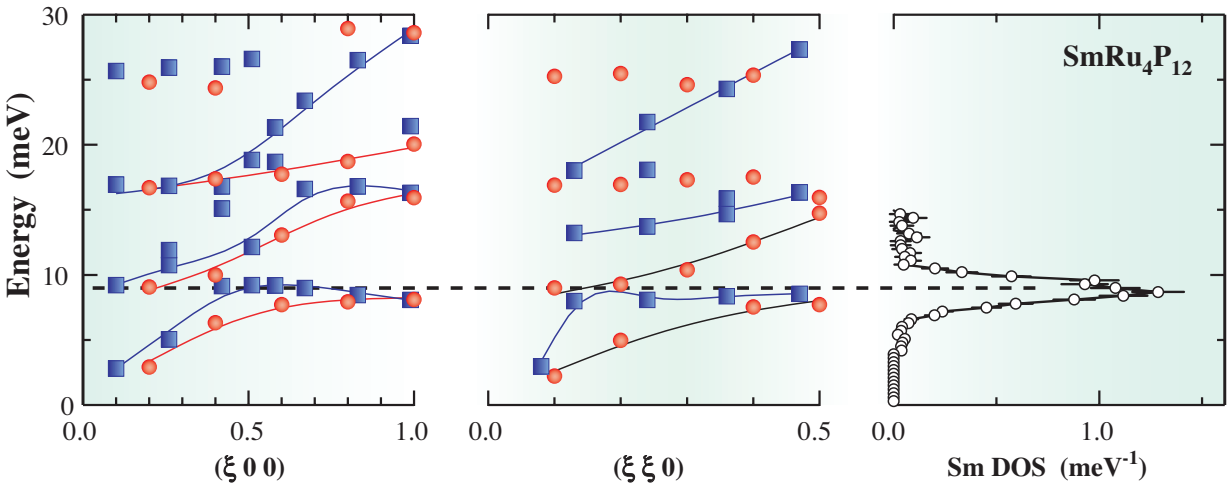


Fig. 2. Phonon dispersion in higher symmetry directions in $SmRu_4P_{12}$ obtained by IXS (left and middle) and measured partial phonon density of states associated with Sm atomic motion (right). The blue squares (red circles) show the phonon energy of the longitudinal (transverse) modes in each direction. The solid curves are guides for the eye. The dotted line is the excitation energy observed by ^{149}Sm NRIS.

Satoshi Tsutsui[a,*], Hisao Kobayashi[b,c] and Alfred Q. R. Baron[a,d]

[a] SPring-8/JASRI
[b] Graduate School of Material Science, University of Hyogo
[c] JST/CREST
[d] SPring-8/RIKEN

*E-mail: satoshi@spring8.or.jp

References

[1] G.A. Slack, Handbook of Thermoelectrics, Ed. By D. Rowe, CRC press 407 (1995).
[2] *S. Tsutsui, H. Kobayashi, D. Ishikawa, J.P. Sutter, A.Q.R. Baron, T. Hasegawa, N. Ogita, M. Udagawa, Y. Yoda, H. Onodera, D. Kikuchi, H. Sugawara, C. Sekine, I. Shirotani and H. Sato: J. Phys. Soc. Jpn. 77 (2008) 022601.*
[3] S. Tsutsui *et al.*: Hyperfine Interact. **168** (2006) 1073.
[4] S. Tsutsui *et al.*: Physica B **383** (2006) 142.
[5] S. Tsutsui *et al.*: J. Phys. Soc. Jpn. **76** (2007) 065003.
[6] S. Tsutsui *et al.*: J. Phys. Soc. Jpn. **77** (2008) A257.
[7] M.M. Koza *et al.*: Nature Materials **7** (2008) 805.
[8] M. Christensen *et al.*: Nature Materials **7** (2008) 811.

Giant Negative Thermal Expansion in Magnetic Nanocrystals

Most solids expand when they are heated but a property known as negative thermal expansion (NTE) has been observed in a number of materials, including the oxide ZrW_2O_8 [1] and the framework material $Zn_xCd_{1-x}(CN)_2$ [2]. This unusual behaviour can be understood in terms of low-energy phonons, while the colossal values of both positive and negative thermal expansion recently observed in another framework material, $Ag_3[Co(CN)_6]$, has been explained in terms of the geometric flexibility of its metal-cyanide-metal linkages [3]. Thermal expansion can also be stopped in some magnetic transition metal alloys below their magnetic ordering temperature, a phenomenon known as the Invar effect, and the possibility of exploiting materials with tunable positive or negative thermal expansion in industrial applications has led to intense interest in both the Invar effect and NTE.

Here, we report our recent finding of giant negative thermal expansion in magnetic nanocrystals of CuO and MnF_2 [4]. The cupric oxide, CuO, is a unique transition metal monoxide that was clarified by us to show strong charge-spin-lattice coupling and ferroelectric properties below its magnetic (antiferromagnetic) transition [5]. This strong charge-spin-lattice coupling has recently received intense attention and has been renamed with the term "multiferroics." Our previous structure study suggested small anomalies in the lattice parameters at its magnetic transition temperature (Néel temperature T_N) and the disappearance of thermal expansion below T_N (i.e., zero thermal expansion). CuO fine particles with sizes narrowly distributed around ~5 nm were prepared by ball-milling from large (~cm) pure single crystals grown by a chemical vapor transport method. The high-resolution TEM image suggests that they are of crystalline nature (Fig. 1). A surprising result concerning the ball-milled nanoparticles is the absence of the lattice defects that one might expect from the balling process (as is the case in our ball-milled submicron particles (Fig. 1)).

The powder X-ray diffraction experiments were carried out at beamline **BL02B2** using a large Debye-Scherrer camera with an imaging plate. XRD data were collected at various temperatures from 300 K to 20 K with 0.01° steps from 0.00° to 75.00° for 2θ. The wavelength of the incident X-ray was tuned to approximately 0.5 Å using the Si double monochromator.

The lattice constants of the nanocrystals at various temperatures were analyzed by the Rietveld method. Nanoparticle CuO has the single crystal structure, as shown in Fig. 2. We found a large NTE effect ($\beta=-1.06\times10^{-4}K^{-1}$) for 5 nm nanocrystals of CuO below its magnetic ordering temperature (Fig. 3). By comparison the renowned NTE compound ZrW_2O_8 has $\beta=-2.6\times10^{-5}K^{-1}$ [1]. A similar result was observed for nanoparticles of MnF_2 but not for NiO. Larger particles

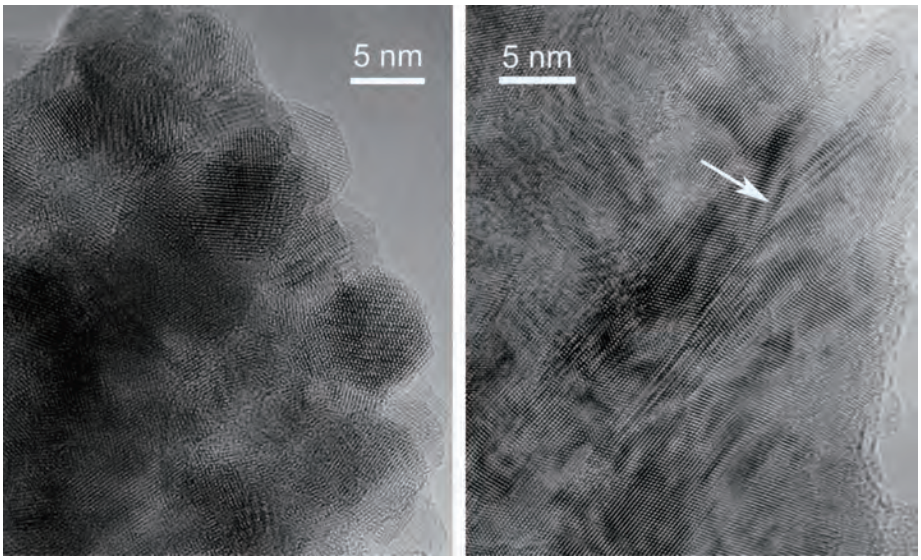


Fig. 1. Electron micrograph of nanocrystals (the left) and submicron particles of ball-milled CuO.

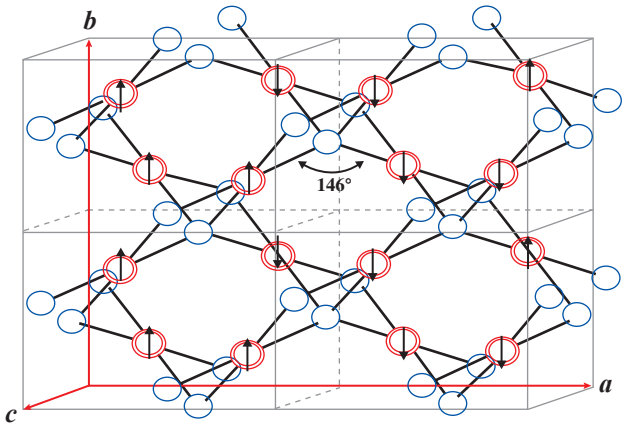


Fig. 2. Crystal structure of CuO. The arrows represent the ordered spins below its magnetic transition temperature.

of CuO and MnF_2 also show a prominent Invar effect below their magnetic ordering temperature constant, whereas this behavior is not observed in NiO. We propose that the NTE effect in CuO (which is four times larger than that observed in ZrW_2O_8) and MnF_2 is a general property of nanoparticles in which there is strong coupling between magnetism and the crystal lattice, i.e., magnetostriction.

As is highlighted by Goodwin in Nature Nanotechnology [6], "if the link between magnetostriction and the NTE in nanoparticles proves to be general – and the materials science community will no doubt explore this possibility – then these results really are a very significant advance. Nearly all high-end functional materials show some form of magnetic ordering – this includes high-temperature superconductors, colossal magnetoresistance manganites and the rapidly expanding family of multiferroics. These are precisely the type of materials used in multicomponent devices, where compatibility between mechanical properties is paramount." Moreover, the present finding suggests that "the particle size affects their fundamental thermodynamics in nanocrystalline magnets. Particle size has always been an important variable in materials science, but now the field has a clear indication of how it might be used to vary – and even invert – the complex interdependencies among fundamental parameters such as temperature, pressure and magnetism. If these principles can be extended to multiferroic materials, where magnetic order and electric polarization are linked, one might hope to develop nanoscale switches and sensors with previously unimaginable electronic responses to changes in temperature or pressure."

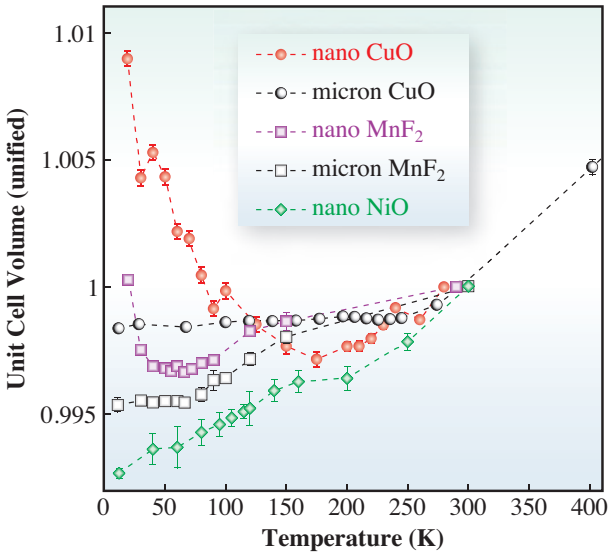


Fig. 3. Negative thermal expansion in nanocrystals of CuO and MnF_2, but not NiO. The unit cell volumes are normalized by their room-temperature values, respectively.

X. G. Zheng

Department of Physics, Saga University

E-mail: zheng@cc.saga-u.ac.jp

References

[1] T.A. Mary *et al.*: Science **272** (1996) 90.
[2] A.E. Phillips *et al.*: Angew. Chem. Int. Ed **47** (2008) 1396.
[3] A.L. Goodwin *et al.*: Science **319** (2008) 794.
[4] *X.G. Zheng , H. Kubozono, H. Yamada, K. Kato, Y. Ishiwata, C.N. Xu: Nature Nanotechnology **3** (2008) 724.*
[5] X.G. Zheng *et al.*: Phys. Rev. Lett. **85** (2000) 5170; J. Phys. Soc. Jpn. **70** (2001) 1054; J. Appl. Phys. **92** (2002) 703; Phys. Rev. B **69** (2004) 104104.
[6] A.L. Goodwin: Nature Nanotechnology **3** (2008) 711.

Recent Findings on Metal Nanoparticles as New-Type Hydrogen-Storage Materials

The search for materials enabling efficient storage and safe transport of fuel gases, particularly hydrogen gas, has focused on hydrogen-storage alloys, metal-organic frameworks, carbon materials and many more. Hydrogen-storage alloys provide the best way to store hydrogen compactly and safely under mild condition as a consequence of the stability of their hydride. Most recently, metal nanoparticles have attracted much attention as advanced materials of new hydrogen-storage alloys [1-4]. It is well known that metal nanoparticles exhibit characteristic chemical and physical properties that are quite different from those in bulk metals owing to high surface-to-volume ratios and unique electronic states. Since the hydrogen-storage properties of metals are strongly related to their electronic states, novel hydrogen-storage properties are expected in metal nanoparticles. Here we report the recent findings about hydrogen-absorption properties of Pd and core (Pd)/shell (Pt) nanoparticles.

As shown in Fig. 1, Pd nanoparticles having 6.1 nm diameter absorb hydrogen, and the hydrogen composition under 101.3 kPa of hydrogen pressure at 303 K is 0.22 H/Pd. In the desorption process the curve does not completely return to the starting point in the case of Pd nanoparticles [2,3], while for bulk Pd, it is completely reversible [2]. The origin of this phenomenon has been a puzzle so far. In order to clarify the location of hydrogen, the surface or the body, and its chemical form, molecular, atomic or hydride, we carried out *in situ* powder X-ray diffraction (XRD) measurement using synchrotron radiation with a 51.148 pm wavelength at beamline **BL02B2**.

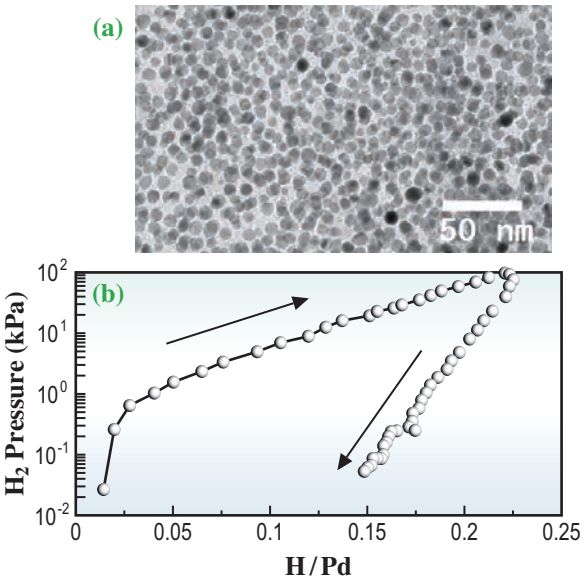


Fig. 1. **(a)** TEM images and **(b)** PC isotherms of Pd nanoparticles at 303 K. Isotherm was measured along directions of arrows.

Pd nanoparticles showed a diffraction pattern corresponding to the metallic face-centered-cubic (fcc) lattice under different hydrogen pressures (Fig. 2(a)). The positions of the diffraction peaks were shifted continuously to the lower-angle side in response to hydrogen pressure. The hydrogen-pressure dependences of the lattice constants at 303 K were determined by Le Bail via fitting to the diffraction patterns, and are shown in Fig. 2(b). It can be seen that the lattice constants increase with hydrogen pressure, indicating that Pd atoms within the lattice are forced apart; this can only be a consequence of hydrogen atoms essentially penetrating the inside of the Pd lattice and expanding it. The lattice constant decreases with hydrogen desorption, and the lattice constant at 0 kPa is larger by 0.006 Å than that of the pristine sample, indicating that the lattice constant does not completely return to the same value as in the pristine sample, i.e., the lattice constant shows hysteresis in the course of hydrogen absorption/desorption. Surprisingly, this hysteresis behavior is exactly the same as that observed in the PC hydrogen adsorption isotherm at 303 K. The present results reveal that hydrogen atoms are strongly trapped and highly stabilized in the lattice of Pd nanoparticles, compared with bulk Pd, resulting in the incomplete recovery of the PC isotherm observed at 303 K [2].

We also applied core/shell-type nanoparticles as hydrogen-storage materials for the first time, and their hydrogen-storage properties were investigated [1]. Pd/Pt core/shell nanoparticles comprising a Pd-core with a diameter of 6.1±0.9 nm and a Pt-shell with a thickness of about 1.1 nm were used as the target material. The solid-state ^{2}H NMR measurement of Pd/Pt nanoparticles under 86.7 kPa of deuterium gas at 303 K was performed to investigate the absorption site of deuterium inside the nanoparticles (Fig. 3(b)). In the ^{2}H NMR spectra for Pd and Pt nanoparticles having a diameter of 5.1 nm under 86.7 kPa of $^2H_2$ gas, we could see absorptions at 34 and –36 ppm [4], respectively, indicating the existence of deuterium absorbed inside the lattice of the Pd or Pt nanoparticles. The wide absorption for Pd/Pt particles covers the range containing peaks for Pd and Pd nanoparticle samples. This result indicates that the deuterium disperses inside both Pd and Pt lattices.

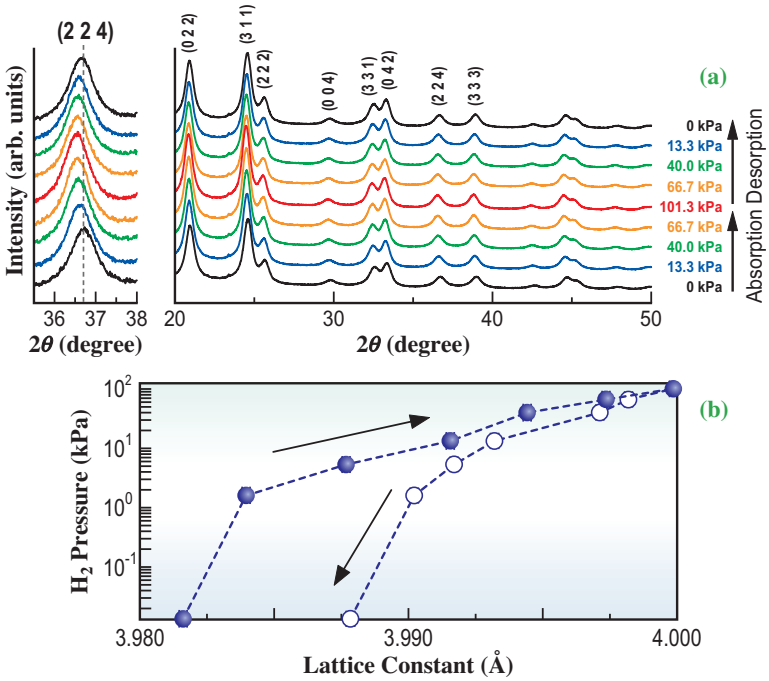


Fig. 2. **(a)** *In situ* synchrotron XRD patterns of Pd nanoparticles with hydrogen absorption/desorption at 303 K. **(b)** Lattice constants of Pd nanoparticles obtained by fitting of XRD patterns (● absorption; ○ desorption). Lattice constants were plotted following the directions of the arrows.

However, the highest intensity was observed between the peak positions for Pd and Pt samples, implying that most of the deuterium is concentrated in the interfacial region between the Pd-core and the Pt-shell in Pd/Pt nanoparticles. These results mean that the atomic arrangements or chemical potential around the core/shell interface boundary is different from those of Pd or Pt nanoparticles, which implies that such a hetero-interface provides a favorable environment for metal-hydride formation (Fig. 3(a)) [1]. We gained a new revelation that the core/shell boundary plays an important role in the formation of the hydride phase of the Pd/Pt nanoparticles.

It is hoped that the new findings obtained in this research will provide a clue to the development of practical hydrogen-storage materials.

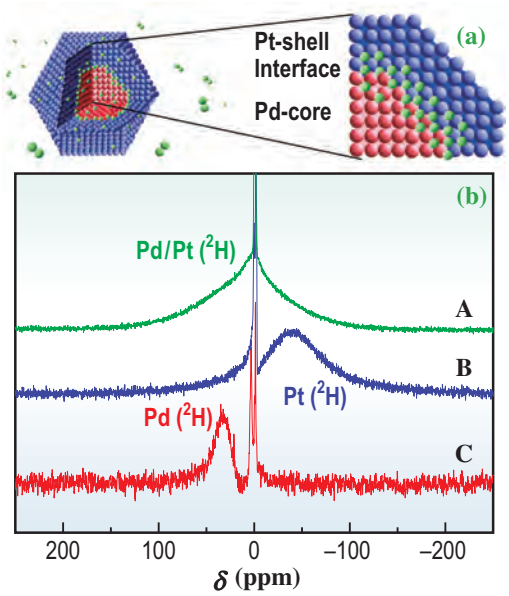


Fig. 3. **(a)** Image of hydrogen storage of Pd/Pt nanoparticles (green=hydrogen, red=Pd, blue=Pt). **(b)** Solid-state ^{2}H NMR spectra for the samples of (A) Pd/Pt, (B) Pt, and (C) Pd nanoparticles under 86.7 kPa of deuterium gas at 303 K.

H. Kobayashi [a], M. Yamauchi [a,b,c], H. Kitagawa [a,d,e,f,*] and M. Takata [g]

[a] Department of Chemistry, Kyushu University
[b] JST-PRESTO
[c] Catalysis Research Center, Hokkaido University
[d] Department of Chemistry, Kyoto University
[e] JST-CREST
[f] INAMORI Frontier Research Center, Kyushu University
[g] SPring-8/RIKEN•JASRI

*E-mail: kitagawa@kuchem.kyoto-u.ac.jp

References

[1] *H. Kobayashi, M. Yamauchi, H. Kitagawa, Y. Kubota, K. Kato and M. Takata: J. Am. Chem. Soc.* ***130*** *(2008) 1818.*
[2] H. Kobayashi *et al.*: J. Am. Chem. Soc. **130** (2008) 1828.
[3] M. Yamauchi *et al.*: J. Phys. Chem. C **112** (2008) 3294.
[4] M. Yamauchi and H. Kitagawa: Chem. Eng. Trans. **8** (2005) 159.

Rational Design of Iron Oxides with Square Planar Coordination

The coordination number in ionically bonded structures is governed by the relative size of oppositely charged ions, which, to a first approximation, may be regarded as charged rigid spheres. Each ion tries to surround itself symmetrically with the largest possible number of oppositely charged neighbors. Unusual coordination beyond the constraint of the ionic model may occur in association with highly directional covalent bonding, as realized, for example, in many silicates and sulfides. A successful approach for exploring unusual coordinations in molecular compounds is the use of organic ligands with specific sterical constraints. This cannot be applied, however, to nonmolecular inorganic solids.

Iron, one of the most abundant elements in the earth, forms an uncountable number of oxides, some of which have been widely used in industry as low-cost ferrite magnets and pigments. In almost all of them, the iron ions are tetrahedrally or octahedrally coordinated. However, we recently succeeded in a low-temperature synthesis of $SrFeO_2$, a new compound bearing an unprecedented square-planar oxygen coordination around Fe^{2+} (Fig. 1(b)) [1]. $SrFeO_2$ is isostructural with "infinite layer" cupric superconducting oxides, and exhibits a magnetic order far above room temperature in spite of the two-dimensional structure.

The target compound was obtained by the reductive reaction using CaH_2 as a reducing agent of a well-known perovskite $SrFeO_3$ (Fig. 1(a)). The synchrotron powder X-ray diffraction (XRD) experiment was carried out with a large Debye-Scherrer camera installed at beamline **BL02B2**, using an imaging plate as a detector. The synchrotron XRD patterns of the sample were indexed assuming the tetragonal unit cell with a=3.99107(3) Å and c=3.47481(5) Å. The Rietveld refinement from the synchrotron data assuming the space group of $P4/mmm$ converged to R_{wp} = 6.04% and χ^2 = 4.41 (see Fig. 2).

$SrFeO_2$ transforms back up to $SrFeO_{3-y}$ upon heating in 0.1 MPa oxygen atmosphere. The oxygen uptake proceeds via the brownmillerite-type intermediate $SrFeO_{2.5}$, which is already formed below 390 K, increasing the potential for its application in low-cost catalysis, oxygen ion conduction or oxygen

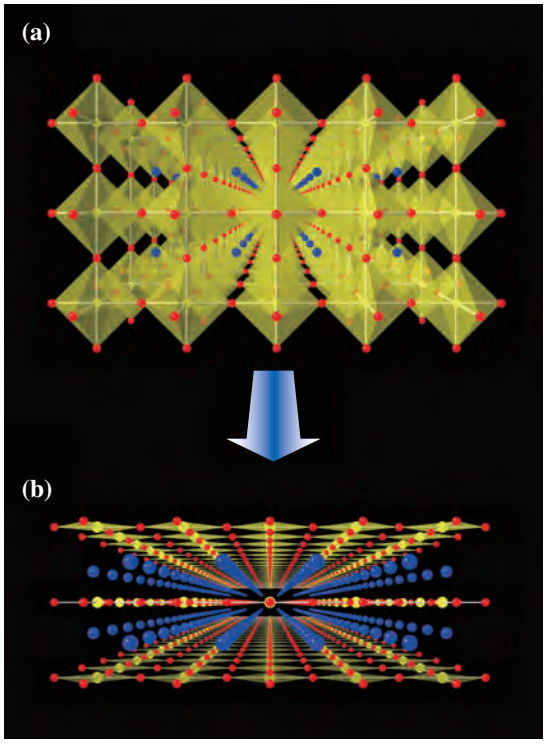


Fig. 1. Structural transformation from **(a)** cubic perovskite $SrFeO_3$ to **(b)** infinite-layer $SrFeO_2$ via topotactic route. Iron, strontium and oxygen atoms are represented as blue, green and yellow spheres, respectively.

gas absorption at reduced working temperatures.

Subsequently, we reported the synthesis of the complete solid solution of $Sr_{1-x}Ca_xFeO_2$, together with its thermal stability measured by *in situ* XRD [2]. The robust nature of the square-planar coordination against both chemical substitution and temperature allows extensive tuning of the physical properties to meet industrial demands. Furthermore, we showed the synthesis of a spin-ladder $Sr_3Fe_2O_5$ through reactions of the double-layered perovskite $Sr_3Fe_2O_7$ with CaH_2 (see Fig. 3) [3]. Together with $SrFeO_2$, this finding establishes new avenues for the solid-state chemistry of ferrous oxides with the square-planar coordination potentially including a serial ladder system $Sr_{n+1}Fe_nO_{2n+1}$ (n=integer), and for the solid-state physics of multiple-spin ladders. $Sr_3Fe_2O_5$ exhibits an antiferromagnetic order owing to interladder coupling, but at a significantly reduced temperature compared with $SrFeO_2$, reflecting dimensional reduction.

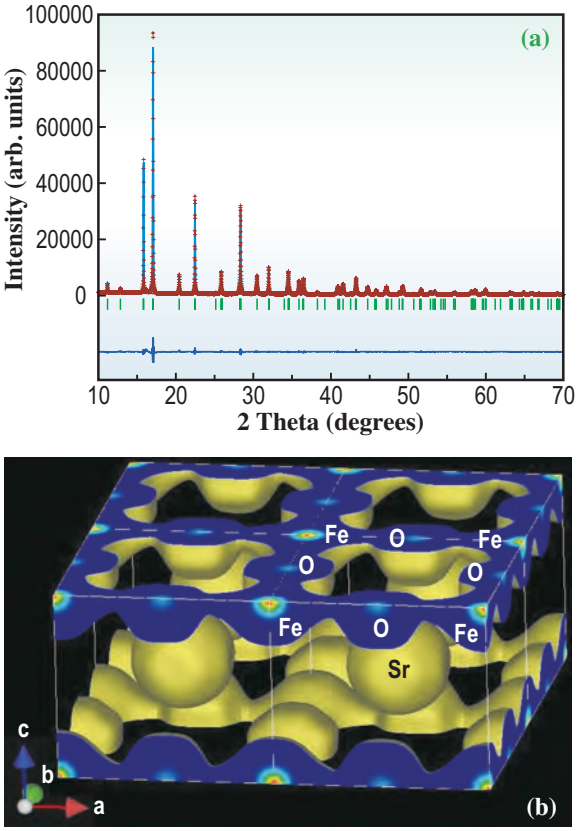


Fig. 2. **(a)** Structural characterization of $SrFeO_2$ by Rietveld refinement of high-q-resolution synchrotron X-ray diffraction at room temperature measured at BL02B2. The wavelength was 0.77747 Å. The solid lines and the overlying crosses and bars indicate the calculated intensities, the observed intensities and the positions of calculated Bragg reflections. The difference between the observed and calculated profiles is plotted at the bottom. **(b)** The electron density in $SrFeO_2$ obtained by the maximum entropy method (MEM).

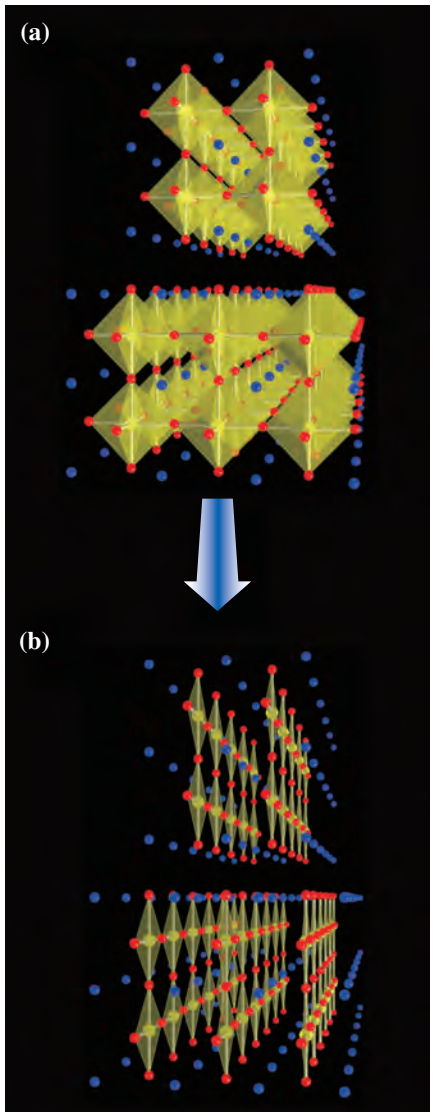


Fig. 3. Structural transformation from **(a)** cubic perovskite $Sr_3Fe_2O_7$ to **(b)** infinite-layer $Sr_3Fe_2O_5$. Iron, strontium and oxygen atoms are represented as blue, green and yellow spheres, respectively.

Hiroshi Kageyama

Department of Chemistry, Kyoto University

E-mail: kage@kuchem.kyoto-u.ac.jp

References

[1] Y. Tsujimoto *et al.*: Nature **450** (2007) 1062.
[2] C. Tassel *et al.*: J. Am. Chem. Soc. **130** (2008) 3764.
[3] *H. Kageyama, T. Watanabe, Y. Tsujimoto, A. Kitada, Y. Sumida, K. Kanamori, K. Yoshimura, N. Hayashi, S. Muranaka, M. Takano, M. Ceretti, W. Paulus, C. Ritter, G. André: Angew. Chem. Int. Ed. 47 (2008) 5740.*

Helical X-Rays Probe Crystal Chirality

Handedness or chirality is found in many complex materials such as proteins, sugars and pharmaceuticals as well as in simpler materials like low quartz and tellurium. They have two crystalline forms that are mirror images of each other, like our right and left hands. Often, the two structures of these so-called enantiomers can have very different chemical and biological properties. For example, thalidomide has two forms: right (R)-thalidomide is effective against morning sickness, on the other hand, left (S)-thalidomide is teratogenic and causes birth defects.

Linearly polarized visible light typically changes its polarization direction depending on whether it passes through a 'left'- or 'right'-handed form of an enantiomer, providing a convenient means of distinguishing them. This phenomenon is known as optical activity, which is effective only for transparent and thin materials. On the other hand, simple X-ray Bragg diffraction, a popular material analysis technique, cannot differentiate between the two, unfortunately.

Our team at the RIKEN SPring-8 Center in Harima and the UK have shown that right and left circularly polarized (RCP and LCP) X-rays of right energy can distinguish 'left' from 'right' low quartz [1].

When the energy of X-rays is tuned to a specific value, that of the silicon *K* absorption edge, X-ray scattering is able to distinguish the particular symmetry of unoccupied states of silicon ion. This process is called resonant scattering, in which the selection rules in diffraction are different from those of normal X-ray scattering. It is known that resonant scattering is sensitive to the crystal symmetry [2], for example, the screw axis, and that forbidden diffraction in normal scattering can become allowed in resonant scattering. We have applied this feature to low quartz with circularly polarized X-rays.

Quartz is the most abundant mineral on earth and has a screw axis in its crystal structure. The screw axis determines the handedness of quartz depending on its form, right screw or left screw, as shown in Fig. 1. Our experiments, carried out at RIKEN beamline **BL17SU**, show that the "forbidden" reflection 001 is observed at the resonant energy of the silicon *K* absorption edge (Energy=1.85 keV). In addition, the intensity depends on the crystal form (right- or left-handed) as well as the helicity of the X-ray beam, as shown in Fig. 2. Another important aspect of resonant X-ray diffraction is that the intensity depends on the rotational angle of the sample, i.e., the azimuthal angle. The intensity of the diffracted X-ray beam is independent of the azimuthal angle for normal X-ray diffraction, however, it changes according to the crystal structure in resonant scattering. Figure 3 shows the intensities of the diffracted beam of 001 reflection for right and left quartz and for right and left circularly polarized X-rays as a function of

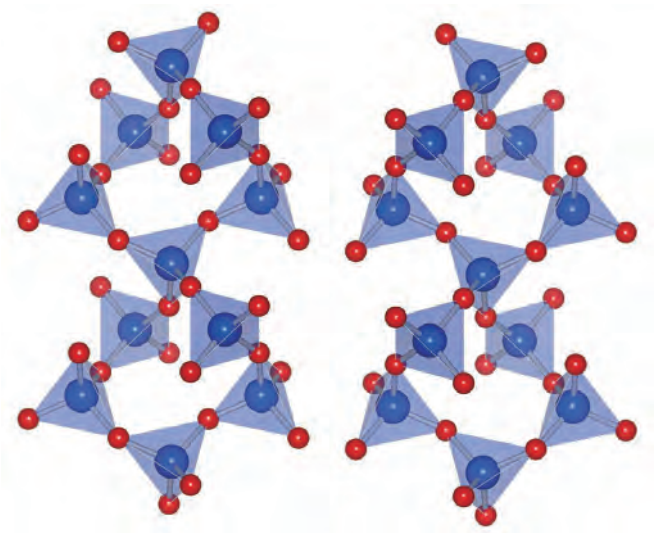


Fig. 1. Views of atomic structures of R-quartz (right) and L-quartz (left) along the a*- and b*- axes, respectively. Blue and red spheres represent silicon and oxygen atoms, respectively.

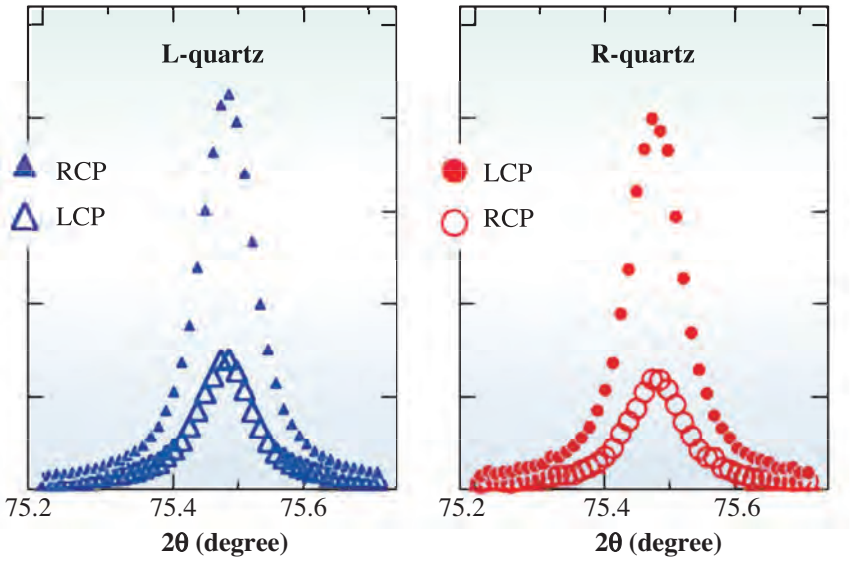


Fig. 2. Reflection profile of 001 of R-quartz and L-quartz measured with a left circularly polarized (LCP) incident beam and a right circularly polarized (RCP) incident beam.

the azimuthal angle. The results clearly show that the helicity of the X-ray beam couples with the handedness of the crystal. The periodicity of 120 degrees in each azimuth scan corresponds to the screw structure in quartz. This technique is expected to be useful for studying the chirality of other materials in general, including biomaterials, liquid crystals and multiferroics.

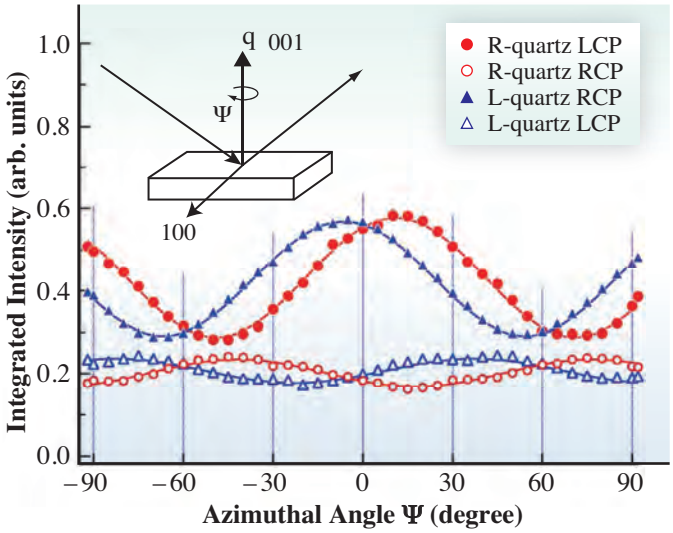


Fig. 3. Integrated intensity of reflection 001of R-and L-quartz as a function of azimuth angle Ψ. Filled (open) circles represent the intensity of reflection 001 of R-quartz measured with LCP (RCP) incident beam, and filled (open) triangles represent the intensity of reflection 001 of L-quartz measured with RCP (LCP) incident beam.

Yoshikazu Tanaka*, Ashish Chainani and Shik Shin

SPring-8/RIKEN

*E-mail: ytanaka@riken.jp

References

[1] *Y. Tanaka, T. Takeuchi, S.W. Lovesey, K.S. Knight, A. Chainani, Y. Takata, M. Oura, Y. Senba, H. Ohashi and S. Shin: Phys. Rev. Lett.* ***100*** *(2008) 145502.*
[2] V.E. Dmitrienko: Acta Crystallogr. Sect. A **39** (1983) 29.

Materials Science:



SPring-8 has a number of beamlines for spectroscopic and diffraction experiments to investigate the properties of various kinds of materials in a wide photon energy range from the infrared (IR) to the hard-X-ray region. Magnetic circular dichroism (MCD) and photoemission spectroscopy (PES; including angle-resolved PES) studies are the important methods both at the soft- and hard-X-ray beamlines. A new MCD method has been developed at BL25SU very recently. Matsui and coworkers presented the possibility of obtaining the layer-resolving magnetic information by diffraction spectroscopy technique combined with MCD. It is expected that this new method will be popular among many users. Conventional MCD measurement has an advantage in element-specific measurements and a high sensitivity for characterizing magnetic moments for dilute magnetic matter. BL23SU, BL25SU and BL39XU are mainly used for MCD studies. Activities concerning Fe nanowires and a dilute magnetic semiconductor are presented. Although there is no report of angle-resolved PES in this chapter; the activities are very high at BL17SU, BL23SU and BL25SU. A very precise observation of the metastable chemisorption state of oxygen on the Si surface is introduced as a representative study of PES in the soft-X-ray region here. The status of the hard X-ray photoemission spectroscopy (HAXPES) studies at SPring-8 is very high and is really in the frontier of science. HAXPES measurement is available at BL15XU, BL19XU, BL29XU, BL46XU and BL47XU. One can access information on really bulk-sensitive electronic structures very easily. Evidence of the recoil effect in the valence band region and the observation of buried interface electronic structures for a magnetic electronic-device material are introduced as hot topics in HAXPES studies.

ELECTRONIC & MAGNETIC PROPERTIES

Compton scattering experiment (at BL08W) is one of the studies complementary to neutron scattering or other magnetic probes for magnetism investigation. Combined with theoretical calculations, the magnetic information of the kagome staircase structure $Co_3V_2O_8$ is shown. Inelastic X-ray scattering (including resonant inelastic scattering; RIXS or resonant X-ray emission; RXES) is a very powerful technique with a high energy resolution in the hard-X-ray region. Here, we present information related to the phonons in the new Fe-based high-Tc superconductors (at BL35XU) and the pressure-induced valence anomaly in TmTe (at BL12XU).

IR microspectroscopy studies are underway at BL43IR. In this chapter, the imaging of the phase separation of the EuO ferromagnetic semiconductor and the effect of carrier doping by X-ray irradiation of organic materials are introduced.

We believe that these activities are really the research frontier of science and may play an important role in the progress of materials sciences.

Toyohiko Kinoshita



Resolving Subsurface Magnetism at Atomic Scale by "Diffraction Spectroscopy"

Future data storage densities will soon need to exceed one terabyte (10^{12} bytes) per square inch, requiring bits just 10 nm or less across. However, this is the scale at which surface magnetism appears. Thus, it is critical to understand unusual magnetic effects from a *nano*scopic point of view. The magnetism of outermost atoms can be detected individually by magnetic STM, whereas much difficulty lies in the case of subsurface atoms. So far, several methods have been developed for probing the magnetic structure of buried interfaces and multilayers. Recently, Amemiya *et al*. have succeeded in evaluating the magnetic moments of surface and subsurface using the emission angle dependence of Auger electron probing depth [1]. However, no atomic-layer resolved characterization technique for subsurface magnetic structures has been developed until now.

A newly developed technique, *diffraction spectroscopy*, enables direct access to the subsurface region, which connects surface and bulk worlds [2]. We combined two existing techniques: X-ray absorption spectroscopy and Auger electron diffraction (AED) measurement. X-ray absorption near edge structure (XANES) and X-ray magnetic circular dichroism (XMCD) measurements by Auger electron yield detection are powerful analysis tools for the electronic and magnetic structures of surfaces. However, all the information from atoms within the electron mean-free-path range is averaged into the obtained spectra. Forward-focusing peaks (FFPs) in AED patterns indicate the directions of atoms surrounding the excited atom. Taking advantage of the FFP as an excellent element- and site-selective probe, we disentangled spectra from different atomic layers.

The spin reorientation transitions (SRTs) of a magnetic epitaxial film from in-plane to perpendicular direction are intriguing phenomena. A Ni ultrathin film on a Cu(001) surface exhibits both SRT and reversal SRT, which are regarded as a basic starting point of nanoscale magnetism. We used *diffraction spectroscopy* to visualize both the magnetic and electronic properties of subsurface layers on the atomic scale in a nondestructive way.

We used the display-type analyzer (DIANA) [3,4] installed at the circularly polarized soft X-ray beamline **BL25SU** for measuring AEDs. As illustrated in Fig. 1(a), electrons emitted from the sample were energy-analyzed and their angular distributions were projected onto a fluorescence screen. The Ni LMM AED pattern excited with normal incident soft X-rays (852.8 eV) are shown in Fig. 1(b). The fcc cluster indicates the relation of crystal orientation and FFPs. FFPs clearly appear along the directions of atoms surrounding excited atoms in the AED pattern. The intensity at an extremely low emission angle especially in the [100] direction is mainly due to the emission from the outermost surface atoms. The FFPs in the [101] and [001] directions indicate the existence of Ni atoms at the second and third layers, respectively.

We obtained a XANES spectrum by monitoring Auger electron intensity while scanning excitation photon energy. The intensity of different FFPs corresponds to the signal of different atomic layers. Figure 2(a) shows the atomic-layer resolved Ni L_3-XANES spectra of a 15 ML Ni film. The first- to fourth-layer spectra were extracted from [100], [101], [001] and [103] FFP intensities, respectively. Note that the intensity of the so-called 6-eV satellite is diminished in the surface layer spectrum. This is due to the atomic and electronic structures peculiar to the outmost surface layer where atoms bond to a relatively few neighboring atoms. The L_3 peaks in the spectra of the surface layer shift to higher photon energy compared to those in the spectra of interior layers by about 0.1 eV.

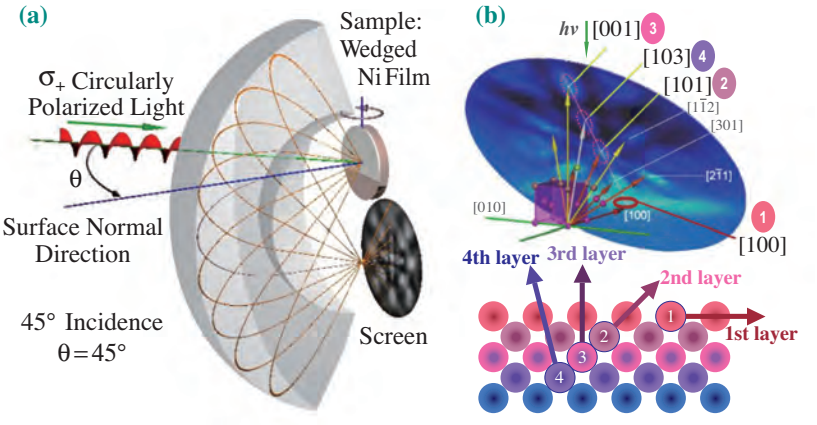


Fig. 1. **(a)** Schematic diagram of display-type analyzer. An Auger electron diffraction (AED) snapshot is taken in a short time, typically 1 sec. **(b)** AED pattern of Ni thin film (kinetic energy: 841.0 eV) together with fcc cluster. Electron-emitting atoms are specified from forward focusing peaks.

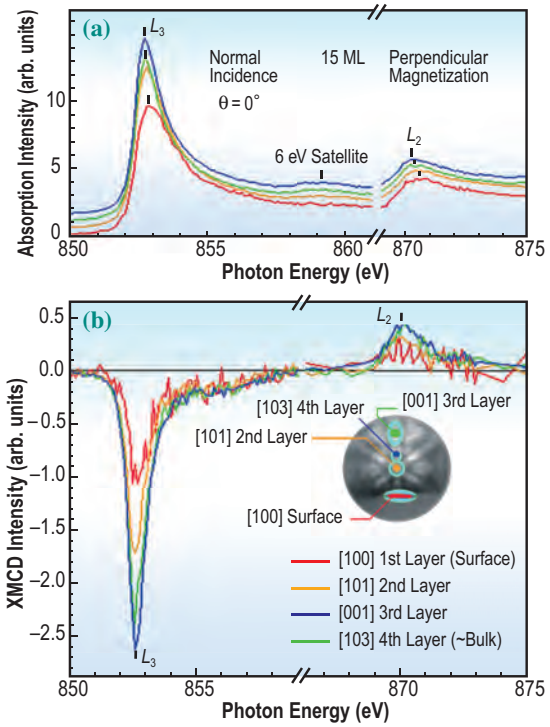


Fig. 2. **(a)** Atomic-layer-resolved Ni L-XANES and **(b)** X-ray magnetic circular dichroism (XMCD) spectra of perpendicularly (15 ML) magnetized Ni films.

The L_3 shifts correspond to the surface core level shifts.

The XMCD spectrum is the difference between the Ni *L*-XANES spectra excited with positive (σ_+)- and negative (σ_-)-helicity light. Figure 2(b) shows the atomic-layer-resolved XMCD spectra for the 15 ML perpendicularly magnetized films. We analyzed Ni magnetic structures of various film thicknesses on the atomic scale and deduced the spin (μ_{spin}^{eff}) and orbital (μ_{orb}) magnetic moments for each atomic layer.

The orbital magnetic moments are more enhanced at the surface layers compared with the spin magnetic moments in the case of 8 ML (in-plane); the variations in the moments are rather small in the case of 15 ML (perpendicular). The orbital is sensitive to the local bonding configuration, while the spin reflects the long-range magnetic ordering. At a thickness beyond SRT, the magnetic moment orientation in a perpendicular direction is caused by the spin magnetic moment in the interior layers, whereas in the region below SRT, where the spin magnetic moment is small, the orbital magnetic moment of the surface layers determines the orientation to be in-plane. SRT at 10 ML is based on such a subtle balance of magnetic moments. Knowing exactly how these magnetic moments change throughout the structure will be useful for making perpendicular magnetic recording devices. Perpendicular magnetic domains are stably packed closer together for greater density than in-plane magnetic domains, which leads to more data per square inch.

In conclusion, we have developed a direct method for atomic-layer resolved analysis of electronic and magnetic structures for surfaces and thin films. This technique opens a door for the study of the correlations of the atomic, electronic, and magnetic structures of nanostructures at the surfaces.

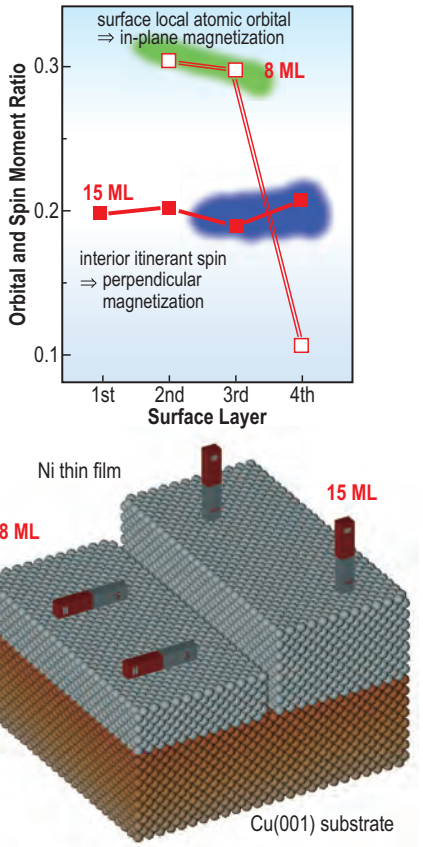


Fig. 3. Ratio of orbital to spin components ($\mu_{orb}/\mu_{spin}^{eff}$) of each atomic layer in the Ni thin film on a Cu(001) surface.

Fumihiko Matsui[a,*], Tomohiro Matsushita[b] and Hiroshi Daimon[a]

[a] Graduate School of Materials Science, Nara Institute of Science and Technology
[b] SPring-8/JASRI

*E-mail: matui@ms.naist.jp

References

[1] K. Amemiya *et al.*: Phys. Rev. B **71** (2005) 214420; *ibid.* **72** (2005) 201404(R).
[2] *F. Matsui, T. Matsushita, Y. Kato, F.Z. Guo, M. Hashimoto, K. Inaji and H. Daimon: Phys. Rev. Lett.* ***100*** *(2008) 207201.*
[3] H. Daimon: Phys. Rev. Lett. **86** (2001) 2034.
[4] T. Matsushita *et al.*: Phys. Rev. B **75** (2007) 085419.

Magnetic Ordering and Fluctuation in One-Dimensional Fe Nanowires

Magnetism in one-dimensional (1D) systems is a classical problem but still a hot topic. Because of the simplicity and fewer parameters of the systems, this problem was treated in theoretical studies early in the 20th century. It has been proved by theories that long-range ferromagnetic order in 1D is prohibited at finite temperatures in principle. Even if all magnetic moments are initially aligned in 1D, spin flips take place owing to thermal fluctuation at finite temperatures. Accordingly, 1D spin systems are inevitably broken up into shorter magnetic domains, and total magnetization becomes nearly zero. However, ferromagnetic ground states can appear if strict one-dimensionality is broken by orbital degeneracy or quasi-1D geometry. From this point of view, we fabricate 1D Fe nanowires grown on vicinal Au surfaces and examine the magnetism in 1D by X-ray magnetic circular dichroism (XMCD).

The growth of Fe nanowires on Au(788) [1] is illustrated in Fig. 1. Fe atoms dosed on the stepped Au surface preferentially adsorb at step edges, thereby decorating them. At an Fe coverage of 0.07 ML, an array of monatomic chains is formed and the second-row growth begins. As Fe coverage is increased, 1D Fe nanowires grow in a step-flow growth mode. However, the morphology of such nanowires gradually changes depending on Fe coverage. The nanowires show periodically meandered shapes above ~0.3 ML owing to the faster growth in fcc regions than in hcp regions. Fe stripes reach adjacent ones in the fcc regions, and 2D networks are formed at around 0.6 ML.

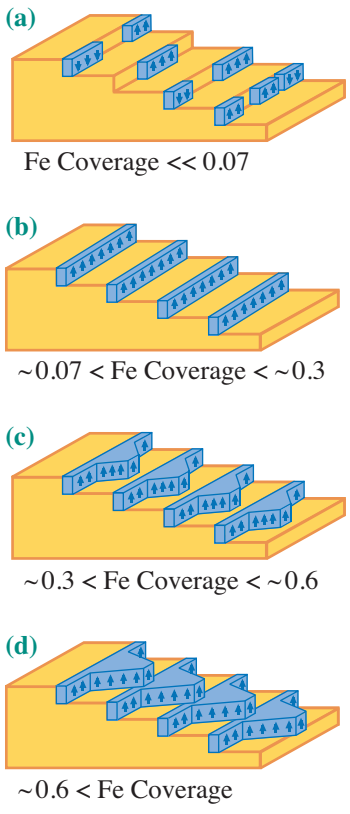


Fig. 1. Schematics of the growth manner of Fe on a Au(788) surface. **(a)** 1D fragments of Fe below 0.07 ML. **(b)** Complete formation of 1D monatomic Fe chains at 0.07 ML. **(c)** Periodically meandered quasi-1D nanowires of Fe between 0.3 ML and 0.6 ML. **(d)** 2D networks of Fe above 0.6 ML.

Figure 2(a) shows an XMCD spectrum for 1D monatomic chains of Fe (0.07 ML) [2], which was taken at **BL25SU**. Fe $L_{2,3}$ absorption edges are related to excitations from the 2*p* core level into unoccupied 3*d* valence states. The strong dichroism directly proves the existence of magnetic moments and their alignment in the external field. From the XMCD spectrum, we estimated the orbital moment to the effective spin moment ratio $m_L / m_s^{eff} = 0.26$, which is five times as large as 0.05 obtained for 2D Fe monolayers. Such an increasing in orbital magnetic moment with a decrease in coverage is mainly due to the reduction in atomic coordination.

Figure 2(b) shows the temperature dependence of magnetization at different Fe coverages. It is clear that MCD intensity decreases as temperature increases. Furthermore, we found that, as the coverage is decreased, 1D nanowires show a faster decay with *T*. Particularly, in the case of monatomic chains, magnetization rapidly drops with a slight increase in temperature. These results suggest that the orbital magnetic moment is enhanced in 1D nanowires, but that the large magnetization is rapidly suppressed with increasing temperature owing to intensive fluctuation in lower dimensions. As a result, magnetization is decreased as Fe coverage is decreased at a finite temperature of $T = 18$ K, as shown in Fig. 2(b). Presumably, cooling the samples down to a temperature low enough to suppress thermal fluctuation may yield a giant magnetization in reduced dimensionality.

Figure 3(a) shows the magnetization curves for monatomic chains. We can clearly see a phase transition from ferromagnetic to superparamagnetic. At the lowest temperature, the magnetization curve shows a hysteresis loop, where each domain is blocked in a fixed magnetization state (up or down) as a result of the freezing of thermal fluctuation. However, the curve is not a simple square like

hysteresis loop, and the remanence at the zero field is much smaller than the saturation magnetization. This implies that thermal fluctuation still seems to be not negligible in monatomic chains. As temperature increases, the coercive field disappears at the blocking temperature T_B. Above T_B, the magnetization spontaneously reverses because of thermal agitation, and typical superparamagnetic reversible S-shaped curves are observed. Furthermore, blocking temperature decreases with decreasing coverage, which is a general trend observable in low dimensionality.

Finally, we focus on magnetization reversal in Fe nanowires [3]. In the case of monatomic chains, the magnetization process is based on single spin flips, and domain boundaries can move site to site. If the growth of nanowires ideally proceeds in a step-flow growth mode, magnetization reversal behavior is independent of Fe coverage, i.e., size of nanowires. As mentioned above, however, the nanowires show the periodically meandered shapes at higher coverages. Since structural constrictions often serve as nucleation, annihilation and pinning centers for domain boundaries, magnetization reversal in quasi-1D nanowires occurs as macrospins flip to the opposite direction. Finally, the magnetization process drastically changes when the 2D networks of Fe are built up at around 0.6 ML. Superparamagnetic fluctuation is strongly suppressed, leading to a remanence-to-saturation ratio of nearly 1 [Fig. 3(b)] and the coherent rotation of the entire magnetization under the action of the external field. These results indicate that the size and overall shape of nanowires have a decisive effect on magnetic properties, such as fluctuation, domain patterns and magnetization processes.

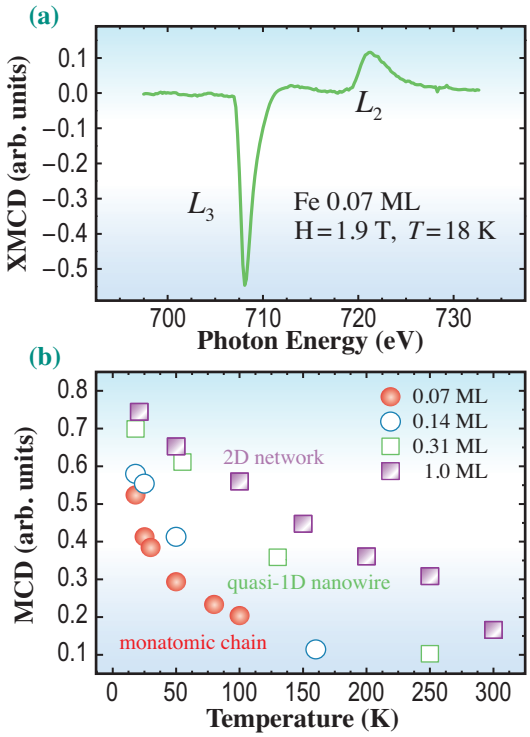


Fig. 2. **(a)** XMCD spectrum of 1D monatomic chains of Fe on Au(788). **(b)** Temperature dependence of magnetization per Fe atom of 1D nanowires on Au(788).

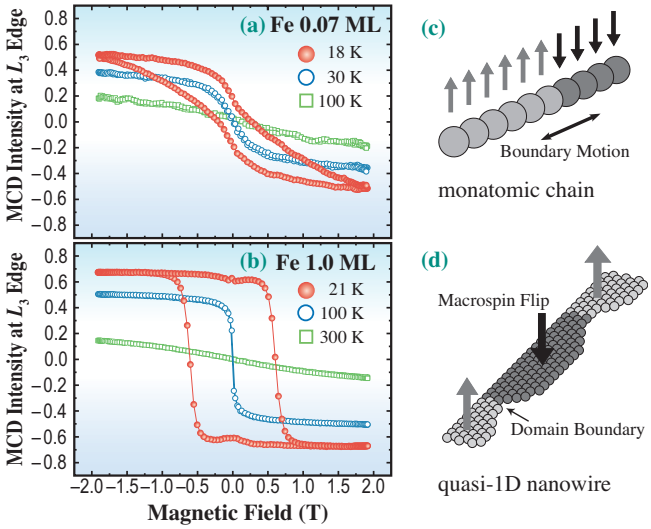


Fig. 3. Magnetization curves of **(a)** monatomic chains (0.07 ML) and **(b)** 2D monolayer (1.0 ML). Magnetic domain structures in **(c)** monatomic chains and **(d)** periodically meandered nanowires. The black and gray atoms are magnetized into and out of the surface, respectively.

Susumu Shiraki

Graduate School of Frontier Sciences,
The University of Tokyo

E-mail: shiraki@k.u-tokyo.ac.jp

References

[1] S. Shiraki *et al.*: J. Phys. Soc. Jpn. **74** (2005) 2033.
[2] H. Fujisawa *et al.*: Phys. Rev. B **75** (2007) 245423.
[3] *S. Shiraki, H. Fujisawa, T. Nakamura, T. Muro, M. Nantoh and M. Kawai: Phys. Rev. B* ***78*** *(2008) 115428.*

Nature of Magnetic Coupling between Mn Ions in As-Grown $Ga_{1-x}Mn_xAs$ – Systematic Temperature and Magnetic Field Dependent XMCD –

$Ga_{1-x}Mn_xAs$ is the prototypical and most well-characterized diluted magnetic semiconductor (DMS) [1]. Although many studies have been performed intensively to obtain a high Curie temperature (T_C) exceeding room temperature, it has not been achieved yet. Because $Ga_{1-x}Mn_xAs$ is grown under thermal non-equilibrium conditions, it is difficult to avoid the formation of various kinds of defect and/or disorder, which might lead to any non-ferromagnetic component. The characterization of the non-ferromagnetic Mn ions is therefore a clue to identifying how they are related to ferromagnetic ordering and eventually to improving the ferromagnetic properties of $Ga_{1-x}Mn_xAs$ samples. However, it has been difficult to extract the above information through conventional magnetization measurement owing to the large diamagnetic response of the substrate and the unavoidable mixture of magnetic impurities. We have performed an X-ray magnetic circular dichroism (XMCD) measurement to address the problem.

X-ray magnetic circular dichroism (XMCD) is defined as the difference between X-ray absorption spectra (XAS) intensities of a ferromagnetic material for circularly polarized photons that are parallel and antiparallel to the orientation of the magnetization of the material. One can investigate and/or characterize the magnetic properties of a specific magnetic element. In the soft X-ray region (400 eV - 2000 eV), especially, the information on the spin electronic structures can be obtained directly because the $L_{2,3}$ absorption edge of transition metals ($2p$ - $3d$) exists. Using the sum rules for the XAS and XMCD signal [2], the spin and orbital magnetic moments of a specific element can also be estimated quantitatively.

In the present study, in order to characterize the magnetic behaviors of substitutional Mn (Mn_{sub}) and interstitial Mn (Mn_{int}), we performed systematic T (sample temperature)- and H (magnetic field)-dependent XMCD studies in the Mn $L_{2,3}$ absorption edge region of $Ga_{1-x}Mn_xAs$. The experiments were performed at beamline **BL23SU** using the XMCD apparatus shown in Fig. 1. T and H can be scanned from < 6 K to room temperature and from 0 to 10 T, respectively. Recently, we have improved the XMCD measurement system for the effective measurement for a short time by installing a nonstop measurement system [3]. Using the nonstop measurement system, we can perform systematic T- and H-dependent XMCD measurements under many experimental conditions. We prepared two as-grown samples with different Mn concentrations, $x = 0.042$ and 0.078, whose T_C values were ~60 and 40 K, respectively. The XAS were obtained by the total electron yield mode. The measurements were carried out without surface treatment and H was applied to the sample perpendicular to the film surface.

Figure 2 shows the XAS (μ^+ and μ^-) in the photon energy region of the Mn L_3 absorption edge and the

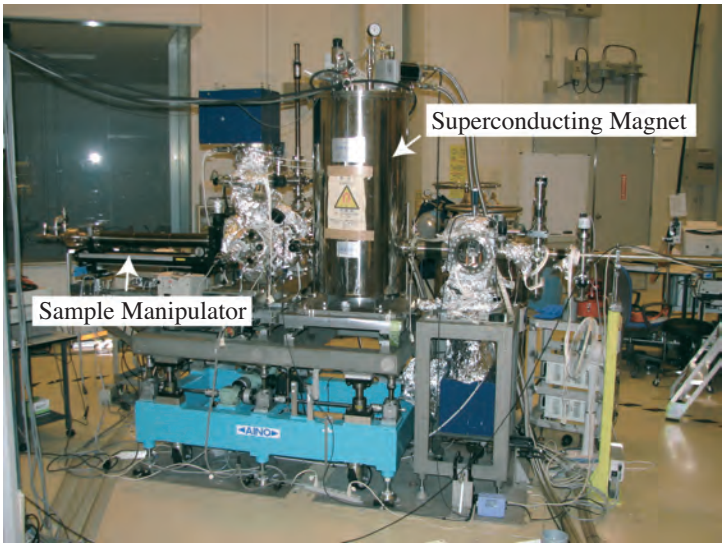


Fig. 1. XMCD apparatus of the soft X-ray beamline BL23SU.

corresponding XMCD spectra, defined as (μ^+ - μ^-), at T = 20 K and H = 0.5 T for x = 0.078. Here, μ^+ (μ^-) refers to the absorption coefficient for the photon helicity parallel (anti-parallel) to the Mn 3d majority spin direction. The magnitude of XMCD signals shows significant T and H dependences. Using these XAS and XMCD spectra, we applied the XMCD sum rules [2]. The spin magnetic moments (M_S) at T = 20 K and H = 0.5 T are estimated to be M_S = 2.5 ± 0.2 and 1.7 ± 0.2 (μ_B per Mn) for x = 0.042 and 0.078, respectively.

Figure 3 shows the H dependence of M_S at several temperatures for x = 0.042 [panel (a)] and 0.078 [panel (b)] obtained by the XMCD measurements. Above 0.5 T, M_S increases almost linearly as a function of H. At T = 20 K, the slope (dashed lines) and $M_S|_{H\to 0T}$ are smaller for x = 0.078 than for x = 0.042, suggesting that the anti-ferromagnetic (AF) interaction becomes stronger for x = 0.078 than for x = 0.042. This is reasonable because the number of Mn_{int} is expected to be larger for larger Mn concentrations. Assuming that the M_S per Mn_{sub} is 5 (μ_B per Mn) and the M_S of Mn_{int} is antiparallel to that of Mn_{sub}, the ratio of Mn_{int} atoms in the intrinsic component (R_{int}) is estimated to be 0.26 for x = 0.042 and 0.33 for x = 0.078 from $M_S|_{H\to 0T}$ at 20 K. Therefore, this means that the number of Mn_{int} ions should be strongly related to T_C, namely, Mn_{int} ions suppress the ferromagnetic properties by ordered spins of Mn_{sub} ions.

In conclusion, we have investigated the T, H and Mn concentration dependences of the ferromagnetism in as-grown $Ga_{1-x}Mn_xAs$ samples by XMCD measurements. The present results indicate that the AF interaction between Mn_{sub} and Mn_{int} ions, which is enhanced as the Mn concentration x increases, plays an important role in determining the magnetic behavior of $Ga_{1-x}Mn_xAs$. In addition, the number of Mn_{int} ions should be strongly related to T_C. These findings should give a valuable insight into the inhomogeneous magnetic properties of many DMS's [4].

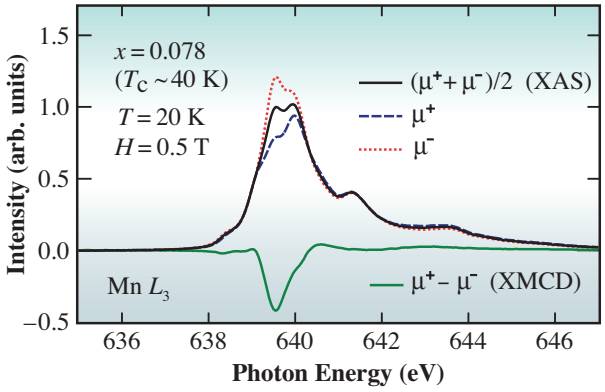


Fig. 2. XAS and XMCD spectra of x=0.078 at T=20 K and H=0.5 T in the photon energy region of the Mn L_3 absorption edge.

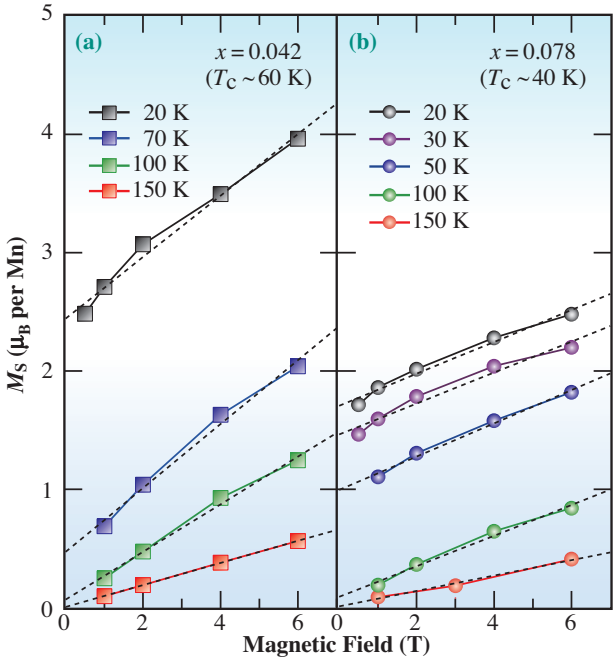


Fig. 3. H and T dependences of M_S **(a)** x=0.042 and **(b)** x=0.078. The dashed lines show fitted straight lines above H = 0.5 T.

Yukiharu Takeda

SPring-8/JAEA

E-mail: ytakeda@spring8.or.jp

References

[1] H. Ohno: Science **281** (1998) 951.
[2] B.T. Thole *et al.*: Phys. Rev. Lett. **70** (1993) 694.
[3] Y. Fukuda *et al.*: JAEA-Technology 2007-007.
[4] *Y. Takeda, M. Kobayashi, T. Okane, T. Ohkochi, J. Okamoto, Y. Saitoh, K. Kobayashi, H. Yamagami, A. Fujimori, A. Tanaka, J. Okabayashi, M. Oshima, S. Ohya, P. N. Hai, M. Tanaka: Phys. Rev. Lett.* ***100*** *(2008) 247202.*

SR-PES and STM Observation of Metastable Chemisorption State of Oxygen on Si(110)-16×2 Surface

With the decrease in MOS device size down to the 65 nm node, the thickness of the SiO_2 gate insulator now falls into the region of 1.2 nm or less, which makes detailed understanding and precise control of the initial oxidation of Si surfaces even more indispensable. This situation applies not only to the conventional Si(001) surface but also to the Si(110) surface, which, from its higher hole mobility [1] and inevitable use in the multi-gated transistors [2], forms a key surface in next-generation CMOS technology. Despite this importance, knowledge of the kinetics of the initial oxidation of the Si(110) surface has been quite limited.

Among various aspects of kinetics in Si oxidation, one of the hot issues is the presence of metastable oxidation states. They are important because they form one of the crucial reaction pathways in Si oxidation. On the Si(111)-7×7 surface, molecularly adsorbed states of oxygen at adatom's dangling bonds are metastable [3], while on the Si(001)-2×1 surface the silanone species (Si=O) is metastable [3,4]. These metastable adsorption states change into more stable oxidation states after annealing. In contrast to the well-understood Si(111) and Si(001) surfaces, however, the Si(110) surface has no information as regards the presence/absence of the metastable adsorption states of oxygen on it. In this study, we conducted high-resolution photoelectron spectroscopy (PES) at SPring-8 to investigate the oxidation states of the Si(110)-16×2 clean surface after the room-temperature (RT) adsorption of oxygen molecules. The impacts of mild 300°C annealing have been investigated as well. Comparative scanning tunneling microscopy (STM) was also conducted to observe atomistic changes after the annealing.

PES measurements were conducted at the surface-chemistry endstation of beamline **BL23SU**. By chemical *ex situ* and thermal *in situ* treatments, we obtained a 16×2 reconstructed surface, which is indicative of the cleanliness of this Si(110) surface. Excitation photons with energies at 365 and 687 eV were used, and photoelectrons with a take-off angle of 20° were collected. Similar chemo-thermal treatment was applied as well for the STM [5].

Figure 1(a) shows the Si 2*p* spectrum of the Si(110)-16×2 clean surface after a RT exposure to 10 L (1 L = 1.0×10^{-6} Torr·s) oxygen molecules. In addition to the bulk peak, at least five components were observed in the spectrum: three suboxide species (Si^{n+}: n = 1 - 3) and two surface core-level shifts (SCLS) at α(+0.30 eV) and β(-0.33 eV). The SCLS components are related to the 16×2 surface reconstruction. The presence of higher suboxides like Si^{2+} and Si^{3+}, in addition to primitive Si^{1+}, suggests that the initial oxides are somewhat aggregated even for this small-dose (10 L), small oxygen coverage (0.4 ML), low-temperature (RT) adsorption.

The mild annealing at 300°C for 15 min drastically changes the oxide structure. The Si 2*p* spectrum after the annealing (Fig. 1(b)) shows a decrease in the level of Si^{2+} and an increase in those of the Si^{3+} components. The emergence of the Si^{4+} component is also observed. These results strongly suggest the onset of further aggregation of the oxides by the annealing. Furthermore, the binding energies of the Si^{2+} and Si^{3+} species shift towards higher energies,

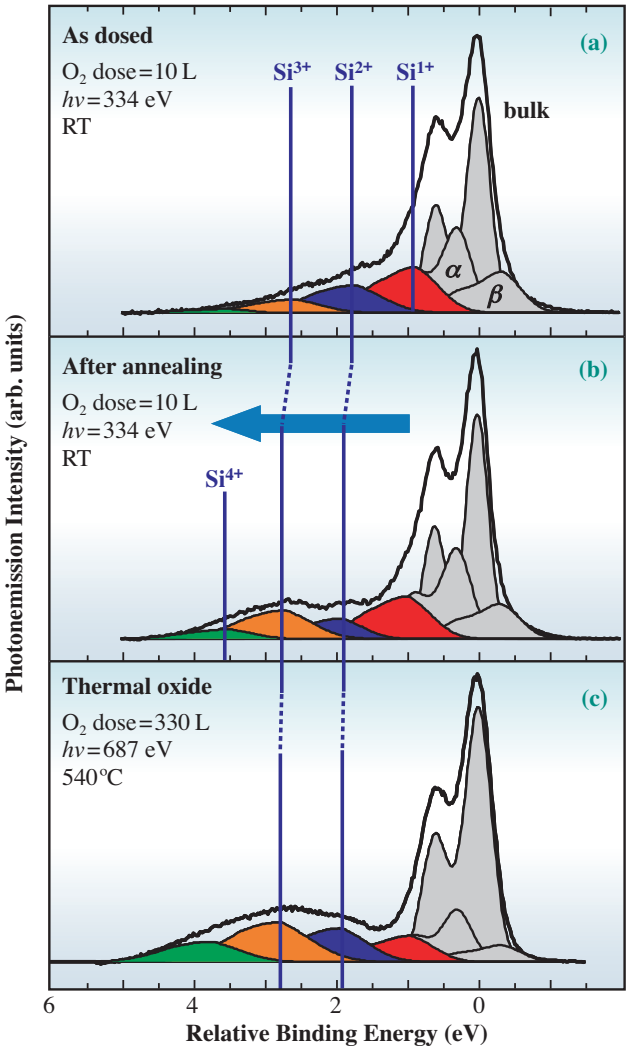


Fig. 1. Si 2*p* spectra of **(a)** as O_2-exposed, **(b)** as-annealed, and **(c)** as thermally oxidized (1 ML) Si(110)-16×2 surfaces.

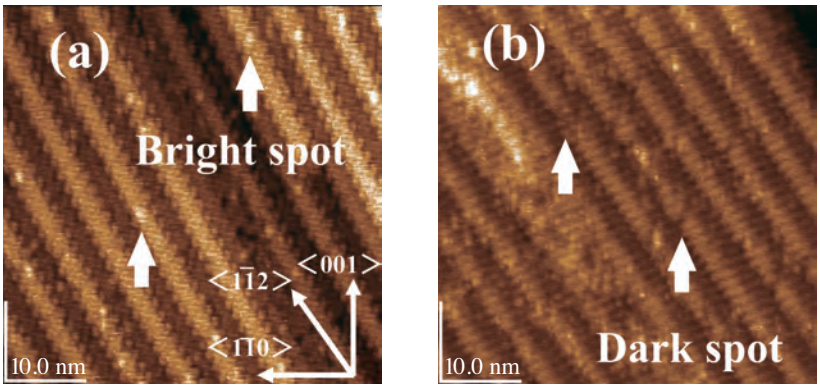


Fig. 2. Filled-state STM images of **(a)** as O_2-exposed and **(b)** as-annealed Si(110)-16×2 surfaces.

approaching those of thermal oxides shown in Fig. 1(c). Such peak shifts of Si suboxides have been already reported for the Si(001)-c(4×2) surface adsorbed with oxygen molecules at low temperatures [6]. According to Ref. [6], the shifts are attributed to deviations in the Si-O-Si angle or in Si-O bond length from the corresponding equilibrium values. Using this scheme, the peak shifts observed in the annealed Si(110):O surface (Fig. 1(b)) are understood to have arisen from the relaxation of locally strained oxidized structures into energetically more stable ones. In other words, the RT adsorption of oxygen molecules onto the Si(110)-16×2 surface results in metastable adsorption states.

This change in the oxidation states with annealing is observed by STM as well. Figure 2(a) shows the unoccupied-state STM image from the Si(110)-16×2 surface adsorbed with oxygen at RT. The small bright spots seen at the pentagon pairs (PPs), the unit for the Si(110)-16×2 surface reconstruction, correspond to reacted sites. Figure 2(b) shows an STM image of the surface after the 300°C, 15-min annealing. Dark spots larger than the bright spots in Fig. 2(a) can now be seen. Combining these with the results of the PES, the small bright spots at PPs before the annealing are related to metastable oxidation states, and the larger dark spots to stable oxidation sites. Figure 3 illustrates the possible oxidation structures before and after the annealing. In RT adsorption, energetically metastable oxidation states, such as adsorption at dangling bonds, are present (Fig. 3(a)). After the annealing, on the other hand, oxygen atoms move to more stable sites, most probably to the backbonds of PP adatoms (Fig. 3(b)). The actual oxidized states after the annealing could be more disordered, because a closer look at the dark spots in the STM image in Fig. 2(b) no longer shows the ordered PP structure. The oxidation caused by the annealing is accompanied by the collapse of the 16×2 reconstruction structure.

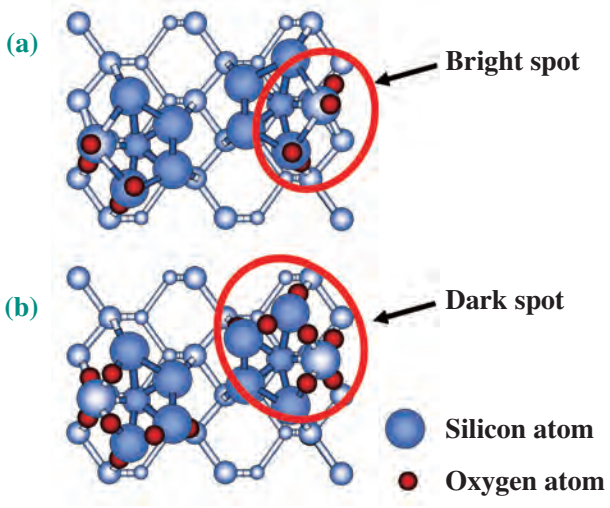


Fig. 3. Possible oxidation structure of **(a)** as O_2-exposed and **(b)** as-annealed Si(110)-16×2 surfaces.

Maki Suemitsu

Research Institute of Electrical Communication,
Tohoku University

E-mail: suemitsu@cir.tohoku.ac.jp

References

[1] T. Sato *et al.*: Phys. Rev. B **4** (1971) 1950.
[2] L. Chang *et al.*: Proc. IEEE **91** (2003) 1860.
[3] K. Sakamoto *et al.*: Phys. Rev. B **68** (2003) 075302.
[4] Y.J. Chabal *et al.*: Phys. Rev. B **66** (2002) 161315.
[5] *Y. Yamamoto, H. Togashi, A. Kato, Y. Takahashi, A. Konno, Y. Teraoka, A. Yoshigoe, H. Asaoka, M. Suemitsu: Appl. Surface Sci.* ***254*** *(2008) 6232.*
[6] H.W. Yoem *et al.*: Phys. Rev. B **59** (1999) R10413.

Recoil Effect of Photoelectron in the Fermi-Edge of Simple Metals

In X-ray photoelectron spectroscopy, the emitted electron kicks the atom from which it is ejected in accordance with the conservation of momentum. For an atom with mass M in free space, the recoil energy δE is simply estimated as $\delta E = (m/M)E_{kin}$, where m is the electron mass, and E_{kin} is the electron kinetic energy. This gives rise to a loss in E_{kin} of the emitted photoelectron. This recoil effect is usually negligible because of the enormous mass difference between the atom and the electron, as long as the excitation energy is not very large. Quite recently, however, clear evidence of recoil effects has been found in the hard X-ray photoelectron spectra of graphite [1]. Under the excitation of the core level by X-ray photons with an energy of several keV, the photoelectron spectra show a remarkable shift and broadening as compared to the case of excitation by soft X-rays. Similar spectroscopic features of recoil effects have been observed in other fundamental processes such as elastic electron scattering and neutron scattering [2].

In the present study, we have investigated the recoil effects in the photoelectron spectra for valence levels [3]. In the core level spectra, one may expect that the recoil effect should be observed because core electron is localized around the atom (see Fig. 1). On the other hand, since Bloch electrons in a valence band are delocalized all over the crystal (Fig. 1), it is not clear whether the recoil momentum is shared by all the atoms of the crystal. This would result in no observable recoil effect, just like the recoilless transition in the in the Mössbauer effect. In contrast to this naïve expectation, we have found a clear evidence of the recoil effect for conduction electrons in a simple metal from our experiments.

Hard X-ray photoelectron spectra of Au and Al at the excitation energy of 7940 eV and soft X-ray spectra of 880 eV were measured at the undulator beamlines **BL29XU** and **BL17SU**, respectively, using hemispherical electron energy analyzers.

Figure 2 shows the photoelectron spectra around the Fermi edge of Au (diamonds) and Al (circles) measured at 20 K with the excitation energy of 7940 eV. The binding energy scale is calibrated by assuming that the recoil energy in Au (M=197) is negligible. It is clear that the Fermi edge of Al (M=27) is shifted to higher binding energy. This shift is due to the kinetic energy loss of photoelectron from the Fermi level in Al because of its lighter atomic mass compared to Au, and is an evidence of the recoil effect of Bloch electrons. Furthermore, the edge profile has a slightly larger slope for Al than for Au. Conventional fitting analysis of these Fermi edge profiles using the Fermi-Dirac function (not shown) elucidates an energy shift of 120 meV in Al relative to Au, and Gaussian widths of 160 meV for Al and 124 meV for Au. The broadening of the width in Al is also a sign of the recoil effect because the contribution of the instrumental energy resolution to the width is the same in these spectra.

Soft X-ray spectra of Au (diamonds) and Al (circles) measured at 50 K with the excitation energy of 880 eV are shown in Fig. 3. Although the difference of the spectrum between Al and Au is small in this excitation energy, recoil effect does exist even in soft X-ray spectra.

The observed recoil effect of photoelectrons in the Fermi edge has been theoretically interpreted.

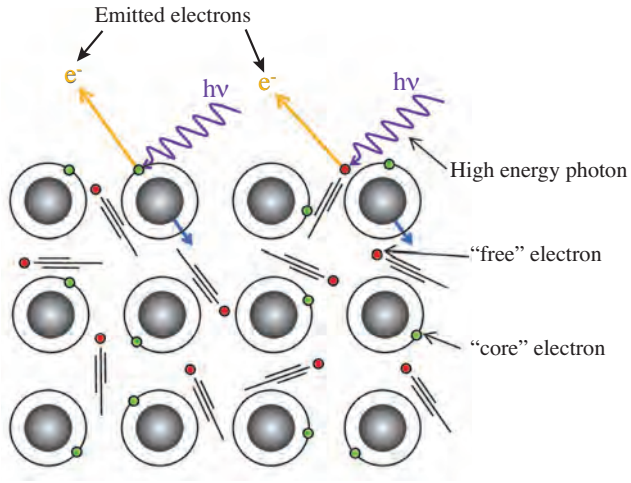


Fig. 1. When a photon (hν) of sufficient energy hits a sample, it can excite the emission of electrons. For a metal, these electrons can come either from specific atoms (green circles) or from the sea of 'free' valence electrons (red) that extends over the whole sample.

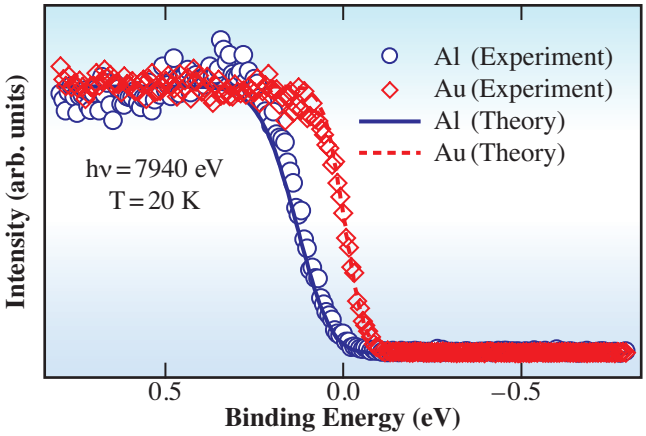


Fig. 2. Photoelectron spectra near Fermi edge of Al (circles) and Au (diamonds) with excitation energy 7940 eV. The zero point of the binding energy is chosen at the observed value of the chemical potential of Au. The solid line and the dotted line indicate the theoretical curves calculated by the Debye model.

A model calculation of Bloch electrons based on the isotropic Debye model (solid and dotted lines in Figs. 2 and 3) reproduces well the experimental spectra. Details of the calculation are described in Ref. [3]. The existence of the photoelectron recoil effect means that the electron is coupled with the crystal lattice, and the wave function of the electron follows adiabatically the atomic motion. Therefore, it is quite surprising that the Bloch electron in the valence band of Al, which is a typical material where the nearly free electron picture works well, shows remarkable recoil effects. The finding of recoil effects in Bloch electrons indicates a new spectroscopic aspect of X-ray photoelectron spectroscopy, and due care must be taken to interpret changes at and near the Fermi level when using hard X-rays. The magnitude of the recoil effect depends essentially on the mass of the component atoms. Since the photoelectron spectra reflect also the nature of the electronic state in the initial state, the recoil effect in the valence levels of composite materials poses an interesting problem. If the material is composed of atoms with big mass differences, and if the valence levels are made of hybridized orbitals originating in specific atomic species, the modification of the photoelectron spectra will depend on the local density of states of the level.

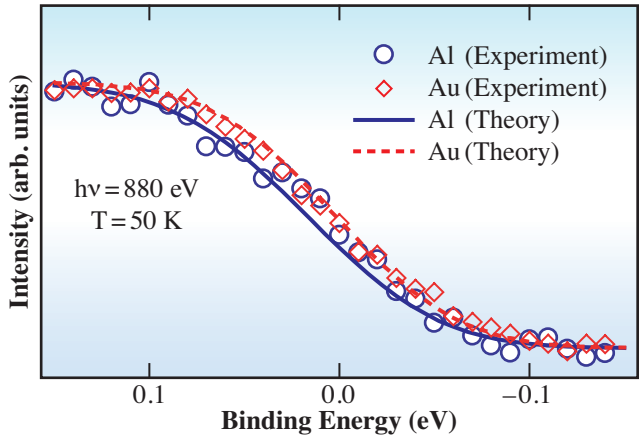


Fig. 3. Photoelectron spectra near Fermi edge of Al (circles) and Au (diamonds) with excitation energy 880 eV. The zero point of the binding energy is chosen at the observed value of the chemical potential of Au. The solid line and the dotted line indicate the theoretical curves calculated by the Debye model.

Yasutaka Takata[a,*] and Yosuke Kayanuma[b]

[a] SPring-8/RIKEN
[b] Graduate School of Engineering, Osaka Prefecture University

*E-mail: takatay@spring8.or.jp

References

[1] Y. Takata *et al.*: Phys. Rev. B **75** (2007) 233404.
[2] M. Vos *et al.*: Phys. Rev. B **78** (2007) 024301.
[3] *Y. Takata, Y. Kayanuma, S. Oshima, S. Tanaka, M. Yabashi, K. Tamasaku, Y. Nishino, M. Matsunami, R. Eguchi, A. Chainani, M. Oura, T. Takeuchi, Y. Senba, H. Ohashi, S. Shin and T. Ishikawa: Phys. Rev. Lett.* ***101*** *(2008) 137601.*

Detection of the Valence Band in Buried Co_2MnSi-MgO Tunnel Junctions by Means of Hard X-Ray Photoemission Spectroscopy

The Co_2YZ (Y = transition metal, Z = main group element) Heusler compounds have attracted scientific and technological interest for their potential use as materials for magneto-electronic devices [1]. From *ab initio* calculations it was concluded that these compounds have peculiar transport properties because the minority-spin density at the Fermi energy ε_F vanishes, wherefore they are called half-metallic ferromagnets. One major technology where Co_2 based Heusler compounds are used is on tunneling magneto resistive (TMR) junctions. High TMR ratios of 179% at room temperature and 683% at 4.2 K were demonstrated for fully epitaxial magnetic tunnel junctions with Co_2MnSi films as both lower and upper electrodes and MgO tunnel barrier [2]. To develop high performance spintronic devices with Heusler compound based thin films as ferromagnetic electrodes, it is essential to clarify the electronic structures of these films interms of the half-metallic nature.

For the present study [3], multi component thin film arrangements were used (see [2,3] and references there for details). Polycrystalline bulk material was used for comparison (see [4] for details). The HAXPES (hard X-ray photoemission spectroscopy) experiments were performed at beamline **BL15XU**. The photon energy was fixed at 5.94677 keV using a double crystal monochromator and a Si(333) post monochromator. The photo emitted electrons were analyzed for their kinetic energy and detected by means of a hemispherical analyzer (Scienta). The overall energy resolution (monochromator plus analyzer) was set to 250 meV, as verified by spectra of the Au valence band at ε_F. Spectra close to ε_F were taken with a resolution of 150 meV. The angle between the electron spectrometer and photon propagation is fixed at 90°. The photons are p-polarized. For the thin films, a near normal emission ($\theta = 2°$) detection angle was used.

A wide energy scan photoelectron spectrum of the Co_2MnSi/MgO thin film system is shown in Fig. 1. It demonstrates the demanding task of high energy valence band spectroscopy. The intensity of the valence band is about 200 times lower compared to the dominant emission from the Co 2*p* states and becomes only weakly visible in the spectrum taken with reduced energy and intensity scales.

Figure 2 compares valence band spectrum of bulk Co_2MnSi to spectra from a Co_2MnSi layer buried underneath MgO/AlO_x with different thickness of the MgO interlayer. The spectrum of the thin film in Fig. 2(b) agrees well with the bulk sample. However, the emission is strongly suppressed in the film with the 20 nm thick MgO layer. In particular, the peak in the density of states at -1.3 eV is clearly resolved. The low lying *s*-band below -8 eV is only seen in Fig. 2(a) and 2(b). This part, in addition to the lower parts of the *p*- and *d*-bands, is covered by the emission from oxygen 2*p* states of MgO in Fig. 2(c) where the oxide is 20 nm thick. The similar structure of the valence band close to ε_F in the thin films and the bulk material is obvious.

In Fig. 3, the valence band spectra for different MgO thicknesses are directly compared by scaling

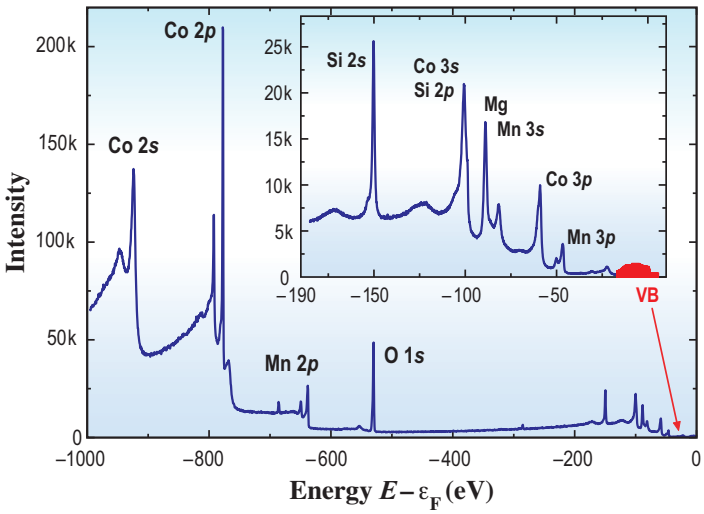


Fig. 1. High kinetic energy survey spectrum of Co_2MnSi/2 nm MgO/1 nm AlO_x. The inset shows the energy range of the semi-core level and the valence band.

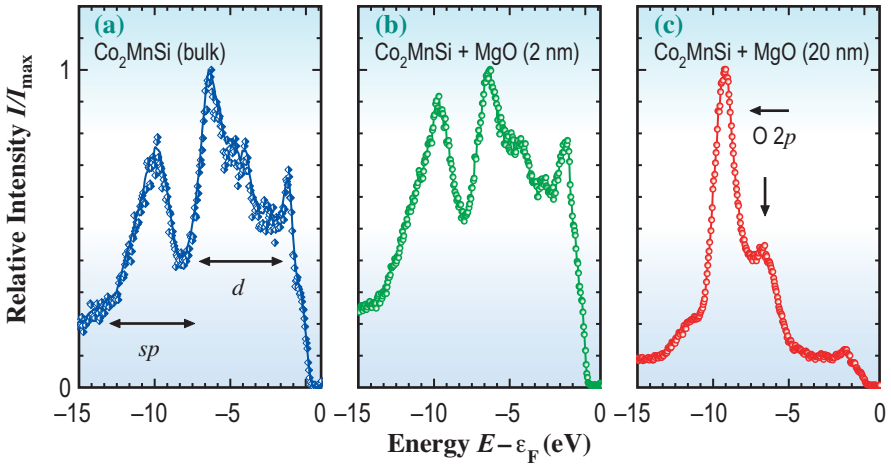


Fig. 2. High kinetic energy photoemission spectra of buried Co_2MnSi. The spectrum from bulk material **(a)** is compared to thin films with different thickness 2 nm **(b)**, 20 nm **(c)** of the MgO interlayer. Co_2MnSi valence bands and oxygen 2*p*-states are indicated by arrows in **(a)** and **(c)**, respectively.

up the intensity of the 20 nm layer. The identical structure of the spectra, in particular close to the Fermi energy, is easily recognized. The high intensity with a center at about -1.3 eV is due to emission from flat *d*-bands belonging to minority states localized in the Co planes and the highly localized Mn *d* majority states (e_g). The Co t_{2g} like states mainly define the upper energy of the minority valence bands, whereas the lower intensity at the Fermi energy arises from steep delocalized majority *d*-bands with t_{2g} character.

The obtained result confirms the promise of an epitaxial, single-crystalline Co_2-based Heusler compound film as a ferromagnetic electrode for spintronic devices. In particular it was shown that buried Co_2MnSi films exhibit the same valence density of states like bulk samples that is typical for halfmetallic ferromagnets for spintronic applications. In summary, the present study demonstrates the feasibility of HAXPES to explore the valence band electronic structure in metallic layers deeply buried under oxide films.

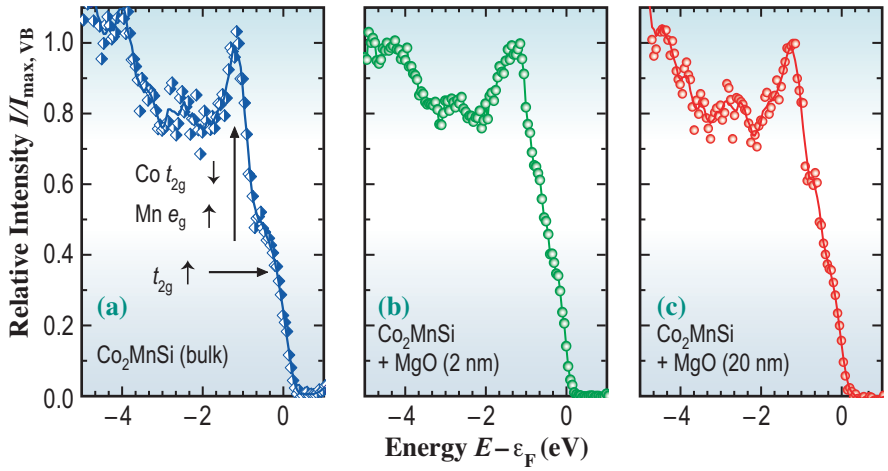


Fig. 3. Comparison of the Co_2MnSi valence band spectra close to ε_F. *d*-states with different character are indicated by arrows.

Gerhard H. Fecher [a,*], Claudia Felser [a] and Keisuke Kobayashi [b]

[a] Institute of Inorganic and Analytical Chemistry, The Johannes Gutenberg University, Germany
[b] Dept. of Materials Infrastructure, Beamline Station, NIMS

*E-mail: fecher@uni-mainz.de

References

[1] C. Felser *et al.*: Angew. Chem. Int. Ed. **46** (2007) 668.
[2] T. Ishikawa *et al.*: J. Appl. Phys. **103** (2008) 07A919.
[3] *G.H. Fecher, B. Balke, A. Gloskowskii, S. Ouardi, C. Felser, T. Ishikawa, M. Yamamoto, Y. Yamashita, H. Yoshikawa, S. Ueda, K. Kobayashi: Appl. Phys. Lett.* ***92*** *(2008) 193513.*
[4] B. Balke *et al.*: Phys. Rev. B **74** (2006) 104405.

Experimental Magnetic Form Factors in $Co_3V_2O_8$: A Combined Study of *Ab Initio* Calculations, Polarized Neutron Diffraction and Magnetic Compton Scattering

A detailed study combining first principles calculations, magnetic Compton scattering (MCS) and polarized neutron diffraction (PND) has been carried out leading to new insights into the magnetic properties of the kagome staircase structure $Co_3V_2O_8$. *Ab initio* wave functions obtained by cluster calculations yield a theoretical model for analyzing the real space magnetization and momentum space spin density simultaneously. The two crystallographically inequivalent Co ions on the cross-tie (Co_c) and spine sites (Co_s) reveal significantly different magnetic moments in the zero-field ferromagnetic structure, which do not saturate by applying an external magnetic field along the easy axis *a*. The increased bulk magnetization has been found on the V and O sites leading to a clarification of the superexchange and super-superexchange pathways in this system. From the Co3*d* orbital occupation a covalent character could be deduced for the cross-tie site giving a reasonable explanation for its relatively weak magnetic moment.

$Co_3V_2O_8$ represents the 3*d* transition metal ortho-oxo-vanadates labeled as kagome staircase structures and crystallizes in the orthorhombic space group Cmca [1]. Its crystallographic structure is characterized by edge-sharing CoO_6 octahedra forming buckled layers of corner-sharing triangles, the kagome staircases, which are separated along the *b* axis by VO_4 tetrahedra. The magnetic exchange is mainly effectuated by a 90° Co-O-Co intralayer pathway. The ferromagnetic structure reveals two strongly different magnetic moments for the Co_c and Co_s of 1.54 μ_B and 2.73 μ_B respectively [2], despite the fact that both Co^{2+} ions apparently present high-spin configurations as macroscopic measurements exhibit saturation of the cross-tie moments [3]. In the kagome staircase structure several nearest and next-nearest neighbor exchange interaction pathways are possible. Investigating the magnetization density, which is reflected by the respective magnetic form factors of the ions, may reveal preferred exchange pathways with the presence of magnetization on the involved O sites. Eventual induced magnetization on the empty *d*-shell of V sites would allow interlayer coupling by super-superexchange. Therefore, MCS and PND experiments have been carried out leading to the spin density in momentum space and the magnetization density in real space, respectively.

However, detailed and precise analysis of these quantities are required in order to determine the exact contribution of the atomic species involved in the studied system. In this context, density functional (DFT) based electronic structure calculations are carried out in order to get better understanding and newer insights into the observed phenomena.

Ab initio wave functions have been derived by hybrid DFT-based quantum chemical cluster calculations for the two different CoO_6 clusters. These were used to build up a theoretical model able to be refined to the real and momentum space quantities at the same time. Such a correlated refinement is possible as the unpaired electron density must be reflected in a similar way in real space as well as in momentum space. The fact that the MCS technique probes only the spin part of the magnetic moment has been handled by refining the size of the magnetic moment only on the PND data; the magnetic Compton profiles (MCP), which are depicted in Fig. 1, have been normalized and analyzed concerning their line shape. In doing so the occupation of the molecular orbitals relevant to the Co3*d* and the magnetic moments of all involved species could be derived. The sum of the obtained magnetic moments within

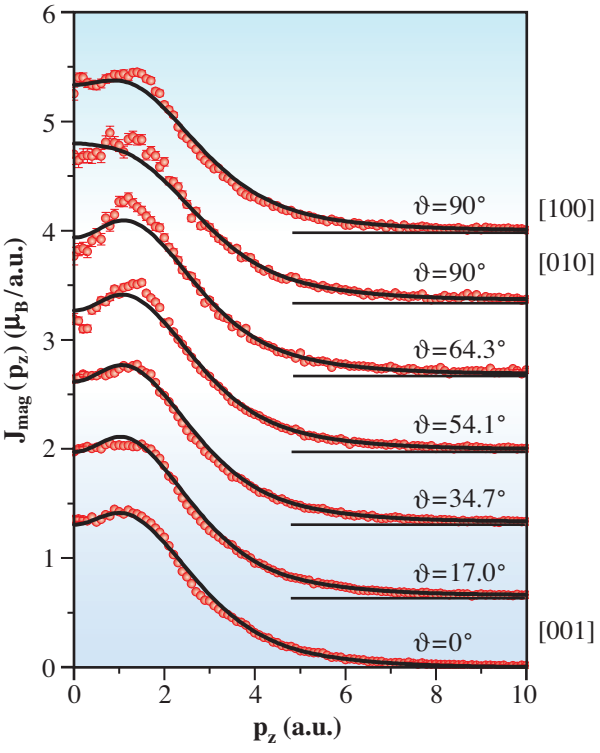


Fig. 1. Observed (dots) and calculated (solid lines) MCPs yielding the projection of the momentum spin density onto different scattering vectors.

the unit cell is in good agreement with macroscopic measurements [3]. Astonishingly the Co magnetic moments do not saturate, but remarkable induced magnetization can be found on the V and O sites which can be seen in Fig. 2 ($\mu(Co_c)$=1.54 μ_B, $\mu(Co_s)$=2.87 μ_B, μ(V)=0.41 μ_B, μ(O1)= 0.05 μ_B, μ(O2)=0.35 μ_B, μ(O3)=0.36 μ_B). The unpaired electron density has been found to be equally distributed between the t_g and e_{2g} levels for Co_s, but in the case of Co_c only 30% of the magnetic signal stems from the e_{2g} orbitals. Therefore the conclusion can be drawn that covalence, as a consequence of the spin transfer from the surrounding O2 and O3 ions, is the reason for the reduced magnetic moment of the cross-tie Co ions. Furthermore, from the individual orbital occupations it could be deduced that the preferred superexchange interaction pathways are Co_s-O2-Co_s and Co_c-O3-Co_s [4].

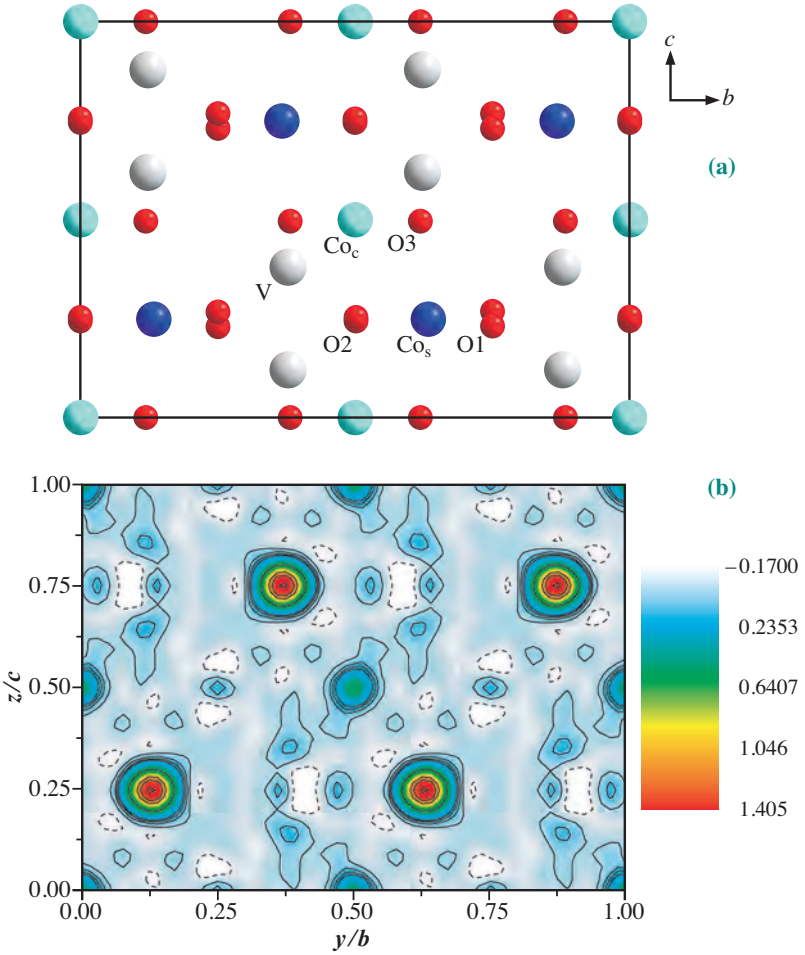


Fig. 2. Crystal structure (upper panel **(a)**) and calculated magnetization density (lower panel **(b)**) as a projection onto the *b*-*c* plane.

N. Qureshi[a,b,*], M. Zbiri[b] and Y. Sakurai[c]

[a] Institute for Materials Science, University of Technology Darmstadt, Germany
[b] Institut Max von Laue - Paul Langevin, France
[c] SPring-8/JASRI

*E-mail: qureshi@ph2.uni-koeln.de

References

[1] H. Fuess *et al.*: Acta. Crystallogr. Sect. B: Struct. Sci. **26** (1970) 2036.
[2] Y. Chen *et al.*: Phys. Rev. B **74** (2006) 014430.
[3] N.R. Wilson *et al.*: J. Phys. Condens. Matter **19** (2007) 145257.
[4] *N. Qureshi, M. Zbiri, J. Rodriguez-Carvajal, A. Stunault, E. Ressouche, T.C. Hansen, M.T. Fernandez-Diaz, M.R. Johnson, H. Fuess, H. Ehrenberg, Y. Sakurai, M. Itou, B. Gillon, Th. Wolf, J.A. Rodriguez-Velamazan and J. Sanchez-Montero: Phys. Rev. B* **79** *(2009) 094417.*

Phonons in the New Iron-Based High-Temperature Superconductors

The new iron-pnictide superconductors discovered by Hosono and coworkers [1] present a fantastic opportunity for new science. With transition temperatures in excess of 50 K, they are interesting systems both in themselves, and as compared to the only other system with $T_c > 50$ K, the copper oxides, which remain poorly understood, even after 20 years of concerted research. The very first question, then, is if the new superconductors are phonon mediated, like MgB_2? or if their mechanism is more complex? Calculations of phonon properties appeared very quickly, and suggested superconductivity in these new materials was not phonon mediated [2]. However, our experimental results [3], as discussed below, show that the phonon properties differ significantly from simple calculations, suggesting conclusions based on those calculations that the phonon role in superconductivity should be considered cautiously.

Our technique of choice for these measurements was inelastic X-ray scattering (IXS) at beamline **BL35XU**, as it allows access to small samples: phonon densities of states (DOS) were measured using ~50 mg powder samples, and while phonon dispersion was measured using a small (~20×100×150 μm^3) single crystal. The powder samples of LaFeAsO (non superconducting) and $LaFeAsO_{0.9}F_{0.1}$ (T_c = 27 K) were synthesized at Tokyo Institute of Technology, while powder and a single crystal of $PrFeAsO_{1-y}$ (T_c = 48 K for powder and 36 K for the single crystal) were prepared at AIST using high-pressure synthesis.

IXS measurements from powder samples give an approximation to the phonon DOS, which we call a "pseudo-DOS." While not being precisely the DOS, which requires incoherent scattering, this provides similar information, which can be compared against various models. Figure 1 shows the results of *ab initio* GGA (general gradient approximation) pseudo-potential calculations for the tetragonal non-magnetic structure as compared against measurements from several samples. First, looking only at the calculations, we can see that most of the features of the DOS (Fig. 1(a)) are preserved in the pseudo-DOS (Fig. 1(b)). Meanwhile, the measurements are similar across all materials, and like the calculation, have a triplet peak structure. However, again, across all materials, the highest energy peak is ~5 meV softer than the calculation, a discrepancy that is very large by the standards of modern pseudo-potential calculations. This difference is also consistent with other work [2,4].

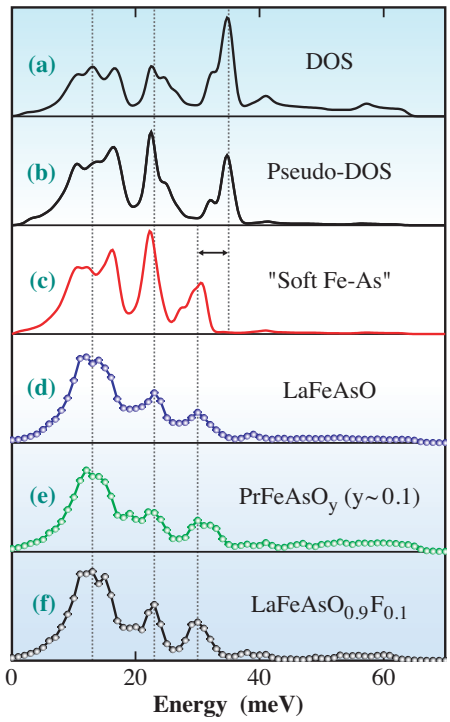


Fig. 1. Calculated and measured densities of states (DOS). **(a)** The DOS, **(b)** pseudo-DOS and **(c)** the effect of softening only the Fe-As bond (see text). **(d)**-**(f)** The pseudo-DOS extracted from measurements of three samples at room temperature. Vertical lines are at 13, 23, 30 and 35meV, which clearly shows the improved agreement with the soft Fe-As model.

In order to understand the origin for the softening, we examined the calculations in more detail, and measured dispersion from a single crystals. The calculated dispersion relation near 35 meV, the third phonon DOS peak, is somewhat complex (Fig. 2). The relevant bands consist primarily of in-plane FeAs motion at zone center (Γ), but apart from Γ point they begin to mix with the *c*-axis polarized motion of the FeAs layers, and across the fast-dispersing oxygen modes. However, the peak in the pseudo-DOS is nearly entirely from Fe-As motion. This can be demonstrated by softening *only* the Fe-As force constant matrix in the calculations. By a reduction of the nearest neighbor interactions by 30%, the third peak of the "soft Fe-As" pseudo-DOS falls to near the experimental value. Moreover, this reduction has only small effect on other peaks, and the total spectrum agrees reasonably well with the experiment as shown in Fig. 1(c). This model, at least in first approximation, is supported by measurements of a single crystal of $PrFeAsO_{1-y}$ (y~0.1). Figure 3 compares the spectra along Γ-X between the experiment and the soft

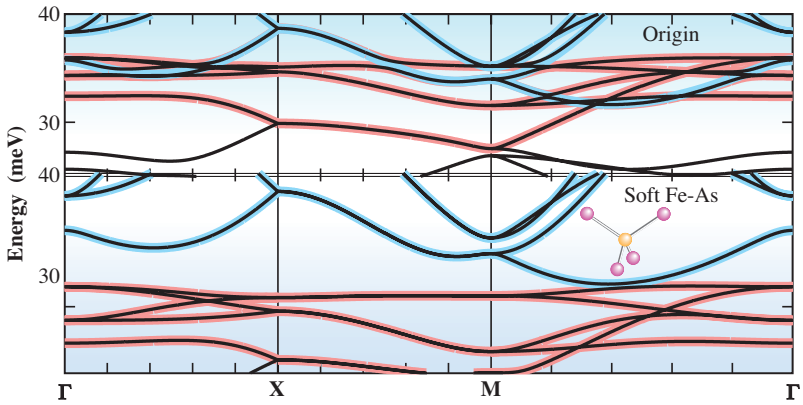


Fig. 2. Original LDA (top) and the "soft Fe-As" (bottom) calculated dispersions around the third peak, 35 meV, of the phonon DOS. Red (blue) shading indicates Fe-As (oxygen) modes. The effect of the soft Fe-As bond is primarily to shift the Fe-As modes to lower energy, as compared to the original calculations.

Fe-As model calculation in the (300) Brillouin zone. Though the low energy region has a slightly complex structure, the high energy part clearly shows the softening of the longitudinal optical modes from ~35 to 30 meV, essentially as expected from our model (see also Fig. 2).

The discrepancy between the measurement and the calculations suggests the existence of some interaction that is not properly included in the calculations. It is known that the LDA (local density approximation) calculations of the Fe-based layered system usually under-estimate the lattice constant *c* and Fe-As bond distance (Fe-As calculated bond distance 2.337 Å *vs.* 2.4 Å measured), and this tendency is consistent with the soft Fe-As model. We also note that another large discrepancy between the calculations and experiments is known about the amplitude of the magnetic moment on the iron atoms (calculation: 1- 2 μ_B, and the measured: ~0.3 μ_B). In fact our recent detailed phonon measurements with single crystals show that the measured dispersion along many symmetrical directions including Γ-X are in reasonable agreement with calculations of the *magnetically ordered* parent compound. This has interesting implications for the presence of short-lived magnetism. Taken together, this work suggests that the phonon system of thismaterial is not yet understood, and that conclusions about the relation between phonons and superconductivity based on simple calculation should be considered with caution.

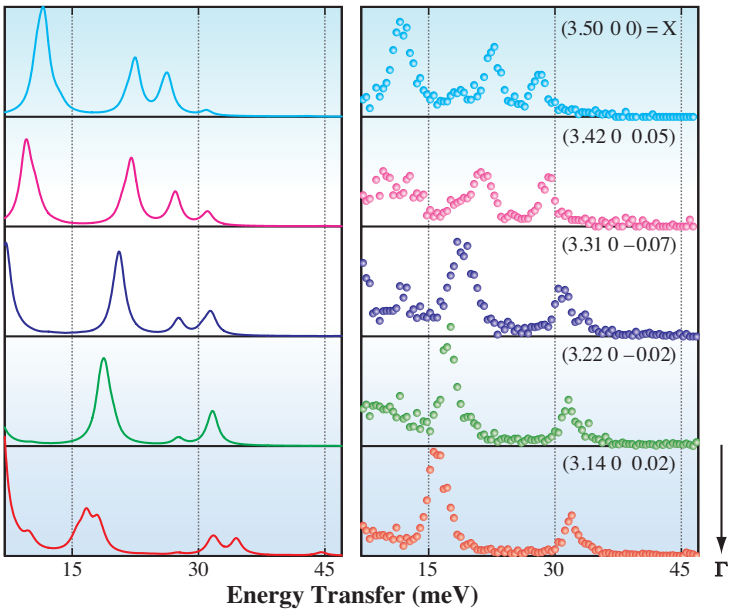


Fig. 3. Comparison of the measured dispersion for $PrFeAsO_{1-y}$ (y~0.1) at room temperature (right panel) and "soft Fe-As" calculation (left).

Tatsuo Fukuda[a,b,c,*] and Alfred Q.R. Baron[a,c,d]

[a] SPring-8/RIKEN
[b] SPring-8/JAEA
[c] TRIP (JST)
[d] SPring-8/JASRI

*E-mail: fukuda@spring8.or.jp

References

[1] Y. Kamihara *et al.*: J. Am. Chem. Soc. **130** (2008) 3296; H. Hosono *et al.*: J. Phys. Soc. Jpn. **77** (2008) Supp. C 1.
[2] D.J. Singh and M.-H. Du: Phys. Rev. Lett. **100** (2008) 237003; L. Boeri *et al.*: Phys. Rev. Lett. **101** (2008) 026403.
[3] *T. Fukuda, A.Q.R. Baron, S. Shamoto, M. Ishikado, H. Nakamura, M. Machida, H. Uchiyama, S. Tsutsui, A. Iyo, H. Kito, J. Mizuki, M. Arai, H. Eisaki, and H. Hosono: J. Phys. Soc. Jpn. 77 (2008) 103715.*
[4] A.D. Christianson *et al.*: Phys. Rev. Lett. **101** (2008) 157004.

Pressure-Induced Valence Anomaly in TmTe Probed by Resonant X-Ray Emission Spectroscopy

The Kondo effect is arguably one of the most studied many body problems in solid state physics. Exotic, non-Fermi liquid physics is expected when more than one screening channel of conduction electrons is present, such as in the case of intermediate-valent Tm compounds. This situation is known as the *n*-channel Kondo (NCK) problem. A particularly intriguing case of NCK effect is foreseen in intermediate-valent Tm compounds where the valence fluctuation of the Tm ion occurs between two magnetic states ($J=6$ and $J=7/2$).

Among Tm intermediate-valent compounds, TmTe appears as an outstanding example of the interplay between structural, magnetic and electronic degrees of freedom under pressure. Divalent semiconductor at ambient conditions, TmTe is supposed to reach trivalency at the completion of the volume collapse transition (VCT) around 6 GPa. But in the vicinity of the VCT and before trivalency is reached, TmTe shows singular behaviors which one is tempted to associate with more exotic effects in relation to an NCK effect: The resistivity presents a Kondo-like maximum at low temperature and antiferromagnetic (AF) order suddenly reappears under pressure. We measured the electron response of TmTe under pressure using X-ray absorption spectroscopy in the partial fluorescence yield (PFY-XAS) and resonant X-ray emission spectroscopy (RXES). The measurements were performed at beamline **BL12XU**. The compressibility was measured by X-ray diffraction (XRD) at beamline **BL10XU**. Hydrostatic pressure was achieved by using silicon oil as a pressure transmitting medium.

Figure 1 summarizes the pressure dependence of the Tm L_3 PFY-XAS spectra and of the Tm $2p_{3/2}\,3d_{5/2}$ RXES spectra collected at the maximum of the Tm^{2+} resonance, in the top and bottom panel, respectively. The intensity ratio between the two main structures at 8644 and 8651 eV in the PFY-XAS spectra, corresponding, respectively, to the transitions to the empty Tm^{2+} and Tm^{3+} 5*d* states, is seen to markedly decrease with pressure, signifying notable changes of the Tm electronic state. This is corroborated by the strong decrease of the RXES signal. The spectra calculated within the Anderson Impurity Model (AIM) are reported in Fig. 1 as well.

Figure 2(a) shows the pressure dependence of the Tm valence *v* extracted through fitting the PFY-XAS and RXES spectra and from the theoretical calculations. As soon as the gap closes and TmTe enters the metallic regime, above 2 GPa, the valence

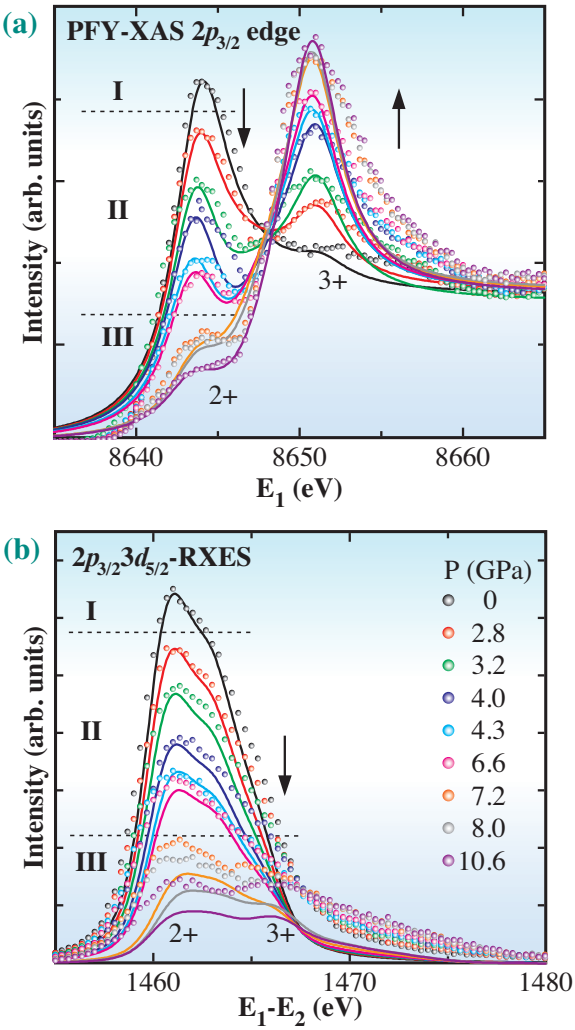


Fig. 1. **(a)** PFY-XAS spectra measured for TmTe at the Tm L_3 edge for various pressures up to 10.6 GPa (dots); **(b)** The $2p_{3/2}3d_{5/2}$ RXES spectra measured with an incident energy of 8644 eV (dots). The solid lines in both panels are the spectra calculated using the AIM.

abruptly increases to reach 2.55 at 4.3 GPa, coinciding with the isostructural VCT. The valence in the collapsed state, 2.55, is much lower than the near trivalent state reported in previous compressibility measurements under pressure. Above 4.3 GPa, the valence levels off as the volume recovers a normal compressibility behavior. As seen in the inset, the plateau coincides with a discontinuity in the evolution of *v* with respect to volume.

The *f-d* hybridization *H* and the energy difference between the Tm divalent and trivalent configurations E_{Tm2+}-E_{Tm3+} are derived from the AIM calculations and shown in Fig. 3. Above 2.1 GPa, *H* significantly strengthens while TmTe becomes metallic. The

concomitant decay of the magnetic moment suggests a progressive Kondo screening by the conduction electrons as P increases. Above 4.3 GPa, H becomes invariant over further compression while E_{Tm2+}-E_{Tm3+} retrieves its low pressure (P<2 GPa) value. This plateau behavior bears the most significant results of our study as it reveals novel Kondo effects. Based on the NCK interpretation of valence fluctuating Tm impurities, the Kondo temperature T_K is supposed to reach a maximum near v=2.4. As it seems, this value matches well the measured TmTe valence in the 4.3–6.5 GPa range. Hence, the NCK effect is expected to be largest in this pressure range. Here we speculate that, when more than one screening channels are involved, the contribution of the Kondo screening to the localization is sufficient to counterbalance the concomitant pressure-induced delocalization through band widening. It follows that the plateau-like regime in the pressure dependence of v and H is likely induced by the growing NCK scattering of the conduction electrons from the local magnetic moments. The peculiarity of the NCK effects on the Tm valence is further stressed by the contrast with the monotonic electron delocalization usually observed in other compressed f-electron systems that is consistent with a single-channel Kondo picture.

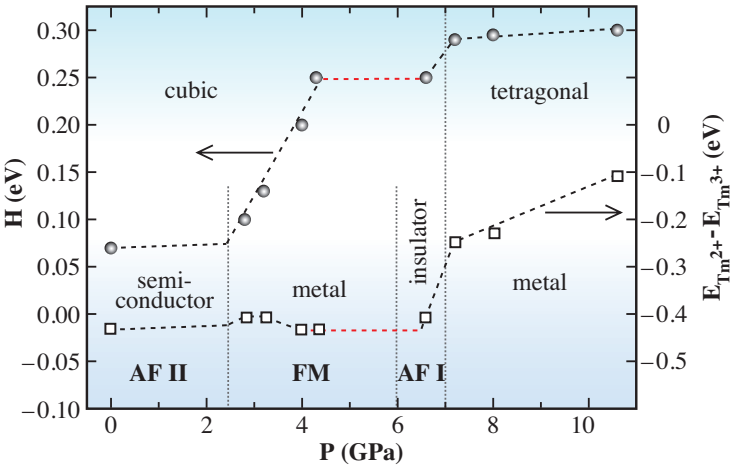


Fig. 3. Pressure dependence of the hybridization (full circles) and the energy difference between the Tm divalent and trivalent configurations (open squares) used in the AIM calculations, along with the structural properties and the electronic and magnetic ground states of TmTe. The dashed line is a guide for the eye.

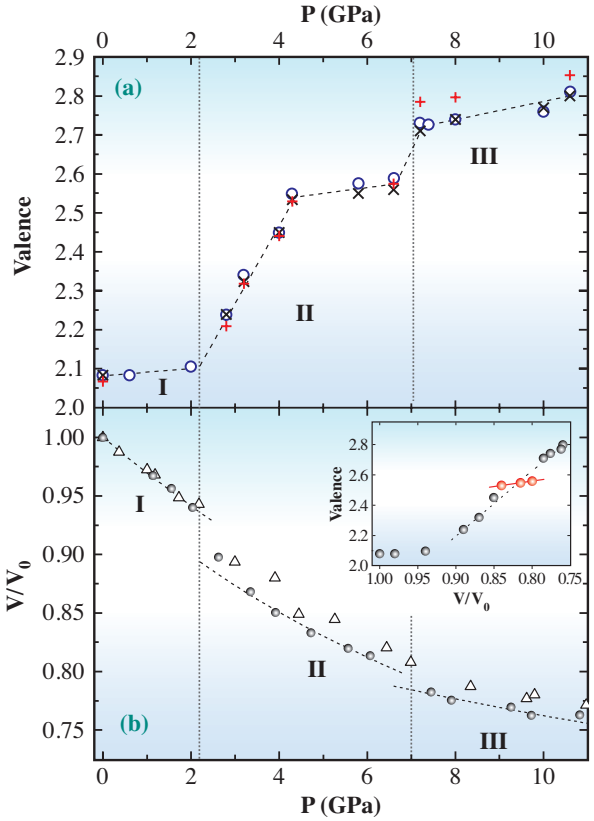


Fig. 2. **(a)** Pressure dependence of the thulium valence in TmTe as determined by PFY-XAS (blue circles), RXES (black crosses), and the calculations (red pluses). The dashed line is a guide for the eye; **(b)** Pressure dependence of the relative volume of TmTe as determined by XRD in this study (full circles). The dashed curves are Birch-Murnaghan equation of states fitted to our data. The relation between the valence from the PFY-XAS data and the volume is shown in the inset.

Ignace Jarrige[a,*], Jean-Pascal Rueff[b] and Yong Q. Cai[c]

[a] SPring-8/JAEA
[b] Synchrotron SOLEIL, France
[c] National Synchrotron Light Source II, Brookhaven National Laboratory, USA

*E-mail: jarrige@spring8.or.jp

References

[1] *I. Jarrige, J.-P. Rueff, S.R. Shieh, M. Taguchi, Y. Ohishi, T. Matsumura, C.-P. Wang, H. Ishii, N. Hiraoka and Y.Q. Cai: Phys. Rev. Lett.* ***101*** *(2008) 127401.*

Infrared Magneto-Optical Imaging on Phase Separation of Solids

In first-order transitions such as the magnetic transition in magnetic materials and the Mott transition in strongly correlated electron systems, physical properties drastically change. Around the transition point, the phase separation in which both phases coexist sometimes appears. Anomalous physical properties often originate from the phase separation, for instance, the colossal magnetoresistance of Manganese oxides [1] and the magnetic-field-induced superconductor-insulator transition of organic superconductors [2] are believed to originate from the phase separation. The domain size of the phase separation is typically on the nanometer scale. Owing to the lattice distortion or trapped magnetic polaron, however, micrometer-sized domains sometimes appear. Such large domains and the electronic structure of each domain can be identified by infrared imaging. The target material dealt with in this study, namely, electron-doped europium monoxide (EuO), has a large magnetoresistance [3], whose origin is still debated to be trapped magnetic polarons. Therefore, the detecting of the large domain size as well as the inhomogeneity of the sample surface near the ordering temperature/magnetic field is important for studying the magnetic polaron scenario.

EuO is a ferromagnetic semiconductor with a Curie temperature (T_C) of around 70 K. With excess Eu electron doping or the substitution of Gd^{3+} or La^{3+} for Eu^{2+} ions, T_C increases up to 150 K and electrical resistivity drops by twelve orders of magnitude below T_C. Since the magnetic moment originates from local Eu^{2+} $4f^7$ electrons, electron-doped EuO has larger magnetic moments than colossal magnetoresistance manganites, which exhibit a similar insulator-to-metal transition at T_C. Therefore, electron-doped EuO is attracting attention as a next generation functional material for spintronics devices.

Infrared reflectivity spectra [$R(\omega)$] and spatial images with unpolarized light were obtained at the infrared magneto-optical station of beamline **BL43IR** [4]. Infrared $R(\omega)$ imaging was performed in the 6000 to 12000 cm^{-1} wave number range at 10 cm^{-1} resolution at different temperatures from 40 to 80 K in magnetic fields of up to 5 T. To acquire spatial imaging data, a total of 1681 spectra were obtained in a 200 × 200 μm^2 region in steps of 5 μm with a spatial

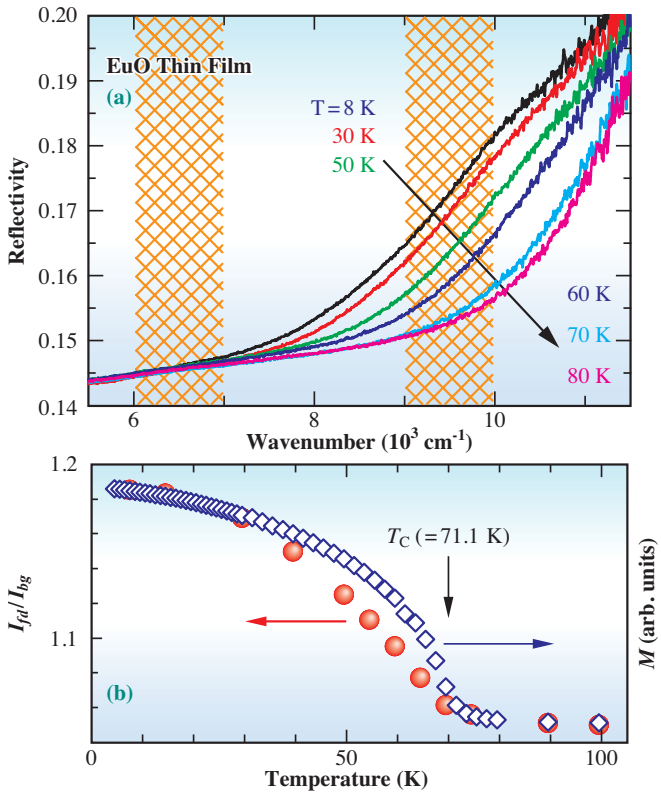


Fig. 1. **(a)** Temperature dependence of the reflectivity spectrum $R(\omega)$ of a EuO thin film in the wave number range of 4000 – 12000 cm^{-1}. **(b)** Temperature dependence of the intensity ratio between the absorption edge of the exciton of the Eu $4f \rightarrow 5d$ transition (I_{fd}) integrated at 9000 – 10000 cm^{-1} and the background intensity (I_{bg}) at 6000 – 7000 cm^{-1}. The temperature dependence of magnetization (open diamonds) is also plotted.

resolution better than 5 μm. The spatial images and the temperature dependence of the reflectivity spectrum were plotted using the intensity ratio of the absorption edge of the exciton of the Eu $4f \rightarrow 5d$ transition (I_{fd}) integrated over 9000 – 10000 cm^{-1} to the background intensity (I_{bg}) in the 6000 – 7000 cm^{-1} range, as shown in Fig. 1.

To investigate the phase separation in the magnetic-field-induced paramagnetic-to-ferromagnetic transition, we performed infrared imaging under magnetic fields at 80 K, which that is slightly higher than T_C, as shown in Fig. 2(a). The figure indicates that the paramagnetic state at $B = 0$ T becomes ferromagnetic as magnetic field increases. A similar magnetic-field-induced insulator-to-metal transition has been observed in manganites in spite of its different origin. The spatial distribution is plotted in Fig. 2(b). The figure shows that the distribution width normalized by that at $B = 0$ T exhibits an approximately twofold increase at 3 T and then decreases at 5 T. Such an anomalous temperature-dependent width can be explained in terms of the magnetic polaron scenario, in which a large magnetic polaron is generated by applying a magnetic field. In other words, the phase transition from a uniform paramagnetic state to a uniform ferromagnetic state via the inhomogeneous magnetic polaron state appears with increasing magnetic field at a temperature slightly higher than T_C.

We use these results as a basis for discussing the domain size of the magnetic polaron state in EuO. The spatial resolution of about 5 μm used in this work is larger than this domain size. However, changes in the spatial distribution width can be detected. In such cases, the domain size is about one-tenth of the spatial resolution of the used microscope, i.e., about several 100 nm. This is the first direct observation of the inhomogeneity due to magnetic polaron domains [5].

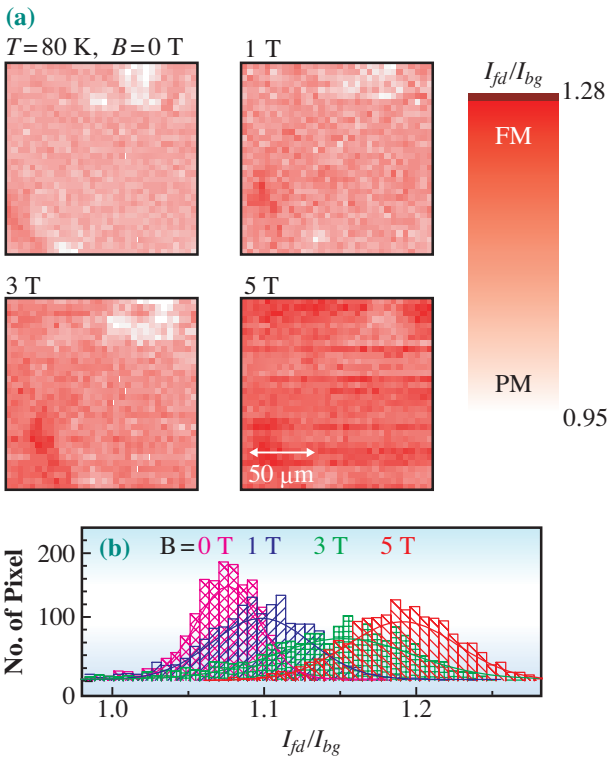


Fig. 2. **(a)** Magnetic field dependence of I_{fd}/I_{bg} of a EuO thin film at $T = 80$ K that is slightly higher temperature than T_C. **(b)** Statistical distributions and Gaussian fittings of I_{fd}/I_{bg} derived from **(a)**.

Shin-ichi Kimura

Institute for Molecular Science, UVSOR Facility

E-mail: kimura@ims.ac.jp

References

[1] L. Zhang *et al.*: Science **298** (2002) 805.
[2] T. Nishi *et al.*: Phys. Rev. B **75** (2007) 014525.
[3] A. Mauger and C. Godart: Phys. Rep. **141** (1986) 51.
[4] S. Kimura *et al.*: Nucl. Instrum. Meth. A **467-468** (2001) 893-896.
[5] *S. Kimura, T. Ito, H. Miyazaki, T. Mizuno, T. Iizuka and T. Takahashi: Phys. Rev. B* ***78*** *(2008) 052409.*

Infrared Optical Probe of Carrier Doping by X-Ray Irradiation in Organic Dimer Mott Insulator κ-(BEDT-TTF)$_2$Cu[N(CN)$_2$]Cl

Organic charge transfer salts based on the BEDT-TTF molecule have been recognized as a highly correlated electron system. Among them, κ-(BEDT-TTF)$_2X$ with X = Cu(NCS)$_2$, and Cu[N(CN)$_2$]Y (Y = Br and Cl) (Fig. 1) have attracted considerable attention from the point of view of the strongly correlated electron system. The strong BEDT-TTF dimer structure makes the conduction band effectively half-filling. In such strongly correlated electron systems, the Mott insulating phase appears and the first-order Mott insulator – metal transition takes place with the application of hydrostatic pressure, which must broaden the conduction bandwidth with respect to the effective Coulomb repulsion energy on the dimer. Thus, the κ-(BEDT-TTF)$_2X$ family has been considered to be the bandwidth controlled Mott system in comparison to the filling controlled one in inorganic perovskites such as high-T_c copper oxides.

X-ray irradiation usually induces disorders in a crystal, for example, the displacement of the atomic position. In the case of molecular materials, the irradiation produces molecular defects, which are generated by radiolysis under ionizing radiation. These molecular defects permanently remain; in contrast, the irradiation damage in inorganic materials is only due to atomic displacements and can be restored with proper heat treatment. These defects and disorders decrease electrical conductivity in general because of enhanced electron scattering [1]. An increase in conductivity by X-ray irradiation, however, has been observed in the organic Mott insulator κ-(BEDT-TTF)$_2$Cu[N(CN)$_2$]Cl, as shown in Fig. 2 [2]. The irradiation-induced defects expected at the donor and/or anion molecule sites might cause a local imbalance in the charge transfer in the crystal. Such local modulation of the charge transfer becomes an effective mean of doping carriers into half-filling Mott insulators. In order to investigate the change in the electronic state caused by possible carrier doping induced by X-ray irradiation into organic dimer-Mott insulators, infrared optical reflectivity spectra were measured in a typical bandwidth controlled Mott insulator, κ-(BEDT-TTF)$_2$Cu[N(CN)$_2$]Cl [3]. Synchrotron irradiation light was used for infrared

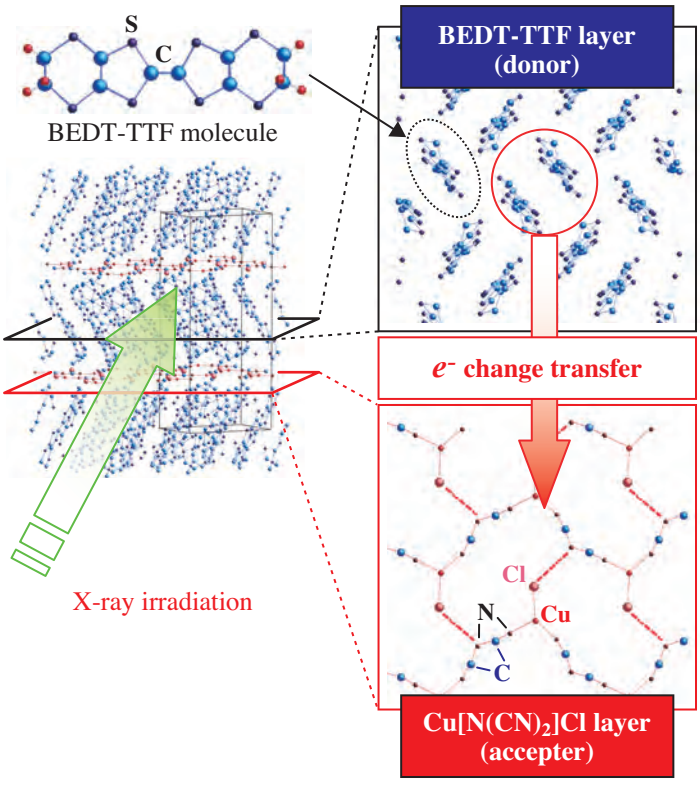


Fig. 1. Crystal structure of κ-(BEDT-TTF)$_2$Cu[N(CN)$_2$]Cl. The two-dimensional conduction plane consists of BEDT-TTF donor molecules, which is sandwiched by insulating Cu[N(CN)$_2$]Cl anion molecule layers.

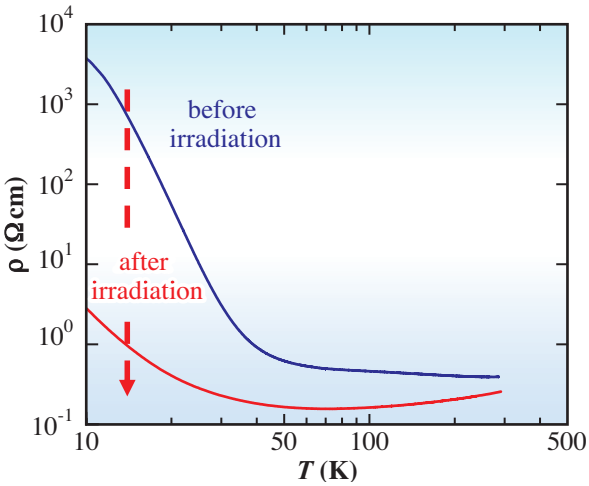


Fig. 2. Temperature dependence of the resistivity of κ-(BEDT-TTF)$_2$Cu[N(CN)$_2$]Cl before and after 350 hours of X-ray irradiation.

reflectivity measurement at beamline **BL43IR**.

In the optical reflectivity spectra (Fig. 3) of κ-(BEDT-TTF)$_2$Cu[N(CN)$_2$]Cl obtained after X-ray irradiation using a tungsten tube (40 kV, 20 mA), it was observed that the spectral weight was transferred from the high-energy region to low-energy region. This means that the interband transitions in dimer bands and Hubbard bands in the mid-infrared region are suppressed drastically and the low-energy Drude-like part is enhanced by compensation. The observed optical spectra suggest that the Mott insulator changes into essentially a metal due to small shift of the carrier number from the half-filling in the conduction band by X-ray irradiation.

As for the future application of this X-ray irradiation technique, a conductive circuit and dots can be made artificially on molecular crystals by controlling the local irradiated position, which will be useful for fabricating organic electronic devices.

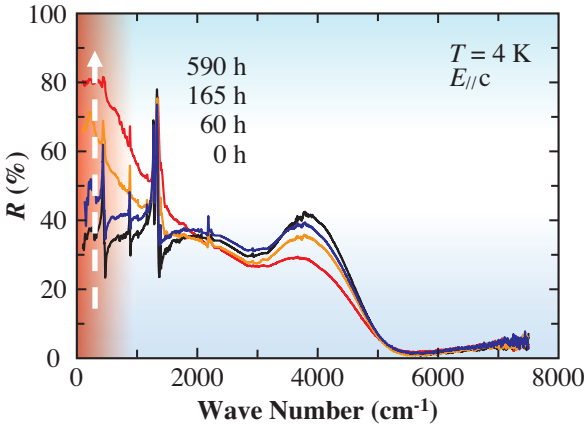


Fig. 3. Optical reflectivity spectra of κ-(BEDT-TTF)$_2$Cu[N(CN)$_2$]Cl at 4 K. Reflectivity in far-infrared region increases with increasing X-ray irradiation time. Concurrently, we observe a decrease in the magnitude of the interband transition in the mid-infrared region at around 3500-4000 cm^{-1}.

Takahiko Sasaki

Institute for Materials Research, Tohoku University

E-mail: takahiko@imr.tohoku.ac.jp

References

[1] J.G. Analytis *et al.*: Phys. Rev. Lett. **96** (2006) 177002.
[2] T. Sasaki *et al.*: J. Phys. Soc. Jpn. **76** (2007) 123701.
[3] *T. Sasaki, N. Yoneyama, Y. Nakamura, N. Kobayashi, Y. Ikemoto, T. Moriwaki and H. Kimura: Phys. Rev. Lett.* ***101*** *(2008) 206403.*

Chemical

Target materials of *Chemical Science* widely spread from simple molecules to complex biosystems across different length scales. Synchrotron X-ray diffraction analysis combined with complementary spectroscopic techniques such as XAFS and NRVS (nuclear resonance vibrational spectroscopy) provide the fundamental structure of simple molecular solids/liquids and a full three-dimensional picture of the hierarchical structure of complex materials. Precise and accurate structural study is essential for understanding the functional properties and mechanisms of these materials in combination with the electronic states studied by PES and XES with a synchrotron light source as well. The trend in Chemical Science studies is going toward dynamics study as demonstrated by the topics collected in *Research Frontiers 2008*. Their outlines are summarized below.

The structure of liquid water has been the issue in materials sciences during the past century. X-ray emission study on the liquid structure provided definite evidence of the coexistence of two species, fourfold and less than fourfold hydrogen-bonded structures, which supports a two-component model. Molecules exhibit a peculiar configuration in the liquid phase even for simple diatomic molecules such as N_2 and O_2. X-ray diffraction measurement at high pressures revealed that diatomic linear molecules tend to take mutually parallel and X-shaped configurations in dense-liquid states as a result of the strengthening of intermolecular interactions. Precise structural study is essential for understanding the distinct behavior of mixed-valence one-dimensional metal chains. Single-crystal X-ray diffraction measurement determine the Pt-Pt distances accurately and allow the average oxidation number of Pt atoms in Pt-Pt chain compounds. The structural study of ionic liquids is a hot topic in chemistry and chemical engineering. A detailed analysis of high energy X-ray and neutron diffraction data reveals that the dominant chain structures consisting of several atoms joined by hydrogen bonding in the liquid state of $Cs(FH)_{2.3}F$, which are not observed in the solid state. The biological nitrogen fixation in microorganisms is investigated by EXAF and NRV. A Fe_6S_9 cage with an interstitial atom is shown to play a key role in the fixation. Selective chemical bond breaking or control of chemical reaction is attempted by ionizing of a target core using well-tuned soft X-rays. *Ab initio* structural determination from powder diffraction data is expanded to medium-size pharmaceuticals.

Katsutoshi Aoki

SCIENCE



Liquid Structure of Water: Observation of Two Structural Motifs

One intriguing question about water, under debate for the last 100 years, is whether liquid water is a continuum of different hydrogen bonding configurations, or could instead consist of a mixture of relatively well-defined species. This debate was initiated in 1892 when Röntgen proposed that water contains a mixture of two components, one ice-like and one unknown [1]. The traditional view of water as a continuum of distorted hydrogen bonds around near-tetrahedral local structure goes back to the work of Bernal and Fowler [2], who in 1933 successfully analyzed the early X-ray diffraction data on water in terms of a disordered quartz-like structure. This picture has been widely used in X-ray and neutron diffraction studies, infrared (IR) and Raman spectroscopy. However, mixture models are also utilized in some cases. For example, in 2004, an X-ray absorption spectroscopy (XAS) study has proposed the existence of two different species with the dominant one related to structures with highly distorted hydrogen bonds and the other more ice-like [3].

Here, we introduce our recent X-ray emission study on the liquid structure of water performed at beamline **BL17SU** [4] (see Fig. 1 for experimental setup). Water can occur in three states: solid (ice), liquid, or gas (water vapor), i.e., three forms of water. The difference between liquid and gas phase water is hydrogen bonding. While gas phase water is an isolated molecule without hydrogen bonding, liquid water has hydrogen bonding that connects molecules. The crystalline ice is where the fraction of hydrogen-bonded molecules reaches the limit; every water molecule is hydrogen bonded with up to four other molecules, i.e., fourfold hydrogen bonded structures. X-ray emission spectroscopy (XES) is used to directly probe the occupied electronic states through radiant decay of a valence electron to fill a vacancy in a core level. Although the valence electrons are delocalized in a condensed phase, the involvement of the core level makes XES a very local spectroscopy with atom-specific sensitivity. The O1*s* core-hole lifetime is of the order of 3-4 femtoseconds. This time scale is much shorter than any rearrangements of the hydrogen bonding network, and XES thus provides an instantaneous sampling of frozen configurations. Let us take a look the XES spectra of water in three states. Figure 2 shows the XES spectra of liquid water at various temperatures, ice and gas phase water. Spectra of gas phase water and crystalline ice show a simple three peak structure that is attributable to valence molecular orbitals of the water molecule

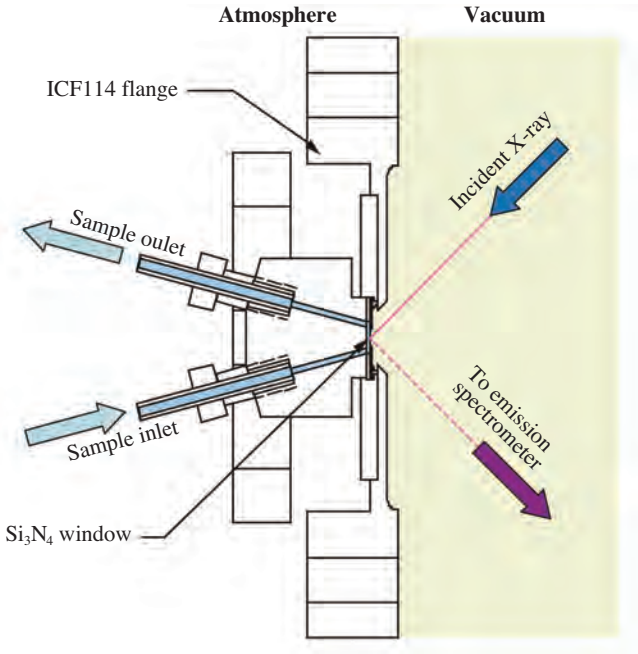


Fig. 1. Schematic of the experimental setup. The liquid flow cell and its internal flow channel are shown in cross-sectional drawings. Samples at ambient condition were fed through a tube connected to the inlet port, passing the surface of the window and then drained from the outlet port using an aspiration pump. A 150-nm-thick Au-coated Si_3N_4 window was used to separate the liquid flow from the high vacuum and to transmit the incoming and outgoing soft X-rays.

(see Fig. 3). The gas phase is at the highest emission energy (527 eV), the crystalline ice at the lowest (525.7 eV), while the liquid peaks are in between. An interesting thing is that in the spectra of liquid water, there are two sharp peaks ($1b_1$' and $1b_1$") in the region of $1b_1$ state. There are also energy shifts in the relative energy positions for different temperatures.

What is the assignment of the two $1b_1$ peaks of liquid water? The answer is found in the measured spectra. As is commonly accepted, the fraction of hydrogen bonded molecules decreases with increasing temperature, while the number of distorted or broken hydrogen bonds increases. The higher energy $1b_1$" peak increases with temperature relative to the $1b_1$' peak, and we can assign the $1b_1$' and $1b_1$" peaks as due to fourfold and less than fourfold hydrogen-bonded structures in the liquid, respectively. The assignment of the $1b_1$' peak as due to a structures in the liquid with ice-like coordination is consistent with the coinciding peak location of the $1b_1$' peak of the liquid (525.9 eV) and the sharp low-energy $1b_1$ peak of crystalline ice at 525.7 eV. The position of the liquid $1b_1$" peak is much closer in energy to the

gas phase value, which is also consistent with the interpretation of liquid water as a distribution of structures where the hydrogen bonds are significantly weakened or distorted.

The XES spectra of water in three states and the temperature dependence of liquid water leads us to interpret the two peaks as representing tetrahedral-like and highly distorted structural motifs. The existence in the experiment of two distinct lone-pair peaks provides evidence against an unstructured continuum model of the liquid, but is easily explained within a two-component mixture model.

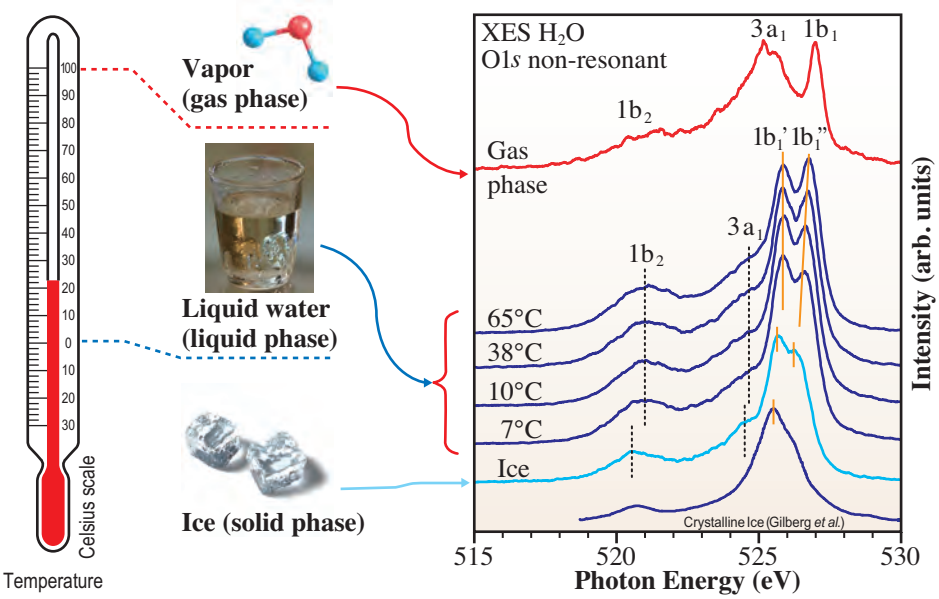


Fig.2. O 1*s* soft X-ray emission spectra of gas phase water, liquid water at different temperatures and amorphous and crystalline ice. The excitation energy is 550 eV, well above the ionization threshold. Peak components are labeled on the basis of the molecular orbitals for a water molecule. The XES spectra of ice (amorphous) and crystalline ice from Gilberg *et al.* [5] are included for comparison. In a previous study by Gilberg *et al.*, both crystalline and amorphous or polycrystalline ice were studied using high resolution XES, where the spectrum of the amorphous ice is rather similar to that in the current study. The energy scale of the spectrum of crystalline ice is adjusted on the basis of the very similar amorphous ice spectra.

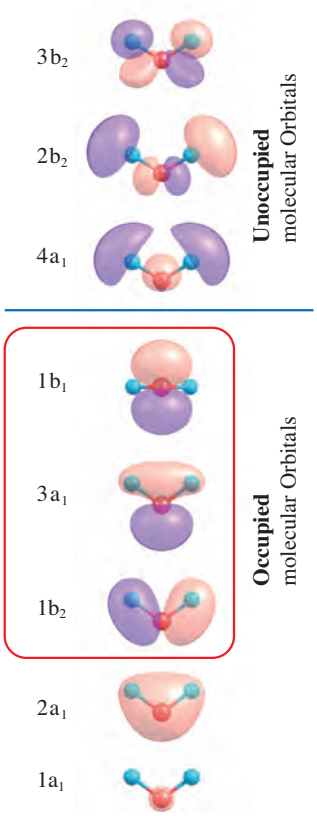


Fig. 3. Schematic of the five occupied and the lowest three unoccupied molecular orbitals of the isolated molecule. In principle, three occupied states indicated by a red box were observed by XES.

T. Tokushima[a,*], Y. Harada[a,†] and S. Shin[a,b]

[a] SPring-8/RIKEN
[b] Institute for Solid State Physics (ISSP), The University of Tokyo

*E-mail: toku@spring8.or.jp

† Present address: Department of Applied Chemistry, The University of Tokyo

References

[1] W.C. Röntgen: Ann. Phys. Chem. **45** (1892) 91.
[2] J.D. Bernal and R.H. Fowler: J. Chem. Phys. **1** (1933) 515.
[3] P. Wernet *et al.*: Science **304** (2004) 995.
[4] *T. Tokushima, Y. Harada, O. Takahashi, Y. Senba, H. Ohashi, L.G.M. Pettersson, A. Nilsson and S. Shin: Chem. Phys. Lett.* ***460*** *(2008) 387.*
[5] E. Gilberg *et al.*: J. Chem. Phys. **76** (1982) 5093.

Orientational Correlations in High-Pressure Fluid Oxygen and Nitrogen

Diffraction studies of the liquid structure at high pressures have led to a much improved understanding of the properties of materials in general. New phenomena, like the liquid-liquid phase transition in phosphorus, have been found. Investigations at GPa pressures, however, pose extreme difficulties during the experiment, as well as while processing raw data.

The structure of the high-pressure phases of oxygen, most abundant element on Earth, has been studied experimentally over the past. These investigations have aimed at determining the structure of crystalline phases, sometimes at extremely high pressure [1]. Concerning fluid phases at high pressure, it has been known for quite a long time that oxygen has an anomalously high crystallization pressure, about 5.9 GPa, at room temperature whereas nitrogen crystallizes just above 2.5 GPa. The structure of fluid oxygen and nitrogen has not yet been studied by diffraction methods just below the crystallization pressure. The purpose of the present study [2] was to provide this missing piece of experimental information and furthermore, to understand the –disordered– fluid structure.

X-ray diffraction experiments were conducted using the high-energy X-ray diffraction beamline **BL04B2**. The energy of the (focused, 40 micron wide) monochromatic X-ray beam was 37.6 keV. For improving counting statistics, an imaging plate detector was used. Sample loading was carried out by compression and oxygen and nitrogen acted as their own pressure media. The diffraction patterns of fluid samples were measured in a diamond anvil cell (DAC) at pressures of 2.5 GPa (fluid N_2), 0.9, 1.2, 4.3 and 5.2 GPa (fluid O_2). Raw data were corrected by usual methods, with a special attention to the subtraction of the scattering from the DAC.

Resulting 'total scattering' structure factors (sf), *F(Q)*, are shown in Fig. 1 for fluid oxygen and nitrogen. Note that for oxygen, structure factors at 0.9 and 1.2 GPa are rather similar, just as they are at 4.3 and 5.2 GPa; for this reason, structural modeling (see below) was carried out only at 1.2 and 4.3 GPa. Since direct Fourier transformation to *r* space would be prone to truncation errors, it is safer to apply an inverse method for the transition to real space. One of the possibilities is the application of the Reverse Monte Carlo (RMC) method [3], which is also capable of providing large structural models that are consistent with the measured sf. In each RMC calculation, 5000 molecules were put in cubic boxes and several hundreds of successful moves/atom were completed.

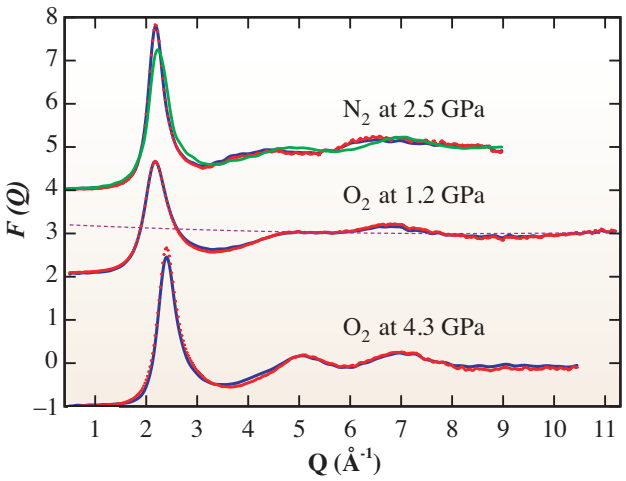


Fig. 1. Experimental (red dots) and RMC simulated (blue line) structure factors for high-pressure fluid phases of nitrogen and oxygen. For fluid nitrogen at 2.5 GPa, results for the highest packing fraction reference (hard sphere) system are also shown (green line). The quadratic background refined by RMC modeling is shown for the 1.2 GPa oxygen sf (magenta dotted line).

Calculations were conducted by the RMC++ software [4]. Hard sphere Monte Carlo (HSMC) calculations of molecular assemblies, with the same parameters (density; bond-length constraints) as the RMC runs, have also been carried out for the three systems. These calculations provided reference structures which possess all features that originate to excluded volume (pure steric) effects. Differences between hard sphere and RMC structures are characteristic to the nature of intermolecular interactions.

Figure 1 compares experimental structure factors to *F(Q)*'s of the corresponding RMC models. For achieving such a level of consistency with experiment, a particular feature of the RMC++ software, the possibility of refining a –small– quadratic background for the experimental sf, had to be exploited. This step was necessitated by the extreme experimental conditions for which the standard data processing software cannot be made fully prepared.

Distance dependent orientational correlation functions were determined in terms of easy-to-understand mutual orientations of two molecules, as depicted by Fig. 2. As it is explained in the figure, 'parallel', 'X(cross)-shaped', 'T-shaped', or 'chain-like', have been considered. The ratio of ‘regular’ pairs, which could be categorized according to the 4 specific arrangements shown in Fig. 2, was more than 25% of all pairs found below 3.5 Å. Figure 3 summarizes results obtained for the three systems. The most striking features are undoubtedly the very strong peaks of the orientational correlation functions

representing the parallel and the 'X-shaped' arrangements at the closest distances, up to about 3.5 Å. It is immediately apparent that these, parallel and 'X-shaped,' correlations for oxygen (at both pressures) are much stronger than they are for nitrogen. It could also be shown (*c.f.* Fig. 3) that the real systems realize orientational correlations that are inherent to the 'frozen' HSMC systems. In other words, the *character* of orientational correlations found in high pressure fluid nitrogen and oxygen resembles to that featuring hard sphere reference systems; the *extent* of these correlations is, on the other hand, different. From this finding it may be conjectured that correlations between magnetic moments of O_2 molecules do not bring about specific orientational forces.

In conclusion, we have performed X-ray diffraction experiments on high-pressure fluid nitrogen (at 2.5 GPa) and oxygen (at 0.9, 1.2, 4.3 and 5.2 GPa) [2]. Site-site and center-center radial distribution functions, as well as distance dependent orientational correlations have been determined by using RMC modeling. Well defined orientational correlations were found in all of the materials, particularly below about 3.5 Å. In agreement with *ab initio* molecular dynamics simulations [5] (conducted for lower temperature and pressure), the dominant mutual arrangement of O_2 molecules appears to be the parallel one. Here, however, the importance of 'X-shaped' configurations has also been revealed. It is expected that the present results will boast high level computer simulation studies, aiming at a detailed understanding of the microscopic behavior of high pressure condensed phases of oxygen.

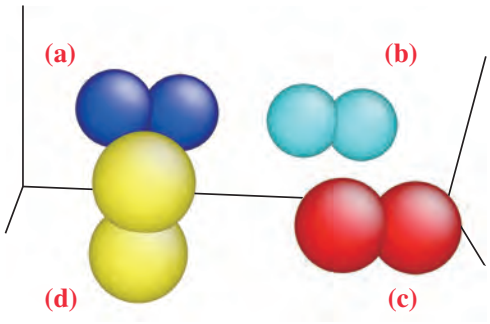


Fig. 2. Specific orientations of molecular pairs considered in this work. **(a)**-**(b)**: chain-like configuration; **(b)**-**(c)**: parallel configuration; **(c)**-**(d)**: T-shaped configuration; **(d)**-**(a)**: X-shaped configuration.

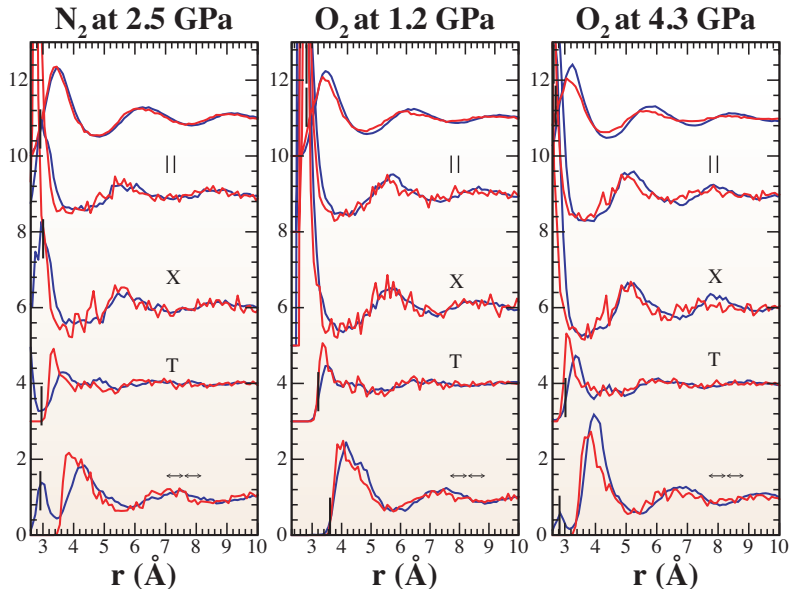


Fig. 3. Orientational correlation functions for high pressure fluid nitrogen and oxygen, as obtained directly from particle coordinates (red lines). Results for the highest packing fraction reference (hard sphere) system are also shown (blue lines). Center-center correlation functions are also shown for comparison (uppermost curves). Vertical bars show the 'significance limits,' above which distance the number of pairs of molecules was sufficient for achieving decent statistics for the given arrangement. (The curve pairs are shifted along the *y*-axis.)

L. Temleitner[a], L. Pusztai[a,*], Y. Akahama[b] and S. Kohara[c]

[a] Research Institute for Solid State Physics and Optics, Hungary
[b] Department of Material Science, University of Hyogo
[c] SPring-8/JASRI

*E-mail: lp@szfki.hu

References

[1] H. Fujihisa *et al.*: Phys. Rev. Lett. **97** (2006) 085503.
[2] *L. Temleitner, L. Pusztai, Y. Akahama, H. Kawamura, S. Kohara, Y. Ohishi and M. Takata: Phys. Rev. B 78 (2008) 014205.*
[3] R.L. McGreevy and L. Pusztai: Molec. Simul. **1** (1988) 359.
[4] G. Evrard and L. Pusztai: J. Phys.: Condens. Matter **17** (2005) S1.
[5] T. Oda and A. Pasquarello: Phys. Rev. Lett. **89** (2002) 197204.

Crystal Structures of the Odd and Even Electron One-Dimensional Metal–Metal Bonded Chain Compounds

Mixed valency (MV) is at the heart of many interesting properties, electrical, magnetic and optical or a combination thereof, and is in many cases the source of a wide range of instabilities. The presence of MV has been the driving force in the development of highly conducting and superconducting materials, molecular magnetism and also of highly colored complexes [1]. MV was first realized in inorganic compounds and in particular, one-dimensional (1D) chain compounds of platinum. However, most 1D mixed-valent metal complexes are semiconducting except for $K_2[Pt(CN)_4]Br_{0.3}\cdot 3H_2O$(KCP(Br)) and $K_{1.62}[Pt(C_2O_4)_2]\cdot 2H_2O$ (α-K-OP), which show metallic conduction in a limited range of temperature [2].

Our approach to construct highly conducting metal–metal bonded solids is to start with a platinum dimer having sulfur ligands, such as $[Pt^{II}_2(RCS_2)_4]$ (RCS_2^- = a dithiocarboxylato), and to partially oxidize it. Here, we used ClO_4^- as a counterion in the electrocrystallization and organic solvents. In choosing the divalent Pt–Pt dimer, we expect a decrease in the Coulomb repulsion *U* by sharing an unpaired electron through a Pt–Pt bond, and the presence of the delocalized sulfur orbitals should favor an increase in the charge-transfer energy *t*. Following the above strategy, we have succeeded in obtaining high-quality crystals of the partially oxidized 1D Pt–Pt chain compounds, $[Pt_2(MeCS_2)_4]_4ClO_4\cdot 5PhCN$(**1**) and $[Pt_2(EtCS_2)_4]_5(ClO_4)_2$ (**2**) from the corresponding dimers.

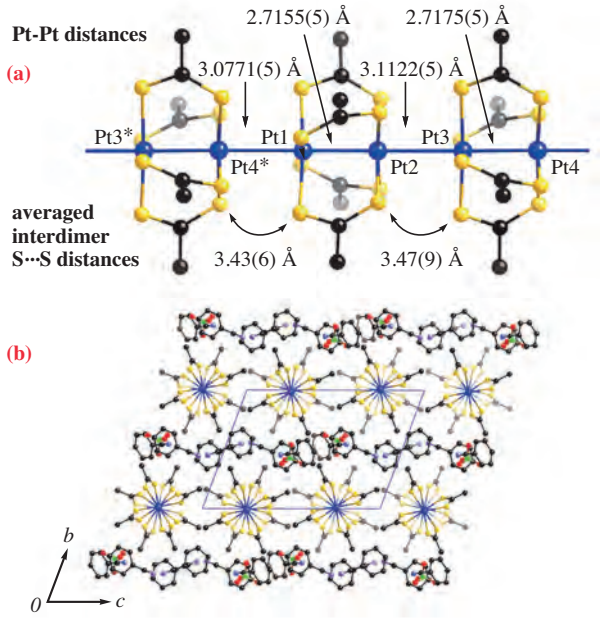


Fig. 1. **(a)** Repeat unit of the 1D chain $\{[Pt_2(MeCS_2)_4]_4\}_n^{n+}$ in **1** at 204 K and **(b)** view of the unit cell along the chain axis (*a* axis).

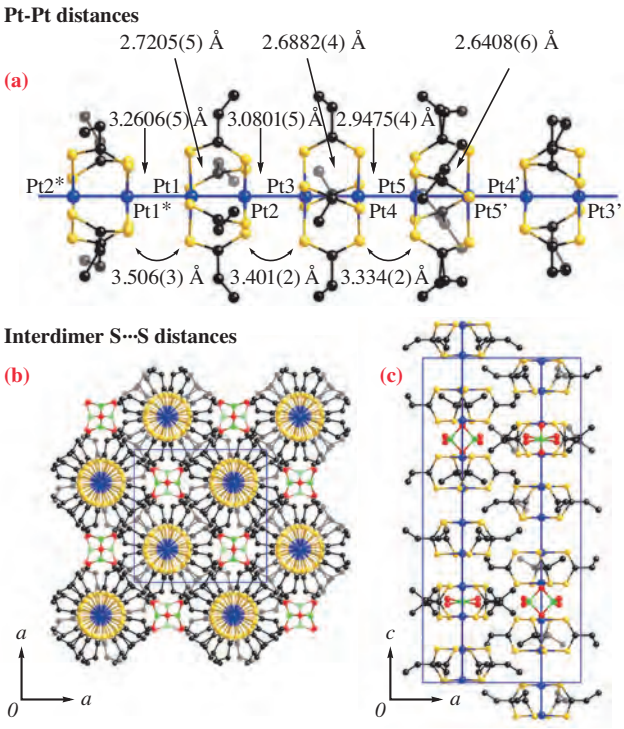


Fig. 2. **(a)** Repeat unit of the 1D chain $\{[Pt_2(EtCS_2)_4]_5\}_n^{2n+}$ in **2** at 298 K and a view of the packing projected down the **(b)** *c* and **(c)** *a* axes.

Crystal structures were determined from data collected on single crystals of **1** and **2** using synchrotron radiation of beamline **BL02B1** [3]. The structure of **1** (triclinic, $P\bar{1}$) consists of alternating cationic and solvated anionic layers; the former is built of stacks of Pt–Pt dimers forming chains adjacent of one another, while the latter contains ClO_4^- solvated by benzonitrile molecules (Fig. 1). One period of the linear chain has two diplatinum units, and the Pt–Pt dimers are almost equidistant from one another forming the spine with notably short interdimer S···S distances. The intradimer Pt–Pt distances are intermediate between those of Pt^{2+}–Pt^{2+} and Pt^{2+}–Pt^{3+}. The molar ratio of $Pt_2(MeCS_2)_4$ cation to ClO_4^- is 4:1, in agreement with the results of elemental analyses. Therefore, the average formal oxidation state of the platinum atom of **1** is +2.125.

The structure of **2** (tetragonal, $P4/nnc$) is shown in Fig. 2, consisting of 1D Pt–Pt chains segregated by the ClO_4^-. The diplatinum units are stacked with a twist of the $EtCS_2^-$ ligands forming the Pt–Pt chain with a helical arrangement of the ligands. In the Pt–Pt

chain, five diplatinum units form a pentamer, and both the intra- and interdimer Pt–Pt distances are shorter at the center of the pentamer (a midpoint of Pt5–Pt5' bond). The Pt1–Pt2 distance is intermediate between those of Pt^{2+}–Pt^{2+} and Pt^{2+}–Pt^{3+}, the Pt3–Pt4 is close to that of Pt^{2+}–Pt^{3+}, and the Pt5–Pt5' is intermediate between those of Pt^{2+}–Pt^{3+} and Pt^{3+}–Pt^{3+}. The ClO_4^- ions are incorporated simultaneously into the spaces formed partially by four 1D chains. Consequently, the interdimer Pt···Pt distance adjacent to the ClO_4^- is lengthened by the steric hindrance. Therefore, it is considered that the periodicity of the helical arrangement of the ligands is strongly correlated with the number of ClO_4^- ions. Since the molar ratio of $Pt_2(EtCS_2)_4$ to ClO_4^- has been confirmed to be 5:2 by elemental analyses, the average oxidation number of the platinum atoms of **2** is +2.2.

1 exhibits high electrical conductivity (4.2–8.0 S cm^{-1}) at room temperature along the 1D chain and metallic behavior surviving down to 125 K in contrast to 250 K for KCP(Br). To our knowledge, it is the most stable ambient pressure metallic 1D mixed-valent metal complex known. The electrical conductivity of **2** is 0.33–1.2 S cm^{-1} at room temperature and shows typical semiconducting behavior. The observed semiconducting behavior of **2** can be ascribed to the electronic localization due to the formation of pentamers within the chains.

The magnetic susceptibility χ_M of **1** is almost temperature independent (*ca.* 1.1×10^{-4}emu·mol^{-1}), which is attributed to Pauli paramagnetism, and gradually decreases with decreasing temperature to an almost spin-singlet state. On the other hand, **2** appears to be non-magnetic except for a very small Curie-like paramagnetic behavior originating from impurities and/or lattice and end-of-chain defects.

From electronic considerations as shown in Fig. 3, the one unpaired electron (odd electron) for every four dimers in **1**, i.e., twice the length of the *a* axis, is unlikely to pair, and consequently, the charge and spin degrees of freedom survive resulting in metallic conduction. On the other hand, **2** has lost the spin degree of freedom owing to the pentamer formation with electron pair formation since two unpaired electrons (even electrons) are present per unit cell, and the charge density wave (CDW) state has appeared.

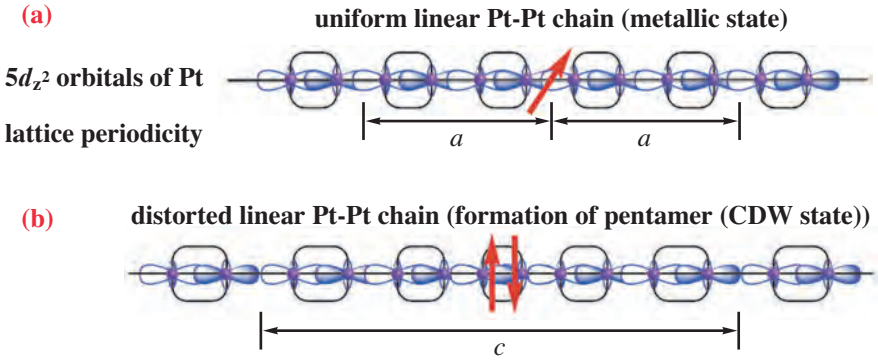


Fig. 3. Schematic representation of the spin states and lattice periodicities of the linear Pt–Pt chains for **(a) 1** and **(b) 2**.

Minoru Mitsumi*, Yoshiki Ozawa and Koshiro Toriumi

Department of Material Science, University of Hyogo

*E-mail: mitsumi@sci.u-hyogo.ac.jp

References

[1] P. Day; Molecules into Materials: Case Studies in Materials Chemistry–Mixed Valency, Magnetism and Superconductivity; World Scientific Publishing: Singapore (2007).
[2] H.R. Zeller *et al.*: J. Phys. Chem. Solids **35** (1974) 77; A. Kobayashi *et al.*: Solid State Commun. **26** (1978) 653.
[3] *M. Mitsumi, H. Ueda, K. Furukawa, Y. Ozawa, K. Toriumi and M. Kurmoo: J. Am. Chem. Soc.* ***130*** *(2008) 14102.*

Structural Collapse of Fluorohydrogenate Anions in Molten $Cs(FH)_{2.3}F$ Detected by High-Energy X-Ray and Neutron Diffraction Studies Combined with RMC Calculation

The authors have been working on a series of onium fluorohydrogenates, $Cat^+(FH)_nF^-$, called ionic liquids such as dialkylimidazolium and pyrrolidinium salts, the vacuum-stable composition n of which always falls to 2.3 [1,2]. Vibrational spectroscopic studies suggest the presence of $(FH)_2F^-$ (C_{2v}) and $(FH)_3F^-$ (D_{3h}) and the absence of FHF^- ($D_{\infty h}$) and neutral HF monomers or oligomers in these liquid salts. This observation explains their nonvolatile nature while the other conventional fluorohydrogentates including alkali salts such as $Cs(FH)_{2.3}F$ more or less have dissociation pressures in the liquid state to lose HF by evacuation. Oligofluorohydrogenate anions, $(FH)_nF^-$, have been structurally characterized in solid states by X-ray crystallography [3]. However, the characterization of these salts in liquid state by diffraction methods has never been reported so far. In the present study [4], we chose $Cs(FH)_{2.3}F$ as a sample for structural characterization since it has an eutectic temperature of 16.9°C, lower than room temperature, at this composition [5].

The salt was prepared by the reaction of CsF and excess of anhydrous HF. The composition was adjusted to $n = 2.3$ by evacuation of the salt to yield a liquid at 16.9°C. For neutron diffraction experiments, a deuterated version of the salt was prepared in the same manner using DF instead of HF. High-energy X-ray diffraction measurement was performed on beamline **BL04B2** at SPring-8 using an incident energy of 113.8 kV. Pulsed neutron diffraction measurement was carried out at the Intense Pulsed Neutron Source, Argonne National Laboratory. Reverse Monte Carlo (RMC) simulation was performed on an ensemble of 3300 particles with a random starting configuration using the RMCA program code [6].

The calculated X-ray weighted total and partial structure factors and neutron-weighted total and partial structure factors of $Cs(FH)_{2.3}F$ in liquid state from the RMC model are shown in Fig. 1. The agreement between the total RMC and experimental structure factors is excellent, indicating that the short

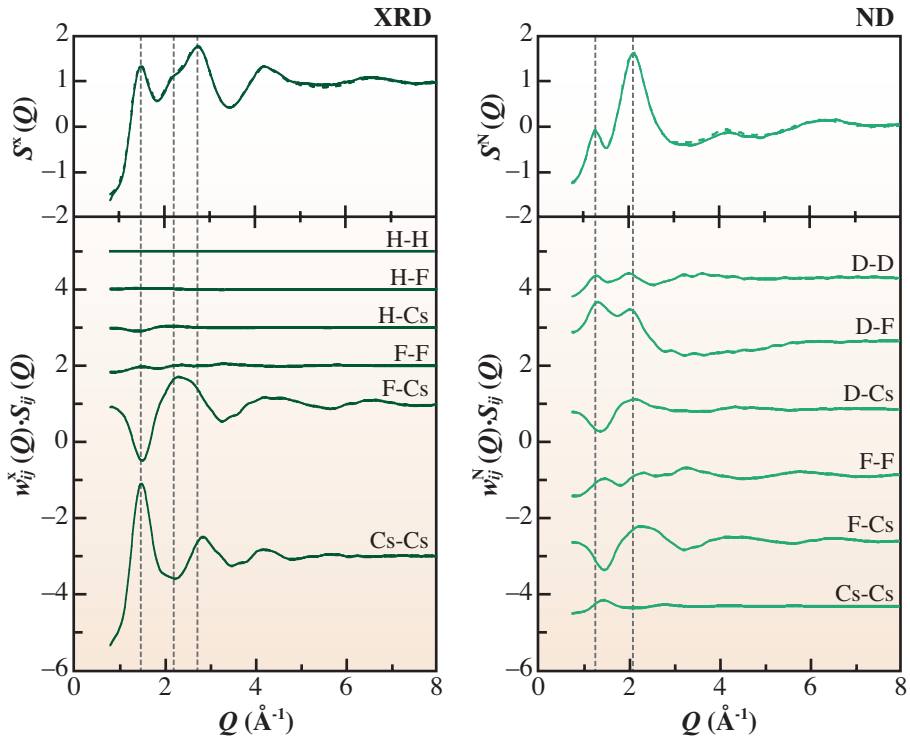


Fig. 1. Calculated X-ray-weighted and neutron-weighted total structure factors $S^{X,N}(Q)$ and associated weighted partial structure factors $w_{ij}^{X,N}\cdot S_{ij}(Q)$ obtained from the RMC model for liquid $Cs(FH)_{2.3}F$. Dotted lines: experimental data; solid lines: RMC model, where w_{ij} denotes the X-ray-weighted or neutron-weighted factor. Successive curves are displaced upward for clarity. Dashed lines are guides to the eye.

and intermediate-range orders of liquid $Cs(FH)_{2.3}F$ are well reproduced using the RMC model. Figure 2 shows a 20-Å-thick snapshot of the RMC model. Chain analysis of the RMC model revealed that the dominant chains consist of five atoms and the average number of atoms per chain is 4.4. Furthermore, a detailed analysis of the atomic configuration revealed that $(FH)_2F^-$ is the major entity in the liquid, and asymmetric FHF^- are formed in the liquid state. The chain analysis also showed that only 2.6% of the molecules form branched chains. These results suggest that branched molecules such as $(FH)_3F^-$ that existed in the solid state collapse into linear $(FH)_2F^-$ and $(HF)_n$, and a part of $(FH)_2F^-$ dissociates further to asymmetric FHF^- ($C_{\infty v}$, note that the symmetry of this anion in the solid state is $D_{\infty h}$) and neutral $(HF)_n$ oligmers in the liquid state. This model provides a reasonable explanation for the vacuum instability of the salt. Thus, in the case of vacuum-unstable fluorohydrogenates such as $Cs(FH)_{2.3}F$, the anions in the solid state are not preserved in the liquid state, releasing HF to have a dissociation pressure. This contrasts with the nonvolatile fluorohydrogenate ionic liquids, the HF dissociation pressure of which under ambient conditions is practically zero. The difference in the preservation of the anionic structures by melting should be caused by the difference in the interactions between the cationic and anionic species in the salts forming aggregates of ions in the liquid state of zero solvent system.

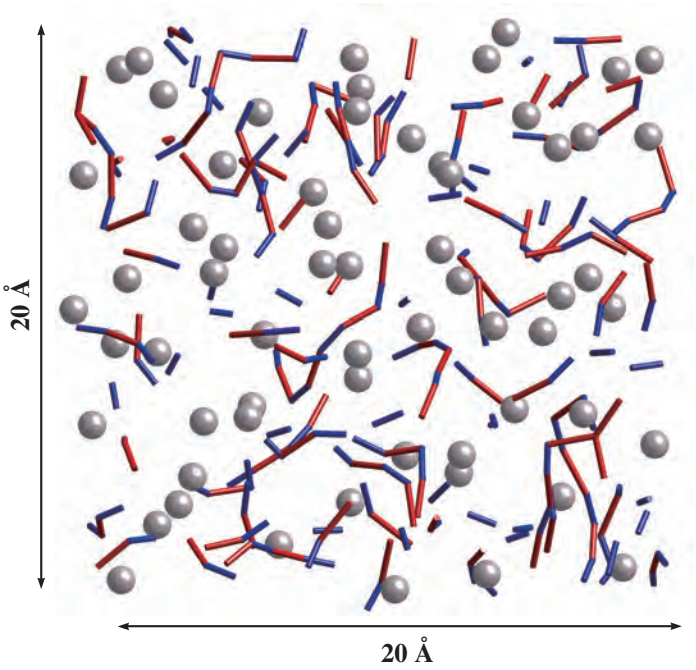


Fig. 2. A 20-Å-thick snapshot of the RMC model. Sticks represent H-F chains. Blue: H-F covalent bonds; red: H…F hydrogen bonds. Gray spheres represent the cesium ions.

Rika Hagiwara[a,*], Kazuhiko Matsumoto[a] and Shinji Kohara[b]

[a] Graduate School of Energy Science, Kyoto University
[b] SPring-8/JASRI

*E-mail: hagiwara@energy.kyoto-u.ac.jp

References

[1] R. Hagiwara *et al.*: J. Electrochem. Soc. **150** (2003) D195.
[2] K. Matsumoto *et al.*: Electrochem. Solid-State Lett. **7** (2004) E41.
[3] J.E. Huheey *et al.*: Inorganic Chemistry, Principles of Structure and Reactivity, Harper & Row, New York, 1993, Chap. 8, p. 290.
[4] *S. Kohara, M. Takata, K. Matsumoto, R. Hagiwara, K. Suzuya, H. Morita, J. E. Sievenie, C. J. Benmore: J. Chem. Phys.* ***129*** *(2008) 014512.*
[5] R.V. Winsor and G.H. Cady: J. Am. Chem. Soc. **70** (1948) 1500.
[6] R.L. McGreevy and L. Pusztai: Mol. Simul. **1** (1988) 359.

NifB-co, a Key FeMo-co Precursor, is a Fe_6S_9 Core with an Interstitial Light Atom

All life depends on the input of the element nitrogen into the biosphere by biological nitrogen fixation (the reduction of dinitrogen to ammonia, $N_2 \rightarrow 2NH_3$) performed only by diazotropic microorganisms. These microorganisms achieve N_2 fixation using a family of metalloenzymes, called nitrogenases (N_2ases). Biological N_2 fixation is responsible for about half of the protein available for human consumption. The other half is produced using natural gas in fertilizer factories by the Haber-Bosch process. A better understanding of N_2ases may have an impact on our ability to transition to a more sustainable energy economy.

The active site of Mo-N_2ase, which is contained within the so-called MoFe protein (one of the component proteins in Mo-N_2ase), is a remarkable [7Fe-9S-Mo-X-homocitrate] cluster, called the iron-molybdenum cofactor (FeMo-co). FeMo-co is regarded as one of the most complex Fe-S clusters found in biology (Fig. 1). The exact identity of the interstitial light atom X is unknown; it can be assigned to C, N, or O. Knowledge of the FeMo-co biosynthetic assembly process, and the nature of X, is critical to understanding the N_2ase catalytic mechanism.

Figure 1 shows the current understanding of the biosynthetic pathways for Mo-N_2ase [1]. A key metabolic intermediate in the biosynthesis of FeMo-co is NifB-co, a low-molecular weight Fe-S cluster. In addition to being a precursor of FeMo-co, NifB-co is also hypothesized to be the precursor of FeV-co and FeFe-co, suggesting that NifB-co forms the core portion that is common among all three N_2ase active site cofactors.

Recently, we used two synchrotron radiation techniques, namely *K*-edge extended X-ray absorption fine structure (EXAFS) and nuclear resonance vibrational spectroscopy (NRVS) to probe the structural and dynamics of the Fe sites of NifB-co bound to the small protein NifX (NifX:NifB-co) (**BL09XU**) [2]. EXAFS is a well-developed technique [3], capable of solving the local structure (typically within 5 Å) of the probed atom (in our case, Fe). NRVS is a novel vibrational spectroscopy [4]. The NRVS experiment involves scanning an extremely monochromatic X-ray beam ($\Delta E \sim 1$ meV) through a nuclear resonance. Apart from the 'zero phonon' (recoil-free) Mössbauer resonance, there are additional transitions that correspond to nuclear excitation plus excitation or de-excitation of vibrational modes.

Figure 2 shows the EXAFS and NRVS spectra of NifX:NifB-co and the simulations. Spectra for FeMo-co are also shown to help calibrate and interpret the NifX:NifB-co results. The EXAFS simulation of NifX:NifB-co reveals a set of S ligand at ~2.3 Å and a set of Fe next nearest neighbors at ~2.6 Å. A set of Fe-Fe interactions at 3.7 Å is also clear, which has so far been observed only in Fe-S centers for FeMo-co. The above features can be viewed as a strong indicator for the presence of the Fe_6S_9 core in NifB-co, similar with the trigonal prism core in a matured FeMo-co. Three different structural models (Fig. 3) have been used in the EXAFS simulation, the best fit was obtained by using the 6Fe model. Furthermore, a search profile in the simulation confirms a Fe-X interaction with ~1 atom at 2.06 Å, consistent with the same interaction in a maturated FeMo-co. This is the first time this interaction has been reported in NifB-co, and is highly significant for the understanding

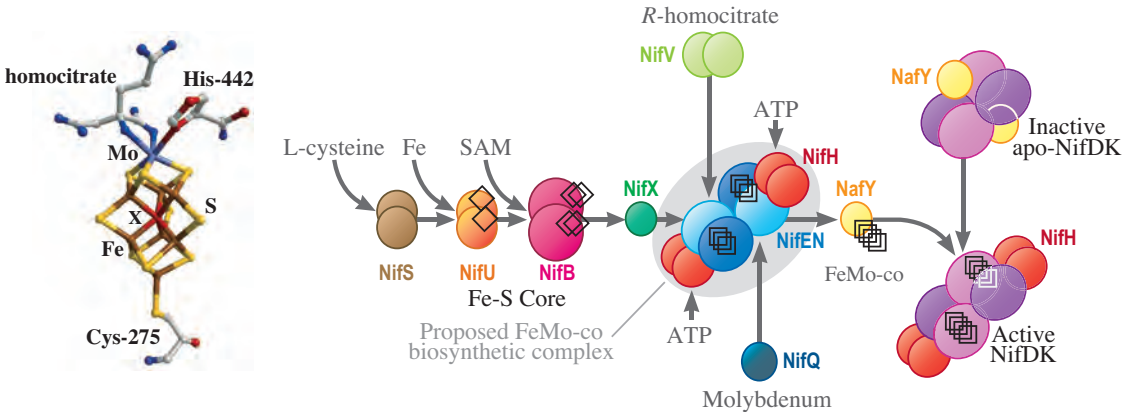


Fig. 1. Left: the structure of FeMo-co as determined by X-ray crystallography on the Mo-N_2ase enzyme (Protein Data Bank: 1M1N). Right: Proposed scheme for FeMo-co biosynthesis showing the proposed roles of NifB, NifX, NifH, NafY, and the MoFe protein (NifDK) N_2ase [1].

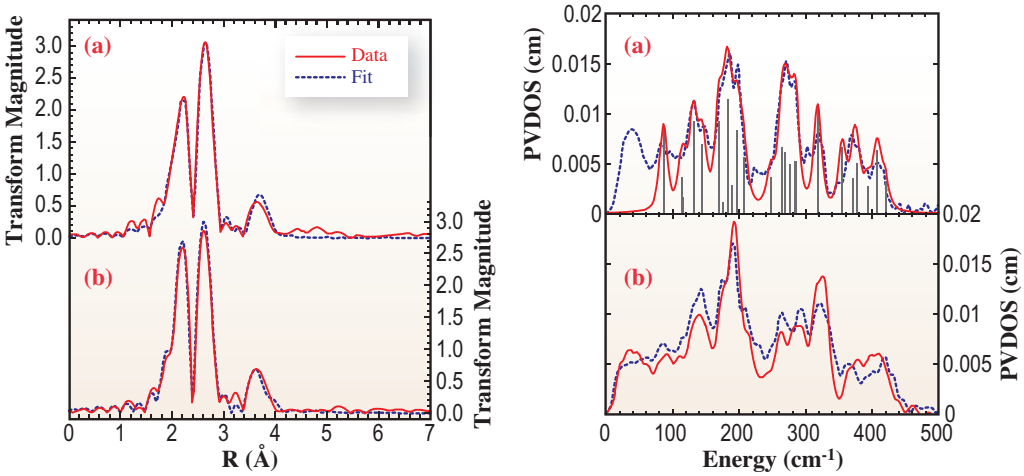


Fig. 2. Left: Fe *K*-edge Fourier transformed EXAFS of **(a)** NifX:NifB-co (---) with the 6Fe model fit (---), and **(b)** data (---) and fit (---) of NafY:FeMo-co. Right: **(a)** NRVS of NifX:NifB-co (---) and the 6Fe model fit (---); **(b)** NRVS of NafY:FeMo-co (---) and NMF:FeMo-co (---).

of FeMo-co maturation and the N_2ase catalytic mechanism. In our simulation, X is simulated as N atom, C, and O also can obtain similar results. In addition, measurements in the Mo *K*-edge region conclusively demonstrate the absence of Mo in NifB-co.

The NRVS spectrum of NifX:NifB-co shows similar spectral features as the NRVS of NafY:FeMoco (FeMo-co bound to the small protein NafY) and NMF:FeMoco (FeMo-co isolated in *N*-methylformamide (NMF)) (Fig. 2). Features above 250 cm^{-1} are primarily due to Fe-S stretching modes. The most striking feature is the intensity observed between 180 and 200 cm^{-1} in the NifX:NifB-co NRVS. This feature is considered to arise from the breathing modes of the Fe_6S_9 core of FeMo-co in the presence of the interstitial light atom X [5], indicating that the interstitial light atom has already been incorporated into the NifB-co cluster. A simulation using the models in Fig. 3 confirms this assignment, while a model without this interstitial atom results in the absence of this 180-200 cm^{-1} band.

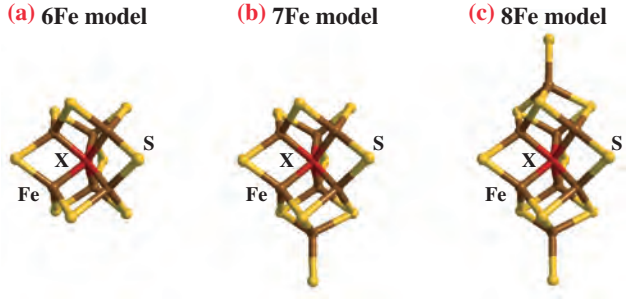


Fig. 3. Proposed models for NifB-co as described in the text. **(a)** 6Fe **(b)** 7Fe **(c)** 8Fe. Color code: Fe (brown), sulfur (yellow), interstitial atom X (red).

Taken together, the EXAFS and NRVS data show that NifB-co, the key FeMo-co biosynthetic intermediate, is most likely to consist of a Fe_6S_9 cage (Fig. 3). The presence of an interstitial atom in NifB-co is confirmed for the first time. This finding is significant because it rules out the possibility that the interstitial atom is incorporated in a later stage of the FeMo-co biosynthetic pathway - it implies that the function of the NifB enzyme is to perform the reaction of synthesizing this unique structure. This study demonstrates that EXAFS and NRVS are a powerful combination to reveal the structural information in the iron-containing metalloproteins.

Yisong Guo[a], Simon J. George[b], Luis M. Rubio[c] and Stephen P. Cramer[a,b,*]

[a] Dept. of Applied Science, University of California, USA
[b] Physical Biosciences Division, Lawrence Berkeley National Lab., USA
[c] Dept. of Plant and Microbial Biology, University of California, USA

*E-mail: spjcramer@ucdavis.edu

References

[1] L.M. Rubio and P.W. Ludden: Ann. Rev. Microbiol. **62** (2008) 93.
[2] *S.J. George, R.Y. Igarashi, Y. Xiao, J.A. Hernandez, M. Demuez, D. Zhao, Y. Yoda, P.W. Ludden, L.M. Rubio and S.P. Cramer: J. Am. Chem. Soc.* ***130*** *(2008) 5673.*
[3] J.J. Rehr and R.C. Albers: Rev. Mod. Phys. **72** (2000) 621.
[4] J.T. Sage *et al.*: J. Phys.: Condensed Matter **13** (2001) 7707.
[5] Y. Xiao *et al.*: J. Am. Chem. Soc. **128** (2006) 7608.

Grasping Carbon – Bonding Nature of Penta- and Hexacoordinated Carbon by Experimental Electron Density Distribution Analysis

Carbon is a central element of chemistry. It enjoys a limitless molecular diversity in millions of molecules, and yet, for new students of chemistry and experienced researchers alike, the structures of carbon compounds are typically understood in terms of the very simplest of bonding concepts. Whether di-, tri-, or tetracoordinate, carbon obeys the octet role with great predictability and has four 2-electron covalent bonds. In another words, carbon has four hands to grasp neighboring atoms. On the reaction path, however, most organic molecules take intermediate structures, in which the carbon atom of the reaction center forms more than four bonds. A hypervalent compound has bonds exceeding the number of bonds expected from the octet role. Because the reaction intermediate has additional bonds, hypervalent compounds are considered to be models of intermediate states.

The pentacoordinated carbon compound is synthesized aiming at the model of the intermediate state of S_N2 reaction. The central carbon atom of the compound has an sp^2-hybridization state, which is the same as the very famous intermediate of the S_N2 reaction. The carbon atom forms three covalent bonds. The carbon atom and the bonding three atoms lie on the same plane. The empty *p*-orbital is orientated perpendicular to the plane. Oxygen atoms form two hypervalent bonds with the central carbon atom by donating the lone pair electron to the empty p-orbital of the carbon. Then, three-center four-electron bonds are formed.

The hexacoordinated carbon compound is an extension of making the pentacoordinated compound. The central carbon atom has an *sp*-hybridization state. The carbon atom forms two covalent bonds with linear geometry. Four oxygen atoms coordinate to the central carbon atom by donating lone pairs to empty π*- or *p*-orbitals. Then, two three-center four-electron bonds are formed.

Since the hypervalent bond, in general, is weaker than the coordination bond, and shows a shallow and broad energy minimum, the evaluation of their bonding nature by theoretical calculations is sometimes difficult. X-ray diffraction, on the other hand, gives the total electron density distribution in crystal. If highly accurate and precise data were obtained, we can see all the chemical bonds in the molecule as they are. To understand the detail of the bonding nature, the electron configurations of hypervalent carbon compounds as models for reaction intermediates were clarified experimentally by electron density distribution analyses using single-crystal diffraction data [1,2].

The diffraction data of both crystals were measured at beamline **BL04B2** using a MacScience imaging plate diffractometer. In order to reduce absorption and extinction effects, we use small crystals and high-energy X-rays (37.8 keV) for measurements. The data were collected with some different crystal orientations to ensure high redundancies. The electron density distributions of valence electrons were derived by a multipole expansion method, following normal crystal structure analyses using spherical atom models.

Figure 1 shows the molecular structure of the pentacoordinated carbon compound. The compound lies on the crystallographic twofold axis through C1 and C11, which is a hypervalent carbon. The atom C11 is placed on the sp^2-plane, that is formed with by C1 and C12, and symmetry related C12. The atoms O1 and its twofold axis related atom coordinate to C11 from both sides of the sp^2-plane. The distance of C11-O1 is short enough to form a bond. Thus, the geometry of the hypervalent carbon atom is trigonal bipyramid. Because of the symmetry, two apical C-O bonds are identical. Figure 2 shows an isosurface static model map, and bond paths and bond critical points of hypervalent bonds. In the map, one of the two lone pairs in the sp^3-orbital on each oxygen atom is oriented towards the empty *p*-orbital of the central carbon atom. Such geometry of the orbital indicates the dative nature of the hypervalent bonds.

Figure 3 shows the molecular structure of the hexa-coordinated carbon compound. The bond

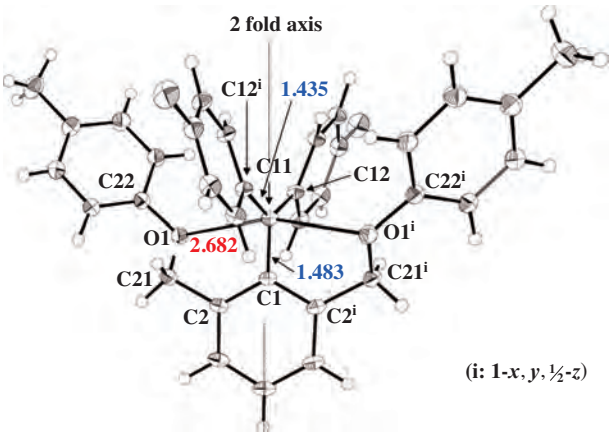


Fig. 1. Molecular structure of the pentacoordinated carbon compound. Bond distances are given in Å.

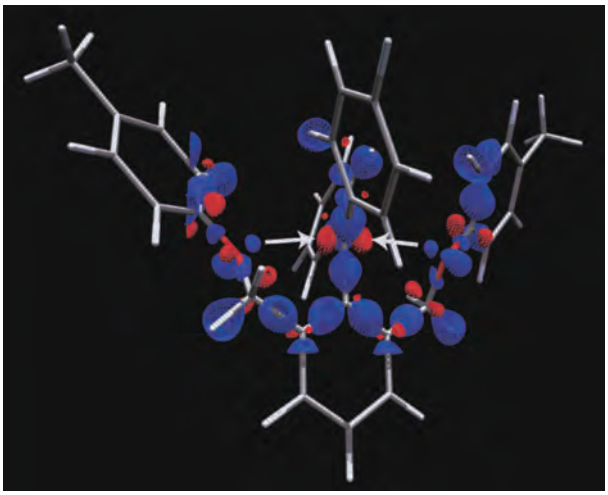


Fig. 2. Isosurface static model map of the penta-coordinated carbon compound. The isosurfaces are drawn in red and blue for electron-poor and electron-rich regions, respectively.

distance for both C17-C9 and C17-C26 is 1.3 Å, which indicates the double bond formations rather than single bonds. The C9-C17-C26 is slightly bent. The angle is 167°. The oxygen atoms are placed on the equatorial positions, and they are in contact with the central carbon atom. The distances were not identical. The O-C-O angles largely deviated from those of regular octahedral geometry. Figure 4 shows the isosurface Laplacian map of electron density distribution and bond paths. In the equatorial plane, the atom C17 has no charge concentration. This is well consistent with the consideration from orbital arrangements; in this region, the empty π*-orbitals should be arranged. The bond paths start from the electron rich oxygen atoms to the central carbon, passing through the electron depression region around the carbon. These indicate that dative character of the bonds. All the C-O bond paths are curved. This indicates poor orbital overlapping of the hypervalent bonds for this compound.

The total electron densities of the compounds were analyzed quantitatively using Bader's "Atoms in Molecule" theory. They also reveal the dative character of the hypervalent bonds in both compounds.

In conclusion, the detailed bonding nature of hypervalent bonds can be derived by experimental method. Therefore, if some conditions are satisfied, the electron configuration of reaction intermediate can be analyzed by this method, and valuable chemical information can be derived in chemistry.

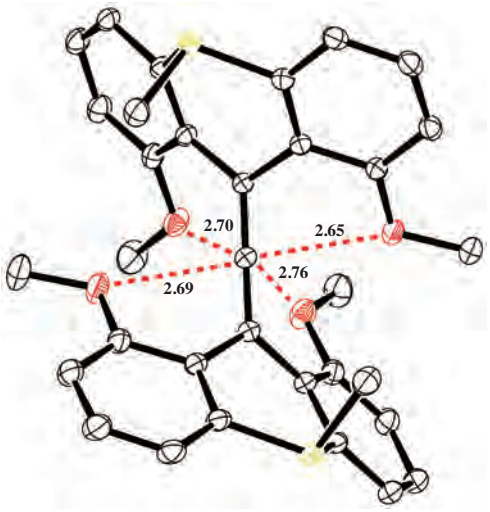


Fig. 3. Molecular structure of the hexacoordinated carbon compound. Bond distances are given in Å.

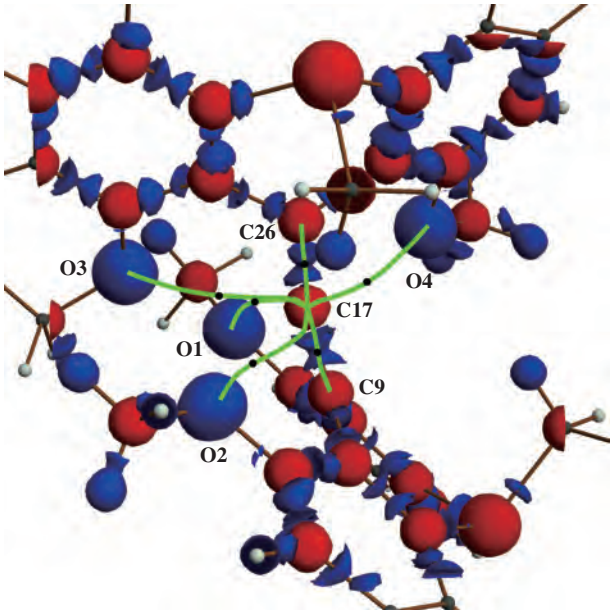


Fig. 4. Isosurface Laplacian distribution plot of the hexacoordinated carbon compound with six bond paths to C17 (green lines). The isosurfaces are drawn in red and blue for electron depressed and electron-concentrated regions, respectively.

Daisuke Hashizume

Advanced Technology Support Division, RIKEN (Wako)

E-mail: hashi@riken.jp

References

[1] K.-y. Akiba *et al.*: J. Am. Chem. Soc. **127** (2005) 5893.
[2] *T. Yamaguchi, Y. Yamamoto, D. Kinoshita, K.-y. Akiba, Y. Zhang, C.A. Reed, D. Hashizume, F. Iwasaki: J. Am. Chem. Soc.* ***130*** *(2008) 6894.*

Selective Chemical Bond Breaking Induced by Resonant Inner-Shell Excitation of Acetone Molecule on the Ar Clusters

Active control of chemical reaction using photoexcitation is one of the main issues of photochemistry [1]. Inner-shell photoexcitation is a notable phenomenon associated with selective chemical bond breaking, and it has been a topic of considerable interest to many researchers [1,2]. The following is a scenario of selective chemical bond breaking. An inner-shell electron is generally localized around a specific atom in a molecule. When an inner-shell electron is ionized or excited in a molecule, the electronic relaxation of the core hole occurs at the initially excited atomic site, and final positive charges in valence orbitals, which are produced via Auger decay, are expected to be localized around the excited sites. Consequently, selective bond scission can be expected depending on the excitation of different atomic site. This concept is called "site-specific fragmentation" and it offers possibilities of controlling chemical reactions through selective bond breaking.

Since the pioneering work by Eberhardt *et al.* in 1983 [2], a number of investigations have been carried out to show the site-specific fragmentation. However, less prominent site selectivity has been reported for the fragmentation of isolated molecules. On the other hand, a remarkable site selectivity has been observed in the photostimulated desorption of some thin polymer films on a metal surface [1]. In order to interpret the different ionic fragmentation processes, the following model has been proposed (Fig. 1). In an isolated molecule, the excess energy afforded at a core-excited site is dissipated over the molecule ahead of the fragmentation. The excited molecule loses the memory of the excited site, and nonspecific fragmentation, i.e., statistical fragmentation, becomes dominant. On the other hand, for a molecule deposited on the surface, the excess energy rapidly flows into the substrate. As a result, the statistical fragmentation is suppressed and specific fragmentation becomes dominant. According to this model, a substrate that absorbs excess energy is indispensable for the occurrence of specific fragmentation induced by inner-shell excitation.

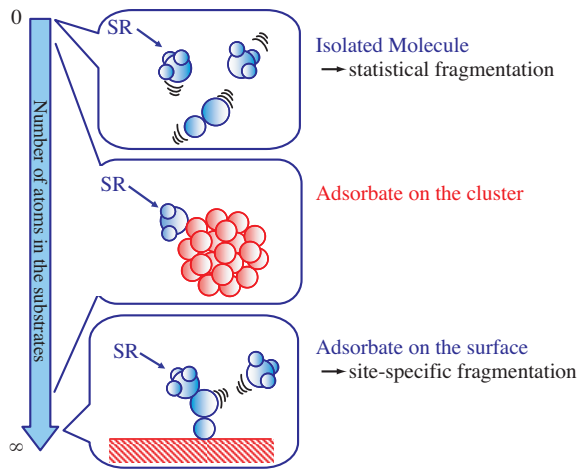


Fig. 1. Illustration of the substrate size dependence on the ionic fragmentation processes.

Under these circumstances, we have focused on the fragmentation processes of a small molecule adsorbed on clusters [3]. Nanoclusters are regarded as an intermediate state between an isolated species and a condensed phase, and easily controlled in size and constituent atoms. In this study, inner-shell photoexcitation and fragmentation of acetone-argon heteroclusters, $[(CH_3)_2CO]Ar_n$, have been investigated. In the photofragmentation of molecules on the clusters, the clusters are expected to behave like a substrate that releases the excess energy from the excited molecule and produces the specific fragmentation even under the isolated condition. Experiments were carried out at the soft X-ray photochemistry beamline **BL27SU**. The experimental setup is illustrated in Fig. 2. The heteroclusters were produced by a "pickup technique." The cluster beam was crossed with a soft X-ray beam in the ionization region and the ions produced were mass-analyzed using a time-of-flight mass spectrometer.

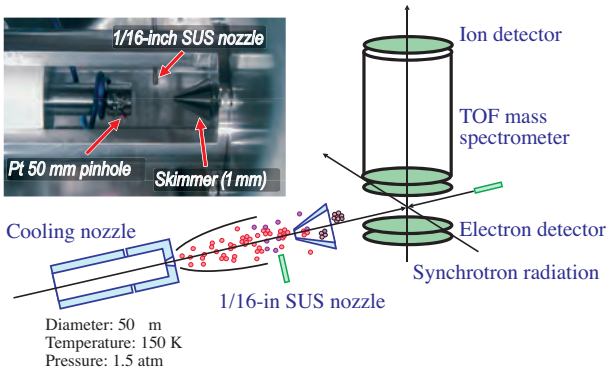


Fig. 2. Schematic layout of the experimental setup.

Figure 3 shows the yield curves of various fragment ions of (a) acetone molecule and (b) $[(CH_3)_2CO]Ar_n$, in the O *K*-edge region. The total ion yield (TIY) curve is also indicated on the top of each spectrum. A clear resonance peak observed at 531 eV can be assigned to the O 1*s* → π*(C=O) resonant excitation, and a small hump observed at

~544 eV is assigned to the σ* shape resonance [4]. A remarkable difference can be seen between the spectra of the isolated acetone molecule and those on the argon clusters. All the partial ion yield (PIY) curves of the acetone molecule mimic that of the photoabsorption spectrum, and it is suggested that the statistical fragmentation processes are dominant. On the other hand, in the case of heteroclusters, the selective enhancement of the O^+ formation can be observed at the O 1*s* → π*(C=O) resonance excitation, while the PIY curves of other fragment ions show only weak resonance features.

A selective C=O bond scission is expected at the O 1*s* → π*(C=O) resonance, because of a strong repulsive character of the Auger final state. Following inner-shell electron excitation, a resonantly excited molecule emits an electron through resonant Auger transitions, and spectator Auger decay, which produces a two-hole one-electron (2h–1e) state, usually gains most of the intensity [5]. The resonant Auger decay following the O 1*s* excitation is considered to preferentially create two holes in the molecular orbitals that have a high population near the O atom. The vacant C=O bonding orbital and the spectator electron in the π*(C=O) orbital are expected to weaken the C=O bond and result in the selective C=O bond scission.

Furthermore, the selective O^+ formation only on the argon clusters should be interpreted by the suppression of statistical fragmentation channels [1]. For the inner-shell-excited acetone molecule, both statistical and specific fragmentations are possible. Because the energy dissipation within the molecule is very rapid and all dissipation processes lead to statistical fragmentations, the former is dominant in the isolated molecule (Fig. 3(a)). On the other hand, when the excited molecule is an adsorbate on the substrate, the substrate can act as an excess energy buffer against the statistical fragmentation of the excited molecule. In the $[(CH_3)_2CO]Ar_n$ clusters, the argon cluster can absorb the excess energy from the excited acetone molecule, and a major part of the clusters causes the evaporation of neutral Ar atoms instead of molecular fragmentation. The selective O^+ formation suggests that either the nonespecific fragmentation is suppressed or the suppression of the specific fragmentation is nonessential. The present results demonstrate that the small cluster is likely to play the role of an excess energy buffer and it produces the selective ionic fragmentation.

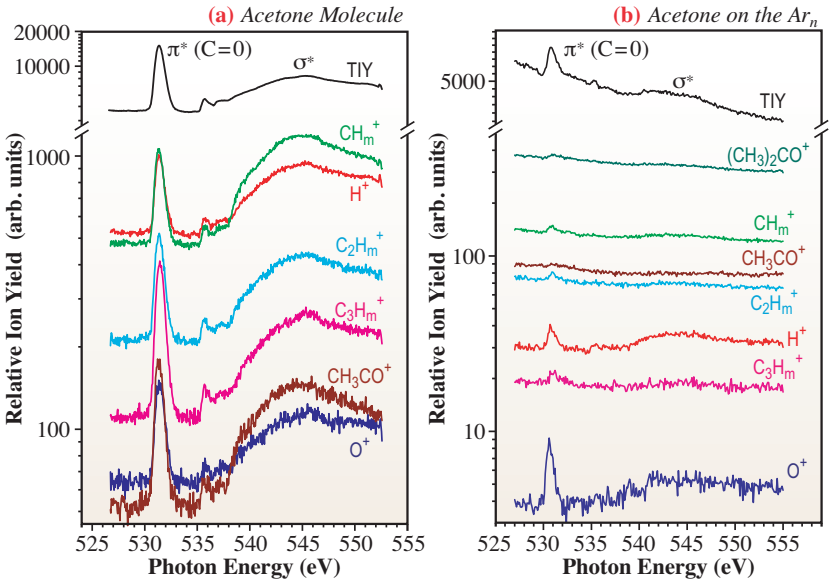


Fig. 3. TIY and PIY spectra of various fragment ions formed by the photoionization of **(a)** an isolated acetone molecule and **(b)** heteroclusters in the O *K*-edge region.

Yusuke Tamenori

SPring-8/JASRI

E-mail: tamenori@spring8.or.jp

References

[1] S. Wada *et al.*: J. Phys.: Condens. Matter **18** (2006) S1629, and references therein.
[2] W. Eberhardt *et al.*: Phys. Rev. Lett. **50** (1983) 1038.
[3] *Y. Tamenori, K. Okada, K. Tabayashi, T. Gejo and K. Honma: Chem. Phys. Lett.* ***462*** *(2008) 40.*
[4] K.C. Prince *et al.*: J. Phys. Chem. A **107** (2003) 1955.
[5] D.B. Thompson *et al.*: J. Phys. B: At. Mol. Opt. Phys. **32** (1999) 2649.

A Molecular Knife
- Control of Chemical Reactions using Core Ionization -

When we cut a corner from a sheet of paper, we usually use a pair of scissors (Fig. 1). When the piece of paper is small, a knife is necessary. However, when the target becomes smaller and smaller towards the size of a molecule, a molecular assembly, or a nanoscale device, we have not yet found an appropriate cutting tool. As a candidate for such a molecular knife, we may consider localized photoexcitation. In contrast to valence electrons delocalized over the entire molecule, core electrons can be localized near the nucleus of one particular atom. Accordingly, controlled bond breaking following photoexcitation or photoemission of localized core electrons can be considered a molecular knife.

To select an atom not only of one specific element, e.g., carbon but also in a specific chemical environment inside the molecule, the corresponding core-electron binding energy differences, that is, chemical shifts in ESCA, can be used. This quantity has been used to study site-specific fragmentation [1], where bonds around the site of core-ionized atoms are dissociated selectively.

In this work, we employed an energy-selected-photoelectron photoion/photoion-photoion coincidence (PEPICO/PEPIPICO) method [2] to study site-specific fragmentation caused by Si:2*p* core-level photoionization of $F_3SiCH_2CH_2Si(CH_3)_3$ (FSMSE) in the vapor phase. The coincidence apparatus was installed at the c branch of **BL27SU** [3]. FSMSE was chosen for this study because the chemical environment of a Si atom bonded to three F atoms (as denoted here Si[F]) is very different from that of Si bonded to three methyl groups (Si[Me]). Therefore, the two peaks in the photoelectron spectrum (PES) of FSMSE vapor assigned to Si[Me]:2*p* and Si[F]:2*p* photoelectron emission [4] are clearly separated in Fig. 2(a). The PEPICO spectra measured in coincidence with the Si[Me]:2*p* and Si[F]:2*p* photoelectrons are shown in Figs. 2(b) and 2(c), where site-specific fragmentation is clearly evident. For example, the site selectivity for the production of $F_3SiCH_2CH_2^+$ and F^+ is almost 100%. The bond dissociations mostly occur at the Si site where the photoionization has taken place. Site-specific



Fig. 1. Molecular knife.

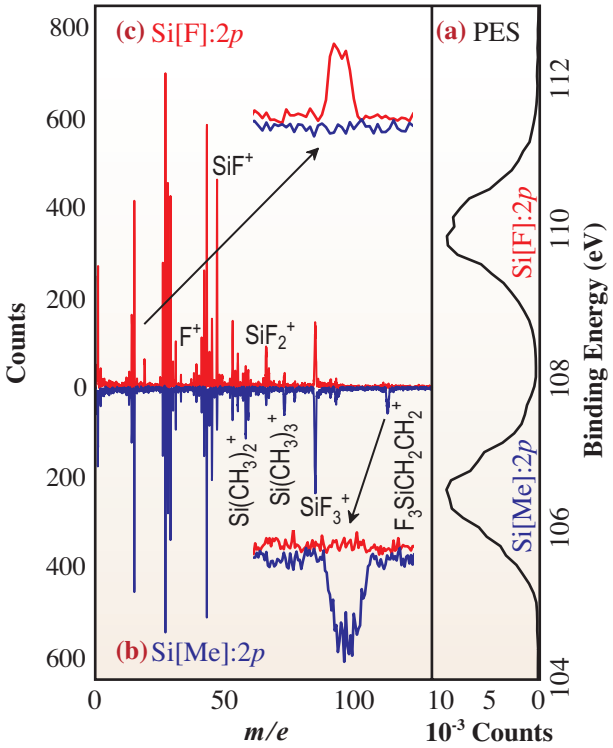


Fig. 2. **(a)** Si:2*p* PES of FSMSE vapor. **(b)** and **(c)** PEPICO spectra measured in coincidence with the Si[Me]:2*p* and Si[F]:2*p* photoelectrons. The insets show the regions of F^+ and $F_3SiCH_2CH_2^+$ with enlarged scales.

fragmentation is also revealed in ion-pair formation. Figure 3 shows the PEPIPICO counts of $F_3SiCH_2CH_2^+$–$Si(CH_3)_3^+$ and SiF^+–$SiCH_3^+$ *versus* the photoelectron binding energy, together with the PES of FSMSE. The site selectivity for the production of these ion pairs was also almost 100%.

Site-specific fragmentation thus offers an approach to control chemical reactions by selecting the sites at which holes are created. The elucidation of the details of the fragment production mechanism brings the goal of a molecular knife one step closer to realization.

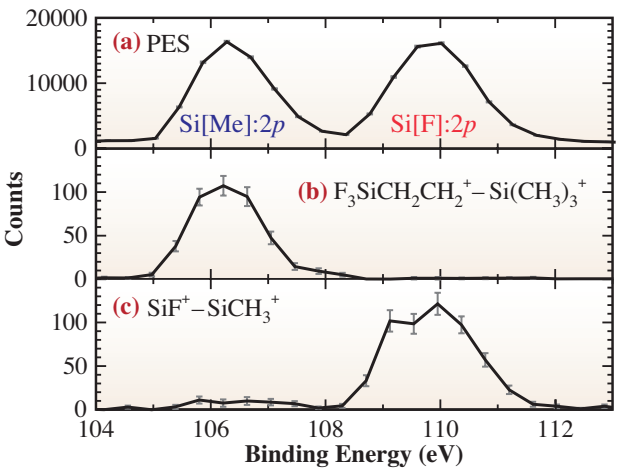


Fig. 3. **(a)** Si:2*p* PES of FSMSE vapor. **(b)** and **(c)** Plots of the PEPIPICO counts of $F_3SiCH_2CH_2^+$–$Si(CH_3)_3^+$ and SiF^+–$SiCH_3^+$ *versus* the photoelectron binding energy.

S. Nagaoka[a,*], G. Prümper[b] and K. Ueda[b]

[a] Graduate School of Science and Engineering, Ehime University
[b] Institute of Multidisciplinary Research for Advanced Materials, Tohoku University

*E-mail: nagaoka@ehimegw.dpc.ehime-u.ac.jp

References

[1] S. Nagaoka *et al.*: J. Chem. Phys. **129** (2008) 204309 and references cited therein.
[2] G. Prümper *et al.*: J. Electron Spectrosc. Relat. Phenom. **144-147** (2005) 227.
[3] H. Ohashi *et al.*: Nucl. Instrum. Methods A **467-468** (2001) 529.
[4] *S. Nagaoka, G. Prümper, H. Fukuzawa, M. Hino, M. Takemoto, Y. Tamenori, J. Harries, I. H. Suzuki, O. Takahashi, K. Okada, K. Tabayashi, X.-J. Liu, T. Lischke and K. Ueda: Phys. Rev. A* ***75*** *(2007) 020502(R).*

Ab Initio Structure Determination of Medium-Sized Pharmaceuticals

Crystal structure determination from powder diffraction (SDPD) has attracted wide interest because of its huge potential to accelerate the design, synthesis, and characterization of materials. During the past decade, many SDPD studies have shown the methodology, software, and also the actual *ab initio* structural determinations. Presently, the structure of a small molecule with less than 30 atoms and approximately 10 degrees of freedom can be routinely solved from powder diffraction data using several software on a single personal computer. The SDPD for large systems such as medium-sized pharmaceuticals with more than 20 degrees of freedom and 100 atoms is still a very difficult task. High resolution powder diffraction data and additional analytical techniques have been normally required for SDPD in these cases. In the present study, we have performed SDPD for a medium-sized pharmaceutical, prednisolone succinate as shown in Fig. 1, using high-resolution synchrotron X-ray powder diffraction data at SPring-8.

The *d*-spacing range of the data collected at beamline **BL02B2** was $d > 1.0$ Å, which is much wider than that of normal laboratory data, $d > 2.0$-1.4 Å. The structure determination has been carried out using the original Genetic Algorithm (GA) system [1]. There were seven torsion angles in the succinate part of the molecule. The number of degrees of freedom in one molecule is thirteen, namely, three positional parameters, three orientation parameters, and seven torsion angles. The number of molecules in a crystallographic asymmetric unit was evaluated from the unit cell volume as two. Therefore, the total number of degrees of freedom became twenty-five, because one positional parameter must be fixed in the case of non-centro-symmetric space group. Rietveld refinement was carried out using the structure model determined using the GA. The reliability factors, R_{wp} and R_I, of the final structure analysis by the Rietveld refinement reach less than 3% and 5%, respectively. The crystal structure of prednisolone succinate is shown in Fig. 2. It clearly shows that the molecules are located parallel to the 101 direction. The reasonable structure including hydrogen atoms of medium-sized pharmaceutical with no checkCIF alert relating to the fundamental structure, such as interatomic distances and bond angles, has been determined from powder diffraction data in the present study.

In the final stage of the analysis, data covered with a wide *d*-spacing range, $d \geq 1.0$ Å, was required to reach a correct solution. It is normally very difficult to measure the powder diffraction peaks of medium-sized pharmaceuticals in the $d \approx 1.0$ Å resolution

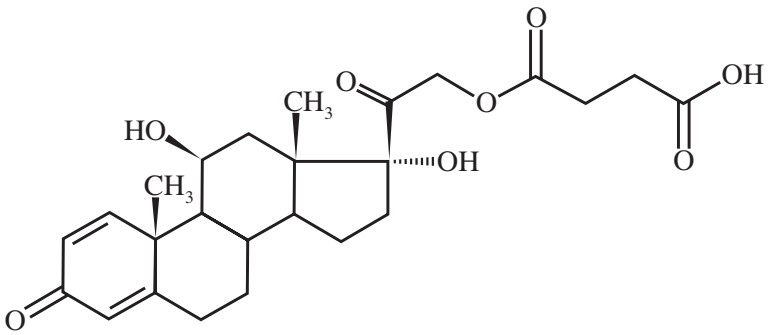


Fig. 1. Structural formula of prednisolone succinate.

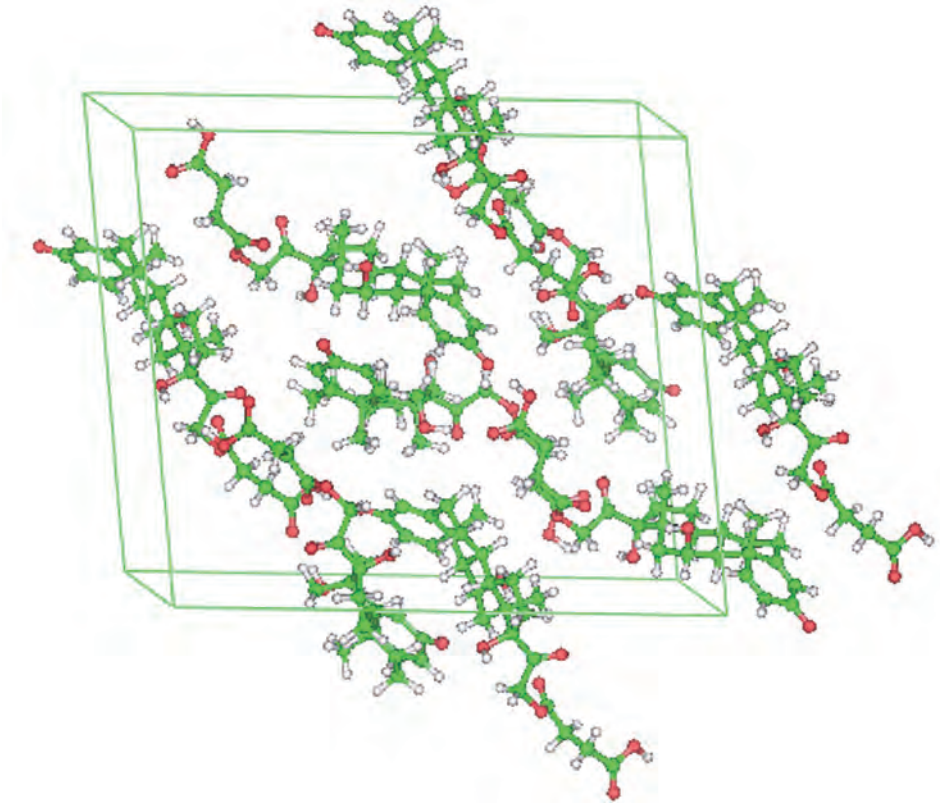


Fig. 2. Crystal structure of prednisolone succinate from powder diffraction data obtained at SPring-8.

range, because the peak intensity of Bragg reflection in this range is intrinsically weak with less than 1% of the maximum intensity. Furthermore, considerable peak overlaps and peak broadenings prevent the recognition of the higher angle peaks. In the powder diffraction experiment at SPring-8, an X-ray beam with the high-energy resolution, $\Delta E/E \approx 10^{-4}$, and sufficiently high intensity is available. Powder data at SPring-8 is the most appropriate for SDPD, which enables us to expand the limit of SDPD.

Eiji Nishibori*, Shinobu Aoyagi and Makoto Sakata

Department of Applied Physics, Nagoya University

*E-mail: o47271a@cc.nagoya-u.ac.jp

References

[1] *E. Nishibori, T. Ogura, S. Aoyagi and M. Sakata: J. Appl. Cryst.* ***41*** *(2008) 292.*

EARTH & PLANETARY



Advances in synchrotron radiation techniques and current challenges in the study of Earth materials have made the remarkable growth in Earth and planetary science research possible. New beamline techniques and analytical methods, of which developments and upgrades are still continuing, allow us to produce significant new results. Furthermore, recently developed *in situ* simultaneous measurement systems, combining synchrotron radiation techniques with non-synchrotron techniques, have yielded outstanding results, including numerous breakthroughs. In this chapter, we have selected three outstanding and two representative studies published in 2008 among many articles on Earth and planetary science research.

Nakamura and Tsuchiyama studied small particles from the short-period comet 81P/Wild 2 that were obtained by the Stardust mission using micro X-ray diffraction, micro X-ray tomography, and field emission scanning electron microscope. They found that the crystalline particles from the comet were mineralogically, texturally, and compositionally similar to chondrules, suggesting that classical models of the formation of the solar system need major modifications. Irifune and Higo demonstrated the utility of a combination method of X-ray diffraction, radiography, and ultrasonic measurements with a large-volume press apparatus, and studied the sound velocities of minerals in the Earth's mantle transition zone at pressures up to 20 GPa and temperatures up to 1800 K to understand the composition of the mantle transition region. They found that the seismic velocitiy of the pyrolite composition is consistent with typical seismological models in the upper to middle parts of the region, and in the lower part of the region the subducted slab materials are stagnant around the 660 km discontinuity. Hirose *et al*. have, for the first time, observed high electrical

SCIENCE

conductivity of post-perovskite under the conditions of the lowermost mantle of the Earth using an X-ray diffraction and electrical conductivity measurement system with a laser-heated diamond anvil cell. Their results suggested that a post-perovskite layer above the core-mantle boundary markedly affects the rotational vibration of the Earth through strong electromagnetic coupling between the fluid outer core and the solid mantle. Nakajima and colleagues presented an *in situ* high-pressure and high-temperature X-ray diffraction study of iron carbide (Fe_3C) and iron hydride (FeH_x) with a large-volume press apparatus, examining the effects of carbon and hydrogen on the melting temperature of iron at high pressures up to 30 GPa. They obtained detailed melting curves of Fe_3C and FeH_x at high pressures that led them to conclude that the temperature of iron in the outer core is significantly affected by carbon and hydrogen. The last topic is by Lee *et al*., who examined the local structure change of oxygen in $MgSiO_3$ glass at high pressures by X-ray Raman spectroscopy in a diamond anvil cell. Their results provided important information about transport properties of magma in the Earth's mantle.

Yasuo Ohishi



Chondrules in the Short-Period Comet 81P/Wild 2

The formation of the early solar system is recorded in primitive solid materials such as meteorites and interplanetary dust particles. In 2006, the Stardust spacecraft (Fig. 1(a)) returned to Earth with many small rock particles that have been successfully recovered from a short-period comet 81P/Wild 2 (Fig. 1(b)) [1]. The particles from the comet were captured in a very low density material, aerogel. The particles are very primitive dust having been present in the outer regions of the early solar system, because short-period comets originally formed as Kuiper-belt objects that currently locate at 30-50AU from the Sun (Fig. 2). In fact, the comet 81P/Wild 2, now orbiting between Mars and Jupiter, had been circulating on a wider orbit reaching the Kuiper belt [1]. On the other hand, asteroids, much closer (3-5AU) to the Sun (Fig. 2), are parent bodies of the primitive class of meteorites, chondrites, and they formed by the accretion of solid particles in the inner regions of the early solar nebula. Through studies of chondrites, the formation of small planetary bodies in the inner solar system is understood, but the formation of those in the outer solar system remains poorly understood. Therefore, cometary materials are the best sample for the elucidation of the evolution of outer solar system.

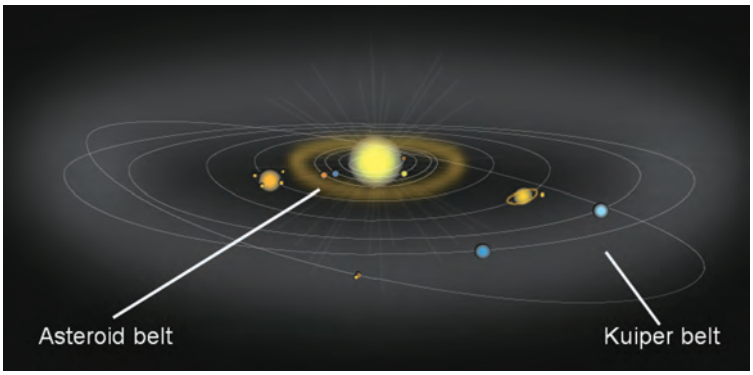
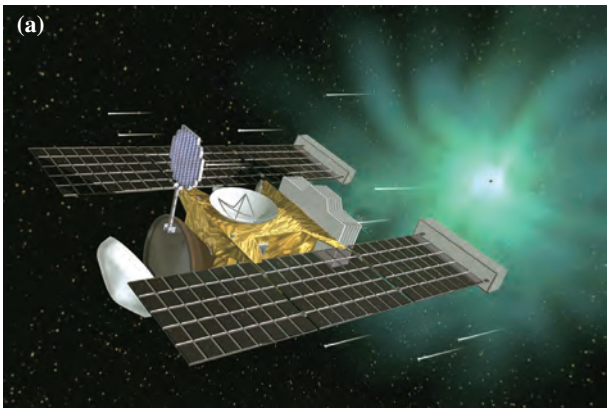


Fig. 2. Illustration of solar system showing location of asteroid belt and Kuiper belt. Short-period comets formed as small planetary bodies in the Kuiper belt.



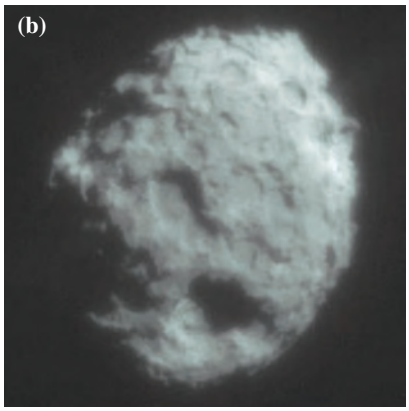


Fig. 1. **(a)** Illustration showing the Stardust spacecraft approaching short-period comet 81P/Wild 2. Small particles from the comet are captured by an aerogel grid poking out of the spacecraft. **(b)** Photograph of comet 81P/Wild 2 taken by an on-board navigation camera. This image was taken within a distance of 500 kilometers from the comet's nucleus. The diameter of the nucleus is approximately 5.5 km.

Chondrules are a major component of chondrites and were formed around 4.565 Gyr by the solidification of totally or partially melted Mg, Fe, Si, and O-rich silicates typically smaller than 1 mm in diameter. Abundant chondrules in chondrites, up to 80 vol% of the rocks, indicate that high-temperature heating events, that melted solid dust particles at temperatures of ~1500 °C or higher, commonly took place in the inner solar nebula. However, it is unknown whether chondrules were present in the outer regions of the early solar system.

The authors and co-investigators listed in [2,3] performed multidisciplinary analyses of small particles from the comet. The particles were first analyzed by X-ray diffraction at beamline **BL37XU** using a thin 6-keV beam to characterize bulk mineralogy. Then the particles were again exposed to a 9-keV X-ray at beamline **BL47XU** for microtomography analysis to characterize internal structures at submicron spatial resolution. Up to now, six samples were found to have bulk mineralogy rich in well-crystalline olivine, low-Ca pyroxene, and FeNi metal and to show a porphyritic internal structure suggestive of high-temperature partial melting during formation (Fig. 3(a)).

To observation of a polished surface of the six samples using a field emission scanning electron

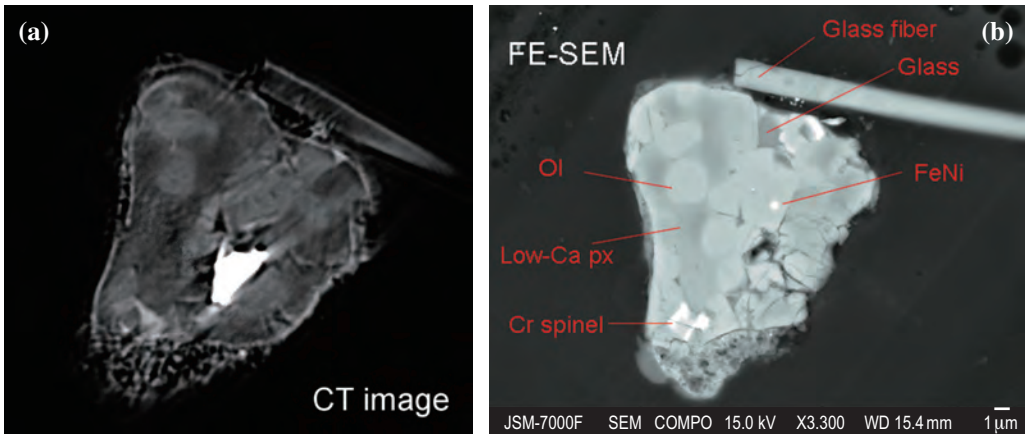


Fig. 3. **(a)** CT image of a particle C2054,0,35,6,0 (Torajiro) from comet 81P/Wild 2. This cross section is chosen to best reproduce the real image of the polished surface shown in **(b)**. **(b)** FE-SEM image of polished surface of Torajiro, showing porphyritic texture that are very similar to chondrules in chondritic meteorites from asteroids.

microscope (FE-SEM) revealed that they really show igneous texture (Fig. 3(b)) and have mineral compositions and concentrations of major and most minor elements that are very similar to those of chondrules in primitive meteorites derived from asteroids. Oxygen isotope ratios show a wide range from −50 to +5 ‰ in $\delta^{18}O_{SMOW}$, nearly along the slope = 1 mass independent fractionation line that characterizes chondrules in carbonaceous chondrites that comprise the outer asteroid belt (Fig. 4). Furthermore, highly heterogeneous oxygen isotope ratios within a single particle suggest that they formed by remelting of prexisting solid precursors. Therefore, these particles are pieces of chondrules formed through the least degree of melting, crystallization, and elemental and isotope equilibration at high temperatures. The presence of chondrules in a short-period comet from the Kuiper belt indicates that chondrules migrated from hot inner nebula regions to cold outer regions and spread widely over the early solar nebula. Our study concludes that a large-scale outward transportation of solid particles took place in the early solar system, reinforcing modifications to current models for solar system formation.

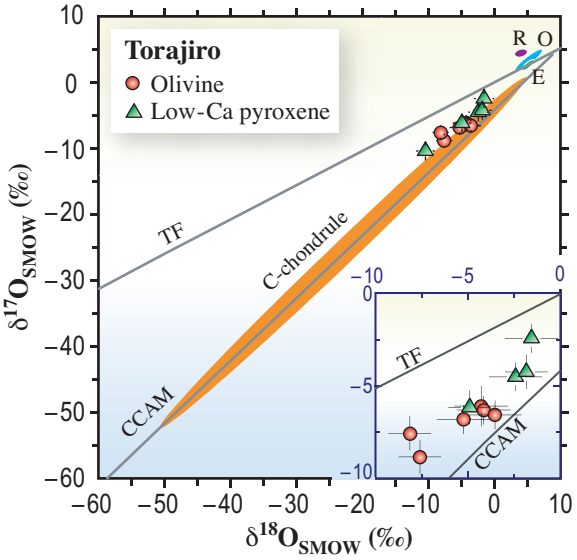


Fig. 4. Oxygen isotope ratios of olivine and low-Ca pyroxene crystals in Torajiro. The ratios are heterogeneous within the particle, suggesting that the particle formed through partial melting.

Tomoki Nakamura[a,*] and Akira Tsuchiyama[b]

[a] Department of Earth and Planetary Science, Kyushu University
[b] Department of Earth and Space Science, Osaka University

*E-mail: tomoki@geo.kyushu-u.ac.jp

References

[1] D. Brownlee *et al.*: Science **314** (2006) 1711.
[2] *T. Nakamura, A. Tsuchiyama, T. Akaki, K. Uesugi, T. Nakano, A. Takeuchi, Y. Suzuki and T. Noguchi: Meteoritics and Planetary Sciences* ***43*** *(2008) 247.*
[3] *T. Nakamura, T. Noguchi, A. Tsuchiyama, T. Ushikubo, N.T. Kita, J.W. Valley, M.E. Zolensky, Y. Kakazu, K. Sakamoto, E. Mashio, K. Uesugi, T. Nakano: Science* ***321*** *(2008) 1664.*

Composition of the Mantle Transition Region Constrained by Sound Velocity Measurements at High Pressure and Temperature

The Earth's mantle is divided into three layers, namely, the upper mantle (30 km-410 km in depth), mantle transition region (410 km-660 km), and lower mantle (660 km-2900 km), by sharp discontinuous changes in both seismic velocities (Vp and Vs) and density at depths of 410 km and 660 km. The upper mantle is known to consist of a rock called "pyrolite" (Fig. 1(a)) [1], which is composed mainly of three minerals, olivine, pyroxene, and garnet, on the basis of petrological studies of deep-seated materials delivered to the surface of the Earth via volcanic eruptions or tectonic movements. Laboratory sound velocity measurements of pyrolite also confirmed that the Vp and Vs of this rock are consistent with those observed seismologically for the upper mantle.

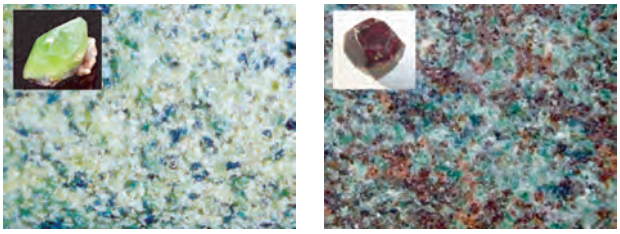


Fig. 1. Examples of mantle rocks: **(a)** pyrolite and **(b)** piclogite, where inlets are crystals of olivine and garnet, respectively, which are the predominant minerals in these rocks. Note that pyrolite and piclogite are names of hypothetical rocks, and the pictures displayed here are those of natural peridotite and eclogite rocks, which are closely related to these hypothetical rocks.

In contrast, the composition of the mantle transition region (MTR, hereafter), as well as of the lower mantle, remains unresolved. As the sources of the mantle rocks are limited to those at depths shallower than ~200 km, laboratory sound velocity measurements of the candidate materials and comparison of these results with seismic velocities are the only way to estimate the composition of the deeper part of the mantle. However, it has been difficult to precisely determine the sound velocities of high-pressure phases at pressures (13-24 GPa) and temperatures (1700-1900 K) equivalent to those of MTR.

It has been acknowledged that olivine in pyrolite composition transforms to modified spinel and spinel structures under the P, T conditions of MTR, while pyroxene dissolves in garnet, forming a high-pressure phase called "majorite." Pyrolite is composed of ~60% of the high-pressure forms of olivine plus ~40% of majorite in this region of the mantle, as confirmed by phase equilibrium studies at high pressure and high temperature. However, an alternative model composition, called "piclogite" (Fig. 1(b)) [2], has also been proposed for this region. Piclogite possesses a range of compositions with lesser amounts of the olivine relative to majorite, in contrast to pyrolite, and it has been difficult to conclude which composition is better in the light of seismological constraints, as the sound velocities of these high-pressure phases have never been measured under the P, T conditions of MTR.

We have developed techniques for precisely measuring the sound velocities at pressures up to ~20 GPa and temperatures up to ~1800 K, by a combination of synchrotron radiation and ultrasonic measurements with a large-volume multianvil apparatus at beamline **BL04B1** [3]. On the basis of these techniques, we measured the sound velocities of the spinel form of olivine (ringwoodite) [3] and majorite [4] in pyrolite composition. The results demonstrated that both Vp and Vs of majorite with the realistic mantle composition are significantly lower than the corresponding velocities of ringwoodite (Fig. 2). The Vp and Vs of the two candidates for the composition of MTR, pyrolite and piclogite, can be

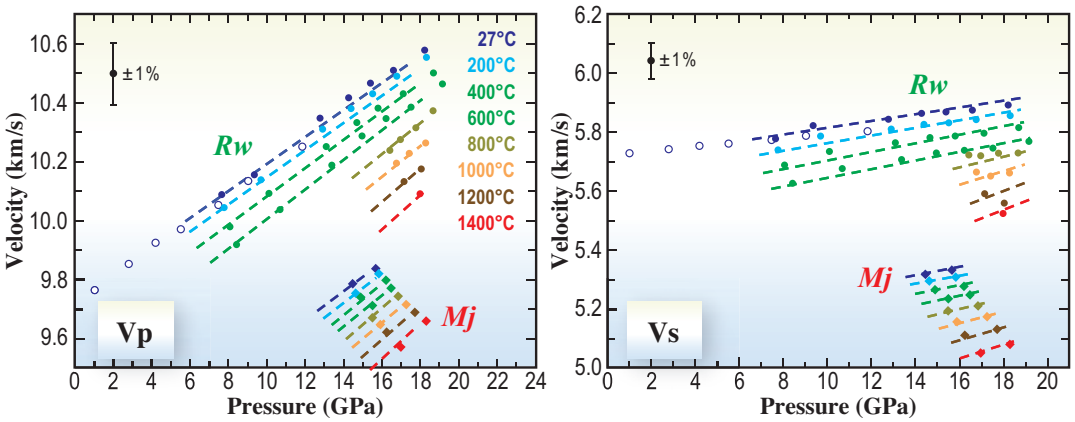


Fig. 2. Sound velocities (Vp, Vs) of ringwoodite (Rw) and majorite (Mj) at high pressure and high temperature determined by the present measurements of combined *in situ* X-ray and ultrasonic observations.

calculated using the present sound velocity data on ringwoodite and majorite, because both of these two rocks crystallize to assemblages mainly of these two high-pressure phases in different proportions.

Figure 3 illustrates the variations in Vp and Vs in pyrolite and piclogite composition based on the present measurements, which are compared with those obtained using seismological models (PREM and AK135). It is seen that the velocities of pyrolite are consistent with those seismologically observed in the upper to middle parts of MTR, while they (particularly Vs) become significantly lower than the seismological models in the lower part of this region. Piclogite yields an even lower Vs in the middle to lower parts of MTR, and is found inappropriate as the composition for this region.

Thus, the present result demonstrates that pyrolite is the best model composition for MTR except for its bottom region. We tested various compositions for this region, and found that only harzburgite, which is the main component of a sinking oceanic plate (referred to as a "subducting slab"), should have Vp and Vs consistent with those of the seismological models (Fig. 3). Thus, it is most likely that the upper mantle and upper to middle parts of this region are composed of pyrolite, while the bottom part of the latter region is made of subducted slab materials trapped around the 660 km discontinuity (Fig. 4), where the density of the surrounding mantle increases substantially.

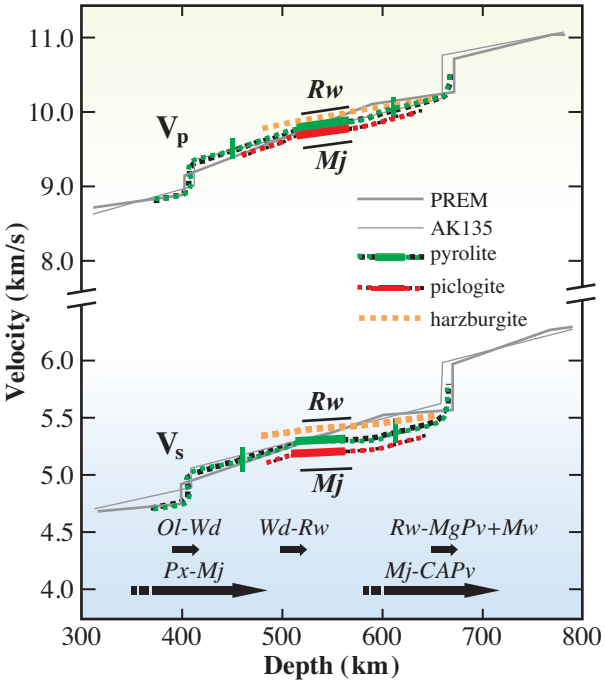


Fig. 3. Comparisons of sound velocities of pyrolite (green), piclogite (red), and harzburgite (orange) with those seismologically derived (PREM and AK135). Phase transitions in these lithologies are shown in the lower part of the figure. Ol=olivine, Wd=wadsleyite, Rw=ringwoodite, Px=pyroxene, Mj=majorite, MgPv=$MgSiO_3$ perovskite, Mw=magnesiowustite, CaPv=$CaSiO_3$ perovskite.

It has been demonstrated that some of the subducting slabs are stagnant at and around the 660 km discontinuity by some seismological observations. The fate of such "stagnant slabs" has been a matter of debate in conjunction with the possible mode of mantle convection [5]. The present study suggests that most of the slabs stagnant around this depth may form a thick (~100 km) layer of harzburgite just around the 660 km discontinuity, although some cold and thick slabs may penetrate deeper into the lower mantle and could reach the mantle-core boundary. As the thermally equilibriated harzburgite is less dense than the surrounding pyrolite mantle, once the ringwoodite to perovskite (+ magnesiowustite) transition takes place in these compositions [6], it is likely that the harzburgite layer will be gravitationally stable in the top region of the lower mantle.

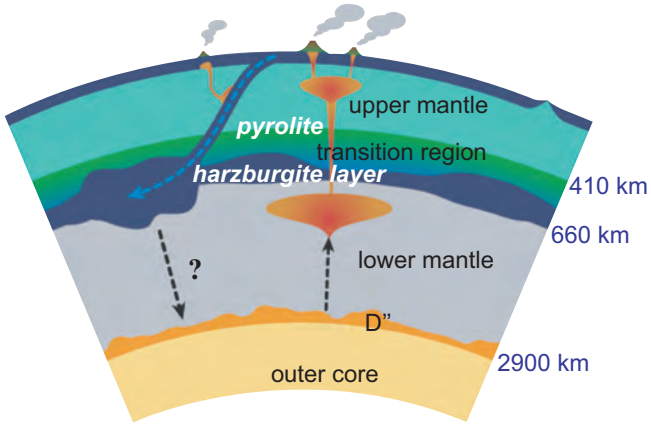


Fig. 4. Proposed model for the composition, structure, and dynamics in the mantle based on the present study, suggesting that the upper mantle and the upper to middle parts of MTR are composed of pyrolite composition, and a thick layer of harzburgite may exist near the 660 km seismic discontinuity. "Flushing" of the stagnant slab down into the lower mantle is questionable, as the harzburgite layer is gravitationally stable at the top of the lower mantle.

Tetsuo Irifune[a,*] and Yuji Higo[b]

[a] Geodynamics Research Center, Ehime University
[b] SPring-8/JASRI

*E-mail: irifune@dpc.ehime-u.ac.jp

References

[1] A.E. Ringwood: J. Geophys. Res. **67** (1962) 857.
[2] D.L. Anderson and J.D. Bass: Nature **320** (1986) 321.
[3] *Y. Higo, T. Inoue, T. Irifune, K. Funakoshi, B. Li: Phys. Earth Planet. Inter.* ***166*** *(2008) 167.*
[4] *T. Irifune, Y. Higo, T. Inoue, Y. Kono, H. Ohfuji, K. Funakoshi: Nature* ***451*** *(2008) 814.*
[5] Y. Fukao *et al.*: Rev. Geophys. **32** (2001) 291.
[6] A.E. Ringwood and T. Irifune: Nature **331** (1988) 131.

The Electrical Conductivity of Post-Perovskite in Earth's D" Layer

Recent discovery of a phase transition from perovskite to post-perovskite suggests that the physical properties of the Earth's lowermost mantle, called the D" layer, may be different from those of the overlying mantle. A possible existence of a highly electrically conductive layer has been often suggested in the deepest mantle from geophysical modeling, where post-perovskite phase is dominant. The direct measurement of silicate post-perovskite has never been performed before.

We measured the DC electrical conductivity of $(Mg_{0.9}Fe_{0.1})SiO_3$ perovskite and post-perovskite phases at high pressure and temperature in a laser-heated diamond-anvil cell (DAC) (Fig. 1), up to 143 GPa and 3000 K corresponding to the condition at the D" layer of the mantle [1]. All the measurements were made at beamline **BL10XU** in order to identify the crystal structure from the XRD patterns. The resistance of starting material was ~10^9 Ω, and it dropped by several orders of magnitude after the synthesis of perovskite or post-perovskite upon heating at high pressure. The electrical conductivity was estimated from the measured resistance and sample geometry that is defined by the length between the electrodes, laser spot size, and thickness of the perovskite or post-perovskite layer. We have determined the electrical conductivity of perovskite phase to 117 GPa. The conductivity obtained at 37 GPa and ~2000 K was about 1 S/m (Fig. 2), which is reasonably consistent with the earlier measurements at 23 GPa in a multi-anvil apparatus [2]. The conductivity decreased remarkably between 58 and 104 GPa. This could be due to the high-spin to low-spin transition of iron in perovskite [3]. The conduction in the high-spin perovskite is dominated by a small-polaron process of electron hopping between ferrous and ferric iron sites. The unpaired electrons in the 3*d* orbital play important roles in this process, but the number of unpaired electrons of ferric iron decreases from five to one at this spin-pairing transition, thus resulting in a significant reduction in the conductivity. Similar reduction in the electrical conductivity has been observed for (Mg, Fe)O ferropericlase between 50 to 70 GPa at room temperature [4], and it has been attributed to the iron spin-pairing transition as well.

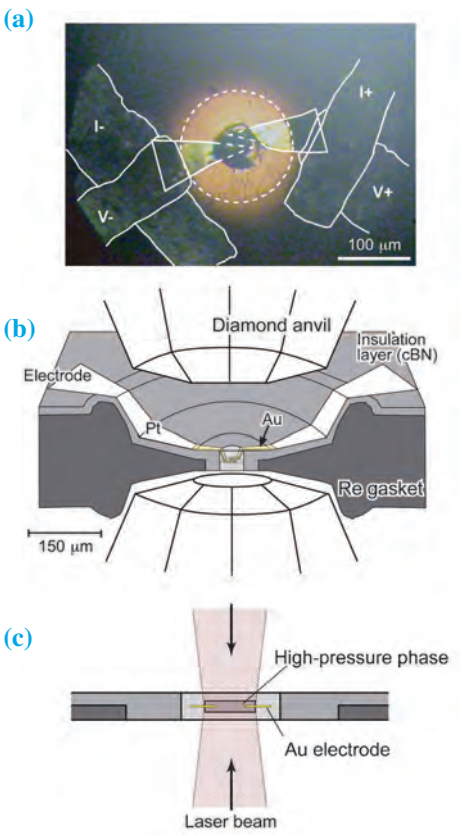


Fig. 1. **(a)** Microscopic image of the sample and electrodes. The quasi-four-terminal electrical resistance measurements were performed at high temperature (direct current of 1 mA was applied through I+ to I-, and the voltage drop between V+ and V- was recorded). **(b)** Schematic drawing of the configuration in a DAC. **(c)** Close-up view of the sample during heating by laser. About 30 or 50-μm areas of the sample and Au electrodes were heated from both sides. Only high-temperature part of the sample transformed to high-pressure phase.

The exceedingly high electrical conductivity of post-perovskite was observed in a couple of separate experiments (Fig. 2). The conductivity increased by three orders of magnitude when perovskite transformed to post-perovskite upon heating to ~2000 K for 20 min at 143 GPa. The sample showed the conductivity of >10^2 S/m (siemens per meter) with minimal temperature dependence. The high conductivity of post-perovskite was reconfirmed when post-perovskite was synthesized directly from the amorphous starting material by heating to 2000 K for 30 min at 129 GPa. After the complete pressure release, the sample was examined under both transmission electron microscope (TEM) and field-emission-type scanning electron microscope (FE-SEM) with a spatial resolution of 1.0-nm. We observed no metal-like phase throughout the sample. The post-perovskite phase has a stacked SiO_6-octahedral sheet structure with interlayer (Mg, Fe) ions. The high conductivity likely reflects the short Fe-Fe distance in the (Mg, Fe) layer, which is shorter than that in perovskite.

These results indicate that the electrical conductivity of (Mg, Fe)SiO_3 post-perovskite is much higher than that of perovskite (Fig. 2). A layer with a high electrical conductivity above the core-mantle boundary would enhance the electromagnetic (EM) coupling between the fluid core and solid mantle. It has been suggested that if the conductance of this layer is $>10^8$ S (at least 3×10^7 S), the resultant exchange of angular momentum between the core and mantle would be sufficient to change the length of a day on decadal timescales by a few milliseconds, as has been observed [5]. Our measurements indicate that the conductance of the D" layer may be 4×10^7 S (the conductance is related to the conductivity and thickness of the layer), which is marginally high enough to account for the decadal variations in length of a day. In addition, the EM coupling also affects the periodic precession of the Earth's axis of rotation (nutation). The high conductance of the post-perovskite-rich D" layer may explain the retrograde 18.6- and 1.0-year nutations that have been observed.

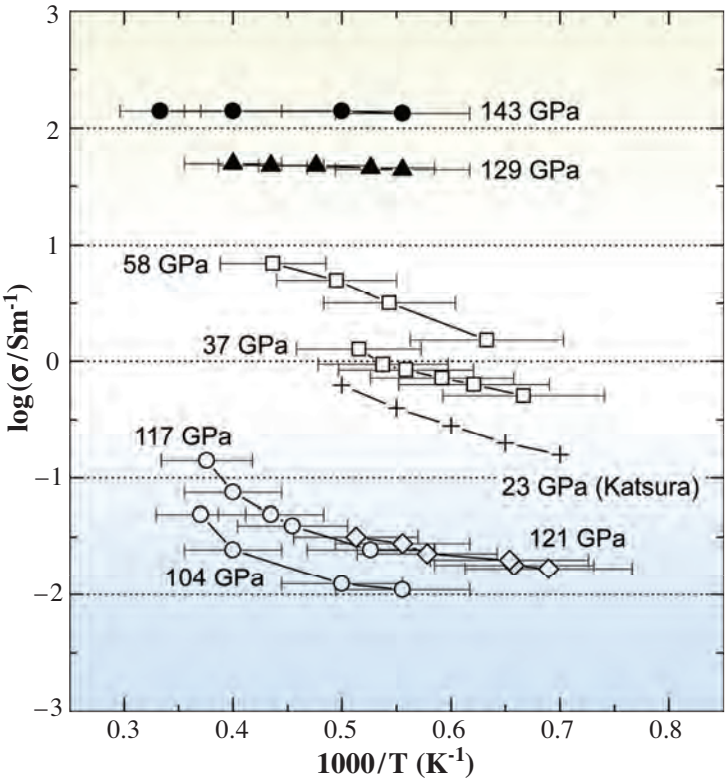


Fig. 2. Electrical conductivity (σ) of perovskite and post-perovskite as a function of reciprocal temperature. Different symbols show the results of different set of experiments. Open and closed symbols indicate measurements of perovskite and post-perovskite, respectively. Previous data on perovskite by Katsura *et al.* [2] are also presented by crosses.

Kei Hirose[a,b,*], Kenji Ohta[a] and Katsuya Shimizu[c]

[a] Department of Earth and Planetary Sciences, Tokyo Institute of Technology
[b] Institute for Research on Earth Evolution, Japan Agency for Marine-Earth Science and Technology
[c] Center for Quantum Science and Technology under Extreme Conditions, Osaka University

*E-mail: kei@geo.titech.ac.jp

References

[1] *K. Ohta, S. Onoda, K. Hirose, R. Sinmyo, K. Shimizu, N. Sata, Y. Ohishi and A. Yasuhara: Science* ***320*** *(2008) 89.*
[2] T. Katsura *et al.*: Nature **395** (1998) 493.
[3] K. Ohta *et al.*: Proc. Jpn. Acad. Ser. B. **83** (2007) 97.
[4] J. Badro *et al.*: Science **305** (2004) 383.
[5] R. Holme: in The Core-Mantle Boundary Region, M. Gurnis, M.E. Wysession, E. Knittle, B.A. Buffett, Eds. (American Geophysical Union, Washington, DC, 1998), pp. 139.

Melting Experiments on Fe_3C and FeH_x under High Pressures

The structure of the Earth is divided into three layers, i.e., hydrosphere, the silicate crust and mantle, and the metallic core. The metallic core is further divided into the liquid outer core (2900–5150 km depth corresponding to 136–330 GPa) and solid inner core (5150–6400 km depth corresponding to 330–364 GPa). The temperature of the core has been discussed on the basis of the melting temperature of the core constituent. Because the liquid outer core freezes to form a solid inner core at the inner-outer core boundary (ICB), the temperature at ICB must correspond to the liquidus temperature of the core building material. It is generally assumed that the Earth's core consists mainly of iron. Seismological and experimental studies show that the Earth's outer core is approximately 10% less dense than molten iron under corresponding pressure and temperature conditions, implying that some light elements exist in the core (e.g., Ref. [1]). In the past 50 years after Birch's report, hydrogen, carbon, oxygen, silicon and sulphur are recognized as possible candidates of such light elements. Therefore, the melting temperatures of the iron-light element systems will provide important information to understand the thermal structure of the core. However, most studies on the temperature of the core have been performed in the Fe-S-O system (e.g., Ref. [2]). In this study, in order to evaluate the effects of hydrogen and carbon on the melting temperature of the core, we performed melting experiments on Fe_3C and FeH_x under high pressures at the SPring-8 synchrotron facility [3,4].

In situ X-ray diffraction (XRD) experiments were conducted using a Kawai-type multianvil SPEED-Mk.II installed at beamline **BL04B1**. The starting specimen was a pre-synthesized Fe_3C, which was mixed with MgO powder in order to avoid grain growth during heating. In order to prevent the effect of crystal grain growth, the multianvil apparatus was oscillated during X-ray diffraction measurements.

High-pressure experiments on Fe_3C were performed at 20 and 29 GPa. A series of XRD patterns during heating at 29 GPa is shown in Fig. 1. In the XRD sequences during the heating experiments, the peaks of orthorhombic Fe_3C disappeared, and new peaks identified as those of hexagonal Fe_7C_3 were observed with increases of background due to the presence of a melt. Finally, the Fe_7C_3 peaks disappeared, and only the halo pattern was observed.

In the experiments on FeH_x, a mixture of sponge-like iron and MgO powder in 2:3 atomic ratio was used as a starting material. The sample material was packed into a NaCl container with $LiAlH_4$, which was separated from the sample by a thin MgO disk. Hydrogen was supplied by the thermal decomposition of $LiAlH_4$. The experimental pressure range was 10-20 GPa.

During heating under high pressures, the hydrogenation of iron was observed from the volume change. The hydrogen concentration of FeH_x was estimated from the excess volume compared with that of pure Fe. It was found that FeH_x in the present study at pressures between 10 and 20 GPa are nearly stoichiometric $FeH_{x=1.0}$. The melting temperature of γ-FeH_x was determined from the abrupt change in the XRD patterns of crystal to liquid. The typical change in the XRD pattern due to melting of the sample is

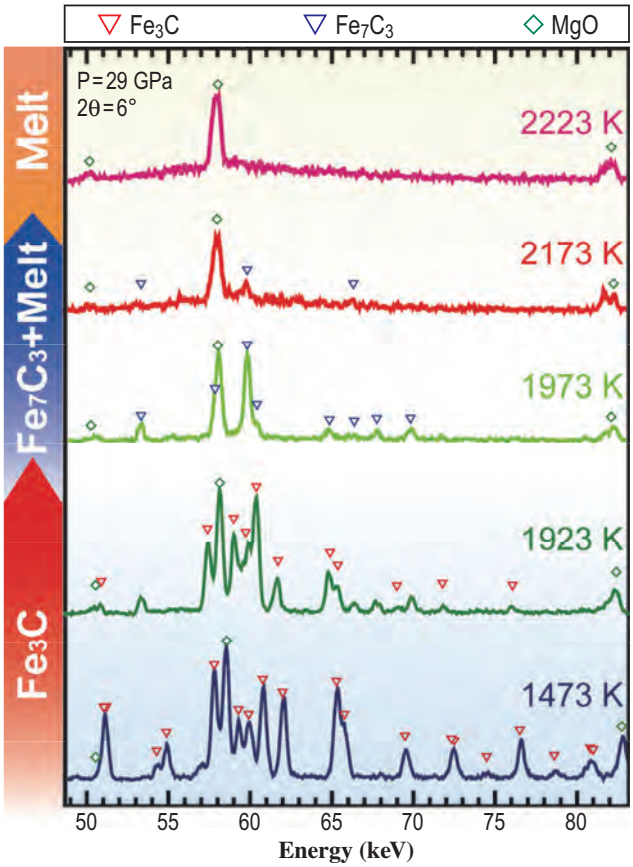


Fig. 1. Diffraction patterns of the Fe_3C during heating experiment at 29 GPa. Red inversed triangles, blue inversed triangles and green diamonds are the diffraction peaks of Fe_3C, Fe_7C_3 and MgO, respectively. During heating, Fe_3C melted incongruently to Fe_7C_3 plus melt between 1923 and 1973 K, and finally all the sample peaks except that of MgO disappeared at 2223 K.

shown in Fig. 2. At 11.5 GPa, the peaks of γ-FeH_x disappeared suddenly between 1423 and 1473 K. At the same time, the background increased due to the presence of a melt.

The phases observed in the Fe_3C and FeH_x experiments are shown in Fig. 3. Under the present experimental pressures, the melting temperatures of FeH_x and Fe_3C are significantly lower than that of pure Fe. The melting temperatures of FeH_x and Fe_3C are 1600 and 1850 K at 20 GPa, respectively, which are less than 2260 K at 20 GPa of Fe calculated by Anderson and Isaak [5] (Fig. 3). Our *in situ* XRD measurements show that hydrogen and carbon can lower the melting temperature of iron dramatically. Using the present observations and thermoelastic parameters for FeH_x [4] and Fe_3C [6], we extrapolated the melting curves for γ-FeH and Fe_3C obtained in our experiments to the core pressure. Those melting temperatures are estimated to be ~2600 and ~2800 K at the core-mantle boundary (CMB). In the present study, we have demonstrated that hydrogen and carbon have a profound effect in lowering the melting temperature of iron. The core temperature was previously proposed to be ~5000 K at ICB and ~4000 K at CMB on the basis of the melting experiments on the Fe-O-S system (e.g., Ref. [2]). If a large amount of hydrogen and/or carbon is present in the Earth's core, it is considered that the temperature of the outer core could be much lower than previous estimates.

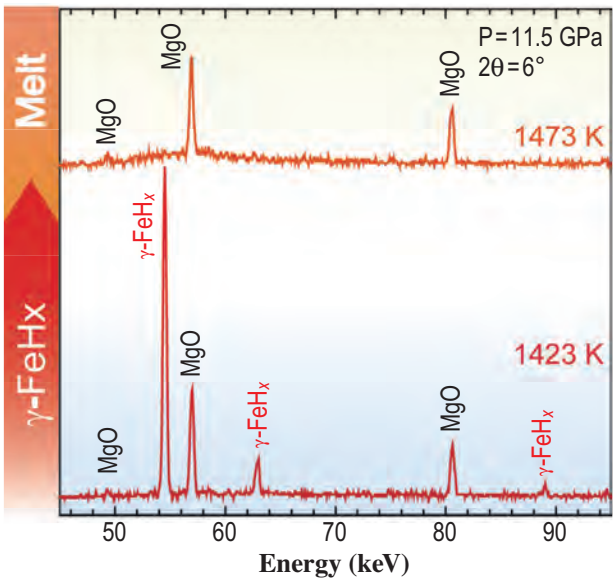


Fig. 2. Diffraction patterns of FeH_x during heating experiment at 11.5 GPa. The peaks of γ-FeH_x disappeared suddenly between 1423 and 1473 K, and a halo due to the presence of a melt was observed. At this pressure, the melting temperature of γ-FeH_x is located between 1423 and 1473 K.

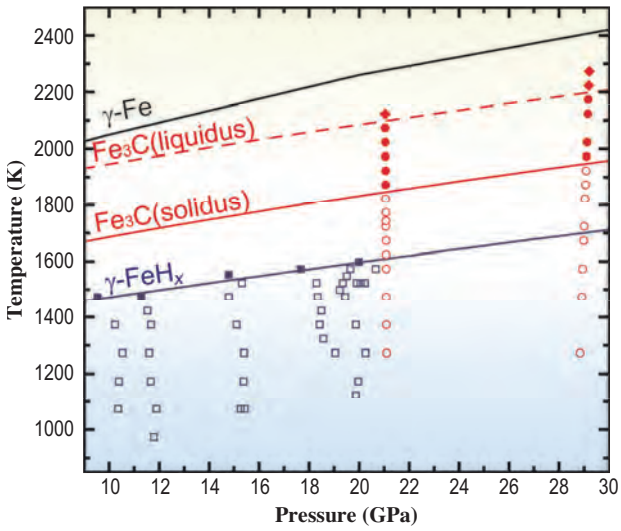


Fig. 3. Experimental results and melting curves for γ-FeH and Fe_3C. Open and solid squares are the γ-phase and melt of FeH, respectively. Open circles, solid circles and solid diamonds are solid Fe_3C, Fe_7C_3 + melt and melt, respectively. Melting curves for γ-FeH_x (blue line) and Fe_3C (red line) are determined in this study. The melting curve for γ-Fe (black line) is referred to Anderson and Isaak [5].

Yoichi Nakajima*, Koichi Sakamaki and Eiichi Takahashi

Department of Earth and Planetary Sciences,
Tokyo Institute of Technology

*E-mail: ynakajim@geo.titech.ac.jp

References

[1] F. Birch: J. Geophys. Res. **57** (1952) 227.
[2] R. Boehler: Annu. Rev. Earth Planet. Sci. **24** (1996) 15.
[3] *Y. Nakajima, E. Takahashi, T. Suzuki, K. Funakoshi: Phys. Earth Planet. Inter. **174** (2009) 202.*
[4] *K. Sakamaki, E. Takahashi, Y. Nakajima, Y. Nishihara, K. Funakoshi, Y. Fukai: Phys. Earth Planet. Inter. **174** (2009) 192.*
[5] O.L. Anderson and D.G. Isaak: Am. Miner. **85** (2000) 376.
[6] Y. Nakajima: Ph.D. thesis, Tokyo Inst. Technol., Tokyo (2009).

Oxygen *K*-edge X-Ray Raman Scattering Study of $MgSiO_3$ Glass at High Pressure

$MgSiO_3$-rich silicate melts can serve the model system for the primary components of the Hadean magma ocean, playing essential roles in the chemical differentiation of the early Earth. Silicate melts at the top of the transition zone and the core-mantle boundary have significant influences on the dynamics and properties of Earth's interior. Diverse macroscopic properties of silicate melts in Earth's interior, such as density and crystal-melt partitioning, depend on their short-range local structures at high pressures and temperatures. In spite of the essential roles of silicate melts in many geophysical and chemical problems, their nature under the conditions of Earth's interior including the densification mechanisms and the atomistic origins of the macroscopic properties at high pressures is not well understood. This is mostly because of their inherent structural disorder and the lack of suitable experimental probes of atomic structure of melts at high pressures.

Formation of tricluster (oxygen triply coordinated by framework cations, such as Al and Si) is known to be one of the dominant factors affecting the melt properties at high pressure. The presence of tricluster can account for the anomalous pressure-induced changes in viscosity and oxygen diffusivity and may significantly enhance the partitioning coefficient of an element between crystals and Mg-silicate melts in Earth's interior and probably explain the low solubility of noble gases in the melt at high pressure. The formation of five- and sixfolded silicon ($^{[5,6]}$Si) in the highly depolymerized $MgSiO_3$ glass is expected to be associated with the formation of the oxygen tricluster, considering similar densification behavior of Si with the fully polymerized silicates. However, experimental evidence for its formation in the silicate melts and glasses at high pressure is lacking. Synchrotron X-ray Raman scattering (also known as inelastic X-ray scattering) with diamond anvil cells (DACs) provides detailed information on the pressure-induced electronic bonding changes for low-z elements in amorphous oxides. Oxygen *K*-edge X-ray Raman scattering is currently the only available *in situ* experimental technique to directly reveal the pressure-induced electronic bonding changes around oxygen atoms in oxide glasses. We explore the local atomic structures of $MgSiO_3$ glass (as a precursor to Mg-silicate melts) using high-pressure X-ray Raman spectroscopy up to 39 GPa where high-pressure oxygen *K*-edge features suggest the formation of tricluster oxygens (oxygen coordinated with three Si frameworks; O) above 20 GPa [1].

While detailed experimental setups can be found in our recent report [1], $MgSiO_3$ glass was loaded into the sample chamber of a Be gasket in a DAC. The X-ray Raman spectra were collected at beamline **BL12XU** of the SPring-8, beamline 13ID-C of Geo Soil Enviro Consortium for Advanced Radiation Sources, and beamline 16ID-C of the High Pressure Collaborative Access Team of the Advanced Photon Source. Figure 1 presents the oxygen *K*-edge spectra of $MgSiO_3$ glass where a dominant feature at 538–539 eV shows negligible changes in the pressure range between 1 atm and approximately 12 GPa. Above 20 GPa, the spectra, however, shows a distinct feature at ~544–545 eV, wherein the spectral features gradually shift to higher energies with increasing pressure. The occurrence of the spectral feature near 545 eV at high pressures may stem from a variety of pressure-induced structural changes in the $MgSiO_3$ glass, such as the formation of the $^{[3]}$O tricluster, an increase in the Mg-O distance, reduction in NBO, and formation of oxygen linking $^{[4]}$Si and highly coordinated silicon, such as $^{[4]}$Si–O–$^{[5,6]}$Si and $^{[6]}$Si–O–$^{[6]}$Si. By comparing these features with those for the known crystalline $MgSiO_3$ and SiO_2 polymorphs with varying oxygen configurations and topology (i.e., bond angle and length), most of the features relevant to the local oxygen configurations observed for the crystalline phases at high pressure, including both the specific bond angles, length effect of crystals, edge-sharing oxygen (537 and 541 eV), and $^{[6]}$Si–O–$^{[6]}$Si (543 eV), cannot explain the significant changes observed for the glasses at high pressures. In particular, pressure-induced changes in the Mg–O distance or the formation of $^{[4]}$Si–O–$^{[5,6]}$Si because of the reduction in NBO can only partially contribute to the occurrence of the spectral features at 545 eV. We suggest that the feature at 545 eV in the $MgSiO_3$ glass at pressures above 20 GPa corresponds to the formation of the triply coordinated oxygen and changes in the short- to medium-range structures that are associated with the formation of the triply coordinated oxygen (i.e., formation of a three-member ring, an increase in bond length, and a decrease in bond angle). The schematic atomic configuration for the oxygen triclusters is also shown in the inset of Fig. 1.

The current results suggest the formation of the oxygen triclusters and associated changes in the

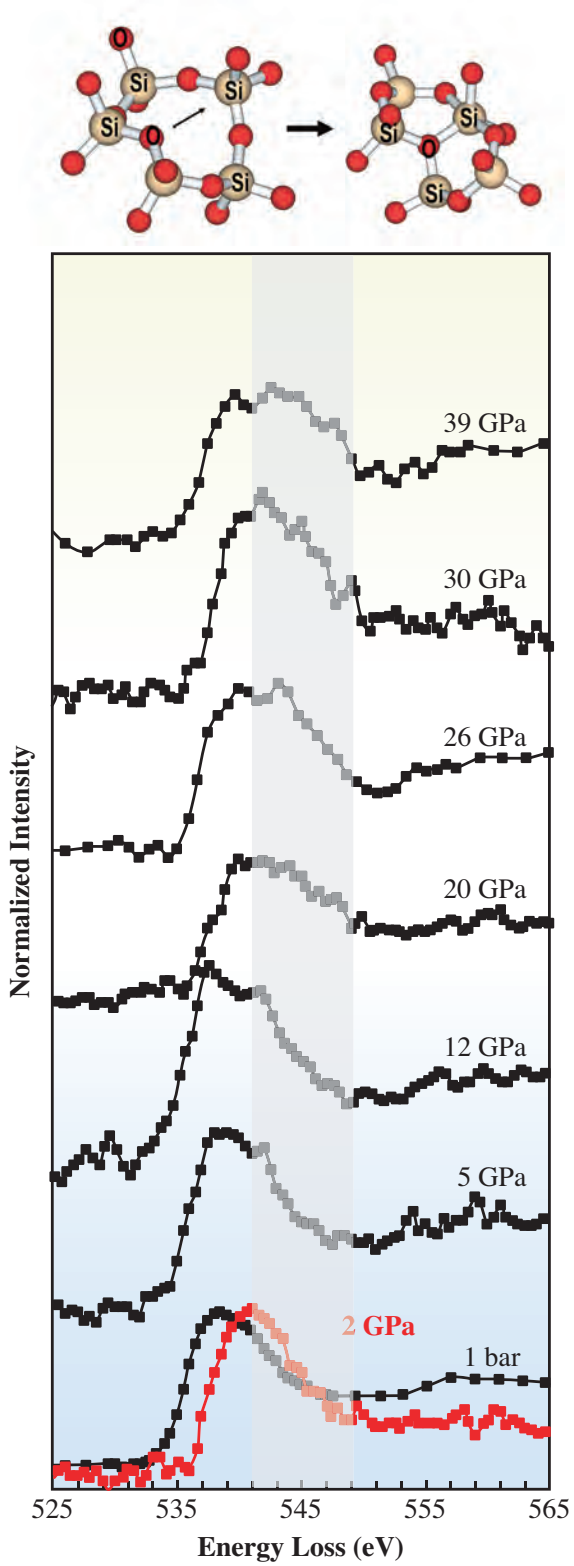


Fig. 1. Oxygen *K*-edge X-ray Raman spectra for $MgSiO_3$ glasses at high pressures [plotted as energy loss (incident energy−elastic energy) *vs.* normalized scattered intensity]. Grey area represents energy range from 543 eV to 551 eV. The schematic mechanism for the formation of the oxygen tricluster is also shown on top of the spectra. Red and yellow spheres refer to oxygen and silicon atoms, respectively.

atomic configuration in short-to-medium range in the $MgSiO_3$ glass at high pressure. These pressure-induced densification certainly affects the thermodynamic (e.g., density, molar volume, and crystal-melt partitioning) and transport properties of silicate melts (e.g., viscosity and diffusivity) in the Earth's interior. The formation of oxygen triclusters can be an efficient densification mechanism in the $MgSiO_3$ melt and may explain the atomistic origin of the high-density Mg-silicate melts at the core-mantle boundary [2,3]. As Changes in the local electronic structure and composition of silicate melts are believed to promote the partitioning of elements between crystalline phases and melts in the Earth's mantle [4,5]. The increase in the fraction of the oxygen triclusters with smaller member rings results in a reduced free volume needed to host elements that are more incompatible. That is, the triclustered oxygens increase the crystal-melt partitioning coefficient of elements, such as radioactive nuclides.

Sung Keun Lee

School of Earth and Environmental Sciences,
Seoul National University, Korea

E-mail: sungklee@snu.ac.kr

References

[1] *S.K. Lee, J.-F. Lin, Y.Q. Cai, N. Hiraoka, P.J. Eng, T. Okuchi, H.-k. Mao, Y. Meng, M.Y. Hu, P.Chow, J. Shu, B. Li, H. Fukui, B.H. Lee, H.N. Kim and C.-S. Yoo: PNAS* ***105*** *(2008) 7925.*
[2] J.A. Akins *et al.*: Geophys. Res. Lett. **31** (2004) L14612.
[3] Q. Williams and E.J. Garnero: Science **273** (1996) 1528.
[4] S.K. Lee *et al.*: Geochim. Cosmochim. Acta **68** (2004) 4189.
[5] V.R. Murthy *et al.*: Nature **423** (2003) 163.

Environmental



SCIENCE

This section covers the various research fields, such as environmental problems and technology, geochemistry and environmental enhancement, that use newly developed functional materials. Not only the development of high-performance materials but also the solution of environmental problems requires the understanding of the mechanisms of phenomena at the atomic level using synchrotron radiation X-rays. Most actual environmental samples and materials have amorphous structures. Thus, the X-ray absorption fine structure (XAFS) method is an indispensable tool for studying them as shown in topics selected in this section.

In the first topic, Hokura *et al*. showed the chemical state of Cd at specific positions in a two-dimensional cellular distribution in hyperaccumulating plant tissues determined using a high-energy μ-XAFS technique. This technique is powerful for obtaining information on the distribution and chemical state of heavy elements.

The second topic concerns the geochemistry of toxic elements. Takahashi studied the chemical states of Te and Se in various solid-water systems on the earth' s surface by the XAFS method, and identified the origin of the large difference in their abundances in marine ferromanganese oxides relative to those in seawater.

The third and fourth topics are photocatalysts to be used for environmentally friendly chemical processes, such as the oxidative decomposition of pollutants and low-temperature NO_x reduction from the exhaust gas. Teramura *et al*. directly showed the formation of Rh particles on a TiO_2 photocatalyst under photoirradiation for the first time by an *in situ* time-resolved energy-dispersive XAFS method. Yamazoe *et al.* developed a new structural analysis method that can estimate the structure of the WO_x unit easily from the XANES spectra at the W L_1-edge and L_3-edge. They applied this method to the estimation of the structure of W oxide species loaded on TiO_2. These studies are leading to the development of more effective photocatalysts.

Tomoya Uruga

Micro X-Ray Fluorescence Imaging and Micro X-Ray Absorption Spectroscopy of Cadmium Hyperaccumulating Plant, *Arabidopsis halleri* ssp. *gemmifera*, using High-Energy Synchrotron Radiation

Arabidopsis halleri grows in Europe and is known to contain more than 10,000 mg kg^{-1} of cadmium and zinc in its shoot [1,2]. This *A. halleri* trait has the potential to be exploited in phytoremediation, a soft method in which plants are used for the cleanup of heavy metal-polluted soils. A Japanese native subspecies of this plant, *Arabidopsis halleri* ssp. *gemmifera* of which an old scientific name is *Arabis gemmifera*, is also known as a cadmium and zinc hyperaccumulator [3]. Since Cd is a highly toxic metal for plants, it is interesting to reveal the mechanism involved in the Cd accumulation of this plant.

The objectives of the present study is to determine the distribution of Cd in the leaves of *A. halleri* ssp. *gemmifera* and also to determine the chemical form of Cd accumulated in the trichomes [4]. The distribution of Cd in the leaves and trichomes was investigated by μ-XRF analysis with the Kirkpatrick-Baez (K-B) mirror. The chemical form of Cd was then studied by Cd *K*-edge (26.7 keV) μ-XANES analysis.

A. halleri ssp. *gemmifera* (Fig. 1) was used in the present study. The plants were cultivated in a nutrient solution of 20 μM Cd. Analytical grade $Cd(NO_3)_2 \cdot 4H_2O$ was used. To reveal the chemical form of Cd in a living plant, the sample with minimal preparation was required for the μ-XANES analysis. Therefore, a thin freeze-dried section of the sample was prepared in order to maintain its tissue structure and chemical state.

The μ-XRF and Cd *K*-edge μ-XANES measurements of the plant leaves were performed using beamline **BL37XU** operated at 8 GeV and *ca*. 100 mA. The X-rays from an undulator were monochromatized by a Si(111) double-crystal monochromator to 37 keV in order to excite the K-lines of cadmium. The beam was focused to a spot size of 3.8 μm (horizontal, H) × 1.3 μm (vertical, V) using a pair of elliptical mirrors in the K-B configuration. The sample on the acryl board was mounted on an x-y translation stage. Fluorescence X-rays were measured using a Si(Li)-SSD in air at room temperature. Cd *K*-edge μ-XANES spectra were measured at the accumulating points of Cd, which were revealed by μ-XRF imaging, in the fluorescence mode. A monochromator stabilization (MOSTAB) system [5] was used to stabilize the X-ray beam position. The XANES spectra of the cadmium sulfate (CdS), cadmium oxide (CdO), cadmium acetate (AcCd), hexakis(imidazole)cadmium(II) nitrate ($(Im)_6Cd(NO_3)_2$), phytochelatin-Cd (PC-Cd) and metallothionein-Cd (MT-Cd) were measured as references.



Fig. 1. Cadmium hyper-accumulating plant, *A. halleri* ssp. *gemmifera*.

The cellular distributions of Cd, Zn, Mn and Ca present in the trichomes were successfully revealed for the first time. The distributions of Cd and Zn are shown in Fig. 2 together with a photograph taken by a digital microscope. High accumulations of Cd, Zn and Mn were found at the base of the trichomes. There is a strong positive correlation between the XRF intensities of Cd and Zn ($r^2 = 0.8674$, $n = 438$, where r and n are the correlation factor and number of data, respectively). In contrast, Ca was highly enriched in the upper part of the trichomes, particularly at the tip, while little was found in the base of the trichomes where Cd highly accumulated. Cd and Zn accumulated in a ring shape at the border between the upper and lower parts of the trichomes. These results indicate that a striking subcellular compartmentalization of Cd and Zn occurs in the vacuole of the trichomes, and this compartmentalization plays an important role in the hyperaccumulating process of this plant.

The Cd *K*-edge μ-XANES spectrum of the plant was successfully measured for the first time by utilizing the K-B mirror for high-energy X-ray focusing and the MOSTAB system. The Cd *K*-edge μ-XANES spectra of the trichomes and reference materials are shown in Fig. 3. The spectrum of reference samples above the absorption edge (26.72–26.76 keV) shows a characteristic difference in shape between Cd with the S ligand and that with the O/N ligand. Thus, the spectrum of Cd with the S ligand (CdS, PC-Cd, MT-Cd) can be distinguished from those of Cd with the O ligand (CdO, $Cd(NO_3)_2$aq, AcCd) and the N ligand ($(Im)_6Cd(NO_3)_2$). The Cd *K*-edge spectra

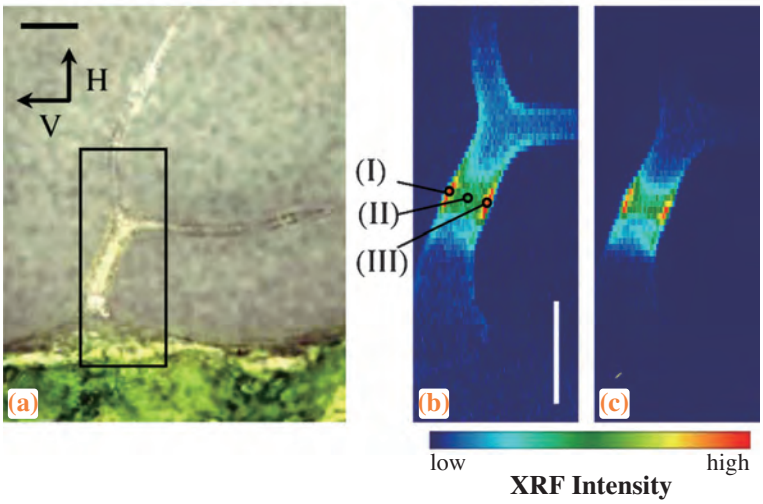


Fig. 2. μ-XRF imaging of trichomes. **(a)** photograph of measured samples showing imaging area, **(b)** Cd, and **(c)** Zn. For the maps, an imaging area of 204 μm (H)×81 μm (V), a beam size of 3.8 μm (H)×1.3 μm (V), a step size of 3 μm (H)×1 μm (V), and a dwell time of 0.3 s/point were used. (I)-(III) show measurement points of Cd μ-XANES. The scale bar is 50 μm [4].

of points (I), (II), and (III) (Fig. 2(b)) in the trichomes are shown in Figs. 3(a)–3(c). It was found that these spectra are similar in shape to those of Cd with the O or N ligand. Therefore, in these specialized cells, the μ-XANES results showed that the majority of Cd exists as a divalent state and binds to the O or N ligand, not the S ligand.

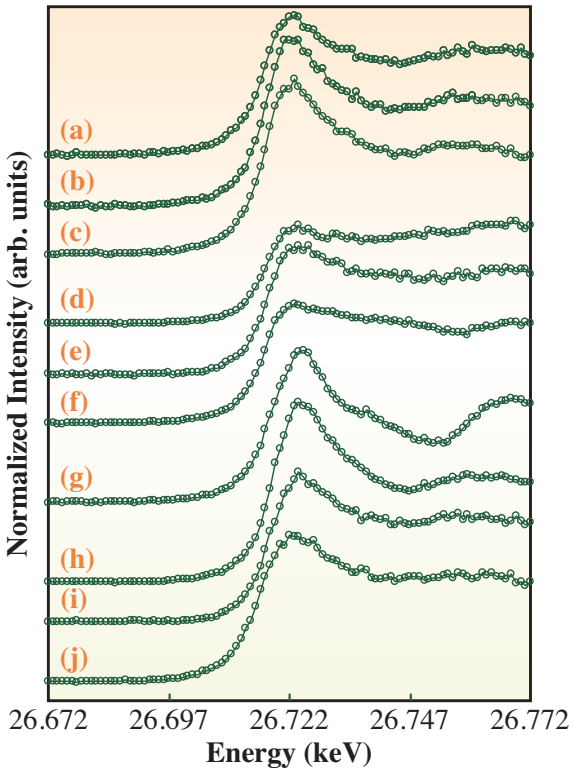


Fig. 3. Cadmium *K*-edge μ-XANES spectra measured at points in Fig. 2 and reference compounds. **(a)** Point I, **(b)** point II, **(c)** point III, **(d)** PC-Cd, **(e)** MT-Cd, **(f)** CdS, **(g)** CdO, **(h)** $Cd(NO_3)_2aq$, **(i)** AcCd and **(j)** $(Im)_6Cd(NO_3)_2$. Beam size: 3.8 μm×1.3 μm, energy step: 1 eV, and dwell time: 1 – 4 s/point [4].

This study has demonstrated the performance of Cd *K*-edge μ-XANES spectroscopy, which was applied here for the first time to plant samples. The combination of μ-XRF and μ-XANES has proved to be an indispensable tool for the study of Cd accumulation in biological samples on a cellular scale. In future research, we will investigate changes in the distribution and chemical form of Cd through the transportation process of Cd.

A. Hokura[a,†], N. Kitajima[b], Y. Terada[c] and I. Nakai[a,*]

[a] Department of Applied Chemistry, Tokyo University of Science
[b] Fujita Co.
[c] SPring-8/JASRI

*E-mail: inakai@rs.kagu.tus.ac.jp

† Present address: Waseda Institute for Advanced Study, Waseda University

References

[1] H. Küpper *et al.*: Planta **212** (2000) 75.
[2] M.P. Isaure *et al.*: Spectrochim. Acta, Part B **61** (2006) 1242.
[3] H. Kubota and C. Takenaka: Int. J. Phytoremediation **5** (2003) 197.
[4] *N. Fukuda, A. Hokura, N. Kitajima, Y. Terada, H. Saito, T. Abe, I. Nakai: J. Anal. At. Spectrom. **23** (2008) 1068.*
[5] T.P. Kudo *et al.*: J. Jpn. Soc. Synchrotron Rad. Res. **16** (2003) 39.

Origin of Difference in Solubility between Tellurium and Selenium into Water at Earth's Surface

Although both tellurium (Te) and selenium (Se) are found in relatively low abundance in the crust, it is possible that the high toxicities of these elements can induce environmental problems. For example, Se contamination has been found in soils, groundwater, and surface waters, which has triggered many studies on the environmental geochemistry of Se. There has been much less studies on Te due to its even lesser quantities in the crust, but Te contamination has also been found in areas associated with mine tailings. Irrespective of the possible problems related to the environment, however, the details of Te behavior in a soil-water system are still unknown. Thus, the comparison of the environmental behavior of Te with that of Se belonging to the same group in the periodic table is important in environmental geochemistry. In addition, it is expected that such comparison will shed light on the differences in their chemical properties, which may help us understand the solubilities of Se and Te in water. Such consideration can be linked to the distribution coefficient of Se between water and ferromanganese oxides in a marine system, which is much larger than that of Te by a factor of 10^5 despite their similar chemical nature.

Among various solid-water systems on earth's surface, the present study [1] focuses on the distributions of Te and Se in a soil-water system, and their speciation in both soil and water phases, which enables us to understand their distribution behaviors on the atomic scale. The samples examined were prepared by the addition of Se(IV), Se(VI), Te(IV), or Te(VI) in synthetic soil-water systems at various soil-water ratios [2]. We conducted an X-ray absorption fine structure analysis (XAFS; experiments were conducted at **BL01B1**) to determine directly the Te and Se species (oxidation state and host phase) in the soil phase, while a high-performance liquid chromatography system connected to ICP-MS (HPLC-ICP-MS) was used to determine the oxidation states of Se and Te in water.

Among these analyses, we conducted an extended X-ray absorption fine structure analysis (EXAFS) to obtain information on the local structures of Se and Te in soil samples. Figure 1 shows the radial structural function (RSF) for EXAFS spectra of Se in the reference materials and soil samples when added as Se(IV) and Se(VI) into a soil-water system. For the sample added with Se(IV), two peaks were observed at 1.25 and 3.10 Å (Fig. 1(a); phase shift uncorrected). These peaks were also found in the RSF of Se(IV) sorbed on ferrihydrite (reference sample; Fig. 1(b)) and correspond to the Se-O and Se-Fe shells, respectively. The similarity of the two RSFs shows that Se(IV) in soils is sorbed on the Fe(III) hydroxide phase. In particular, the presence of Fe in the second shell indicates that Se(IV) forms inner-sphere complexes at the surface of Fe(III) hydroxide. In contrast, the RSF of the sample added with Se(VI) did not exhibit a prominent peak for the Se-Fe shell (Fig. 1(c)), which was almost identical to that of Se(VI) sorbed on ferrihydrite (Fig. 1(d)). The absence of a peak for the Se-Fe shell suggests that an outer-sphere surface complex of selenate is formed at the surface of Fe(III) hydroxide. For Te(IV) and Te(VI), prominent peaks that can be ascribed to the Te-Fe shell were found near 3.20 and 2.70 Å (phase shift uncorrected) in the RSFs of Te(IV) and Te(VI), respectively. The presence of Fe in the second shell showed that both Te(IV) and Te(VI) formed inner-sphere surface complexes at the surface of Fe(III) hydroxide.

The EXAFS analyses showed that the outer-sphere complex is important for the Se(VI) sorbed on Fe(III) hydroxide in soils, while Se(IV), Te(IV), and Te(VI) form inner-sphere complexes. This structural information, in turn, is closely related to the solubilities of the elements in water. In terms of the distribution between soil and water, the Se distribution in water was much higher than that of Te under wide redox

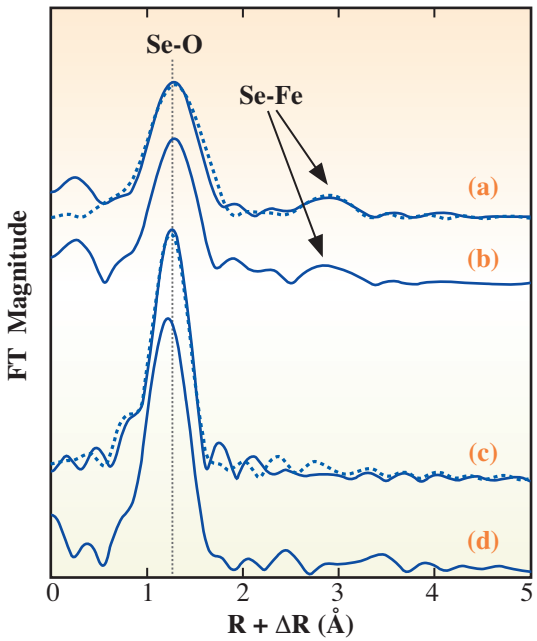


Fig. 1. Radial structural functions of Se(IV) species sorbed on **(a)** ferrihydrite (iron hydroxide) and **(b)** soil, and Se(VI) species sorbed on **(c)** ferrihydrite and **(d)** soil.

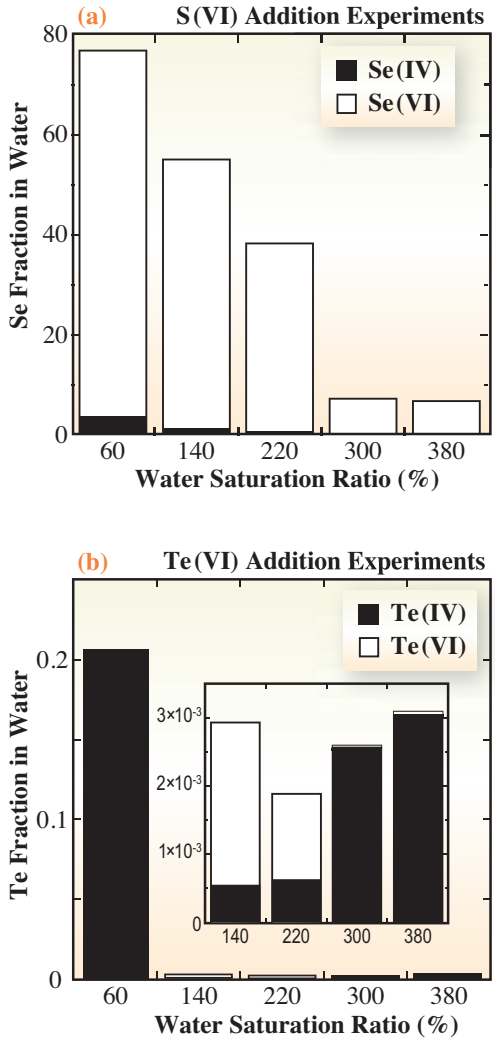


Fig. 2. Dissolved fraction of **(a)** Se and **(b)** Te in water in distribution experiments of Se and Te in soil-water system. Initial concentrations of Se and Te were 150 mg/kg in the system. The horizontal axis indicates the volume ratio of water to soil. When the ratio was large, Eh decreased (= more reducing) owing to the small content of oxygen dissolved in water.

conditions (Fig. 2). For Se, selenate is the predominant species in water even under reducing condition due to the much higher solubility of Se(VI) than Se(IV). Furthermore, the much smaller distribution of Te in water was primarily due to the larger affinities of Te(IV) and Te(VI) to Fe(III) hydroxide than Se(VI), which originates from the formation of the inner-sphere complexes of Te(IV) and Te(VI) at the surface of Fe(III) hydroxide.

This difference can be finally ascribed to the stability of the oxyanion of Se(VI) compared with those of Se(IV), Te(IV), and Te(VI). Based on the effective ionic radius at sixfold coordination (r/Å), the ionic potential (IP;=z/r; z: charge of the ion) of Se^{6+} was 14.3 $Å^{-1}$, which is much larger than those of Se^{4+} (8. 0 $Å^{-1}$), Te^{4+} (4.1 $Å^{-1}$), and Te^{6+} (10.7 $Å^{-1}$). The ion with a larger IP forms stable oxyanions, which may not form an inner-sphere complex at the surface of Fe(III) hydroxide without the bonding of Se-O-Fe or Te-O-Fe.

Finally, the difference between Se and Te found in this study can be used to explain the large difference in abundance between Se and Te in marine ferromanganese oxides relative to those in seawater (Fig. 3). The enrichment factor of Te in ferromanganese crusts relative to the mean abundance in seawater is larger than that of Se by more than four orders of magnitude. This is most likely due to the formation of outer- and inner-sphere complexes of Se and Te, respectively, when reacted with the ferromanganese oxides. The high stability of Se(VI) oxyanions induces a large Se abundance in seawater, which is not the case for Te(IV) and Te(VI) that prefer to form hydroxides rather than oxyanions.

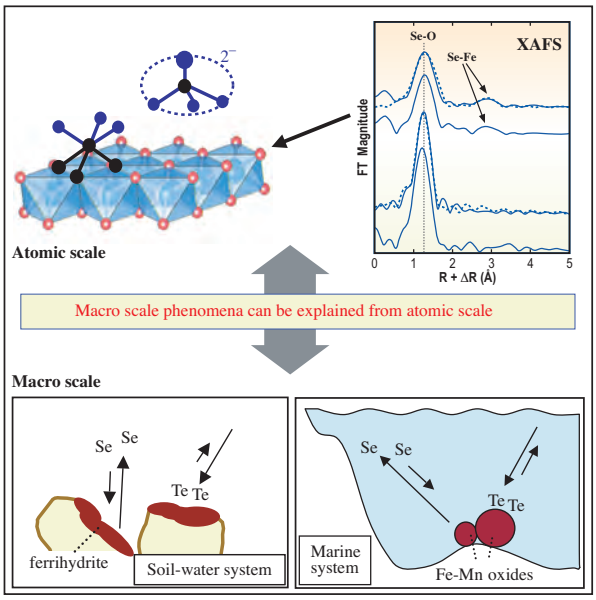


Fig. 3. Schematic showing that difference between solid-water distributions of Se and Te in soil-water and marine systems may be caused by difference between structures of Se and Te species sorbed on ferrihydrite (outer- or inner-sphere complex). Understanding the interactions of metal ions and solid on the atomic scale reveals the macroscopic phenomena observed at earth's surface.

Yoshio Takahashi

Department of Earth and Planetary Systems Science, Hiroshima University

E-mail: ytakaha@hiroshima-u.ac.jp

References

[1] *T. Harada and Y. Takahashi: Geochim. Cosmochim. Acta 72 (2008) 1281.*
[2] Y. Takahashi *et al.*: Environ. Sci. Technol. **38** (2004) 1038.

Snapshots of Metal Nanoparticles Generated on TiO_2 Photocatalyst: *In Situ* Time-Resolved Energy-Dispersive X-Ray Absorption Fine Structure Analysis

A photocatalytic system qualifies as a candidate for an environmentally friendly chemical process under ambient condition using solar light. It is well known to utilize a TiO_2 photocatalyst for the oxidative decomposition of pollutants and poisonous and hazardous organic compounds. Since 1970s, a noble metal was often loaded onto a TiO_2 photocatalyst as a modifier to enhance photocatalytic activity. The photodeposition method enables the easy to loading of various metal species as cocatalysts on semiconductor photocatalysts because the introduction of a photocatalyst and a metal precursor into an aqueous solution involving alcohol as a sacrificial reagent and the illumination of this suspension with a light source. Time-resolved energy-dispersive XAFS (DXAFS) [1,2] analysis is an up-to-date method for rapidly observing the structural changes of various materials *in situ*. Recently, some groups have reported DXAFS studies on kinetics and dynamics of catalysis with several synchrotron radiation sources in the world. However, the DXAFS analysis has not been applied applies to photocatalytic reactions involving photodeposition, although several *ex situ* and *in situ* XAFS studies on the photocatalytic reactions were reported. In this study, we inve+stigated the formation of Rh particles on a TiO_2 photocatalyst under photoirradiation by *in situ* DXAFS analysis at beamline **BL28B2** [3].

The photocatalyst used in this study was the anatase phase of TiO_2 calcined in a furnace in air at 673 K for 3 h before photodeposition. The photodeposition of Rh metal particles onto a TiO_2 photocatalyst was carried out in a closed batch system. 0.5 g of TiO_2, 0.8 ml of $RhCl_3 \cdot 3H_2O$ solution (0.095 mol/L) and 3.2 ml of alcohol were introduced into the reactor made of Pyrex® glass with a flat glass ceiling window for illumination after Ar bubbling for 10 min. The amount of residual Rh ions in the filtrate was determined using a sequential inductively coupled plasma (ICP) spectrometer. Rh *K*-edge (around 23.2 keV) X-ray absorption fine structure (XAFS) measurements were performed at beamline BL28B2. The main equipment used for DXAFS spectroscopy at beamline BL28B2 in this study consists of a polychromator, which is set to a Laue configuration with net plane Si(422), and a position-sensitive detector (PSD), which is mounted on a $\theta-2\theta$ diffractometer, as shown in Fig. 1. The exposure time of the PSD was 267 msec per shot. 50 snapshot spectra were accumulated to obtain one spectrum; therefore, we observed a spectral variation every 13.35 s in this study.

Figure 2 shows a series of Rh *K*-edge X-ray absorption near edge structure (XANES) spectra for the Rh species in the presence of TiO_2 as a photocatalyst and methanol as a sacrificial reagent under photoirradiation and references, $RhCl_3$ in solution as a precursor and Rh foil. The XANES spectra obtained before and after photoirradiation were consistent with those of the $RhCl_3$ solution and Rh foil as references, respectively. The energy position of the absorption edge consecutively shifted to a low-energy side with an increasing in time for photoirradiation. Accordingly, the evolved electron under photoirradiation was trapped by the Rh trivalent ions adsorbed on the surface and the Rh metal particles deposited on the TiO_2 photocatalyst. In addition, a series of XANES spectra exhibited isosbestic points showing that the transient state between a Rh metal particle and a Rh^{3+} ion cannot be captured in the measurement if any, and we can consider that the spectra consist of simply overlapping spectra of Rh^0 and Rh^{3+}.

Figure 3 shows a series of Fourier transforms (FT) for k^3-weighted Rh *K*-edge EXAFS spectra of the sample shown in Fig. 2 under photoirradiation. Fourier transformation was performed without phase shift correction. The first shell peak located at 1.73 Å disappeared after photoirradiation and an alternative peak appeared at 2.45 Å. This peak is assigned to the Rh-Rh bond of Rh metal, in comparison with the FT spectrum of the Rh foil as a reference. The peak height linearly increased with photoirradiation time

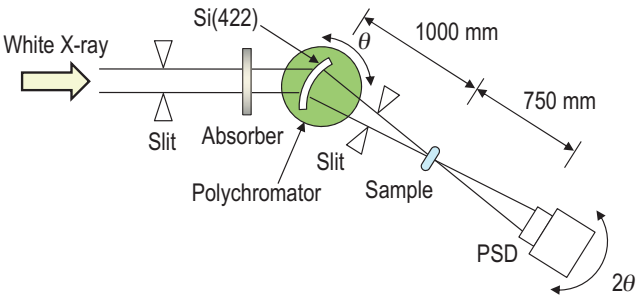


Fig. 1. Schematic view of DXAFS spectrometer for Laue geometry with net plane Si(442).

and saturated after 90 min. This is possibly due to the consumption of all Rh ions in the aqueous solution or the inhibition of Rh metal particle formation. The residual Rh trivalent ions in the filtrate were determined by ICP analysis. There were no ions in the solution in the case of methanol above 90 min of photoirradiation. The amounts of residual Rh trivalent ions linearly decreased with the increasing in photoirradiation time. Accordingly, the formation rate of the Rh metal particles on the irradiated TiO_2 was compatible to the diminution rate of the Rh trivalent ions.

We observed the photodeposition of Rh metal particles onto a TiO_2 photocatalyst from an aqueous solution $RhCl_3$ as a precursor and alcohol as a sacrificial reagent by *in situ* DXAFS analysis. The Rh trivalent ions are adsorbed on the surface of the TiO_2 photocatalyst, followed by reduction to the Rh metal particles by electron acceptance. The formation rate of the Rh metal particles on the irradiated TiO_2 was closely related to the diminution rate of the Rh trivalent ions. The coordination number of the Rh-Rh bond stopped after 90 min of photoirradiation in the presence of methanol as a sacrificial reagent, suggesting the formation of fine Rh metal particles on TiO_2.

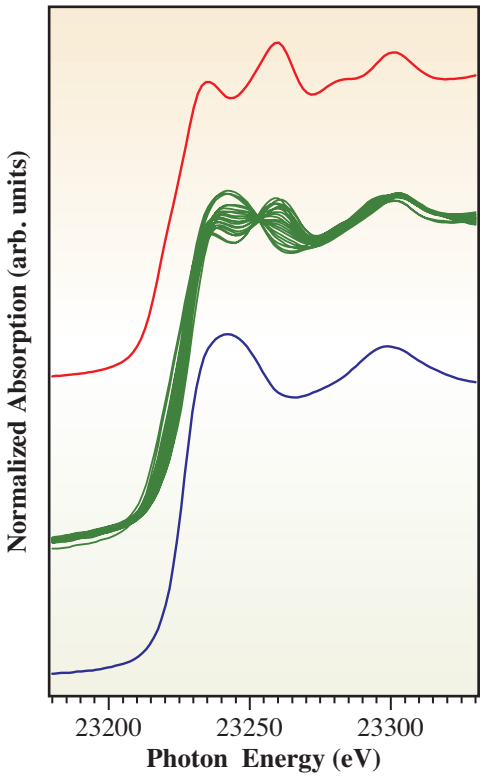


Fig. 2. Series of Rh *K*-edge X-ray absorption near edge structure spectra for Rh species in TiO_2 as photocatalyst and methanol as sacrificial reagent under photoirradiation (green lines) and references, $RhCl_3$ in solution as precursor (blue line) and Rh foil (red line).

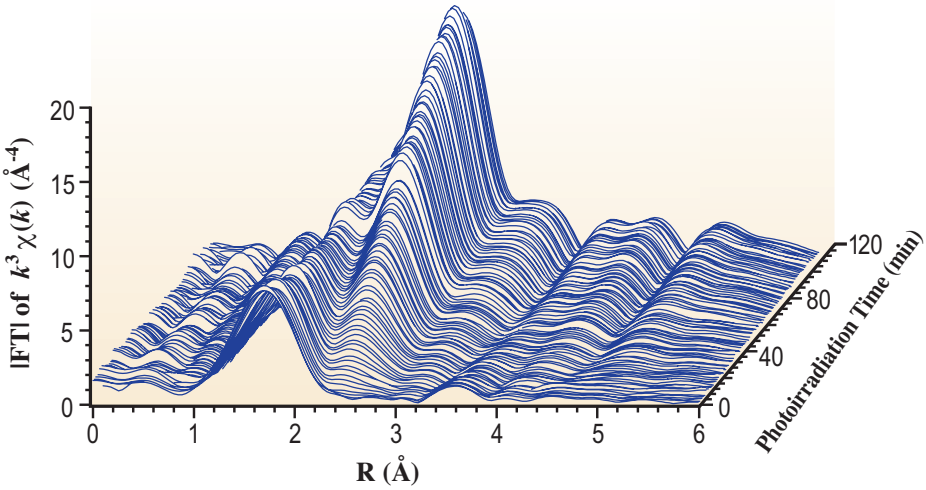


Fig. 3. Series of Fourier transforms (FT) for k^3-weighted Rh *K*-edge EXAFS spectra of sample shown in Fig. 2 under photoirradiation.

Kentaro Teramura[a,*] and Tsunehiro Tanaka[b]

[a] Kyoto University Pioneering Research Unit for Next Generation, Kyoto University
[b] Department of Molecular Engineering, Kyoto University

*E-mail: kentaro.teramura@ kupru.iae.kyoto-u.ac.jp

References

[1] T. Matsushita and R.P. Phizackerley: Jpn. J. Appl. Phys. **20** (1981) 2223.
[2] U. Kaminaga *et al.*: Jpn. J. Appl. Phys. **20** (1981) L355.
[3] *K. Teramura, S. Okuoka, S. Yamazoe, K. Kato, T. Shishido and T. Tanaka: J. Phys. Chem. C* ***112*** *(2008) 8495.*

XAFS Study of Tungsten L_1- , L_3- Edges: Structural Analysis of Loaded Tungsten Oxide Species

A realization of low-temperature NO*x* reduction from an exhaust gas at stationary emission sources, such as factories, boilers, power stations and incinerators, is strongly desired. In addition, some ammonia slips from factories and pig and poultry farms are serious problems from an environmental viewpoint. We found that a TiO_2-based photocatalyst is effective for the abatement of NO (photo-SCR) and the removal of NH_3 (photo-SCO), and that the loading of tungsten (W) oxide species on TiO_2 promotes photocatalyses [1,2]. Not only the loading amount but also the local structure of W oxide species affects the activities. A conventional XAFS analytical method could give us only a vague result for the structure of the loaded W oxide species.

W L_1- and L_3-edge X-ray absorptions have often been used to provide information on the local symmetry, coordination and valence of W oxide species loaded on supports [3]. The valence of the W oxide species is determined by the position of the W L_1-edge. The local symmetry is determined by the area of the pre-edge peak in W L_1-edge XANES. The coordination number and bond distance of the W oxide species are estimated by the analysis of W L_3-edge EXAFS. However, the study of W L_3-edge XANES is limited.

The white line appearing in the L_3-edge XANES of transition metals is mainly attributed to electronic transitions from $2p_{3/2}$ orbitals to vacant *d* orbitals. In the case of Mo L_3-edge X-ray absorption, two white lines are observed in the XANES. The splitting and areas of the two white lines depend on the symmetry of the MoO*x* ($x = 4$, 5, 6) unit because these correspond to the ligand field splitting of the *d* orbitals [4]. Therefore, it is expected that W L_3-edge XANES will reveal the characteristics of the 5*d* orbitals in a manner similar to that of Mo L_3-edge XANES. However, no such relationship between W L_3-edge XANES and the structure has been described. This is because the white line is not distinctly split as is the case for Mo [5].

In the present study, we recorded the W L_1- and L_3-edge X-ray absorption spectra of reference samples, whose structures are already known, at beamline **BL01B1** in a transmission mode. We analyzed the W L_3-edge XANES carefully to clarify the relationship between the splitting of the W L_3-edge white line and the structure of the WO*x* unit. Additionally, we found that the structure of the WO*x* unit can be estimated from the splitting of the W L_3-edge white line and the pre-edge peak area of the W L_1-edge XANES. This new structural analysis method can also easily estimate the structure of the W^{6+} oxide loaded on TiO_2.

Figure 1(A) shows the W L_3-edge XANES spectra of reference samples with the W^{6+} ion. Cr_2WO_6 and Ba_2NiWO_6, which have D_2 and *Oh* symmetries, give two peaks in the white line. On the other hand, WO_3, $H_3PW_{12}O_{40}$, and $(NH_4)_{10}W_{12}O_{41}{\cdot}5H_2O$ samples, which have a distorted WO_6 unit, and $Sc_2W_3O_{12}$ and Na_2WO_4, which respectively have nearly *Td* and *Td* symmetries, exhibit only one peak. However, the second derivatives of the W L_3-edge white line clarify that the white line consists of two peaks ($Sc_2W_3O_{12}$ and Na_2WO_4 give a large peak with a shoulder peak at a low energy), as shown in Fig. 1(B). In general, 5*d* orbitals of the octahedral (tetrahedral) WO_6 (WO_4) unit are split into e_g and t_{2g} (*e* and t_g) orbitals by a ligand field. The poorer the symmetry of WO_6 (WO_4) from *Oh* (*Td*), the smaller (larger) the energy gap of the split 5*d* orbitals. Additionally, the energy gap for the WO_4 unit is smaller than that for the WO_6 unit. Therefore, the energy gap of the two peaks in Fig. 1(B) reflects the splitting of 5*d* orbitals by the ligand field. Additionally, we carried out the deconvolution of the W L_3-edge XANES spectra. All spectra were fitted with two Lorentz functions, whose top positions were determined on the basis of the values of the two peaks in Fig. 1(B), and an arctangent function. Figure 2 shows the results of the deconvolution of WO_3 and Na_2WO_4, as examples. The ratio of the areas under the two peaks (peak 1: peak 2; peak 1 appears at a lower energy than peak 2) for the samples with the WO_6 unit was about 3:2, whereas that for the sample with the WO_4 unit was about 2:3. For the WO_6 (WO_4) unit, the t_{2g} (*e*) orbital appears at a

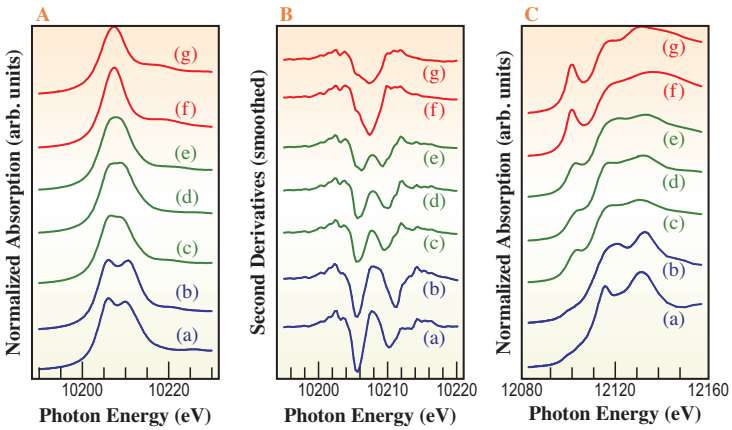


Fig. 1. **(A)** W L_3-edge XANES spectra, **(B)** second derivatives of **(A)**, and **(C)** W L_1-edge XANES spectra of (a) Ba_2NiWO_6, (b) Cr_2WO_6, (c) $(NH_4)_{10}W_{12}O_{41}{\cdot}5H_2O$, (d) WO_3, (e) $H_3PW_{12}O_{40}{\cdot}13H_2O$, (f) $Sc_2W_3O_{12}$ and (g) Na_2WO_4.

lower energy than the e_g (t_g) orbital and the X-ray absorption intensity is t_{2g}:e_g=3:2 (e:t_g=2:3). Thus, the ratios of peak 1:peak 2 reflect the absorption intensities of the split 5*d* states. From the above results, we conclude that the white line in the W L_3-edge XANES indicates the electron transition from the $2p_{3/2}$ orbital to the split 5*d* orbitals.

Figure 1(C) shows the W L_1-edge XANES spectra of the reference samples. The pre-edge peak is mainly attributed to the forbidden electron transition from a 2*s* orbital to 5*d* orbitals. The less symmetric structure of W oxide species (distortion from the *Oh* symmetry) provides a larger pre-edge peak because this forbidden electron transition is induced by mixing p orbitals of tungsten and ligand into empty d orbitals. Therefore, Na_2WO_4 and $Sc_2W_3O_{12}$ exhibit a large pre-edge peak. We found that the combination of the area of the pre-edge peak of the W L_1-edge XANES and the splitting of the W L_3-edge white line provides more reliable information on the structure of the W oxide species. Figure 3 shows the area of the pre-edge peak of the W L_1-edge XANES plotted against the energy gap of the split W L_3-edge white line for the reference samples (represented by red solid circle). Figure 3 reveals an interesting relationship, in that the area of the pre-edge peak has a linear correlation with the energy gap of the split W L_3-edge white line. This linear relationship is supported by density functional theory calculations of the octahedral and tetrahedral W models [2]. Therefore, we conclude that the structure of the W oxide species can be easily estimated by a combination of the pre-edge peak area of the W L_1-edge XANES and the energy gap of the split W L_3-edge white line.

Using this new analytical method, we estimated the structure of the W oxide species loaded on TiO_2 samples from the above linear correlation. The samples used were *x*(2, 4, 12, 20, 40, and 80) molg^{-1} $H_3PW_{12}O_{40}\cdot 13H_2O$ loaded on TiO_2 (*x*HPA/TiO_2). The area of the pre-edge peak of W L_1-edge XANES is plotted against the energy gap of the split W L_3-edge white line for *x*HPA/TiO_2 in Fig. 3 (represented by blue solid square). As shown in Fig. 3, 2HPA/TiO_2 has a WO_6 structure and the amount of WO_4 species increases with an increase in the amount of loaded HPA. These estimated structures of W oxide species were in agreement with the curve fitting analysis results for the W L_3-edge EXAFS [2].

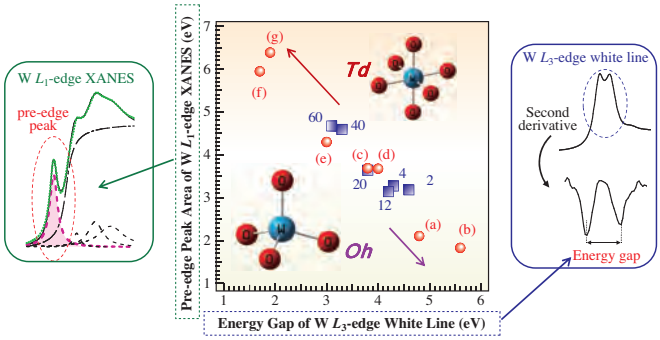


Fig. 3. Dependence of pre-edge peak area of W L_1-edge XANES on energy gap of split W L_3-edge white line of reference samples; (red solid circle): reference samples ((**a**) Ba_2NiWO_6, (**b**) Cr_2WO_6, (**c**) $(NH_4)_{10}W_{12}O_{41}\cdot 5H_2O$, (**d**) WO_3, (**e**) $H_3PW_{12}O_{40}\cdot 13H_2O$, (**f**) $Sc_2W_3O_{12}$ and (**g**) Na_2WO_4), (blue solid square): *x*HPA/TiO_2 samples (*x*=2, 4, 12, 20, 40, 60).

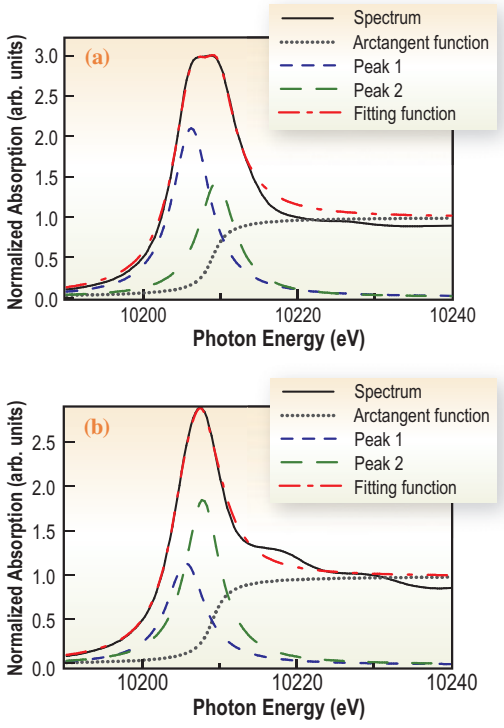


Fig. 2. Deconvolution of W L_3-edge XANES spectra of (**a**) WO_3 and (**b**) Na_2WO_4.

Seiji Yamazoe[a,*], Tetsuya Shishido[b] and Tsunehiro Tanaka[b]

[a] Dept. of Materials Chemistry, Ryukoku University
[b] Dept. of Molecular Engineering, Kyoto University

*E-mail: yamazoe@rins.ryukoku.ac.jp

References

[1] S. Yamazoe *et al.*: Appl. Catal. B **83** (2008) 123.
[2] *S. Yamazoe, Y. Hitomi, T. Shishido and T. Tanaka: J. Phys. Chem. C* ***112*** *(2008) 6869.*
[3] M. Fernández-García *et al.*: J. Phys. Chem B **109** (2005) 6075.
[4] G.N. George *et al.*: J. Am. Chem. Soc. **112** (1990) 2541.
[5] F. Hilbrig *et al.*: J. Phys. Chem. **95** (1991) 6973.

Industrial



SPring-8 has been successfully increasing the use of its cutting-edge facilities by industrial researchers. The most important factor contributing to our success in attracting a wide range of industries is the synchronicity of both the increase in the number of public beamlines dedicated to industrial research and the implementation of various utilization propulsion programs at public beamlines, which have been improved continuously, supported by the Ministry of Education, Culture, Sports, Science and Technology. As of March 2009, SPring-8 accommodates three public beamlines dedicated to industrial research. The first is the Engineering Science Research I (BL19B2) beamline, a standard bending magnet beamline for grazing-incidence X-ray diffraction (GIXD), X-ray reflectivity measurements, powder X-ray diffraction, and X-ray imaging experiments, at which experiments for industrial users have been carried out since the 2001B term. The second is the Engineering Science Research II (BL14B2) beamline, a standard bending magnet beamline, dedicated to XAFS measurements, which began operating for industrial use from the 2007B term. In addition to the two bending magnet beamlines, the third is the Engineering Science Research III (BL46XU) beamline, a standard-type "in-vacuum" undulator beamline, which began operating for industrial use in the 2008A term upon installation of a hard X-ray photoemission spectroscopy system as well as an 8-axis multipurpose X-ray diffractometer. In addition to the three public beamlines, there are three contract beamlines under companies' operation in SPring-8: Industrial Consortium ID (BL16XU), Industrial Consortium BM (BL16B2), and Pharmaceutical Industry (BL32B2). In addition, Hyogo BM (BL08B2) and Hyogo ID (BL24XU), contract beamlines under the local government, are running independent programs for industrial use.

APPLICATIONS

In the present issue, nine topics chosen to represent the outstanding work carried out in the field of Industrial Applications mainly in 2007A and 2007B are introduced here. Although most users of industrial applications had previously belonged to the field of electronics, many researchers from other industrial fields, such as those involving metals, fuel cells, hydrogen storage materials, polymers, cosmetics, and hair care are now joining SPring-8. The topical experiments introduced here were performed using the following techniques: hard X-ray photoelectron spectroscopy (HAXPES; BL47XU), soft X-ray photoelectron spectroscopy (SXPES; BL27SU), X-ray microbeam diffraction (BL24XU), grazing-incidence X-ray diffraction (GIXD; BL46XU), hard X-ray magnetic circular dichroism (BL39XU), nano-XAS and photoemission electron microscopy (BL17SU), powder X-ray diffraction (BL19B2), X-ray microtomography (XMT; BL47XU), and X-ray diffraction (BL40B2).

Three excellent studies from Si and compound semiconductor fields are selected this year as research frontiers of 2008: that is, nondestructive evaluation of band bending and carrier concentration profile in Si shallow junctions using HAXPES and SXPES, respectively, and GaN crystalline quality evaluation using X-ray microbeam rocking-curve mapping. Also, three studies from future electronic device fields are selected. Spectroscopic and structural characterizations were applied to graphene multilayers, ferromagnetic nanosheets, and bit-patterned media. The number of studies in the energy field related to global environmental problems is now rapid increasing. One of the topics is development of hydrogen storage materials using powder X-ray diffraction. The last two topics are directly related to everyday life: that is, damaged hair evaluation using XMT and structural phase transition evaluation in human stratum corneum using X-ray diffraction.

Yoshio Watanabe



Energy Band Bending Profile of Ultra-Shallow Junction in Silicon Studied by Hard X-Ray Photoelectron Spectroscopy

In advanced LSI devices, the gate length of metal-oxide-semiconductor field effect transistors (MOSFETs) is less than 20 nm; thus, short-channel effects, such as threshold-voltage instability and an increase in leakage current, become serious problems (Fig. 1). To solve this problem, X_j, the thickness of the source/drain extension region in a silicon surface, must be reduced to less than 10 nm. This technology is called ultra-shallow junction (USJ), which can be realized by high-concentration, low-energy ion implantation as well as rapid annealing to activate the implanted dopant without any diffusion. Therefore, the depth profile of carrier (activated dopant) concentration is very important for the development of USJ, but it is mostly estimated from electric properties of slant or step-etched samples where etching damage is not negligible.

In this study, we attempt to examine the carrier profile of USJ through the energy band bending profile measured by hard X-ray photoelectron spectroscopy (HX-PES or HAXPES) with as-received samples. Because carriers around USJ reach electrical equilibrium with an inhomogeneous concentration profile and cause energy band bending, the energy band bending profile reflects the carrier profile. The large probing depth of HX-PES gives spectra including signals from the entire USJ region, allowing the estimation of not only the magnitude but also the depth of the band bending caused by USJ. Using this method, we already found direct evidence of band bending in a GaN surface [1].

We prepared two types of USJ sample using a BF_2-implanted n-Si substrate (p^+-Si) and an As-implanted p-Si substrate (n^+-Si). Both dopants were implanted with low kinetic energies for 1×10^{15} atoms/cm^2 and activated by flush-lamp annealing. The depths of doped regions were measured by secondary ion mass spectroscopy (SIMS) as 17.2 nm for B and 12.6 nm for As at a concentration of 5×10^{18} atoms/cm^3. An HX-PES experiment was performed at beamline **BL47XU** with an incident X-ray energy of 8 keV. The photoelectron detection angle was 89 degrees relative to the sample surface and the total energy resolution was estimated to be 0.3 eV from the Fermi-edge spectrum of Au.

Figure 2 shows Si1*s* spectra of the samples. The peaks differ in energy position but are assigned to elemental silicon and not to silicon oxides that appear at a binding energy of more than 1843 eV. The difference in Si1*s* peak position originates not from the chemical shift but from the Fermi level shift of silicon because the valence band spectra shift by just the same energy of Si1*s*. In the photoelectron spectrum, the Fermi level is set to the origin of binding energy and photoelectron peaks of semiconductor samples may shift with carrier type and concentration. Therefore, it is considered that the Si1*s* peak appears at a higher binding energy in n^+-Si than in p^+-Si and the difference of 1.06 eV is nearly equal to the silicon band gap of 1.12 eV.

Figure 3 shows Si1*s* spectra of p^+-Si and n-Si substrates with relative binding energies. The peak of p^+-Si is obviously asymmetric and has a small tail on the higher energy side. This is because the Fermi level of p^+-Si varied in the depth direction and the Si1*s*

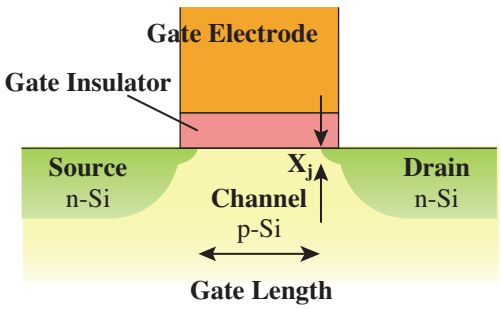


Fig. 1. Schematic of MOSFET.

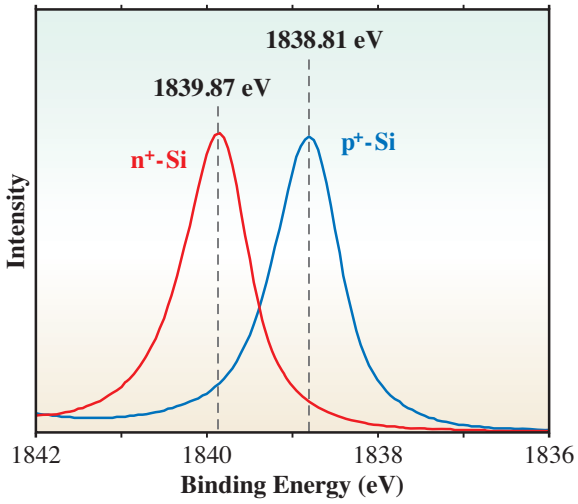


Fig. 2. Si1*s* photoelectron spectra of p^+-Si and n^+-Si USJ samples. Si1*s* peaks of surface oxide are outlying and very weak. The difference in peak energy originates not from the chemical shift, but from the Fermi level shift of the samples.

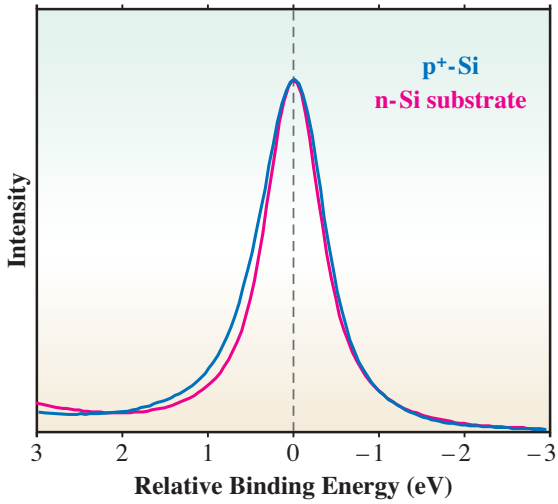


Fig. 3. Si1*s* photoelectron spectra of p⁺-Si USJ sample and n-Si substrate. The spectra are calibrated with a peak energy of 0.0 eV and normalized with peak height.

spectrum consisted of peaks with different energy positions originating from the probing depths of HX-PES. When a thin p⁺-Si layer is activated by many carriers, the difference in Fermi level between the p⁺-Si and n-Si substrates is about 1 eV; thus, the migration of carriers results in energy band bending (Fig. 4). This suggests that HX-PES can provide both the magnitude and depth of energy band bending in silicon with USJ.

In the case of a GaN surface, the N1*s* spectrum showed a large asymmetric peak and we could derive its energy band bending profile by peak deconvolution [1,2]. However, the band gap of silicon is smaller than that of GaN and the degree of energy band bending also decreases. Consequently, an HX-PES experiment with a higher energy resolution is necessary for obtaining precise energy band bending profiles of silicon.

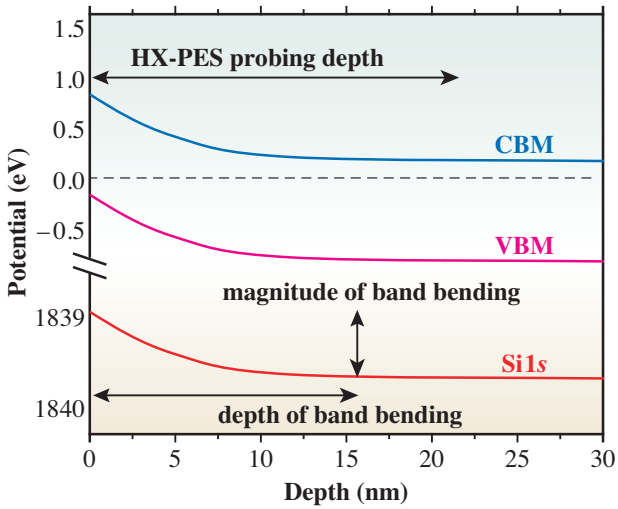


Fig. 4. Example of energy band diagram for p⁺-Si USJ sample. Note that the depth scale is incorrect here.

Masahiko Yoshiki

Corporate Research & Development Center,
Toshiba Corporation

E-mail : masahiko.yoshiki@toshiba.co.jp

References

[1] *M. Yoshiki, S. Saito, S. Nunoue, E. Ikenaga, K. Kobayashi: User Exp. Report, 2005B0807* (in Japanese).
[2] *M. Yoshiki, M. Suzuki, Y. Tsuchiya, R. Ichihara, S. Saito, S. Takeno: Houshyakou **22**(1) (2009) 20* (in Japanese).

Chemical Analyses of Heavily Doped Boron in Silicon-Based Shallow Junctions by Soft X-Ray Photoelectron Spectroscopy

Semiconductor device technology for large-scale integrated circuits has been advanced by pursuing aggressive scaling down of device feature sizes. The formation of an ultra-shallow junction, in which impurity atoms are heavily doped into a very shallow region near the surface of a single crystalline silicon (Si) wafer, is a key process in keeping this trend. An important impurity is boron (B), which produces holes in the doped region, forming Si-based p-n junctions. In up-to-date nanoscale transistors, the depth of the doped layer, the so-called junction depth, must be as small as a few tens of nm on the surface of a Si wafer. In actual doped layers, B concentration is excessively high in the near surface region, as shown in Fig.1. Some of the B atoms that occupy the lattice site in crystalline Si must be electrically activated. The rest of these B atoms that occupy the interstitial sites in the crystalline Si form clusters, particularly in the heavily doped region. Such B clusters do not contribute to electrical conduction, thereby degrading the electrical properties of devices. On the other hand, the thermal diffusion of B atoms during thermal annealing, which activates B atoms, should be suppressed in order to preserve the small junction depth. Thus, the development of process technology, which results in the high activation rate of B in a heavily doped shallow junction, is a significant challenge. To achieve such process technology, the chemical analysis of B atoms in shallow junctions is strongly required.

The detection of chemical bonding states of B, whose concentration in Si is in the order of 1% or less, using Al Kα radiation excited photoelectron spectroscopy (XPS) is difficult because the photoionization cross section of B is small. Thus, we performed soft X-ray photoelectron spectroscopy at beamline **BL27SU**, where intensive soft X-ray was available at a photon energy of 500 eV, in order to increase the photoionization cross section. In addition, we achieved concentration depth profiling of B having different chemical bonding states by using step-by-step etching. Figure 2 shows the B 1*s* spectra with the etched depth as a parameter for a heavily doped shallow layer. The B 1*s* spectra arising from unoxidized B can be decomposed into three spectra having binding energies of 187.1 eV (BEL), 188.3 eV (BEM) and 189.6 eV (BEH). Therefore, three different chemical bonding states of B exist in the doped layer.

The concentration of B related to each spectrum (with BEL, BEM or BEH) was evaluated from the B 1*s* spectral intensity normalized by the Si 2*p* spectral intensity obtained from the same sample, in which the concentration of B was calculated from the normalized spectral intensity by using the ratio of the photoionization cross section of B 1*s* to that of Si 2*p*, the ratio of the inelastic mean free path of B 1*s* to that of Si 2*p* and the concentration of Si (5.0×10^{22} cm^{-3}) [1]. Depth profiles of B concentrations evaluated from three spectra, BEL, BEM and BEH, and the total concentration of B including oxidized B denoted as "all boron" are shown in Fig. 3. The three different chemical bonding states of B exhibit different depth profiles. The depth profile of hole concentration evaluated by Hall effect measurement combined with step-by-step etching is also shown in Fig. 3.

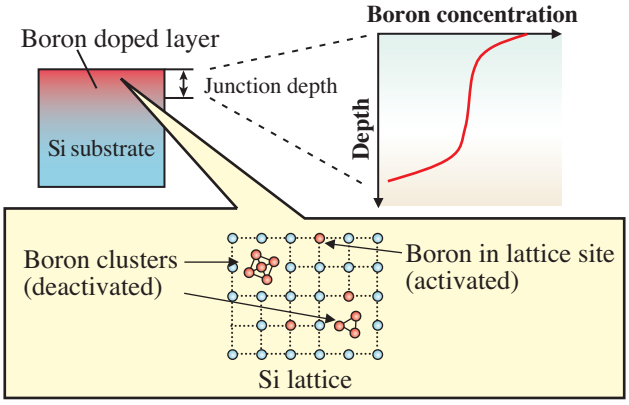


Fig. 1. Schematic diagram of B-doped shallow junction formed on surface of crystalline Si and depth profile of B concentration. In the B-doped region, B atoms are incorporated into a Si crystal at interstitial sites to form clusters and at lattice sites.

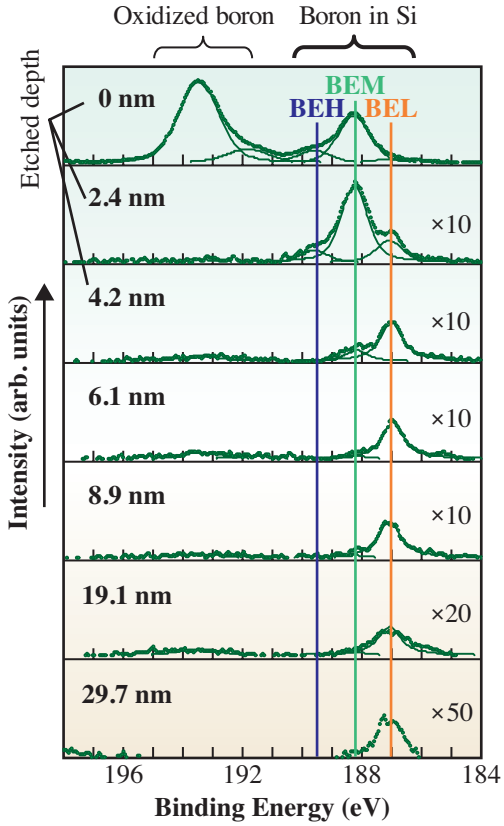


Fig. 2. B 1*s* spectra are shown with various etching depths. Photoelectron spectra arising from B are decomposed into three spectra having different binding energies, denoted by BEL, BEM and BEH.

According to this figure, the carrier concentration profile agrees well with the B concentration profile of BEL. Therefore, the binding energy of BEL is assigned to electrically activated B, and binding energies of BEM and BEL are assigned to B clusters.

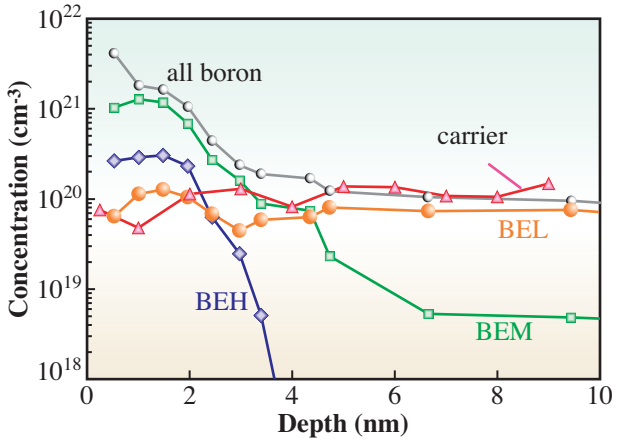


Fig. 3. Concentration depth profiles of B evaluated from BEL, BEM, BEH and total B including oxidized B. The profile of carrier concentration evaluated by Hall effect measurement is also shown. The depth profile of carrier concentration agrees well with the B concentration evaluated from BEL.

Present chemical analyses enabled the discrimination of three chemical bonding states of impurity atoms in the shallow junctions. The basic understanding of impurity activation in semiconductors for the development of new process technologies for future semiconductor devices is strongly anticipated.

Kazuo Tsutsui[a,*], Hiroshi Iwai[b] and Takeo Hattori[b]

[a] Interdisciplinary Graduate School of Science and Engineering, Tokyo Institute of Technology
[b] Frontier Research Center, Tokyo Institute of Technology

*E-mail: ktsutsui@ep.titech.ac.jp

References

[1] *K. Tsutsui, T. Matsuda, M. Watanabe, C.-G. Jin, Y. Sasaki, B. Mizuno, E. Ikenaga, K. Kakushima, P. Ahmet, T. Maruizumi, H. Nohira, T. Hattori and H. Iwai: J. Appl. Phys.* ***104*** *(2008) 093709.*

Excellent Crystallinity of Truly Bulk Ammonothermal GaN

Gallium Nitride (GaN) has attracted a great attention for its material properties that are useful for applications in short-wavelength optoelectoelectronic and high power electronic devices such as white or color light emitting diodes (LEDs), blue laser diodes (LDs), UV detectors and high power-high frequency transistors [1]. However, the currently available optoelectronic and electronic devices are manufactured mainly by heteroepitaxial methods, in which a variety of substrates, different than GaN, is applied, including sapphire, silicon carbide, silicon, zinc oxide, and many others [1]. The well-known disadvantages of heteroepitaxy are: lattice mismatch, thermal-expansion-coefficient difference, and/or chemical incompatibility, which in effect lead to nitride epilayers with high stress, high dislocation density, and mosaic crystal structure. This limits seriously the lifetime and power of aforementioned devices. During the past decade, an enormous effort was put into overcoming these fundamental obstacles, and an impressive progress was done, especially in high-efficiency LEDs or LDs manufacturing. However, it is widely expected that even these highly-engineered devices can benefit from the use of native (i.e. GaN) substrates and bring real technological breakthroughs.

At the moment, the main source of GaN substrates is the HVPE technique which is advantageous from the point of view of high growth rate, and yields crystalline GaN layers of a few millimeter thickness. However, this method by its own suffers from all disadvantages of heterogeneous (sapphire) substrates on which the growth is initiated. Even after removal of non-native substrate the thus-obtained free-standing GaN layer is highly stressed, and the resulting GaN wafers are typically highly bowed.

An ideal and ultimate solution to the problem are GaN substrates sliced from truly-bulk GaN crystals. Due to a high covalency and an extremely high decomposition pressure at the melting point it is not possible to grow GaN by standard melt-growth method. Therefore, many growth methods have been developed, including solution growth from Ga melt, Ga-Na alloys, and a variety of flux-assisted methods, in which the pressures range from atmospheric to as high as 20 kbar.

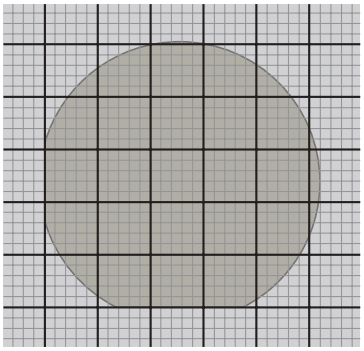


Fig. 1. 1-inch AMMONO-GaN substrate.

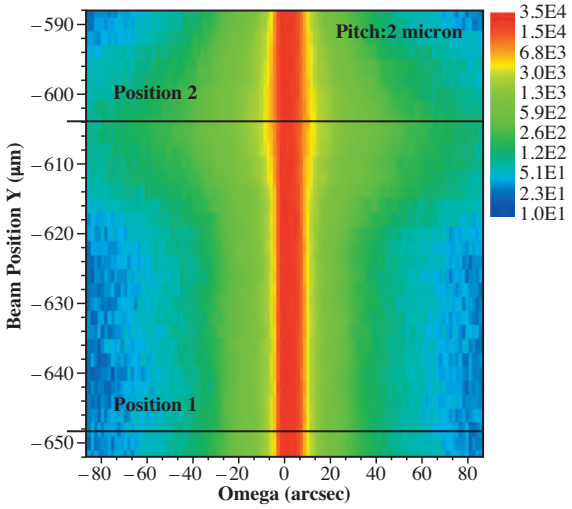


Fig. 2. X-ray micro-beam Omega-scan map for a 2-μm pitch.

Despite spectacular results and low dislocation density of grown crystals, these techniques suffer from relatively low dissolution of GaN in the melt, low controllability of the process, difficulties in implementing seeds, and limited scalability.

The ammonothermal method is a straightforward counterpart of hydrothermal technology, used in α-quartz commercial production. GaN-containing feedstock is dissolved in supercritical ammonia solution in one zone of the high pressure autoclave, then transported through solution by means of convection, and finally crystallized in the second zone, preferably on GaN seeds. The typical temperatures and pressures applied are 0.1- 0.3 GPa and 500°C – 900°C, respectively. The crucial point is the choice of mineralizer – the ionic substance added to the reaction zone in order to increase a reversible dissolution of GaN in ammonia. In the ammonothermal method of growing bulk GaN single crystals, invented, developed and implemented by the AMMONO company in collaboration with Nichia Corporation (AMMONO-Bulk Method), the growth is carried out in so called ammonobasic regime, where the mineralizer introduces NH_2^- ions to the solution. Our team has showed for the first time negative temperature coefficient of solubility ($\partial S/\partial T|_p < 0$) in ammonobasic environment [2,3]. As a consequence, the chemical transport of GaN is directed from the low-temperature zone of the autoclave to the high-temperature zone. Furthermore, as convection is a driving force for the mass transport, one has to place the high-temperature zone (with seeds) below the low-temperature zone (with feedstock) in order to obtain an efficient re-crystallization.

In general, the main benefits one can gain from application of ammonothermal method are: (i) the possibility of growing high-diameter seeds with excellent structural properties, (ii) repeatable and highly controlled re-crystallization process at close-to-equilibrium conditions (this enables, upon

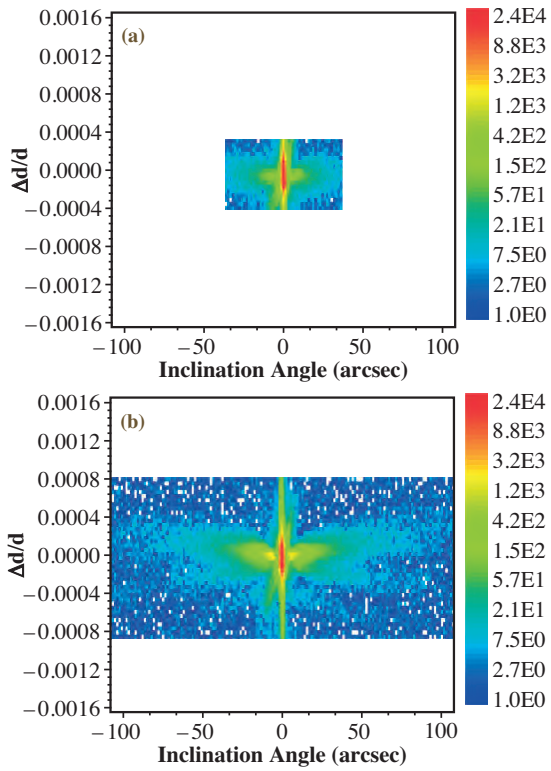


Fig. 3. X-ray micro-beam reciprocal-space maps. **(a)** Position 1; **(b)** Position 2.

request, either dissolution or crystallization of seeds by simple change of thermal conditions), (iii) relatively low growth temperatures, and (iv) excellent scalability of the process with the size of autoclaves. Moreover, as the long-duration processes are possible, one can grow large crystals and slice them in arbitrary directions (*c*-, semi-polar or non-polar planes).

Since the AMMONO-Bulk Method enables growth of high-quality seeds that can be further multiplied and re-grown without a noticeable loss of quality, the AMMONO-GaN crystals are characterized by excellent structural properties. In Fig. 1 we introduce a typical 1-inch AMMONO-GaN substrate, i.e., an oriented and polished wafer which was sliced from a larger AMMONO-GaN crystal. All structural data shown below were measured on as-grown AMMONO-GaN crystals of various shapes and dimensions which did not influence their properties.

The pure hexagonal phase of ammonothermally grown GaN was confirmed by powder diffractometry of pulverized crystals [3]. Excellent crystalline quality was confirmed by the Synchrotron Radiation Microbeam (SRM) measurements on the (0002) plane. Such investigations were performed by means of the synchrotron radiation SPring-8 facility, at beamline **BL24XU**. An AMMONO-GaN sample was scanned along the [11-20] direction with the 0.76 μm × 30 μm X-ray beam. As a result a set of rocking-curve maps was obtained. For example, in Fig. 2 a 60 μm-range scan with a 2 μm pitch is demonstrated. Then, two positions were chosen in which the widths of rocking curves were relatively lower (Position 1) and higher (Position 2). In these two positions, structural properties of AMMONO-GaN were illustrated by reciprocal-space maps, as shown in Fig. 3 where (a) corresponds to the Position 1, and (b) corresponds to the Position 2. In both cases, the general conclusion is that AMMONO-GaN crystals reveal excellent single-crystal structure, without mosaicity and low-angle grain boundaries.

Rocking curves measured for a number of AMMONO-GaN samples (#1 - #4) are shown in Fig. 4. Thanks to high monochromaticity, excellent collimation, and a very low diameter of the X-ray microbeam, the FWHM values of rocking curves of the level of 10 arcsec was achieved. Perfect crystallinity was also manifested by large radius of curvature (higher then 1000 m in the best crystals) and low dislocation density (below 10^4 cm^{-3}) [3].

The excellent structural properties of crystals (FWHM value of X-ray rocking curve of about 10 arcsec), combined with advantages of the method itself (seed-multiplication, repeatability, scalability), allow us to claim that AMMONO-Bulk Method is an extremely promising technology for fabricating high-quality, large diameter GaN substrates. Moreover, high scalability of the method will play a crucial role in further improving its cost-effectiveness when implemented in the industrial scale.

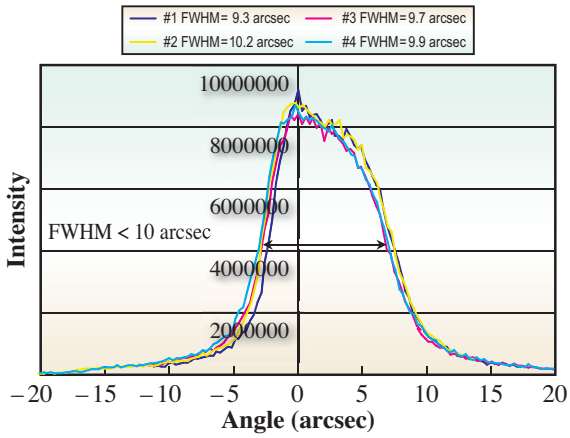


Fig. 4. X-ray microbeam rocking curves for AMMONO-GaN.

Robert Dwiliński[a,*], Marcin Zając[a] and Yasuo Kanbara[b]

[a] Ammono Sp. z o.o., Poland
[b] Nichia Corporation

*E-mail: dwilinski@ammono.com

References

[1] S.C. Jain *et al.*: J. Appl. Phys. **97** (2000) 965.
[2] R.T. Dwiliński *et al.*: United States Patent no. 6,656,615 B2 (02.12.2003).
[3] *R. Dwiliński, R. Doradziński, J. Garczyński, L.P. Sierzputowski, A. Puchalski, Y. Kanbara, K. Yagi, H. Minakuchi, H. Hayashi: J. Crystal Growth* ***310*** *(2008) 3911.*

Analysis of the Electronic and Crystal Structures of Graphene Multi-layers by Hard X-Ray Photoelectron Spectroscopy and Grazing Incidence X-Ray Diffraction

Graphene has been considered to be one of materials for future electronic devices since it was discovered in 2004 [1] in which it was shown to have an extremely high electron mobility and thermal conductivity [2]. On the other hand, low-temperature synthesis, which is essential for various electronic applications, has not been achieved yet [3]. Recently, we have succeeded in synthesizing graphene multi-layers at low temperatures of 510 and 620°C. In this paper, two approaches to low-temperature graphene synthesis will be introduced.

A novel carbon composite structure consisting of graphene multi-layers and aligned multi-walled carbon nanotubes (MWNTs) has been obtained at a temperature of 510°C [4]. The composite structure, which was synthesized by chemical vapor deposition (CVD), has graphene multi-layers combined with the upper ends of vertically aligned MWNTs on a substrate. Figure 1(a) shows a cross-sectional image of the composite on a silicon substrate by scanning electron microscopy (SEM). A flat structure on vertically aligned MWNT bundles is clearly observed. Analyzing this flat structure by transmission electron microscopy (TEM) in Fig. 1(b), we have found that the flat structure is composed of multiple graphite domains next to each other, whose thickness was estimated to be approximately 18 nm. This thickness can be controlled by the growth condition and catalyst composition [4]. Furthermore, from the growth-time dependence, it is found that graphene multi-layers were firstly synthesized, which implies the possibility of low-temperature synthesis of graphene.

The CVD process was performed at 510°C. As a catalyst, a 2.6-nm cobalt (Co) film on a 5-nm titanium nitride (TiN) film was used. While the obtained structure is clearly different from usual MWNTs, its origin has not been completely understood yet. To elucidate roles of catalyst films in synthesizing the composite, we have investigated the electronic structures of the composite by hard X-ray photoelectron spectroscopy (PES). The PES measurements were performed at beamline **BL47XU**, using SES-R4000 analyzer.

Figure 2 shows Co 2*p* core level spectra of (a) the usual MWNTs grown from an 1-nm Co film and (b) the composite structure measured by PES. The PES spectrum indicates that the catalyst after synthesizing the composite mainly consists of pure cobalt. On the other hand, the catalyst for the MWNTs was mainly oxidized. Taking into account the fact that the Co film was mostly oxidized before synthesis, these results mean that the Co film of the composite was much more reduced during the growth, implying that high catalyst activity of the Co film is one of the origins of the composite structure.

At a higher temperature of 620°C, graphene multi-layers can be synthesized [5]. The quality of graphene is better and their domain size is bigger than the former case. Figure 3(a) shows SEM images of the samples observed after CVD growth. A film-like structure with multiple domains was observed on the substrate. Analyzing the cross-sectional structures of this flat structure by TEM in Fig. 3(b), we have found that the flat structure is composed of graphene

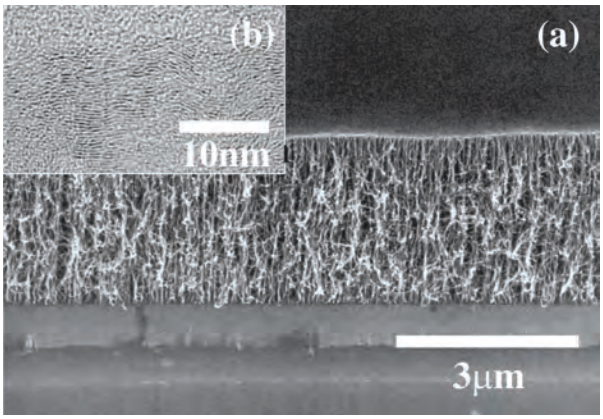


Fig. 1. **(a)** SEM image of the new carbon structure composed of graphene multi-layers and MWNTs; **(b)** TEM image of the graphene multi-layers.

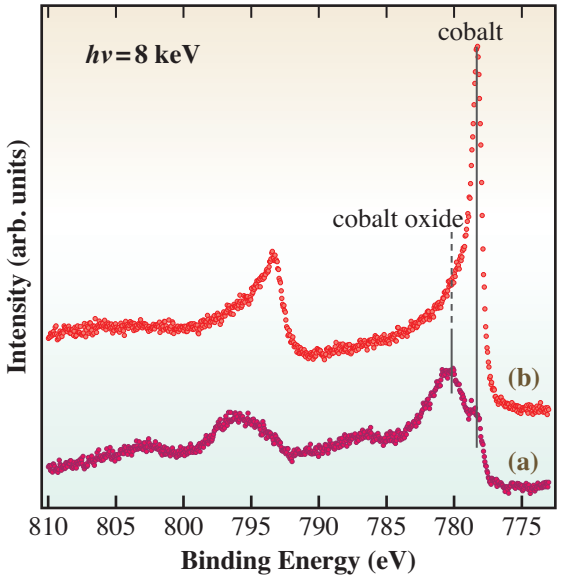


Fig. 2. Co 2*p* core level spectra of **(a)** usual MWNTs and **(b)** the composite structure.

multi-layers, whose thickness was estimated to be approximately 13 nm. The thickness of graphene multi-layers can be controlled by the growth condition and catalyst composition as in the former case.

Graphene multi-layers were obtained by hot-filament CVD at 620°C. As a catalyst, an iron (Fe) film with a thickness of 100 nm on a silicon substrate was used. To elucidate roles of catalyst films in synthesizing graphene, we have investigated the crystal and electronic structures of graphene by grazing incident X-ray diffraction (GIXRD). The GIXRD measurement was performed at beamline **BL46XU**, using ATX-GSOR.

Figure 4 shows the XRD patterns of (a) before and (b) after CVD process measured by GIXRD. After CVD, several new structures were found, which were assigned to be originated form graphene multi-layers and iron carbide (Fe_3C). In the case of MWNT synthesis, this kind of metal carbide has also been observed [6]. Taking into account that there was no crystallized structure originated from Fe before CVD, these observations indicate that formation of graphene multi-layers and Fe_3C occurs successively or at the same time. Although the direct contribution of Fe_3C to the synthesis of graphene is not clear, it implies that the role of Fe_3C may be important in the synthesis process of graphene.

In summary, we show two approaches to graphene synthesis at a temperature lower than those reported previously. The low-temperature synthesis methods reported here have brought the application of graphene to electronic devices one step closer to practical use. We will also continue to investigate the mechanisms by which the graphene multi-layers form, in order to develop future electronic devices, such as graphene-based transistors.

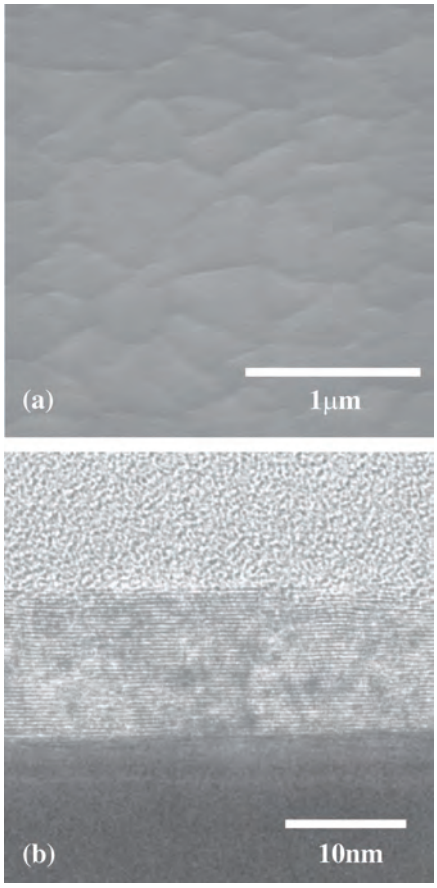


Fig. 3. **(a)** SEM image of the graphene multi-layers. **(b)** TEM image of the graphene multi-layers.

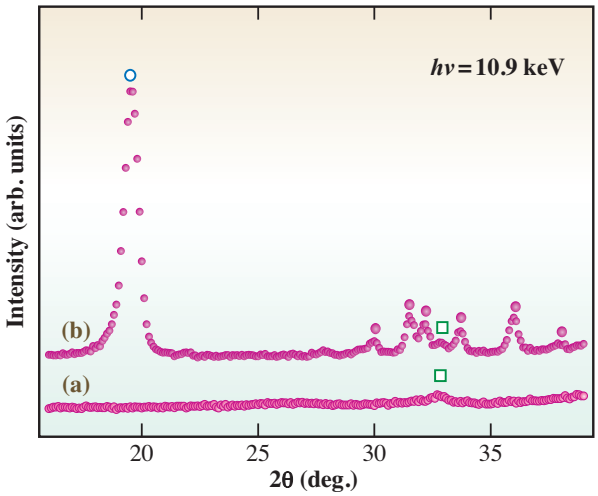


Fig. 4. XRD patterns of **(a)** before the CVD growth and **(b)** after the CVD growth of graphene multi-layers. Open circles: graphen multi-layers, open square: Fe, solid circles: Fe_3C.

D. Kondo[a,b,c,*], S. Sato[a,b,c], M. Nihei[a,b,c] and Y. Awano[a,†]

[a] Nanoelectronics Research Center, Fujitsu Lab. Ltd.
[b] Fujitsu Limited
[c] CREST-JST

*E-mail: kondo.daiyu@jp.fujitsu.com

[†] Present address: Department of Electronics and Electrical Engineering, Keio University

References

[1] K.S. Novoselov *et al.*: Science **306** (2004) 666.
[2] A.A. Balandin *et al.*: Nano Lett. **8** (2008) 902.
[3] M. Yudasaka *et al.*: J. Vac. Sci. Technol. A **13** (1995) 2142.
[4] *D. Kondo, S. Sato and Y. Awano: Appl. Phys. Express* ***1*** *(2008) 074003.*
[5] *D. Kondo et al.: Abst. 36th Fullerene Nanotubes General Symposium 2-15, 2009.*
[6] K. Nishimura *et al.*: Jpn. J. Appl. Phys. **43** (2004) L471.

Effects of Ion Implantation in Fabrication of Bit Patterned Media by Micro-XMCD Measurement

Hard disk drives (HDDs) adopting a perpendicular magnetic recording were commercialized in 2005. However, by conventional perpendicular magnetic recording using granular media, it is difficult to achieve an areal density of beyond 1 Tbit/in^2 because of thermal instability [1]. Bit-patterned media (BPM), in which a bit is recorded per magnetic dot arrayed periodically, has been proposed as the next-generation system. The BPM is expected as the most promising candidate systems for overcoming the restriction of thermal stability. We have studied techniques of design, fabrication and magnetic characterization in order to establish design guidelines for the BPM. In 2006, we demonstrated experimentally that when the dot-dot spacing, which is an important parameter for BPM design, is small, the recording performance deteriorates because of the magnetostatic interaction between dots [2]. In 2007, a sensitive element-specific hard X-ray micro-magnetometer at beamline **BL39XU** was used to characterize the magnetic properties of the Co-Pt dot arrays patterned by FIB with 30 keV Ga ions in a small area of μm order [3]. It was found that as the dot size decreases, the intensity of X-ray magnetic circular dichroism (XMCD) drastically decreases. This suggests that the dot edges were damaged magnetically by Ga ions implantation. The width of the damaged dot edge was estimated to be about 13 nm from the decrease in XMCD intensity [4]. This result suggests that BPM with an areal density of 1 Tbit/in^2 cannot be achieved by FIB with 30 keV Ga ions. Therefore, we proposed that ions with lower energies should be used to solve the problem and that the magnetic properties of Co-Pt dots fabricated by using Ar-ion etching with a energy as low as 200 eV should be evaluated.

Co-Pt magnetic dot arrays were prepared by directly etching a continuous film using electron beam (EB) lithography. Firstly, a 20-nm-thick $Co_{80}Pt_{20}$ continuous film with a perpendicular magnetic anisotropy was deposited by magnetron sputtering at room temperature. The anisotropy field (H_k) of the original film was estimated to be 8 kOe from the saturation field of the in-plane magnetization curve. In the subsequent process, dot arrays of an EB resist with a size of 20~100 nm and a dot-dot spacing of 100 nm were patterned by EB exposure. Finally, Co-Pt dot arrays were transferred through the EB resist mask by using Ar-ion etching with an energy of 200 eV. Figure 1 shows the SEM images of the Co-Pt arrays with dot sizes of 100, 70 and 20 nm before and after ion etching. All images show ideal sizes with regular alignments.

The magnetic properties of the Co-Pt dot arrays were evaluated by using the micro-magnetometer mentioned above, which is based on XMCD, as shown in Fig. 2. The magnetometer has a spatial resolution of 2.5 μm. XMCD signals were measured

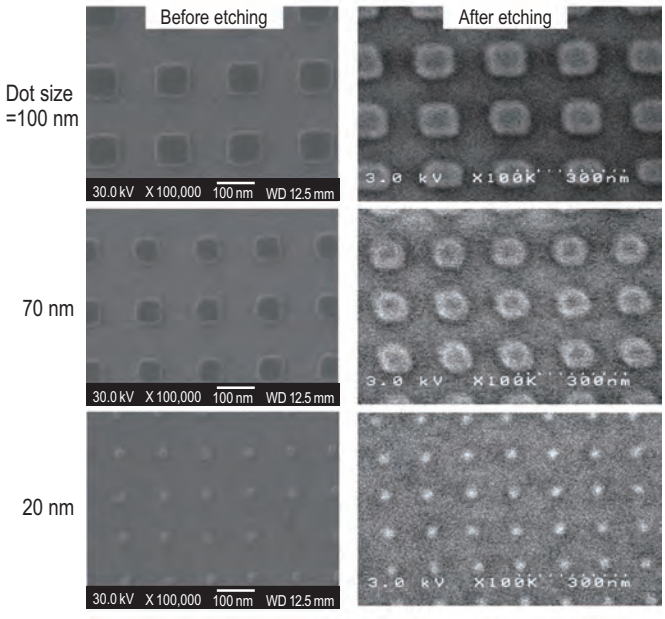


Fig. 1. SEM images of electron beam resist and Co-Pt magnetic dots before and after Ar ion etching.

in an X-ray fluorescence mode in which fluorescence yields were detected using a silicon drift detector. Element-specific magnetic hysteresis (ESMH) measurements were performed by changing the magnetic field and fixing the energy at the Pt L_3 edge ($h\nu$=11.56 keV) on the basis of the assumption that the XMCD amplitude of Pt is proportional to the total magnetization of the Co-Pt dots.

In Fig. 3, plots of closed circles show ESMH curves at the Pt L_3 edge of the original film (a) and dot arrays with various dot sizes (b-d) for an out-of-plane component. The ESMH curve of the 70 nm dot array patterned by FIB with 30 keV Ga ions is also shown by open circles in Fig. 3(c). Vertical axes of Fig. 3 denote that the XMCD intensities are normalized by Pt fluorescence yield, that is, they are proportional to the magnetic moment per Pt atom. Saturated XMCD intensities for dots of 100, 70 and 20 nm sizes were not reduced compared with that of the original film. It was found that the etching by low-energy Ar ions does not deteriorate the magnetization of the dots. Furthermore, the coercivity (H_c) of 20 nm dot arrays is 7.5 kOe, which is comparable to the H_k of the original film. By comparison with ESMH curves in Fig. 3(c) with 70 nm dot arrays, the H_c of the dot arrays

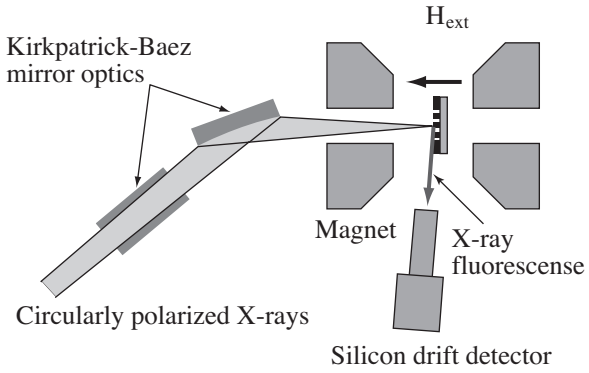


Fig. 2. Schematic view of element-specific hard X-ray micro-magnetometer based on X-ray magnetic circular dichroism.

fabricated by 200 eV Ar ions was found to be larger than that by 30 keV Ga ions. This may result from an accelerated deterioration of crystallinity or amorphization by Ga ion implantation. These results confirm that the etching using Ar ions cause slight damage on not only the magnetization but also the anisotropy field. It was concluded that the etching process using lower energy ions is effective for the realization of BPM with an areal density of 1 Tbit/in^2.

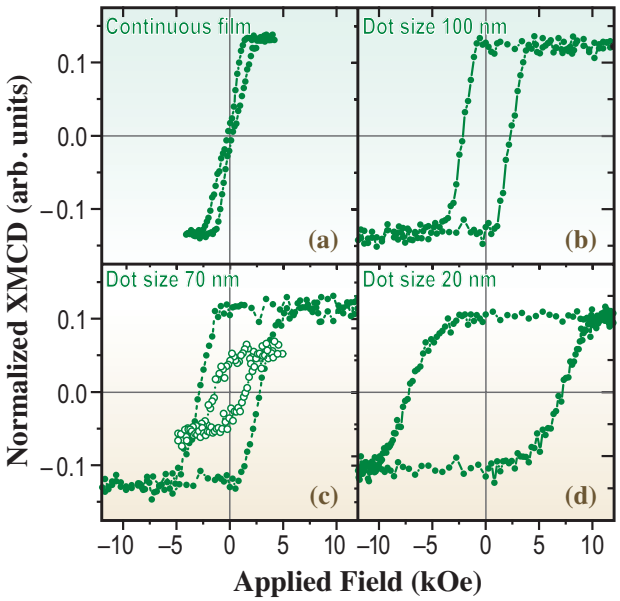


Fig. 3. ESMH curves at Pt L_3 edge of original film **(a)** and magnetic dot arrays with various dot sizes **(b-d)** obtained by 200 eV Ar ions. ESMH curves with 70 nm dots obtained by Ga ions with an energy of 30 keV are also shown in **(c)**.

Y. Kondo[a,*], J. Ariake[a] and M. Suzuki[b]

[a] Research Institute of Advanced Technology, Akita Prefectural R&D Center
[b] SPring-8/JASRI

*E-mail: kondo@ait.pref.akita.jp

References

[1] N. Honda, K. Ouchi: Digests of Intermag 2006, FB-02, San Diego (2006) p. 562.
[2] Y. Kondo *et al.*: J. Magn. Soc. Jpn. **30** (2006) 112.
[3] M. Suzuki *et al.*: AIP Conf. Proc. **879** (2007) 1699.
[4] *Y. Kondo, T. Chiba, J. Ariake, K. Taguchi, M. Suzuki, M. Takagaki, N. Kawamura, B. M. Zulfakri, S. Hosaka, N. Honda: J. Magn. Magn. Mater.* ***320*** *(2008) 3157.*

X-Ray Nanospectroscopic Characterization of Single Molecular Ferromagnetic $Ti_{1-x}Co_xO_2$ Nanosheet

Recent developments in nanotechnology require the investigation of local electronic structures of individual nanostructures, which is essential in understanding their interesting physical properties. Currently, scanning probe microscopy and electron probe microanalysis occupy a central position in the characterization of these nanostructures. In these techniques, however, it is almost always difficult to monitor how the local electronic structure changes in an individual nanostructure.

Photoelectron emission microscopy (PEEM) provides some clues to answer this issue, as it provides a simple probe of local electronic structures of nanomaterials directly in real space with a high spatial resolution (<100 nm). In particular, PEEM combined with synchrotron radiation is ideally suited for studying nanomaterials since it allows the element-specific imaging of local electronic and domain structures owing to the tunability of photon energy and polarization in synchrotron radiation.

We present here, for the first time, nanoscale PEEM measurements of a single molecular ferromagnetic $Ti_{0.8}Co_{0.2}O_2$ nanosheet [2,3], which allow not only the determination of the local electronic structure of a 1-nm-thick ferromagnetic material but also the characterization of the chemical states of stacking structures.

A $Ti_{0.8}Co_{0.2}O_2$ nanosheet (Fig. 1) is a new room-temperature (RT) ferromagnetic nanomaterial derived from a layered titanate by exfoliation. In many ways, the $Ti_{0.8}Co_{0.2}O_2$ nanosheet represents an ideal system for addressing the feasibility of PEEM in nanomaterial researches. $Ti_{0.8}Co_{0.2}O_2$ nanosheets exhibit the ultimate two-dimensional nature with a thickness of ~1 nm, which is a model system for investigating the lower detection limit of PEEM. Our focus in this study is on the unexplored electronic properties of an individual $Ti_{0.8}Co_{0.2}O_2$ nanosheet.

Samples used here are monolayer films composed of well-dispersed $Ti_{0.8}Co_{0.2}O_2$ nanosheets. A colloidal suspension of $Ti_{0.8}Co_{0.2}O_2$ nanosheets (with a lateral dimension of 2~10 μm) was synthesized from layered titanate by exfoliation. Monolayer films of $Ti_{0.8}Co_{0.2}O_2$ nanosheets were fabricated by Langmuir-Blodgett deposition.

X-ray nanospectroscopic measurements were performed at beamline **BL17SU**. We have conducted nanoscale X-ray absorption spectroscopy (nano-XAS) with a high spatial resolution using PEEM.

Since the number of emitted secondary electrons is proportional to the X-ray absorption intensity, the PEEM contrast directly reflects the XAS intensity. For nano-XAS measurement, we scanned the photon energy and obtained a secondary electron emission

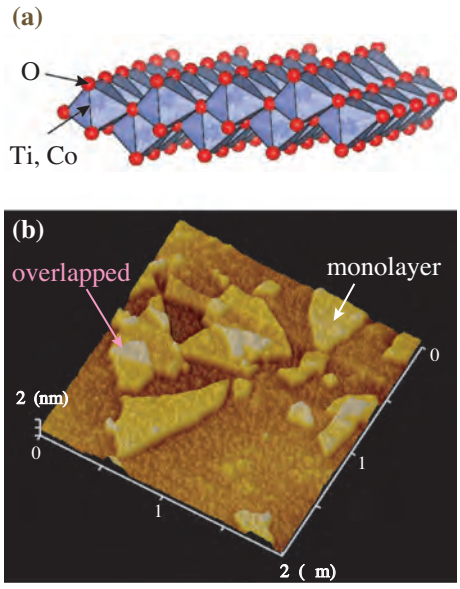


Fig. 1. **(a)** Structure of two-dimensional $Ti_{0.8}Co_{0.2}O_2$ nanosheet. Ti and Co atoms are coordinated with six oxygen atoms and the resulting Ti(Co)O6 octahedra are joined via edge sharing to produce the two-dimensional lattice. The thickness of the nanosheet is about 0.75 nm, and the nanosheet consists of two edge-shared octahedra. **(b)** AFM image of $Ti_{0.8}Co_{0.2}O_2$ nanosheets. The monolayer and overlapped nanosheets are observed.

PEEM image at each photon energy. In nano-XAS measurements, we chose the appropriate regions of interest (ROIs) in the PEEM image and integrated the intensities in ROIs to obtain nano-XAS intensity. It should be noted that, due to a sample drift during the measurements, it is rather difficult to obtain a reliable nano-XAS spectrum with a high spatial resolution, and therefore, drift correction was applied to all images using image analysis to reduce the drift within 20 nm.

Figure 2(a) shows the PEEM image of a single molecular $Ti_{0.8}Co_{0.2}O_2$ nanosheet. The image was taken at the area where the coverage of the nanosheet is comparatively low to observe the local electronic structure within an individual nanosheet. Figure 2(b) shows the Co 2*p* nano-XAS spectra for five different areas in the nanosheet shown in Fig. 2(a). The ROI of each spectrum is about 400 nm by 400 nm. The Co 2*p* X-ray absorption peak is observed only in the nanosheet region. The nano-XAS spectra of the different areas in the nanosheet show a clear resemblance, which indicates that the electronic structure and chemical state of doped Co is uniform in a single nanosheet. It is suggested that there is no Co concentration distribution or Co segregation in the single nanosheet.

The Co 2*p* X-ray absorption spectra in Fig. 2(b) show complex multiplet structures due to Coulomb interaction between the Co 2*p* core hole and 3*d* electrons. From the comparison of the spectral line shape and peak position with atomic-multiplet simulations, the valence of doped Co ions in the $Ti_{0.8}Co_{0.2}O_2$ nanosheet was estimated to be Co^{2+}.

In summary, we have investigated the local electronic structures of ferromagnetic $Ti_{0.8}Co_{0.2}O_2$ nanosheets by state-of-the-art X-ray nanospectroscopy techniques. Our results clearly indicate the feasibility of PEEM in addressing some fundamental issues on the determination of the local electronic structure of an individual $Ti_{0.8}Co_{0.2}O_2$ nanosheet. We should also note the characteristics and sensitivity of PEEM. Compared with other microscopy techniques, PEEM offers a convenient means of direct material characterization in real space with a high spatial resolution. PEEM is also a nondestructive method without any contact to samples, and therefore, it is ideal for the study of nanomaterials already incorporated into devices. With these characteristics, our method is therefore expected to provide a powerful and versatile technique for the nanoscale characterization of different nanomaterials and other nanosheets including graphene sheets.

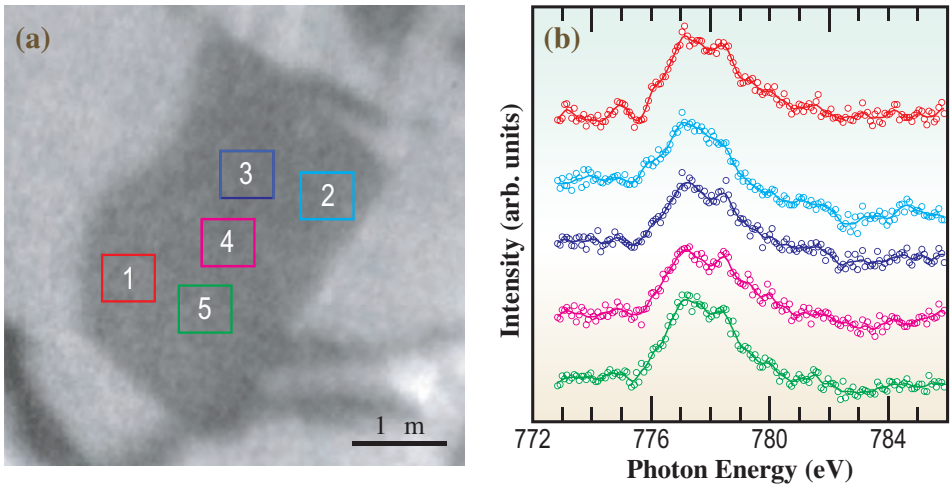


Fig. 2. **(a)** PEEM image of single molecular $Ti_{0.8}Co_{0.2}O_2$ nanosheet on Au substrate taken at photon energy of 773 eV. Five different areas (1–5) with sizes of about 400×400 nm^2 are shown in the figure. **(b)** Co 2*p* nano-XAS spectra for five different areas in $Ti_{0.8}Co_{0.2}O_2$ nanosheet. The numbers and colors of each spectrum correspond to the area shown in **(a)**.

Kanta Ono

Institute of Materials Structure Science,
High Energy Accelerator Research Organization (KEK)

E-mail: kanta.ono@kek.jp

References

[1] Y. *Kotani, T. Taniuchi, M. Osada, T. Sasaki, M. Kotsugi, F. Z. Guo, Y. Watanabe, M. Kubota and K. Ono: Appl. Phys. Lett.* ***93*** *(2008) 093112.*
[2] M. Osada *et al.*: Phys. Rev. B **73** (2006) 153301.
[3] M. Osada *et al.*: Adv. Mater. **18** (2006) 295.

Development of Hydrogen Storage Materials by Crystal Structure Analysis of Light Element Hydrides

Hydrogen storage is one of the key technologies that should be developed to utilize hydrogen as a clean energy source. The development of safe and efficient hydrogen storage materials is indispensable for the popularization of fuel-cell vehicles. Thus, hydrogen storage alloys have been mainly investigated, but the gravimetric hydrogen density of these alloys is lower than 3 mass%. In recent years, complex hydrides that consist of light elements, such as $LiBH_4$ and $LiNH_2$, have attracted considerable attention as new hydrogen storage materials [1] because of their high gravimetric hydrogen density ($LiBH_4$: 18.5 mass%; $LiNH_2$: 8.8 mass%). Generally, these complex hydrides release hydrogen by thermal decomposition reaction but cannot absorb hydrogen. Namely, the reversible hydrogen storage reaction in these complex hydrides is difficult. However, it has recently been reported that reversible hydrogen storage is possible in a $NaAlH_4$ system with a Ti catalyst and in a $LiNH_2$+LiH mixture system. Furthermore, it was found that the mixture of Mg_3N_2+$4Li_3N$ exhibits reversible hydrogen storage functions in which hydrogen of 9.1 mass% density of can be stored [2,3]. In this system, intermediate phases, such as $Li_2Mg(NH)_2$, are created in the reaction process according to the following formula:

$$3Mg(NH_2)_2 + 12LiH \leftrightarrow 3Li_2Mg(NH)_2 + 6LiH + 6H_2$$

$$\leftrightarrow Mg_3N_2 + 4Li_3N + 12H_2$$

It is expected that the intermediate phases will be important in the reversible reaction. However, the intermediate phases are novel hydrides and their structures are unknown. As a result, the reversible reaction mechanism has not yet been clarified. Therefore, these crystal structure analyses have been performed in order to understand the reaction mechanism. The diffraction intensities from hydrogen and lithium atoms are very low; thus, the highly brilliant X-ray source at beamline **BL19B2** was used for the diffraction measurement.

The mixture of Mg_3N_2+$4Li_3N$ was prepared by ball milling. First, the mixture was hydrogenated at a hydrogen pressure of 9.5 MPa, and then pressure-composition (p-c) isotherm measurement during the dehydrogenation process was performed at 523 K using the conventional Sieverts apparatus [4]. At several dehydrogenation stages of p-c isotherm measurement, the sample was taken out and the X-ray powder diffraction was measured. The crystal structure was analyzed by the Rietveld method using the computer program RIETAN. The result of p-c isotherm measurement and the sampling points are shown in Fig. 1. At the sampling points A, B and C, the hydrogen pressures (and the amounts of hydrogen desorption) are 9.5 MPa (0.0 mass%), 6.0 MPa (3.1 mass%) and 0.06 MPa (4.9 mass%), respectively. According to the amount of hydrogen desorbed during the p-c isotherm measurement, the following chemical formulas of samples A, B and C were estimated:

A: $3Mg(NH_2)_2$+12LiH,

B: $Li_4Mg_3(NH_2)_2(NH)_4$+8LiH+[$4H_2$], and

C: $3Li_2Mg(NH)_2$+6LiH+[$6H_2$].

The analyzed crystal structures of $Mg(NH_2)_2$, $Li_4Mg_3(NH_2)_2(NH)_4$ and $Li_2Mg(NH)_2$ are shown in Fig. 2. These crystal structures are similar to those of the anti-CaF_2 type. Namely, anions ($\{NH_2\}^-$ or $\{NH\}^{2-}$) are in the FCC-type arrangement and cations

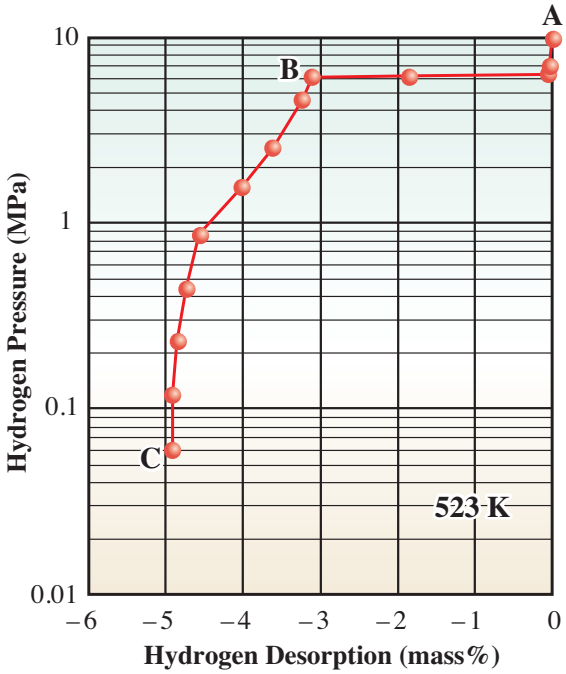


Fig. 1. p-c isotherm during dehydrogenation of Mg_3N_2+$4Li_3N$ mixture at 523 K after hydrogenation. A, B and C indicate the sampling points for the X-ray measurement.

(Mg^{2+} and Li^{+}) are located at eight interstitial sites. Nitrogen atoms coordinate at tetrahedral sites around cations. In $Mg(NH_2)_2$, Mg^{2+} ions are located at two cation sites and the other six cation sites are vacant. In $Li_4Mg_3(NH_2)_2(NH)_4$ and $Li_2Mg(NH)_2$ formed during the dehydrogenation process, Mg^{2+} and Li^{+} ions are randomly distributed among the cation sites. Consequently, the cation sites are Mg-rich, Li-rich or vacant according to the chemical composition [5].

As a result of this structure analysis, it is considered that the dehydrogenation reaction is related to the diffusion of Li^{+} ions at cation sites of $Mg(NH_2)_2$. Namely, Li^{+} ions diffuse from LiH to $Mg(NH_2)_2$ crystal and then decompose $\{NH_2\}^{-}$ into $\{NH\}^{2-}$ and H^{+}. The created H^{+} ions in $Mg(NH_2)_2$ attach to the side of LiH and combine with H^{-}. Consequently, H_2 gas is released. Hydrogenation is induced probably by the reverse process, which begins with the dissociation of a hydrogen molecule. The dehydrogenation of the $Mg(NH_2)_2$+LiH system is illustrated in Fig. 3. Furthermore, it has been clarified that the reversibility of the hydrogenation and dehydrogenation reaction of the $Mg(NH_2)_2$+LiH system is caused by the similarity in the structures of imides and amides. In the future, the development of catalysts or additives that enhance the diffusion of Li^{+} ions will be necessary for practical use. Crystal structure analysis will be important in future research of new hydrogen storage materials.

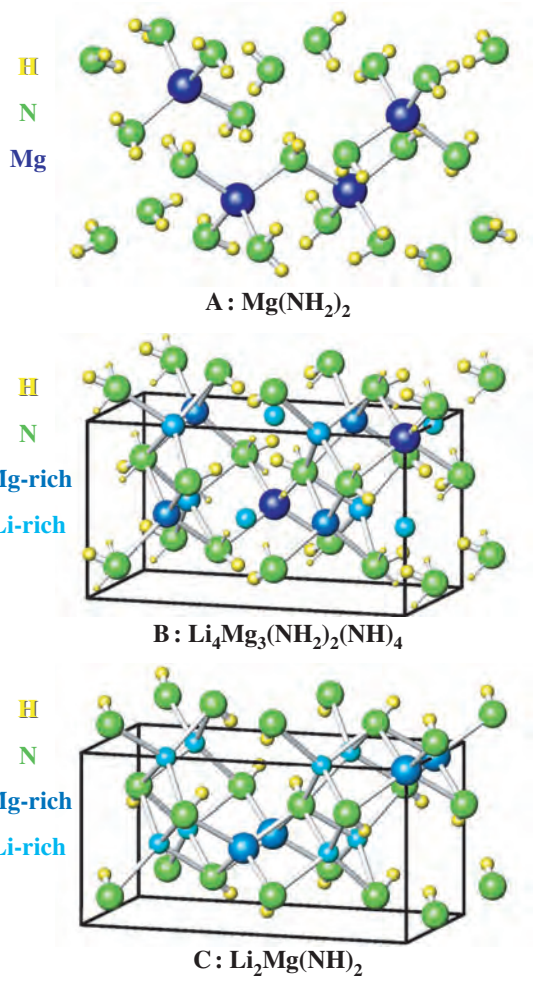


Fig. 2. Crystal structures of $Mg(NH_2)_2$, $Li_4Mg_3(NH_2)_2(NH)_4$ and $Li_2Mg(NH)_2$. The small light blue and large dark blue spheres represent the Li-rich and Mg-rich sites, respectively.

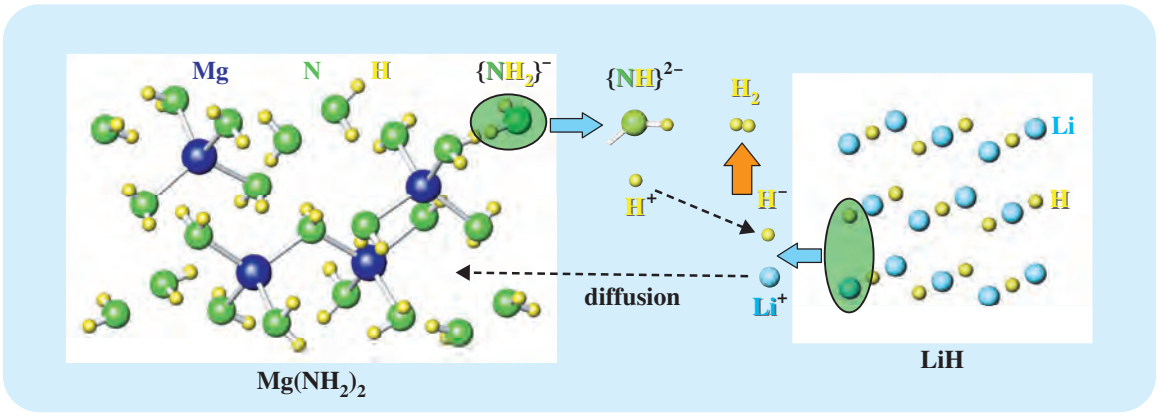


Fig. 3. Illustration of dehydrogenation of $Mg(NH_2)_2$+LiH system.

Tatsuo Noritake[a,*], Shin-ichi Towata[a] and Shin-ichi Orimo[b]

[a] TOYOTA Central R&D Labs., Inc.
[b] Institute for Materials Research, Tohoku University

*E-mail: e0553@mosk.tytlabs.co.jp

References

[1] S. Orimo *et al.*: Chem. Rev. **107** (2007) 4111.
[2] Y. Nakamori *et al.*: J. Power Sources **138** (2004) 309.
[3] Y. Nakamori *et al.*: Appl. Phys. A **80** (2005) 1-3.
[4] M. Aoki *et al.*: J. Alloys Comp. **428** (2007) 307.
[5] *T. Noritake, M. Aoki, S. Towata, Y. Nakamori and S. Orimo: Mater. Res. Soc. Symp. Proc.* ***971*** *(2007) 0971-Z07.*

Imaging of Damaged and Undamaged Hairs using X-Ray Microtomography

The market of hair-care products in Japan is large with about 200 billion yen sales per year. In particular, damage care is important because of the increasing opportunities to perform hair coloring, bleaching and permanent waving in Japanese consumers. To evaluate the degree of hair damage, many methods such as tensile strength, flexibility and amino acid analyses, are developed. However, structural information on hair damage, such as that on the locations of damaged parts and how hair damage proceeds in these location, seems insufficient. Electron and atomic force microscopes have been used for damaged hair observation. However, they cannot provide a three-dimensional microstructure of hair, and sometimes, they need specific preprocessing techniques, for example, slicing and staining. Thus, we aim to obtain a three-dimensional microstructure of hair without preprocessing. This structural information is expected to provide new aspects on care methods for damaged hair.

Beamline **BL47XU** was designed for application to various imaging technologies. It is mainly used for experiments involving X-ray photoelectron spectroscopy and microtomography in a hard X-ray region. X-ray computerized tomography (CT), which was originally developed for medical diagnosis, is a nondestructive technique for three-dimensional observation using a strong penetrating power of X-rays. Recently, a CT method with a high spatial resolution (X-ray microtomography, XMT) has been developed. Using highly collimated X-ray beams from a synchrotron radiation light source and using a high-spatial-resolution image detector, XMT with a simple projection geometry reaches a spatial resolution of 1 μm [1]. On the other hand, X-ray microscopy using several types of X-ray imaging device, such as a Fresnel zone plate (FZP), refractive lenses, and total reflection mirrors, has been developed. Currently, a spatial resolution of several tens of nm is achievable in the hard X-ray region. For example, the spatial resolution of 30 nm has been achieved with a FZP [2]. Therefore, combining such X-ray microscopy optics with XMT is expected to result in very high spatial resolution three-dimensional imaging.

Edge-enhanced refraction contrast imaging can also be realized with the slightly off-focus condition of the X-ray microscopy optics. This method enables the observation of light materials, whose absorption is too small in the hard X-ray region to observe with absorption contrast [3,4]. By this method, the three-dimensional microstructure of hair without preprocessing could be obtained. Figure 1(a) shows an X-ray transmission image of a human hair not subjected to any chemical treatment. Using a series of transmission images, CT images are produced. One of the CT images is shown in Fig. 1(b). Hair consists of three parts, namely, medulla, cortex and cuticle. Features of these parts are observed in this sliced section image.

To obtain a three-dimensional image, layers of CT images are piled on top of each another. Figure 2 shows a three-dimensional image of hair without chemical treatment. This image shows features of the cuticle, cortex and medulla. In the cortex, some microstructures of submicron size are aligned in the length direction of a hair shaft. In addition, these

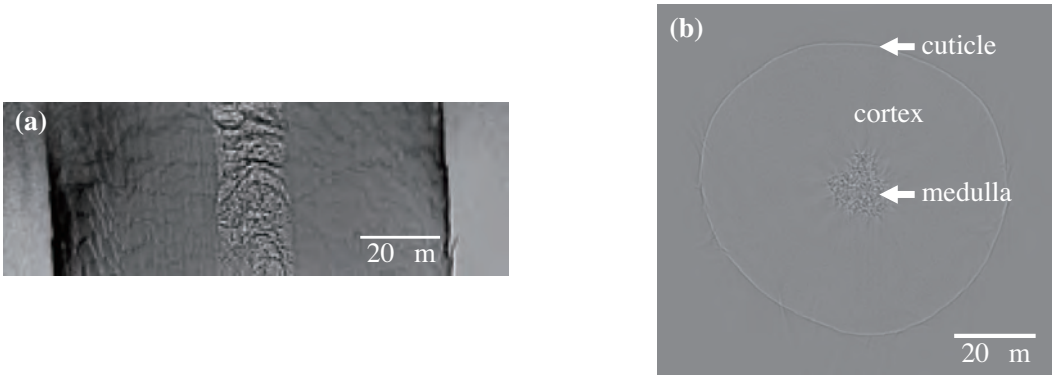


Fig. 1. **(a)** X-ray transmission image of hair obtained in off-focus edge-enhance mode. **(b)** CT image. X-ray energy: 9.8 keV; pixel size: 88 nm.

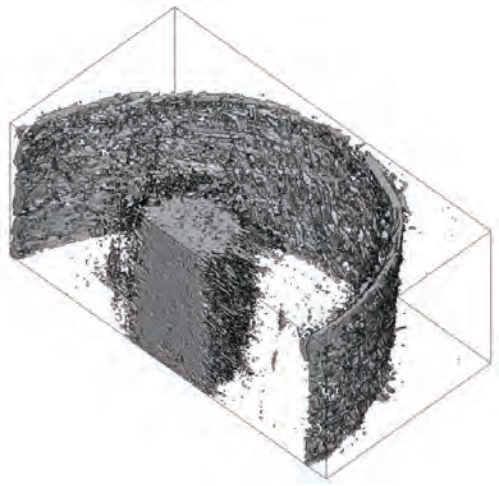


Fig. 2. Three-dimensional image of hair without chemical treatment.

microstructures increased by chemical treatments (e.g., permanent waving), as shown in Fig. 3. Edge-enhanced refraction contrast imaging enables the observation of the boundary between two structures with different electron densities. We consider that the microstructures in the cortex are cavities produced by chemical treatments, such as permanent waving. The number of microstructures was observed to proportionally increase with the extent of damage. In addition, the number of microstructures tended to decrease with repair treatments using a certain kind of oil.

Using edge-enhanced refraction contrast imaging, the three-dimensional microstructure of hair could be observed without the preprocessing of hair samples. We found that the number of microstructures in the cortex increased with chemical treatments. Although other experiments will be conducted to confirm the structural change quantitatively, the increase in the number of microstructures seems to provide a new aspect of hair damage. Edge-enhanced refraction contrast imaging is a useful tool for hair science.

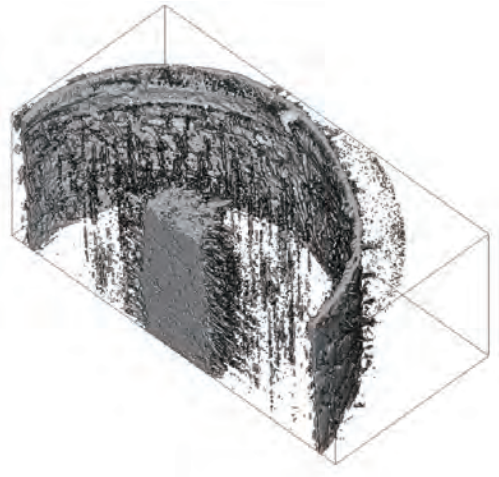


Fig. 3. Three-dimensional image of hair with chemical treatment (permanent waving).

Kouji Takehara[a,*], Takafumi Inoue[b] and Kentaro Uesugi[c]

[a] Kanebo Cosmetics Inc. Cosmetic Laboratory
[b] Kanebo Cosmetics Inc. Basic Research Laboratory
[c] SPring-8/JASRI

*E-mail: takehara.kouji@kanebocos.co.jp

References

[1] K. Uesugi *et al.*: AIP Conf. Proc. **705** (2003) 1316.
[2] A. Takeuchi *et al.*: Rev. Sci. Instrum. **73** (2002) 4246.
[3] A. Snigirev *et al.*: Rev. Sci. Instrum. **66** (1995) 5486.
[4] S.W. Wilkins *et al.*: Nature **384** (1996) 335.

X-Ray Diffraction Analysis of Intercellular Lipid Structure in Human Stratum Corneum Collected by Less Invasive Method

Stratum corneum (SC), the outermost layer of skin, is an important organization as a barrier function of a mammalian skin, which regulates not only the evaporation of water from the body but also the invasion of exogenous hazards. SC is a very thin layer of about 10 μm and composed of corneocytes and an intercellular lipid matrix [1]. The ordered structure of the intercellular lipid matrix plays an important role in skin barrier function. Although some skincare cosmetics claim their efficacy on the barrier function, precise mechanisms on an intercellular lipid structure remain to be elucidated. Recently, some structural analyses of intercellular lipids in mammalian SC by X-ray diffraction have shown more detailed lipid structure models [2,3]. In mammalian SC, the longitudinal arrangement of lipid molecules, consisting of long and short lamellar structures with repeat distances of about 13 nm and 6 nm, respectively, has been observed by small-angle X-ray diffraction (SAXD). In the lateral arrangement of lipid molecules, hexagonal and orthorhombic hydrocarbon-chain packing has been observed by wide-angle X-ray diffraction (WAXD). However, these previous studies were often carried out using nonhuman SC samples, and studies with human SC have been limited. The purpose of this study is to establish a technique for analyzing the structure of intercellular lipids using synchrotron X-rays with a very small amount of SC sample collected less invasively from a healthy human volunteer.

SC samples were collected from the forearm and cheek of a healthy volunteer with a water soluble adhesive tape. SC samples were isolated by extensive washing with water to remove adhesive materials. After adjusting the water content of the isolated SC samples to about 30 wt%, a piece of each sample (about 3 mg) was immediately sealed in a capillary tube before X-ray diffraction measurements.

X-ray diffraction measurements were performed at beamline **BL40B2** using 15 keV X-rays, and the scattered X-rays were detected using an imaging plate system (R-AXIS IV; Rigaku, Tokyo, Japan). The sample-to-detector distance was about 400 mm and the exposure time was 30 s. The diffraction pattern was circular-averaged to obtain a radial intensity profile.

The temperature of the sample was controlled using a temperature regulator (FP900 Thermo System; Mettler-Toledo K. K., Tokyo, Japan) and measured with a thermocouple embedded in the sample holder. All the experiments were performed in a heating scan from 15 °C to 120 °C at a rate of 0.5 °Cmin^{-1}. The X-ray diffraction profile was recorded every 2.5 °C.

The profiles of the human SC sample at 25 °C, 45 °C, and 85 °C in the small-angle and wide-angle regions are shown in Figs. 1(a) and 1(b), respectively. The value of S is given by $S=(2/\lambda)\sin(2\theta/2)$, where 2θ is the scattering angle and d is the repeat distance. At 25 °C, some broad peaks correspond to repeat distances of 13.6 nm (S=0.0736 nm^{-1}) and 6.3 nm

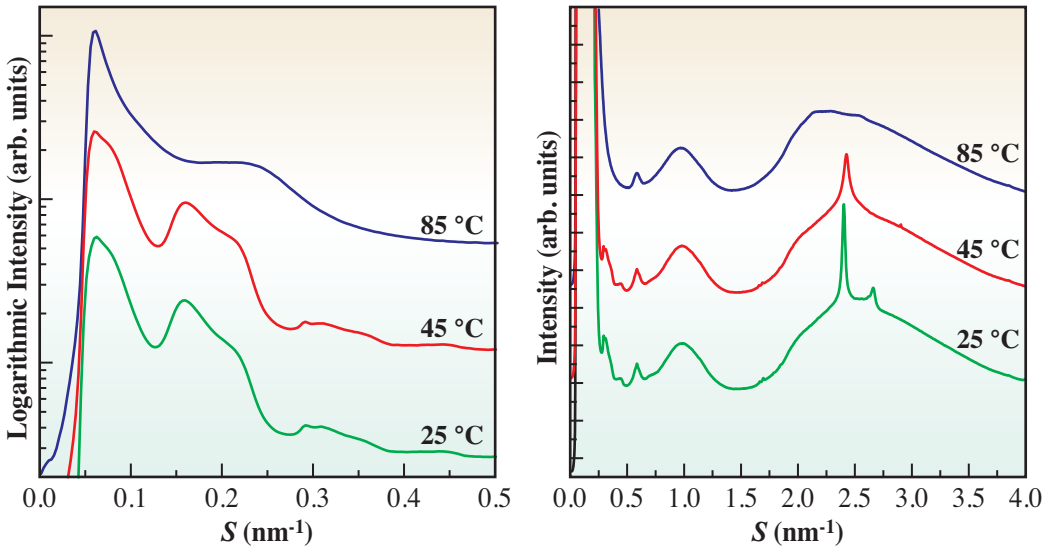


Fig. 1. X-ray diffraction profiles of human SC. **(a)** Small-angle and **(b)** wide-angle regions at 25 °C, 45 °C and 85 °C. Each plot is moved upward successively so as to see it easily. The reciprocal spacing is expressed by $S = (2/\lambda)\sin\theta$, where λ is the wavelength of the X-ray and 2θ is the scattering angle.

(S=0.16 nm^{-1}) among others (Fig. 1(a)). At 25 °C, two diffraction peaks (S=2.4 nm^{-1} and 2.7 nm^{-1}, corresponding to spacings of 0.42 nm and 0.37 nm, respectively) were observed superposed on a broad hump peak derived from soft keratin (Fig. 1(b)). Therefore, we could obtain a sufficient number of diffraction patterns for the analysis of a small amount of human SC sample.

The SAXD and WAXD data from the SC are plotted against temperature in Figs. 2(a) and 2(b), respectively. The intensity of the X-ray profile is represented by a contour line. On SAXD (Figs. 1(a) and 2(a)), as the temperature increased, the intensity for the lamellar structure with S=0.0736 nm^{-1} decreased and that for the lamellar structure with S=0.16 nm^{-1} also decreased. The latter peak deviated to a higher angle and disappeared above 80 °C. On WAXD (Figs. 1(b) and 2(b)), around 40 °C, the SC lipids underwent a structural transition from the orthorhombic state to the hexagonal state, which was consistent with the previous study on mouse SC by Hatta *et al.* [4]. The diffraction peaks at S=2.4 nm^{-1} and 2.7 nm^{-1}, which were derived from the hydrocarbon-chain packing of the orthorhombic state, disappeared at about 40 °C. Above 40 °C, the diffraction peak at S=2.43 nm^{-1}, which was due to the hydrocarbon-chain packing of the high-temperature hexagonal state, appeared instead. Above 40 °C, the lattice constant of the hydrocarbon-chain packing in the high-temperature hexagonal state gradually increased with an increase in temperature. Above 80 °C, the high-temperature hexagonal state, as well as the above-mentioned lamellar structure in the SAXD, disappears. These phase transitions were reversible, since recrystallization was observed upon cooling from 120 °C to 25 °C (data not shown).

It is interesting that a distinct phase transition occurrs around the body temperature, which may explain the result obtained in the previous study indicating that percutaneous absorption of some drugs depends on the temperature [5]. We consider that the X-ray diffraction analysis of intercellular lipid structure in human SC obtained by tape stripping is a promising technique for the development of new cosmetics based on the structural change of intercellular lipids. At present, a further detailed examination about the relationship between the intercellular lipid structure in human SC and the barrier function of skin is necessary.

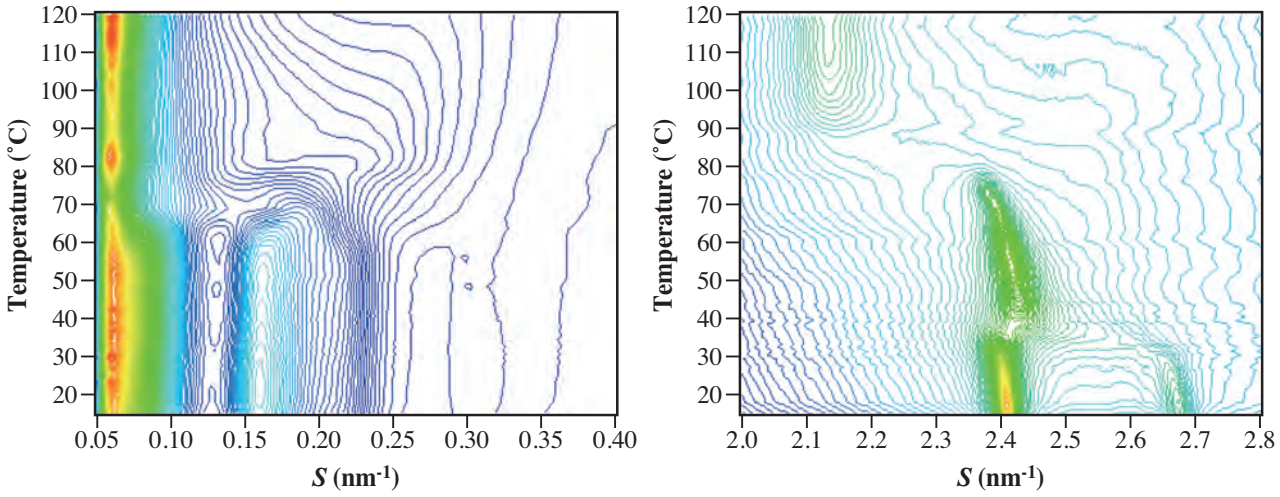


Fig. 2. Intensity contour maps of SAXD **(a)** and WAXD **(b)** in stratum corneum of human. The intensities are shown by colored lines. High-to-low intensities are shown in red-to-violet contours.

Naomi Kunizawa[a,*] and Ichiro Hatta[b]

[a] Shiseido Research Center
[b] SPring-8/JASRI

*E-mail: naomi.kunizawa1@to.shiseido.co.jp

References

[1] P.M. Elias and G.K. Menon: Adv. Lipid Res. **24** (1991) 1.
[2] N. Ohta *et al.*: Chem. Phys. Lipids **123** (2003) 1.
[3] J.A. Bouwstra *et al.*: J. Invest. Dermatol. **97** (1991) 1005.
[4] I. Hatta *et al.*: Biochim. Biophys. Acta – Biomembranes **1758** (2006) 1830.
[5] N. Ohara *et al.*: Int. J. Pharm. **105** (1994) 31.

INSTRUMENTATION &



Methodology

In the last decade, synchrotron radiation has become an indispensable tool for analyzing the nano- and pico-worlds. The increasing brightness of this light source accompanied by its enhanced X-ray optics performance has made it much easier to investigate 'dynamics' in the nano- and pico-world. A number of new instruments and methods challenging faster dynamics have been developed, greatly benefiting numerous research fields.

In this volume, we present three of the many exciting new developments related to 'dynamics' . The first one is a method for determining the elastic constant of material under high pressure using inelastic X-ray scattering. The coupling of elastic motion and X-rays causes a small shift of scattered X-ray energy, the spectrum of which is used to derive the elastic constant. The second one is the development of a 'time-resolved' XMCD-PEEM system to make pump-probe PEEM measurements, which enables time-resolved photoemission and magnetization reversal measurements. On the contrary, the third one is a method for cancelling the effect of dynamics to have a 'lifetime-broadening free' X-ray absorption spectroscopy.

Based on our operations experience, we are certain that these new developments in instrumentation/methodology will soon find wide a variety of applications.

Tetsuya Ishikawa



Precise Determination of Elastic Constants by Inelastic X-Ray Scattering

Precise measurement of the elastic properties of materials in extreme conditions is crucial for both materials and earth sciences. However, it is difficult to measure elastic velocities on small and/or optically opaque materials, especially when they are contained within complex sample environments. In earth science, for example, seismic wave observations are an important source of information about the earth's interior: in principle, the thermal and chemical structure of the earth may be investigated by comparing measured seismic velocities with the elastic properties of candidate materials measured in the lab in controlled environments. However, conventional techniques such as ultrasound interferometry (UI) and Brillouin light scattering (BLS) are not easily applied, as UI usually requires large sample volumes and BLS requires optically transparent samples.

High resolution inelastic X-ray scattering (IXS) is a technique that may be used to determine elastic

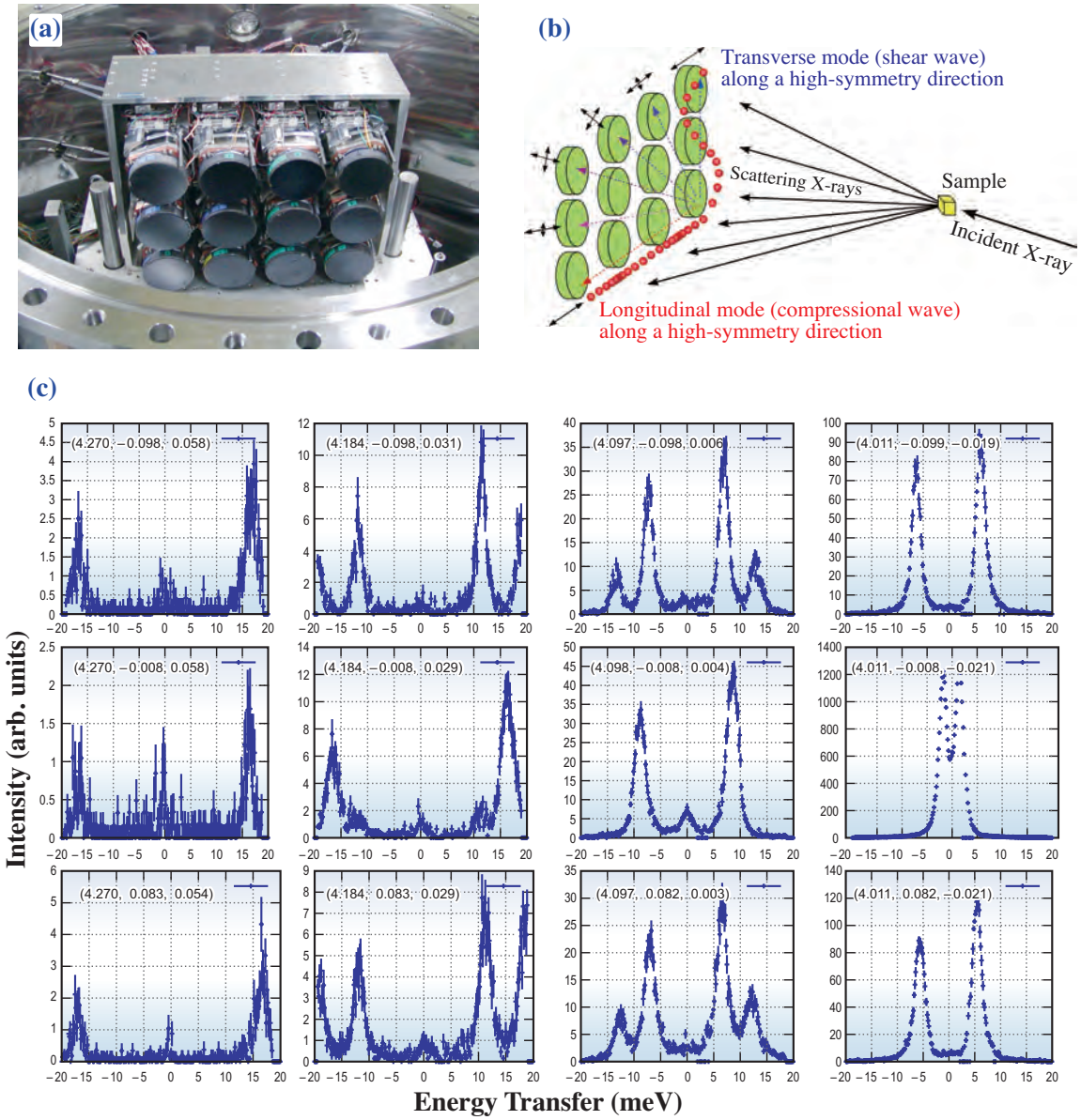


Fig. 1. **(a)** Photograph of the two-dimensional analyzer array. **(b)** Schematic drawing of detectable phonons at one scattering position. Colored broken arrows indicate phonon propagation direction and thin black arrows the detectable phonon polarizations. **(c)** Representative IXS spectra obtained using the 12-analyzer array. The reciprocal lattice coordinate for each analyzer is shown in the figure, and the Bragg point would be just off the figure on the right-hand side.

constants from small opaque samples under extreme conditions: the measured acoustic phonon velocity, as wavenumber approaches zero, corresponds to that of the elastic wave. As the ~20 keV X-rays used in IXS are penetrating and can be focused to a few micron size, they are an interesting probe of elastic constants. This has been demonstrated by several groups with the uncertainties around 3% in bulk modulus. However, to maximize utility, the precision of the determination should be improved. In the case of (Mg,Fe)O, for example, uncertainties of 3% in sound velocity and bulk modulus corresponds to uncertainties of 450 K in temperature and 17% in iron content, respectively. We have achieved the precision of 0.4% in bulk modulus using special characteristics of beamline **BL35XU** and a new method of analysis [1].

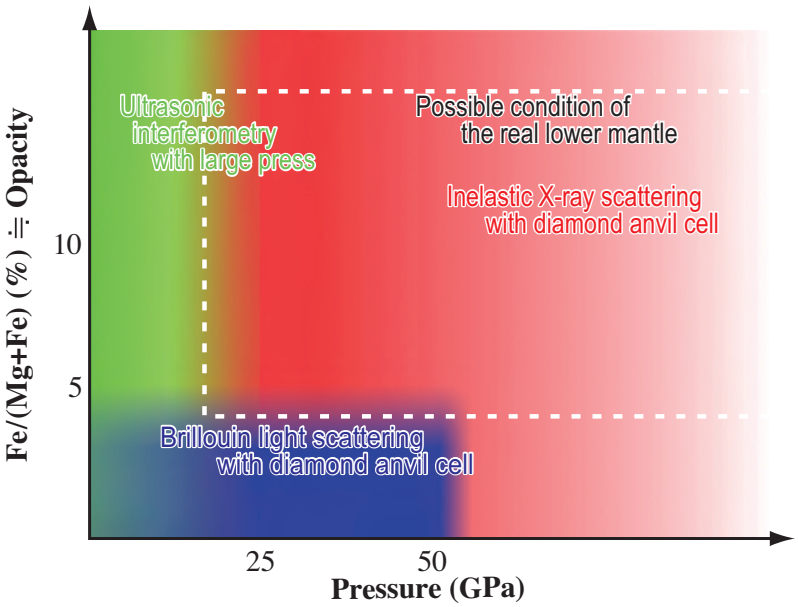


Fig. 2. Regions in pressure-opacity (iron content) space where elastic constants of a single crystal can be measured by UI and large press with a solid pressure medium (green), BLS and DAC (blue), and IXS and DAC (red). White broken lines indicate possible conditions of the real lower mantle. The pressure region for UI with large press would be limited because a single crystal may be broken by a buffer rod and a pressure medium at higher pressure. In the case of BLS with DAC, signals from longitudinal velocities might be covered by that from diamond anvils at higher pressure. This technique is difficult to apply to opaque materials. Since IXS with DAC does not suffer from those, the region is potentially the widest.

A single crystal of magnesium oxide, a known material, was used to characterize our method. MgO, being cubic, has only 3 independent elastic constants, and therefore it is sufficient, in principle, to measure sound velocities along limited high symmetry directions, e.g. [1 0 0] (longitudinal only) and [1 1 0] directions (longitudinal and transverse). However, redundancy is highly desirable to reduce errors. The unique two-dimensional analyzer array at BL35XU [2] allows simultaneous collection of data at twelve *k* points, clustered around a central momentum transfer, making the system well matched to this problem (Fig. 1). Elastic constants were obtained by fitting Christoffel's equation [3] to measured phonon energies at *arbitrary k* points. The redundancy and quality of the data allowed isolation of a correction term to the alignment of $(\Delta H\ \Delta K\ \Delta L) = (0.0056 \pm 0.0005, -0.0080 \pm 0.0007, 0.0043 \pm 0.0012)$ – the importance of this correction (neglecting it leads to an error of 1.9% in bulk modulus) demonstrates the sensitivity of the method. The elastic constants determined in this analysis were 293.9±1.0, 95.2±0.2, and 154.9±0.2 GPa for C_{11}, C_{12}, and C_{44} respectively, consistent with those measured by other techniques. The uncertainties are much better than 1%, and about one order of magnitude better than previously published IXS work.

This technique is now being applied to materials under extreme conditions. Here, the combination of IXS and diamond anvil cells (DACs) can cover the widest area for single crystal samples in pressure-composition (or opacity) space (See Fig. 2). However, one should note that the sample thickness in a DAC is only a few percent of the 1 mm thickness used in the present test. Thus the efficiency and redundancy of the multi-analyzer array becomes crucial for high pressures, and efforts should be made to maximize the flux onto the sample.

Hiroshi Fukui[a,*] and Alfred Q.R. Baron[a,b]

[a] SPring-8/RIKEN
[b] SPring-8/JASRI

*E-mail: fukuih@spring8.or.jp

References

[1] *H. Fukui, T. Katsura, T. Kuribayashi, T. Matsuzaki, A. Yoneda, E. Ito, Y. Kudoh, S. Tsutsui, and A.Q.R. Baron: J. Synchrotron Rad.* ***15*** *(2008) 618.*
[2] A.Q.R. Baron *et al.*: J. Phys. Chem. Solids **69** (2008) 3100.
[3] B.A. Auld: Acoustic Fields and Waves in Solids, Vol. 1 (1973) Krieger Pub., Malabar.

Construction and Development of Time-Resolved XMCD-PEEM System using Femtosecond Laser Pulse at BL25SU

Although ultrafast dynamics measurements became accessible with the development of ultrafast laser technology, their combination with pulsed synchrotron radiation is becoming an even more powerful technique. Ultrafast magnetization dynamics in micron-sized magnetic materials is now one of the issues relating to the development of faster and higher density data storage devices. In this article, we introduce a time-resolved magnetization imaging system using a stroboscopic pump-probe method [1] installed in **BL25SU**.

Magnetic domain imaging was performed by combining the X-ray magnetic circular dichroism with photoelectron emission microscopy (XMCD-PEEM). The achieved lateral resolution was ~100 nm. The time evolution of magnetic domain structures was obtained by a pump-probe method. The probe light was circularly polarized X-ray pulses, which were isolated bunches in a several bunch mode operation of the SPring-8 storage ring shown in Fig. 1. In this mode, twelve isolated bunches containing 1.6 mA were separated by 342.1 ns (repetition rate of 2.92 MHz) with an additional 342.1-ns-long bunch train. The temporal resolution was estimated to be ~100 ps, because of jitter (~60 ps) and the X-ray pulse width (~40 ps). The pump was the magnetic field pulses switched by the femtosecond laser pulses. The repetition rate of the laser pulse was tuned to 2.92 MHz so as to be synchronized with the isolated bunches. The diagram of the pump-probe system is shown in Fig. 1.

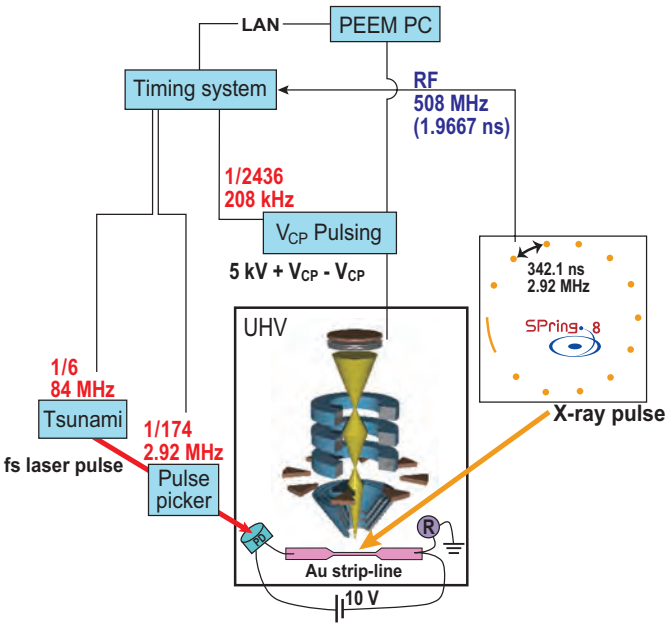


Fig. 1. Diagram of the pump-probe system. The timing system [details in Ref. 2] is triggered by the rf signal and distributes output signals to the custom-build V_{CP} system, the oscillator (Tsunami), and the pulse picker, which reduce the frequency of the laser pulse to the same as that of a single bunch.

Electrons projected by the X-rays from the bunch train were gated off with a custom-built power supply dropping the voltage synchronized with the bunch train, since they did not provide time-resolved signals. Figure 2 shows the measured characteristics of the power supply, where the PEEM image intensity is plotted as a function of the delay time between the bunch train and the gating out period of the channel plate. When the bunch train overlaps with the gating out period, all the electrons excited by radiation from the bunch train are blanked out. This leads to the lowest intensity (III in Fig. 2) because the PEEM intensity is only from the isolated bunches.

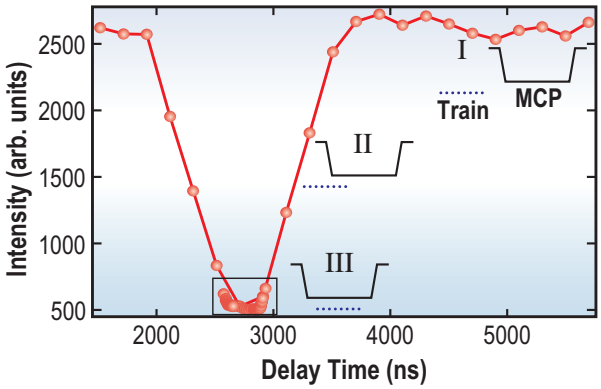


Fig. 2. Evaluation of the pulsing of the channel plate voltage power supply. The y axis is the PEEM image intensity and the x axis is the delay between the bunch train and the period for which the channel plate voltage is turned off.

Magnetization dynamics has been observed for $Fe_{20}Ni_{80}$ (FeNi) disks (6 μm in diameter) fabricated onto a Au stripline (10 μm in width and 100 nm thickness). When the thickness of the magnetic sample is smaller than its radius, with negligible magnetic anisotropy energy, the sample shows closure magnetic patterns to minimize the stray field energy, known as the magnetic vortex structure (Fig. 3(c)). In our experiment, the excitation energy to generate a magnetic event, i.e., a shifting of the core from the

middle of the disk, was provided by the external field pulse turned on by the femtosecond laser pulse in the following way. A fast photodiode connected to the stripline with inversely biased to 10 V was switched on by the femtosecond laser pulse and electric current flowed in the stripline. The current generated magnetic field pulses that acted on the spins in the disks, resulting in the shift of the core positions. The cores move in a direction perpendicular to the field direction.

The time zero, at which the current pulse flowed under the magnetic disk exactly when the X-ray pulses hit the disk, was inferred from the shift of the morphological structure. The shape of the field pulse was obtained as well. Since the PEEM detects electrons, the magnetic field created around the sample distorts the images. As a consequence, the images shift along the stripline perpendicular to the field direction. Figure 3(a) shows the absorption contrast of two FeNi disks on the stripline using the incident X-ray photon energy 5 eV below the Fe-L_3 absorption edge to observe the shape of the disks clearly. A series of PEEM absorption images were taken with a 50 ps delay increment of the femtosecond laser pulse. The integrated intensity over one region, indicated by a red rectangular box in Fig. 3(a), from each image is clipped and aligned with the delay (Fig. 3(b)). At around 0.5 ns, one can see the start of the shift, while the width of the field was around 300 ps (full width at half maximum).

Snapshots of the spin motion of a FeNi disk in 200 ps steps are displayed in Figs. 3(c)-3(g) in which the stripline lies from top to bottom. The orange, green, red, and black arrows in Fig. 3(c) indicate the magnetization of the vortex structure, core polarization, incidence direction of X-rays, and external field direction, respectively. The magnetic structure just before the field pulse is shown in Fig. 3(c). The core is at the middle of the disk. Through Figs. 3(c)-3(g), one can see the core moves upward during the field pulse. The core displacement from the disk center is shown in Fig. 3(h) for 70 ns with 500 ps delay increment. After the core reached the edge of the disk as shown in Fig. 3(g), the core undergoes a one-axial oscillatory motion about the disk center (Fig. 3(h)). The frequency of the core motion is around 50 MHz, which reproduces the observation in Ref. [3].

In summary, we have succeeded in observing magnetization dynamics images in the sub-ns time scale. This method can be applied for time-resolved photoemission and magnetization reversal measurements.

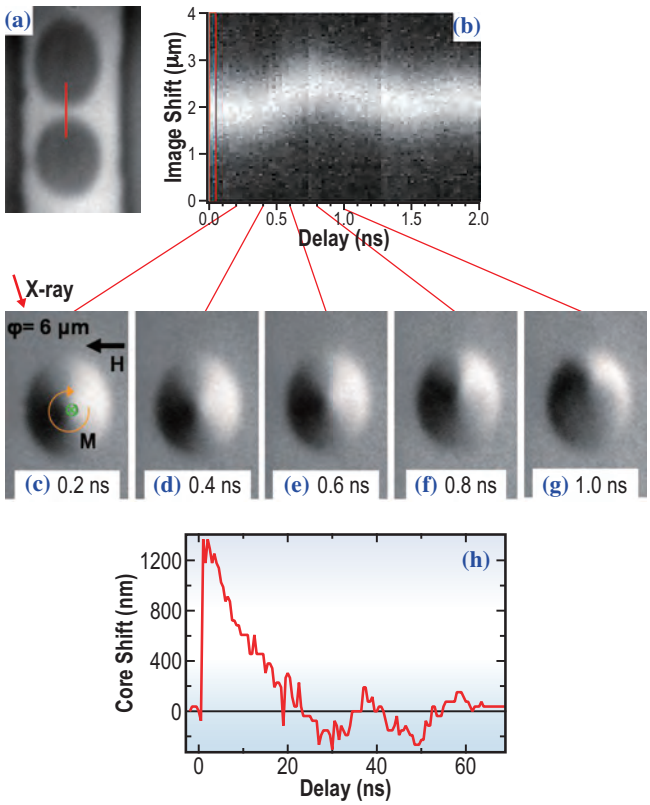


Fig. 3. **(a)** An X-ray absorption contrast image of two FeNi disks (ϕ = 6 μm) on the Au stripline. **(b)** Shape of the magnetic field pulse. Part of the absorption image [red rectangular box in **(a)**] with a 50 ps delay increment is clipped and lined up from left to right. Images **(c)**-**(g)** show the dynamics of the magnetic structure of a FeNi disk obtained with a 200 ps time increment. **(h)** The displacement of the vortex core from the disk center.

Keiki Fukumoto†

SPring-8/JASRI

E-mail: fukumoto@mosk.tytlabs.co.jp

† Present affiliation: TOYOTA Central R&D Labs., Inc.

References

[1] *K. Fukumoto, T. Matsushita, H. Osawa, T. Nakamura, T. Muro, K. Arai, T. Kimura, Y. Otani and T. Kinoshita: Rev. Sci. Instrum.* **79** *(2008) 063903.*
[2] S.-B. Choe *et al.*: Science **304** (2004) 420.
[3] T. Ohshima *et al.*: Proc. Asian Particle Accelerator Conference TUPMA**031** (2007) 145.
[4] K.Yu. Guslienko *et al.*: Phys. Rev. Lett. **96** (2006) 067205.

Is Lifetime-Broadening Free X-Ray Absorption Spectroscopy Really Feasible?

X-ray absorption spectroscopy (XAS) is one of the most powerful and versatile techniques for investigating the composition, structure and electronic structure of matter, and is used not only in physics and chemistry, but now also in a variety of scientific fields such as biology and geology. One of the limiting factors in XAS is the spectral resolution that is restricted by the large natural widths of core-exited states; because of this physical constraint, the details of the core-excited structures are often smeared out of XAS spectra. It has been proposed that lifetime-broadening free XAS can be achieved by scanning over the frequencies of the incoming photons while keeping the emission frequency "fixed at the maximum of the X-ray fluorescence line" [1]. The narrowing of X-ray absorption resonances was experimentally evidenced in previous studies [2,3]. Nowadays, lifetime-broadening free XAS is regarded as a new powerful tool, particularly for studies on the electronic states of solid systems.

In this work, we demonstrate that lifetime vibrational interference (LVI), which arises from a coherent excitation to overlapping intermediate levels, ruins the idea for obtaining XAS in the lifetime-broadening free regime [4]. We have performed an XAS study in the resonant Auger scattering (RAS) mode around the O1*s* → 2π resonance of carbon monoxide. The measurement was performed on beamline **BL27SU**. The monochromatized light was introduced into a cell to which CO molecules were admitted. Emitted electrons were sampled by a hemispherical electron energy analyzer (Gammadata-Scienta SES-2002) placed at right angles with respect to the photon beam. The right panel of Fig. 1 shows the total ion yield curve around the O1*s* → 2π resonance, which essentially corresponds to the conventional XAS profile. The resonance exhibits modulations due to the vibrational levels of the core-excited state. We have measured more than one-hundred RAS spectra to the $1\pi^{-1}$ $A^2\Pi$ final state, in this resonance range with a small photon energy step (15 meV). For an effective presentation of the RAS spectra, they were assembled as a two-dimensional (2D) map shown in Fig. 1. The 2D map is formed of diagonal stripes, each of which corresponds to a certain vibrational level of the final ion state. All stripes consist of "hills" of elliptical shape. It may appear, at first sight, that the hilltop positions simply reflect the vibrational progression of the core-excited state seen in the conventional XAS spectrum; however, a closer inspection reveals that the positions of the hilltops slightly deviate from the vibrational progression. The deviations of the resonance energies are essentially due to the LVI effect.

Figure 2(a) shows a lifetime-broadening free XAS spectrum extracted from the 2D map along the vertical axis. The spectrum corresponds to the cut going through the peak position of the global maximum on the 2D map at the kinetic energy of 516.9 eV. This

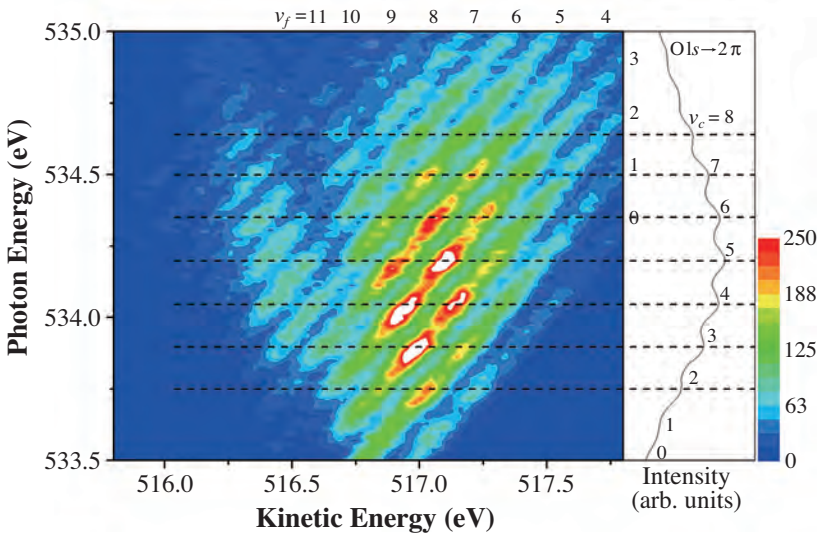


Fig. 1. 2D map of the RAS yields from CO as a function of photon energy and electron kinetic energy, measured around the O1*s* → 2π resonance. A total ion yield curve which essentially describes the conventional XAS profile is shown in the right panel.

extraction method follows the idea suggested in [3]. The spectrum shows sharp peaks with widths that are apparently narrower than the natural width of the core-excited state. However, the peak positions of the resonances do not coincide with the vibrational levels of the core-excited state, but instead follow fully the vibrational progression of the final ion state.

Obviously, XAS beyond the natural width is meaningful only if it gives the same positions of the resonances as the conventional XAS. In an effort to overcome the problem in the XAS profile obtained above, a more sophisticated path that follows the local maxima of the "hills" should be adopted in extracting a lifetime broadening XAS spectrum. By such an extraction method, we can obtain narrow XAS resonance by scanning over photon energy in the vicinity of a hill while keeping kinetic energy fixed at the hilltop. To obtain the rest of the resonances, we must tune the kinetic energy to the corresponding hilltops. Figure 2(b) shows a spectrum thus obtained. The resonance positions seen in the spectrum again disagree with those of the conventional XAS resonances. The peak deviations are due to the LVI.

In conclusion, although the extractions of RAS yields obey the spectral resolution beyond the natural width of the core-excited state, the resonant energies on the extracted XAS spectra deviate from the real resonance energies. The present work demonstrates clearly that interferences arising from coherent core excitation to overlapping electronic/vibrational levels spoil the idea of obtaining XAS spectra in a lifetime-broadening free regime.

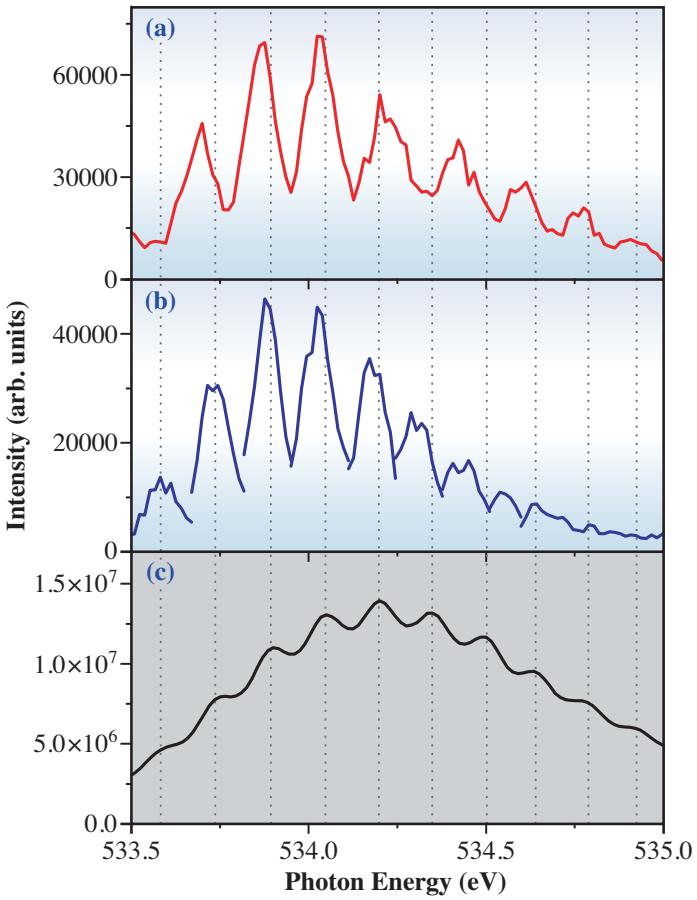


Fig. 2. **(a)** XAS spectrum extracted along the photon energy axis in the 2D map. **(b)** XAS spectrum extracted in the way explained in the text. **(c)** Conventional XAS spectrum.

Y. Hikosaka* and E. Shigemasa

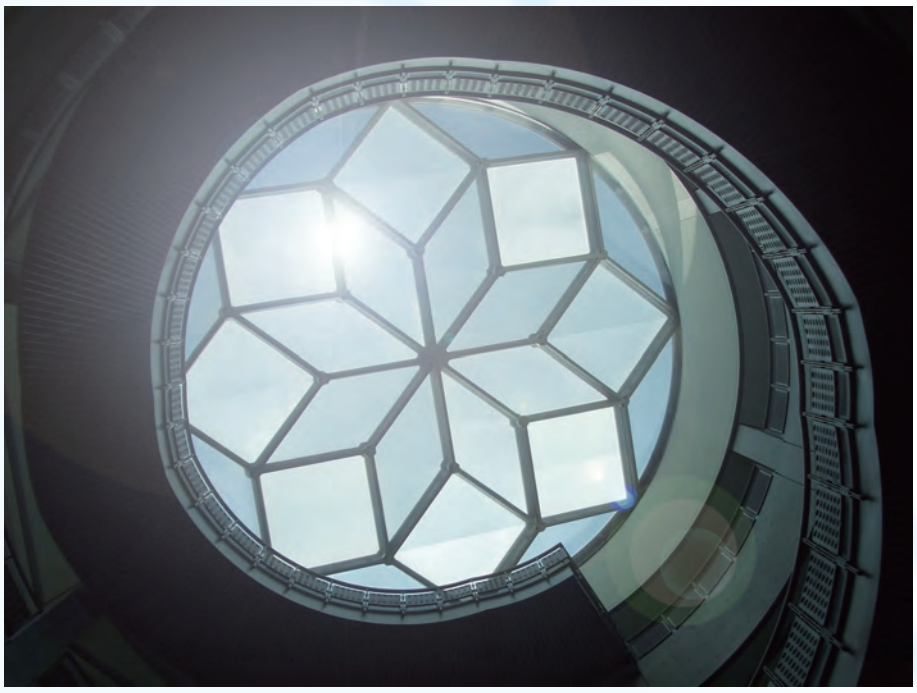
UVSOR Facility, Institute for Molecular Science

*E-mail: hikosaka@ims.ac.jp

References

[1] J. Tulkki and T. Åberg: J. Phys. B **15** (1982) L435.
[2] K. Hämäläinen *et al.*: Phys. Rev. Lett. **67** (1991) 2850.
[3] A. Kivimäki *et al.*: Phys. Rev. Lett. **81** (1998) 301.
[4] *Y. Hikosaka, Y. Velkov, E. Shigemasa, T. Kaneyasu, Y. Tamenori, J. Liu and F. Gel'mukhanov: Phys. Rev. Lett.* ***101*** *(2008) 073001.*

Nuclear



PHYSICS

The linearly polarized photon beam is produced by backward-Compton scattering of laser photons from 8 GeV electrons at BL33LEP. The current LEPS facility studies photoproduction of hadrons in the forward angles, where the high linear polarization plays an essential role to decompose various reaction processes.

The beam polarization is high and can be changed easily by changing the laser polarization. The LEPS covers photon energy region from 1.5 GeV to 2.9 GeV, which is suitable to study creation of strange quark and anti-quark pair near the production thresholds, such as photoproduction of the ϕ meson, hyperons and excited hyperons. The correlation between the polarization angle and the scattering plane (beam asymmetry) reveals the spin-parity combination of exchanged particles.

The first topic we chose is the Σ^{*-} photoproduction. The cross-section and the beam asymmetry of the $\gamma n \rightarrow \Sigma^{*-}K^{+}$ reaction are measured by using the LEPS spectrometer. The aim of the experiment is to know the reaction mechanism and the strength of the transition from a neutron to a Σ^{*-} by emission of a strange meson such as K and K^{*}. The experimental results provide stringent tests for theoretical models for hadrons and their interactions.

The second topic is a photoproduction of another excited hyperon, $\Lambda(1405)$, which is a candidate of a meson-baryon molecule resonance. The experiment has been carried out using a newly developed wide-acceptance counter, which is called TPC. The TPC detects decay products of excited hyperons and distinguishes $\Lambda(1405)$ from Σ^{*0}. We have observed striking energy dependence in the production rate of $\Lambda(1405)$. It could be a consequence of the unique structure of $\Lambda(1405)$.

Takashi Nakano
Research Center for Nuclear Physics
Osaka University



First Production of the Σ* Nucleon Resonance using the LEPS Spectrometer

One of the primary objectives of subatomic physics is to understand the substructure of the proton and other baryons, which are composed of three valence quarks and many gluons. Quarks are the fundamental constituents of the theory of the strong interaction, called QCD, and gluons are particles that mediate the strong force. In other words, gluons play the same role for the strong interaction as photons do for the electromagnetic interaction.

By sending a beam of high-energy photons onto a target containing protons and neutrons, new particles can be produced. This is done at the LEPS detector, located at the SPring-8 facility. High-energy photons are produced by Compton scattering of laser light from the 8 GeV beam of stored electrons. Some of the electron energy is transferred to the laser light, which reflects back from the electron giving it an energy of several GeV. This beam of photons strikes a target, creating new particles.

Baryons containing strange quarks are particularly interesting. There are no strange quarks in the proton or neutron, but there are several baryons known with one strange quark. One of these is known as the Σ baryon, which comes in three charge states: Σ^-, Σ^0 and Σ^+. The Σ^0 is difficult to measure because it overlaps with a nearby baryon resonance with neutral charge called the Λ. However, the Σ^- resonance is easier to measure in the LEPS spectrometer due to its negative charge, beamline **BL33LEP**. An excited state of this resonance, the Σ^{*-}, was measured for the first time just recently using LEPS [1].

Shown in Fig. 1, the vertical axis is the cross section (representing the probability to create this particle) and the horizontal axis is the energy of the photon in the nuclear reaction $\gamma n \rightarrow K^+ \Sigma^*$. The K^+ particle contains an anti-strange quark, and is typically seen in coincidence with the Σ baryons. The Σ^{*-} particle is not observed directly, but its presence is deduced by measuring the K^+ and then using conservation of momentum and energy to calculated the unique mass of the Σ*.

The four panels shown in Fig. 1 represent different center-of-mass (cm) angles, measured from the beam axis, of the K^+ as detected in the LEPS spectrometer. The points are the data and the curve represents the theoretical calculation. The theoretical model used here is based on quantum field theory, using Feynman graphs to calculate the probability to produce the above nuclear reaction. Details of the calculation are given in Ref. [2].

From comparison of the data and calculation, the value of the coupling constant (representing the overall strength of the nuclear reaction) between the neutron and the produced particles (the K^+ and Σ^{*-}). This, in turn, is proportional to the probability to produce a strange quark/anti-quark pair by the photon. Knowledge of these coupling constants enables theorists to make more quantitative predictions of the probability to produce other particles such as the Θ^+ pentaquark (see Ref. [3]).

Shown in Fig. 2, the vertical axis is the beam asymmetry (representing the probability of producing the reaction along the electric field of the photon) and the horizontal axis is the azimuthal angle around the beam axis, ϕ. The three panels on the left side are for detection of the ground-state Σ^- baryon and the three panels on the right are for detection of the excited-state Σ^{*-} baryon. In each case, the photon energy used increases in going from top to bottom panel. The curves are not theoretical predictions, but are simple fits to the function cos(2ϕ). Not only is the amplitude of the fitted function bigger for the left panel, the phase also changes sign for the right panel. This signifies that the reaction dynamics are sensitive

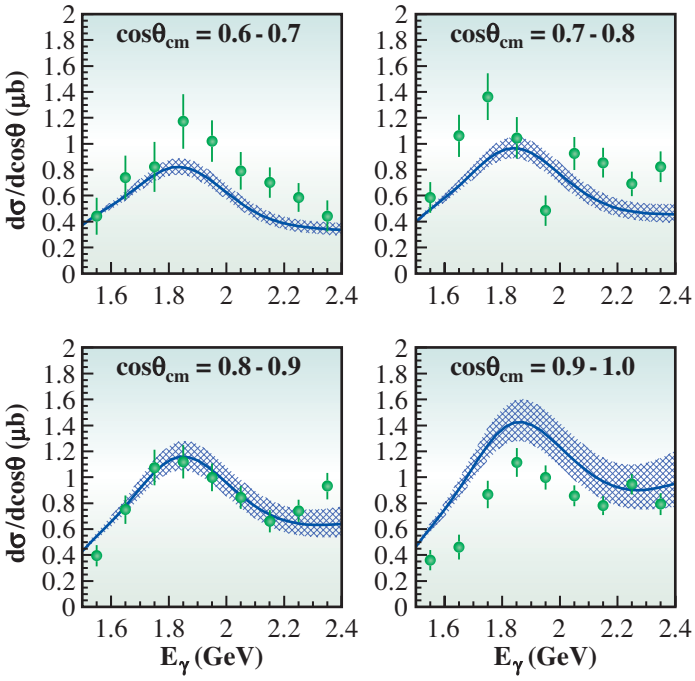


Fig. 1. Cross sections for the reaction $\gamma n \rightarrow K^+ \Sigma^{*-}$ as a function of photon energy. The curve is from the theoretical model of Ref. [2].

to the direction of the photon polarization. Hence, the Σ^- is produced in a different manner than the Σ^{*-} is produced. This is perhaps surprising since the primary difference between these two cases is simply the spin of the quarks.

Figure 3 summarizes the results presented in the previous figure. The vertical axis gives the amplitude of the fit at ϕ=0°, and the horizontal axis is the beam energy. The top panel is for production of Σ^- and the bottom panel for Σ^{*-}. The curve in the lower panel is from the same theoretical model as for Fig. 1. Here, this model predicts that the beam asymmetry should be nearly zero, meaning that the reaction is predicted to have little sensitivity to the photon polarization. Clearly, the theoretical model needs to be improved, which is only possible now that the data are measured.

In summary, the LEPS Collaboration has measured for the first time with high precision the probability to produce a Σ^* baryon using the reaction $\gamma n \rightarrow K^+ \Sigma^{*-}$ using the photon beam (γ) incident on the neutron (n) at the SPring-8 facility. The beam asymmetry was also measured, which is the first time ever for a Σ^* baryon. The cross sections are in reasonable agreement with theory, but improvements in the theoretical model are necessary to get agreement with the beam asymmetry.

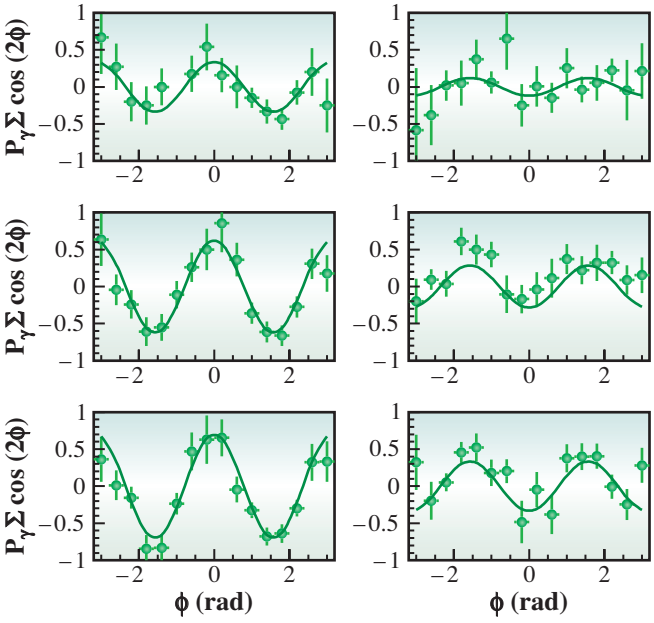


Fig. 2. Beam asymmetry as a function of the azimuthal angle ϕ for production of the Σ^- (left panels) and the Σ^{*-} (right panels). The beam energy increases from top panel to bottom panel.

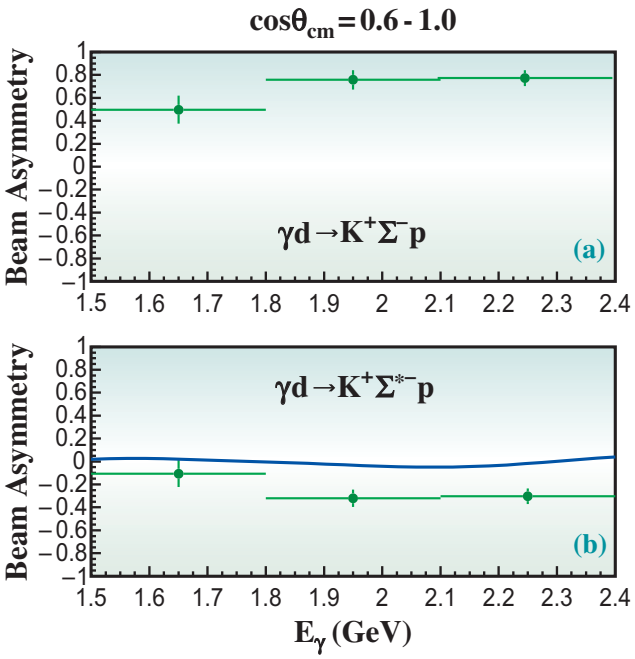


Fig. 3. Beam asymmetry as a function of photon energy for the Σ^- **(a)** and the Σ^{*-} **(b)**. The curve in the bottom panel is from the model of Ref. [2].

Ken Hicks for the LEPS Collaboration

Department of Physics and Astronomy,
Ohio University, USA

E-mail: hicks@ohioedu

References

[1] *K. Hicks, D. Keller, H. Kohri, D.S. Ahn, J.K. Ahn, H. Akimune, Y. Asano, W.C. Chang, S. Daté, H. Ejiri, S. Fukui, H. Fujimura, M. Fujiwara, S. Hasegawa, T. Hotta, K. Imai, T. Ishikawa, T. Iwata, Y. Kato, H. Kawai, Z.Y. Kim, K. Kino, N. Kumagai, S. Makino, T. Matsuda, T. Matsumura, N. Matsuoka, T. Mibe, M. Miyabe, Y. Miyachi, M. Morita, N. Muramatsu, T. Nakano, M. Niiyama, M. Nomachi, Y. Oh, Y. Ohashi, H. Ohkuma, T. Ooba, J. Parker, C. Rangacharyulu, A. Sakaguchi, T. Sasaki, P.M. Shagin, Y. Shiino, A. Shimizu, H. Shimizu, Y. Sugaya, M. Sumihama, Y. Toi, H. Toyokawa, A. Wakai, C.W. Wang, S.C. Wang, K. Yonehara, T. Yorita, M. Yoshimura, M. Yosoi and R.G.T. Zegers: Phys. Rev. Lett.* ***102*** *(2009) 012501.*
[2] Y. Oh *et al.*: Phys. Rev. C **77** (2008) 045204.
[3] T. Nakano *et al.*: Phys. Rev. Lett. **91** (2003) 012002.
[4] H. Kohri *et al.*: Phys. Rev. Lett. **97** (2006) 082003.

Photoproduction of Λ(1405) and Σ⁰(1385) on the Proton at E_γ ≈ 1.5–2.4 GeV

The quark model has succeeded in explaining the fundamental properties of hadrons, such as the mass, spin and parity. Despite great success of the quark model, there remain several mysteries in the understanding of hadrons. For example, some hadrons are predicted by the quark model but not observed experimentally (missing resonance), and the masses of some hadrons are significantly different from quark-model predictions.

Hyperons are particles consisting of three quarks with a strange quark. Photoproduction of hyperons is of interest because we can search for a missing resonance that couples to a *K*-meson hyperon pair rather than a pion nucleon pair. The cross section of hyperon photoproduction depends on its production mechanism and the form factor of the hyperon. Figures 1(a) and 1(b) show Feynman diagrams for hyperon photoproduction for t-channel K^- exchange process and s-channel direct reaction with a nucleon resonance (N^*) that couples to $K\Lambda$. By investigating cross sections of hyperon photoproduction in detail, we can extract the contribution of s-channel reaction and search for missing resonances. Some theorists predicted nucleon resonances that couple to $K\Sigma$(1385) and $K\Lambda$(1405). Therefore, it is important to study these resonances.

In addition to searching for missing resonances, it is of interest to study the internal structure of hyperon resonances. Both of Σ(1385) and Λ(1405) hyperons contain u, d and s quarks. The Σ(1385) hyperon is firmly established as a three-quark baryon (q^3 baryon). On the contrary, the internal structure of the Λ(1405) hyperon is ambiguous [1]. In the quark model, Λ(1405) is assigned as a *p*-wave q^3 baryon. However, the mass of Λ(1405) is much smaller than the quark-model calculation, and therefore, Λ(1405) is widely considered as a candidate for a kaon-nucleon molecular state or a q^4 anti-q pentaquark baryon.

Photoproduction of Σ(1385) has been measured by the CLAS Collaboration at TJNAF. A theoretical calculation by Oh *et al.* [2] using an effective Lagrangian was then compared with the data and the contributions from nucleon resonances were discussed. Experimentally, Λ(1405) has been studied in meson-induced and proton-induced reactions so far. However, understanding of the photoproduction of Λ(1405) is very limited because of the lack of experimental data.

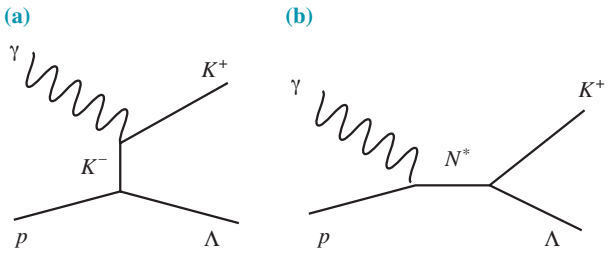


Fig. 1. Feynman diagrams of hyperon photoproduction.

We have studied photoproduction of Λ(1405) and Σ(1385) hyperons on the proton for an energy range of 1.5-2.4 GeV at the Laser-Electron Photon facility at SPring-8 (LEPS), beamline **BL33LEP**. We measured production cross sections of Λ(1405) and Σ(1385). This is the first measurement of the cross section of Λ(1405) photoproduction. The production cross section of Λ(1405) decreased largely in the higher photon energy region with respect to that of Σ(1385). Thus, the production mechanisms or form factors for these two hyperons must be quite different. The production cross sections were compared with theoretical calculations. We found that the production cross sections of Λ(1405) could not be explained by a conventional theoretical model. Thus, an exotic production mechanism, such as nucleon resonance contribution, might be necessary to understand the photoproduction of Λ(1405) [2]. A brief overview of the experiment is described below.

In this experiment, forward going K^+'s from the $\gamma p \rightarrow K^+X$ reaction were detected in the LEPS spectrometer. Using the energy-momentum conservation and measuring the momentum of a K^+-meson and the energy of a photon, we can obtain the missing mass of the $\gamma p \rightarrow K^+X$ reaction, MM(K^+), which corresponds to the masses of Λ(1405) and Σ(1385). However, in principle, it is impossible to separate Λ(1405) and Σ(1385) in *MM*(K^+) because the intrinsic widths of these resonances, 36 MeV/c^2 for Σ(1385) and 50 MeV/c^2 for Λ(1405), are much larger than their mass difference.

To distinguish these two resonances, a time projection chamber (TPC) was used together with the LEPS spectrometer to facilitate the detection of the decay products of these hyperon resonances. Figure 2 shows a schematic view of the experimental setup. The main decay mode of Σ(1385) is the Λπ channel, where Λ is the ground state. On the other hand, Λ(1405) is prohibited from decaying into a Λπ pair due to the conservation of isospin. Thus, Σ(1385) production can be identified by detecting a Λ hyperon. Both of Λ(1405) and Σ(1385) decay into the Σπ channel, where Σ is the ground state, but we can estimate the contamination of Σ(1385) using the yield obtained from its Λπ decay mode and the known

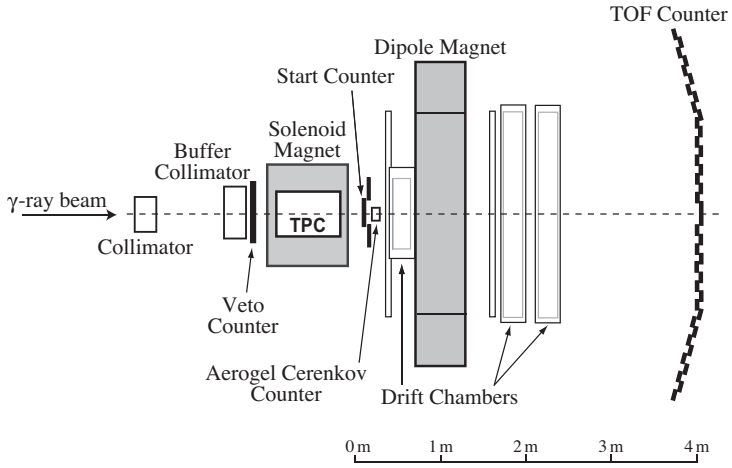


Fig. 2. Schematic view of experimental setup.

branching ratio of the Λπ and Σπ decay channels of Σ(1385). The production ratios of Λ(1405) to Σ(1385) were obtained in two photon energy ranges. The scattering angle of K^+ in the center-of-mass frame, Θ_K was required to satisfy $0.8<\cos\Theta_K<1.0$. The production ratios of Λ(1405) to Σ(1385) were obtained as $\Lambda(1405)/\Sigma(1385)\approx0.54$ and 0.084 for $1.5<E_\gamma<2.0$ GeV and $2.0<E_\gamma<2.4$ GeV, respectively. The absolute values of the production cross sections were obtained from high statistics liquid hydrogen data with the input of production ratios of Λ(1405)/Σ(1385) obtained above. The differential cross sections of Λ(1405) production were found to be $d\sigma/d(\cos\theta)\approx0.43$ μb and 0.072 μb for $1.5<E_\gamma<2.0$ GeV and $2.0<E_\gamma<2.4$ GeV, respectively. Those of Σ(1385) production were $d\sigma/d(\cos\theta)\approx0.80$ μb and 0.87 μb for $1.5<E_\gamma<2.0$ GeV and $2.0<E_\gamma<2.4$ GeV, respectively.

The production cross sections of Σ(1385) were almost constant with respect to the photon energy and consistent with a theoretical prediction in both photon energy ranges. Closed circles with error bars in Fig. 3 show the experimental data for the cross sections of Λ(1405) production and a solid line and a shaded area show theoretical calculations. The production cross section in the lower photon energy region is much higher than theoretical values. The production mechanisms that are not considered in the theoretical model are necessary to explain the production cross section of Λ(1405) in this photon energy region. Recently, Jido and Kanada-En'yo have proposed a nucleon-like molecular state consisting of K^+K^-p, which decays into $K^+\Lambda(1405)$ [3]. If this nucleon resonance is created in the intermediate state, the production cross section is enhanced. However, in view of our limited statistics, further data are needed for more quantitative discussions, which will be available in future experiments at SPring-8/LEPS. We already obtained data with higher statistics to study photoproduction of Λ(1405) at SPring-8/LEPS, and more precise data will be shown in the near future.

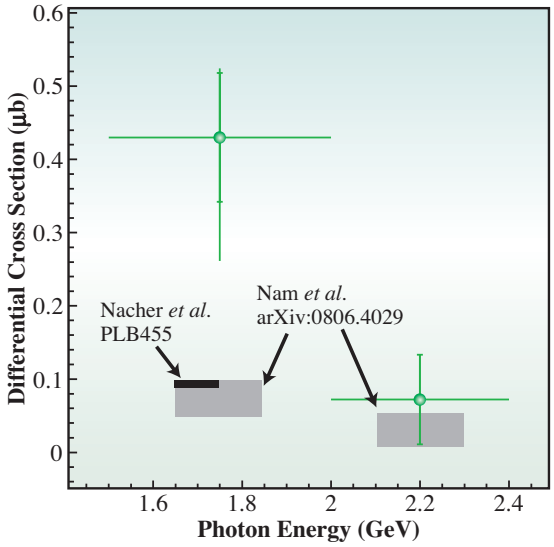


Fig. 3. Differential cross section of Λ(1405) photoproduction.

Masayuki Niiyama for the LEPS Collaboration

RIKEN (Wako)

E-mail: niiyama@rcnp.osaka-u.ac.jp

References

[1] R.H. Dalitz: Euro. Phys. J. C **15** (2000) 748 .
[2] Y. Oh *et al.*: Phys. Rev. C **77** (2008) 045204.
[3] *M. Niiyama, H. Fujimura, D.S. Ahn, J.K. Ahn, S. Ajimura, H.C. Bhang, T.H. Chang, W.C. Chang, J.Y. Chen, S. Daté, S. Fukui, H. Funahashi, K. Hicks, K. Horie, T. Hotta, K. Imai, T. Ishikawa, Y. Kato, K. Kino, H. Kohri, S. Makino, T. Matsumura, T. Mibe, K. Miwa, M. Miyabe, N. Muramatsu, M. Nakamura, T. Nakano, Y. Nakatsugawa, Y. Ohashi, D.S. Oshuev, J.D. Parker, N. Saito, T. Sawada, Y. Sugaya, M. Sumihama, J.L. Tang, M. Uchida, C.W. Wang, T. Yorita and M. Yosoi: Phys. Rev. C **78** (2008) 035202.*
[4] D. Jido and Y. Kanada-En'yo: Phys. Rev. C **78** (2008) 035203.



Accelerators & Beamlines Frontiers

Beam Performance

Developments and Upgrades of Storage Ring

Improvement of Dynamic Aperture by Counter-Sextupole Magnets

In the SPring-8 storage ring, there are four magnet-free long straight sections of 30 m length. These long straight sections were installed in 2000 by locally rearranging quadrupole and sextupole magnets. At that time, we maintained the periodicity of the cell structure, particularly that of sextupole field distribution along the ring, since the high periodicity leads to the large dynamic aperture. To maintain the periodicity as high as possible, we adopted a scheme in which "betatron phase matching" and "local chromaticity correction" are combined. The betatron phase matching keeps the dynamic aperture for on-momentum particles large and the latter enlarges that for off-momentum ones with local chromaticity correction by focusing sextupole magnets (SFL) in matching cells. However, the nonlinear kick of the SFL slightly breaks the periodicity and reduces the dynamic aperture.

To improve the symmetry of the storage ring, we installed "counter-sextupole magnets" (SCT) in every long straight section in 2007 [1-3]. These magnets are placed π apart from the SFL in the horizontal betatron phase, so they can minimize the harmful nonlinear kick of the SFL. After installing the SCT, we confirmed the enlargement of the dynamic aperture by measuring the injection efficiency. Figure 1 shows the dependence of the injection efficiency on the gaps of the in-vacuum undulators, ID20 and ID23. From the measurement, we found that the injection efficiency is improved by 6% by the SCT, which contributes to the stable top-up operation.

Recently, to investigate the nonlinear dynamics of the storage ring, especially the effect of the SCT, we directly measured the dynamical aperture. Observing the survival rate of the stored beam after instantly giving the horizontal displacement by the pulse bump magnets, we measured the horizontal dynamical aperture. The survival rate is given by the ratio of the stored currents before and after the kick caused by the bump magnets, or that of the voltage sums of 4 electrodes of the turn-by-turn beam position monitors. The latter can give the decay process of the survival rate as well as the oscillation of the beam, so it is suitable to analyze the nonlinear dynamics.

Figure 2 shows the dependence of the survival rates obtained by turning the SCT on and off, from which we can estimate the dynamic aperture. Note that the reduction of the survival rate at both the ends in the case of the SCT on is limited not by the dynamical but the physical apertures. This is found from the decay process of the survival rate. In the case of the SCT on, the survival rates at the ends suddenly drop at the first turn, which means that the stored electrons are lost because of the physical aperture. Thus, the dynamic aperture with the SCT is larger than that as observed in Fig. 2. The measured dynamic aperture in the case of turning the SCT off is estimated to be the horizontal displacements at which the survival rate decreases. We find that the estimated dynamic aperture fairly well agrees with that estimated by computer simulation.

To investigate the mechanism of limiting the dynamic aperture, we analyzed the beam oscillation after the sudden displacement. The Fourier analysis of the oscillation gives the dependence of the betatron tune on the displacement, i.e., the amplitude, as shown in Fig. 3. The circles and crosses in the figure represent the horizontal and vertical betatron tunes,

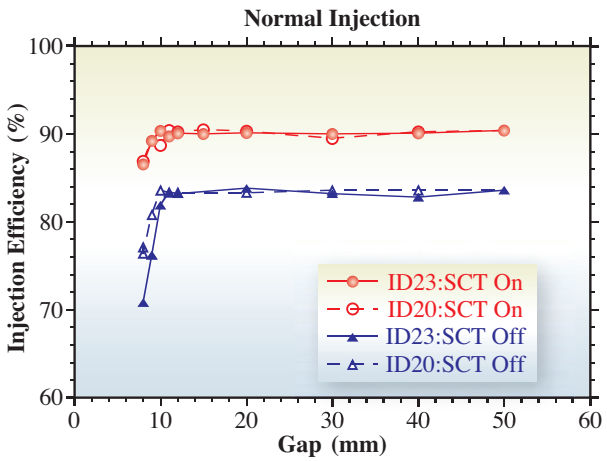


Fig. 1. Injection efficiency *vs.* in-vacuum undulator gaps.

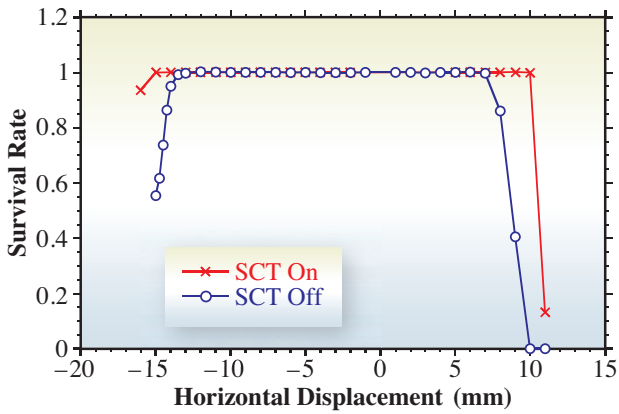


Fig. 2. Dependence of the survival rate on the displacement caused by the bump magnet.

respectively, and the dotted lines denote the calculated ones. As expected, we find from Fig. 3 that the amplitude-dependent tune shift is reduced by the SCT, and namely, that the nonlinear kick is weakened. Plotting the horizontal and vertical tunes on a map, we obtain the tune diagram shown in Fig. 4. The axes indicate the fractional parts of the betatron tunes, and the dashed lines represent the nearest third-order resonances, and the dotted lines represent the higher ones. Then we can conclude that, in the case of the SCT off, the dynamic aperture is limited by the normal sextupole resonance $n_x+2\,n_y=77$.

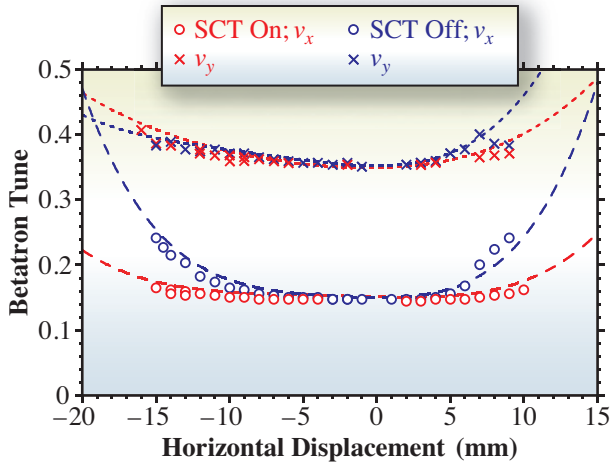


Fig. 3. Amplitude-dependent tune shift.

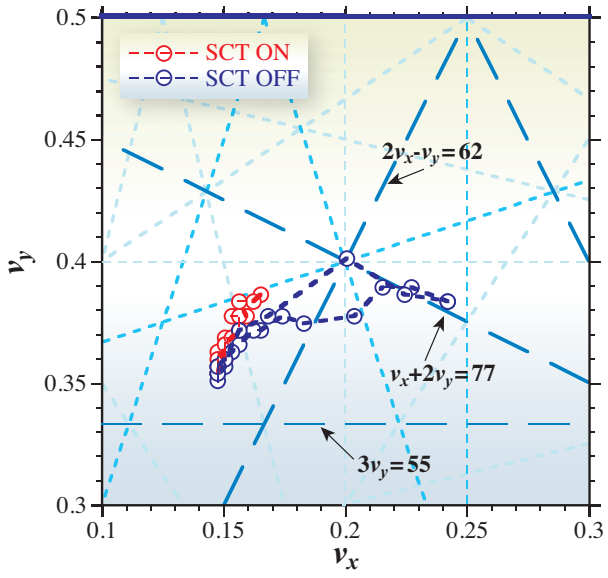


Fig. 4. Tune diagram.

Short-Bunch Operation with Low-α Optics

The length of circulating electron bunches can be made shorter by changing the storage ring optics to that having a smaller value of momentum compaction factor α. For the nominal optics in user time the lowest order term (see below) is $\alpha_0=1.68\times10^{-4}$ and the rms bunch length σ is 13 ps at the limit of zero bunch current. Since the bunch length σ is proportional to the square root of α at low bunch current, we can reduce σ by adopting low-α optics for generating shorter X-ray pulses.

The momentum compaction factor α represents the dependence of path length on momentum deviation Δp/p of an electron and can be written as $\alpha=\alpha_0+\alpha_1(\Delta p/p)+\alpha_2(\Delta p/p)^2+\ldots$. Although the lowest order term α_0 is dominant in conventional optics, its value can be lowered by changing quadrupole strengths in the arc section in exchange for increasing the emittance. Figure 5 is an example of such low-α optics, where optical functions are shown for a quarter of the storage ring. We see that the horizontal dispersion function η_x is positive at arc sections and negative at straight sections, and this enables us to reduce α. For the optics shown in Fig. 5, the reduction factor in α_0 is 11 although the emittance increases by a factor of 7. The value of α_0 can be reduced further by carefully tuning quadrupole strengths. In such optics with an extremely small α_0, however, the next order term α_1 (Δp/p) is dominant and the energy oscillation of electrons within a bunch becomes unstable. We then need to reduce α_1 at the same time and this can be carried out by tuning sextupole strengths in the arc section.

We optimized quadrupole and sextupole strengths and carried out beam tests with low-α

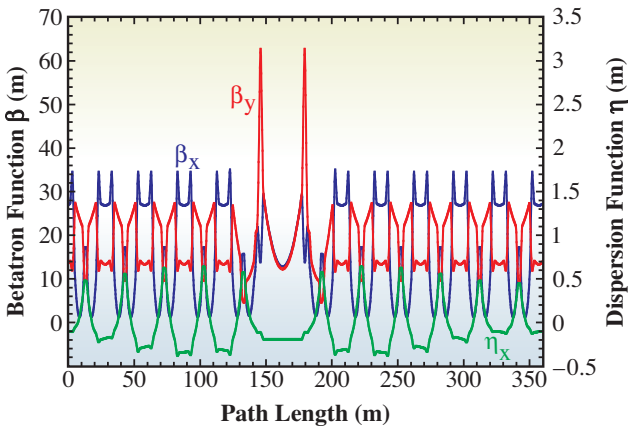


Fig. 5. Low-α optics. The horizontal and vertical betatron functions (β_x and β_y) and dispersion function (η_x) are shown for a quarter of the ring.

optics. By reducing α_0 and α_1 and measuring the bunch length σ with an optical streak camera at a low bunch current of 0.01 mA, we obtained the α_0-dependence of σ as shown in Fig. 6. The shortest bunch length of 2.2 ps was achieved for the optics with $\alpha_0=5.8\times10^{-6}$. This optics with $\sigma=2.2$ ps, however, has a very short beam lifetime due to a narrow range of energy acceptance. For stable beam operation of this optics, we further need to carefully tune the sextupoles. In addition, we also found by computer simulations that octupole magnets are effective in controlling α_2 and enlarging the energy acceptance. Further studies on these are necessary for the stable operation of the low-α optics.

To observe the performance of the low-α optics, we carried out a test experiment in the 25-m-long undulator beamline. A total current of 0.14 mA was stored in 12 bunches. The optics used has $\alpha_0=1.61\times10^{-5}$ and the bunch length was measured to be $\sigma=4$ ps. The data analysis is in progress.

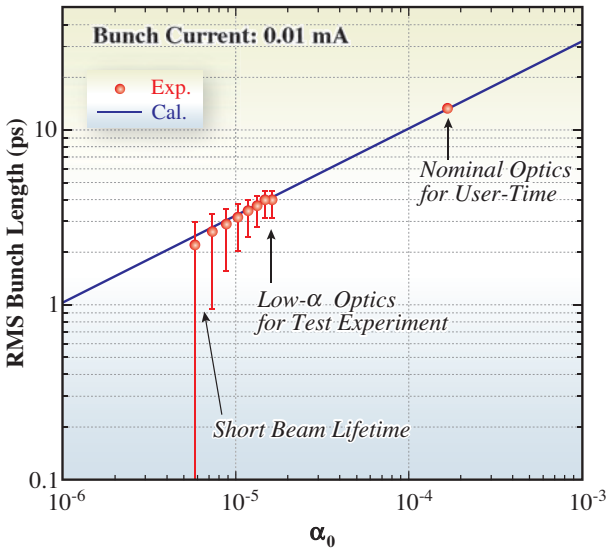


Fig. 6. RMS bunch length at a low bunch current of 0.01 mA as a function of α_0. The experimental data was obtained using an optical streak camera whose time-scale had been calibrated with a stored beam. The timing jitter was estimated to be 2.5 ± 1 ps and corresponding error bars are shown.

Suppression of the Filling Pattern Dependence of the BPM Signal Processing Electronics

The signal processing electronics of the storage ring beam position monitors (BPMs) were replaced during the summer shutdown of 2006 and it was found that they had the filling pattern dependence as large as over a hundred micrometers, as reported in Research Frontiers 2007. In addition, it was reported in Research Frontiers 2007 that the countermeasure to suppress the filling pattern dependence was to attach the band pass filters (BPFs) at the input of each channel of the electronics, and preliminary results showed the effectiveness of the BPF. In 2008, the production version BPF was made, attached to all the electrode channels, and the performance was evaluated using the actual beam.

The BPFs were attached during the short shutdown period from the end of October to the beginning of November. After the storage ring operation was restarted, no significant indication concerning the filling pattern dependence was reported for ordinary user operations.

During the machine study period, the effect of BPF was evaluated. As a measure of the effect, root mean square (RMS) values between two different measurements of the closed orbit distortion (COD), averaged over all the BPM, were used, which were defined as

$$RMS_x\,(A\text{-}B)=\sqrt{\frac{\sum_{i=1}^{N_{BPM}}\left(x_i^A-x_i^B\right)^2}{N_{BPM}}},\quad RMS_y\,(A\text{-}B)=\sqrt{\frac{\sum_{i=1}^{N_{BPM}}\left(y_i^A-y_i^B\right)^2}{N_{BPM}}}$$

where RMS_x is in the horizontal direction and RMS_y is in the vertical direction, the superscripts A and B indicates the two different measurements: measurement A and measurement B, i runs through 1 to the number of BPM N_{BPM}, x_i and y_i are the measured position values in the horizontal and vertical directions of i-th BPM.

The filling patterns in Table 1 were selected for the evaluation. These filling patterns were taken from the typical user runs. The storage ring was operated with 100 mA total stored current for all the patterns in Table 1. The change in the measured values of the COD between two different patterns was estimated using the RMS values between the COD measurements of the two different filling patterns, which were expressed as $RMS_{x/y}$*(FP1-FP2)* according the equation, where *FP1* and *FP2* are the indices of the filling patterns.

During the evaluation runs, the periodic COD correction was switched off. The COD correction was carried out during ordinary user runs to compensate the drift of the beam orbit itself. However, the correction process induced an artificial jump of COD by exciting the steering magnets that introduced some difficulties in evaluating the filling pattern dependence of the electronics.

The stored beam had to be discarded and refilled for the filling pattern to be changed, and it took approximately or over 20 minutes. During the time of the filling pattern change, the COD continued to drift. The RMS values between two different filling patterns, $RMS_{x/y}(FP1\text{-}FP2)$, should be compared with the RMS values caused by the orbit drift in the same amount of time for the filling pattern change. For comparison, we used the same procedure except for changing the filling pattern: the beam was discarded and refilled without changing the filling patterns and calculated RMS values, $RMS_{x/y}\ (FP1_1\text{-}FP1_2)$, where $FP1_1$ and $FP1_2$ are the indices of the two different measurements of the same filling pattern $FP1$.

Table 1 shows the RMS values of the differences between the COD measurements just before the discard and just after the refill of the beam with a different filling pattern. Table 2 is for the RMS values of the differences between the COD measurements just before the discard and just after the refill of the beam without changing the filling pattern. The time intervals of the two measurements in both Tables 1 and 2 were about the same, and the RMS values in both tables showed no significant difference. The main effect on the RMS values in both Tables 1 and 2 was the drift of the closed orbit during the interval of two measurements. Therefore, no significant differences in the measured beam position attributed to the filling pattern dependence of the electronics were observed.

In Fig. 7, the RMS evolution from the beginning of the measurement for the evaluation, $RMS_{x/y}(t\text{-}t_0)$, is shown. The RMS values were obtained for the differences in the position data from the reference COD measurement that was carried out at the beginning, t_0, of the evaluation runs. The filling patterns were changed in the order that is indicated in the figure: multi-bunches, 203 bunches, 1/12+10 s, and 1/14+12 s. Each filling pattern was repeated twice to estimate the reproducibility.

The RMS tended to increase almost monotonically in both x and y directions, regardless of the change in the filling pattern. No significant jump of the data between the different filling patterns was observed in the plot. The drift of the closed orbit was the dominant effect of the evolution of the RMS values.

Thus, the closed orbits can be set continuously across any filling pattern for the ordinary user run of the storage ring.

Table 1. RMS values of differences between two different filling patterns: $RMS_{x/y}(FP1\text{-}FP2)$

filling pattern 1	filling pattern 2	Δt (min. : sec.)	RMS_x (mm)	RMS_y (mm)
multi-bunches	203 bunches	24:20	6.8	2.9
203 bunches	1/12+10s	19:48	4.2	4.5
1/12+10s	1/14+12s	21:41	5.9	2.4
1/14+12s	multi-bunches	18:25	4.0	4.3

multi-bunches: 12 units composed of 160 sequential buckets filled with some 50-μA current each followed by 43 empty buckets were equally spaced around the storage ring.

203 bunches: equally spaced 203 buckets, i.e., every 12 buckets, were filled with 0.5-mA current each.

1/12+10s: Consecutive 203 buckets were filled with electrons; 203 buckets corresponds to 1/12 of the total bucket number of 2436 of the storage ring. The remaining 11/12 part of the ring is filled with equally spaced 10 isolated bunches with 1.5-mA current each, i.e., every 203 buckets were filled with 1.5-mA current. The current of 1/12 part was 85 mA.

1/14+12s: Consecutive 174 buckets were filled with electrons; 174 buckets correspond to 1/14 of the total bucket number of the storage ring. The remaining 13/14 part of the ring is filled with equally spaced 12 isolated bunches with 1.6-mA current each, i.e., every 174 buckets were filled with 1.6-mA current. The current of 1/14 part was 80 mA.

Table 2. RMS values of differences between two different times of the measurement within the same filling pattern: $RMS_{x/y}\ (FP1_1\text{-}FP1_2)$

filling pattern 1	filling pattern 2	Δt (min. : sec.)	RMS_x (mm)	RMS_y (mm)
multi-bunches	multi-bunches	12:14	5.1	2.8
203 bunches	203 bunches	21:30	6.4	1.9
1/12+10s	1/12+10s	20:21	6.6	2.3
1/14+12s	1/14+12s	18:48	3.3	2.3

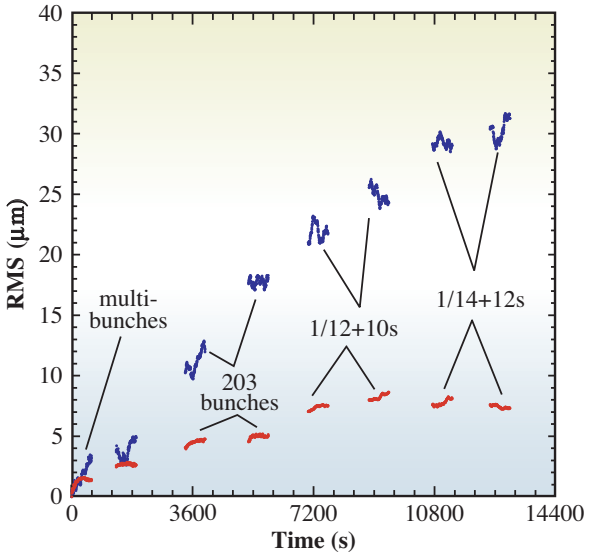


Fig. 7. RMS values of the difference between the measured position data from the measurement at the reference time. Horizontal axis: time in seconds from the starting time: $\Delta t = t\text{-}t_0$. Vertical axis: RMS values in μm: $RMS_{x/y}(t\text{-}t_0)$. Blue marks are in horizontal direction ($RMS_x(t\text{-}t_0)$). Red marks are in vertical direction ($RMS_y(t\text{-}t_0)$). The filling patterns are indicated in the plot. Explanations of each filling pattern are described in the caption of Table 1. Each filling pattern was repeated twice. The blank regions between the data points were the time for discard and refill of the beam, in which the COD measurements could not be carried out.

Development of Bunch-by-Bunch Feedback

Currently, a high-current bunch of more than 10 mA/bunch can be stored in the storage ring by suppressing the horizontal and vertical mode-coupling single-bunch instabilities with the bunch-by-bunch feedback system (BBF). However, the high gain or short feedback damping time of less than 1 ms of the BBF is necessary to suppress these instabilities. Simultaneously, a wide horizontal acceptance of the BBF is required to suppress the horizontal betatron motion excited by the formation of the injection bump orbit. To meet those requests, we increased the feedback strength by introducing of high-power amplifiers, and we are constructing a high-efficiency horizontal kicker (Fig. 8). For the longitudinal feedback for possible low-energy high-current operation in the near future, the new type of longitudinal kicker with high shut impedance per unit length is also under construction.

Moreover, we are developing a tune-tracking RFKO system for the booster synchrotron based on the bunch-by-bunch feedback system. Currently, the booster is operating every seconds during the wait of the injection to stabilize the system. However, the on-demand operation of the booster is preferred for saving of electricity. With this mode, betatron tune drift occurs in this operation mode because of the unstable temperature of the magnet system and it is difficult to perform the bunch purification by RFKO. To overcome this tune drift, we are testing the tune tracking RFKO system shown in Fig. 9. The main bunch is excited by the bunch-by-bunch feedback system and the oscillation signal is sent also to the RFKO system. The bunch-by-bunch feedback system uses an FIR filter less than ten taps and the tracking speed to the tune is fast enough. The tune shift between the main bunch and satellite bunches produced by the current dependent tune shift is also intended to be compensated by the BBF by careful adjustment of the phase of the FIR filters. In a preliminary test, we obtained the purity of 10^{-8} to 10^{-9}, which is not sufficient for the required purity of 10^{-10}; further development is necessary.

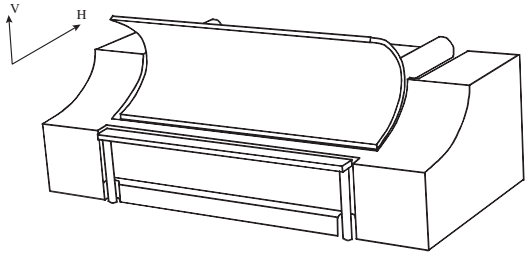


Fig. 8. High-efficiency horizontal kicker. One quadrant is shown with a large horizontal electrode of full shape. The vertical kicker electrode is also shown in the bottom of the figure.

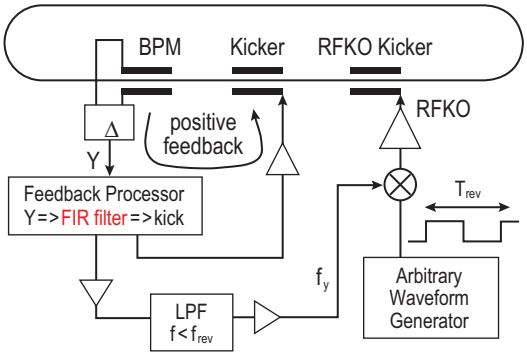


Fig. 9. Tune tracking RFKO system. The vertical betatron motion of the main bunch is excited by the feedback processor (positive feedback loop). The oscillation signal is also fed to the RFKO system to kick out the satellite bunches. The negative vertical tune shift of the main bunch is intended to be compensated by the feedback.

Beam Loss Monitor

One of the major concerns in the SPring-8 storage ring (SR) is irradiation-induced damage due to beam loss to the environment surrounding the accelerator. In 2003, a vacuum leakage was caused by the meltdown of a vacuum chamber at the injection section during the time of a beam abort [4]. In addition, demagnetization of permanent magnets for the in-vacuum insertion devices (IDs) is caused by the irradiation of circulating electron beam in the SR [5].

To observe a beam loss, to manifest its mechanism, and to handle it, a beam loss monitoring system has been developed. The beam loss monitor is composed of a beam loss detector and a noise detector. The former detects secondary particles with PIN photodiodes, of which the spectral range of the sensitivity is 780 ~ 1100 nm, the radiant sensitive area is 2.65×2.65 mm^2 and no reversed bias voltage is given, when a circulating electron beam hits a vacuum chamber and is lost. The latter is used to compensate for background noises (see Fig. 10). Each detector is shielded by an aluminum chassis of 50×80×34 mm^3 and is set to characteristic points in the tunnel of the SR such as the injection point, the beam dump point, the chamber for the irradiation experiment (SS48),

and the entrance of the long in-vacuum ID (ID19). These signals are extracted through a shielded two-pair twist cable into a signal processing circuit outside the tunnel, and then digitized using a digital recorder (GR-7500). The signal is monitored in the central control room.

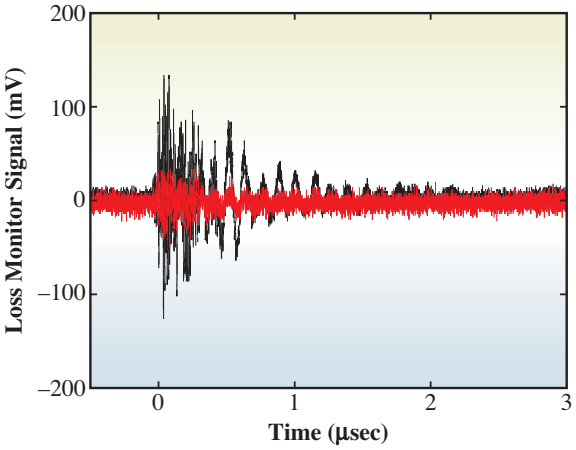


Fig. 10. Background noise detected using a beam loss monitor before (black) and after (red) compensation, when the injection bump magnet is turned on.

By monitoring beam losses with beam loss monitors set around the SR, it can be specified where the beam loss occurs. A typical beam loss signal on the nominal injection is shown in Fig. 11. The beam loss signal was observed at the injection point and at the SS48. An injected beam coherently oscillates around the reference orbit because of the off-axis injection scheme. From Fig. 11, we see that a part of the injected beam hits the vacuum chamber and is lost at the injection point and at the SS48. In this case, one can expect that, by locally deforming the reference orbit around there, this part can survive and achieve an equilibrium beam distribution, and the injection efficiency from the injector to the SR will improve. An example of such experiments is shown in Fig. 12, where the bump orbit was locally set in the vertical direction at the SS48. The average injection efficiency became higher as the height of the local bump was increased. This indicates that the irradiation damage due to beam loss surrounding the SR on the timing of nominal injection can be more or less suppressed.

In the future, we will strategically install additional beam loss monitors to watch and handle beam losses effectively.

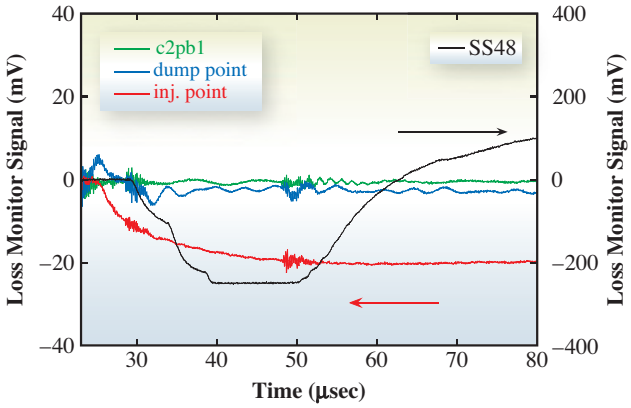


Fig. 11. Beam loss signal measured using a beam loss monitor on nominal injection. "c2pb1" denotes beam loss monitor set near absorber-3 of cell-2 in SR.

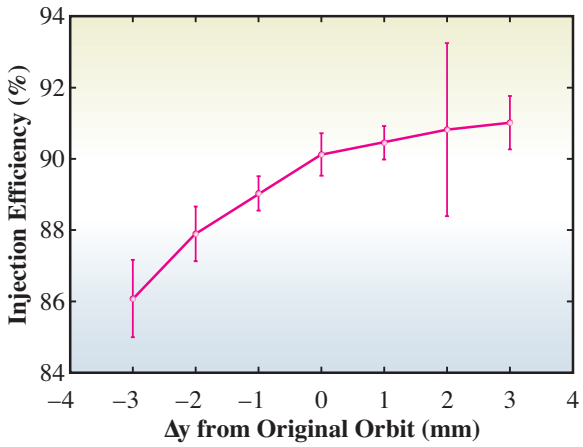


Fig. 12. Injection efficiency (SR/SSBT) dependent on vertical local bump orbit at SS48.

Development of Accelerator Diagnostics Beamlines

The generation of short X-ray pulses is now a challenge at SPring-8. The visible streak camera at the accelerator diagnostics beamline I (BL38B2) provides crucial information on the longitudinal bunch structures of the electron beam essential to tackle the challenge. One approach to generate shorter synchrotron radiation pulses is to shorten the bunch length itself by decreasing the momentum compaction factor α of the storage ring. The natural bunch length is proportional to the square root of factor α. The longitudinal bunch profiles measured using the streak camera confirmed that the bunch length was successfully shortened to about one-third by decreasing α by one order (Fig. 13). Another approach to obtain short X-ray pulses is by slitting a

vertically tilted bunch. By giving a pulsed vertical kick to an electron bunch, the head-tail oscillation of the bunch can be excited in the presence of nonzero vertical chromaticity. Figure 14 shows the vertical beam tilt observed using the streak camera operated in the dual-time scan mode. The maximum observed difference between the head and tail of the bunch was about 2 mm. Further studies to obtain short X-ray pulses by this method are in progress.

The accelerator diagnosis beamline II (BL05SS) has an ID light source and two optics hutches. In April 2008, we successfully delivered the first ID light to the optics hutch II that contains a cryogenically cooled monochromator. We are now investigating the diagnostics of both the transversal and longitudinal properties of the electron beam by observing the imprints on the spectral, spatial, and temporal characteristics of the synchrotron radiation of the ID. The magnet array mounted on the ID is of Halbach type with 51 periods 76 mm long. The maximum value of the deflection parameter K is 5.8 when the magnet gap is minimum at 20 mm. The spectral photon fluxes of the ID were measured for both the regular user optics (ε=3.4 nm·rad) and the low-α optics mentioned above (ε=24.8 nm·rad). Figure 15 and Fig. 16 show spectral fluxes of the 1st and 19th harmonics, respectively. The peak of higher harmonics as high as 19 is clearly observed, which shows success of the elaborate tuning of the magnetic field in the assembling of the ID. The observed spectra of the low-α optics show reduction of the peak intensity and growth of the tail in the low-energy region, which are distinct imprints of large emittance of the electron beam.

We have been developing a method for the real-time measurement of the energy spread of the electron beam on the basis of idea of observing the divergence of monochromatic higher harmonics of the ID in the vertical direction. The vertical divergence is sensitive to the energy spread of the electron beam because of the small vertical emittance of SPring-8, while the horizontal divergence is dominated by the horizontal emittance. To demonstrate our idea, we observed the vertical profile of the 19th harmonics of the ID while changing the effective beam energy spread. The effective energy spread was increased by exciting the beam energy oscillation by modulating the phase of the RF voltage at the synchrotron

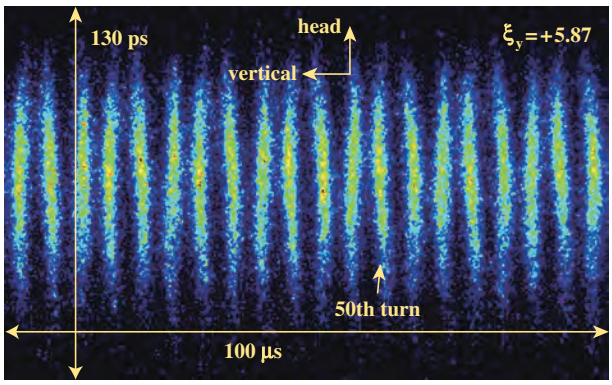


Fig. 14. Excited head-tail oscillation of a stored electron bunch observed using the visible streak camera operated in the dual time scan mode.

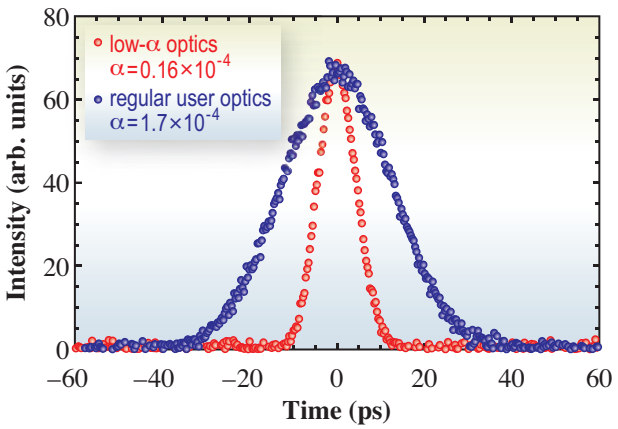


Fig. 13. Longitudinal bunch profiles measured for low-α and regular user optics, respectively. The bunch length was successfully made shorter by decreasing α.

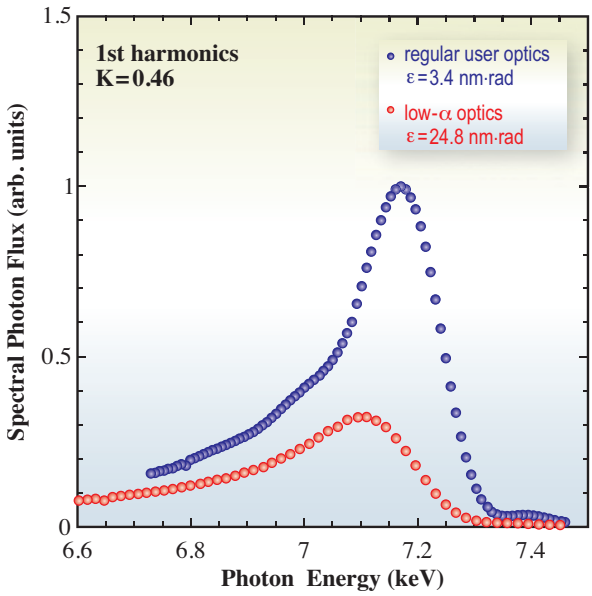


Fig. 15. Spectral photon fluxes of the 1st harmonics of the ID. The magnet gap was 80 mm and the deflection parameter K was 0.46. The blue and red dots show the spectra measured for the regular user and the low-α optics, respectively.

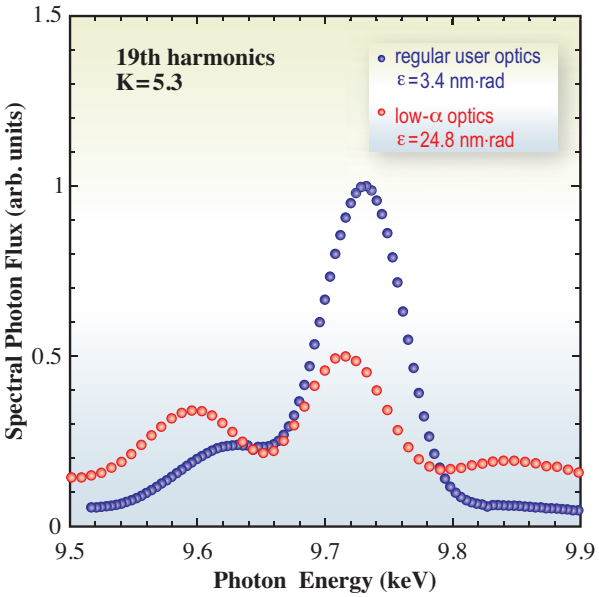


Fig. 16. Spectral photon fluxes of the 19th harmonics of the ID. The magnet gap was 22 mm and the deflection parameter K was 5.3. The blue and red dots show the spectra measured for the regular user and the low-α optics, respectively.

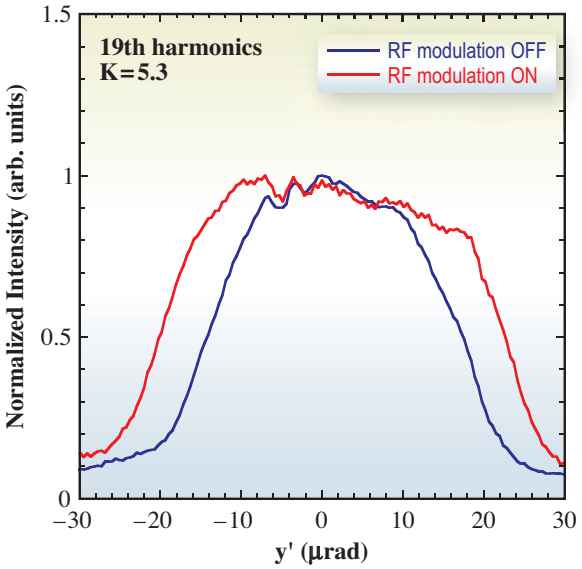


Fig. 17. Measured vertical profiles of the 19th harmonics of the ID with and without the phase modulation of the RF voltage. The magnet gap was 22 mm. The red line shows the data with RF phase modulation of 4 degrees corresponding to the effective beam energy spread of 0.27%. The blue line shows the data without the modulation when the beam energy spread is 0.11%.

frequency (f_s~ 2 kHz). An X-ray CCD camera was used and the exposure time was set at 30 ms, which is sufficiently longer than the period of the energy oscillation. Preliminary results are shown in Fig. 17. Although preliminary, the results are promising and encourage us to develop, by employing a fast-gated camera, turn-by-turn diagnostics of the energy spread of a nonequilibrium beam such as an injection beam that is expected in the future from the C-band XFEL driver.

To observe the temporal structure of X-ray pulses from the ID, we are investigating the characteristics of an X-ray streak camera such as dependence of the temporal resolution on the photon energy. With the aim of developing optical diagnostics for expected next-generation light sources, we are preparing to observe shorter X-ray pulses generated by low-α operation of the ring and by slitting vertically tilted bunch obtained by exciting head-tail motion.

At the diagnosis beamline II, the so-called edge radiation from the bending magnets upstream and downstream of the ID straight section can be observed. Formerly, a movable mirror to direct FIR laser beam to the electron beam traversing the straight section was installed downstream of the lower bending magnet for a plan in progress to generate Compton-backscattered MeV γ-ray photons. By applying the mirror to direct the edge radiation into the atmosphere, we observed the edge radiation with microwave detectors. The intensities in the 50-75 GHz and 75-110 GHz frequency bands were measured by increasing the current of a single-bunch beam. The measured turn-by-turn intensities in the two bands varied temporally and the time-averaged intensities showed nonlinear dependence on the bunch current (Fig. 18), which suggested that we detected coherent synchrotron radiation originating from single bunch instabilities.

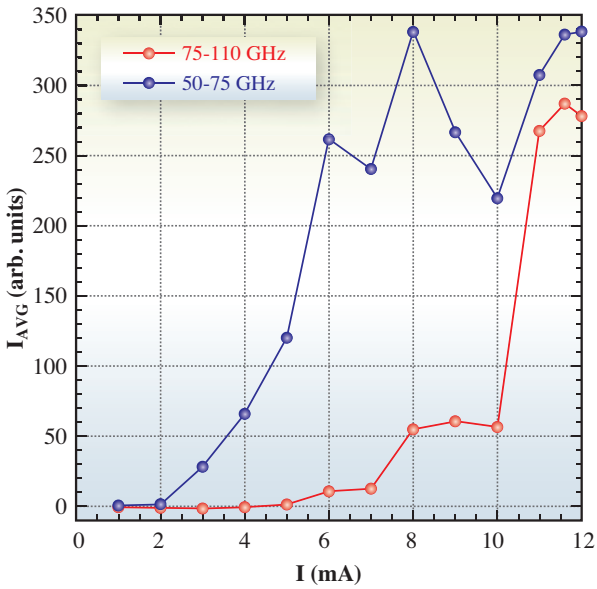


Fig. 18. Time-averaged intensities of the edge radiation measured in the 50 - 75 GHz and 75 - 110 GHz microwave bands as functions of the current of single-bunch beam.

Investigation of Misreading of Pressure Measurement by Radiation

The vacuum pressures of the SPring-8 storage ring became better, with the increase in the integrated beam dose until the summer shutdown of August 1997. However, after the summer shutdown, the pressure readings of the Bayard-Alpert vacuum gauge (ionization gauge) around the photon absorbers did not decrease.

Assuming that the pressure readings of the ionization gauges are affected by the synchrotron radiations scattered by the photon absorbers, radiation shields were added around the gauge heads and cables. In addition to the shields, U-shape pipe or a permanent magnet was installed in 2001 between the gauge duct and the beam duct of the storage ring to eliminate the photoelectrons. As a result of the countermeasures, the pressure at the Absorbers (AB3) and the Crotch Absorbers (CR1) became equivalent to the pressure at the Straight Section Chambers (SC1), as shown in Fig. 19. Figure 19 shows the pressure rise normalized by the beam current and the product of the beam current and the beam lifetime as a function of the integrated beam dose.

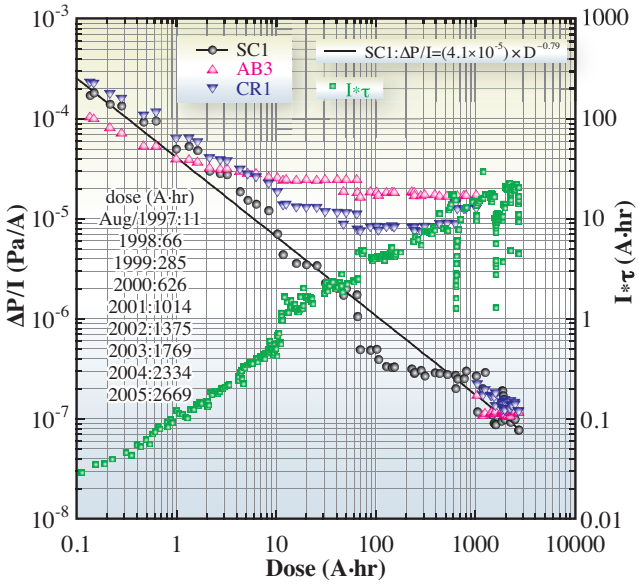


Fig. 19. Pressure rise normalized by beam current ($\Delta P/I$) and the product of the beam current and beam lifetime ($I \cdot \tau$). The beam lifetime was measured when the gaps of all Insertion Devices were fully opened in the beam filling of multi-bunch mode. The pressures at Straight Section Chambers (SC1) that are far from the photon absorber decreased with increasing integrated beam dose. However, the pressures at Absorbers (AB3) and Crotch Absorbers (CR1) did not decrease after 10 A·hr of beam dose.

Some effects of irradiation to the gauge cable and a large amount of electronic inflow to the gauge head are expected. However, very little is known about the effect of irradiation to the gauge head. To investigate the mechanism for misreading of the vacuum pressure, we conducted the irradiation experiment of the vacuum gauge at the accelerator diagnosis beamline II (BL05SS), as shown in Fig. 20. The experimental result of the collector currents against the pressure is shown in Fig. 21. When the collector electrode is irradiated at the pressure of less than 0.1 Pa, the collector currents indicate a constant value of 2×10^{-11} A. Because the collector currents are expected to be caused by the photoelectric emission of the photoelectric effect or the Compton scattering, the collector currents are constant against the pressure change.

Meanwhile, when the collector electrode is not irradiated, the photoelectric emission is not generated and the collector currents decrease with pressure. The ion currents of the collector electrode are generated by the residual gases ionization by X-ray, so the collector currents correlate with the pressure.

A part **[A]** of Fig. 21 is considered to be the residual gases ionization. However, the cause of part **[B]** is the residual gas ionization or another process is not confirmed.

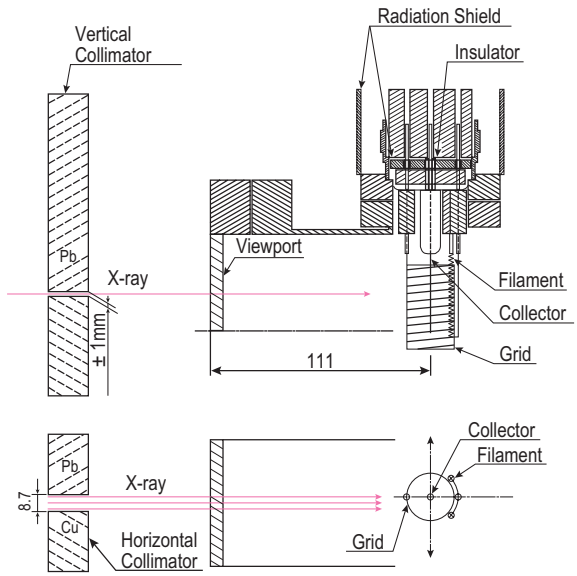


Fig. 20. Experimental setup at the front-end of the Accelerator Diagnosis Beamline II (BL05SS). The gauge head is installed in the vacuum chamber with the view port. The chamber is set on XZ precision motorized stages, so as to move the collector electrode. The collector current of irradiated gauge head is measured under various pressures.

The photoelectric emission by the photoelectric effect or by the Compton scattering is deduced to be dominant factor for the misreading of the vacuum pressure, and the ionization of residual gases is almost negligibly small under 1×10^{-4} Pa. However, between the gauge head and the electric connector, there is atmospheric air. If the X-rays irradiate the atmospheric air gases between the gauge head and electric connector, the gases are ionized and a large amount of collector currents are generated. It is known empirically as a necessity of the radiation shield for the electric connector; this indicates that the cause of misreading is the ionization of atmospheric air between the gauge head and electric connector.

In this investigation, the causes of the misreading of the Bayard-Alpert vacuum gauge (ionization gauge) by irradiation were confirmed. It is necessary to further investigate about the atmospheric air ionization process between the gauge head and electric connector, and the photoelectric emission mechanism of the photoelectric effect or the Compton scattering from the collector electrode.

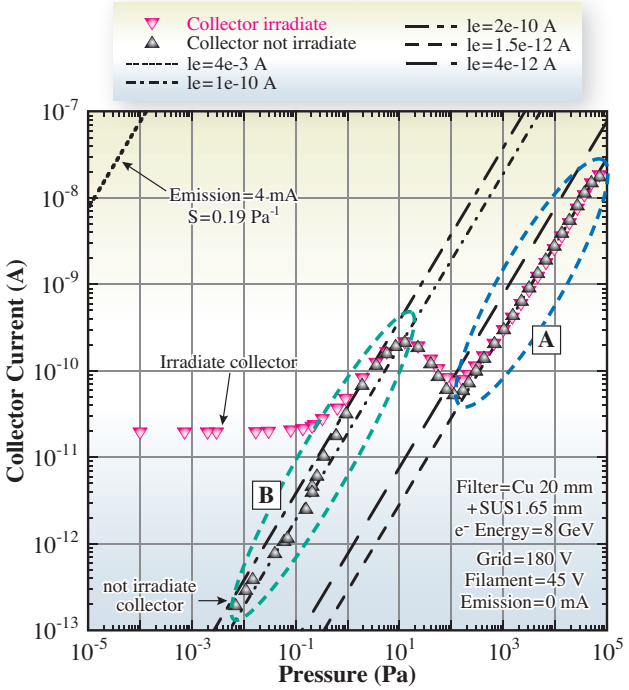


Fig. 21. An experimental result of the measured collector currents against the pressure. The emission current of the gauge is shut off, so the collector current cannot flow under normal circumstances. The symbol ▽ indicates the collector currents with the irradiation and the symbol △ without the irradiation.

Research and Development of Femtosecond Pulse X-Ray Generation

The generation of an X-ray with an energy of 10.7 keV and a pulse width of 600 fs in two standard deviations can be achieved if we install superconducting crab cavities and a minipole undulator in one of the long straight sections of the SPring-8 storage ring. The flashing repetition of such an X-ray is the same as that of the preexisting synchrotron radiation, or that of the electron bunches circulating around the ring. This feature complements the low repetition of the X-FEL, which has extraordinarily high temporal intensities. This method, in addition, can supply a femtosecond X-ray without causing any disturbance to users on the other beam lines at SPring-8. Its principle of generation, performance expected with design parameters, and R&D issues have been described in previous reports [6,7].

Because the stability of the electron orbit in the storage ring is insensitive to the common phase shift among deflecting cavities, the RF power from a 1 MW klystron, a power amplifier, is quartered and supplied to four crab cavities. Each is fed into the cavity through a fast high-power phase shifter newly developed for precise deflecting phase control (Fig. 22). The achieved performance of this phase shifter through high-power tests was as follows: the phase-adjusting range was ±1.5 degrees under a full reflection power of 300 kW and the frequency response of the phase change was from DC to 1 kHz (−3 dB). This response speed is sufficient to suppress the individual phase fluctuation of crab cavities, which is caused mainly by their change in resonant frequency. The test results of a crab cavity at KEK show that the resonant frequency of the cavity is

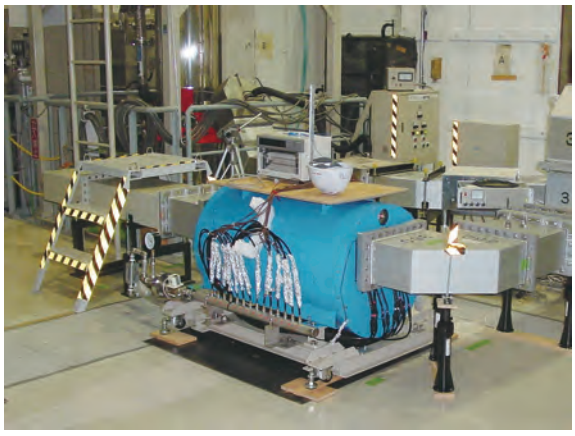


Fig. 22. 300 kW fast phase shifter in the magnetic shield (blue). Incident power travels from right to left and is reflected with a variable-position short plate found under the ladder bridge.

predominated by mechanical vibration and a change in liquid helium pressure, and that the phase fluctuation spectra lie mainly below 1 kHz.

Superconducting crab cavities have been developed at KEK and are being utilized for the crab crossing of the B-factory (KEK-B). Our crab cavity needs little modification, because our RF accelerating frequency is almost the same as that of KEK-B; moreover, our beam current is much smaller than theirs. Taking advantage of our low beam current, we are developing a SPring-8-type tuner with a simple mechanism to improve the reliability and stability of the resonant frequency of the crab cavities.

Developments and Upgrades of Linac

High-Resolution Integrator Circuit for Beam Charge Monitoring [8]

For top-up injection to the SPring-8 storage ring, about every 20 seconds, the linac shoots an electron beam whose beam charge is about 1 nC. In the future, the beam charge will be decreased owing to more frequent beam injection to the storage ring to minimize the stored beam current variation. Presently Fast Gated Integrator and Boxcar Averager Modules (Stanford Research Systems) are equipped as integrator circuits for signal processing. When the beam charge is decreased for the frequent beam injection, the measurement error of the present integrator circuit will be nonnegligible owing to the noise of the integrator. To maintain or improve the resolution, we developed a new integrator circuit to reduce the noise level to 1/10 of the present integrator circuit.

The principle of the new integrator circuit, which is identical as the principle of the present integrator, is as follows: The principal elements are a gate switch and an accumulator (a 6- or 12-m long coaxial cable) connected to a high-impedance sum amplifier as shown in Fig. 23. An input pulse signal is fed to the accumulator via the opened gate switch. When the gate is closed, the input signal is confined in the accumulator, that is, the signal repeats reflections at both ends of the accumulator. As a result, the signal pulse becomes dull in shape and is averaged as the signal transfers forward and backward. This averaged voltage is proportional to the integral of the signal voltage while the gate is open.

The S/N ratio at the accumulator stage can be maximized by minimizing the length of the accumulator that affects the signal attenuation. The minimum accumulator length is determined on the basis of the pulse width of the input signal including the rise and fall times of the gate switch. We have therefore focused on enhancing the transient response of the gate switch.

A transfer switch (SW-283-PIN, M/A-COM) was adopted as the gate switch to terminate all ports for eliminating switching noises generated at an open port. The rise time of the gate switch is determined from the root sum square of the rise times of the transfer switch and the control voltage. To avoid lengthening the rise time of the gate switch, a fast circuit was developed to generate control voltages for

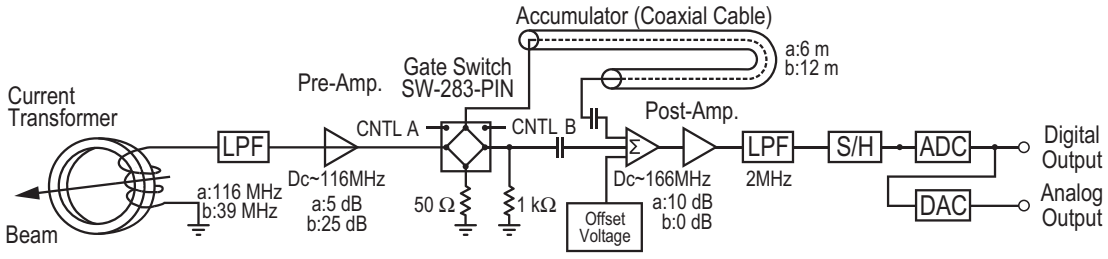


Fig. 23. Block diagram of developed integrator circuit. "a:" denotes the parameter for a short (1 ns) pulsed beam measurement, while "b:" denotes the parameter for a long (40 ~ ns) pulsed beam measurement.

the transfer switch. The circuit is composed of a transistor bridge circuit and clipping diodes as shown in Fig. 24. The control voltages of -0.1 and -7.9 V are instantaneously inverted by the external gate pulse. We finally obtained the rise time of 2 ns (10-90%).

The resolution of the developed integrator circuit was measured as 0.65 pC under conditions of a range of 2 nC and a gate width of 20 ns, that is, the resolution of the developed integrator circuit has been significantly improved to 1/12 of that of the present integrator with the same range and gate width conditions. The linearity of the output voltage to the time integral of the input voltage was measured with a gate width condition of 20 ns. The obtained output voltages showed good linearity with its deviation of 0.14% rms. The observed performance of the integrator sufficiently satisfies our requirement for the future low-current operation of the linac.

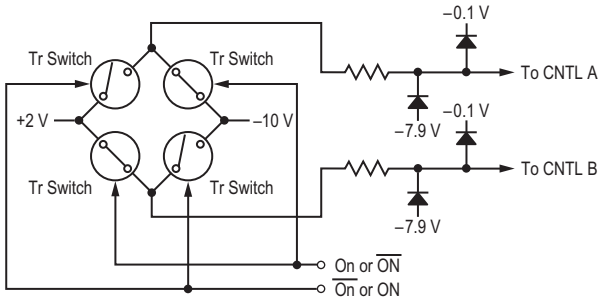


Fig. 24. Block diagram of the circuit to generate control voltages for SW-283-PIN.

RF Gun Development

Upgrade of 3D UV laser pulse shaping system

To minimize the beam emittance of a photocathode RF gun, the laser pulse shape should be optimized in three dimensions. One of the candidates for a reliable 3D laser pulse shape was the cylindrical beer-can-shaped (spatially top-hat and temporally square) pulse. The 3D UV laser pulse shaping system combined with a deformable mirror (transverse: 2D) assisted by a genetic algorithm and a chirped pulse stacker (longitudinal: 1D) was completed at SPring-8.

In 2007, we installed a new UV pulse stacking system that consisted of three birefringent α-BBO crystal rods [9] to fix the optical delays between neighboring microchirped pulses in the previously developed mechanical pulse stacker [10]. To avoid the interference caused by stacking, orthogonally polarized chirped pulses are alternatively stacked with an optical delay. The optical delay period should be 1.2~1.3 times longer than the microchirped pulse duration to generate a homogeneous electron bunch at the cathode. This method, which introduces additional chirp to avoid interference, as shown in Fig. 25, is referred to as “chirped pulse stacking” [10]. The optimal chirp of a micropulse minimizes interference caused by stacking to make the plateau of a combined pulse flat. This chirping was carried out with group delay dispersion (GDD) in whole transport optics and additional adjustable chirping introduced by DAZZLER (AO-modulator) at the fundamental wavelength.

A birefringent crystal that resembles a conventional retardation plate works on the basis of a principle for time delay. It does introduce a certain temporal delay between two orthogonally polarized components of a linearly polarized incident beam. The angle of rotation of each crystal axis against incident polarization is 45° to make twin pulses. Then a pulse train with equivalent intervals is connected smoothly with additional pulse stretching introduced by DAZZLER (Fig. 25). These α-BBO crystal rods can be used as a pulse stacker in the super broadband wavelength region (189−3500 nm). To obtain the longest square laser pulse duration of 32 ps with four birefringent crystals, the crystals must generate temporal delays of $\Delta t = 2.0$, 4.0, 8.0, and 16 ps. The 4-, 8-, or 16-ps squarely combined pulse is generated by rotating the crystal axis parallel to the incident polarization at each corresponding crystal as shown in Fig. 25.

Proposal of Z-polarization Schottky emission gun with hollow laser incidence

By focusing a radial polarized beam on the photocathode (Fig. 26), the laser’s electric field is generated in the laser propagation direction (Z-direction) at the focus point. The Z-field oscillates with a periodic time of ~2.6 fs at the fundamental Ti:Sapphire laser light (~790 nm), for example. By introducing a hollow laser incidence, the generated Z-polarization field can exceed an electrical field of 1 GV/m even with a fundamental wavelength from compact femtosecond Ti:Sapphire laser systems. In a 1 GV/m field, the work function of the copper cathode decreases by ~2 eV [11]. This Schottky effect can be used as a gate of the photoemission process. Thus, a laser-induced Schottky-effect-gated photocathode gun using the Z-polarization of the laser source was proposed [11] as a future multi-bunch high brightness electron source with a low charge.

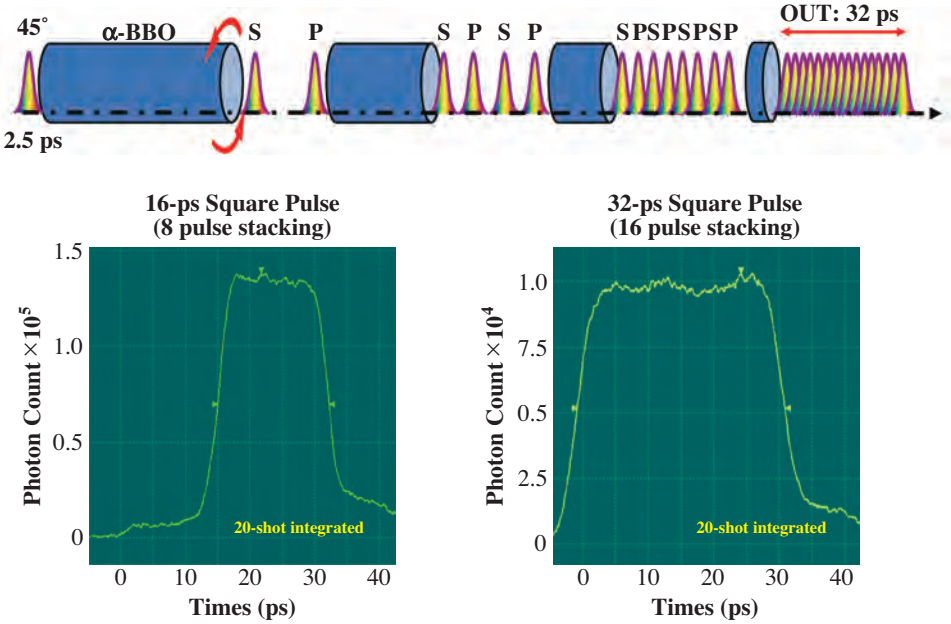


Fig. 25. Measurement results obtained using a streak camera (Fesca-200) of UV-laser pulses stacked with BBO crystal rods. For instance, the rotation angle of the first crystal rod against incident polarization works as a half waveplate in our mechanical pulse stacker. By rotating the first crystal rod, switching between 16- and 32-ps square pulses is available.

We have conducted a feasibility study of this laser-induced Schottky effect on the photocathode by comparing radial and azimuthal polarizations. In this experiment, the linear polarization of the incident laser only switches from the vertical to the horizontal direction. Note that we can keep the same photon densities at the focus point during experiments comparing radial and azimuthal polarizations. In this method, we can separately verify the Schottky effect due to the Z-field from the multiphoton process.

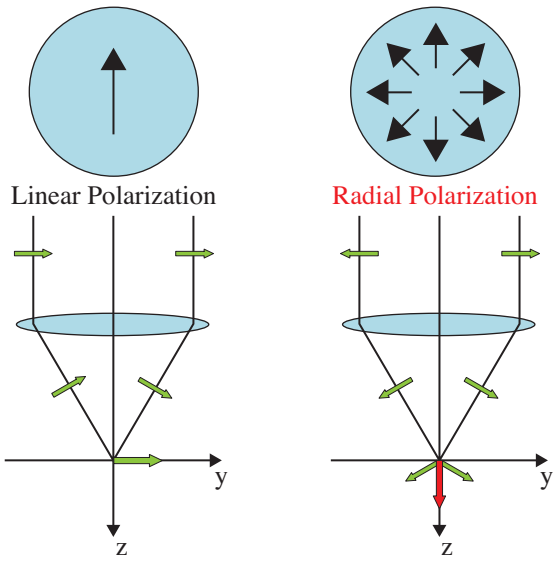


Fig. 26. Principle of Z-polarization optical field on cathode generated from radial polarization.

Haruo Ohkuma*, Hiroto Yonehara, Hirofumi Hanaki

SPring-8/JASRI

*E-mail: ohkuma@spring8.or.jp

References

[1] SPring-8 Research Frontiers 2006, p. 179.
[2] SPring-8 Research Frontiers 2007, p. 188.
[3] K. Soutome *et al.*: Proc. EPAC08 (2008), p. 3149.
[4] M. Oishi *et al.*: SPring-8 Internal Report, SR06-007 (in Japanese).
[5] T. Bizen: Nucl. Instrum. Meth. A **574** (2006) 401.
[6] SPring-8 Research Frontiers 2006, p183.
[7] SPring-8 Research Frontiers 2007, p195.
[8] K. Yanagida *et al.*: Proc. LINAC08 (2008) - to be published.
[9] H. Tomizawa *et al.*: Proc. FEL07 (2007), p. 298.
[10] H. Tomizawa *et al.*: Quantum Electronics **37** (2007) 697.
[11] H. Tomizawa and M. Kobayashi: Proc. FEL07, p. 382.

CONTROLS & COMPUTING

Development of Flexible and Logic-Reconfigurable VME Boards

A real-time control system with complex sequences is a key technology for developing equipment for next-generation light sources, various progressive user experiments and accelerator operations. Software on a CPU and simple AI/AOs and DIOs enable us to build control systems with complex sequences, such as slow feedback routines. However, a fast sequence that requires sub-100-microsecond-order timing is currently impossible to achieve using software on a CPU. Hardware in the form of a hard-wired circuit, on the other hand, enables the realization of a fast sequence. However, hardware sometimes has limited flexibility and requires considerable time and cost to modify sequences.

An I/O flexible and logic-reconfigurable VME board was developed to enable both the fast control and modification of sequences [1]. The board has three main features: (i) flexible I/O selection, (ii) real-time and fast control, and (iii) sequence reconfigurability.

(i) Flexible I/O selection: The I/O parts of the board were physically separated from the base board (see Fig. 1). The I/O parts are simple I/O daughter modules such as an AI/AO or DIO module. The users can choose appropriate I/O daughter modules for their own system, put them on the base board and develop the firmware of the sequences to be carried out. The same base board can be used with different I/Os with a small modification of the logic and without any modification of the hardware, such as printed circuit board design. Two I/O parts can be installed on the base board as daughter modules. Three types of the I/O daughter board are developed: AI/AO, DIO and the Camera Link grabber.

(ii) Real-time and fast control: The base board is mounted with field-programmable gate array (FPGA) chips. The user sequences are on one FPGA chip with 1.5 M gates. The FPGA executes user logic at a base clock frequency of 50 MHz. The FPGA enables real-time and fast control with a microsecond-order response, which software on a CPU at present

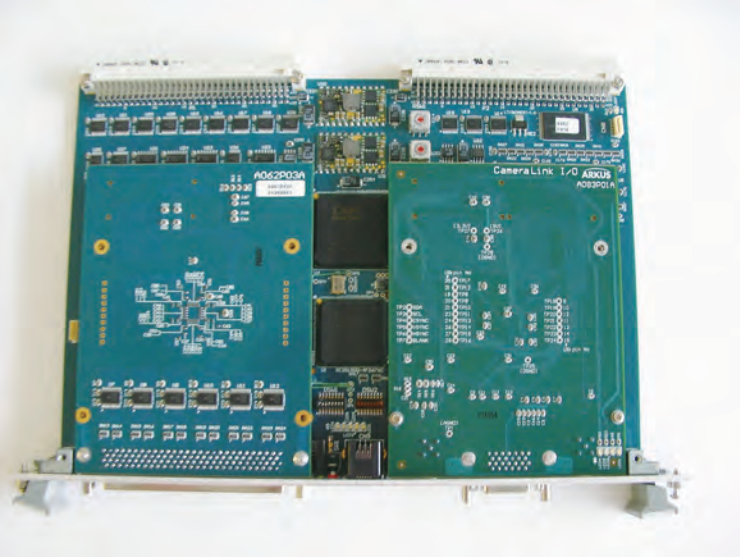


Fig. 1. Photograph of flexible and logic-reconfigurable VME board mounted with DIO (left side) and camera link grabber (right side) daughter boards. The FPGA that execute the users' sequence is mounted in the lower middle part of the base board.

cannot achieve.

(iii) Sequence reconfigurability: An FPGA is reprogrammable. Changing the logic in the FPGA is only the modification of the configuration data of the firmware, which is performed in a few minutes. The feature of reconfigurability enables us to carry out R&D of the sequence because of ease of modification. The users can test several sequences to find the appropriate one for their equipment in a short period of time. This feature is important to facility, such as SPpring-8, where novel measurement systems are developed.

In addition to the above three features, the board has a 256 MB DDR memory as temporal data storage and LEDs for debugging. The block diagram of the board is shown in Fig. 2. The proportional-integral-derivative (PID) feedback system is one of the applications of the board. A base board with the logic for a PID feedback sequence and an AI/AO daughter board function as the feedback system. The board is also applied in many systems, such as the PID system with a pulse width modulation output, a pulse train generator with outputs of a few kHz, screen monitor system with Camera Link camera, a trigger selector that selects a trigger from a 60 Hz pulse and a shutter system that requires an over 80 kHz TTL output.

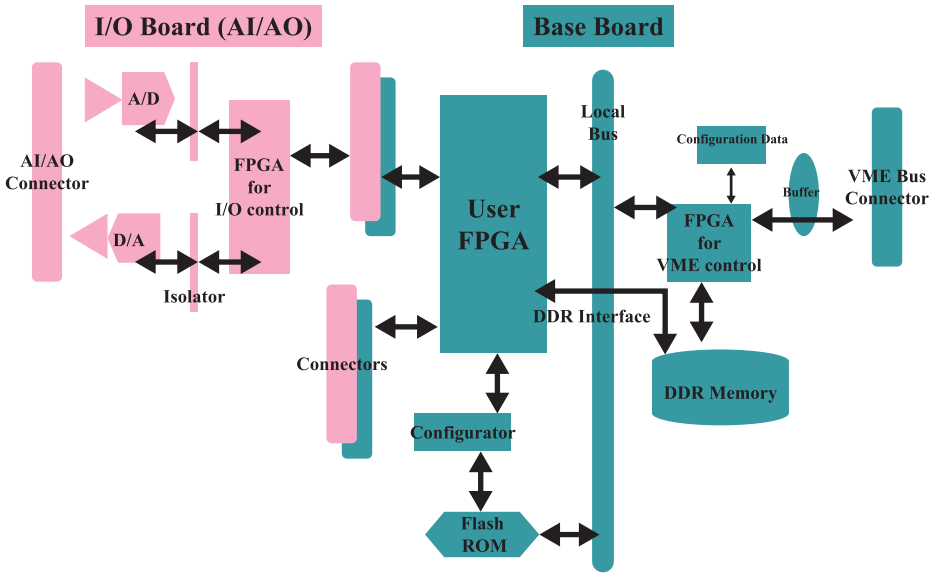


Fig. 2. Block diagram of flexible and logic-reconfigurable VME board. Green blocks are elements on the base board and pink blocks are elements on the I/O daughter board.

T. Hirono

SPring-8/JASRI

E-mail: hirono@spring8.or.jp

References

[1] T. Hirono *et al.*: Proc. ICALEPCS'07, Knoxville, U.S.A. (2007).

New Apparatus & Upgrades

Upgrade at Hyogo Prefectural Beamline BL24XU

BL24XU is the first contract beamline at SPring-8 constructed by Hyogo Prefecture in 1997. For the first decade, the beamline has been operated with the primary mission of promoting synchrotron radiation use to industrial application. The first mission is successfully completed by reviewing the present prosperity for industrial use of synchrotron radiation such as the advent of many exclusive beamlines. We instituted a new mission of industrial contribution for the next decade that aim at providing highly advanced techniques for nanoscience. In this report, beamline upgrade at BL24XU for the new mission is introduced.

BL24XU consists of a hard X-ray undulator source and four experimental hutches. The undulator of the figure-8 type can provide intense X-ray containing every half-order harmonics with each alternative linear polarization. In the first decade configuration, we divided X-ray beam into three branches (A, B, C) by two sets of beam-splitting monochromators. The monochromators have a configured long-offset (2 m) double-crystal geometry using a thin diamond crystal as the first crystal. Branch-A has an end station for protein crystallography experiments, and branch-B has end stations composed of a powder diffractometer and a gas-environed grazing incidence diffractometer for materials science. For the most downstream branch, namely, branch-C, a silicon double-crystal monochromator has been installed to share X-rays with the tandem experimental hatches C1 and C2 for nanobeam application and microbeam diffraction, respectively (C2 was constructed in 2004). The nano/microbeam techniques developed as scientific research by X-ray Optics Laboratory at the University of Hyogo are highly advanced subjects and the demands for the techniques are getting higher. On the other hand, the roles of end stations A and B will stop with the development of other beamlines for the industry. Then, we reconfigured the beamline in 2008 to develop nano/microbeam technique and to give new functions for new application works.

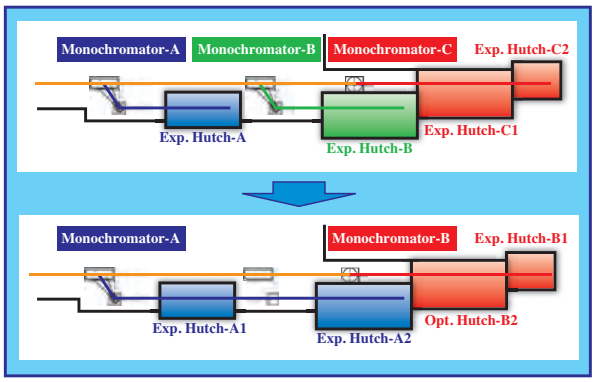


Fig. 1. Schematic upgrade at BL24XU.

Figure 1 shows the beamline configuration before/after the beamline upgrade. One of the beam-splitting monochromator for branch-B was removed and the experimental hutches between A and B was connected by a wide beam transport pipe. The pipe was installed in optical hutch and had to be completely shielded with a 20 mm-thick lead layer. These reconstructions were finished in March 2008. Consequently, we can use a very long experimental setup with tandemly arranged experimental hutches, which were renamed A1 and A2. The previous branch-C was also renamed branch-B. The large propagation length of new branch-A can be used not only for focusing beam but also as a 16-m-long USAXS instrument. The rearrangement of conventional diffractometers has already been completed and opened to use. New apparatuses for USAXS and micro-SAXS are under construction. And GISAXS and Bonse-Hart type SAXS are being planned.

The improvement of nano/microbeams is also an important subject, though a focusing beam with a size of approximately 100 nm is now practical. We are studying a new beam-splitting monochromator that does not disturb the X-ray wavefront to branch-B. For the first crystal of the monochromator an amplitude division type using a thin sapphire single crystal or a wavefront division type using sectioned silicon substrate are being evaluated. Furthermore, new focusing devices using a multilayer technique have been developed to improve both focusing size and efficiency.

The above-mentioned new apparatuses at branch-A, including nano/microbeam optics at branch-B, will help to analyze nanostructures in both real and reciprocal spaces, and will provide powerful complex tools for nanoscience with its operation with another Hyogo prefectural beamline BL08B2.

Hidekazu Takano

Graduate School of Material Science, University of Hyogo

E-mail: htakano@sci.u-hyoko.ac.jp

Upgrade of the SAXS Apparatus at BL40B2

BL40B2 is mainly used in the small angle X-ray scattering (SAXS) measurement of soft materials, proteins, synthetic macromolecules, lipids, and surfactants. It is necessary to observe the wide range from several angstroms to hundreds of nanometers to analyze the structures of these materials. Moreover, the change in the sample cell, detector, and camera length are required for many experiments. We report the introduction of the new equipment for securing user experiment time by performing the measurement smoothly.

Figure 1 shows the layout of the pedestal with the automatic vacuum path rise-and-fall equipment introduced in 2007B. The pedestal has two parallel rails of 5 m, and a vacuum path with a beam stop in which a two-dimensional drive is possible to be fixed downstream of a pedestal. A beam stop can be easily replaced from the side of a vacuum path. The vacuum paths are divided into six pieces and respectively fixed on electric stages. The connection of vacuum paths is attained by uniting a flange face with an O-ring and by using a vacuum pump. Moreover, a guide is prepared on both sides of a surface plate. The slide of the plate that carries the stage on which a flange, a nose, and a sample stage are arranged according to camera length. By changing the vacuum path to make it go up and down, it is possible to perform measurement using seven camera distances of 0.25, 0.5, 1.0, 1.5, 2.0, 3.0, and 4.0 m. The photographs settings of camera lengths at 0.25 and 4 m are shown in Fig. 2. The replacement of such a camera distance is completed in about 5 minutes. Even if all optical alignment and change in wavelength are operated, an experiment using a different camera distance is possible in about 1 hour. The speeding up of setup can be attained with an aid, which carries out the user experiment within a limited time.

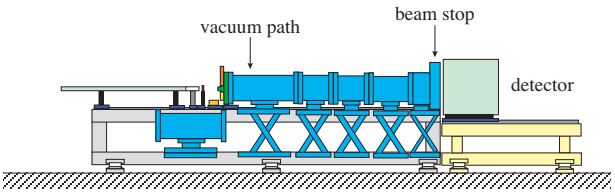


Fig. 1. Layout of apparatus with automatic vacuum path rise-and-fall equipment.





Fig. 2. Photographs settings at BL40B2 of camera lengths of **(a)** 0.25 m and **(b)** 4 m.

Hiroyasu Masunaga

SPring-8/JASRI

E-mail: masunaga@spring8.or.jp

Stabilization of Double-Crystal Monochromator at BL41XU

In SPring-8, double-crystal monochromator mechanisms were developed standards for facilitating the rapid construction of beamlines thirteen years ago. The basic design of the mechanisms has remained unchanged. At present, the mechanisms are used at 27 undulator and bending magnet beamlines. In the ten-year user operation, users' requests for X-ray beams are becoming severer as research studies with SPring-8 are pioneering new fields of science and technology. For example, at beamline BL41XU for structural biology research, the typical sizes of crystalline protein specimens are being reduced down to tens of microns, and users consequently require to obtain highly brilliant X-rays focused into the specimen sizes as stably as possible. However, the micro-focused beam has not been stable enough to reduce the intensity by 26% per hour and to fluctuate it by 13%, as shown in Fig. 1. Such reduction and fluctuation were most likely caused by the instability of the mechanism. Moreover, the synchrotron radiation deteriorated the performance of water-cooled crystals, and damaged the O-rings for the water seal and motor cables in the mechanisms with time. We solved the above problems at BL41XU.

Intensity reduction — Intensity reduction was induced when the diffraction net planes of the two crystals were not held in parallel. We measured temperature at about forty points in the monochromator, such as the coolant water, crystal holder and fine stepper stages. As a result, the angular shift between the net planes was nearly proportional to the temperature changes of the tilt stages for crystal adjustment. The temperatures of the tilt stages were controlled by two means: (a) elimination of heat sources and (b) efficient cooling of the stages. The former was carried out (a-i) by turning off the hold currents of the motors of fine stepper stages and (a-ii) by adding shield parts to block X-ray and electron radiations to the mechanism (Fig. 2). The latter was performed (b-i) by an indirect water cooling of the tilt stages and (b-ii) by changing the temperature of the cooling water from 20.0 to 25.5 °C (the room temperature). Consequently, the temperature difference between the first crystal and the tilt stages decreased from 9.5 to 0.5 °C, and that between the second crystal and the tilt stages from 5.4 to 0.3 °C. The control of stage temperature resulted in the stabilization of microbeam intensity (reduction rate 1% per hour), as shown in Fig. 1.

Intensity fluctuation — The black lines in Figs. 3(a) and 3(b) show the intensity fluctuation and its power spectrum of the monochromatic beam filtered with a narrow slit. Turning off the instruments around the monochromator, such as vacuum pumps and the chiller, one by one, we divided the vibration sources into four types: (A) the chiller to supply the coolant water into the crystal (< 5 Hz), (B) the water paths inside the vacuum chamber (50~100 Hz), (C) scroll vacuum pumps (179, 207 Hz) and (D) something undefined (117 Hz). As shown in Fig. 2, we put new accumulators to control water pressure for the vibration source (A), used the polyurethane inner tubes to smooth the water flow for (B), and put rubber cushions under the scroll vacuum pumps for (C). The intensity fluctuation after the above improvements (red lines in Fig. 3) decreases to the same level as the

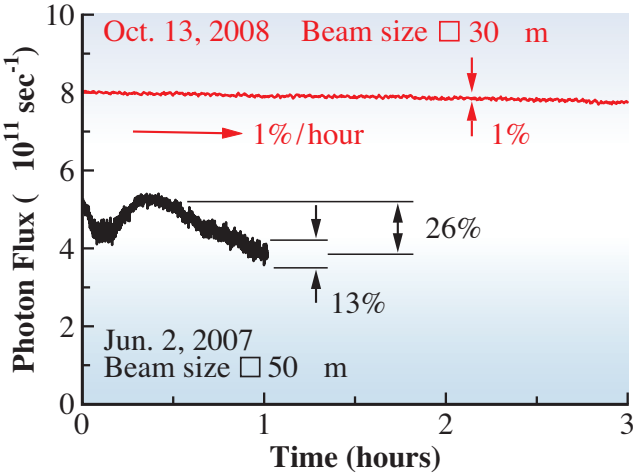


Fig. 1. Changes in microbeam intensity at the experimental station with time. The black and red lines show the beam intensities before and after the stabilization, respectively. The increase in beam intensity was caused by the improvement in crystal performance.

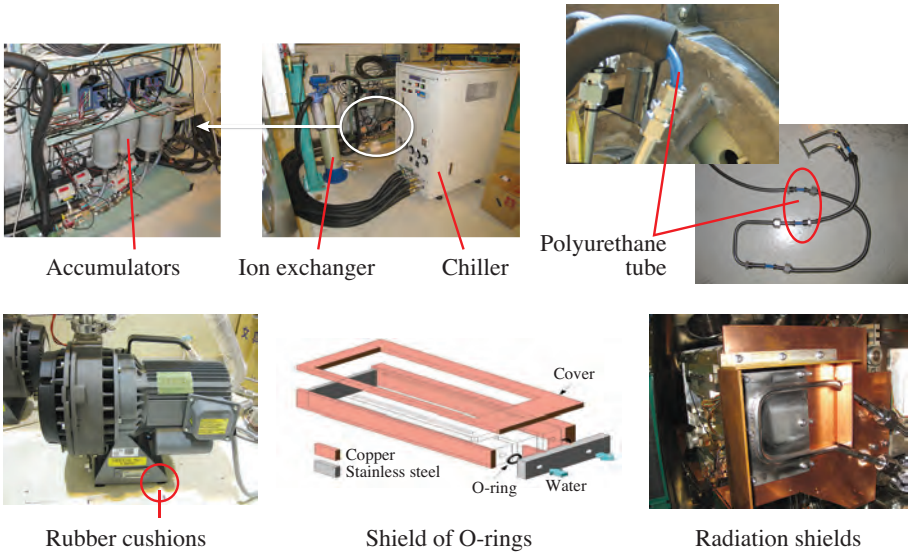


Fig. 2. Parts of the improvements for the stabilization of the monochromator.

instruments around the monochromator were turned off (blue lines in Fig. 3). The intensity fluctuation of the microbeam reduced from 13% to 1% accordingly as shown in Fig. 1.

Radiation damage — The deterioration in crystal performance was mainly caused by the jamming of copper compound in the water paths. Copper ions were dissolved from the crystal holders. We coated all the water paths inside the newly designed crystal holders with nickel. In addition, the coolant water was continuously refined with the ion exchanger shown in Fig. 2. The water paths inside and outside the crystal were changed to shield the O-rings from radiations (Fig. 2). The shield parts for X-ray and electron radiations played a role in the protection of the motor cables.

We are planning to stabilize other beamline monochromators on the basis of the above results.

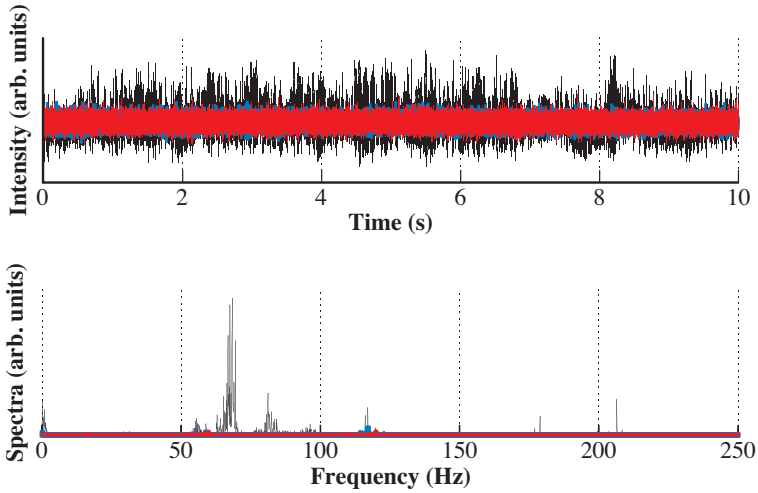


Fig. 3. **(a)** Monochromatic beam intensities filtered with a narrow slit and **(b)** their power spectra. The black and red lines show the data before and after the stabilization, respectively. The blue lines were measured when the instruments around the monochromator were turned off.

Hiroshi Yamazaki[a,*], Yasuhiro Shimizu[a,b] and Nobutaka Shimizu[a]

[a] SPring-8/JASRI
[b] SPring-8/SES

*E-mail: yamazaki@spring8.or.jp

Upgrade of Engineering Science Research III, BL46XU

Recently, the number of SPring-8 users in the field of the industrial application has been remarkably increasing. In order to respond to the growing demand in this field, we upgraded BL46XU as an "Engineering Science Research III" beamline.

In this upgrade of BL46XU, we renewed the multiaxis X-ray diffractometer, and installed a hard X-ray photoemission spectroscopy (HAX-PES) device. Additionally, the small X-ray diffractometer specialized for thin-film analysis (a commercial diffractometer ATX-G, manufactured by RIGAKU), which had been installed in BL13XU, was moved to BL46XU, because it was in high demand from industrial application users. The target field of these instruments is expected to be the development research on functional thin films. Furthermore, the high potential of this beamline with an undulator light source makes it possible to respond to various needs of the industrial application field.

The upgrade of the optical components started in the summer of 2008. This upgrade was mainly for expanding the available energy range of X-rays and for improving the flux density of the X-ray beam. After this modification, the available energy range of X-rays is E = 6 ~ 35 keV and an X-ray beam can be focused at the sample position with a horizontal beam size of about 150 μm using the newly installed mirror-bender devices. Furthermore, a channel-cut monochrometer for HAX-PES was installed in the optics hatch.

The upgrade of the instruments in the experimental hatch was carried out from December of 2008 to February of 2009. As the standard layout, a multiaxis X-ray diffractometer is placed upstream of the experimental hutch, and a HAX-PES device is placed downstream. ATX-G is set in the experimental hatch temporarily after moving the HAX-PES device with adjustable guide rails in case that some users want to use this diffractometer.

The multiaxis X-ray diffractometer, which was manufactured by HUBER, has a basic construction of a four-circle goniometer whose fundamental scattering plane is vertical (four basic axes, χ, ϕ, ω, 2θ), equipped with four additional axes for horizontal scattering plane, ω_z and $2\theta_z$ (see in Fig. 1). A C-type χ cradle is adopted to get a wide scattering angle range (-20° to 160°) by avoiding dead angles. This design enables precise control of the incident angle of X-rays to the sample surface in the measurements of grazing incidence X-ray scattering (GIXS) for thin films. Two types of motorized sample



Fig. 1. Multi-axis X-ray diffractometer.



Fig. 2. X-ray diffractometer specialized for the thin film analysis (ATX-G).

stage, a XYZ stage and a swivel stage, are installed on the φ axis for adjusting sample position precisely. Furthermore, the position of users' optional accessories (e.g., furnace and tensile tester) can be set efficiently using these sample stages in combination with an X-ray camera. To improve the quality of the GIXS data for thin-film samples, we provide a He-gas sample chamber with a kapton dome to reduce background noise due to air scattering around the sample. To respond to various experimental configurations, we provided various optical components and detectors. As optional optical components, a solar slit and crystal analyzers (Si (111), Ge (111), LiF (002)) can be used. For the detectors, we provided a NaI scintillation counter detector and a silicon drift detector as one-dimensional detectors, and a pixel detector (PILATUS) or an imaging plate as a two-dimensional detector. PILATUS is an effective detector for time-resolved X-ray diffraction measurement. Furthermore, an attenuator automatic changer has been installed for X-ray reflectivity spectral measurement of the dynamic range of approximately ~10^{10}.

ATX-G is a conventional X-ray diffractometer specialized for GIXS measurement for thin-film structural analysis (Fig. 2). This diffractometer is easy to use for many company users because many companies have used it in their laboratories, and its specifications specialized for GIXS enable rapid scan motion. Therefore, this diffractometer is efficient for experiments that need to measure many samples in a fixed experimental configuration.

HAX-PES is powerful tool for chemical analysis on the surface and interface of thin films. This technique realizes a large probing depth of photoemission spectroscopy (PES) up to ~ a few tens of nanometers, detecting photoelectrons with high kinetic energy excited by hard-X-rays. Therefore, it is possible not only to observe the intrinsic characteristic of the samples reducing the effect of the contamination on the surface, but also to detect the depth profile of chemical information from the sample in a nondestructive manner. The number of HAX-PES users in the industrial application field has been increasing markedly in BL47XU. HAX-PES installed in BL46XU can enlarge opportunities for the use of this technique. The HAX-PES system is equipped with a VG-SCIENTA photoelectron energy analyzer, R-4000 (Fig. 3). The sample holder has a tilting device to change the detection angle of photoelectrons to the sample surface (take off angle: TOA). One can investigate the depth profile of chemical composition near the sample surface by measuring the TOA dependence of photoemission spectra using the tilting device.

We expected the high performance of this undulator beamline to improve the industrial application of SPring-8 qualitatively and quantitatively. We will operate BL46XU by flexibly researching various demands of industrial users.

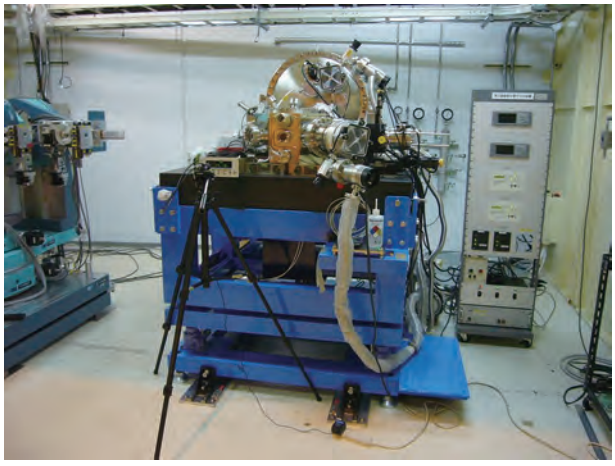


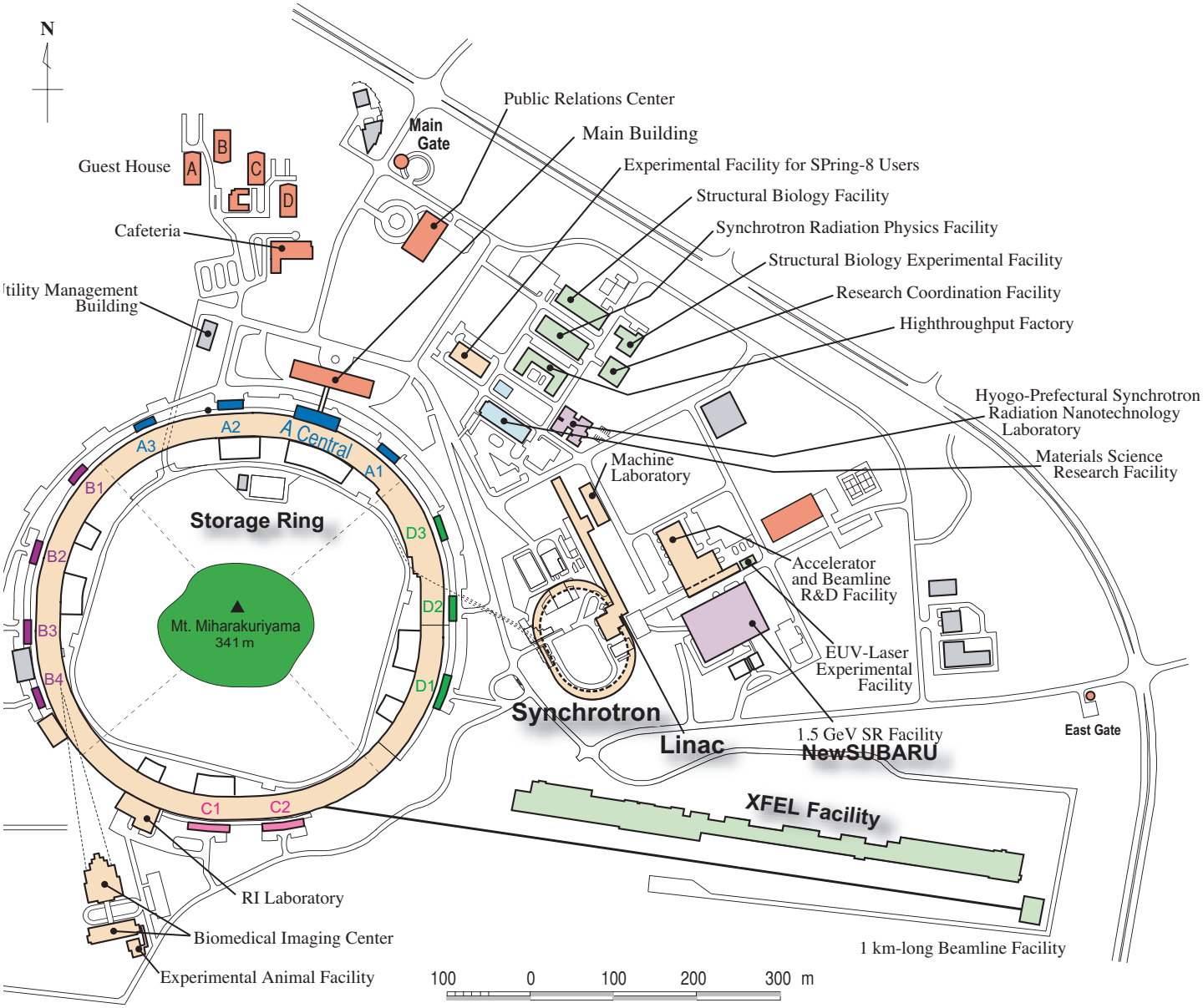
Fig. 3. The device for hard X-ray photoemission spectroscopy.

Masugu Sato

SPring-8/JASRI

E-mail: msato@spring8.or.jp

Facility Status



I. Introduction

Topics of SPring-8 in 2008 and Efforts toward the Next Decade

It was the last year that the SPring-8 celebrated its 10th anniversary since its start of operation in 1997. The year 2008 is, hence, positioned as the first year for the SPring-8 to initiate new efforts toward the next decade. The major milestones that the SPring-8 has so far reached in its history are shown in the Table I.

Following the SPring-8 Advisory Council (SAC) in March 2000 and JASRI International Advisory Council (JIAC) in July 2006, RIKEN and JASRI jointly established an international review committee called the "SPring-8 Academic Review Committee (SPARC)" this year. The missions given to this committee was (1) to measure and evaluate the scientific performance of academic research carried out at the SPring-8, (2) to help the public become better informed of the scientific values of research at the SPring-8, and (3) to advise on the future plans proposed. To accomplish these missions, SPARC meetings were held at the SPring-8 campus, from November 17 to 19, 2008. As shown in Table II, the review committee selected twelve research activities as the outstanding achievements from academic viewpoint among a wide range of scientific and technological activities carried out at the SPring-8, covering life science, chemical science, materials science, earth and planetary science, environmental science, and industrial application. Also closely examined were the future plans and prospects for each activity, which were rated highly by the SPARC board panel. For details of the review results, please refer to the following URL:

http://www.spring8.or.jp/en/about_us/committees/reports/sparc_report

Since RIKEN and JASRI have collaboratively started formulating the upgrade program of the SPring-8 by setting 2019 as the target year, the presentations and recommendations from the SPARC should be of great help for both research organizations to further develop and improve not only the SPring-8 accelerator complex and its beamlines, but its effective utilization. To promote scientific and technological achievements at the SPring-8 as during the last decade, it is essential for the SPring-8 to upgrade its accelerator complex as well as its beamlines at an appropriate timing in the near future, thus enabling itself to compete and collaborate with other world-leading synchrotron radiation facilities. To successfully evolve the SPring-8 in the right direction, the SPring-8 upgrade committee has proposed a large-scale upgrade plan over the next

Table I. Major milestones

Jul. 1987	Recommendations for the "Promotion of Comprehensive R&D on Advancement of Light Science and Technology" (Inquiry No. 11) was submitted by MEXT.
Oct. 1988	Japan Atomic Energy Research Institute and RIKEN established a collaborative team for the synchrotron radiation facility research and development.
Jun. 1989	Harima Science Garden City in Hyogo Prefecture was chosen as the construction site.
Dec. 1990	Japan Synchrotron Radiation Research Institute was founded.
Nov. 1991	SPring-8 construction started.
Oct. 1994	"Law regarding Promotion of Common Use of the Synchrotron Radiation Facility" was enforced and Japan Synchrotron Radiation Research Institute was assigned as the "Organization for promoting synchrotron radiation research."
Mar. 1996	Recommendations for the "Effective Utilization and Management of Large-Scale Synchrotron Radiation Facility (SPring-8)" (Inquiry No. 20) was submitted by MEXT.
Mar. 1997	The generation of synchrotron radiation was confirmed.
Oct. 1997	Start of SPring-8 Operation.
Jan. 2000	Start of NewSUBARU Operation.
Mar. 2000	SPring-8 Advisory Council (SAC).
Apr. 2000	Drafting of the XFEL development concept (compact and low-cost).
Sep. 2002	Report on the First Interim Review of SPring-8 by MEXT.
Oct. 2003	RIKEN was reorganized as an Independent Administrative Institution.
Jun. 2004	The "top-up" operation began.
Apr. 2005	Construction of a 250 MeV test apparatus SCSS began.
Oct. 2005	Japan Atomic Energy Research Institute withdrew from the management of SPring-8 and the management by two bodies, JASRI and RIKEN, began.
Mar. 2006	XFEL was certified as Key Technology of National Improtance in Third-Stage Basic Plan for Science and Technology.
Apr. 2006	RIKEN and JASRI established joint project office for the XFEL project.
Jun. 2006	Laser oscillation of 49 nm UV rays was acheived in the test apparatus SCSS.
Jul. 2006	"Law regarding Promotion of Common Use of the Synchrotron Radiation Facility" was revised.
Jul. 2006	JASRI International Advisory Council (JIAC).
Mar. 2007	JASRI was approved as a Registered Institution for Promoting Synchrotron Radiation Research.
Jul. 2007	Report on the Second Interim Review of SPring-8 by MEXT .
Oct. 2007	SPring-8 10th Anniversary Ceremony and Symposium.
Nov. 2008	SPring-8 Academic Review Committee (SPARC).

Table II. Outstanding achievements

In-vacuum Undulator Sources.
Advanced Beamline Technology.
Structural Studies on Membrane Proteins.
Structural Studies on Macromolecular Assemblies.
Real-time SAXS Analysis of Periodosome.
Motion of Potassium Channel Revealed by Single Molecule Tracking.
Rational Design of Nanoporous Materials with Chemical Functionality.
Probing Bulk States of Correlated Electron Systems by High-Resolution Resonance Photoemission.
Phase Change Mechanism of Rewritable Optical Media.
Post-perovskite Phase of $MgSiO_3$ at 120 GPa: Nature of the Mantle-core Boundary.
Advancing the Understanding of Automobile Exhaust Gas Catalysts.
Interfacial Magnetism between FM/AFM Bilayers in Magnetic Sensor Heads.

decade. In order to design a detailed plan, the working group for the SPring-8 upgrade plan was formed on October 10, 2008, comprised of scientists and engineers of RIKEN and JASRI who will lead the next generation. The working group has started closely examining the upgrade processes needed for the accelerator complex, X-ray sources, and effective utilization of the SPring-8.

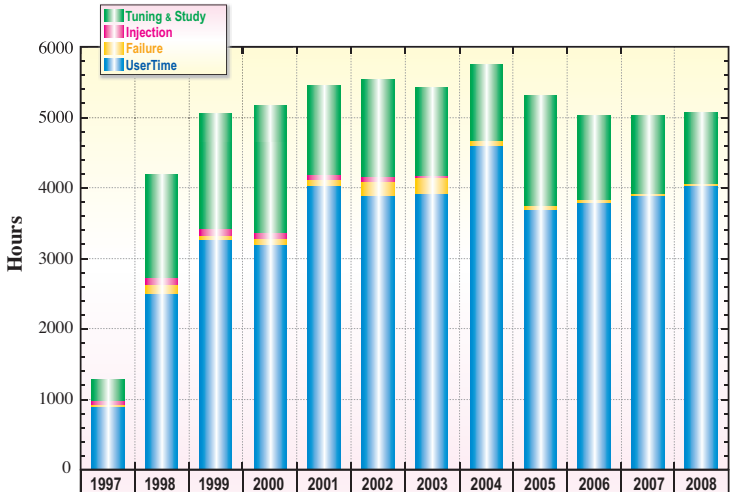
Currently, an X-ray free electron laser (XFEL) facility is being constructed at the SPring-8 campus with completion slated for 2011. Owing to juxtaposing XFEL, the SPring-8 will become a unique large-scale third-generation synchrotron radiation facility, forming a center-of-excellence for advanced photon science. Also currently under construction is the electron beam transport system designed to inject the high quality electron beam generated by the XFEL linac to the SPring-8 storage ring.

II. Machine Operation

The operation statistics since the facility was opened to users are shown in Fig. 1. In 2008, the total operation time of the accelerator complex was 5078.5 hours. The operation time of the storage ring was 5063.4 hours, of which 79.7% (4037.8 hours) was made available to the users. The down time resulting from failure accounted for 0.76% (30.7 hours) of the user time; in 2008, no great loss of user time exceeding several hours occurred. Since 2004, there has been no injection time because top-up injection was introduced. Concerning user service operation, the high availability (ratio of net user time to planned user time) was achieved, e.g., 99.0% in 2008. The total tuning and study time of 1010 hours was used for machine tuning, and the study of the linac, booster synchrotron and storage ring, and also for the beamline tuning and study.

Operations in three different filling modes were provided for the following user time: percentages 18.7% in the multi-bunch mode, 44.2% in the several bunch mode, such as the 203-bunch mode (203 equally spaced bunches) and 37.1% in the hybrid filling mode such as a 1/14- partially filled multi-bunch with 12-isolated bunches. In 2008, the several bunch mode was the dominant filling mode. In particular, 203-bunch mode reached 24.1% of the total user time. For the hybrid filling mode, 1.0 mA, 1.4 mA, 1.6 mA, or 3.0 mA, is stored in each isolated bunch. An isolated bunch purity better than 10^{-10} is routinely maintained in the top-up operation. Table III shows a summary of the beam filling patterns.

Table IV shows a summary of the useful beam parameters of the storage ring.



	1997	1998	1999	2000	2001	2002	2003	2004	2005	2006	2007	2008
Accelerator Operation Time	1286.0	4189.6	5051.6	5167.5	5456.1	5542.9	5419.5	5759.2	5317.1	5026.2	5027.9	5078.5
Storage Ring Operation Time	1270.6	4135.4	4863.9	4972.9	5340.6	5484.1	5328.5	5736.7	4781.3	5008.5	5019.2	5063.4
Tuning & Study (Acc. & BL)	304	1457.6	1624.2	1815	1276.5	1394.9	1245.8	1085.9	1559.2	1193.6	1100.3	1010
Injection	50	110	95.2	70.4	59.3	60.8	39.2	0	0	0	0	0
Failure	26	110	57.2	88.7	87.1	190.5	208.5	82.4	59.7	42.5	27.6	30.7
User Time	906	2512	3275	3193.4	4033.2	3896.7	3926	4590.9	3698.2	3790.1	3900	4037.8
Planned Time	984	2712	3432	3352	4176	4152	4176	4680	3762	3840	3936	4080
Availability (%)	97.2	96.7	98.2	97.4	98	95.3	95	98.1	98.3	98.7	99.1	99

Fig. 1. Operation statistics since the facility became available to users.

Table III. Filling patterns

	bunch current (mA)	life time (h)
Multi-bunch (160 bunch-train × 12)	0.05	~ 200
203 bunches	0.5	25 ~ 30
4 bunch-train × 84	0.3	35 ~ 50
11 bunch-train × 29	0.3	35 ~ 50
1/7 - filling + 5 single bunches	3.0 (single)	18 ~ 25
1/14 - filling + 12 single bunches	1.6 (single)	18 ~ 25
2/29 - filling + 26 single bunches	1.4 (single)	18 ~ 25
4/58 - filling + 53 single bunches	1.0 (single)	18 ~ 25

Table IV. Beam parameters of SPring-8 storage ring

Energy [GeV]	8
Number of buckets	2436
Tunes (ν_x / ν_y)	40.15 / 18.35
Current [mA]:	
single bunch	12
multi bunch	100
Bunch length (σ) [psec]	13
Horizontal emittance [nm·rad]	3.4 *
Vertical emittance [pm·rad]	6.8 *
Coupling [%]	0.2
RF Voltage [MV]	16
Momentum acceptance [%]	±3 (±200 MeV)
Beam size [μm]: (σ_x / σ_y)* [μm]	
Long ID section	294 / 10
ID section	301 / 6
BM section	107 / 13
Beam divergence [μrad]: ($\sigma_{x'}$ / $\sigma_{y'}$)* [μrad]	
Long ID section	13 / 0.7
ID section	12 / 1.1
BM section	56 / 0.6
Operatinal chromaticities: (ξ_x / ξ_y)	+2 / +6 **
Lifetime [hr]:	
100 mA (multi-bunch)	~ 200
1 mA (single bunch)	~ 20
Horizontal dispersion [m]:	
Long ID section	0.103
ID section	0.107
BM section	0.032
Fast orbit stability (0.1 – 200 Hz) [μm]:	
horizontal (rms)	~ 4
vertical (rms)	~ 1

* Assuming 0.2% coupling for "Low Emittance Optics"
** With bunch-by-bunch feedback

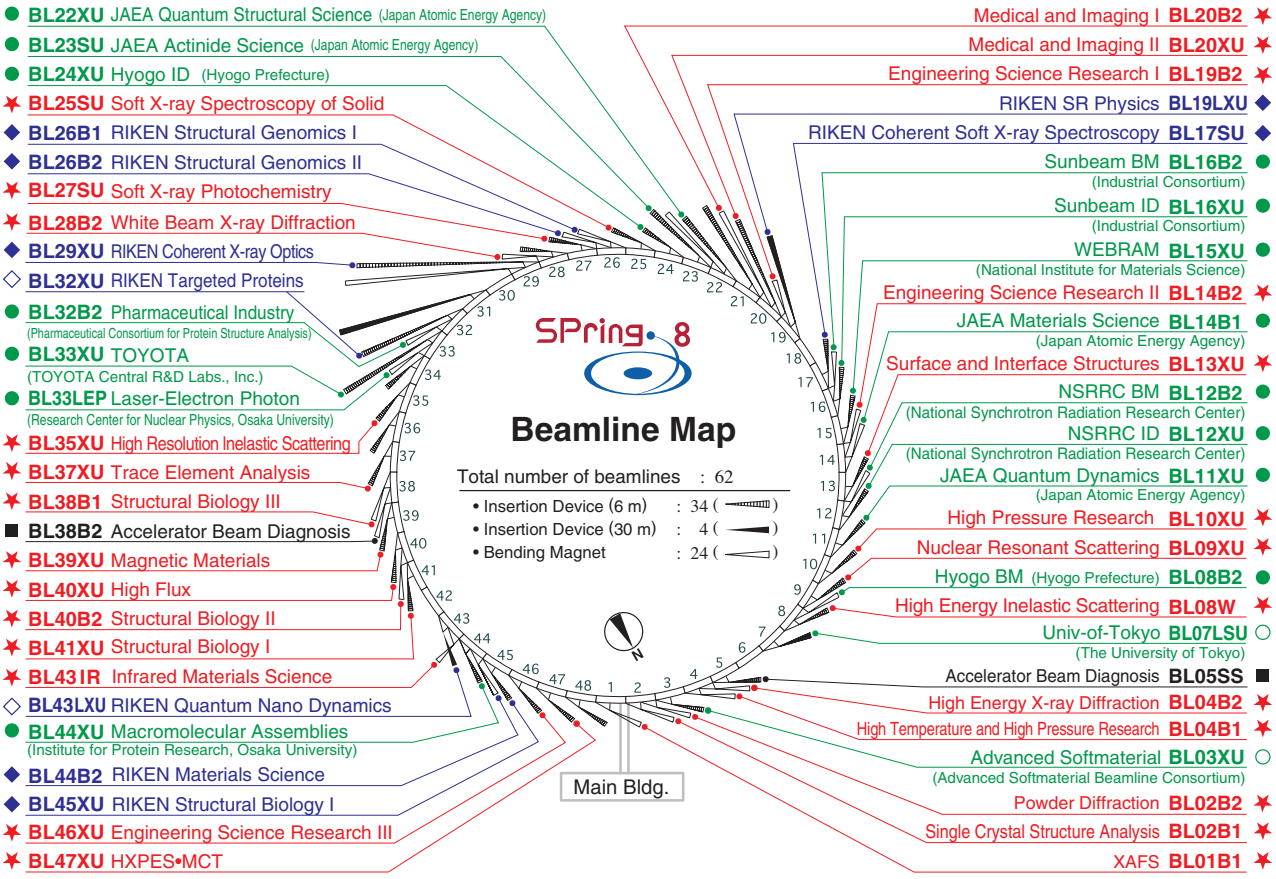
III. Beamlines

The SPring-8 storage ring can accommodate up to 62 beamlines: 34 insertion devices, 4 long undulators, and 24 bending magnets. At the time of writing, 50 beamlines are in operation, covering a wide variety of research fields of synchrotron radiation science and technology. The beamlines are classified into the following four types:

(1) Public Beamlines
(2) Contract Beamlines
(3) RIKEN Beamlines
(4) Accelerator Diagnostics Beamlines

There are now 26 public beamlines in full operation. The beamlines, which are proposed and constructed by external organizations such as universities, research institutes, private companies, and so forth, are called contract beamlines, and are exclusively used by the contractors for their own research purposes. At present, 15 contract beamlines are in operation. The contract beamlines includes NSRRC BM (BL12B2) and NSRRC ID (BL12XU) beamlines, which were contracted by the National Synchrotron Radiation Research Center in Taiwan. These are the first contract beamlines installed at the SPring-8 by a foreign organization. Currently, two new contract beamlines are under construction: Advanced Softmaterial (BL03XU) and Univ-of-Tokyo (BL07LSU) beamlines. Those beamlines constructed by RIKEN are called RIKEN beamlines, and are used for RIKEN's own research activities. RIKEN is now operating seven RIKEN beamlines, and is constructing a new beamline called RIKEN Targeted Proteins (BL32XU). In addition, two accelerator diagnostics beamlines are in operation.

To display the beamline portfolio of the SPring-8, the beamline map is shown in Fig. 2 together with the beamline classification. Research field of each beamline is presented in Table V.



BL: Beamline
B1, B2: Bending Magnets
XU: X-ray Undulator
SU: Soft X-ray Undulator
W: Wiggler

IR: Infrared Radiation
LEP: Laser-Electron Photon
LXU: Long-length X-ray Undulator
LSU: Long-length Soft X-ray Undulator
SS: Straight Section

WEBRAM: Wide Energy Range Beamline for Research in Advanced Materials
NSRRC: National Synchrotron Radiation Research Center, Taiwan

HXPES•MCT: Hard X-ray Photoelectron Spectroscopy, Micro-Tomography

★ : Public Beamlines
● : Contract Beamlines
◆ : RIKEN Beamlines
■ : Accelerator Diagnostics Beamlines
○ ◇ : Planned or Under Construction

Fig. 2. Beamline map.

Table V. List of beamlines

BL #	Beamline Name	(Public Use)	Areas of Research
★ Public Beamlines			
BL01B1	XAFS	(Oct. 1997)	XAFS in wide energy region (3.8 to 113 keV). XAFS of dilute systems and thin films. Quick XAFS with a time resolution of seconds to as tenth seconds.
BL02B1	Single Crystal Structure Analysis	(Oct. 1997)	Single crystal structure analysis in X-ray wide energy range. Precise X-ray diffraction analysis of the lattice or charge modulation originated from the phase transition at low temperature.
BL02B2	Powder Diffraction	(Sep. 1999)	Accurate structure analysis of crystalline materials using powder diffraction data by Rietveld refinements and maximum entropy method (MEM).
BL04B1	High Temperature and High Pressure Research	(Oct. 1997)	Mineral physics at high temperature and high pressure. Energy-dispersive X-ray diffraction and X-ray radiography using the large-volume press.
BL04B2	High Energy X-ray Diffraction	(Sep. 1999)	Structural analysis of glass, liquid, and amorphous materials. X-ray diffraction under ultra high-pressure. Precise single crystal structure analysis.
BL08W	High Energy Inelastic Scattering	(Oct. 1997)	Magnetic Compton scattering. High-resolution Compton scattering. High-energy Bragg scattering. High-energy fluorescent X-ray analysis.
BL09XU	Nuclear Resonant Scattering	(Oct. 1997)	Lattice dynamics using nuclear inelastic scattering. Time domain Mössbauer spectroscopy, especially under the extreme conditions. Coherent X-ray optics using nuclear resonant scattering. Nuclear excitation by electron transition (NEET). Surface structures and residual strain analysis.
BL10XU	High Pressure Research	(Oct. 1997)	Structure analysis and phase transitions under ultra high pressure (DAC experiment). Earth and planetary science.
BL13XU	Surface and Interface Structures	(Sep. 2001)	Atomic-scale structural analysis of an ultra-thin film, nanostructure and surface, using in-air measurements (room temperature to 500 ºC) and in-vacuum measurements (20 to 1300 K).
BL14B2	Engineering Science Research II	(Sep. 2007)	XAFS in wide energy region (3.8 to 72 keV). XAFS of dilute systems and thin films.
BL19B2	Engineering Science Research I	(Nov. 2001)	Residual stress measurement. Structural analysis of thin film, surface, interface. Powder diffraction. X-ray imaging, X-ray topography. Ultra-small angle X-ray scattering.
BL20XU	Medical and Imaging II	(Sep. 2001)	Microimaging. Hard X-ray microbeam/scanning microscopy, imaging microscopy, micro-tomography, phase-contrast microtomography with Bonse-Hart interferometer, X-ray holography, coherent X-ray optics, and other experiments on X-ray optics and developments of optical elements. Medical application. Microangiography, refraction-enhanced imaging, radiation therapy, phase-contrast CT using interferometer. Ultra-small angle scattering.
BL20B2	Medical and Imaging I	(Sep. 1999)	Medical research mainly involves micro-radiography, micro-tomography and refraction-contrast imaging on biological specimens and small animals. Imaging techniques involve the evaluation and development of various kinds of optical elements for novel imaging techniques.
BL25SU	Soft X-ray Spectroscopy of Solid	(Apr. 1998)	Observation of electronic structures by photoemission spectroscopy (PES). Observation of electronic band structures by angle resolved photoemission spectroscopy (ARPES). Magnetic state study by magnetic circular dichroism (MCD) of soft X-ray absorption. Element-specific magnetization curve measurements by MCD analysis of atomic arrangements by photoelectron diffraction (PED). Observation of magnetic domains by photoelectron emission microscope (PEEM).
BL27SU	Soft X-ray Photochemistry	(May 1998)	Industrial research of functional material. Atomic and molecular spectroscopy by high resolution electron spectroscopy. Surface analysis and solid state physics.
BL28B2	White Beam X-ray Diffraction	(Sep. 1999)	White X-ray diffraction. Time-resolved energy-dispersive XAFS (DXAFS). Medical applications. White X-ray topography.
BL35XU	High Resolution Inelastic Scattering	(Sep. 2001)	Material dynamics on ~meV energy scales using inelastic X-ray scattering (IXS) and nuclear resonant scattering (NRS).
BL37XU	Trace Element Analysis	(Nov. 2002)	X-ray microbeam spectrochemical analysis. Ultra trace element analysis. High energy X-ray fluorescence analysis.
BL38B1	Structural Biology III	(Oct. 2000)	Routine data collection for macromolecular crystallography.
BL39XU	Magnetic Materials	(Oct. 1997)	X-ray magnetic circular dichroism (XMCD) spectroscopy and element-specific magnetometry under multiple-extreme conditions. Micro-XMCD. X-ray emission spectroscopy. Resonant X-ray magnetic scattering.
BL40XU	High Flux	(Apr. 2000)	Time-resolved diffraction and scattering experiments. Microbeam X-ray diffraction experiments. Quick XAFS.
BL40B2	Structural Biology II	(Sep. 1999)	Noncrystalline small and wide angle X-ray scattering
BL41XU	Structural Biology I	(Oct. 1997)	Structural biology. Macromolecular crystallography. Ultra-high resolution structural analysis.
BL43IR	Infrared Materials Science	(Apr. 2000)	Infrared microspectroscopy. Magneto-optical spectroscopy.
BL46XU	Engineering Science Research III	(Nov. 2000)	Structural characterization of thin films by X-ray diffraction and X-ray reflectivity measurement. Residual stress measurement. Time resolved X-ray diffraction measurement. Hard X-ray photoemission spectroscopy.
BL47XU	HXRES·MCT	(Oct. 1997)	Hard X-ray photoelectron spectroscopy. Projection type micro-tomography. Imaging type micro-tomography. Hard X-ray microbeam/scanning microscopy.

BL #	Beamline Name	(First Beam)	Areas of Research
	● Contract Beamlines		
BL08B2	**Hyogo BM** (Hyogo Prefecture)	(Jun. 2005)	XAFS in a wide energy region. Small angle X-ray scattering for structural analyses of polymer and nanocomposite materials. X-ray topography. Imaging. Powder diffraction with a high angular resolution.
BL24XU	**Hyogo ID** (Hyogo Prefecture)	(May 1998)	Structure analysis of small bio-crystals for industry. Surface/interface analysis for industry by fluorescent X-ray analysis, strain measurements and grazing incidence X-ray diffraction. Microbeam formation studies for materials and life sciences.
BL12XU	**NSRRC ID** (National Synchrotron Rad. Res. Center, Taiwan)	(Dec. 2001)	High resolution non-resonant or resonant inelastic X-ray scattering. High resolution near-edge X-ray Raman scattering. Phase transitions under high-pressure, low and high temperatures. High-resolution X-ray absorption and emission spectroscopy. X-ray physics and optics.
BL12B2	**NSRRC BM** (National Synchrotron Rad. Res. Center, Taiwan)	(Oct. 2000)	X-ray absorption spectroscopy. Powder X-ray diffraction. High resolution X-ray scattering. Protein crystallography.
BL15XU	**WEBRAM** (National Institute for Materials Science)	(Jan. 2000)	Hard X-ray photoelectron spectroscopy. Highly precise X-ray powder diffraction
BL16XU	**Sunbeam ID** (Industrial Consortium)	(Oct. 1998)	Characterization of thin films for ULSI and magnetic devices, catalysts, functional materials, and structural materials by X-ray diffraction, fluorescence X-ray analysis, X-ray magnetic circular dichroism, and imaging with X-ray microbeam.
BL16B2	**Sunbeam BM** (Industrial Consortium)	(Oct. 1998)	Characterization of industrial materials by X-ray absorption fine structure measurements, X-ray diffraction and other methods.
BL32B2	**Pharmaceutical Industry** (Pharmaceutical Consortium for Protein Structure Analysis)	(Apr. 2002)	Protein structure analysis for structure-based drug design: Design and optimization of new leading compounds based on pharmacodynamic action mechanism elucidated at the molecular level which obtained from a detailed interaction analysis of receptor-drug complexes.
BL33XU	**TOYOTA** (TOYOTA Central R&D Labs., Inc.)	(Apr. 2009)	Time-resolved XAFS. Characterization of industrial materials, such as catalysts, secondary batteries, fuel cells.
BL33LEP	**Laser-Electron Photon** (RCNP, Osaka University)	(Jun. 1999)	Meson photoproduction from nucleon and nucleus. Photoexcitation of hyperons, nucleon resonances, and other exotic states. Photonuclear reactions. Beam diagnoses. Test and calibration of detectors with GeV photon beam.
BL44XU	**Macromolecular Assemblies** (IPR, Osaka University)	(May 1999)	Crystal structure analysis of biological macromolecular assemblies (e.g. membrane complexes, protein complexes, protein-nucleic acid complexes, and viruses).
BL11XU	**JAEA Quantum Dynamics**	(Oct. 1998)	Nuclear scattering. Surface and interface structure with MBE. Inelastic X-ray scattering. XAFS.
BL14B1	**JAEA Materials Science**	(Dec. 1997)	Materials science under high-temperature. *In situ* study on catalysis using dispersive XAFS. X-ray diffraction for structure physics.
BL22XU	**JAEA Quantum Structural Science**	(May 2002)	Materials science under high-pressure. Resonant X-ray scattering. Speckle scattering. Residual stress/strain distribution analysis.
BL23SU	**JAEA Actinide Science**	(Feb. 1998)	Surface chemistry with supersonic molecular beam. Biophysical spectroscopy. Photoelectron spectroscopy. Magnetic circular dichroism.
	◆ RIKEN Beamlines		
BL17SU	**RIKEN Coherent Soft X-ray Spectroscopy**	(Sep. 2003)	High resolution photoemission spectroscopy. Soft X-ray emission spectroscopy for liquid and biological samples. Soft X-ray diffraction spectroscopy. Surface science.
BL19LXU	**RIKEN SR Physics**	(Oct. 2000)	Any research field requiring the highly brilliant X-ray beam.
BL26B1	**RIKEN Structural Genomics I**	(Apr. 2002)	Structural genomics research based on single crystal X-ray diffraction.
BL26B2	**RIKEN Structural Genomics II**	(Apr. 2002)	Structural genomics research based on single crystal X-ray diffraction.
BL29XU	**RIKEN Coherent X-ray Optics**	(Dec. 1998)	X-ray optics, especially coherent X-ray optics.
BL44B2	**RIKEN Materials Science**	(Feb. 1998)	Macromolecular crystallography.
BL45XU	**RIKEN Structural Biology I**	(Jul. 1997)	Time-resolved and static structures of non-crystalline biological materials using small-angle scattering and diffraction techniques.
	■ Accelerator Diagnostics Beamlines		
BL05SS	**Accelerator Beam Diagnosis**	(Mar. 2004)	Accelerator beam diagnosis. R&D of accelerator components. Production of MeV γ-ray photons.
BL38B2	**Accelerator Beam Diagnosis**	(Sep. 1999)	Accelerator beam diagnosis. R&D of accelerator components.

IV. User Program and Statistics

IV-1. Program Overview

JASRI calls for public use proposals twice a year. The submitted proposals are reviewed by the Proposal Review Committee (PRC). As for General Proposals, 560 proposals out of 782 submitted proposals were approved in the research term 2007B, and 558 out of 754 proposals were approved in 2008A. Since the start of the Long-term Program in 2000B, 22 Long-term Proposals have been implemented. In 2008A, three new proposals were approved. During the past year, a total of 11 proposals were carried out. During 2007B and 2008A, Nanotechnology Support Proposals, Industrial Application Proposals, Medical Bio Trial Use Proposals and Medical Bio EX Proposals were called for as the Priority Field Proposals. Out of 225 submitted proposals, 161 proposals were approved in 2007B, and 191 out of 255 proposals were approved in 2008A. The proposal statistics is shown in Table VI for the period from 1997B to 2008A, in which Power User Proposals and JASRI Proposals are excluded. During the period from 2003B to 2008A, 11 user groups have been designated as Power User groups (PUs), which include six PUs active in 2007B and 2008A. To date, a total of 2,226 shifts have been used by PUs, of which 579 shifts were spent from 2007B to 2008A.

The SPring-8 consistently provided 2,140 hours of user beamtime in 2007B, and 2,231 hours in 2008A. Since the start of operation in 1997, the SPring-8 has succeeded in providing users with the total beamtime of 41,119 hours. In 2007B, 965 experiments were conducted by 6,752 users at public and contract beamlines, and 1,001 experiments by 6,731 users in 2008A. During the period from the start of operation in 1997 up to 2008A, a total of 13,551 experiments were conducted by 91,330 users.

The beamtime available to the users, the number of experiments conducted, and the number of user visits at the public and contract beamlines are summarized in Table VII and in Fig. 3.

Figure 4 shows the breakdown of the approved proposals sorted by user affiliation and of the number of experiments conducted at the public and contract beamlines during the period from 1997B to 2008A. The percentages of experiments conducted by users from abroad were 3.8% in 2007B and 6.9% in 2008A.

Since the SPring-8 is a public facility widely open not only to academia but to industrial sectors, JASRI established the Industrial Application Division in 2005. The division's coordinators specializing in the fields of SR industrial applications are available for consultation with new users. The division also has the experiment support personnel who provide technical advice and support. Currently, Industrial Application Proposals account for approximately 20% of total proposals conducted at the public beamlines. From 2007B, the SPring-8 has introduced the SPring-8 Measurement Service, in which the personnel of the Industrial Application Division can carry out XAFS measurements on behalf of users at BL14B2. This new program is expected to provide convenience for companies that have difficulty in retaining their own specialized staff, and to meet the needs for quick access.

Table VI . Numbers of submitted proposals and approved proposals in each research term

Research Term	Beamtime available to users at each beamline	Submission deadline	Number of submitted proposals	Number of approved proposals
1997B: 1997.10 - 1998.03	168	1997.1.10	198	134
1998A: 1998.04 - 1998.10	204	1998.1.6	305	229
1999A: 1998.11 - 1999.06	250	1998.7.12	392	258
1999B: 1999.09 - 1999.12	140	1999.6.19	431	246
2000A: 2000.02 - 2000.06	204	1999.10.16	424	326
2000B: 2000.10 - 2001.01	156	2000.6.17	582	380
2001A: 2001.02 - 2001.06	238	2000.10.21	502	409
2001B: 2001.09 - 2002.02	190	2001.5.26	619	457
2002A: 2002.02 - 2002.07	226	2001.10.27	643	520
2002B: 2002.09 - 2003.02	190	2002.6.3	751	472
2003A: 2003.02 - 2003.07	228	2002.10.28	733	563
2003B: 2003.09 - 2004.02	202	2003.6.16	938	621
2004A: 2004.02 - 2004.07	211	2003.11.4	772	595
2004B: 2004.09 - 2004.12	203	2004.6.9	886	562
2005A: 2005.04 - 2005.08	188	2005.1.5	878	547
2005B: 2005.09 - 2005.12	182	2005.6.7	973	624
2006A: 2006.03 - 2006.07	220	2005.11.15	916	699
2006B: 2006.09 - 2006.12	159	2006.5.25	867	555
2007A: 2007.03 - 2007.07	246	2006.11.16	1099	761
2007B: 2007.09 - 2008.02	216	2007.6.7	1007	721
2008A: 2008.04 - 2008.07	225	2007.12.13	1009	749

Table VII. SPring-8 user operation results

Research Term	User Time (hours)	Public BL		Contract BL	
		Experiments	Users	Experiments	Users
1997B: 1997.10 - 1998.03	1,286	94	681	–	–
1998A: 1998.04 - 1998.10	1,702	234	1,252	7	–
1999A: 1998.11 - 1999.06	2,585	274	1,542	33	467
1999B: 1999.09 - 1999.12	1,371	242	1,631	65	427
2000A: 2000.02 - 2000.06	2,051	365	2,486	100	794
2000B: 2000.10 - 2001.01	1,522	383	2,370	88	620
2001A: 2001.02 - 2001.06	2,313	474	2,915	102	766
2001B: 2001.09 - 2002.02	1,867	488	3,277	114	977
2002A: 2002.02 - 2002.07	2,093	545	3,246	110	1,043
2002B: 2002.09 - 2003.02	1,867	540	3,508	142	1,046
2003A: 2003.02 - 2003.07	2,246	634	3,777	164	1,347
2003B: 2003.09 - 2004.02	1,844	549	3,428	154	1,264
2004A: 2004.02 - 2004.07	2,095	569	3,756	161	1,269
2004B: 2004.09 - 2004.12	1,971	555	3,546	146	1,154
2005A: 2005.04 - 2005.08	1,880	560	3,741	146	1,185
2005B: 2005.09 - 2005.12	1,818	620	4,032	187	1,379
2006A: 2006.03 - 2006.07	2,202	724	4,809	226	1,831
2006B: 2006.09 - 2006.12	1,587	550	3,513	199	1,487
2007A: 2007.03 - 2007.07	2,448	781	4,999	260	2,282
2007B: 2007.09 - 2008.02	2,140	739	4,814	226	1,938
2008A: 2008.04 - 2008.07	2,231	769	4,840	232	1,891
	41,119	10,689	68,163	2,862	23,167

Note: The numbers of long-term proposals are counted by beamline, that is, if two beamlines were used for one experiment, those are counted as two experiments.

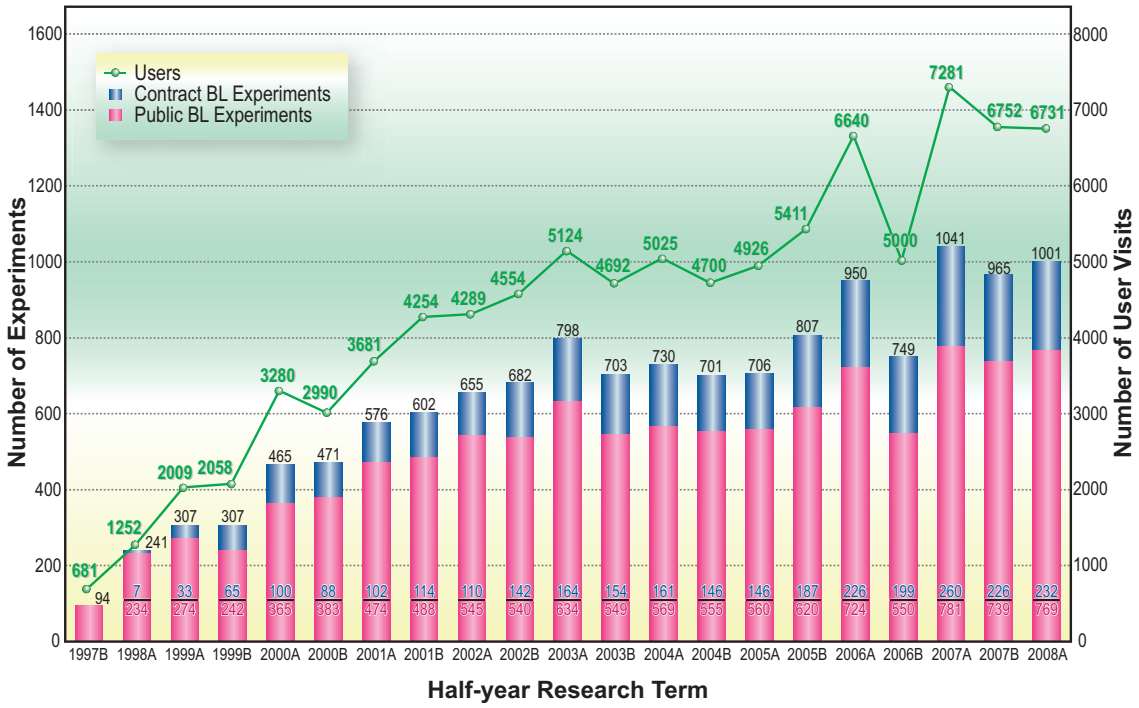


Fig. 3 . Numbers of user visits and conducted experiments.

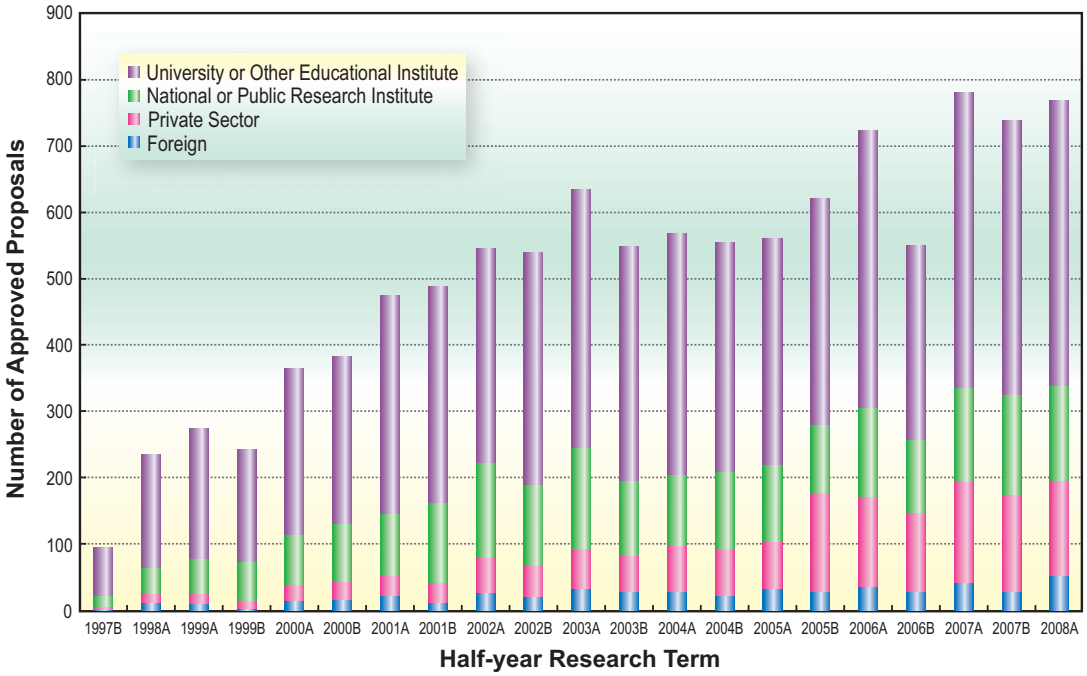


Fig. 4 . Number of approved proposals by affiliation of applicants (public beamlines).

IV-2. Types of Research (Proprietary and Non-Proprietary Research)

With respect to the handling of research results obtained by using the SPring-8, there are two types of research at the SPring-8: proprietary and non-proprietary research. For research to be considered non-proprietary, users must submit the SPring-8 Experiment Report within 60 days of the completion of each experiment to make the results available to the public. Users can use beamlines free of charge if their research is non-proprietary. As for proprietary research, the research proposals are reviewed only from the viewpoint of feasibility, safety, sociality, and ethics. In this type of research, users are charged beamtime fee of 480,000 yen/shift based on cost recovery for the SPring-8 beamline operation. In return, the SPring-8 Experiment Reports need not be submitted.

IV-3. Types of Proposals

A. General Research Program

(i) General Proposal

JASRI calls for General Proposals twice a year. Once approved, the validity of each proposal is six months. Up to 10% of total beamtime is allocated to proprietary proposals.

(ii) Long-term Proposal

Beamtime is reserved for Long-term Proposals for three years in order to promote research expected (a) to produce outstanding results in the field of science and technology, (b) to establish a new research field or experimental method, and (c) to significantly improve industrial base technology by fully utilizing the characteristics of the SPring-8. The call for Long-term Proposals and the review process take place twice a year prior to those for General Proposals. For this type of proposal, proprietary research is not available. The review process consists of two steps: application forms are reviewed initially and applicants who meet certain criteria will proceed to the interview.

(iii) Urgent Proposal

This system is designed for users with urgent needs to conduct experiments of great scientific significance. The PRC reviews the submitted proposals on a rolling basis and promptly determines whether to approve or reject them.

(iv) Budding Researchers Support Proposal

The Budding Researchers Support Program intends to encourage doctoral students with an exploratory and original research proposal or research theme who are expected to contribute to the development of synchrotron radiation research. Under the program, successful applicants will be provided with domestic travel and lodging expenses. At the time of experiment at the SPring-8, applicants must be doctoral students who can show initiative, work independently, and be self-reliant when conducting research at the SPring-8. All applicants are required to obtain permission to apply from their Ph.D. advisor, who must be included as a project team member.

(v) Non-proprietary Grant-aided Proposal

The Non-Proprietary Grant-Aided Program is intended for research proposals that have been reviewed and approved for a large research grant available in Japan. Under the program, the proposals are exempt from scientific review process; and only the feasibility and the safety of the experiment are considered. These proposals are given priority consideration up to 5% of entire user beamtime, and 20% of user beamtime for each beamline. Instead, users are required to pay a program fee of 131,000 yen/shift.

(vi) Time-designated Proposal

The time-designated use is intended for users wishing to conduct proprietary research in a particular time period. Submitted proposals are promptly reviewed through a simplified process. Users are charged beamtime fee of 720,000 yen/shift for proprietary use (incl. 50% premium).

(vii) SPring-8 Measurement Service

The staff of JASRI perform measurements on behalf of users, and users can choose whether to come to the SPring-8 and be present during the measurements or to simply send their samples to the SPring-8. The service is intended to provide convenience for companies and research institutes that find it difficult to retain specialized staff and to accommodate the need for quick access. Application for the service is considered a proprietary proposal and is subject to the proprietary beamtime fee and user fee applicable to Time-designated Proposals (calculated in two-hour increments).

B. Priority Research Program

The Priority Research Program is categorized into the following two types: the priority field type and the priority user type. As for the priority field type, JASRI designates the research fields of strategic

importance. As for the priority user type, eligible candidates, who are highly familiar with the public beamlines and their methodological approaches, and who are expected to deepen the academic fields of SR science and technology, are designated as power users. JASRI has been providing active support for this program to produce a number of high-quality results.

B-1) Priority Field Type

Currenty, the following three types of research are designated under the priority field type:

(i) Nanotechnology Support Proposal (period of designation: FY2007-FY2011)

Based on the achievements gained through the Nanotechnology Support Project (a national project from FY2002 to FY 2006), the research field of nanotechnology and nano-materials has been designated as the priority field. The purpose of this system is to support research in the field of nanotechnology and nano-materials for innovation creation in 5-10 years time.

(ii) Industrial Application Proposal (period of designation: FY2007-FY2011)

This field is aimed at promoting the expansion of industrial application fields by attracting new users, developing basic technology through the industry-academia-government cooperation, and promoting the project whose achievements contribute to companies and society. JASRI provides intensive support in the categories of "new users," "new area," "industrial base consortium," and "advanced technology development." To meet the needs of industrial users, JASRI calls for Industrial Application Proposals four times a year for the three public beamlines (BL14B2, BL19B2 and BL46XU) dedicated to industrial applications.

(iii) Medical Bio Trial Use Proposal and Medical bio EX proposal (period of designation: FY2006-FY2009)

Aiming at establishing new experimental methods in the field of medical bio, there are two types of proposals in this field: Medical Bio Trial Use Proposal and Medical Bio EX Proposal. The Medical Bio Trial Use Proposal is intended for the promotion of the beamline use by new users, who seek to develop and establish a new approach to solving problems at the forefront of medical biology research. The Medical Bio EX Proposal, which is an expanded and developed form of the Medical Bio Trial Use Proposal, is designed for research aiming to discover the causes of major diseases and to develop their diagnostic and treatment methods.

B-2) Priority User Type

(i) Power User Proposal

Power User Proposals are non-proprietary proposals designed for designated power user groups (PUs) to produce outstanding results in the field of pioneering use of SR using up to 20% of beamtime allocated to beamlines accepting PUs. The power user designation period is five years. PUs are subject to an interim review of research achievements, equipment development, and user support by the Power User Review Committee at the end of the third year and whether to continue or discontinue the power user status is determined. When the designation period is completed, a post implementation review is conducted by the Committee. JASRI invites applications for power user positions once a year, which takes place before the proposal calls for research term A.

IV-4. Beamtime Allocation

The beamtime allocation of public beamlines is arranged in a way that more than 50% of the total beamtime is allocated to the public use proposals (proposals submitted in response to the calls for proposals and approved by the PRC), while up to 20% is allocated to JASRI's own research proposals. The remaining beamtime is used for seminars, trainings, setup/removal and adjustment of equipment for user experiments, and proposals with special needs and requirements (Urgent, Time-designated, and Power User Proposals). The conceptual scheme of the beamtime allocation at the public beamlines is shown in Fig. 5 below.

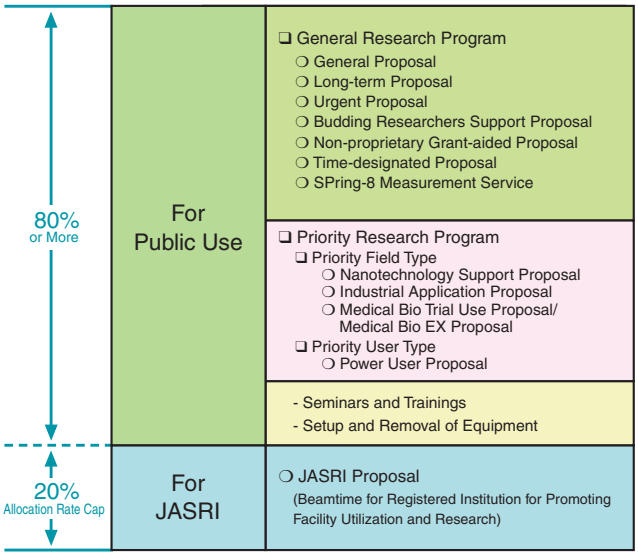


Fig. 5. Conceptual scheme of beamtime allocation at public beamlines.

IV-5. Research Outcome

When users conduct non-proprietary experiments, they are required to submit the SPring-8 Experiment Report to JASRI within 60 days of the completion of their experiments. When the research results obtained through the use of the SPring-8 are published in academic journals and other publications, the project leaders are requested to report to JASRI.

As of March 2009, the number of registered refereed papers is 4,447: out of which, 3,505 papers resulted from the use of public beamline, 685 papers from that of contract beamlines, 668 papers from that of RIKEN beamlines, and 321 papers from hardware/software R&D. The papers resulting from the use of two or more beamlines are counted at each beamline. Figure 6 shows the annual statistics of refereed papers.

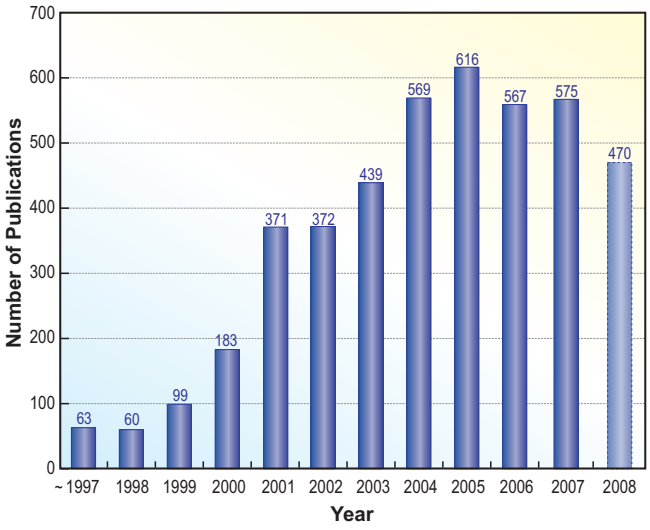


Fig. 6. Number of refereed publications as of March 2009.

V. Budget and Personnel

Since the start of operation in 1997, the SPring-8 had been jointly managed by RIKEN, JAERI (JAEA, as it is known today), and JASRI. Since JAERI withdrew from the management of the SPring-8 on September 30, 2005, the SPring-8 has been administered by RIKEN and JASRI in a unified manner.

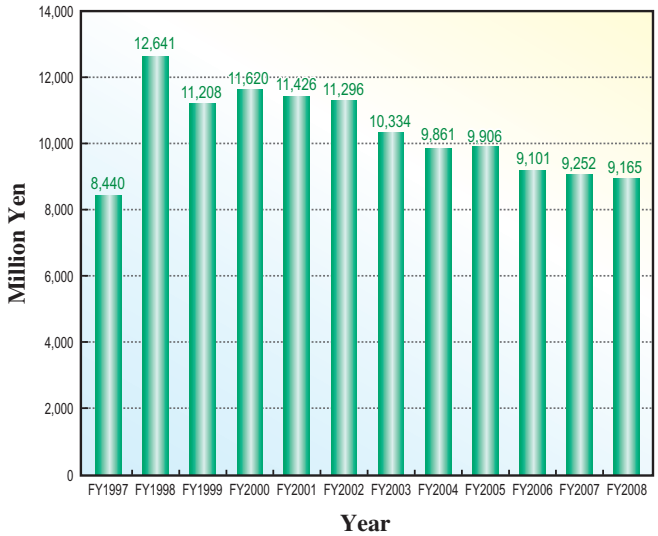
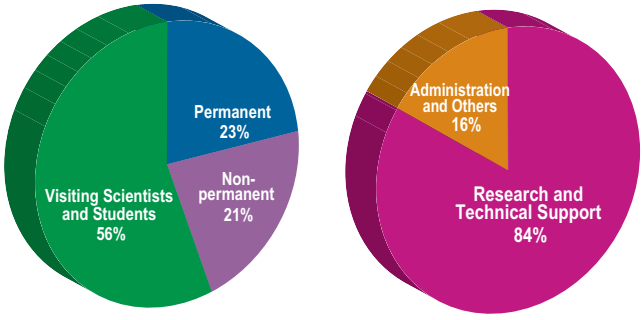


Fig. 7. SPring-8 budget.

The following figure (Fig. 7) shows the annual budget allocated to the operation, maintenance, and promotion of the use of the SPring-8 from FY1997 to date. The budget for FY2008 is 8.96 billion yen. The total number of staff of JASRI, RIKEN and XFEL project amounts to 1,225 as of October 2008 as shown in Fig. 8.



	by Type			by Field		Total
	Permanent	Non-permanent	Visiting Scientists and Students	Research and Technical Support	Administration and Others	
JASRI	234	142	147	374	149	**523**
RIKEN	52	84	466	562	40	**602**
XFEL	1	35	72	102	6	**108**
	287	**261**	**685**	**1038**	**195**	**1233**

Fig. 8. Personnel at SPring-8: JASRI, RIKEN and XFEL (FY2008).

VI. Research Complex

The facilities of the SPring-8, XFEL and NewSUBARU are forming a center-of-excellence at the SPring-8 campus, where JASRI, public beamline users, contractors of contract beamlines, RIKEN, and the University of Hyogo work in close cooperation to form a research complex playing their own roles to deliver high-quality results in the field of synchrotron radiation science and technology. Figure 9 shows the SPring-8 research complex and the operational and management of each research facility. The organizational charts of RIKEN and JASRI, which form the kernel of this research complex, are shown in Fig. 10 and Fig. 11, respectively.

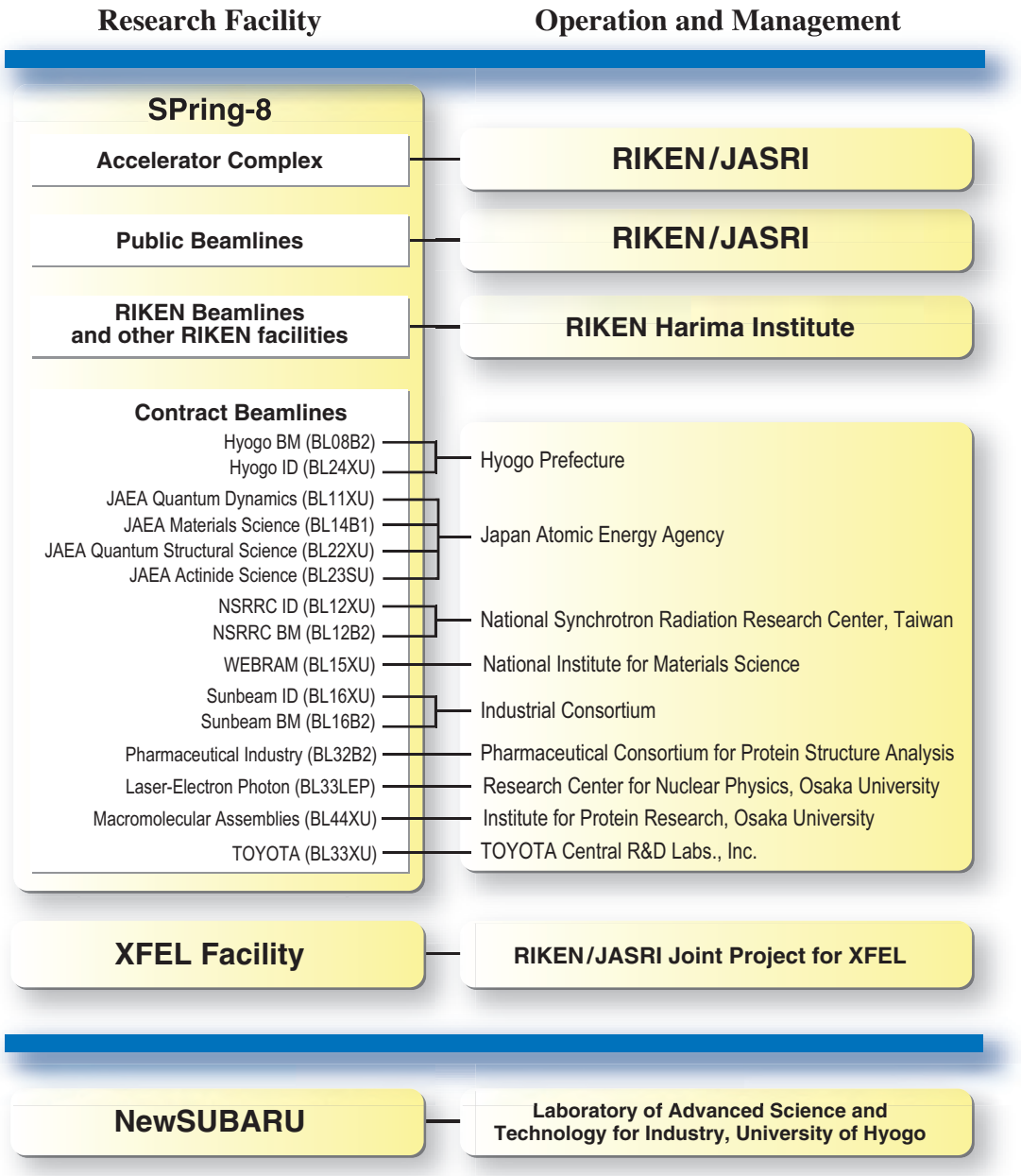


Fig. 9. SPring-8 research complex.

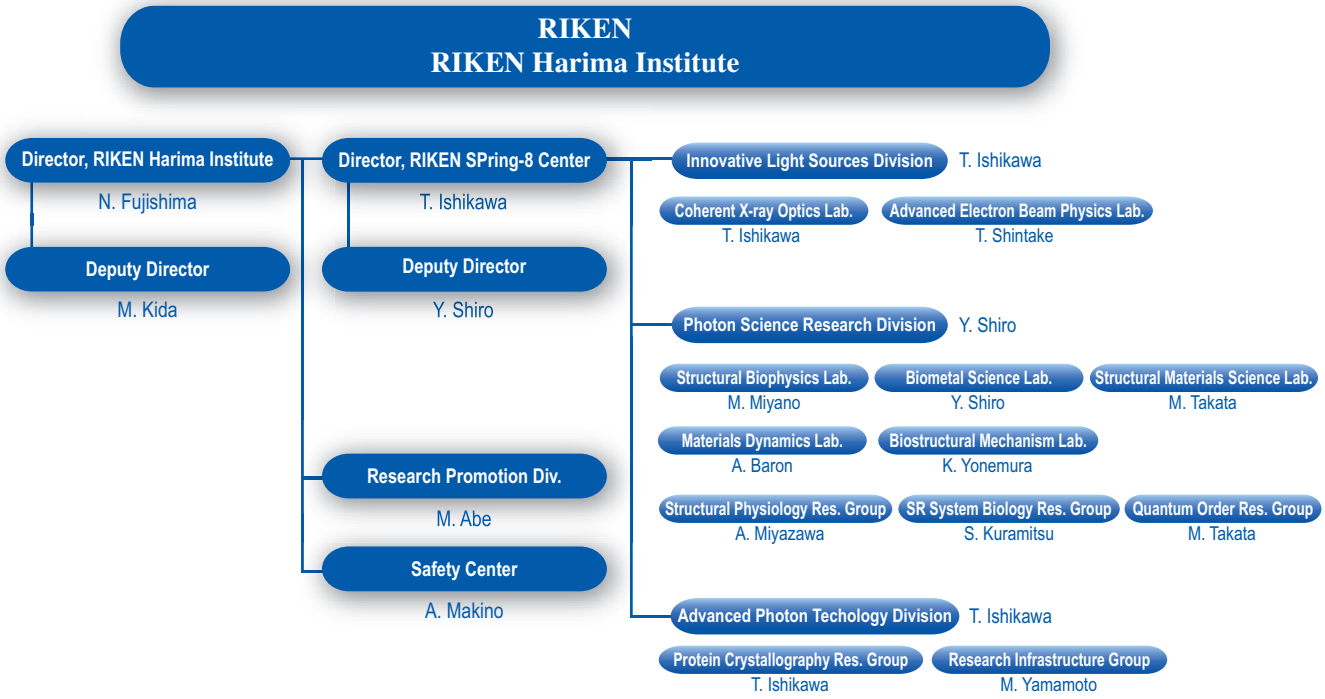


Fig. 10. RIKEN Harima chart as of April 2009.

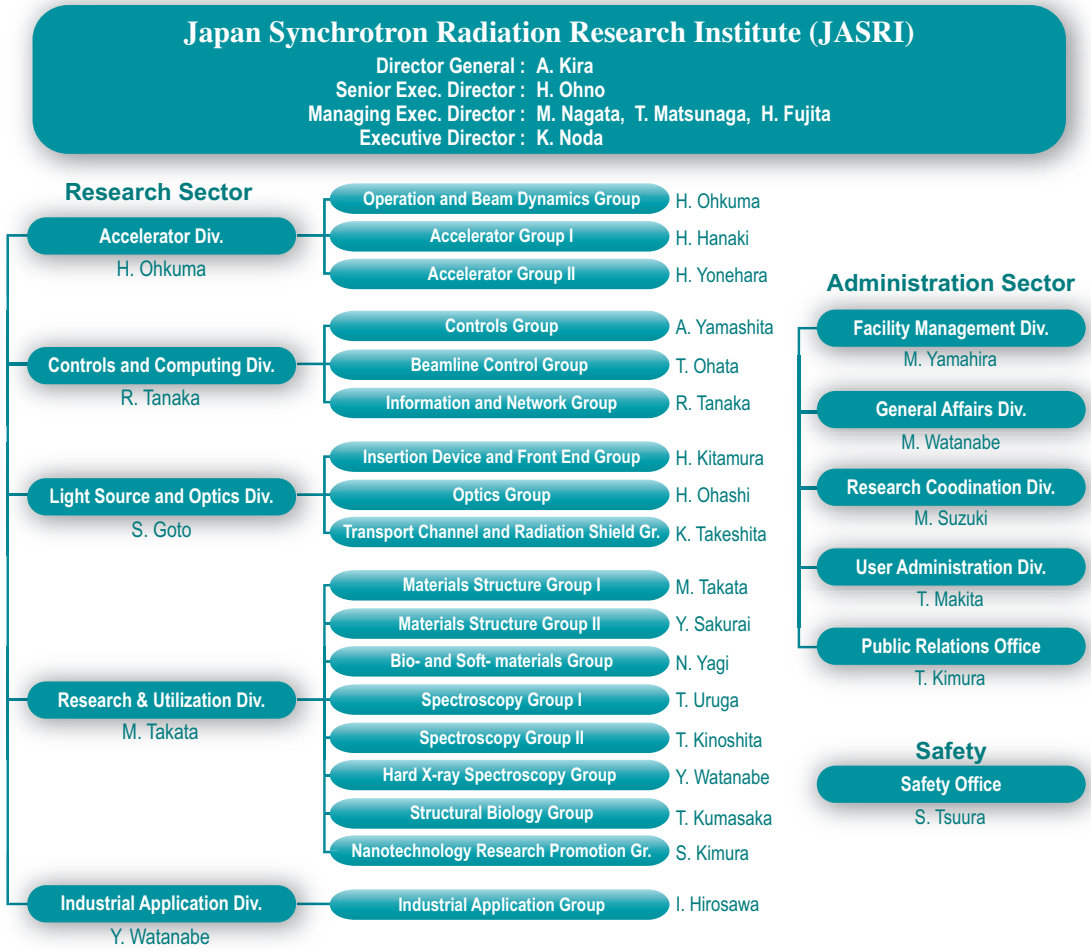


Fig. 11. JASRI chart as of April 2009.

VII. Users Societies, Conferences and Other Activities

SPring-8 Users Society

In order to promote and advance the research activities of users, the **SPring-8 Users Society** was established in May 1993 and made a substantial contribution to the SPring-8 construction. Now that the construction phase is over, their primary focus has shifted to the support for the upgrade of the SPring-8 facilities and the promotion of the SPring-8 utilization. To that end, the SPring-8 Users Society has nine commissions, under which 35 scientific research groups are formed to facilitate communication and information exchange between the facility and the experts. Among them two research groups have been newly organized in the fields of environmental science and educational use of synchrotron radiation. Most of research groups have renewed their two-year projects starting April 2008. Upon completion of each two-year project, their activity reports are prepared. In March 2009, the report entitled "Future Prospects for Scientific Activities at the SPring-8" is to be published to commemorate the 10th anniversary of the SPring-8. As of December 31, 2008, the SPring-8 Users Society has 1,448 members.

The **Industrial Users Society of the SPring-8** was established in September 1990 to promote the use of the SPring-8 by the member of companies. It has also made efforts in the development of the SPring-8 user program. Eight research groups have been organized representing various fields of applications. These research groups have played a significant role in enhancing communication among the industrial sector, JASRI, and the MEXT. Owing to their activities, the percentage of industrial applications has increased up to 20% in terms of the number of proposals approved. In addition to the activities of the research groups, the Society provides information on the trends of the synchrotron radiation facilities in Japan and abroad, and their latest research achievements. The Society consists of 71 companies and one organization as of December 31, 2008.

Conferences and Workshops

The conferences and workshops organized, sponsored, or hosted by JASRI, RIKEN or both in 2008 are listed below.

- 21th Annual Meeting of Japanese Society for Synchrotron Radiation Research, January 12-14, 2008 - Ritsumeikan University Biwako-Kusatsu Campus, Shiga
- The 3rd XFEL Symposium, January 16, 2008 - Marunouchi My Plaza, Tokyo
- The Memorial Lecture for the 10th Anniversary of Industrial Applications, January 23, 2008 - Conference Square M+, Tokyo
- The Report Meeting of SPring-8 Medical-bio Trial Use in FY2008, January 31, 2008 - Public Relations Center, SPring-8
- SPring-8 GPCR Symposium - Frontier on Integral Membrane Proteins in Crystal Structure Determination, February 26, 2008 - Public Relations Center, SPring-8
- The Meeting 2007A on Research Activities of Priority Research Proposals (Priority Field: Industrial Application), February 29, 2008 - National Museum of Emerging Science and Innovation, Tokyo
- The 9th Symposium on Accelerator Power Supply, March 6-7, 2008 - Public Relations Center, SPring-8
- Forefront of Nanotechnology Synchrotron Radiation Use Research, May 7, 2008 - Mielparque-Osaka, Osaka

- The 3rd International Conference on Diamond for Modern Light Sources,
  May 20-23, 2008 - Awaji Yumebutai · International Conference Center, Hyogo
- SPring-8 Workshop for a NanoDynamics Beamline, May 22-23, 2008 - Public Relations Center, SPring-8
- Workshop on the New Applications of Advanced X-ray Imaging Techniques in Materials Science,
  July 30, 2008 - Tokyo Station Conference, Tokyo
- The 11th Japanese XAFS Conference, August 6-8, 2008 - Egret Himeji, Hyogo
- The 6th International Conference on Borate Glasses, Crystals and Melts (BORATE2008),
  August 18-22, 2008 - Egret Himeji, Hyogo
- SPring-8 IUCr2008 Satellite Meeting on X-ray and Neutron Techniques for Nano-Structural Research,
  August 21-23, 2008 - Public Relations Center, SPring-8
- The 7th Annual Meeting of Structural-Biological Whole Cell Project of *Thermus thermophilus* HB8,
  September 13-15, 2008 - Public Relations Center, SPring-8
- Outlook for Active Use of SPring-8 is Soft Matter Dynamics,
  September 30, 2008 - Structural Biology Facility, SPring-8
- The 1st Workshop on the SPring-8 Budding Researchers Support Program,
  October 29, 2008 - National Museum of Emerging Science and Innovation, Tokyo
- Beam Physics Workshop 2008 at SPring-8, November 6-7, 2008 - Public Relations Center, SPring-8
- Synchrotron Radiation Industrial Applications Seminar - SPring-8/SAGA-LS Collaboration -
  November 7, 2008 - Sun Messe Tosu, Saga
- The 4th XFEL Symposium, December 12, 2008 - Tokyo International Exchange Center, Tokyo

Users Meeting

The meetings for users jointly organized by JASRI and the SPring-8 Users Society, and those organized by JASRI and the Industrial User Society of the SPring-8 are listed below.

- The 5th Report Meeting on SPring-8 Industrial Application,
  September 18-19 - National Museum of Emerging Science and Innovation, Tokyo
- The 12th SPring-8 Symposium
  October 30-November 1, 2008 - National Museum of Emerging Science and Innovation, Tokyo

Other Activities

- The 16th SPring-8 Open House
  April 27, 2008
- The 8th SPring-8 Summer School 2008
  July 11-14, 2008 - Kamitsubo Hall, SPring-8
- The 2nd AOFSRR Summer School - Cheiron School 2008
  September 29-October 8, 2008 - Public Relations Center, SPring-8

Project XFEL

Late in the 20th century, theoreticians discovered that a free electron laser (FEL) based on the self-amplified spontaneous emission (SASE) scheme has exceptional ability to produce ultrabrilliant, coherent radiation in a short wavelength region, including extreme ultraviolet (EUV), soft X-rays, and even hard X-rays. With great enthusiasm, the construction of X-ray FEL (XFEL) facilities was started in 21st century at Stanford Linear Accelerator Center (SLAC) in the US, Deutsches Elektronen-Synchrotron (DESY) in Germany, and SPring-8 in Japan. From the very beginning, the SPring-8 XFEL project claimed the importance of "compactness" in order to realize widespread distributions of XFEL machines for developing diverse fields of photon science.

This unique concept is based on the combination of Japan's original technologies: short-period invacuum undulators, high-gradient C-band linacs, and an ultralow-emittance thermionic electron gun. To verify the concept, the SPring-8 Compact SASE Source test accelerator (SCSS) was constructed in 2005. After many trials and developments, the SCSS finally achieved a stable saturation of the lasing power at a wavelength region of 50 to 61 nanometers in 2007. Succeedingly, the SCSS started to deliver the intense EUV radiation to users from May, 2008. The stable, robust operations to be achieved have been highly appreciated by a number of researchers, and provided great expectations for performance of the 8-GeV XFEL machine, which will start user operation in 2011.

Tetsuya Ishikawa

SPRING-8 COMPACT SASE SOURCE PROJECT
SCSS SPRING-8 COMPACT SASE SOURCE

Progress of the XFEL Project

1. Status of XFEL Construction

In FY2006, a five-year construction project of an 8-GeV XFEL facility was launched at SPring-8. This project was designated as one of the key technologies of national importance. Over the past three years, the construction has been progressing satisfactorily. Below we summarize our major achievements in 2008: (i) a large number of accelerator components were produced at factories; (ii) the manufacture of undulators was started; (iii) the specifications of XFEL beamline were determined; (iv) the electron-beam transport line from the 8-GeV linac to the SPring-8 storage ring was designed; and (v) the accelerator tunnel and undulator hall were completed.

Hereafter, we describe more details of the activities in XFEL construction. First, we have performed the reoptimization of accelerator parameters to provide a set of high-quality electron beams. To this purpose, we have performed start-to-end simulations from an electron gun to an 8-GeV beam dump. In these simulations, resistive wall wake fields in the undulator have been included. With these parameters, SASE-FEL radiation properties have been precisely evaluated. A summary of performance as well as the temporal profile are shown in Table 1 and Fig. 1, respectively.

To facilitate beam commissioning, we started to investigate beam commissioning-related subjects, i.e., the distribution of electron beam loss including dark current from the C-band acceleration system, the alignment-error tolerance of the accelerator structure, the effect of accelerator-structure vibration on beam quality, and the introduction of an rf deflector cavity for

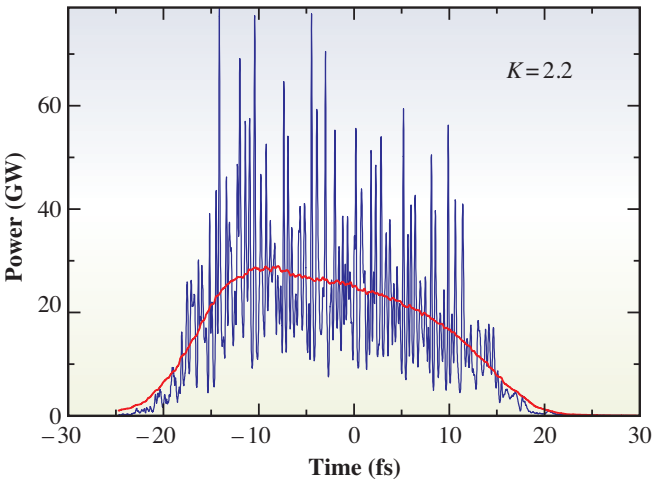


Fig. 1. Temporal profile of XFEL radiation at K=2.2. The red line shows a guide after smoothing.

Table 1. FEL radiation parameters at K=2.2 (for fundamental radiation)

FEL parameter	4.4×10^{-4}
Radiation wavelength (nm)	0.13
Photon energy (keV)	9.9
Bandwidth	9.2×10^{-4}
Source size (μm, rms)	33
Angular divergence (μrad, rms)	0.73
Beam size @ sample position (μm, rms, 100 m from ID exit)	80
Peak power (GW)	29
Pulse energy (mJ/pls)	0.78
Photons per pulse (phs/pls)	5.0×10^{11}
Pulse width (fs, FWHM)	30
Repetition rate (Hz)	60 (max) to 1 (min)
Power ratio of higher-order harmonic (2nd:1st)	1.3×10^{-4}
Power ratio of higher-order harmonic (3nd:1st)	2.8×10^{-3}



Fig. 2. Test bunker for high-power rf components.

measuring slice emittance and shot-by-shot longitudinal phase space.

A test bunker for high-power rf components was constructed in the SPring-8 site, as shown in Fig. 2, (i) to ensure the performance of the delivered rf components under a high-power condition, (ii) to establish an aging procedure for stable operation with design rf power and acceleration gradient and (iii) to accumulate fundamental data on dark current generation and aging period. The first high-power test was successfully performed: we confirmed to achieve a high acceleration gradient of 35 MV/m at a repetition rate of 60 Hz.

A new field correction procedure for an in-vacuum undulator was established with a manufactured prototype undulator in order to achieve the high field quality required for SASE XFEL. The new procedure consists of the following steps; the conventional field correction is performed first to compensate phase and multipole-field errors in the field measurement bench with the vacuum vessel removed. To install the vacuum vessel, magnet arrays are detached from the mechanical frame and then built again inside it. The field distribution is then measured with the developed *in situ* field measurement system named SAFALI (self aligned field analyzer with laser instrumentation). A possible gap deformation during the above assembly process is analyzed with the measured phase error distribution and corrected by adjusting the ball screws supporting the magnet array assembly. Figure 3 shows the results of the new correction procedure. We found that the final phase errors in the new method are sufficiently suppressed down to the same level as that obtained in the bench with the vacuum vessel removed.

We achieved three progresses on the beam diagnostic system. First, a beam position monitor with a target resolution better than 1 μm has been developed. The detection sensitivity to a transverse displacement (Fig. 4) has been evaluated. This result, combined with the measured noise-level of a new DAQ (data acquisition) system, shows that a resolution of 30 nm is possible. Second, a screen monitor has been developed for measuring a small beam profile of a few tens of micrometer scale. As shown in Fig. 5, we have distinguished a 2.5-μm object. Third, two types of timing monitor system have been developed. One is a fast current transformer for the electron beam, and the other is an in-vacuum photodiode system for FEL radiation. Both the measurement systems have pulse responses of

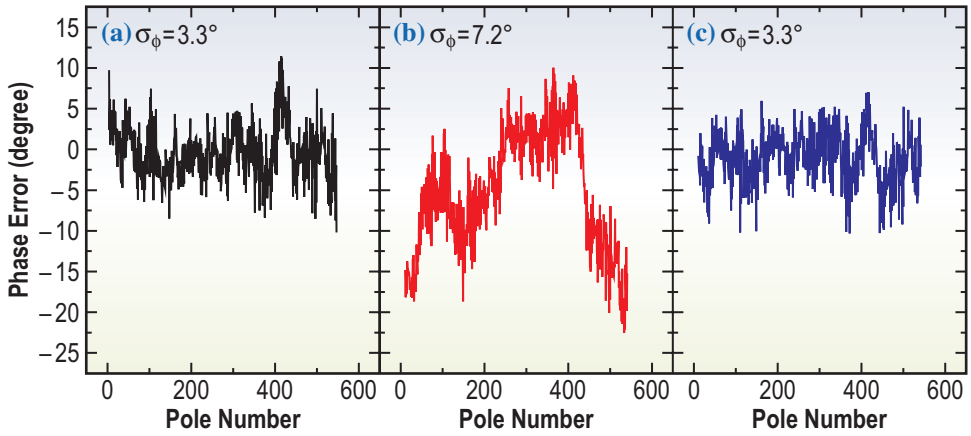


Fig. 3. Phase error distributions **(a)** before and **(b)** after reinstallation of magnet arrays and **(c)** after correction of gap deformation.

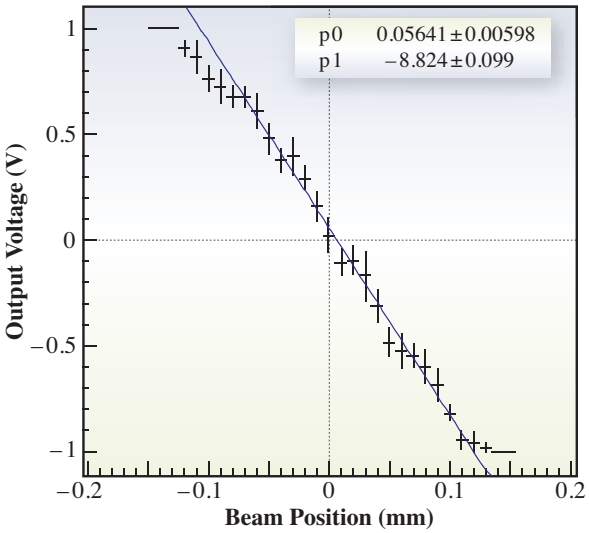


Fig. 4. Output voltages of beam position monitor measured at different beam positions.

~100 ps with an arrival timing accuracy of about 1 ps.

The R&D of LLRF (low level rf) and timing systems was carried out at the test accelerator. An electron beam time-jitter of about 46 fs in STD has been achieved at a position downstream of the C-band acceleration system. This result showed that the LLRF system almost satisfies the stability requirement for XFEL. To apply the developed systems in the XFEL accelerator on a scale of several hundred meters, an optical timing and reference rf signal transmission system using the WDM (wavelength division multiplex) method has been developed. The adopted WDM system using one optical fiber to transmit the rf signals generated by the master oscillator can handle five frequency signals corresponding to each multistage cavity

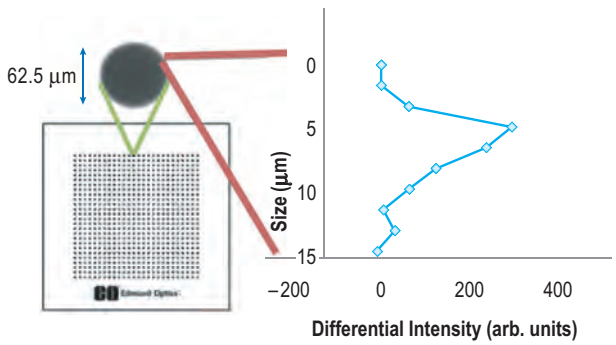


Fig. 5. Resolution of optical system of screen monitor. The dot diameter is 62.5 µm. The graph shows that the sharpness (resolution) of the dot edge is about 4 µm (FWHM). Edge sharpness is obtained by a differential operation of dot contrast.

acceleration unit for the velocity bunching. The experiment on optical signal transmission using an optical fiber of 500 m length revealed a very low noise characteristic of the system, as shown in Fig. 6, which never enhances the noise of the master oscillator through the transmission.

With respect to the R&D of vacuum technology, a laser beam welding procedure was established for a wide and square vacuum vessel that is used in a bunch compressor and a chicane where the energy-chirped electron beam becomes wider in the horizontal plane. A special rf contact for such a vessel was also developed to reduce impedance.

A remote-I/O card, called OPT-RMT i-DIO, was developed to realize a fast and precise control of a power supply for electromagnets even under a severe noise environment. High performance was confirmed by a test using an engineering sample of the OPT-RMT i-DIO and a prototype power supply. The developed FL-net test tool, which checks communication with a PLC, was tested in the rf test bunker. We found that the test tool is useful for debugging the configuration of a FL-net memory map. This will be used in a factory test before delivery to avoid a FL-net missconfiguration.

The XFEL facility can contain five photon beamlines. In 2008, the design work for the central beamline (BL3) has been completed. The beamline layout in the experimental hall as well as a detailed configuration are shown in Fig. 7 and Fig. 8, respectively. The main aim of this beamline is to manage hard X-ray FEL with a photon energy

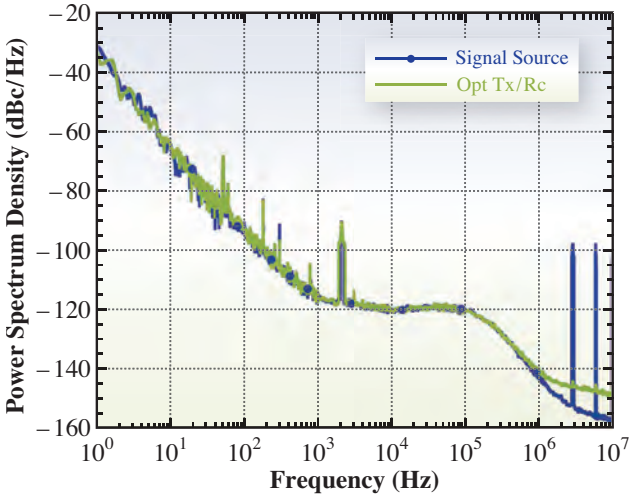


Fig. 6. Degradation of rf signal quality due to noise of optical rf signal transmission system. The increase in the level of noise at around 1 MHz corresponds to about 7 fs.

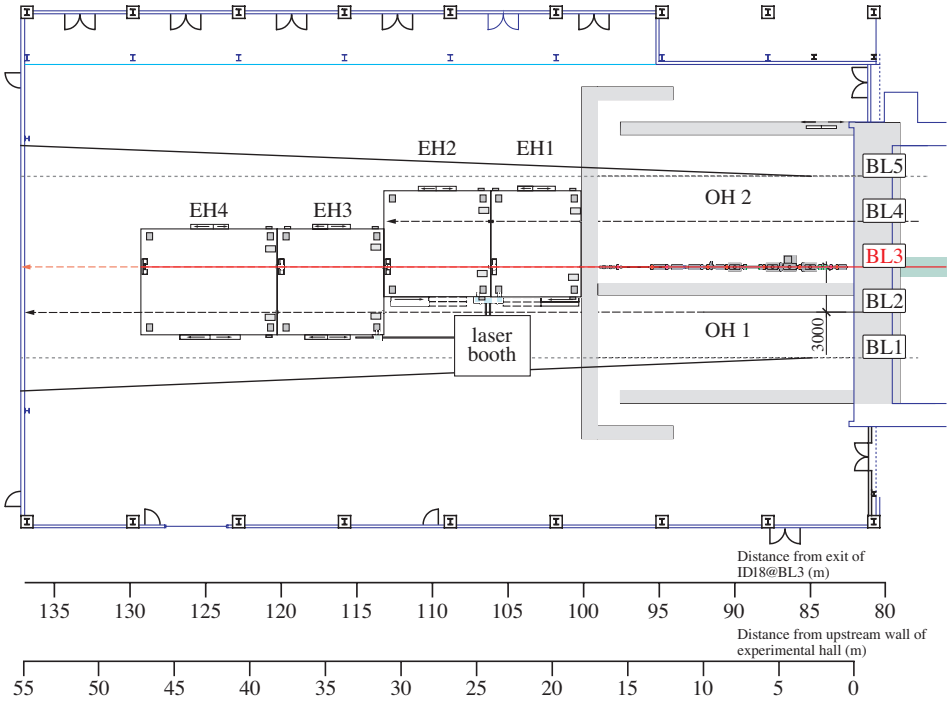


Fig. 7. Layout in experimental hall. Beamline optics are contained in the optics hutch, while experimental instruments are installed in experimental hutches. Synchronized lasers are set in the laser booth and distributed to experimental hutches.

above several keV; however, softer X-rays can be transported by adopting differential-pumping systems. A double-crystal monochromator and a pair of double-mirror systems are employed as principal beamline optics. The former delivers monochromatic X-rays in the range of 4 to 30 keV (with Si 111 diffraction), while the latter works as a low-pass filter below ~8 keV or ~15 keV. The beamline components are contained in the optics hutch. Four experimental hutches for installing experimental instruments are set.

Most of foreseen XFEL experiments demands shot-by-shot measurement to cope with the instability inherent in the SASE process. To realize these experiments, a feasibility study of the dedicated data acquisition (DAQ) system has been started. Accordingly, the X-ray two-dimensional detector

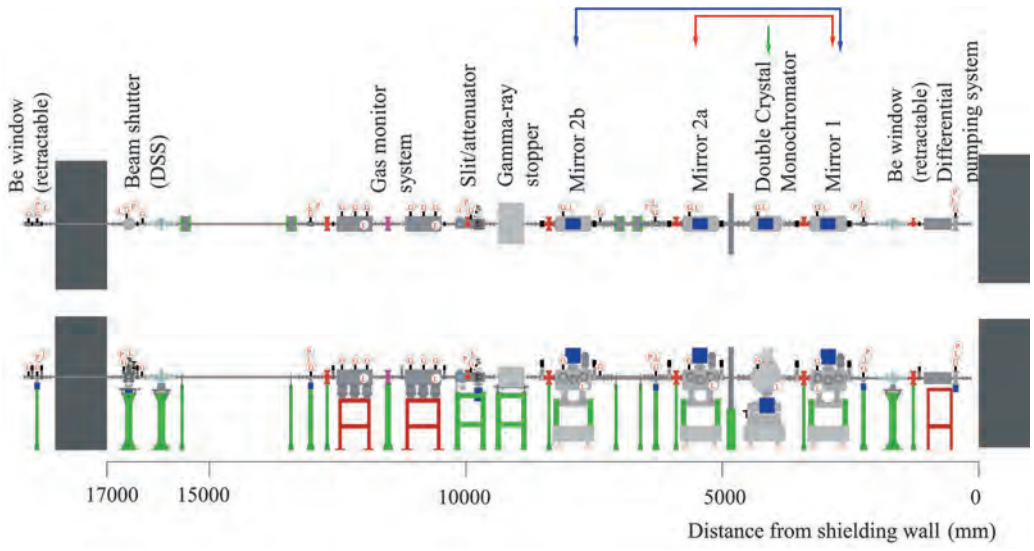


Fig. 8. Beamline configuration of BL3. A monochromator (green arrow), and a pair of mirrors 1 & 2a (red arrow) or 1 & 2b (blue arrow) are exclusively utilized as main optical components.

should record frame data at an XFEL repetition rate of 60 Hz with a high full-well capacity. The study including that of radiation damage has revealed the feasibility of the use of the direct detection charge-coupled device (CCD) in XFEL experiments, and yielded the concept of the multiport CCD sensor for XFEL. The finalized design has 64 readout ports with 2k×2k 50 μm square pixels, and each pixel has a full-well capacity of 5 M electrons (Fig. 9).

The building construction has progressed on schedule. Figure 10 shows an aerial photograph of the construction site. The building frame and exterior finish were completed for both the accelerator and undulator buildings. The accelerator tunnel and undulator hall were made of radiation-shielding concrete walls whose thicknesses are 2 and 1.5 m, respectively. Soil improvement for the undulator building was carried out by a replacement method using crushed stones. A stable and high-density artificial rock bed with a maximum depth of 16 m was formed by rolling crushed stone layers at every 40 cm in depth, as shown in Fig. 11. The completion of both the accelerator and undulator buildings is scheduled in March 2009. A soil survey of the tunnel construction site for the beam transport line to the SPring-8 synchrotron was carried out in October 2008. This tunnel construction will be completed in March 2010.

2. Operation Status of SCSS Test Accelerator

The 250-MeV SCSS test accelerator was constructed in 2005 to perform basic R&D of the accelerator systems designed for 8-GeV XFEL. The first SASE FEL saturation was achieved in September 2007 (Fig. 12) [1]. Since May 2008, the extremely

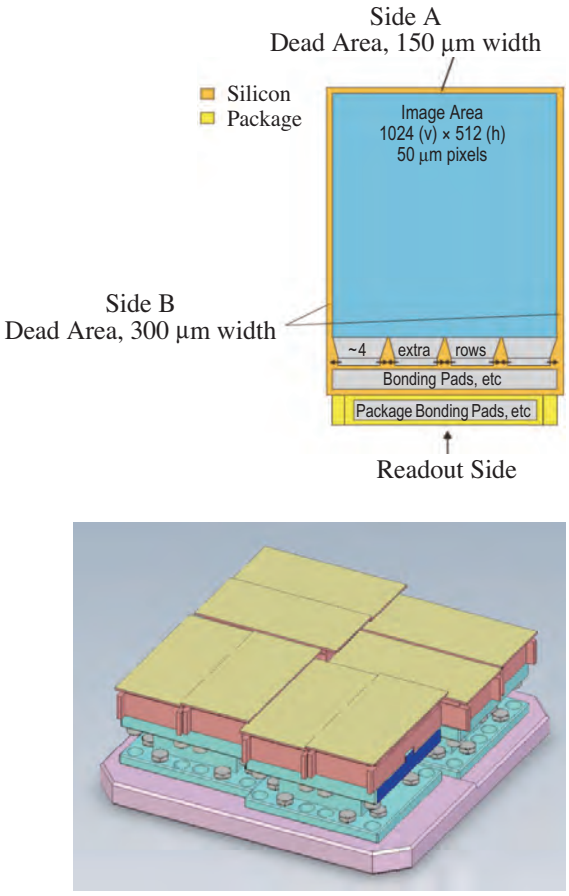


Fig. 9. Schematic sensor format of multiport charge-coupled devices (MP-CCDs) with eight readout nodes (left), and a tiled detector with a stepped array of eight devices with a total pixel number of 2k×2k (right). Each readout node operating a 5 M pixel/sec readout rate enables synchronization to an XFEL repetition rate of 60 pps. The tiled detector has a through hole at the center whose size can be controlled by remote.



Fig. 10. Aerial photograph of XFEL construction site taken in November 2008.



Fig. 11. Rolling procedure for forming stable and high-density artificial rock bed.

intense FEL radiation in the EUV (extreme ultraviolet) region has been provided for users. User operation has been conducted over several months without any serious problems with the machine.

We introduce the R&D of accelerator components. A CeB_6 cathode assembly, which had been stably used for about twenty thousands hours, was first replaced by a new one in January 2008. Figure 13 shows part of the exchange procedures in the accelerator tunnel and the old cathode just before being replaced. The cathode assembly was replaced without any serious problems. It took only one week including the processes of charging the voltage up to 500 kV and raising the temperature up to ~1800 K. We could successfully reproduce the saturation of SASE FEL power with the new virgin cathode. This result verified the following issues: (i) the present design of the cathode assembly is suitable for quick and reliable exchange, (ii) the quality control of CeB_6 single crystals is sufficiently high for SASE FEL reproducibility, and (iii) the beam tuning procedure after the cathode replacement is well established.

For the C-band acceleration system, the target performance was achieved in September 2008: a stable SASE FEL saturation has been confirmed with an acceleration gradient of 37 MV/m at a repetition rate of 60 Hz. The reliability of this high-gradient operation has been confirmed through a long-period operation over several months. Fault rate is kept small with an almost the same level as that in the low-gradient operation.

An event-synchronized data-acquisition system with a distributed shared-memory network has been installed and tested in the control system of the SCSS test accelerator. Fifty-four signals from the beam monitoring system such as current transformers, beam position monitors (BPM), and photodiode intensity monitors, have been successfully collected with 60 Hz

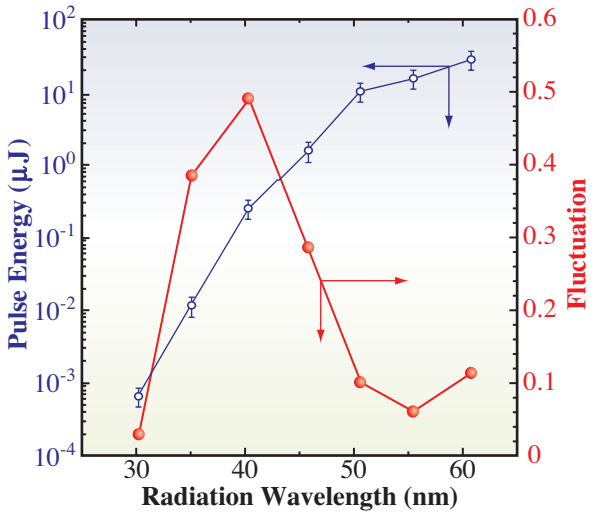


Fig. 12. Dependences of pulse energy and intensity fluctuation on radiation wavelength.

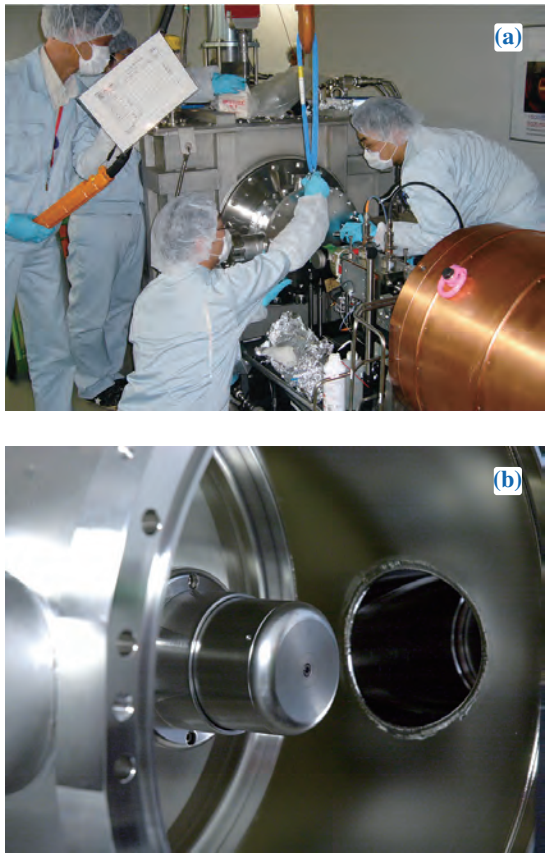


Fig. 13. One scene in cathode exchange procedures at CeB_6 thermionic gun **(a)** and gun electrode with single-crystal CeB_6 cathode just before the first replacement **(b)**. The central dark part on the flat-shaped wehnelt is a CeB_6 crystal.

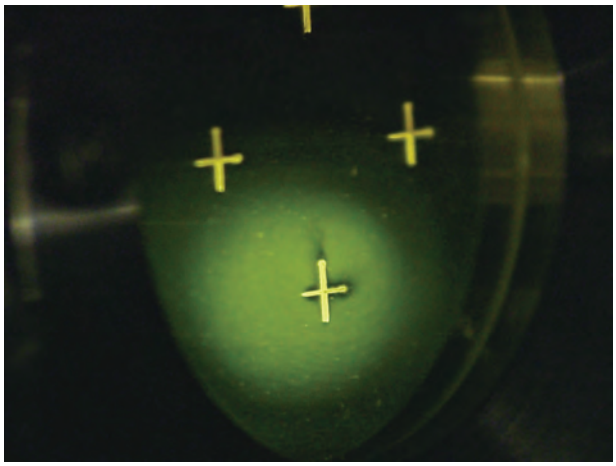


Fig. 14. Spatial profile of EUV radiation measured with YAG(Ce) crystal.

of beam operation cycles. The accumulated data are stored on a relational database for pulse-to-pulse correlation investigation. The BPM data have also been used for the effective correction of beam orbit and energy drifts.

After the first observation of the power saturation of FEL radiation, the accelerator parameters have been continuously optimized in order to improve FEL performance. This effort led us to achieve stable FEL radiation in the wavelength range between 50 to 60 nm during the user operation described below. Figure 14 shows the laser profile at the entrance of the experimental station.

Since the beginning of the user operation in May, we have conducted a user operation for 71 days for 10 user groups involving approximately 60 scientists including foreign researchers. The targets of the experiments are categorized into the following four groups: technical research preparatory for XFEL experiments; science with gas phase targets as atoms, molecules and clusters [2,3]; imaging and diffraction; and high-energy-density and warm matter.

In parallel with the user operation, we have continued to upgrade the EUV-FEL beamline. The plan is schematically shown in Fig. 15. The EUV-FEL can be delivered to four experimental stations at branches D, E, F and G, which is selected by a switching mirror. In 2008, we have developed branches B, D and E. In branch B, we have installed common diagnostics and optics such as a Ce:YAG fluorescent crystal to monitor beam profile, gas-filled attenuators to control pulse energy, nondestructive intensity monitors to measure pulse energy, and switching mirrors to steer the photon beam to branches D, E (G) and F. At the moment, an unfocused FEL beam can be steered to branches D and E. A focusing device will be installed in 2009.

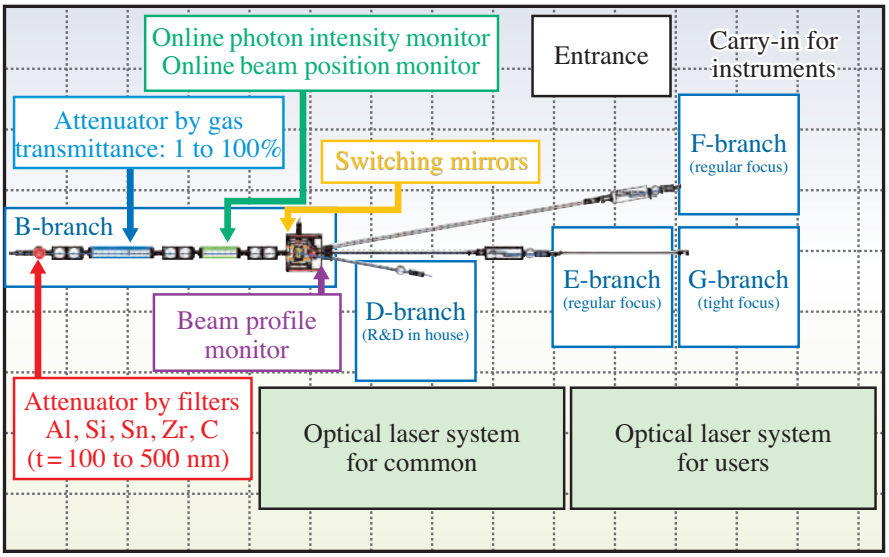


Fig. 15. Layout of EUV-FEL beamline.

SPring-8 Joint-Project for XFEL

Project-XFEL@riken.jp

References

[1] T. Shintake *et al.*: Nature Photonnics **2** (2008) 555.
[2] T. Sato *et al.*: Appl. Phys. Lett. **92** (2008) 154103.
[3] H. Fukuzawa *et al.*: Phys. Rev. A **79** (2009) 031201(R).

NewSUBARU

The 1.5 GeV synchrotron radiation ring named NewSUBARU is the main facility of the Laboratory of Advanced Science and Technology for Industry (LASTI) at the University of Hyogo. NewSUBARU is at the site of SPring-8 and can provide light beams from IR to soft X-rays. We have achieved storing 500 mA at 1GeV and 200 mA at 1.5 GeV. At present, NewSUBARU has six bending section beamlines (BL-2, BL-3, BL-5, BL6, BL-10, and BL-11), two short undulator beamlines (BL-7a and BL-7b), a long undulator beamline (BL-9) and an optical-klystron beamline (BL-1), as shown in Fig. 1.

NewSUBARU research activities for this year include the basic characteristic research of the NewSUBARU electron storage ring, neutron spectrum measurement generated by a gamma-ray photonuclear reaction, the completion of material analysis BL-5 beamline construction for industrial use, studies of microfluid devices and diffraction gratings for the X-ray Talbot interferometer using the LIGA (Lithographie, Galvanoformung and Abformung) process, and the development of new technologies for EUV (Extreme Ultraviolet) lithography. The entire useful energy range of the BL-5 is in the region from 50 to 4000 eV and X-ray absorption spectrum of every atom from Li to Sn can be measured using this beamline. BL-5 is managed and maintained by the Synchrotron Analysis LLC (Limited Liability Company), which is composed of industrial companies. A 2.5-dimensional structure grating with a high aspect ratio was required for the X-ray Talbot interferometer, which was used to observe a rabbit liver tissue with cancer, and micro fluid device for DNA sequence have been demonstrated using the LIGA process. The microscope, wavefront metrology system and new resist with a small LER (line edge roughness) and a high sensitivity to EUV lithography have been developed.

Most of our research activities are being conducted in collaboration with industries, government research institutes and other universities. We will continue to respond to the research, education and community's demand by offering new science and technologies.

Shinji Matsui
Director of LASTI, University of Hyogo

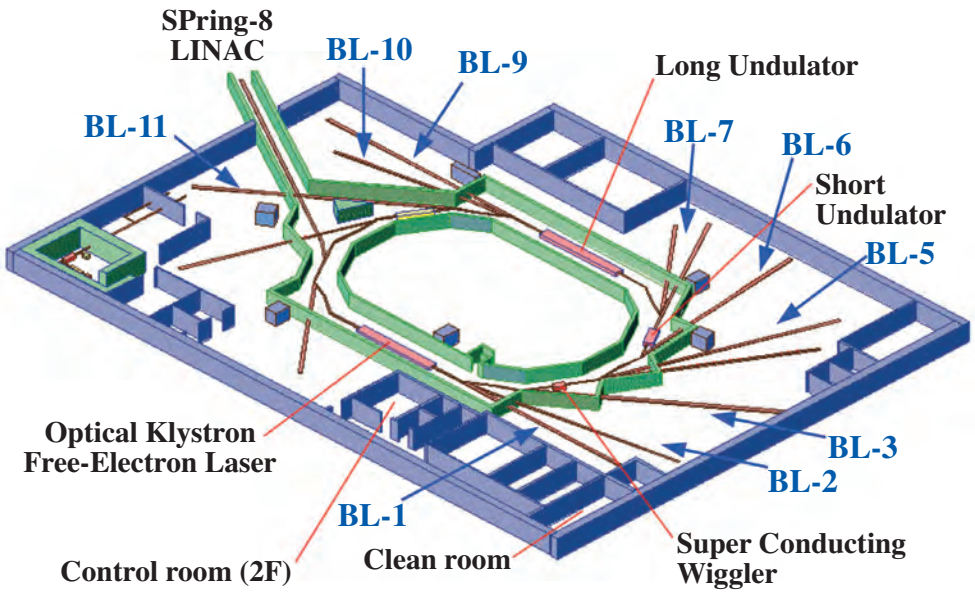


Fig. 1. Beamline arrangement in NewSUBARU.

Construction of a High-Resolution Beamline BL-5 for Soft X-Ray Spectroscopic Analysis on Industrial Materials

The X-ray absorption fine structure (XAFS) technique in the soft X-ray region has attracted much attention from the industrial world as a powerful tool for investigating the electronic and geometric structures of industrial materials. In addition, photoemission spectroscopy (PES) technique is also an effective means for researching the electronic structure of material surfaces in the soft X-ray region. Thus, there is a need for the analysis ability in the soft X-ray region to increase with the development of nanotechnology in the industrial yields. A new beamline was constructed in response to such a demand in the industrial world (Fig. 1). The decision on the optical design and specifications of end stations was made in cooperation with the University of Hyogo and industrial companies joining Synchrotron Analysis LLC, as described below. This beamline is anticipated to prosper the co-research with University of Hyogo and industrial companies, and expected to advance the analysis abilities of industrial companies.

A high-resolution beamline was constructed at BL-5 of NewSUBARU, where a 30-m-long beamline can be built. The light source of BL-5 is the bending magnet, which can provide photons in the region of up to 4000 eV. BL-5 consists of two branch lines for use in the wide range from 50 eV to 4000 eV. BL-5A, which is mounted with a double-crystal monochromator, can be used in the energy range of 1300-4000 eV. On the other hand, BL-5B is mounted with a valid-line-spacing grating monochromator, which is designed to cover the energy range of 50-1300 eV using three kinds of grating. The incident beam from the bending magnet is provided for two branch lines through different windows of a mask. Therefore, these two branch lines can be employed simultaneously.

A layout of the BL-5A is shown in Fig. 2. InSb crystals and Si crystals are prepared for a double-crystal monochromator. Toroidal mirrors are used as a pre-mirror and a focusing mirror of BL-5A. XAFS measurement in the total electron yield mode and fluorescence XAFS measurement using SSD (SII Vortex) can be performed. The fluorescence XAFS spectra can be measured for samples at the end station filled with He gas.

A layout of BL-5B is shown in Fig. 3. The constant-deviation monochromator consisting of a demagnifying spherical mirror and a varied-line-spacing plane grating (VLSPG), which can provide high resolution, simple wavelength scanning with fixed slits, was mounted on BL-5B. The optical system consists of a first mirror (M0), a second mirror (M1), an entrance slit (S1), a pre-mirror (M2), and three kinds of plane grating (G), an exit slit (S2) and a focusing mirror (M3). The deviation angle of the monochromator is 175°. The VLSPG achieves high resolution in the extreme ultraviolet region by diminishing various kinds of aberration. In the case of the VLSPG, the groove parameters can be expressed in the following form by expanding the groove density N with coefficients a_i:

$$N(w)=N_0\,(1+a_1 w+a_2 w^2+a_3 w^3+\cdots)\,,$$

where N_0 is the groove density at the center of the grating and w is the distance from the center of the grating along the direction of light traveling. Aberrations, such as defocus, coma, and spherical aberration, were computed with the present geometrical and ruling parameters. For BL-5B, we use three kinds of grating with groove densities of 100, 300 and 800 grooves/mm at the center of the grating, N_0 and the space variation parameters a_1, a_2



Fig. 1. Constructed high-resolution beamline BL-5 for soft X-ray spectroscopy analysis of Industrial Materials.

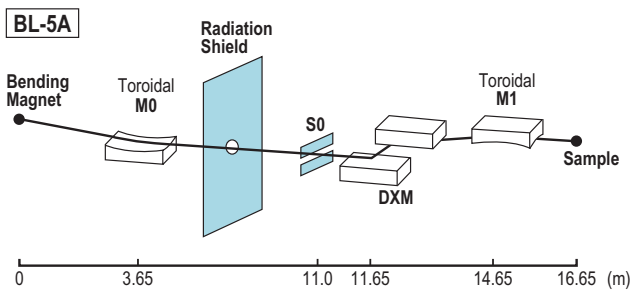


Fig. 2. Layout of BL-5A.

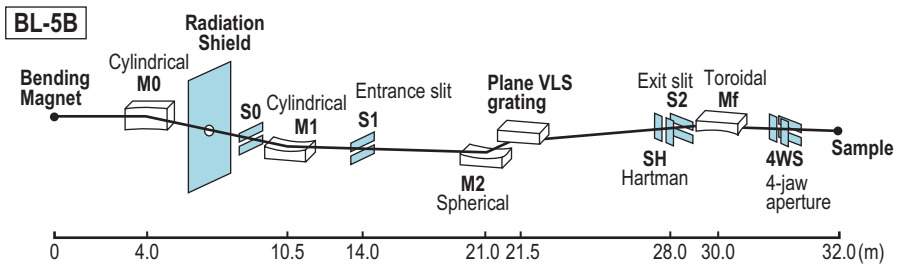


Fig. 3. Layout of BL-5B.

and a_3 are determined to minimize the aberration in the specified photon wavelength region to -3.0727×10^{-4}, 7.1×10^{-8} and -1.7×10^{-11}, respectively. Figure 4 shows the calculated resolving powers at entrance and exit slit widths of 50 and 100 μm with the slope error limit. A total resolving power of about 3000 can be realized in the entire energy region. Two measurement chambers are prepared at the end station of BL-5B. The XAFS spectra in the total electron yield mode and fluorescence XAFS spectra using SDD (EDAX) can be measured in a high vacuum chamber. In addition, the photoelectron spectrum can be measured using spherical electron analyzer (VG Sienta, R3000) in an ultra high-vacuum chamber. The chambers can be replaced by each other within 1 hour.

The B *K*-edge and N *K*-edge NEXAFS spectra of hexagonal-boron nitride (h-BN) measured at BL-5B are shown in Fig. 5 and Fig. 6, respectively. The B *K*-edge NEXAFS spectrum was measured using G1 with 100 grooves/mm. On the other hand, the N *K*-edge NEXAFS spectrum was measured using G2 with 300 grooves/mm. The entrance and exit slit widths were 100 μm. NEXAFS measurement was performed in the total electron yield (TEY) mode.

The maintenance and management of BL-5 are performed by Synchrotron Analysis LLC, which is a consortium of user companies, under the supervision of the LASTI staff. The companies that wish to use BL-5 have to join Synchrotron Analysis LLC, with the payment of a membership fee. If users want help with measurements at BL-5, operators of Synchrotron Analysis LLC can assist them.

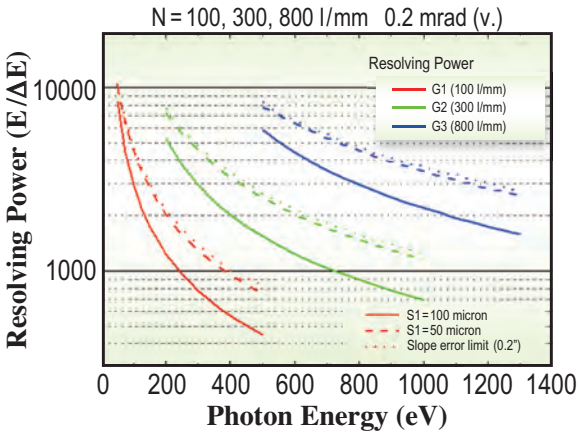


Fig. 4. Calculated resolving power of BL-5B.

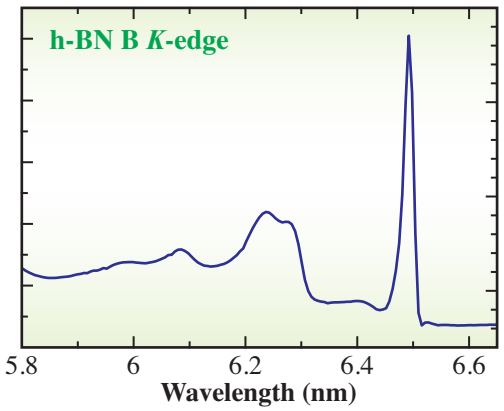


Fig. 5. B *K*-edge NEXAFS spectrum of h-BN.

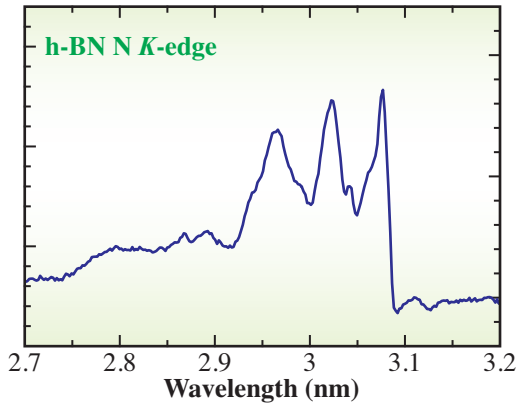


Fig. 6. N *K*-edge NEXAFS spectrum of h-BN.

Kazuhiro Kanda

LASTI, University of Hyogo

E-mail: kanda@lasti.u-hyogo.ac.jp

Editor
Seishi Kikuta
SPring-8 / JASRI

Editing & Layout
Marcia M. Obuti-Daté
SPring-8 / JASRI

Printing
Fuji Xerox Cross Works Co., Ldt.

J A S R I
Library and Information
Users Administration Division

1-1-1 Kouto, Sayo-cho, Sayo-gun
Hyogo 679-5198 • JAPAN
Tel. +81-(0)791 58-2797 Fax. +81-(0)791 58-1869

frontiers@spring8.or.jp
http://www.spring8.or.jp/

© **SPring-8 / JASRI**
July 2009



Japan Synchrotron Radiation Research Institute
1-1-1 Kouto, Sayo-cho, Sayo-gun, Hyogo 679-5198 JAPAN
http://www.spring8.or.jp